Narayanasamy Sabari Arul
Vellalapalayam Devaraj Nithya *Editors*

Two Dimensional Transition Metal Dichalcogenides

Synthesis, Properties, and Applications

Springer

Two Dimensional Transition Metal Dichalcogenides

Narayanasamy Sabari Arul ·
Vellalapalayam Devaraj Nithya
Editors

Two Dimensional Transition Metal Dichalcogenides

Synthesis, Properties, and Applications

Springer

Editors
Narayanasamy Sabari Arul
Department of Chemical and Biochemical Engineering
Dongguk University
Seoul, Korea (Republic of)

Vellalapalayam Devaraj Nithya
Gobichettipalayam, Tamil Nadu, India

ISBN 978-981-13-9044-9 ISBN 978-981-13-9045-6 (eBook)
https://doi.org/10.1007/978-981-13-9045-6

This Springer imprint is published by the registered company Springer Nature Singapore Pte Ltd.
The registered company address is: 152 Beach Road, #21-01/04 Gateway East, Singapore 189721, Singapore

Preface

The great accomplishment of graphene has been pursued by an equally inspiring surge for the expansion of other 2D materials isolated from its original van der Waals crystal that can form atomic sheets with extraordinary properties. Among them, transition metal dichalcogenides (TMDs) are layered materials which are composed of type MX2 of group VIA, where M is a transition metal atoms (M=Mo, W and X=S, Se, Te), and are emerging next-generation semiconductor materials. Depending on the arrangement of the atoms, the structures of 2D TMDs can be categorized as trigonal prismatic (hexagonal, H), octahedral (tetragonal, T), and their distorted phase (T0). Depending on their chemical compositions and structural configurations, atomically thin 2D materials can be categorized as metallic, semimetallic, semiconducting, insulating, or superconducting. Two-dimensional TMDs exhibit unique electrical and optical properties that evolve from the quantum confinement and surface effects that arise during the transition of an indirect bandgap to a direct bandgap when bulk materials are scaled down to monolayers. The tunable bandgap in TMDs is accompanied by strong photoluminescence (PL) and large exciton binding energy, making them a potential candidate for a variety of optoelectronic devices, including solar cells, photodetectors, light-emitting diodes, and phototransistors. For instance, unique properties of MoS_2 including direct bandgap ($\sim$1.8 eV), good mobility ($\sim$700 $cm^2\ V^{-1}s^{-1}$), high current on/off ratio of $\sim 10^7$–10^8, large optical absorption ($\sim 10^7\ m^{-1}$ in the visible range), and a giant PL arising from the direct bandgap (1.8 eV) in monolayer have been studied widely for various electronics and optoelectronics applications.

This book solely focuses on the "transition metal dichalcogenides (TMDs)" and deals with the "synthesis, properties, and application" aspects of the materials. Moreover, the current challenges and future perspectives on the development of 2D TMDs are comprehensively discussed in this book with the hope that the book will

provide a deep insight into the state of the art of transition metal dichalcogenides. We would like to thank the editorial assistance and patience as well as Springer for the invaluable help in the organization of the editing process.

Seoul, Korea (Republic of) Narayanasamy Sabari Arul
Gobichettipalayam, India Vellalapalayam Devaraj Nithya

Contents

Editors and Contibutors

About the Editors

Narayanasamy Sabari Arul received his Ph.D. in Nanoscience and Technology from Bharathiar University, Tamil Nadu, India, following which he has worked as a visiting Ph.D. research fellow at Lunghwa University of Science and Technology, Taiwan and Brain-Korea (BK21) Postdoctoral Fellow at Hanyang University, Seoul, South Korea and Assistant Professor in Dongguk University-Seoul, South Korea. His research interests include synthesis of metal oxide nanocomposites and thin films, nanomaterials, quantum dots, perovskites and two-dimensional dichalcogenides for photocatalysts, photovoltaic cells, memory devices, supercapacitors, and electrochemical sensors. He has published more than 45 SCI journal articles and 20 papers in proceedings of international conferences and holds one US and Korean Patent. Dr. Arul also serves as a referee for various journals in Springer, Elsevier, Royal Society of Chemistry and Institute of Physics.

Vellalapalayam Devaraj Nithya received her Ph.D. in Physics from Bharathiar University, Tamil Nadu, India, and had completed her Masters from same University. Her research interests mainly focus on metal oxide nanostructures and their applications for energy storage devices with special emphasis on supercapacitors and Li-ion batteries. She has been the recipient of many awards and fellowships including the INSPIRE fellowship by the Department of Science and Technology, Government of India. She has presented her research work in many seminars and workshops and has published over 20 research papers in journals of international repute.

Contributors

Dan A. Allwood The University of Sheffield, Sheffield, UK

Yu Cai Department of Chemical and Biological Engineering, University of Colorado Boulder, Boulder, CO, USA

Hongzheng Chen Department of Polymer Science and Engineering, Zhejiang University, Hangzhou, People's Republic of China

Wenchao Chen College of Information Science and Electronic Engineering, Zhejiang University, Hangzhou, People's Republic of China

Vinod R. Dhanak Department of Physics, University of Liverpool, Liverpool, UK

Mukulika Dinara School of Basic Sciences, Indian Institute of Technology, Bhubaneswar, Odisha, India

James T. Gibbon Department of Physics, University of Liverpool, Liverpool, UK

Linji Gong CAS Key Laboratory for Biomedical Effects of Nanomaterials and Nanosafety, Institute of High Energy Physics, Chinese Academy of Sciences, Beijing, People's Republic of China;
University of Chinese Academy of Sciences, Beijing, People's Republic of China

L. Gouda Department of Chemistry and the Institute of Nanotechnology, Bar-Ilan University, Ramat-Gan, Israel

Zhanjun Gu CAS Key Laboratory for Biomedical Effects of Nanomaterials and Nanosafety, Institute of High Energy Physics, Chinese Academy of Sciences, Beijing, People's Republic of China;
University of Chinese Academy of Sciences, Beijing, People's Republic of China

Mohammad Rezwan Habib State Key Laboratory of Silicon Materials, College of Information Science and Electronic Engineering, Zhejiang University, Hangzhou, People's Republic of China

Ting Huang Key Laboratory for Soft Chemistry and Functional Materials of Ministry of Education, School of Chemical Engineering, Nanjing University of Science and Technology, Nanjing, China

G. Kakavelakis Department of Materials Science and Technology, University of Crete, Gallos, Greece

I. Kaliakatsos Department of Electronic Engineering, Hellenic Mediterranean University, Crete, Greece

Tao Liang State Key Laboratory of Silicon Materials, Department of Polymer Science and Engineering, College of Information Science and Electronic Engineering, Zhejiang University, Hangzhou, People's Republic of China

Liangxu Lin University of Wollongong, Wollongong, AU, Australia;
Wuhan University of Science and Technology, Wuhan, China

Xiaoheng Liu Key Laboratory for Soft Chemistry and Functional Materials of Ministry of Education, School of Chemical Engineering, Nanjing University of Science and Technology, Nanjing, China

K. Petridis Department of Electronic Engineering, Hellenic Mediterranean University, Crete, Greece

Rajeswari Ponnusamy Centre for Nano and Material Sciences, Jain University, Ramanagaram, Bangalore, India

Chandra Sekhar Rout Centre for Nano and Material Sciences, Jain University, Ramanagaram, Bangalore, India

Ze Xiang Shen Division of Physics and Applied Physics, School of Physical and Mathematical Sciences (SPMS), Nanyang Technological University, Singapore, Singapore

Huanxing Su State Key Laboratory of Quality Research in Chinese Medicine and Institute of Chinese Medical Sciences, University of Macau, Macau SAR, People's Republic of China

Y. Tischler Department of Chemistry and the Institute of Nanotechnology, Bar-Ilan University, Ramat-Gan, Israel

Mingsheng Xu State Key Laboratory of Silicon Materials, College of Information Science and Electronic Engineering, Zhejiang University, Hangzhou, People's Republic of China

Jiaxu Yan Key Laboratory of Flexible Electronics (KLOFE), Jiangsu National Synergistic Innovation Center for Advanced Materials (SICAM), Institute of Advanced Materials (IAM), Nanjing Tech University (Nanjing Tech), Nanjing, People's Republic of China;
Division of Physics and Applied Physics, School of Physical and Mathematical Sciences (SPMS), Nanyang Technological University, Singapore, Singapore

Hongfei Yin Key Laboratory for Soft Chemistry and Functional Materials of Ministry of Education, School of Chemical Engineering, Nanjing University of Science and Technology, Nanjing, China

Wen-Yan Yin College of Information Science and Electronic Engineering, Zhejiang University, Hangzhou, People's Republic of China

Min Zhang Key Laboratory for Soft Chemistry and Functional Materials of Ministry of Education, School of Chemical Engineering, Nanjing University of Science and Technology, Nanjing, China

Shaowei Zhang University of Exeter, Exeter, UK

Chapter 1
Two-Dimensional Transition Metal Dichalcogenides: An Overview

Tao Liang, Yu Cai, Hongzheng Chen and Mingsheng Xu

Abstract Two-dimensional materials attract enormous research attentions owing to the fascinating properties and great potential applications in electronics, optoelectronics, spintronics, energy conversion, and storage. Among them, two-dimensional transitional metal dichalcogenides exhibit exceptional properties such as tunable bandgaps, phase transition, and superconductivity. As such, two-dimensional transitional metal dichalcogenides have been extensively studied focusing on the property, synthesis, modification, and devices. Furthermore, the combination of different two-dimensional transitional metal dichalcogenides brings in versatile functionalities and the proof-of-concept electrical devices such as tunneling field-effect transistors, light-emitting diodes and photovoltaics have been demonstrated in the planar or vertical heterostructures. Thus in this chapter, we summarize the basic knowledge and previous research results about the two-dimensional transitional metal dichalcogenides, emphasizing the atom structure, band structure, and electrical applications.

1.1 Introduction

Since graphene was first isolated from highly oriented pyrolytic graphite (HOPG) in 2004 [1], the excellent properties of graphene are motivating rapidly growing research enthusiasms in the layered materials, especially when they are thinned down to the atomic thickness. For layered transition metal dichalcogenides (TMDs), two-dimensional (2D, referring to few-layer and monolayer herein) ones exhibit distinct

T. Liang · M. Xu (✉)
State Key Laboratory of Silicon Materials, College of Information Science and Electronic Engineering, Zhejiang University, Hangzhou 310027, People's Republic of China
e-mail: msxu@zju.edu.cn

T. Liang · H. Chen
Department of Polymer Science and Engineering, Zhejiang University, Hangzhou 310027, People's Republic of China

Y. Cai
Department of Chemical and Biological Engineering, University of Colorado Boulder, Boulder, CO 80309-0596, USA

N. S. Arul and V. D. Nithya (eds.), *Two Dimensional Transition Metal Dichalcogenides*,
https://doi.org/10.1007/978-981-13-9045-6_1

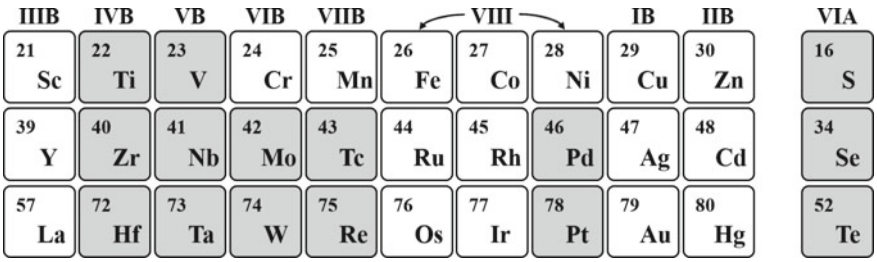

Fig. 1.1 Known layered TMDs in the periodic table highlighted with shadow

properties from the bulk counterparts owing to the quantum confinement effect and broken inversion symmetry.

Thus, increasing research efforts are devoting to this field, and the fantastic properties of 2D TMDs are continuously being revealed. Depending on the filling state for the *d* band of the metal elements, 2D TMDs can be semiconductors with varied band structures, semimetals, true metals, and superconductors, which determine their roles in the electronic devices. The already known layered TMDs are outlined in a periodic table with shadow background (Fig. 1.1), and a majority of their 2D counterparts have been theoretically predicted and experimentally synthesized. In this chapter, the atoms arrangement, band structure, and electronic applications of the most studied 2D TMDs are reviewed. Other aspects of the 2D TMDs such as synthesis methods, characterization technique, application in catalysts, and heterostructure assembly can be found in details in the following chapters. The readers can also refer to a comprehensive review for more information about 2D materials [2].

1.2 Group VIB TMDs (MoS_2, WS_2, $MoSe_2$, WSe_2, $MoTe_2$, WTe_2)

1.2.1 Atoms Arrangement and Band Structure

As one of the most widely studied group VIB TMDs in the twentieth century, MoS_2 attracted a lot of research interest focusing on its tribological properties [3]. The renewed research interest in group VIB MX_2 (M = Mo and W, X = S, Se, and Te) following the discovery of graphene concentrates upon the electronic and catalytic properties of 2D counterparts. The tunable bandgap, high carrier mobility, and large surface area of 2D MX_2 render them potential application in electronics [4], optoelectronics [5], and catalysts [6]. Moreover, the reduced dimension along the vertical direction provides an ideal platform to study solid-state physics such as robust excitonic effects [7], spin-orbit coupling [8, 9], and many-body interactions [10], which are difficult to be observed in the bulk materials.

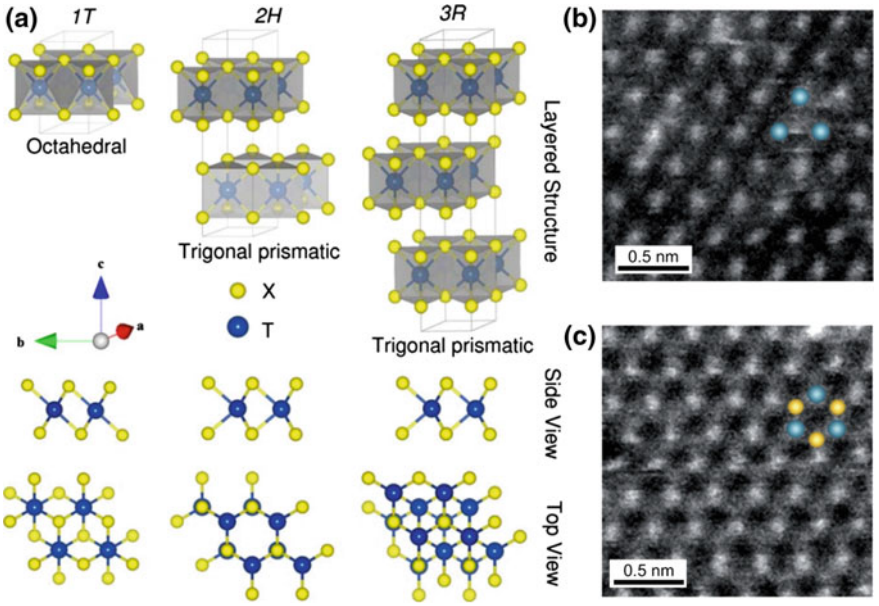

Fig. 1.2 **a** Ball-and-stick model of 1T, 2H, and 3R polymorphs of group VI TMDs [14]. Reproduced by permission of the Royal Society of Chemistry. **b**, **c** Atomic resolution STEM images of 1T (**b**) and 1H (**c**) phase of monolayer MoS_2. Blue and yellow balls represent Mo and S atoms, respectively [15]. Copyright 2013. Reprinted with permission from Macmillan Publishers

In similarity to graphite, MX_2 monolayers are held together by interlayer van der Waals (vdW) force to construct the bulk materials. The vdW force is several orders of magnitude weaker than the in-plane covalent bonding, making it feasible to obtain the monolayers through top-down routes including mechanical and liquid exfoliation. As such, most of the early theory verification and demonstration of proof-of-concept electronic devices based on 2D MX_2 were realized through this route [4, 5, 8, 11–13]. Different from the planar carbon sp^2 hybridization within each graphene layer, monolayer MX_2 is in fact composed of three sublayers of atoms, with one metal (M) sublayer sandwiched between two sublayers of chalcogenide (X) atoms, as shown in Fig. 1.2a [14]. Each M atom is sixfold coordinated with X atoms, forming either trigonal prismatic or octahedral geometry. In the trigonal prismatic atom arrangement, the above three X atoms are vertically above the below ones, while they stagger in the octahedral geometry.

The bulk MoS_2 shows polymorphs depending on the atoms arrangement in each monolayer and the relative position between monolayers. The three most commonly observed polymorphs of MoS_2 are 1T, 2H, and 3R. The number (1, 2, and 3) represents the layer number in the unit cell, and the letter stands for symmetry (T-trigonal, H-hexagonal, and R-rhombohedral). Figure 1.2b and c shows the atomic resolution scanning transmission electron microscopy (STEM) images for monolayer 1T and 1H MoS_2, respectively [15], consistent with the corresponding ball-and-stick model

in Fig. 1.2a. For sulfide and selenide, the 2H phase is stable, and the 1T phase is metastable, while for telluride, the 1T phase is more energetically favorable. The 2H phase could be converted to 1T phase under certain conditions, such as Li-ion intercalation, strain, electron beam, laser beam irradiation, as well as plasma bombardment. Conversely, the 1T phase could also be converted to 2H phase [16–20]. The most prominent feature of the group VIB TMDs is the layer-dependent band structure tunability. In the bulk materials, they own an indirect bandgap, which changes to direct one when being thinned down to monolayer limit [11].

Figure 1.3a–c shows the MoS_2 band structure of varied layer numbers calculated by density functional theory (DFT) [21]. In the bulk form, MoS_2 owns an indirect bandgap of about 1.2 eV. The valence band maximum (VBM) locates at the Γ point, and the conduction band minimum (CBM) locates in the middle of Γ-K direction in the Brillouin zone (Fig. 1.3a). As the layer number reduces, the VBM and CBM shift due to quantum confinement effects (Fig. 1.3b). A direct bandgap of about 1.9 eV is finally achieved in monolayer MoS_2 with both VBM and CBM sitting in the Brillouin zone K point (Fig. 1.3c). Other group VIB TMDs exhibit similar band structure evolution as a function of layer number [21–24]. Figure 1.3d shows the calculated band structure of monolayer WS_2 [21]. A direct bandgap of ~2.1 eV is predicted, in contrast to the ~1.3 eV indirect bandgap in the bulk form [21].

As a result of the band structure evolution, the photoluminescence (PL) emission dramatically increases when layer reduces (Fig. 1.3e). The PL quantum yield in monolayer MoS_2 is 100-fold higher than bilayer MoS_2 and four orders of magnitude higher than bulk MoS_2 (inset in Fig. 1.3e). Similarly, the electroluminescence (EL) efficiency in monolayers is also higher than the bulk materials [12], due to more efficient exciton generation and photon emission. The monolayer bandgap in the range of 1–2 eV, corresponding to the visible and near infrared spectrum range, and the direct bandgap nature render monolayer group VIB TMDs for constructing high-efficiency photodetectors, photovoltaics, and light-emitting diodes.

1.2.2 Electronics

2D group VIB TMDs are promising candidates for next-generation high-performance transistor channel materials, ascribing to the high conductivity, atomic thickness, and ultra-flat surface without dangling bonds. The first monolayer MoS_2 field-effect transistor (FET) is reported by Kis et al. [4]. The cross-sectional view of the device structure and the electrical connection (Fig. 1.4a), and the transfer and output curves of the device are displayed in Fig. 1.4b.

From the curves, field-effect electron mobility of ~200 cm^2/Vs and current on/off ratio exceeding 1×10^8 were extracted. The mobility is significantly boosted compared with its mostly reported 1–10 cm^2/Vs on SiO_2, ascribing to the suppression of Coulomb scattering by the top deposited HfO_2 layer. Fuhrer and Hone [25] pointed out that the capacitive coupling between the top and bottom gates could result in an overestimation of the mobility and the true mobility is likely in the range of

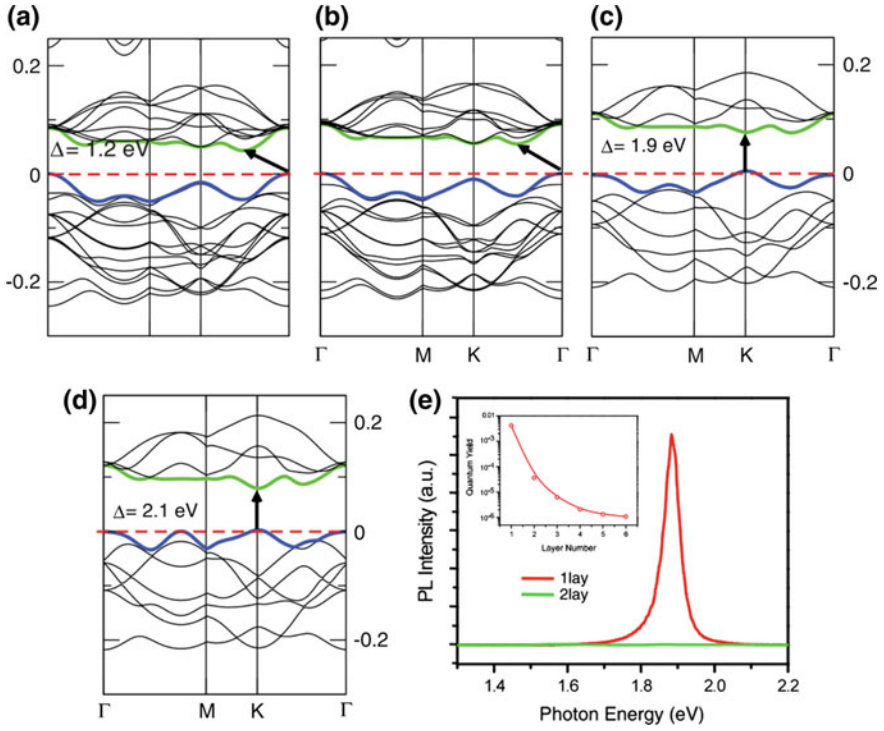

Fig. 1.3 **a**–**d** DFT calculated band structure of bulk MoS_2 (**a**), bilayer MoS_2 (**b**), monolayer MoS_2 (**c**), and monolayer WS_2 (**d**). The arrows indicate the fundamental bandgap, and the horizontal dashed lines indicate the Fermi level [21]. Copyright 2011 by the American Physical Society. Reproduced with permission (**e**) PL spectra for mono- and bilayer MoS_2 samples. The inset shows the PL quantum yield as a function of layer number [11]. Copyright 2010. Reproduced with permission from American Physical Society

2–7 cm^2/Vs. And thus Hall effect measurements were later performed, from which the mobility, contact resistance, and capacitive coupling can be obtained simultaneously [25]. One device exhibited mobility of 168 cm^2/Vs at 4 K and 60 cm^2/Vs at 250 K [25]. Other factors besides Coulomb scattering such as defects, charged impurities, and metal–semiconductor contact are also liable for the measured relatively low mobility in a FET device compared with the theoretical phonon-limited value. For example, through a thiol chemistry route to repair the sulfur vacancies and interface modification, Wang et al. achieved >80 cm^2/Vs electron mobility in monolayer MoS_2 bottom-gated FET [26].

To reduce the Schottky barrier height at the interface between metal electrode and MoS_2 channel, Chhowalla et al. [16] converted part of the MoS_2 flake underneath the metal electrodes from 2H to 1T phase, decreasing the contact resistance from 0.7–10 kΩ μm to 200–300 Ω μm.

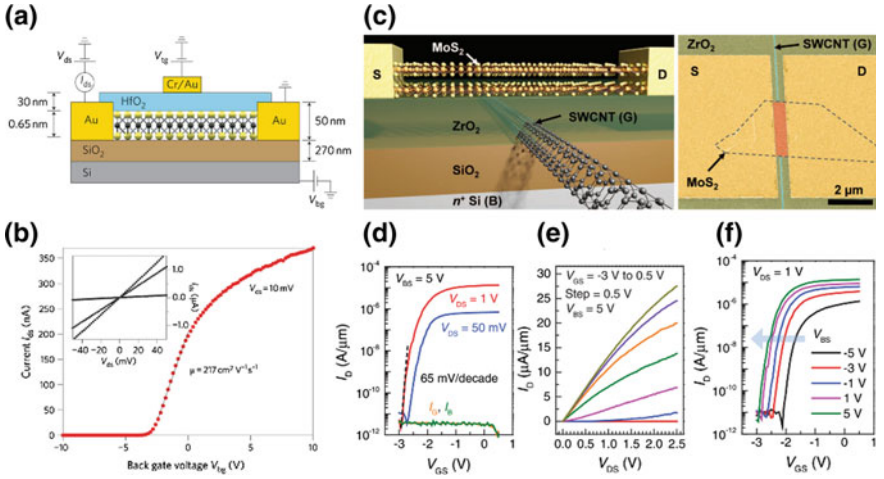

Fig. 1.4 **a** Cross-sectional view of the monolayer MoS_2 FET and the electrical connection for measurement. **b** Room temperature transfer and output (inset) curves for the monolayer MoS_2 FET. The transfer curve is obtained at $V_{ds} = 10$ mV, and the output curves are obtained at $V_{bg} = 0$, 1 and 5 V [4]. Reprinted by permission from Macmillan Publishers Ltd., copyright (2011) **c** 3D schematic (left) and false-colored SEM image (right) of MoS_2 FET with SWCNT gate. **d** I_D-V_{GS} curves of a bilayer MoS_2 FET at $V_{BS} = 5$ V and $V_{DS} = 50$ mV and 1 V. **e** I_D-V_{DS} curves for the device at $V_{BS} = 5$ V and varying V_{GS}. **f** I_D-V_{GS} curves at $V_{DS} = 1$ V and varying V_{BS} [36]. Copyright 2010. Reproduced with permission from AAAS

As a consequence, excellent device performance including high mobility, high on/off current ratio, current saturation, and low subthreshold swing (SS) was realized. Similarly, graphene was tested as an electrode material for MoS_2 FET to realize an ohmic contact [27]. Duan et al. devised an electrode transfer method to address the problem of Fermi-level pinning at the metal–semiconductor interface [28]. Instead of the conventionally evaporated metal electrodes, the transferred metal pads which are vdW interacted with the pre-deposition MoS_2 channel exhibited prominent advantages in maintaining the integrity of the underlying channel material and eliminating metal–semiconductor chemical bonding. The Fermi-level pinning in MoS_2 channel is eliminated and the metal–semiconductor Schottky barrier height is tuned and predicted by Schottky–Mott model. High electron mobility of 260 cm^2/Vs and hole mobility of 175 cm^2/Vs were realized by choosing metals electrodes with appropriate work functions [28]. The electrical performance of MoS_2 FETs is also closely correlated with the layer number and the substrate [29–31]. Compared with MoS_2, the electrical performances of other 2D group VIB TMDs are less investigated. However, they were proposed to exhibit superior electrical performance dictated by the theoretical calculation and existing experimental studies [32–35].

As the traditional silicon-based metal-oxide-semiconductor FET (MOSFET) scales down to the limit, the short channel effects become adversely prominent. Benefiting from the ultrathin and surface bonding-free nature, the 2D group VIB

TMDs are promising candidates to construct high-performance FETs at a reduced channel length. To implement such a conception, a single-walled carbon nanotube (SWCNT) was used as the bottom gate to tune the bilayer MoS_2 FET (Fig. 1.4c) [36]. The effective channel length was about 1 nm in the on state and 3.9 nm in the off state inferred from the simulation. Figure 1.4d–f shows the electrical performance of the MoS_2 FETs gated by SWCNT at a short channel length. A nearly ideal SS of ~65 mV per decade at room temperature and on/off current ratio of ~10^6 were realized. More complicated device components in logical circuits were also devised and preliminarily tested based on group VIB TMDs FET [37–40].

1.2.3 Photo-, Chemical, and Bio- Sensors

The high performance of 2D group VIB TMDs FETs, as well as the large exposed surface, provides a good platform for their applications in sensing light, chemicals, and biomaterials, through a stimulus to electrical signal switch process. For most of the sensing devices based on 2D materials FETs, the change of the carrier concentration in the channel material upon applying a stimulus is responsible for the electrical response, similar to the function of a top gate. The first single-layer MoS_2 phototransistor was reported by Zhang et al. [5] and a photoresponsivity of 7.5 mA/W and a prompt response time of ~50 ms were achieved.

Later, high photoresponsivities of 880 and 2200 A/W were reported by Kis et al. [41] and Li et al. [42], respectively. Figure 1.5a shows a schematic of the single-layer MoS_2 phototransistor and Fig. 1.5b shows the source-drain current versus source-drain voltage (I_{ds}-V_{ds}) curves of the phototransistor under dark and different illumination intensities. The increased current with the illumination intensity was ascribed to the photoelectric and photo-thermoelectric effects [43, 44]. The monolayer MoS_2 FET is also suitable for detection of chemical vapors, especially those of electron donors (Fig. 1.5c). Figure 1.5d shows the conductivity change of monolayer MoS_2 channel upon exposing to a sequence of 0.002% P_0 triethylamine pulses (black line). The amplitude of conductivity change was in proportion to triethylamine concentration and the control experiment of exposure to nitrogen and water vapor confirmed that the observed response was due to interaction of the MoS_2 with triethylamine. The MoS_2 sensor is less sensitive to electron acceptors, owing to the weak n-type nature of the MoS_2 flakes. The MoS_2 FET for label-free bio-detection was also demonstrated [46]. In this device architecture (Fig. 1.5e), the MoS_2 channel was covered with a dielectric layer, which was functionalized with receptors for explicitly capturing the target biomolecules.

When the target biomolecule was captured by the receptor biomolecule, it would induce a gating effect and modulate the current between the source and drain electrodes. Figure 1.5f shows the I_{ds}-V_{gs} (gate voltage) curves of the MoS_2 biosensor at three PH values of the solution. At low PH value (PH = 3), the surface OH groups of the dielectric layer tended to be protonated, causing a positive surface charge and reduced threshold voltage. The source-drain current (I_{ds}) increased with the decrease

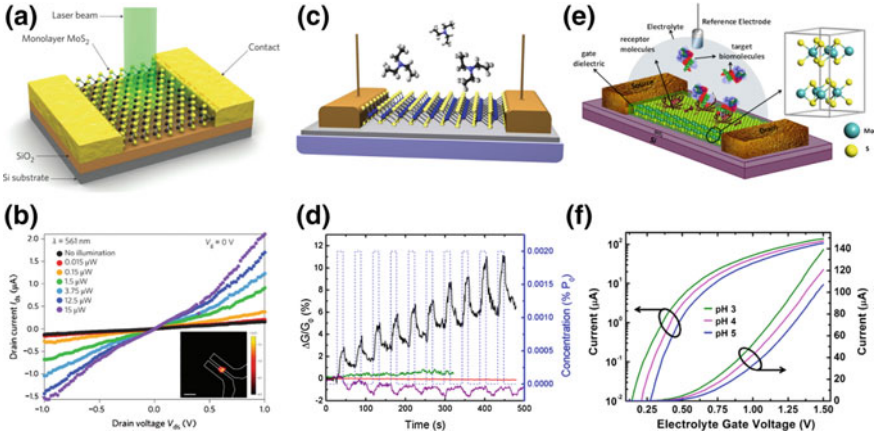

Fig. 1.5 **a** Schematic of the single-layer MoS_2 phototransistor. **b** I_{ds}-V_{ds} curves of the phototransistor under dark and different illumination intensities. The inset image shows the spatial photocurrent map by raster-scanning of a focused laser beam over the device. Scale bar, 5 μm [41]. Copyright (2013). Reprinted with permission from Macmillan Publishers **c** Schematic of the device structure of monolayer MoS_2 chemical sensor. **d** Conductivity variation of monolayer MoS_2 sensor channel upon exposing to a sequence of 0.002% P_0 triethylamine pulses (black line). The dashed blue line shows the pulse timing (15 s on/30 s off) and concentration. The solid red and green lines show the response to nitrogen and water vapor (0.025% P_0), respectively. The purple line shows the response of graphene sensor to water vapor pulses (0.025% P_0) [45]. Copyright 2013 American Chemical Society. Published with permission **e** Schematic of the device structure of MoS_2 biosensor. **f** I_{ds}-V_{gs} curves of the MoS_2 biosensor at three PH values of the solution [46]. Copyright 2014. Reproduced with permission from American Chemical Society

in pH value. The sensitivity as high as 713 for a pH change by 1 unit in the subthreshold region and a wide operable pH range from 3 to 9 were demonstrated. This kind of MoS_2 biosensor was also used for specific protein detection at an ultralow concentration [46].

1.2.4 Tunneling FET

Tunneling FETs (TFET) have been realized in graphene-based van der Waals heterostructures [47, 48]. In those work, 2D MoS_2 or WS_2 layers were inserted between the graphene layers, acting as atomically thin barrier. High-performance TFET characteristics were obtained in such a device structure. Banerjee et al. [49] devised a novel TFET utilizing band-to-band tunneling (BTBT). The device structure is shown in Fig. 1.6a. Under a bias, electrons flow from degenerately doped p-type Ge to the MoS_2 channel in a BTBT way and diffuse to the drain electrode.

In the off state, only the electrons above the conduction band of Ge could move to MoS_2 according to the band alignment between Ge and MoS_2. The current was

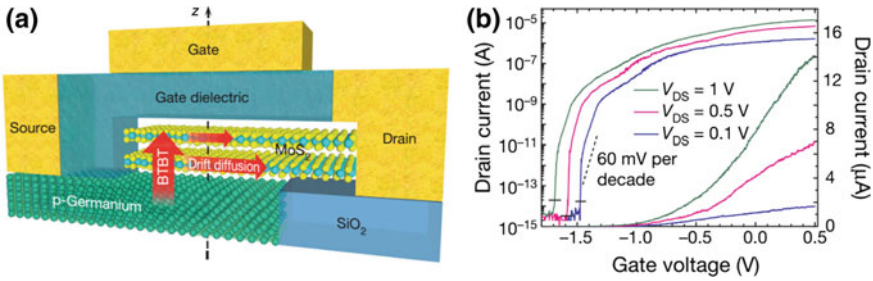

Fig. 1.6 **a** Schematic of the band-to-band tunneling FET. The red arrows show the electron transport path. The electrons band-to-band tunnel (BTBT) from Ge source to MoS_2 channel, and laterally diffuse to the drain electrode. **b** I_{ds}-V_{gs} curves for three different drain voltages of 0.1, 0.5, and 1 V, from which the SS were obtained [49]. Copyright (2015). Reproduced with permission from Macmillan Publishers

low due to the lack of available electrons in the conduction band. As the gate voltage was increased, the MoS_2 conduction band was lowered below the Ge valence band. The electrons in the Ge valence band could flow to the empty states in the MoS_2 channel, leading to an abrupt increase in current. The drain current as a function of gate voltage at three different drain voltages is shown in Fig. 1.6b. Ultralow SS all below 60 mV per decade over about four decades of current were deduced from the three curves, breaking the fundamental limitations on SS in MOSFETs.

1.2.5 Light Emitters and Photovoltaics

Similar to the PL, EL in 2D group VIB TMDs originates from the excitonic recombination. They are supposed to exhibit more efficient light emission being direct bandgap semiconductors in the monolayer limit. In a pioneer work by Steiner et al. [12], a pair of electrodes were deposited and contacted with the single-layer MoS_2. Electrons were injected from one electrode to the conduction band of MoS_2 and combined with holes, forming excitons under a high source-drain voltage. This is known as a hot carrier process, and the light emission is localized in the vicinity of the contacts. 2D p-n junction is more efficient in exciton generation and requires a reduced source-drain bias. Three independent groups reported the construction of 2D p-n junctions within monolayer WSe_2 through local electrostatic doping [50–52]. WSe_2 is selected owing to the ambipolar transport behaviors.

Figure 1.7a shows the device structure of monolayer WSe_2 with two split gates [51]. The two gates could locally dope the channel. When the same polar voltage was applied to the two gates, the devices operated as a resistor (blue and green dash lines in Fig. 1.7b). Whereas when the two gates were applied voltage of opposite polarity, the current rectification was observed (blue and green solid lines in Fig. 1.7b). Thus,

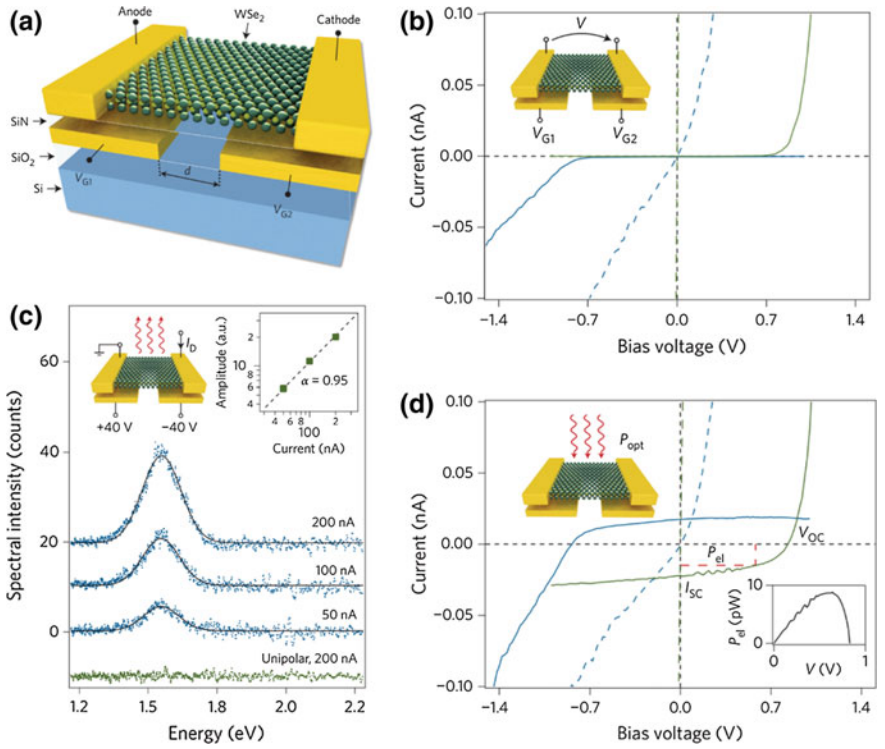

Fig. 1.7 **a** Schematic of the monolayer WSe_2 device with split-gate electrodes. **b** I–V curves of the device in the dark under different biasing conditions: p-n (solid green line; $V_{G1} = -40$ V, $V_{G2} = 40$ V), n–p (solid blue line; $V_{G1} = 40$ V, $V_{G2} = -40$ V), n–n (dashed green line; $V_{G1} = V_{G2} = 40$ V), p–p (dashed blue line; $V_{G1} = V_{G2} = -40$ V). **c** Electroluminescence emission spectra recorded at constant currents of 50, 100, and 200 nA, respectively. The green curve shows that no light emission is obtained under unipolar conduction. The left inset shows the two gate voltages and the right inset shows that the amplitude of the emission intensity on a double-logarithmic scale is linearly dependent on the current. **d** *I–V* curves of the device under illumination. The biasing conditions are the same as (**b**). Inset: electrical power (P_{el}, operating as a diode) versus voltage [51]. Copyright (2014). Reproduced with permission from Macmillan Publishers

the device could operate as a light emitter when a forward current is driven through the device and opposite voltages are applied to the two gates.

Figure 1.7c shows the EL emission spectra at different driving currents. The EL emission is found at the same energy as the PL and the emission intensity increases linearly with the driving current (inset in Fig. 1.7c), indicating that the EL arises from excitonic transition. Vertically standing van der Waals heterostructures are also good platforms for investigating the light emission behaviors of 2D semiconductors. In this kind of structure, the carriers flow perpendicular to the 2D plane. Compared with the planar structure where the carriers flow within the 2D plane, the vertical

structure offers the advantages such as reduced contact resistance, higher current density, and whole device light emission.

For example, a sandwich structure of graphene/BN/MoS_2/BN/graphene was devised [53]. The Fermi level of the two graphene layers could be tuned to align with the conduction and valence band edges of MoS_2, resulting in electrons and holes injection through the BN barrier. EL emission with external quantum efficiency of ~10% was realized. The 2D semiconductors could also be attempted as a light absorption layer in a photovoltaic device. For instance, asymmetric electrodes of Pd and Au were applied in a MoS_2 FET [54]. When the channel was illuminated by light, the generated electron-hole pairs could be separated under the influence of the built-in potential from the space charge at the contacts, giving rise to a photovoltaic effect. The 2D p-n heterostructure could be another viable way for electron-hole pair generation and separation. When the device in Fig. 1.7 was illuminated with light and the two split gates were applied by opposite voltages, a photovoltaic effect was observed (green and blue solid lines in Fig. 1.7d). The power conversion efficiency (PCE) of the device was 0.5% with a filling factor (FF) of 50%. The comparatively low PCE and FF are ascribed to the low absorption of the atomically thin photoactive layer. The strategy of combining 2D TMDs with plasmonic materials or tandem device structure for sufficient light absorption would be used to improve photo-to-electric conversion performance. Other n-type and p-type 2D TMDs would also be combined to construct the p-n junction to fulfill the photovoltaic functionalities [55].

1.2.6 Valleytronics

2D group VIB TMDs also provide a good platform for the study of valley physics. In monolayer group VIB TMDs with broken inversion symmetry, the valence bands are split by spin-orbit coupling. The spin splitting must be opposite at the two inequivalent valleys, labeled K and K' in the first Brillouin zone (Fig. 1.8a). Right (left)-handed circularly polarized light only couples to the K (K′) valleys according to the optical selection rules [56, 57], as has been experimentally demonstrated by valley polarization using polarization resolved PL (Fig. 1.8b) [8, 9, 58, 59]. The circularly polarized EL emission, which is electrically switchable, was also demonstrated in a WSe_2 p-i-n junction [60]. The p- and n-regions are defined by the electric double layer at the electrolyte-solid interface, which could induce a large gate field and break the inversion symmetry of few-layer WSe_2. Figure 1.8c shows the circularly polarized EL emission for two opposite current flow directions. The circular polarization was reversed when the source-drain bias was exchanged. The result was explained by the electron-hole overlap controlled by in-plane electric field [60].

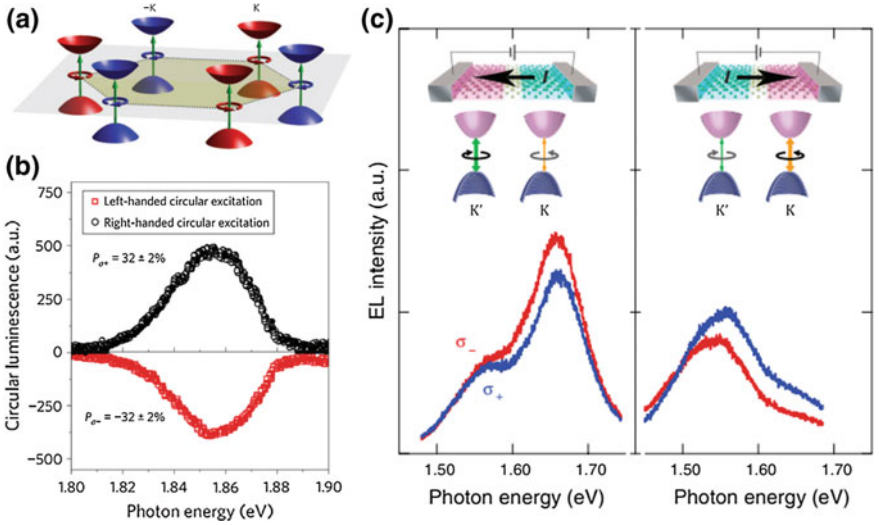

Fig. 1.8 **a** Valley contrasting optical selection rules in a 2D hexagonal lattice with broken inversion symmetry [57]. Reprinted by permission from Macmillan Publishers Ltd., copyright (2014). **b** Polarization resolved PL spectra under circularly polarized excitation [8]. Reprinted by permission from Macmillan Publishers Ltd., copyright (2012). **c** Circularly polarized EL spectra for two opposite current directions. The contribution to EL from two valleys is shown in the bottom [60]. Copyright 2014. Reprinted with permission from Science

1.3 Group VIIB TMDs (ReS_2 and $ReSe_2$)

1.3.1 Atoms Arrangement and Band Structure

Rhenium dichalcogenide (ReX_2, X = S and Se) is a representative-layered group VIIB TMD, although the element Re is discovered late [61]. Similar to group VIB TMDs, the ReX_2 layers are held together by weak vdW force and the Re and X atoms within each layer are covalently bonded.

The difference is that the extra electron in each Re atom brings in a chemical bond between Re atoms. Each four Re atoms arrange in a parallelogram shape and the parallelograms connect to form atomic chains along the principle *b*-axis, which is the shortest axis in the basal plane (Fig. 1.9a) [62]. The *a*-axis is 118.97° apart from the *b*-axis, corresponding to the second-shortest axis. This kind of atoms arrangement of both ReS_2 and $ReSe_2$ is experimentally verified by aberration-corrected STEM, as shown in Fig. 1.9b and c [63]. For ReS_2, the distance between two neighboring parallelograms in the direction of *b* and *a* is measured as 0.34 and 0.31 nm, and that for $ReSe_2$ is 0.39 and 0.35 nm, respectively, in agreement with the theoretical calculations [64].

Unlike the stable H phase observed in MX_2 (M = Mo and W, X = S and Se), ReX_2 shows a distorted 1T structure originating from the Peierls distortion [65], which

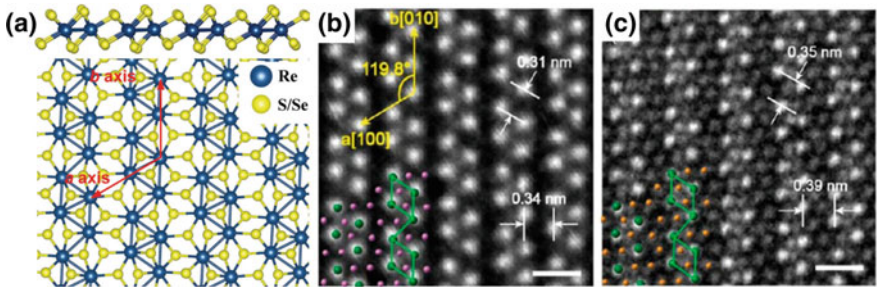

Fig. 1.9 **a** Side view (top panel) and top view (bottom panel) of the atoms arrangement in monolayer ReX_2 (X = S and Se) [62]. Reproduced with permission from Wiley-VCH Verlag GmbH (**b**, **c**) ADF STEM images of monolayer ReS_2 (**b**) and $ReSe_2$ (**c**) [63]. Copyright 2015. Reprinted with permission from American Chemical Society

prevents interlayer-ordered stacking and minimizes the wavefunctions overlap. As a result, the interlayer interaction in ReX_2 is over an order of magnitude lower than that in MoS_2 (18 vs. 460 mV per unit cell). The bulk ReX_2 behaves like vibrationally and electronically decoupled while stacked monolayer counterparts [65]. Thus the bulk ReX_2 can be directly used for study of 2D physics, circumventing the necessity of preparing monolayer samples. The bandgap of layered TMDs is strongly influenced by the layer number. For group VIB TMDs, an indirect to direct bandgap transition occurs when the bulk materials are thinned down to monolayer limit, caused by the exciton confinement effects [11]. As a consequence, both the PL quantum yield and PL emission position vary. However, for ReX_2, the electronic band structure is barely influenced by the layer number, due to the weak interlayer interaction.

Figure 1.10a shows the band structure for monolayer, trilayer, and five-layer ReS_2 by ab initio calculation [66]. The CBM and VBM share the identical position in the Brillouin zone, respectively, giving rise to direct bandgap for monolayer, trilayer, and five-layer ReS_2. The bandgap only varies slightly, from 1.44 eV for monolayer ReS_2, 1.40 eV for trilayer ReS_2, to 1.35 eV for five-layer ReS_2. In fact, the bulk ReS_2 is also a direct bandgap semiconductor with a bandgap of 1.35 eV, predicted by generalized gradient approximation (GGA) [67]. As such, the PL emission for ReS_2 with different layer numbers is a superposition of the emission from individual monolayers. The PL intensity increases as the layer number increases and no significant emission position change is observed due to the similar bandgap (Fig. 1.10b) [65].

1.3.2 Anisotropic Optical and Electrical Properties

Deriving from the atoms arrangement, ReX_2 crystals are supposed to exhibit anisotropic optical and electrical response behaviors. The anisotropic properties of the bulk materials have been documented [68, 69] and that of the few-layer and

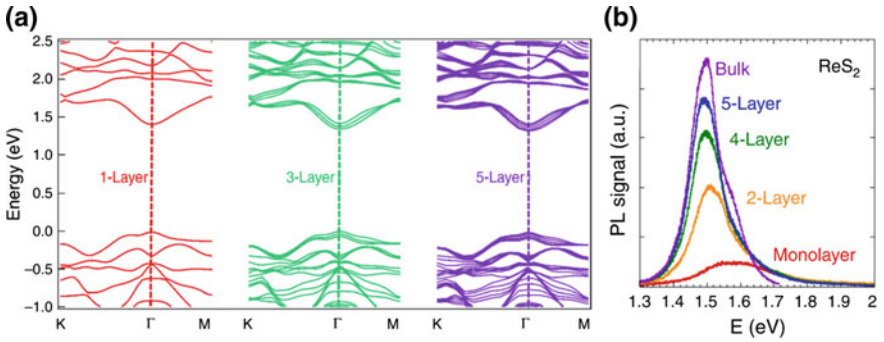

Fig. 1.10 **a** Ab initio calculated band structures of monolayer, trilayer, and five-layer ReS_2 [66]. Reprinted by permission from Macmillan Publishers Ltd., copyright (2015). **b** PL signal of ReS_2 with different layer numbers [65]. Copyright 2014. Reprinted with permission from Macmillan Publishers

monolayer counterparts are the current research focus. The unique anisotropy is not only important for the understanding of physical properties but also fundamental for designing novel kinds of electronic devices.

The anisotropic Raman response of ReX_2 is revealed in several studies [70–73]. Compared with the group VIB TMDs, the Raman spectra of ReX_2 exhibit more bands due to its low symmetry. Figure 1.11a shows an optical image of ReS_2 samples with varied layer numbers obtained by mechanical exfoliation [70]. The Raman spectra for the 1L, 2L, 3L, and 4L ReS_2 are shown in Fig. 1.11b. Note that the peak position of Raman mode I continuously changes with the layer number, from 133.1 ± 0.1 cm^{-1} in the 1L to 136.2 ± 0.2 cm^{-1} in the 4L, while the position of modes III, IV, and V barely varies. Thus the peak position difference between Raman mode I and other modes, such as mode III, can be used to identify ReS_2 layer number in few-layered samples, similar to the work done on MoS_2 [74]. Figure 1.11c exhibits the orientation-dependent polarization response of mode V in the 4L region with unpolarized (black), cross-polarized (blue), and parallel-polarized (red) collection. The cross- and parallel-polarized spectra yield 4-lobed and 2-lobed shapes, respectively, indicating the anisotropic Raman response behavior of thin ReS_2 by angle-resolved polarized Raman spectroscopy technique.

1.3.3 Anisotropic Electrical Properties

The unique atomic structure also renders an anisotropic electron transport behavior for 2D ReX_2. The theoretical calculations have predicted that the conductivity along *b*-axis is higher than other directions [68, 69]. The FET devices were fabricated with the electrodes patterning perpendicular to the ReS_2 *a*- and *b*-axes, respectively, and the transfer curves are shown in Fig. 1.12a [66].

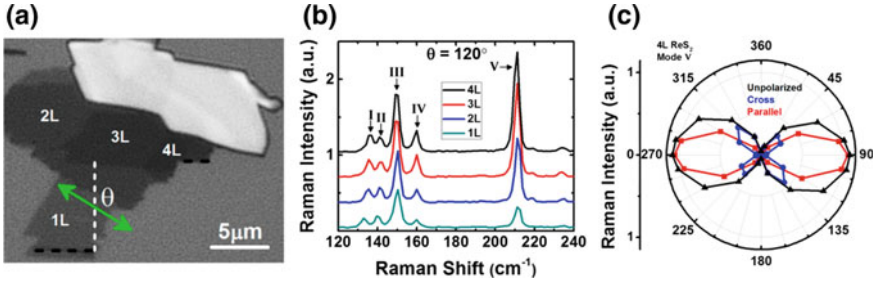

Fig. 1.11 **a** Optical microscopy image of a mechanical-exfoliated ReS_2 sample with 1-4 layers identified. **b** Raman spectra taken in the 1L, 2L, 3L, and 4L ReS_2 regions with an orientation of $\theta = 120°$. **c** Raman intensity of mode V in the 4L region with unpolarized (black), cross-polarized (blue), and parallel-polarized (red) collection [70]. Copyright 2015. Reproduced with permission from American Chemical Society

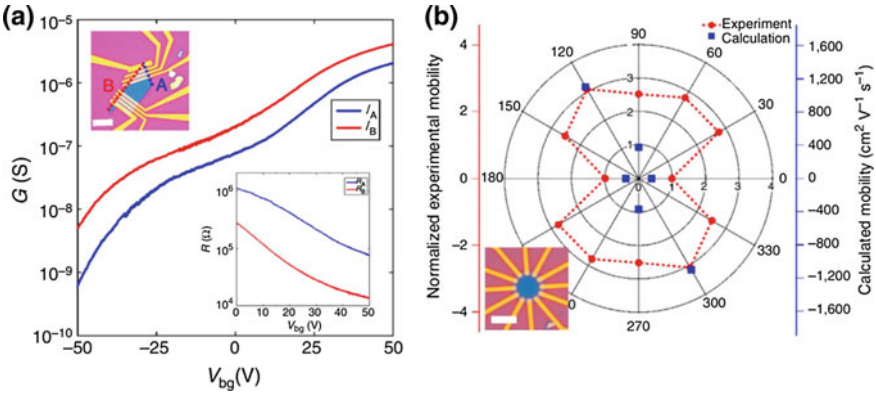

Fig. 1.12 **a** Transfer curves of a quadrilateral-shaped five-layer ReS_2 flake in the A and B directions. The left inset shows the optical microscopy image of the FET device, scale bar, 10 mm, and the right inset shows the four-probe resistance of the same devices as a function of V_{bg}. **b** Experimentally measured field-effect mobilities of a six-layer ReS_2 device along 12 evenly spaced directions in polar coordinate. The blue dots show the calculated mobilities in the same polar coordinate. The optical image of the device is shown inset [66]. Copyright 2015. Reprinted with permission from Macmillan Publishers

Obviously, the current along the *b*-axis is higher than that along the *a*-axis, and the current ratio was also gate dependent. To eliminate the contact resistance, the four-probe resistance was measured (inset in Fig. 1.12a) and the result was consistent with the current trend.

The anisotropic transport behaviors were further evaluated by the device shown in the inset of Fig. 1.12b. The 12 electrodes were separated by 30° apart. The transfer curves of each pair of diagonally positioned electrodes were measured, and the normalized mobility was plotted in a polar coordinate. The field-effect mobility is highly angle dependent and the largest value is 60° from the direction with the

lowest value. The anisotropic ratio of mobility was ~3.1, which is larger than 1.8 for anisotropic black phosphorus [75].

1.3.4 Electronics and Optoelectronic Devices

Since ReX_2 sheets have exhibited a high room temperature mobility above 30 cm^2/Vs and a high on/off current ratio of over 10^6 [76, 77], they are promising for application in electronics. As the synthesis technology for ReX_2 is rapidly developing, especially the controlled sample preparation by CVD with predefined layer number and size [78–81], increasingly more electronic devices based on these materials are emerging. Figure 1.13 shows some elementary logical gates constructed with few-layer ReS_2 channel [82]. Monolayer graphene was applied as the source, drain, and gate electrode, and a kind of ion gel with a high capacitance was used as the dielectric layer.

The graphene electrodes avoid the trap states and Fermi-level pinning in the ReS_2 channel, and the ion gel can tune the electron concentration of the channel within a large range. Figure 1.13a shows an optical image of the logical NOT device and Fig. 1.13b exhibits the reasonable voltage transfer characteristics and the voltage gain exceeding 3.5. For the NAND gate, three transistors are connected in series (Fig. 1.13c). When either or both of the inputs are in the logic states "0," the V_{out} is in the logic state "1," and the V_{out} logic state "0" is only achieved when both the inputs are held at "1" (Fig. 1.13e). For the NOR gate, one transistor is connected in series with two transistors connecting in parallel (Fig. 1.13d). When either or both of the inputs are in the logic states "1," the V_{out} is in the logic state "0," and the V_{out} logic state "1" is only achieved when both the inputs are held at "0" (Fig. 1.13e).

Since the direct bandgap nature of ReX_2 is independent of the layer number, highly performance photodetectors are expected in the few-layer samples owing to improved light absorption compared with the monolayers. A similar device structure designed for group VIB TMDs is also utilized for ReX_2 photodetectors, and high device performance was reported [77, 81, 83–87]. The polarization-sensitive photoresponsivity originating from the high in-plane optical anisotropy was also observed in a $ReSe_2$ photodetector [84]. The EL was also preliminarily proposed and reported in ReS_2 [88] and ReS_2 p-n junction [89], and more efforts are necessary in this area to realize devices with higher performance.

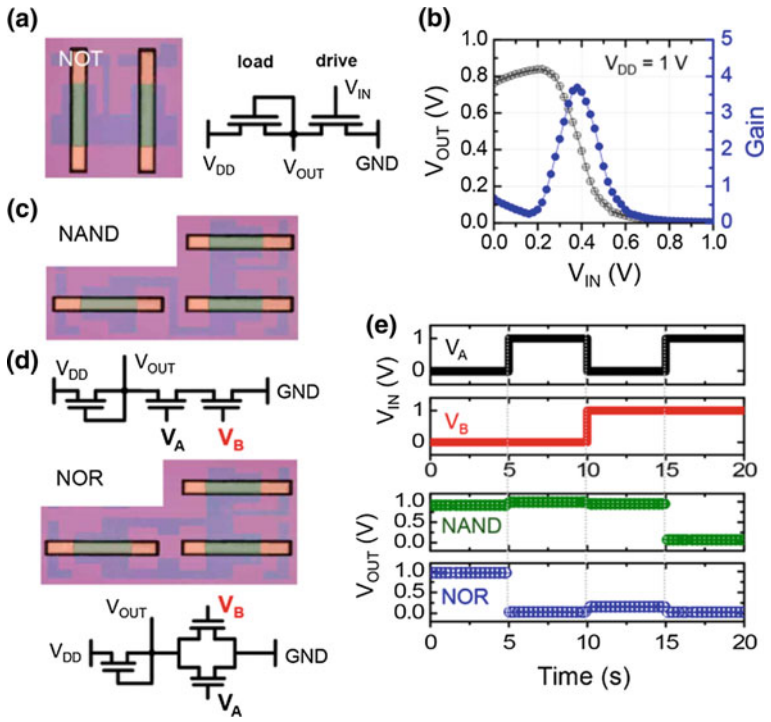

Fig. 1.13 **a** Optical image and schematic band diagram of the NOT gate. **b** Voltage transfer characteristics and signal gain of the NOT gate. (**c**, **d**) Optical images and schematic band diagrams of the **c** NAND and **d** NOR gates. **e** The input and output voltages of the NAND and NOR gates as a function of time [82]. Copyright 2017. Reproduced with permission from American Chemical Society

1.4 Group VIII TMDs (PtS_2 and $PtSe_2$)

1.4.1 Atoms Arrangement and Band Structure

PtX_2 (X = S and Se) crystal possesses a typical 1T-type hexagonal crystal structure, similar to the 1T phase of group VIB TMDs. The Pt atom is in a tilted octahedral site and coordinated by six X atoms. The lattice constants of the hexagonal structure are defined in Fig. 1.14a [90]. Figure 1.14b shows an atom-resolved STEM image of few-layer $PtSe_2$ [91]. The atoms can be clearly identified from the image contrast and the intensity profile along the red line. The fast Fourier transform image is also in agreement with the hexagonal structure of $PtSe_2$. Different from the weak interlayer interaction in group VIIB TMDs and the moderate interlayer interaction in group VIB TMDs as discussed above, the interaction between PtX_2 layers is strong, resulting from the overlapping of the p_z orbital of interlayer X atoms [90–95].

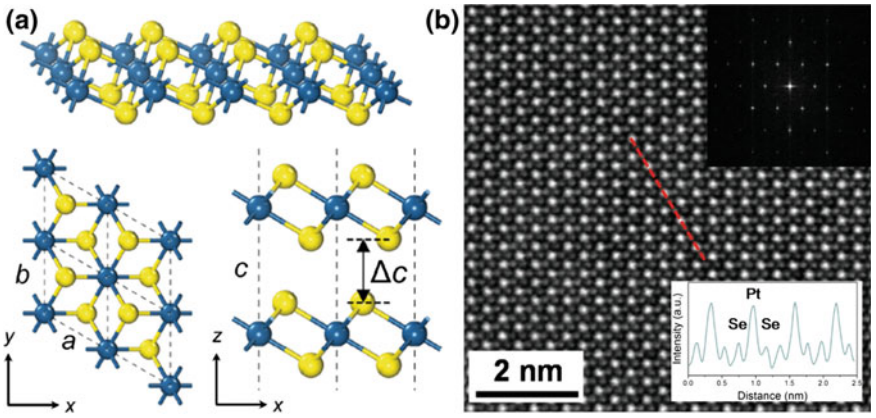

Fig. 1.14 **a** 3D, top, and side view of the 1T PtX_2 (X = S and Se). The blue and yellow balls represent Pt and X atoms, respectively [90]. Reproduced with permission from Wiley-VCH Verlag GmbH **b** Atoms resolved STEM image of few-layer $PtSe_2$. The up inset is the fast Fourier-transformed image showing hexagonal structure and the bottom inset shows the intensity line proline along the red line [91]. Copyright 2017. Reproduced with permission from Wiley-VCH Verlag GmbH

As a result, the band structure of PtX_2 changes dramatically with the layer number. Monolayer $PtSe_2$ is a semiconductor with indirect bandgap. The bandgap narrows in the bilayer and becomes zero in the trilayer, as predicted by the first-principle calculation (Fig. 1.15a–c) [96].

Also, the indirect bandgap could be transformed to direct bandgap under strain [93]. PtS_2 shares a similar band structure evolution with $PtSe_2$ as a function of layer number. The experimentally verified and DFT calculated bandgaps versus number of layers are plotted in Fig. 1.15d [90]. The layer-dependent semiconductor to metal transition is unique in the group VIII TMDs. Note that the value of the bandgap varies depending on the calculation method and the level of theory, as well as the defect concentration [90–96].

1.4.2 Electronic Devices

PtX_2 is predicted to exhibit phonon-limited carrier mobility exceeding 1000 cm^2/Vs at room temperature [97]. Thus they are suitable for high-speed electronic devices. The FETs based on different layer numbers of PtS_2 and $PtSe_2$ were constructed and tested [90, 91]. The output and transfer curves for an 11-nm-thick $PtSe_2$ device are shown in Fig. 1.16a and b. The I_{ds} increased with the positive back gate voltage , indicating the n-type carrier transport. The room temperature electron mobility derived from the linear region of the transfer curve was 210 cm^2/Vs. This mobility is much higher than that of 2D group VIB and VIIB TMDs. Moreover, the device is rather stable, which exhibits negligible degradation after storing in air for one

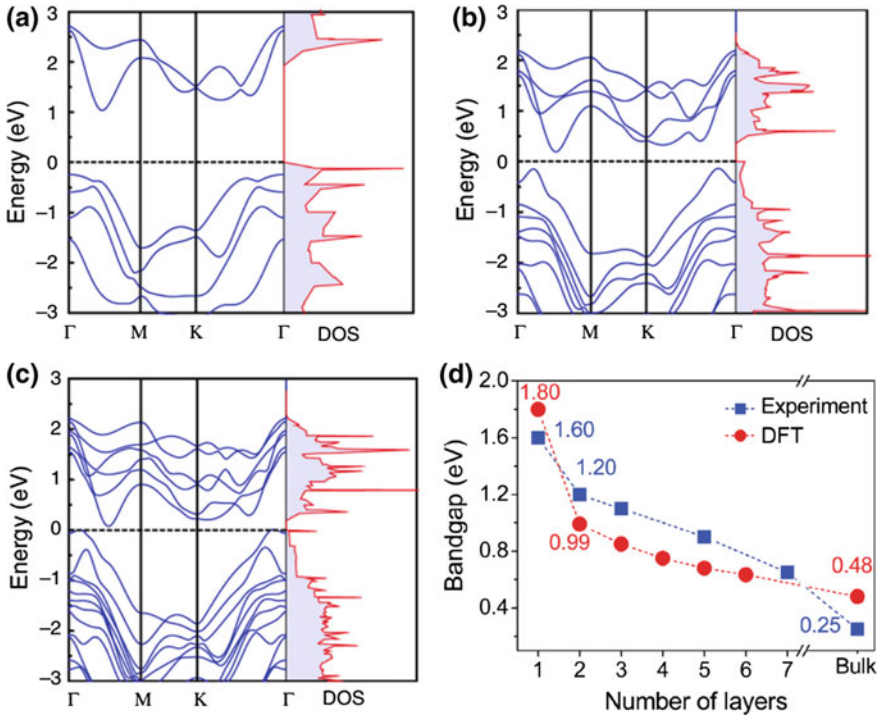

Fig. 1.15 **a**–**c** First-principle calculated band structure of defect-free **a** monolayer, **b** bilayer, and **c** trilayer $PtSe_2$ [96]. Reprinted by permission from Macmillan Publishers Ltd., copyright (2018), **d** Experimentally measured and DFT calculated bandgap as a function of PtS_2 layer number [90]. Copyright 2016. Reproduced with permission from Wiley-VCH Verlag GmbH

year [91]. A FET fully composed of $PtSe_2$ was also reported [98]. A thinner $PtSe_2$ sheet is used as a semiconductor channel material, and the thicker $PtSe_2$ sheet is used as an electrode. The same kind of material within one device yields an Ohmic contact between electrode and channel, which is beneficial for carrier injection. P-type carrier transport was also reported in $PtSe_2$ FET [99]. The different 2H phase resulted from the different synthesis route may be accounted for the observed p-type carrier transport. Photodetectors using the planar FET device configuration based on PtX_2 channel materials have also been realized [91, 96, 98], in analogy to the photodetectors based on group VIB and VIIB TMDs.

The unique advantages for group VIII TMDs photodetectors are the tunable narrow bandgaps, which is an excellent choice for mid-infrared light detection. Figure 1.16c and d shows the time-resolved photocurrent when the device was illuminated with lasers of different wavelengths. For the monolayer $PtSe_2$ FET, a photoresponsivity of 0.9 and 0.15 A W^{-1} was obtained for 632 nm and 1.47 μm illumination, respectively. However, the device showed negligible photoresponse to

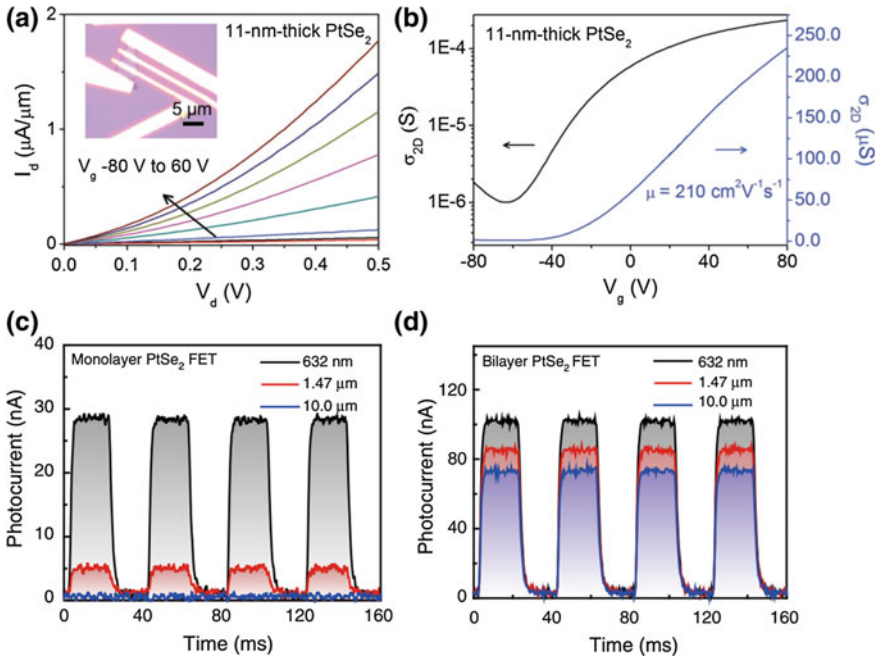

Fig. 1.16 **a**, **b** Output and transfer curves of a 11 nm $PtSe_2$ transistor. The optical image of the device is shown in the inset in (**a**) [91]. Reproduced with permission from Wiley-VCH Verlag GmbH (**c**, **d**) Time-resolved photocurrent of **c** monolayer and **d** bilayer $PtSe_2$ FET at a bias voltage of 0.1 V and zero gate voltage under laser illumination with a wavelength of 632 nm, 1.47 μm, and 10 μm, respectively [96]. Copyright (2018) Reproduced with permission from Macmillan Publishers

a mid-infrared laser illumination ($\lambda = 10$ μm) since the photon energy of the incident laser is far below the bandgap of monolayer $PtSe_2$ (Eg ~ 1.2 eV).

For the bilayer $PtSe_2$ FET, a much higher photoresponsivity of 6.25, 5.5, and 4.5 A W^{-1} was observed for 632 nm, 1.47 μm, and 10 μm illumination, respectively. The broadband mid-infrared photoresponse of bilayer $PtSe_2$ FET was proposed to be originated from the defect-induced bandgap reduction [96]. The $PtSe_2$ FET could also be used as a NO_2 gas sensor [100], in which ultrahigh sensitivity and extremely fast response time are obtained.

A photovoltaic device was proposed and fabricated by transferring $PtSe_2$ thin films onto pre-patterned Si substrates [100], forming $PtSe_2$/n-Si Schottky barrier diodes (SBDs). The schematic of the device structure is shown in Fig. 1.17a and the rectifying characteristics are shown in Fig. 1.17b. A clear photoresponse was observed in the reverse bias region under illumination, as shown in Fig. 1.17c. The energy band diagram at the junction of the SBD under illumination is presented in Fig. 1.17d. J-V curves of the devices with different $PtSe_2$ thicknesses under an incident light intensity (P_{in}) of 4.7 mW/cm^2 are plotted in Fig. 1.17e. As the thickness

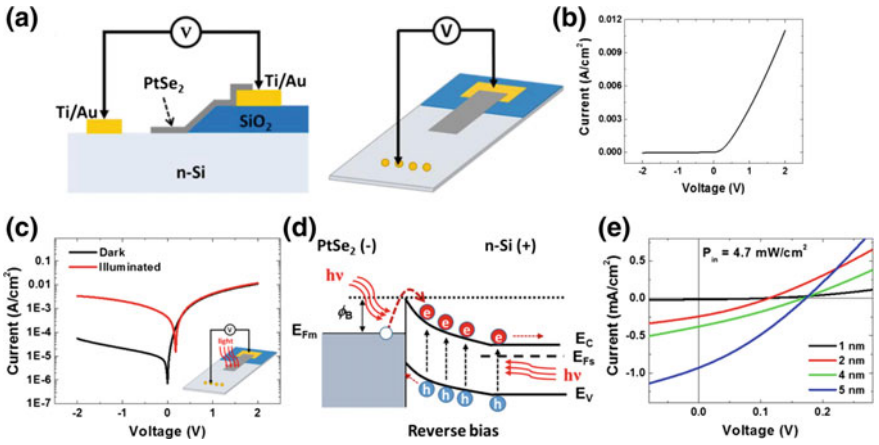

Fig. 1.17 **a** Schematic of the $PtSe_2$/n-Si Schottky barrier diode. **b** J-V curve of the device with a $PtSe_2$ film synthesized from 4-nm-thick Pt on a linear scale. **c** J-V curves of the device with a $PtSe_2$ film synthesized from 4-nm-thick Pt on a semilogarithmic scale under dark and illumination. **d** Energy band diagram of the Schottky junction between $PtSe_2$ and n-Si under reverse bias. **e** J–V characteristics of the devices with different $PtSe_2$ thicknesses under an incident light intensity (P_{in}) of 4.7 mW/cm^2 [100]. Copyright 2016. Reprinted with permission from American Chemical Society

of the $PtSe_2$ layer increases, light absorption enhances and thus the power conversion efficiency increases.

1.5 Other 2D TMDs

In addition to the TMDs discussed above, more 2D TMDs are emerging and attracting increasing attentions. These materials exhibit dramatically different properties mainly due to the varied *d*-orbit electron states of the transition metals and provide versatile platforms for studying fundamental physical conceptions such as charge density wave (CDW), phase transition, and superconductivity.

In the group VB TMDs, VX_2 (X = S and Se) exhibits intrinsic ferromagnetic behaviors and the magnetic moments and strength of magnetic coupling could be tuned by isotropic strain, as predicted by the first-principles calculations [101]. The ferromagnetism has been experimentally verified in both VS_2 and VSe_2 [102, 103]. The CDW behavior was also discovered in VSe_2 [103] and the CDW transition temperature is dependent on the thickness [104, 105]. For VS_2, the stable phase (H or T) relies on the temperature and the thickness [106]. Few-layer VS_2 is metallic [107, 108] and the metal-insulator transition is also observed and influenced by the vdW interaction [108].

The DFT calculation reveals that bulk and few-layers VSe_2 in T and H phase, and monolayer VSe_2 in T phase are metallic, while the H monolayer is a semi-

conductor [109]. 2D $NbSe_2$ is also investigated and the coexistence of CDW and superconducting phase has been observed in monolayer limit [110]. The electronic phase transitions can be achieved by electrostatic gating [111]. A plenty of low-temperature electronic states also appear in 1T-TaS_2, especially the first reported superconductivity in a pristine 1T-TaS_2 [112]. A series of phase transitions in 1T-TaS_2 thin flakes are reported by gate electric field induced Li-ion intercalation [113]. For 2H TaS_2, the superconductivity persists down to 3.5 nm, and the critical temperature increases from 0.5 to 2.2 K as the layers are thinned down [114]. Similarly, the CDW and superconductivity phases were also reported in 2D group IVB TMDs, like $TiSe_2$ [115–117]. The transition temperature could be tuned by the electric field [116]. 2D $HfSe_2$ in group IVB TMDs is a kind of n-type semiconductor, with a relatively small bandgap of ~1.1 eV revealed by scanning tunneling spectroscopy (STS) on a molecular beam epitaxy grown sample [118] and high phonon-limited mobility over 3500 cm^2/Vs predicted by calculation [97].

1.6 Conclusions

In this chapter, the atomic arrangement, band structure, and electronic applications of most of the widely studied 2D TMDs are summarized. Differentiating from graphene and bulk TMDs, 2D TMDs exhibit unique properties and application potential. As the synthesis technique is continuously developing, more 2D TMDs are obtained. For example, 47 kinds of binary, alloy, and heterostructured 2D TMDs have been synthesized by a salt-assisted CVD method in a recent report [119]. The availability of these materials paves the way for a deeper understanding of the physical origins and device applications. At the same time, apart from the optical and electrical applications, 2D magnetism is attracting increasing attentions, exhilarated by the particular magnetic properties discovered in transition metal Cr based 2D materials [120, 121]. As such, low-power and ultra-compact spintronic applications could be expected based on 2D TMDs.

Acknowledgements The work was partially supported by the financial support of the National Natural Science Foundation of China (Grant 51472219 and 51672244).

References

1. Novoselov KS, Geim AK, Morozov SV, Jiang D, Zhang Y, Dubonos SV et al (2004) Electric field effect in atomically thin carbon films. Science 306:666–669
2. Xu M, Liang T, Shi M, Chen H (2013) Graphene-like two-dimensional materials. Chem Rev 113:3766–3798
3. Winer WO (1967) Molybdenum disulfide as a lubricant: a review of the fundamental knowledge. Wear 10:422–452

4. Radisavljevic B, Radenovic A, Brivio J, Giacometti V, Kis A (2011) Single-layer MoS_2 transistors. Nat Nanotechnol 6:147–150
5. Yin Z, Li H, Li H, Jiang L, Shi Y, Sun Y et al (2012) Single-layer MoS_2 phototransistors. ACS Nano 6:74–80
6. Li H, Tsai C, Koh AL, Cai L, Contryman AW, Fragapane AH et al (2016) Activating and optimizing MoS_2 basal planes for hydrogen evolution through the formation of strained sulphur vacancies. Nat Mater 15:48–53
7. Ugeda MM, Bradley AJ, Shi SF, da Jornada FH, Zhang Y, Qiu DY et al (2014) Giant bandgap renormalization and excitonic effects in a monolayer transition metal dichalcogenide semiconductor. Nat Mater 13:1091–1095
8. Zeng H, Dai J, Yao W, Xiao D, Cui X (2012) Valley polarization in MoS_2 monolayers by optical pumping. Nat Nanotechnol 7:490–493
9. Mak KF, He K, Shan J, Heinz TF (2012) Control of valley polarization in monolayer MoS_2 by optical helicity. Nat Nanotechnol 7:494–498
10. Qiu DY, da Jornada FH, Louie SG (2013) Optical spectrum of MoS_2 : many-body effects and diversity of exciton states. Phys Rev Lett 111:216805
11. Mak KF, Lee C, Hone J, Shan J, Heinz TF (2010) Atomically thin MoS2: a new direct-gap semiconductor. Phys Rev Lett 105:136805
12. Sundaram RS, Engel M, Lombardo A, Kruple R, Ferrari AC, Avouris P et al (2013) Electroluminescence in single layer MoS_2. Nano Lett 13:1416–1421
13. Xia F, Wang H, Xiao D, Dubey M, Ramasubramaniam A (2014) Two-dimensional material nanophotonics. Nat Photonics 8:899–907
14. Kuc A (2014) Low-dimensional transition-metal dichalcogenides. Royal Soc Chem, Cambridge, pp 1–29
15. Chhowalla M, Shin HS, Eda G, Li LJ, Loh KP, Zhang H (2013) The chemistry of two-dimensional layered transition metal dichalcogenide nanosheets. Nat Chem 5:263–275
16. Kappera R, Voiry D, Yalcin SE, Branch B, Gupta G, Mohite AD, Chhowalla M (2014) Phase-engineered low-resistance contacts for ultrathin MoS_2 transistors. Nat Mater 13:1128–1134
17. Cho S, Kim S, Kim JH, Zhao J, Seok J, Keum DH et al (2015) Phase patterning for ohmic homojunction contact in $MoTe_2$. Science 349:625–628
18. Song S, Keum DH, Cho S, Perello D, Kim Y, Lee YH (2016) Room temperature semiconductor–metal transition of $MoTe_2$ thin films engineered by strain. Nano Lett 16:188–193
19. Scalise E, Houssa M, Pourtois G, Afanasev V, Stesmans A (2012) Strain-induced semiconductor to metal transition in the two-dimensional honeycomb structure of MoS_2. Nano Res 5:43–48
20. Zhu J, Wang Z, Yu H, Li N, Zhang J, Meng J, Liao M et al (2017) Argon plasma induced phase transition in monolayer MoS_2. J Am Chem Soc 139:10216–10219
21. Kuc A, Zibouche N, Heine T (2011) Influence of quantum confinement on the electronic structure of the transition metal sulfide TS_2. Phys Rev B 83:245213
22. Zhao W, Ghorannevis Z, Chu L, Toh M, Kloc C, Tan PH et al (2013) Evolution of electronic structure in atomically thin sheets of WS_2 and WSe_2. ACS Nano 7:791–797
23. Ruppert C, Aslan OB, Heinz TF (2014) Optical properties and band gap of single- and few-layer $MoTe_2$ crystals. Nano Lett 14:6231–6236
24. Roldán R, Silva-Guillén JA, López-Sancho MP, Guinea F, Cappelluti E, Ordejob P (2014) Electronic properties of single-layer and multilayer transition metal dichalcogenides MX_2 (M = Mo, W and X = S, Se): electronic properties of TMDs. Ann Phys 526:347–357
25. Fuhrer MS, Hone J (2013) Measurement of mobility in dual-gated MoS_2 transistors. Nat Nanotechnol 8:146–147
26. Yu Z, Pan Y, Shen Y, Wang Z, Ong ZY, Xu T, Xin R et al (2014) Towards intrinsic charge transport in monolayer molybdenum disulfide by defect and interface engineering. Nat Commun 5:5290–5297
27. Guimarães MHD, Gao H, Han Y, Kang K, Xie S, Kim CJ et al (2016) Atomically thin ohmic edge contacts between two-dimensional materials. ACS Nano 10:6392–6399

28. Liu Y, Guo J, Zhu E, Liao L, Lee SJ, Ding M et al (2018) Approaching the Schottky-Mott limit in van der Waals metal–semiconductor junctions. Nature 557:696–700
29. Das S, Chen HY, Penumatcha AV, Appenzeller J (2013) High performance multilayer MoS_2 transistors with scandium contacts. Nano Lett 13:100–105
30. Bao W, Cai X, Kim D, Sridhara K, Fuhrer MS (2013) High mobility ambipolar MoS_2 field-effect transistors: Substrate and dielectric effects. Appl Phys Lett 102:042104
31. Zheng J, Yan X, Lu Z, Qiu H, Xu G, Zhou X et al (2017) High-mobility multilayered MoS_2 flakes with low contact resistance grown by chemical vapor deposition. Adv Mater 29:1604540
32. Huang JK, Pu J, Hsu CL, Chiu MH, Juang ZY, Chang YH et al (2014) Large-area synthesis of highly crystalline WSe_2 monolayers and device applications. ACS Nano 8:923–930
33. Zhou J, Liu F, Lin J, Huang X, Xia J, Zhang B et al (2017) Large-area and high-quality 2D transition metal telluride. Adv Mater 29:1603471
34. Empante TA, Zhou Y, Klee V, Nguyen AE, Lu IH, Valentin MD et al (2017) Chemical vapor deposition growth of few-layer $MoTe_2$ in the 2H, 1T′, and 1T phases: tunable properties of $MoTe_2$ films. ACS Nano 11:900–905
35. Nakaharai S, Yamamoto M, Ueno K, Lin YF, Li SL, Tsukagoshi K (2015) Electrostatically reversible polarity of ambipolar α-$MoTe_2$ transistors. ACS Nano 9:5976–5983
36. Desai SB, Madhvapathy SR, Sachid AB, Llinas JP, Wang Q, Ahn GH, Pinter G et al (2016) MoS_2 transistors with 1-nanometer gate lengths. Science 354:99–102
37. Radisavljevic B, Whitwick MB, Kis A (2011) Integrated circuits and logic operations based on single-layer MoS_2. ACS Nano 5:9934–9938
38. Cheng R, Jiang S, Chen Y, Liu Y, Weiss N, Cheng HC et al (2014) Few-layer molybdenum disulfide transistors and circuits for high-speed flexible electronics. Nat Commun 5:5143
39. Wang H, Yu L, Lee YH, Shi Y, Hsu A, Chin ML et al (2012) Integrated circuits based on bilayer MoS_2 transistors. Nano Lett 12:4674–4680
40. Yu L, El-Damak D, Radhakrishna U, Ling X, Zubair A, Lin Y et al (2016) Design, modeling, and fabrication of chemical vapor deposition grown MoS_2 circuits with E-mode FETs for large-area electronics. Nano Lett 16:6349–6356
41. Lopez-Sanchez O, Lembke D, Kayci M, Radenovic A, Kis A (2013) Ultrasensitive photodetectors based on monolayer MoS_2. Nat Nanotechnol 8:497–501
42. Zhang W, Huang JK, Chen CH, Chang YH, Cheng YJ, Li LJ (2013) High-gain phototransistors based on a CVD MoS_2 monolayer. Adv Mater 25:3456–3461
43. Wu CC, Jariwala D, Sangwan VK (2013) Elucidating the photoresponse of ultrathin MoS_2 field-effect transistors by scanning photocurrent microscopy. J Phys Chem Lett 4:2508–2513
44. Buscema M, Barkelid M, Zwiller V, van der Zant HSJ, Steele GA, Castellanos-Gomez A (2013) Large and tunable photothermoelectric effect in single-layer MoS_2. Nano Lett 13:358–363
45. Perkins FK, Friedman AL, Cobas E, Campbell PM, Jernigan GG, Jonker BT (2013) Chemical vapor sensing with monolayer MoS_2. Nano Lett 13:668–673
46. Sarkar D, Liu W, Xie X (2014) MoS_2 field-effect transistor for next-generation label-free biosensors. ACS Nano 8:3992–4003
47. Britnell L, Gorbachev RV, Jalil R, Belle BD, Schedin F, Mishchenko A et al (2012) Field-effect tunneling transistor based on vertical graphene heterostructures. Science 335:947–950
48. Georgiou T, Jalil R, Belle BD, Britnell L, Gorbachev RV, Morozov SV et al (2013) Vertical field-effect transistor based on graphene–WS_2 heterostructures for flexible and transparent electronics. Nat Nanotechnol 8:100–103
49. Sarkar D, Xie X, Liu W (2015) A subthermionic tunnel field-effect transistor with an atomically thin channel. Nature 526:91–95
50. Baugher BWH, Churchill HOH, Yang Y, Jarillo-Herrero P (2014) Optoelectronic devices based on electrically tunable p–n diodes in a monolayer dichalcogenide. Nat Nanotechnol 9:262–267
51. Pospischil A, Furchi MM, Mueller T (2014) Solar-energy conversion and light emission in an atomic monolayer p–n diode. Nat Nanotechnol 9:257–261

52. Ross JS, Klement P, Jones AM, Ghimire NJ, Yan J, Mandrus DG et al (2014) Electrically tunable excitonic light-emitting diodes based on monolayer WSe_2 p–n junctions. Nat Nanotechnol 9:268–272
53. Withers F, Del Pozo-Zamudio O, Mishchenko A, Rooney AP, Gholinia A, Watanabe K et al (2015) Light-emitting diodes by band-structure engineering in van der Waals heterostructures. Nat Mater 14:301–306
54. Fontana M, Deppe T, Boyd AK, Rinzan M, Liu AY, Paranjape M et al (2013) Electron-hole transport and photovoltaic effect in gated MoS_2 Schottky junctions. Sci Rep 3:1634
55. Furchi MM, Pospischil A, Libisch F, Burgdorfer J, Mueller T (2014) Photovoltaic effect in an electrically tunable van der Waals heterojunction. Nano Lett 14:4785–4791
56. Xiao D, Liu GB, Feng W, Xu X, Yao W (2012) Coupled spin and valley physics in monolayers of MoS_2 and other group-VI dichalcogenides. Phys Rev Lett 108:196802
57. Xu X, Yao W, Xiao D, Heinz TF (2014) Spin and pseudospins in layered transition metal dichalcogenides. Nat Phys 10:343–350
58. Cao T, Wang G, Han W, Ye H, Zhu C, Shi J et al (2012) Valley-selective circular dichroism of monolayer molybdenum disulphide. Nat Commun 3:887
59. Jones AM, Yu H, Ghimire NJ, Wu S, Aivazian G, Ross JS et al (2013) Optical generation of excitonic valley coherence in monolayer WSe_2. Nat Nanotechnol 8:634–638
60. Zhang YJ, Oka T, Suzuki R (2014) Electrically switchable chiral light-emitting transistor. Science 344:725–728
61. Rahman M, Davey K, Qiao SZ (2017) Advent of 2D rhenium disulfide (ReS_2): fundamentals to applications. Adv Funct Mater 27:1606129
62. Wen W, Zhu Y, Liu X, Hsu HP, Fei Z, Chen Y et al (2017) Anisotropic spectroscopy and electrical properties of 2D $ReS_{2(1-x)}Se_{2x}$ alloys with distorted 1T structure. Small 13:1603788
63. Lin YC, Komsa HP, Yeh CH, Bjorkman T, Liang ZY, Ho CH et al (2015) Single-layer ReS_2: two-dimensional semiconductor with tunable in-plane anisotropy. ACS Nano 9:11249–11257
64. Murray H, Kelly SP, Chianelli RR (1994) Structure of rhenium disulfide. Inorg Chem 33:4418–4420
65. Tongay S, Sahin H, Ko C, Luce A, Fan W, Liu K et al (2014) Monolayer behaviour in bulk ReS_2 due to electronic and vibrational decoupling. Nat Commun 5:3252
66. Liu E, Fu Y, Wang Y, Feng Y, Liu H, Wan X et al (2015) Integrated digital inverters based on two-dimensional anisotropic ReS_2 field-effect transistors. Nat Commun 6:6991
67. Gehlmann M, Aguilera I, Bihlmayer G, Nemsak S, Nagler P, Gospodaric P et al (2017) Direct observation of the band gap transition in atomically thin ReS_2. Nano Lett 17:5187–5192
68. Ho CH, Huang YS, Tiong KK (1999) In-plane anisotropy of the optical and electrical properties of layered ReS_2 crystals. J Phys: Condens Matter 11:5367
69. Ho CH, Huang YS, Tiong KK (2001) In-plane anisotropy of the optical and electrical properties of ReS_2 and $ReSe_2$ layered crystals. J Alloys Compd 222–226
70. Chenet DA, Aslan OB, Huang PY, Fan C, van der Zande AM, Heinz TF et al (2015) In-plane anisotropy in mono- and few-layer ReS_2 probed by Raman spectroscopy and scanning transmission electron microscopy. Nano Lett 15:5667–5672
71. Wolverson D, Crampin S, Kazemi AS, LLie A, Bending SJ (2014) Raman spectra of monolayer, few-layer, and bulk $ReSe_2$: an anisotropic layered semiconductor. ACS Nano 8:11154–11164
72. Feng Y, Zhou W, Wang Y, Zhou J, Liu E, Fu Y et al (2015) Raman vibrational spectra of bulk to monolayer ReS_2 with lower symmetry. Phys Rev B 92:054110
73. Lorchat E, Froehlicher G, Berciaud S (2016) Splitting of interlayer shear modes and photon energy dependent anisotropic Raman response in N-layer ReSe2 and ReS2. ACS Nano 10:2752–2760
74. Liu KK, Zhang W, Lee YH, Lin YC, Chang MT, Su CY et al (2012) Growth of large-area and highly crystalline MoS_2 thin layers on insulating substrates. Nano Lett 12:1538–1544
75. Xia F, Wang H, Jia Y (2014) Rediscovering black phosphorus as an anisotropic layered material for optoelectronics and electronics. Nat Commun 5:4458

76. Pradhan NR, McCreary A, Rhodes D, Lu Z, Feng S, Manousakis E et al (2015) Metal to insulator quantum-phase transition in few-layered ReS_2. Nano Lett 15:8377–8384
77. Corbet CM, McClellan C, Rai A (2015) Field effect transistors with current saturation and voltage gain in ultrathin ReS_2. ACS Nano 9:363–370
78. He X, Liu F, Hu P, Fu W, Wang X, Zeng Q et al (2015) Chemical vapor deposition of high-quality and atomically layered ReS_2. Small 11:5423–5429
79. Keyshar K, Gong Y, Ye G, Brunetto G, Zhou W, Cole DP et al (2015) Chemical vapor deposition of monolayer rhenium disulfide (ReS_2). Adv Mater 27:4640–4648
80. Cui F, Wang C, Li X, Wang G, Liu K, Yang Z et al (2016) Tellurium-assisted epitaxial growth of large-area, highly crystalline ReS_2 atomic layers on mica substrate. Adv Mater 28:5019–5024
81. Li X, Cui F, Feng Q, Wang G, Xu X, Wu J et al (2016) Controlled growth of large-area anisotropic ReS_2 atomic layer and its photodetector application. Nanoscale 8:18956–18962
82. Dathbun A, Kim Y, Kim S (2017) Large-area CVD-grown sub-2V ReS_2 transistors and logic gates. Nano Lett 17:2999–3005
83. Zhang E, Jin Y, Yuan X, Wang W, Zang C, Tang L et al (2015) ReS_2-based field-effect transistors and photodetectors. Adv Funct Mater 25:4076–4082
84. Zhang E, Wang P, Li Z, Wang C, Song C, Huang C et al (2016) Tunable ambipolar polarization-sensitive photodetectors based on high-anisotropy $ReSe_2$ nanosheets. ACS Nano 10:8067–8077
85. Hafeez M, Gan L, Li H (2016) Large-area bilayer ReS_2 film/multilayer ReS_2 flakes synthesized by chemical vapor deposition for high performance photodetectors. Adv Funct Mater 26:4551–4560
86. Shim J, Oh A, Kang DH, Oh S, Jang SK, Jeon J et al (2016) High-performance 2D rhenium disulfide (ReS_2) transistors and photodetectors by oxygen plasma treatment. Adv Mater 28:6985–6992
87. Yang S, Tongay S, Li Y (2014) Layer-dependent electrical and optoelectronic responses of $ReSe_2$ nanosheet transistors. Nanoscale 6:7226–7231
88. Gutiérrez-Lezama I, Reddy BA, Ubrig N, Morpurgo AF (2016) Electroluminescence from indirect band gap semiconductor ReS_2. 2D Mater 3:045016
89. Najmzadeh M, Ko C, Wu K Tongay S, Wu J (2016) Multilayer ReS_2 lateral p–n homojunction for photoemission and photodetection. Appl Phys Express 9:055201
90. Zhao Y, Qiao J, Yu P (2016) Extraordinarily strong interlayer interaction in 2D layered PtS_2. Adv Mater 28:2399–2407
91. Zhao Y, Qiao J, Yu Z, Hu Z, Lin Z, Lau SP et al (2017) High-electron-mobility and air-stable 2D layered $PtSe_2$ FETs. Adv Mater 29:1604230
92. Wang Y, Li L, Yao W, Song S, Sun JT, Pan J et al (2015) Monolayer $PtSe_2$, a new semiconducting transition-metal-dichalcogenide, epitaxially grown by direct selenization of Pt. Nano Lett 15:4013–4018
93. Miró P, Ghorbani-Asl M, Heine T (2014) Two dimensional materials beyond MoS_2: noble-transition-metal dichalcogenides. Angew Chem Int Ed 53:3015–3018
94. Rasmussen FA, Thygesen KS (2015) Computational 2D materials database: electronic structure of transition-metal dichalcogenides and oxides. J Phys Chem C 119:13169–13183
95. Guo GY, Liang WY (1986) The electronic structures of platinum dichalcogenides: PtS_2, $PtSe_2$, and $PtTe_2$. J Phys C: Solid State Phys 19:995
96. Yu X, Yu P, Wu X, Sing B, Zeng Q, Lin H, Zhou W et al (2018) Atomically thin noble metal dichalcogenide: a broadband mid-infrared semiconductor. Nat Commun 9:1545
97. Zhang W, Huang Z, Zhang W, Li Y (2014) Two-dimensional semiconductors with possible high room temperature mobility. Nano Res 7:1731–1737
98. Su TY, Medina H, Chen YZ, Wang SW, Lee SS, Shih YC, Chen CW et al (2018) Phase-engineered $PtSe_2$-layered films by a plasma-assisted selenization process toward all $PtSe_2$-based field effect transistor to highly sensitive, flexible, and wide-spectrum photoresponse photodetectors. Small 14:1800032

99. Wang Z, Li Q, Besenbacher F (2016) Facile synthesis of single crystal $PtSe_2$ nanosheets for nanoscale electronics. Adv Mater 28:10224–10229
100. Yim C, Lee K, McEvoy N, Brien MO, Riazimehr S, Berner NC et al (2016) High-performance hybrid electronic devices from layered $PtSe_2$ films grown at low temperature. ACS Nano 10:9550–9558
101. Ma Y, Dai Y, Guo M (2012) Evidence of the existence of magnetism in pristine VX_2 monolayers (X = S, Se) and their strain-induced tunable magnetic properties. ACS Nano 6:1695–1701
102. Gao D, Xue Q, Mao X, Wang W, Xu Q, Xue D (2013) Ferromagnetism in ultrathin VS_2 nanosheets. J Mater Chem C 1:5909–5916
103. Xu K, Chen P, Li X, Wu C, Guo Y, Zhao et al (2013) Ultrathin nanosheets of vanadium diselenide: a metallic two-dimensional material with ferromagnetic charge-density-wave behavior. Angew Chem Int Ed 52:10477–10481
104. Yang J, Wang W, Liu Y, Du H, Ning W, Zheng G et al (2014) Thickness dependence of the charge-density-wave transition temperature in VSe_2. Appl Phys Lett 105:063109
105. Zhang Z, Niu J, Yang P, Gong Y, Ji Q, Shi J et al (2017) Van der Waals epitaxial growth of 2D metallic vanadium diselenide single crystals and their extra-high electrical conductivity. Adv Mater 29:1702359
106. Zhang H, Liu LM, Lau WM (203) Dimension-dependent phase transition and magnetic properties of VS_2. J. Mater. Chem. A 1:10821–10828
107. Feng J, Sun X, Wu C (2011) Metallic few-layered VS_2 ultrathin nanosheets: High two-dimensional conductivity for in-plane supercapacitors. J Am Chem Soc 133:17832–17838
108. Guo Y, Deng H, Sun X, Li X, Zha J, Wu J et al (2017) Modulation of metal and insulator states in 2D ferromagnetic VS_2 by van der Waals interaction engineering. Adv Mater 29:1700715
109. Li F, Tu K, Chen Z (2014) Versatile electronic properties of VSe_2 bulk, few-layers, monolayer, nanoribbons, and nanotubes: A computational exploration. J Phys Chem C 118:21264–21274
110. Xi X, Zhao L, Wang Z (2015) Strongly enhanced charge-density-wave order in monolayer $NbSe_2$. Nat Nanotechnol 10:765–769
111. Xi X, Berger H, Forró L, Shan J, Mak KF (2016) Gate tuning of electronic phase transitions in two-dimensional $NbSe_2$. Phys Rev Lett 117:106801
112. Sipos B, Kusmartseva AF, Akrap A (2008) From Mott state to superconductivity in 1T-TaS_2. Nat Mater 7:960–965
113. Yu Y, Yang F, Lu XF, Yan YJ, Cho YH, Ma L Gate-tunable phase transitions in thin flakes of 1T-TaS_2. Nat Nanotechnol 10:270–276
114. Navarro-Moratalla E, Island JO, Mañas-Valero S, Pinilla-Cienfuegos E, Castellanos-Gomes A, Quereda J, Rubio-Bollinger G et al (2016) Enhanced superconductivity in atomically thin TaS_2. Nat Commun 7:11043
115. Chen P, Chan YH, Fang XY (2015) Charge density wave transition in single-layer titanium diselenide. Nat Commun 6:8943
116. Li LJ, O'Farrell ECT, Loh KP, Eda G, Ozyilmaz B, Castro Neto AH (2016) Controlling many-body states by the electric-field effect in a two-dimensional material. Nature 529:185–189
117. Sugawara K, Nakata Y, Shimizu R (2015) Unconventional charge-density-wave transition in monolayer 1T-TiSe2. ACS Nano 10:1341–1345
118. Yue R, Barton AT, Zhu H, Azcatl A, Pena LF, Wang J et al (2015) $HfSe_2$ thin films: 2D transition metal dichalcogenides grown by molecular beam epitaxy. ACS Nano 9:474–480
119. Zhou J, Lin J, Huang X, Zhou Y, Chen Y, Xia et al (2018) A library of atomically thin metal chalcogenides. Nature 556:355–359
120. Gong C, Li L, Li Z, Ji H, Stern A, Xia Y et al (2017) Discovery of intrinsic ferromagnetism in two-dimensional van der Waals crystals. Nature 546:265–269
121. Huang B, Clark G, Navarro-Moratalla E, Klein DR, Cheng R, Seyler KL et al (2017) Layer-dependent ferromagnetism in a van der Waals crystal down to the monolayer limit. Nature 546:270–273

Chapter 2
Preparation Methods of Transition Metal Dichalcogenides

Mukulika Dinara and Chandra Sekhar Rout

Abstract During last past decades, a vibrant research on two-dimensional (2D)-layered materials has emerged a significant attention due to their remarkable physical and chemical properties for potential applications in electronics and optoelectronics. Transition metal dichalcogenides (TMDs) represent a group of 2D-layered materials those exhibit versatile properties depending upon their chemical composition and crystallographic orientation. The properties of TMDs can be monitored through various synthesis ways. A lot of attention has been focused to grow 2D TMDs with various novel approaches to get exotic functionalities in nano-scaled material characterizations as well as device applications. The growth strategies of 2D TMDs are mainly classified into top-down approach and bottom-up approach. We study the various synthesis routes on the development of 2D TMDs under both top-down and bottom-up methods. The mechanical exfoliation and liquid-phase exfoliation are the promising techniques under top-down strategies to develop atomically thin flakes TMDs. Due to lack of fine controllability upon growth parameters, the top-down methods are not well populated and applicable for nano-scaled electronics applications. Oppositely under bottom-up strategy, the wet chemical synthesis, vapor-phase deposition, and electrodeposition are well-handling methods with fine-tuning controllability to synthesize thin-layered nanomaterials with high structural quality and low defect density. In this regard, synthesized materials with various fascinating characteristics through bottom-up strategies have more potential functionalities in nano-scaled device applications rather than top-down strategies. The different synthesis routes provide different functionalities materials upon varying their exciting physical and electrical properties due to effect of process parameters and environmental variations. The structural and morphological evolution upon various synthesis routes strongly influences the materials properties. Developing uniform-layered materials with large area is a fundamental part in wafer-scale fabrication for device applications. Various challenges on growth strategies are being explored to enhance

M. Dinara
School of Basic Sciences, Indian Institute of Technology, Bhubaneswar 751013, Odisha, India

C. S. Rout (✉)
Centre for Nano and Material Sciences, Jain University, Jain Global Campus, Ramanagaram, Bangalore 562112, India
e-mail: r.chandrasekhar@jainuniversity.ac.in; csrout@gmail.com

N. S. Arul and V. D. Nithya (eds.), *Two Dimensional Transition Metal Dichalcogenides*,
https://doi.org/10.1007/978-981-13-9045-6_2

materials performance with better uniformity and structural quality for industrial applications. In this study, various processing routes under different process parameters are elaborately stated and discussed with their influence upon the evolution of materials' qualities. The mostly cited and potentially well-known TMDs such as transition metal sulfides and selenides are reported here with their superior properties and qualities through various synthesis techniques.

2.1 Introduction

A lot of attention has been focused on two-dimensional (2D)-layered materials due to their exciting physical and chemical properties. Among various 2D material graphene is one of the most studied materials due to its unique physical and electronic properties. But vibrant research grows a new family of layered materials namely 2D transition metal dichalcogenides beyond graphene to achieve more extraordinary properties suitable for various applications [1, 2]. TMDs materials are composed of two different group of elements like transition metal (M) (groups 4–10) and a chalcogen (X) element such as sulfur (S), selenium (Se), or tellurium (Te).

Unlike graphene, TMDs exhibit various stimulating properties depending upon their compositional variation and variant nature like semiconductor, metal, semimetal, superconductor depending upon crystallographic orientation and stacking sequence in crystal form or thin film formation. So under monitoring the growth condition through various process and parameters, different types of TMD can be grown to perform various operations like sensing, energy storage, energy conversion, catalysis, memory device, etc. In this context, various synthesis processes of TMDs will be discussed along with their corresponding exciting properties owing to their different electronic and physical structures. Various novel approaches to grow 2D TMD with exotic functionalities are being devoted to lead the materials for potential application in electronics and optoelectronics. In this chapter, we discuss the various preparation methods of mostly cited and popular TMDs materials such as MoS_x, $MoSe_x$, WS_x, WSe_x, VS_x, VSe_x, and also some of ternary TMDs.

There are two main strategies namely bottom-up approach and top-down approach involved to develop 2D nanomaterials [3–5]. The top-down approach is applied in macroscopic scale when initial material is in large dimension and the material is externally processed to get nanostructure geometry through different technologies like mechanical exfoliation, wet chemical exfoliation, ball milling, etc. Oppositely, the bottom-up approach is developed in miniaturization of materials up to their atomic level and also large area uniform layer can be governed through self-assembly process through different synthetic techniques like: wet chemical synthesis, chemical vapor deposition (CVD), electrodeposition, etc. Thin-layered nanomaterials with high quality are produced by bottom-up technique that is highly applicable with great electronic properties and defect-free structure for device application. But bottom-up strategies have some limitation in large scale-production due to expensive synthesis procedure.

In contrary, the top-down strategy is easily handled and cheaper than bottom-up strategy but limitation in poor material formation is still a great challenge for industrial application. Now we will discuss the 2D TMD preparation through both bottom-up and top-down approaches by various methods like mechanical exfoliation, wet chemical exfoliation, chemical vapor deposition, wet chemical synthesis, and electrodeposition. Moreover we will study the different processes with their different parameters which are involved to influence structure evolution and morphological variation of synthesis materials.

2.2 Top-Down Approach

2.2.1 Mechanical Exfoliation Method

The mechanical exfoliation method is a top-down approach to create single or few layers crystal or single or few layer crystalline flakes materials from layered bulk crystals that become commonly used for 2D TMD [6–9]. But the limitations to prepare the TMDs with desired thin film geometry and better efficiency have restricted the method for reliable large area research. Noteworthy the large area TMD preparation through this method is still challenging. Various researchers reported on mechanical exfoliation method to prepare single and multilayer MoS_2 and WSe_2 with high crystalline quality [10, 11]. Typically in this process, a desired TMD layer is peeled off from its bulk crystal by an adhesive scotch tape. The newly cut TMD crystal on scotch tape is further attached in contact with the target substrate and rubbed to achieve desired geometry by using a plastic tweezers. Once the scotch tape is removed, the TMD nanosheets of one layer and multilayer are formed on the substrate.

Figure 2.1 shows the formation of MoS_2 of 1L (monolayer) to 4L (quadruple-layer) on SiO_2-coated Si substrate [12]. Also atomic force microscopy shows the height of respective layers of MoS_2 nanosheets which are 0.8, 1.5, 2.1, and 2.9 nm for 1L to 4L, respectively. Here the optical contrast difference is introduced to identify the layer numbers of mechanically exfoliated TMD nanosheets. Optically identification of the number of TMD layer formation is a key technology that correlates the optical contrast between the layer numbers with respect to the substrate. In this method, the optical contrast of nanosheets (C) and optical contrast of the substrate (CS) can be directly analyzed from its color optical image through ImageJ software. The contrast difference (CD) is obtained by subtracting C from CS. Likewise, for grayscale optical image that comes from the R, G, or B channel, the contrast difference from R, G, or B channel (CDR, CDG, or CDB) is evaluated from the difference of the contrast of nanosheet (CR, CG, or CB) and the contrast of substrate (CSR, CSG, or CSB).

Li et al. [13] studied how to find out the number of nanosheets formation on thick substrate through a contrast optical imaging between grown nanosheets and substrate. Figure 2.2 shows the optical image of 1L-15L MoS_2 nanosheets on 90 nm

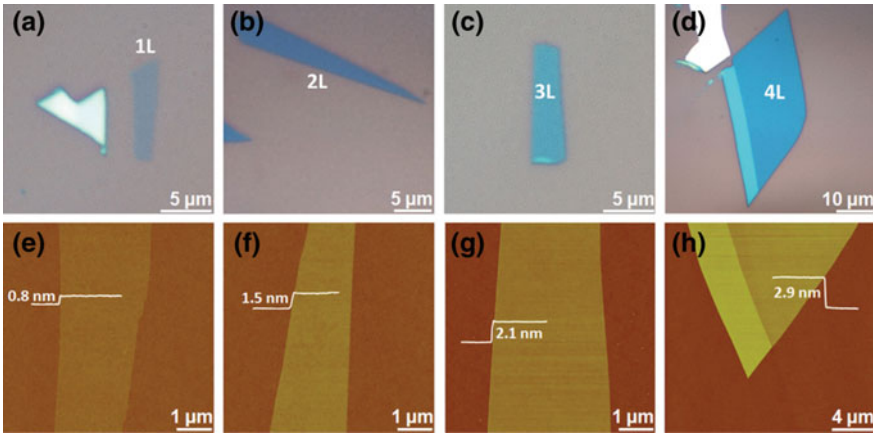

Fig. 2.1 Mechanically exfoliated single and multilayer MoS_2 films on Si/SiO_2. Optical microscope images of single-layer (1L), bilayer (2L), trilayer (3L), and quadrilayer (4L) MoS_2 films (**a**–**d**). Panels **e**–**h** show the corresponding AFM images of the 1L (thickness: ≈0.8 nm), 2L (thickness: ≈1.5 nm), 3L (thickness: ~2.1 nm), and 4L (thickness: ~2.9 nm) MoS_2 films shown in **a**–**d** [12]. Copyright 2012. Reproduced with permission from Wiley-VCH Verlag GmbH

coated Si substrate. The various exposure times were taken to evaluate thickness-dependent contrast difference (shown in Fig. 2.2o, p) that was further verified by AFM (Fig. 2.2q) [13].

2.2.2 Liquid Exfoliation Method

The liquid-phase exfoliation is one of the promising exfoliation techniques to prepare exfoliated TMD nanosheets in large scale. Liquid exfoliation method as a top-down approach exploits to prepare layered TMD nanocomposites and hybrids by mixing and dispersing of different materials [14, 15]. In 1070s, the intercalation method was first demonstrated through a typical procedure where bulk TMD powder was dispersed into lithium compound-based solution for more than a day to allow lithium ions to intercalate to water [16]. The single-layer WS_2, MoS_2, and $MoSe_2$ have been demonstrated by lithium intercalation method [17]. Zeng et al. [18] demonstrated the electrochemical lithiation of layered TMDs: MoS_2, WS_2, TiS_2, TaS_2, ZrS_2. The schematic view of the electrochemical lithiation process is shown in Fig. 2.3.

In this process, the bulk materials of corresponding TMDs were introduced as cathode in electrochemical bath (Step 1 in Fig. 2.4) and lithium foil as an anode functioned to provide lithium ions. Then under galvanostatic discharge mode, lithium intercalation process was done at current density of 0.05 mA. After lithium insertion, the intercalated compound (e.g., Lix(TMD)) was isolated by successive rinsing procedure with acetone and sonication method (Step 2 in Fig. 2.4). Finally 2D nanosheets

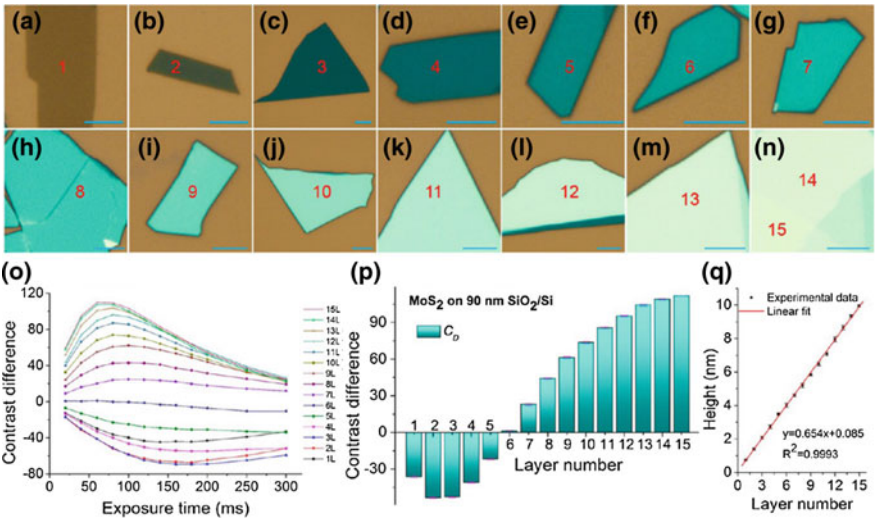

Fig. 2.2 **a**–**n** Color optical images of 1L–15L MoS_2 nanosheets on 90 nm SiO_2/Si. The scale bar is 5 μm for each image. The digitals shown in **a**–**n** indicate the layer numbers of corresponding MoS_2 nanosheets. **o** Plot of measured CD values of 1L-15L MoS_2 nanosheets on 90 nm SiO_2/Si at exposure times of 20, 40, 60, 80, 100, 120, 140, 160, 180, 200, 250, and 300 ms. **p** Plot of CD values of 1L-15L MoS_2 on 90 nm SiO_2/Si at exposure time of 80 ms. **q** Thickness of 1L-15L MoS_2 nanosheets measured by AFM [13]. Copyright 2013. Reproduced with permission from American Chemical Society

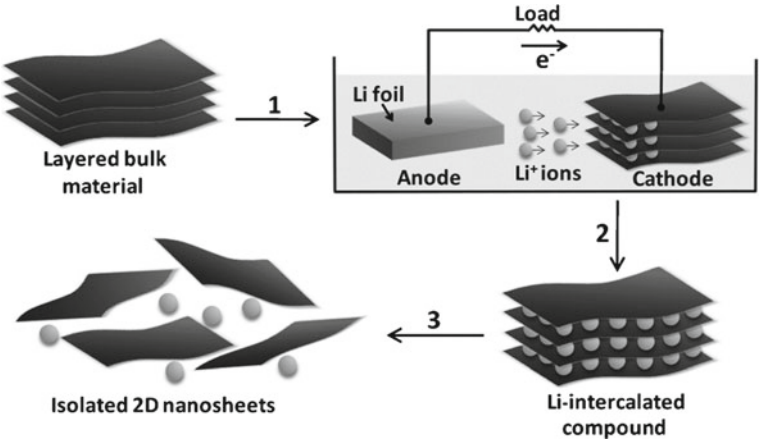

Fig. 2.3 Electrochemical lithiation process for the fabrication of 2D nanosheets from the layered bulk material [18]. Copyright 2011. Reproduced with permission from Wiley-VCH Verlag GmbH

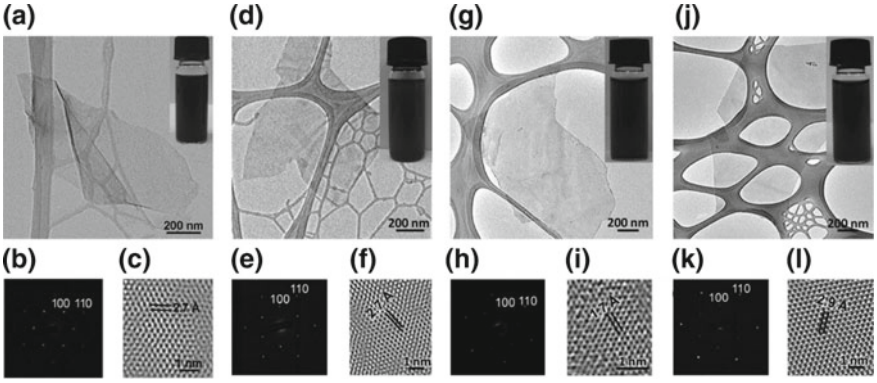

Fig. 2.4 **a** TEM image of a typical MoS_2 nanosheet. Inset: Photograph of the MoS_2 solution. **b** Selected area electron diffraction (SAED) pattern of a single-layer MoS_2 nanosheet. **c** HRTEM image of single-layer MoS_2 nanosheet. **d** TEM image of a typical single-layer WS_2 nanosheet. Inset: Photograph of the WS_2 solution. **e** SAED pattern of a single-layer WS_2 nanosheet. **f** HRTEM image of a single-layer WS_2 nanosheet. **g** TEM image of a typical single-layer TiS_2 nanosheet. Inset: Photograph of a TiS_2 solution. **e** SAED pattern of a single-layer TiS_2 nanosheet. **h** HRTEM image of a single-layer TiS_2 nanosheet. **i** TEM image of a typical single-layer TaS_2 nanosheet. Inset: Photograph of the TaS_2 solution. **j** SAED pattern of a single-layer TaS_2 nanosheet. **k** HRTEM image of single-layer TaS_2 nanosheet [18]. Copyright 2011. Reproduced with permission from Wiley-VCH Verlag GmbH

of corresponding TMDs were obtained (Step 3 in Fig. 2.4). Importantly here lithium plays dual roles by providing Li+ ions for intercalation with bulk materials and by reducing Li(OH) and H_2 gas after reaction with water that phenomena assist the exfoliated nanosheets to apart from water.

In another example, Eda et al. [19] reported chemically exfoliated two-dimensional MoS_2 crystal structure which exhibited thickness of 1–1.2 nm and lateral dimensions of 300–800 nm (Fig. 2.5).

Li intercalation exhibited poor semiconducting nature of MoS_2 film due to rise of a metallic nature and also exfoliated film showed inherent monolayer of non-homogeneous nature due to partial aggregation. Particularly, after exfoliation electronic structure of MoS_2 is changed from semiconducting to metallic and atomic coordination is changed from trigonal prismatic to octahedral [17, 19–21].

Smith et al. [15] reported a large quantity of MoS_2 flakes formation by intercalation route where MoS_2 was viewed in a small number of stacked monolayers (Fig. 2.6). MoS_2 flakes in stacked form consisted of 2–9 monolayer and the length of the flake remained in the range of 280 nm to maximum 430 nm.

The basic advantage of Li intercalation method is fast charge transfer rate and controllable process that yield large-scaled monolayer. The Li intercalation is to be carried out under inert gas environment due to flammability nature of Li. Liquid exfoliation is insensitive to ambient conditions, but it yields a relatively low concentration of monolayer flakes [14]. For electronic or photonic applications, liquid exfoliation is not well suited. After subsequent annealing ion exfoliated nanosheets

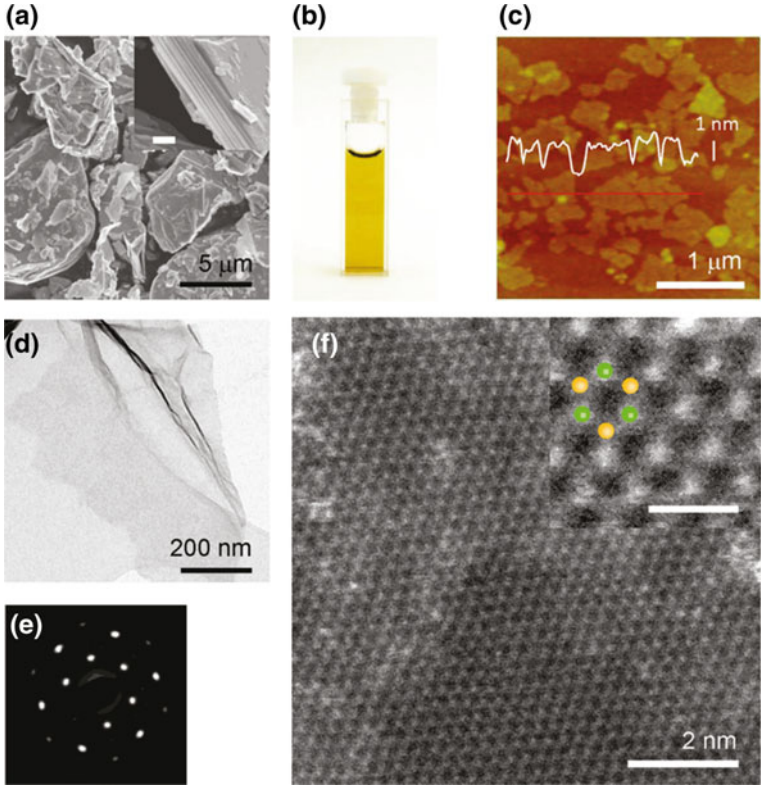

Fig. 2.5 **a** Scanning electron microscopy image of MoS_2 powder. Inset shows higher magnification image of the layered structure. The scale bar is 400 nm. **b** Photograph of a typical chemically exfoliated MoS_2 suspension in water. **c** AFM image of individual exfoliated MoS_2 sheets after annealing at 300 °C. Height profile along the red line is overlaid on the image. The sample was prepared by filtering a small volume (~3 mL) of dilute MoS_2 suspension to minimize overlap between individual sheets. The resulting film was non-homogeneous due to partial aggregation. Regions of the sample where the sheets were isolated were imaged for step height analysis. **d** TEM image of an as-deposited MoS_2 sheet on holey carbon grid. **e** SAED pattern from the MoS_2 sheet in (**d**) showing the hexagonal symmetry of the MoS_2 structure. **f** HAADF STEM image of monolayer MoS_2 annealed at 300 °C in Ar. Inset is a blow-up image showing individual Mo (green dot) and S (orange dot) atoms and their honeycomb arrangement. The scale bar is 0.5 nm. The white blur on the surface of the sheet is possibly due to carbon residues from the intercalation and exfoliation processes [19]. Copyright 2011. Reproduced with permission from American Chemical Society

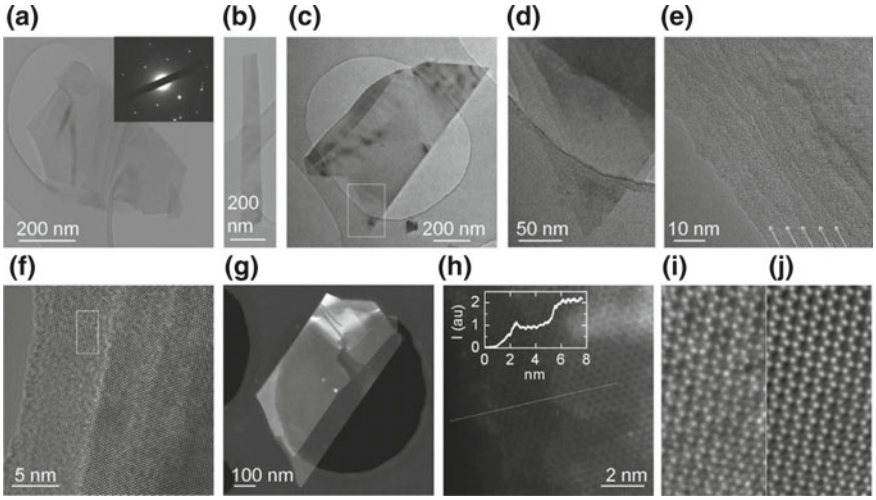

Fig. 2.6 TEM of MoS_2 flakes. **a–c** Typical bright field TEM images of MoS_2 flakes. Inset in (**a**): Typical electron diffraction pattern. **d** A zoomed bright field image of the region in (**c**) indicated by the white square showing layer edges. **e**, **f** Phase contrast HRTEM images of thin MoS_2 flakes showing layer edges. **g** Dark field scanning TEM image of a thin flake clearly illustrates the step edges. **h** An unfiltered aberration corrected high-angle annular dark field (HAADF) STEM image. The HAADF STEM detector was calibrated in units of primary electrons detected. This has enabled quantitative interpretation of *Z*-contrast STEM images and the counting statistics of the signal. Inset: Average signal intensity plotted over the dashed line. **i** A zoomed image of the region in (**f**) indicated by the white square showing the MoS_2 atomic structure. **j** A digitally filtered (low-pass fast Fourier transform (FFT) with spot masking and a 25-point smoothing) image of the marked region in (**f**) clearly showing defect-free hexagonal symmetry [15]. Copyright 2011. Reproduced with permission from Wiley-VCH Verlag GmbH

might be useful in electronics application. But to prepare composite materials in large scale liquid exfoliation will be mostly preferred in rational need.

Interestingly a new approach as a liquid exfoliation technique has been demonstrated to synthesize selenide from aqueous solution by using formic acid which acts as a reducing agent followed by co-reduction process. Remarkably, the HCOOH-reduction route could be applied to prepare other selenide material from aqueous solution like: SnSe, Ag_2Se, CdSe, NiSe, PbSe, and ZnSe [22]. Xu et al. [22] have been reported the VSe_2 synthesis through the same reduction procedure and the synthesized VSe_2 showed 2D ultrathin nanosheets structure with 4–8 Se-V-Se atomic layers. This reduction route also paves a great attention to avoid any expensive organic solvents or high toxic VCl_4 reagent.

2.3 Bottom-up Approach

2.3.1 Wet Chemical Process

Solution-phase reaction offers a synthetic chemistry at low temperature compared to vapor-phase reaction route and provides sophisticated nanostructures like quantum dot, nanorod, nanoparticles, etc. of specific geometry by controlling various process parameters in a predictable manner. The synthesized high quality nanostructured in solution route tailor more surprising properties at low cost that especially attractive for potential application in electronics and optoelectronics. Wet chemical process is a potentially active top-down approach for an alternative of exfoliation route that significantly gives rise to achieve high-purity nanostructured material under proper choice of source materials. Typically wet chemical process offers to direct growth kinetics in a specific direction, i.e., when lateral growth is governed, vertically growth is truncated [23–25].

Generally low-temperature hydrothermal synthesis of TMDs (NiS_2, CoS_2, FeS_2, $NiSe_2$, MoS_2, and $MoSe_2$) has been carried out through sulfurization and selenization reaction between corresponding metal salt and $Na_2S_2O_3$ or Na_2SeSO_3 respectively at ~140 °C [26].

Bilayer MoS_2 nanosheet was reported through a facile hydrothermal route under 2:1 molar ratio of S:Mo at 180 °C for 50 h with sources:ammonium molybdate ($(NH_4)_6Mo_7O_{24},4H_2O$) and sulfur (S) powders [25]. When MoS_2 crystals are exfoliated to monolayer or few thin layer, then some exciting characteristics are emerged like photoluminescence, band gap change, surface area modulation, etc. Splendiani et al. **[**27**]** have reported a surprising characteristic of MoS_2, i.e., change of band gap from indirect to direct upon formation of multilayer to monolayer. Ye et al. [28] reported bilayer MoS_2 nanosheets that show strong photoluminescence spectra from 650 to 850 nm which potentially used in photo-devices. Correspondingly nanosheets structure of MoS_2 exhibited large specific surface area and high adsorption capacity which can give the material to perform as a photochemical catalyst. The above-synthesized MoS_2 nanosheets showed a wrinkled- uneven sheet-like structure (shown in FESEM image) (Fig. 2.7a, b) [28]. Wet chemically synthesized MoS_2 exhibited a well-defined crystal structure with lattice spacing of 0.28 and 0.64 nm across (10 0) and (0 0 2) plane of MoS_2 nanosheets, respectively that have been clearly distinguished by lattice fringe pattern in HRTEM image (Fig. 2.7c) [28].

A novel morphology of MoS_2 with hierarchical nanospheres was reported by hydrothermal treatment with source reagents like sodium fluoride (NaF), molybdenum trioxide (MoO_3), and potassium thiocyanate (KSCN) [29]. The synthesis was performed into sealed autoclave at 220 °C for 48 h. MoS_2 nanospheres have been shown by FESEM and TEM images (Fig. 2.8) under different magnifications. Javed et al. [29] in their study reported that the hierarchical nanospheres exhibit high specific area and porosity that give rise to increase the capacitance value as well as energy and power density of the material. This exciting morphology of MoS_2 through wet

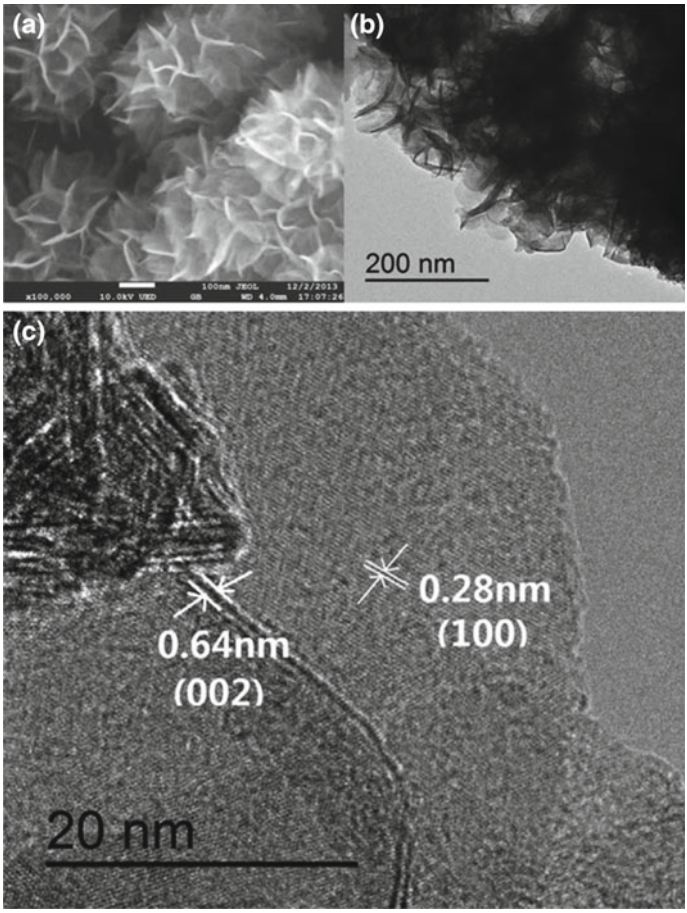

Fig. 2.7 **a** FESEM, **b** TEM, and **c** HRTEM images of MoS_2 prepared by using stoichiometric S and Mo precursors through hydrothermal processing for 50 h [28]. Copyright 2014. Reproduced with permission from Elsevier

chemical route establishes the potentially active structure for supercapacitor application.

Shelke et al. [30] reported hydrothermal synthesis of WS_2 by using WCl_6 and thioacetamide. The source materials were dissolved in 40 ml DI water under continuous stirring for 1 h at room temperature. Then the solution was transferred into stainless steel autoclave and sealed to keep it at 265 °C for 24 h. Finally, the solid products were centrifuged and washed repeatedly with deionized water and ethanol for few minutes and dried in vacuum.

The 1T phase WS_2 of metallic characteristics was prepared through hydrothermal route via direct vacuum filtration technique. In this method, 0.25 mmol of ammonium tungsten oxide hydrate $(NH_4)_6H_2W_{12}O_{40}{\cdot}xH_2O$ and 10 mmol thiourea were

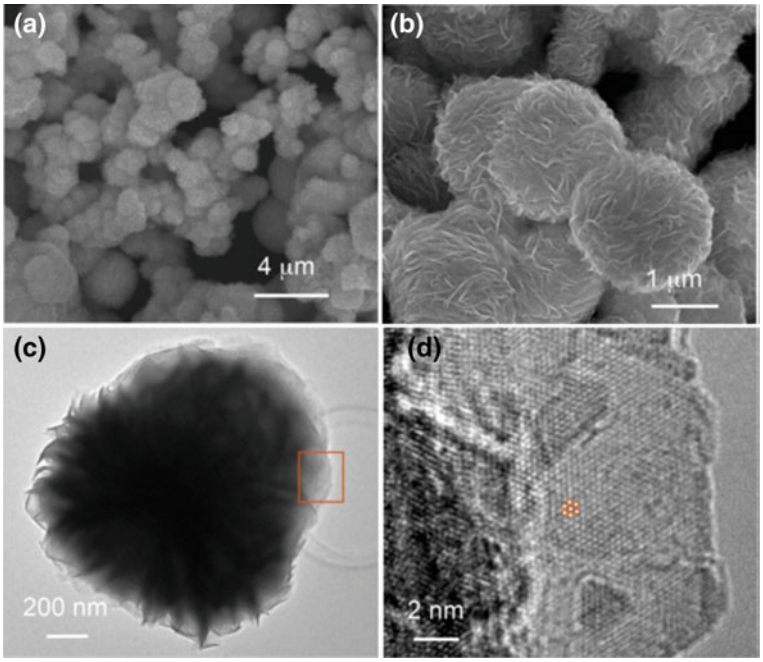

Fig. 2.8 SEM and TEM images of the synthesized MoS_2 spheres. **a** low and **b** high magnification SEM images, **c** low **d** high-resolution TEM images. [29]. Copyright 2015. Reproduced with permission from Elsevier

dissolved in 30 ml of deionized water under continuous stirring to prepare homogeneous solution [31]. Meanwhile, as a catalyst 2.25 mmol $H_2C_2O_4{\cdot}2H_2O$ was added to the solution and adjusted the pH to 2. Subsequently, the above solution was transferred into a Teflon-lined stainless steel autoclave and sealed to keep it at 220 °C for 48 h. After cooling at room temperature, the solid product was centrifuged (at 5000 rpm for 20 min) and washed repeatedly with deionized water and ethanol for few minutes and dried in vacuum (at 60 °C for overnight). The surface morphology of grown WS_2 nanosheets was observed in SEM and TEM images (Fig. 2.9). The hydrothermally grown WS_2 nanosheets showed a uniform flowerlike structure with diameter of 4–6 μm (Fig. 2.9b). Figure 2.9c revealed that each flower unit was consisted of hundreds of WS_2 nanosheets. The TEM image showed the irregular cycle shape and ripple structure of as-grown WS_2 nanosheets indicates the flexible and ultrathin structure of WS2 nanosheets. The high-resolution TEM image (Fig. 2.9e) showed layered WS_2 flakes structure with an interlayer spacing of ~9.2 Å. The chemical composition of the as-grown WS_2 was confirmed by EDS analysis (Fig. 2.9f). Interestingly Cao et al. [32] reported a flowerlike WS_2 nanospheres synthesis through facile hydrothermal route where the nanospheres have formed into numerous aggregate with uniform sizes. As a surfactant cetyltrimethylammonium bromide (CTAB) was used to endorse as well as accelerate the formation of flowerlike nanosheets.

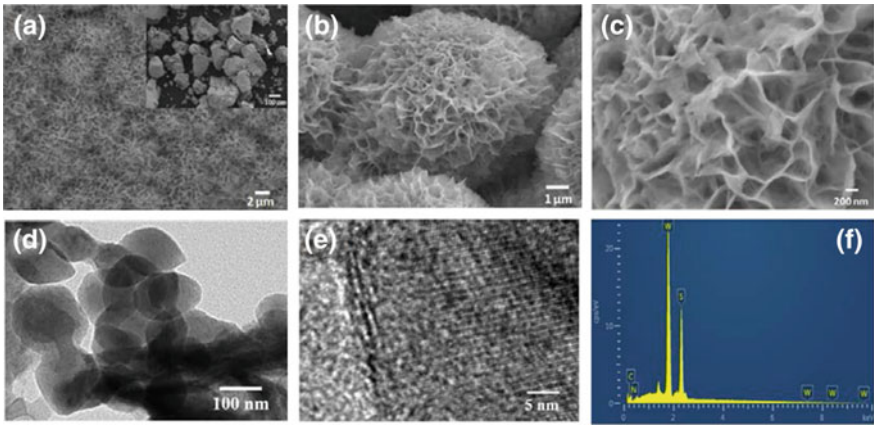

Fig. 2.9 **a** Typical SEM image of surface morphology of as-prepared 1T phase WS_2 nanosheets, inset: SEM image of macroscopic powder; **b** SEM image of uniform flowerlike unit; **c** Amplification of the SEM image of the flowerlike unit; **d** low-magnification TEM image of 1T phase WS_2 nanosheets; **e** HRTEM image of 1T phase WS_2 nanosheets; **f** EDS spectrum for chemical component analysis [31]. Copyright 2017. Reproduced with permission from Institute of Physics

The synthesis WS_2 through facile surfactant-assisted hydrothermal route shows excellent visible-absorption ability that promotes it to perform as a visible photocatalyst. The experimental synthesis was performed by using sodium tungstate (Na_2WO_4, $2H_2O$), hydroxylamine hydrochloride (NH_2OH, HCl), sulfourea (CH_4N_2S), and CTAB dissolved in deionized water under continuous stirring. The pH value of the solution was adjusted to 6 by adding hydrochloric acid (HCl) or ammonia water (NH_3, H_2O). Then the final mixture was transferred into autoclave for heating and then washed and dried as mentioned previously.

The pure phase WS_2 and well-stacked WS_2 formation through surfactant-assisted hydrothermal route was scrutinized through XRD analysis which was confirmed by sharp peak around (002) plane. Moreover well WS_2 nanoflowers formation was displayed by SEM image under low (b) and high magnification mode (c). The SEM image (Fig. 2.10) showed the WS_2 nanoflowers consisted of well-ordered nanospheres like nanosheets with 5 µm diameter that are uniformly arranged throughout the crystals [32].

VS_2 preparation under hydrothermal mode has been performed by using sodium orthovanadate (Na_3VO_4, $12H_2O$) and thioacetamide (TAA) as a source material and carried out the synthesis process at 160 °C for 24 h into an autoclave setup [33]. Interestingly Liu et al. [34] examined morphological variation of grown VS_2 with synthesis temperature (140–200 °C).

Importantly it was noticed that VS_2 nanoparticles size has been increased with increasing temperature and also morphology has been changed from nanoparticles to nanosheet or nanobar (Fig. 2.11a–d). This observation signifies that crystalline VS_2 growth could be obtained under high reaction temperature process.

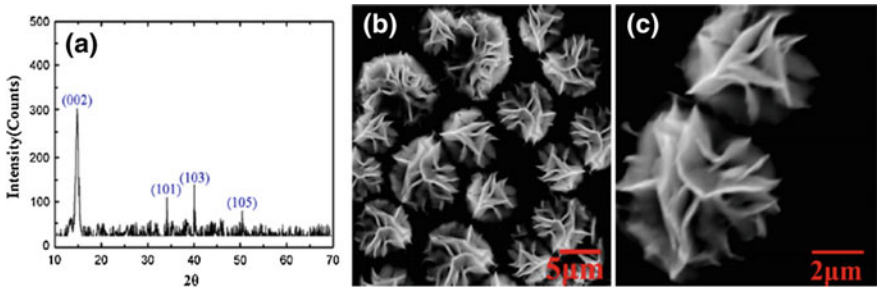

Fig. 2.10 **a** XRD patterns and **b**, **c** SEM image of the flowerlike WS_2 nanospheres [32]. Copyright 2014. Reproduced with permission from Springer Nature

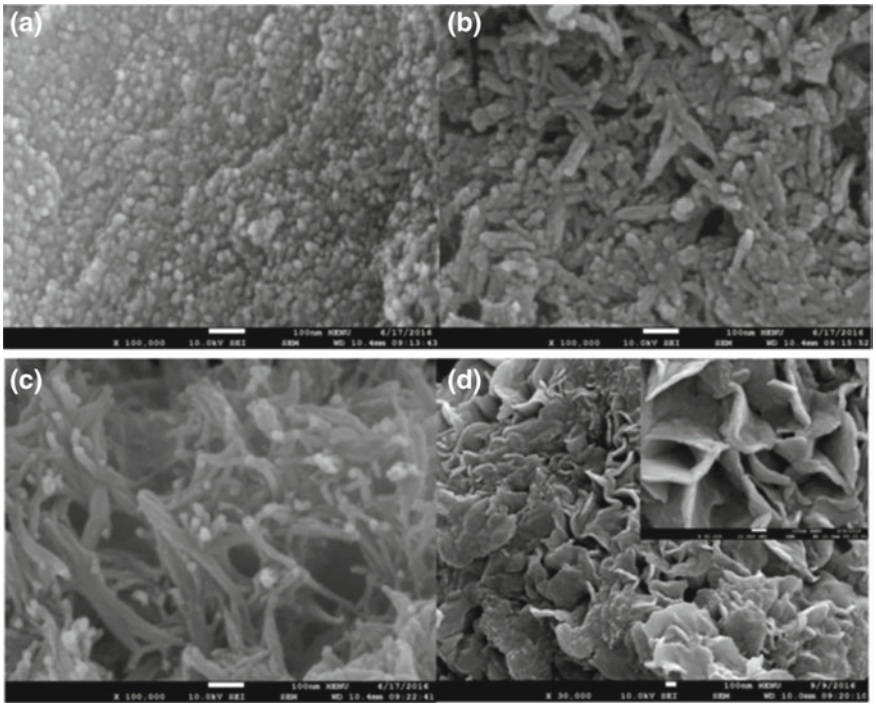

Fig. 2.11 SEM images of VS_2 obtained at **a** 140, **b** 160, **c** 180, and **d** 200 °C [34]. Copyright 2017. Reproduced with permission from Royal Society of Chemistry

Traditionally different approaches in hydrothermal synthesis were carried out to prepare cobalt sulfide of different morphological forms in nanoscale [35, 36]. Co_3S_4 nanocrystal was synthesized by adding $Co(CH_3COO)_2$, $4H_2O$ and thioglycolic acid into 200 mL distilled water under constant stirring for 30 min [36]. Then the desired product was successfully formed through a successive heating, washing, and drying process as mentioned in earlier hydrothermal processes.

Currently, hierarchical hybrid nanostructures have taken a great attention for high-performance electrode material for supercapacitor application. The hierarchical cobalt sulfide as an active electrode material for supercapacitor has been successfully synthesized by vapor-phase hydrothermal route where cobalt chloride hexahydrate ($CoCl_2{\cdot}6H_2O$), urea ($CO(NH_2)_2$), sodium sulfide ($Na_2S{\cdot}9H_2O$), potassium hydroxide (KOH), hydrochloric acid (HCl), and absolute ethanol have been used as reagents to conduct the synthesis [37]. This hierarchical cobalt sulfide was formed in two steps: Initially cobalt basic salt nanowires were formed by adding $CoCl_2{\cdot}6H_2O$ (0.952 g, 4 mmol) and urea (1.201 g, 20 mmol) in 40 mL deionized under constant stirring until a pink homogeneous solution was obtained. Afterward, the above solution and clean nickel foam were moved into a 50 mL Teflon-lined stainless steel autoclave and followed the heat treatment at 95 °C for 8 h. Then after cooling the autoclave at room temperature, the successfully developed nickel foam-coated cobalt nanowires were rinsed with deionized water and dried at 60 °C for 2 h.

Moreover cobalt sulfide/cobalt nanocomposite has been developed on cobalt nanowire-coated nickel foam into sodium sulfide solution and the mixed solution was kept into Teflon-lined stainless steel autoclave to carry thermal reaction at 125 °C for 2 h. Subsequently autoclave solution was cooled down at RT naturally. The resulted hierarchical cobalt sulfide/cobalt nanocomposite on nickel foam was rinsed with DI and ethanol for several times and dried under vacuum at 60 °C for 2 h. The morphology of grown cobalt sulfide/cobalt nanocomposite was shown by SEM and TEM images (Fig. 2.12) that consist of nanowire of several micrometer lengths with 50–70 nm diameters. Liu et al. [37] reported in their study that the hierarchical structure cobalt sulfide-based nanocomposite performs as a more potentially active electrode material than other cobalt basic salt nanowires for supercapacitor owing to its higher specific capacitances, better rate capability, and excellent cycling stability.

A ternary nickel cobalt sulfide was reported with unique architecture by various research groups through wet chemical method. Chen et al. [38] reported $NiCo_2S_4$ nanotube arrays on Ni foam by hydrothermal treatment via two steps process shown schematically in Fig. 2.13.

At first step, $CoCl_2{,}6H_2O$, $NiCl_2{,}6H_2O$ and urea were mixed into deionized water to prepare in situ $NiCo_2(CO_3)_{1.5}(OH)_3$ nanowire. The in situ growth has been carried by hydrothermal treatment of Ni^{2+} and Co^{2+} ion. Then mixed solution was heated at 120 °C for 6 h to get $NiCo_2$ $(CO_3)_{1.5}(OH)_3$ nanowire arrays. In second step, $NiCo_2S_4$ nanotube arrays were synthesized by hydrothermal treatment of $NiCo_2(CO_3)_{1.5}(OH)_3$ nanowire with $Na_2S{,}9H_2O$ at 160 °C for 6 h. In this process, ion-exchange reaction takes an important part to grow various types of nanoparticles and nanotubes. Likewise ion exchange between S^{2-} and $CO_3{}^{2-}$ and OH^- of $NiCo_2(CO_3)_{1.5}(OH)$ takes a fundamental role to form $NiCo_2S_4$ nanowire and as by-products CO_2 and H_2O were

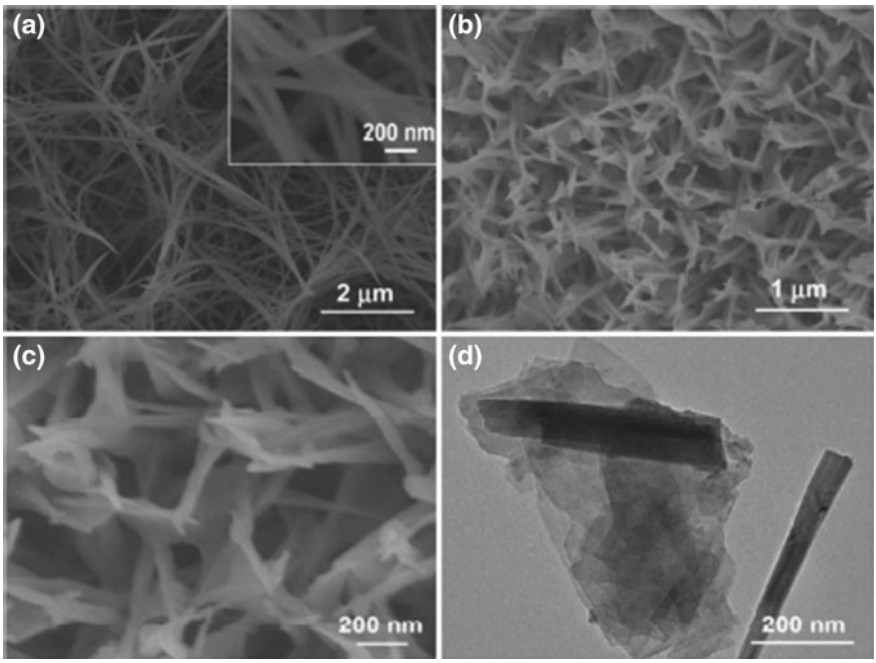

Fig. 2.12 **a** SEM image of the cobalt basic salt nanowires, inset in (**a**) is an enlarged SEM image; **b**, **c** SEM images, **d** TEM image of the cobalt sulfide/cobalt basic salt nanocomposite [37]. Copyright 2017. Reproduced with permission from Royal Society of Chemistry

formed. Typically a continuous ion exchange occurred through diffusion process from the inner $NiCo_2(CO_3)1.5(OH)_3$ nanowire to the surface of as-grown $NiCo_2S4$.

In another report, Cai et al. [39] reported a uniform hybrid nickel cobalt sulfide ($NiCo_2S_4$) nanoparticles attached with reduced graphene oxide (RGO) nanosheets through wet chemical reaction with $Ni(Ac)_2{\cdot}4H_2O$ and $Co(Ac)_2{\cdot}4H_2O$ in a molar ratio 2:1. Interestingly Wu et al. [40] reported a one-step hydrothermal route to prepare nickel cobalt sulfide-reduced graphene oxide (rGO) by $Ni(OAc)_2{\cdot}6H_2O$ and $Co(OAc)_2{\cdot}6H_2O$ aqueous solution that was further mixed with a GO aqueous solution under continuous magnetic stirring.

Further Chen et al. [41] reported nickel cobalt sulfide (NCS) hollow spheres formation through hydrothermal-sulfurization process. In this method, initially nickel cobalt precursors (NCP) have been synthesized by a facile solvothermal method in submicron-sized spheres. Then subsequent sulfurization has changed the NCP to porous structured based nickel cobalt sulfide. Importantly, the geometry of hollow spheres can be tuned by different amount of sulfur source that purposely introduced. NCP preparation was carried out by $Ni(NO_3)_2{\cdot}6H_2O$ and $Co(NO_3)_2{\cdot}6H_2O$ those were dissolved in isopropanol (IPA) under magnetic stirring and also followed by introducing of ethylene glycol (EG). Subsequently sufurization into hydrothermal process was done by adding Na_2S.

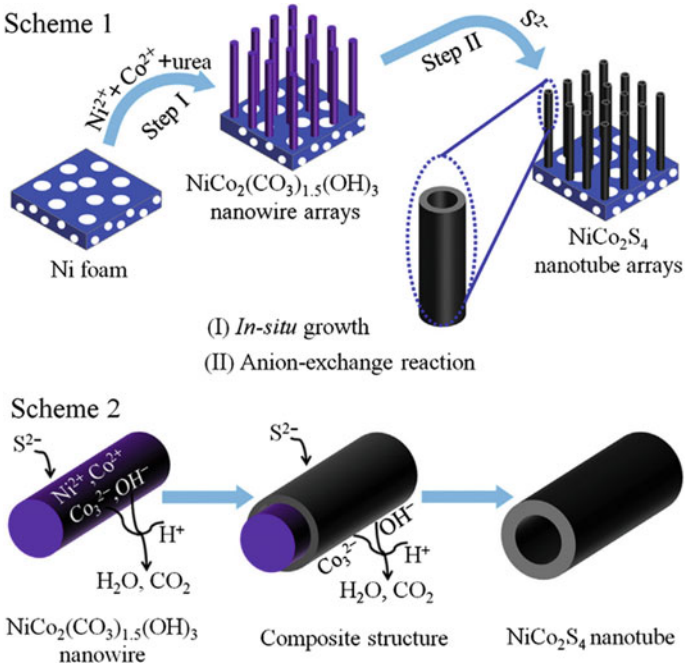

Fig. 2.13 Schematic of the formation of $NiCo_2S_4$ nanotube through the anion-exchange reaction of the $NiCo_2(CO_3)_{1.5}(OH)_3$ nanowires with S^{2-} [38]. Copyright 2014. Reproduced with permission from Elsevier

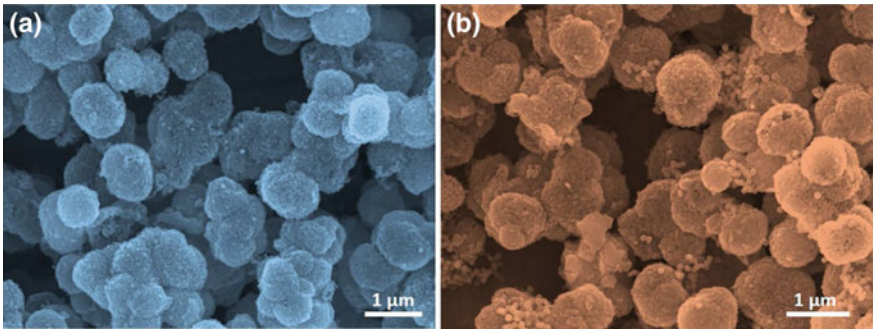

Fig. 2.14 FESEM images of NCS 1 and NCS 2 [41]. Copyright 2016. Reproduced with permission from Nature

Coreshell (NCS 1) and hollowed colloids (NCS 2) structures were formed by introducing different amount of Na_2S like 60 and 120 mg and corresponding FESEM images are shown in Fig. 2.14a, b [40].

Selenization of various transition metals into hydrothermal route is being explored to get various exciting and interesting characteristics at nanoscale. $MoSe_2$ flowerlike

nanostructures were synthesized by a facile hydrothermal method. In this method, sodium molybdate (Na_2MoO_4) and selenium (Se) powder were used as precursors materials in a stoichiometric amount that was placed into a stainless steel autoclave of 50 ml capacity [42]. Then a hydrazine hydrate (N_2H_4, H_2O) and DI water were added under specific amount into the solution and the pH value was adjusted at 12 with introducing NaOH. Then autoclave was sealed to follow the heating process at 180 °C for 48 h. After cooling the autoclave, a black precipitate was obtained and followed by successive treatment like washing drying to get $MoSe_2$ nanostructured materials.

Another report was done on 3D hierarchical flowerlike $MoSe_2$ microspheres formation by wet chemical method via a three-stage growth process like nucleation, oriented aggregation, and self-assembly growth. Tang et al. [43] synthesized $MoSe_2$ nanoflowers by using precursors reagents $Na_2MoO_4{\cdot}2H_2O$, Se, and $NaBH_4$ through hydrothermal treatment at 200 °C by varying reaction time from 6 h to 48 h. Till now synthesis of $MoSe_2$ self-assembled nanostructures remains a great challenge upon controlling the reaction time. Tang et al. reported a morphological evolution by increasing the reaction time. Initially when growth time was taken for 1 h, the $MoSe_2$ nanoparticles were formed of diameter 5–10 nm. Afterward the reaction time was increased to 6 h, the sheet-like nanostructures were formed and by further increase of time to 12 h flowerlike nanostructures were formed by assembling of many nanosheets without existence of any nanoparticles.

Finally when reaction time was prolonged to 48 h, then the nanosheets were assembled gradually into perfect crystalline flowerlike microspheres. The uniform flowerlike morphology of as-prepared $MoSe_2$ was shown by SEM, TEM, and HRTEM images (Fig. 2.15). The uniform flowerlike microspheres (Fig. 2.15a, b) showed the structure of mean diameter about 1.0 μm and each microsphere was consisted of numbers of nanosheets with thickness of 20 nm (Fig. 2.15c). A clear lattice fringe pattern of $MoSe_2$ was observed in HRTEM image which showed hexagonal $MoSe_2$ phase in (100) plane with lattice spacing was about 0.28 nm (Fig. 2.15d). The above synthesis process can be explained by ion reaction mechanism shown by Eqs. (2.1)–(2.4) where Se may well reduce to NaHSe by reaction between Se, H_2O and $NaBH_4$. Correspondingly MoO_4^{2-} may well reduce to Mo^{4+} through ion reaction between Na_2MoO_4, H_2O and $NaBH_4$. Consequently reduced Mo^{4+} and Se^{2-} got reaction with each other and formed $MoSe_2$ nanocrystals [43].

$$2Se + 4BH_4^- + 7H_2O \rightarrow 2HSe^- + B_4O_7{}^{2-} + 14H_2 \tag{2.1}$$

$$4MoO_4{}^{2-} + BH^{4-} + 10H_2O \rightarrow 4Mo^{4+} + BO^{2-} + 24OH \tag{2.2}$$

$$HSe^- + OH^- \rightarrow H_2O + Se^{2-} \tag{2.3}$$

$$Mo^{4+} + 2Se^{2-} \rightarrow MoSe_2 \tag{2.4}$$

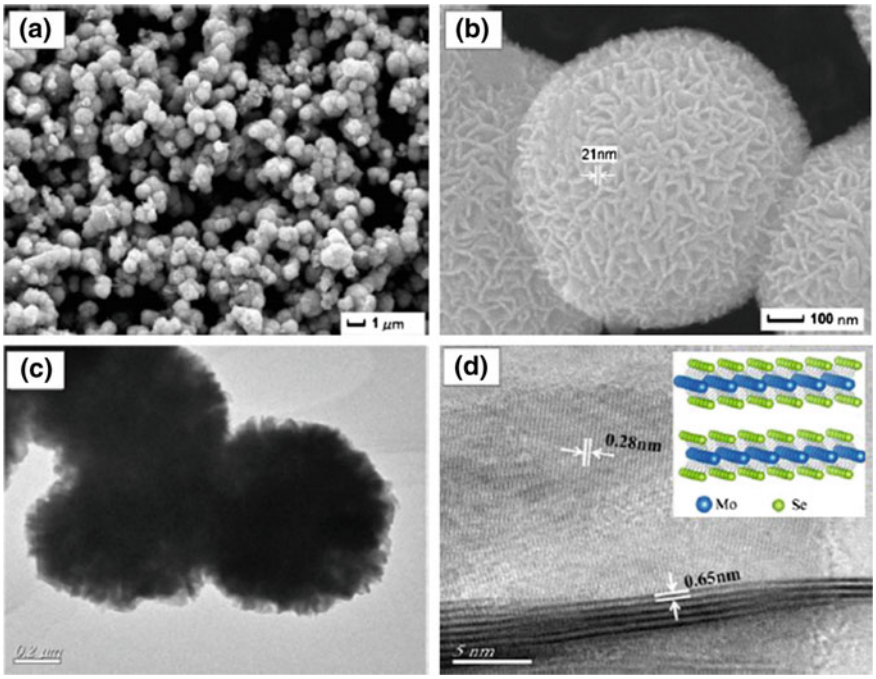

Fig. 2.15 SEM (**a**, **b**), TEM (**c**) and HRTEM (**d**) images of flowerlike $MoSe_2$ microspheres [43]. Copyright 2016. Reproduced with permission from Elsevier

WSe_2 micro-rod and nanoparticles have been synthesized by one-step hydrothermal method by using ammonium tungstate $[(NH_4)_{10}H_2(W_2O_7)_6]$, elemental selenium, and hydrazine monohydrate [44]. The hydrothermally synthesized WSe_2 at nanoscale shows superior electrochemical performance that is potentially applicable for supercapacitor.

In another report, WSe_2-graphene composite nanowire was prepared through wet chemical method that showed exciting photocatalytic behavior where tungsten (vi) oxide (WO_3) and crude selenium (Se) powder were used as source materials of WSe_2 [45]. FESEM images (Fig. 2.16) showed nanowire-like WSe_2 formation on the surface of graphene nanosheet under different magnifications. In this process, WO_3 was first dispersed in deionized water and the solution was followed by dropwise addition of nitric acid.

Subsequently the mixed solution was heated at 120 °C to remove the by-products O_2 and H_2O. Separately an another solution was prepared by mixing anhydrous sodium sulfite (Na_2SO_3) and Se powder with ethylene glycol under continuous stirring at 80 °C to form selenium salt. Then both solutions were transferred into a stainless steel autoclave to follow the heating process for 24 h at 250 °C in an electric furnace. Finally WSe_2 precipitates were obtained after cooling the autoclave at RT. The WSe_2 precipitate was then filtered and heated at 350 K for 12 h to get WSe_2

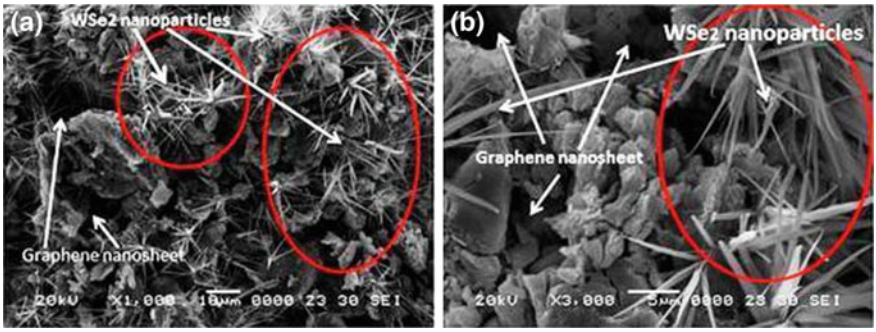

Fig. 2.16 SEM images of WSe_2 graphene composite with different magnifications [45]. Copyright 2017. Reproduced with permission from Nature

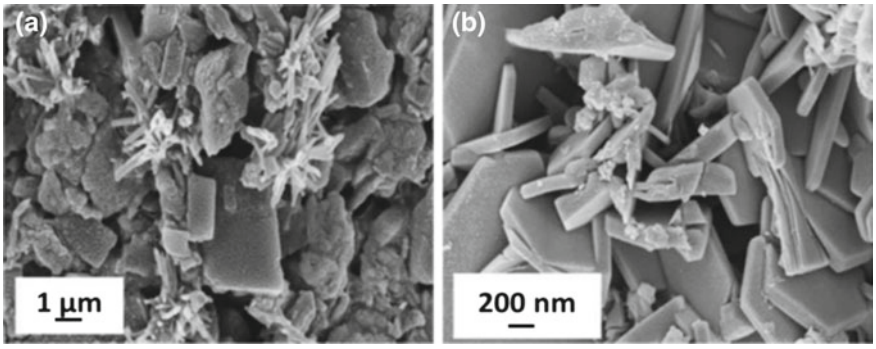

Fig. 2.17 FESEM data showing **a** low and **b** high magnification images of VSe_2 [46]. Copyright 2018. Reproduced with permission from Elsevier

powder. Afterward to prepare WSe_2-graphene composite, WSe_2 and GO powder were taken into 1:1 mass ratio and followed by successive treatments like sonication heating, etc. VSe_2 has been reported through hydrothermal route by using source materials sodium metavanadate ($NaVO_3$) and selenium dioxide (SeO_2) [46]. The hydrothermal synthesis was performed in aTeflon-lined stainless steel autoclave at 200 °C for 24 h. The solid block-like structures of VSe_2 was found through hydrothermal route is shown in Fig. 2.17a, b by low and high magnification FESEM image respectively. The hydrothermally grown VSe_2 showed solid block-like-layered structures evaluated from SEM images (Table 2.1).

2.3.2 Chemical Vapor Deposition

CVD is a preferred method for large area deposition of atomically thin TMD on a relatively matching substrate. TMD growth can be conducted through CVD in

Table 2.1 The preparation of TMD through wet chemical synthesis and their corresponding growth criteria with structural view of grown materials

TMDs	Precursors	Synthesis temperature	Grown structure	Reference
MoS_2	$(NH_4)_6Mo_7O_{24}$, $4H_2O$ and S	180 °C for 50 h	Thin monolayer	[28]
	NaF, MoO_3 and KSCN	220 °C for 48 h	Hierarchical nanospheres	[29]
WS_2	WCl_6 and thioacetamide	265 °C for 24 h	Layered nanosheets	[30]
	$(NH_4)_6H_2W_{12}O_{40}{\cdot}xH_2O$ and thiourea	220 °C for 48 h	Flowerlike nanosheets	[31]
	Na_2WO_4, $2H_2O$, NH_2OH, HCl, CH_4N_2S, and CTAB	18 °C for 72 h	Nanoflowers	[32]
VS_2	Na_3VO_4, $12H_2O$, and TAA	160 °C for 24 h	Layered nanosheets	[43]
$MoSe_2$	Na_2MoO_4 and Se	180 °C for 48 h	Nanoflower	[39]
	$Na_2MoO_4{\cdot}2H_2O$, Se and $NaBH_4$	200 °C for 48 h	3D hierarchical flower	[40]
WSe_2	$(NH_4)_{10}H_2(W_2O_7)_6$, elemental selenium and hydrazine monohydrate	150–170 °C for 48 h	Micro-rod and nanoparticles	[37]
	WO_3 and Se	250 °C for 24 h	Nanowire	[38]
VSe_2	$NaVO_3$ and SeO_2	200 °C for 24 h	Solid block-like structure	[41]

two ways: sulfurization and selenization where vapor-phase reactions in both cases are conducted by transition metal with sulfur and selenium, respectively. TMDs are grown in different morphology and different structural orientations with monolayer, bilayer, and multilayer stacks of different crystallographic orientations in single crystalline, polycrystalline, or pure crystalline form.

Typically the vapor-phase reaction is occurred on transition metal-coated substrate or bare substrate in chalcogen(S or Se) atmosphere or the reaction can be conducted under vapor phase of both transition metal and chalcogen. In CVD, the process parameters, i.e., deposition temperature, temperature ramp, carrier gas flow rate, and vacuum pressure greatly influence the crystal structure, surface morphology, electronic property, and orientation of the grown film. Typically the role of CVD system is to generate vapor precursors of the source material and deliver those vapor reactants through the reactor under specific temperature and pressure. The schematic view of three-zone CVD furnace is shown in Fig. 2.18. The system mainly consists of a reaction chamber equipped with three zones patterned for placement of substrate and subsequent precursors, and heating system with temperature controller. In general, CVD undergoes the growth kinetics by adsorption of reactant species into vapor phase governed above relatively high decompose temperature of respective

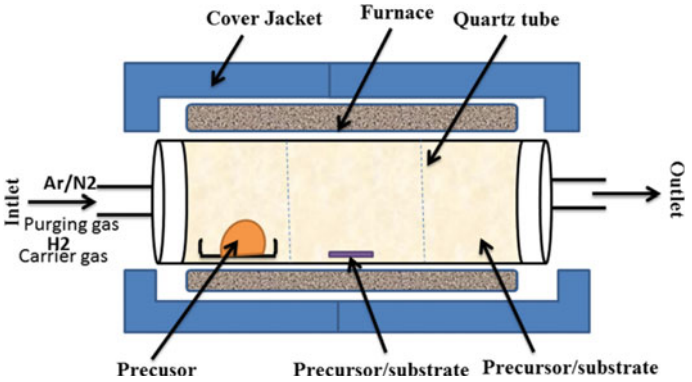

Fig. 2.18 Schematic view of CVD system

precursors into the substrate surface and subsequently heterogeneous reaction get started by formation of newly grown film on the substrate surface and by-product species.

The by-product species are removed from reactor chamber by diffusion process. To transport vaporized reactant into the reactor on to the targeting substrate, carrier gasses (reactive gases such as H_2 and N_2 or inert gases such as Ar) are used with specific flow rate. Typically sulfurization and selenizations are occurred under Ar and H_2 mixed atmosphere with definite ratio that correspondingly participate in nucleation and reduction process. In this process, deposition rate can be willingly adjusted and low deposition rate is mostly preferred for good quality thin film formation. The CVD system is well designed and can be operated with optimum process conditions to generate good quality epitaxial film with uniform film thickness and surface morphology.

2.3.2.1 Sulfurization

Zhan et al. [47] reported MoS_2 growth through sulfurization method where Mo thin film-coated SiO_2 used as a precursor as well as substrate that placed in high-temperature zone and ceramic holder carrying pure sulfur placed in a low-temperature zone. Under specified growth condition, vapor-phase reaction was started at 750 °C by introducing sulfur and successfully governed a large area deposition of polycrystalline MoS_2 atomic layer on SiO_2 substrate with grain size ranging from 10 to 30 nm. The CVD grown MoS_2 film has been shown in Fig. 2.19. Interestingly CVD grown MoS_2 showed a floating morphology with layered orientation(Fig. 2.19a). The as-grown MoS2 showed two- and three-layered structure (Fig. 2.19b, c) with interlayer spacing of ~6.6 ± 0.2 Å. Moreover HRTEM image (Fig. 2.19d) showed Moiré patterns of CVD grown MoS_2 film. Due to scalability nature of CVD, thin film with good uniformity and of any size can be developed. The grown thickness of

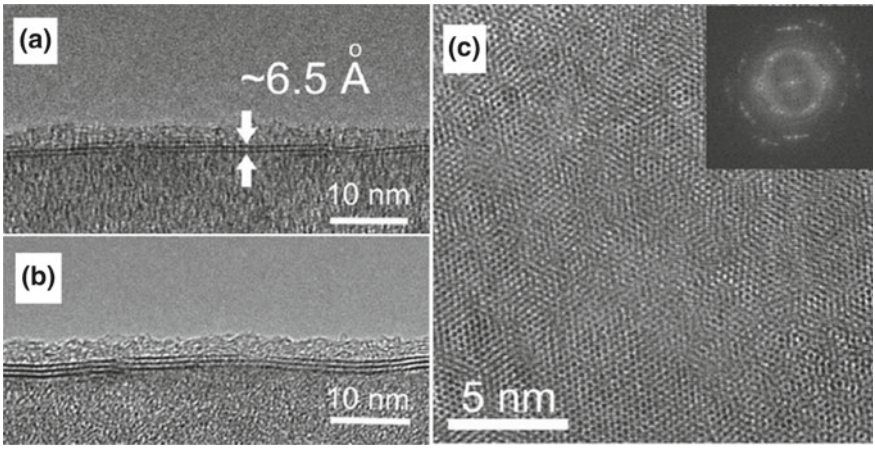

Fig. 2.19 TEM characterizations and chemical elemental analysis of CVD-MoS_2 **c**, **d** Two and three layers of MoS_2. The distance between two layers is about 6.5 Å. **e** A HRTEM image with Moiré patterns. The FFT in the inset reveals a three-layer packing [47]. Copyright 2012. Reproduced with permission from Wiley-VCH Verlag GmbH

MoS_2 is scalable through this CVD method depending upon the as-prepared Mo film and area of the substrate that is fully demanded as per device requirements. Likewise Liu et al. [48] reported the same material through CVD with different approaches by thermal decomposition of the precursor material.

The thermolysis temperature in CVD route is an important parameter to grow high-quality film. So at higher temperature (~1000 °C), $(NH4)_2MoS_4$ precursor is annealed to grow high-quality MoS_2 film. Here decomposition step is easily violated by oxygen which may interrupt to grow sulfide film. So as well as H_2 gas is required to prevent oxidation of as-deposited film into the growth chamber. The gas flow is an important part in CVD system. Shi et al. [49] reported MOS_2 growth in low-pressure CVD on graphene-templated Cu foil. In where they used ammonium thiomolybdate as a precursor that thermally decomposes on graphene to form epitaxial MoS_2 single crystalline hexagonal flakes. Remarkably it was observed that upon introducing a large amount of precursors a continuous MoS_2 film is grown prior flake formation.

Elias et al. [50] reported a large area WS_2 synthesis through sulfurization method where WO_x-coated Si/SiO_2 substrate was heated at high temperature 750–950 °C into sulfur-contained furnace in vapor phase. The grown WS_2 sheet is totally flexible due to its folded or wrinkled nature that signifies different regions of different thickness and stacking. The CVD grown WS_2 film showed hexagonal lattice structure with very small defects which confirm very good crystalline quality of the film (Fig. 2.20a). Also bilayer and trilayer WS2 structure has been evaluated from HRTEM images (Fig. 2.20b, c). Different stacking ordered layer formation of CVD grown WS_2 symbolized the Moire patterns (shown in the inset of figures) that contained to monolayer, bilayer, and trilayer stack at 1, 2, and 2.8 nm, respectively. The edge of single-layered WS2 was shown by HRTEM (Fig. 2.20b, c). Strangely the electronic structure of

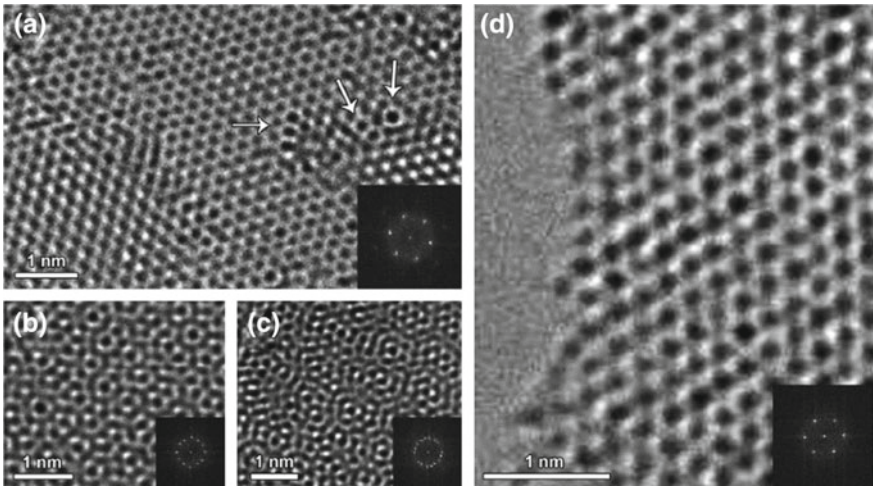

Fig. 2.20 HRTEM images of WS_2 films. Insets show the Fast Fourier Transformation (FFT) of the corresponding TEM micrograph. **a** WS_2 region exhibiting crystalline regions and some defects, such as larger rings, highlighted by arrows. **b**, **c** exhibit a bilayer and trilayer WS_2 with different stacking, revealed by the formed Moire pattern and confirmed by the FFT, and **d** depicts the edge of a single-layer WS_2 film [50]. Copyright 2013. Reproduced with permission from American Chemical Society

grown film was also governed by number of stacking layers which correspondingly notify the energy band structure. In this context, it was examined that the monolayer- and multilayer-stacked structures specify the material property like direct band gap and indirect band gap semiconductor, respectively.

A novel approach to conventional CVD reported as rapid cooling CVD (RCCVD) process by Chao Li. et al. [51] where single crystalline WS_2 was formed with maximum size of 320 μm.

The process parameter optimization and suddenly decrease of temperature were effectively introduced to govern good quality single crystalline film formation. The temperature-growth profile of normal CVD and RCCVD is shown in Fig. 2.21a, b respectively. In RCCVD mode after reaching the synthesis temperature, the system is cooled down rapidly for a while and suddenly reheated at growth temperature. In this process, the control parameters are rapid cooling start time (tRCS), rapid cooling time (tRC), cooling rate, reheating rate and reheating/regrowth temperature (TRG) those should be accordingly maintained to conduct a single crystalline growth.

In the above context, RCCVD paves a great role to synthesize the monolayer and single-crystal WS_2 formation of a large domain size. Moreover domain size can be controlled by optimizing the growth parameters during the rapid cooling stage.

VS_2 nanosheets preparation has been reported by a facile CVD method [52, 53] where vanadium chloride (VCl_3) and sulfur (S) were used as precursors. The VS_2 synthesis was carried out at 500–600 °C on SiO_2/Si substrate under the environment of carrier gasses mixture: N_2 with 10% of H_2. The CVD grown VS_2 nanosheets exhib-

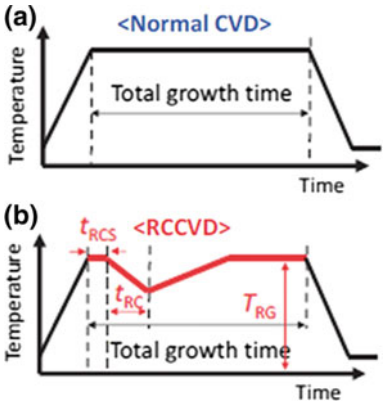

Fig. 2.21 **a**, **b** Time sequence of temperature profile for **a** normal CVD and **b** RCCVD [51]. Copyright 2017. Reproduced with permission from IOP Publishing Ltd

ited mainly two types of VS_2 flakes: hexagonal and half hexagonal VS_2 nanosheets. The characteristics edge length of VS_2 nanostructures is greatly influenced by H_2 flow rate. Ji et al. demonstrated with reducing H_2 flow rate (from 8 sccm to 2 sccm) the edge length of the nanosheet was increased from ~10 μm to ~40 μm [53]. Figure 2.22 shows the morphology of CVD grown VS_2 at 600 °C reported by Yuan et al. where it was shown that VS_2 has been grown in both phases hexagonal and half hexagonal. The repeated observation has been followed (Fig. 2.22d, e) in an another study where VS_2 has been synthesized at slightly lower temperature at 550 °C [53].

2.3.2.2 Selenization Through CVD

Selenization of metal oxide is a common way to form transition metal selenide through CVD route. Typically selenization can be conducted through direct formation of transition metal selenide or through the formation of transition oxide on preferred substrate prior to selenization. Due to low chemical reactivity of selenium, H_2 is mostly required to conduct selenization reaction through a strong reduction process with transition metal oxide precursor to follow the chemical reaction as:

$$WO_3 + 3Se + H_2 \rightarrow WSe_2 + H_2O + SeO_2 \tag{2.5}$$

Huang et al. [54] reported a large area synthesis of WSe_2 monolayer with high crystalline quality through CVD route by selenization of WO_3 and introducing hydrogen as a carrier gas throughout the reaction. The optimized carrier gasses Ar/H_2 were taken into 4:1 to follow better synthesis chemistry. The good crystalline quality of WSe_2 film exhibits hole and electron mobility around 90 and 7 cm^2/Vs, respectively, that signify its applicability in logic circuit integration. To conduct WSe_2 growth, as precursor materials WO_3 and selenium powder was taken and placed into the temperature zone of the center and upper stream area of tube furnace respectively and heated up to 950 and 270 °C to each zone. As a substrate sapphire was used and placed

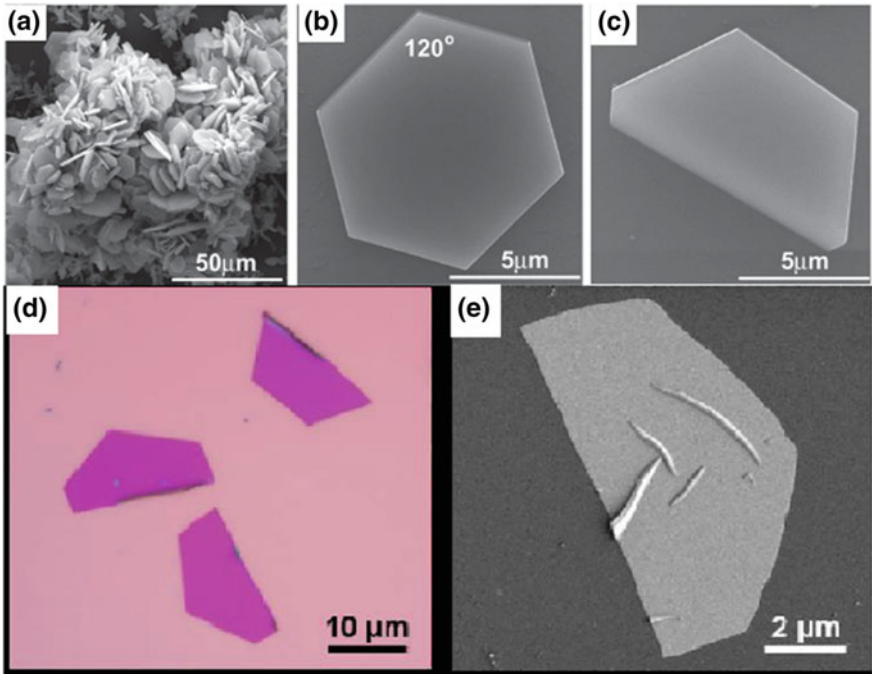

Fig. 2.22 **a** Scanning electron microscope (SEM) images of VS_2 nanosheets (synthesized at 600 °C) with different orientations **b** dominant hexagon [52]. Copyright 2015. Reproduced with permission from Wiley-VCH Verlag GmbH. **c** nearly "half-hexagon" shape for individual crystal, **d** Optical image of the half-hexagon-shaped VS_2 nanosheets (synthesized at 550 °C) and **e** SEM image of a VS_2 nanosheet (synthesized at 550 °C) as grown on SiO_2/Si [53]. Copyright 2017. Reproduced with permission from American Chemical Society

at the downstream side of the furnace. To carry out growth kinetics Ar and H_2 are used as a carrier gasses at 80 and 20 sccm respectively to transmit the selenium and WO_3 vapor toward the targeting substrate. Huang et al. also reported temperature-dependent morphological change due to change of nucleation density in synthesis time. The report showed that synthesized WSe_2 at 850 °C exhibited a triangular-shaped crystal structure with lateral size of 10–50 μm (shown in Fig. 2.23b, while the grown WSe_2 at 750 °C has shown a continuous film formation after merging many small domains into a single domain film (Fig. 2.23c). This should be noticed that the lower synthesis temperature would be responsible for high-density nucleation with better uniformity. WSe_2 monolayer of 0.73 nm thickness was evaluated by atomic force microscopic (AFM) image (Fig. 2.23).

Liu et al. [55] followed the same route to prepare monolayer WSe_2 flakes and studied shape evolution with increasing temperature. It was importantly noticed that with increasing growth time larger single crystalline material could be formed with large domain size in triangular geometry.

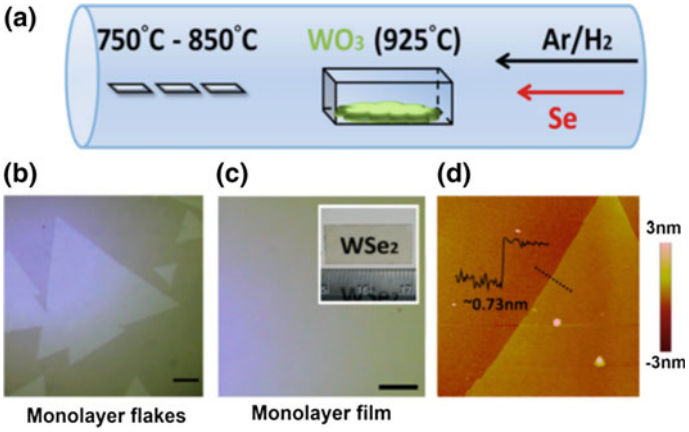

Fig. 2.23 **a** Schematic illustration for the growth of WSe_2 layers on sapphire substrates by the reaction of WO_3 and Se powders in a CVD furnace. A photograph of the setup is also shown. **b**, **c** Optical microscopy images of the WSe_2 monolayer flakes and monolayer film grown at 850 and 750 °C, respectively. Scale bar is 10 μm in length. The inset in (**c**) shows the photograph of a uniform monolayer film grown on a double side polished sapphire substrate. **d** AFM image of a WSe_2 monolayer flake grown at 850 °C on a sapphire substrate [54]. Copyright 2013. Reproduced with permission from American Chemical Society

Many reports were done on $MoSe_2$ synthesis through CVD with monolayer to few layers formation in different crystalline phases [56–59]. The high-quality uniform growth of $MoSe_2$ was reported by using MoO_3 and selenium pellets through CVD under atmospheric pressure. $MoSe_2$ growth temperature has been taken at 750 °C (heating ramp 50 °C/min) for 20 min throughout the reaction [59]. During growth a mixture of Ar and H_2 (15% of Ar) have been used at 50 sccm as a carrier gasses. The schematic view of CVD setup to grow $MoSe_2$ was shown in Fig. 2.24a. This synthesis yielded under ambient pressure a triangular uniform $MoSe_2$ monolayers growth resulting in a large single crystalline islands where the size of triangles was in ranges of few tens to 100 μm or more than 100 μm (Fig. 2.24b, c). The monolayer $MoSe_2$ growth was confirmed by atomic force microscopy (AFM, Fig. 2.24e), by evaluating the thickness of CVD grown triangle of 0.8 nm that correspondingly confirmed the film uniformity through optical micrographs with respect to color homogeneity.

Vanadium diselenide (VSe_2) is a typical TMD-layered material that consists of vanadium atoms sandwiched between two selenium atom layers signifying CdI2-type structure. In case of VSe_2, growth was greatly influenced through van der Waals epitaxial strategy under matching substrate (mica, sapphire, etc.) with grown material. In various reports, VSe_2 growth has been differently approached than conventional TMDs through vapor-phase reaction of corresponding precursors not likely metal oxide reduction process. Due to strong sigma bonding of vanadium oxide precursor, it could not be easy to conduct oxide reduction for selenization. So in this mode

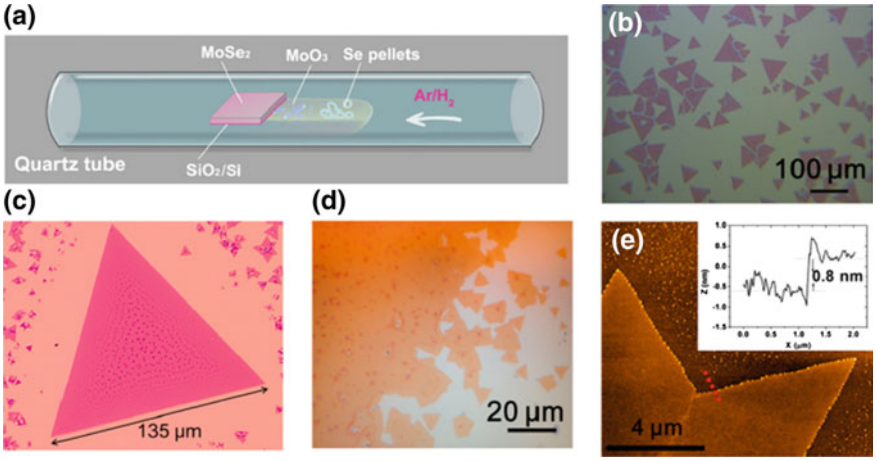

Fig. 2.24 $MoSe_2$ monolayer synthesis and morphology. **a** Schematic of the controlled synthesis of monolayer $MoSe_2$ via CVD. Se pellets and MoO_3 powder are positioned in same ceramic boat at the center of the tube furnace. **b–d** Typical optical images of monolayer triangles and continuous film. Small bilayer domains with darker color can be observed in (**c**) and (**d**). **e** AFM height topography of monolayer $MoSe_2$, and the height profile (inset) showing a thickness of ~0.8 nm, as measured along the red dotted line [59]. Copyright 2015. Reproduced with permission from American Chemical Society

growth kinetics should be differently controlled by other vanadium source material like VCl_3. Zhang et al. [60] reported the growth of 1T VSe_2 mono-crystalline nanosheets with high crystallinity and high electrical conductivity (10^6 S m^{-1}) that is 4–10 times larger than compared to other TMDs.

The CVD grown VSe_2 exhibited uniform crystallinity and compositional uniformity with different shapes of hexagonal and triangular geometry. Moreover compositional uniformity of VSe_2 nanosheets has been evaluated by uniform color contrast image at the corner portion of the triangular nanosheet through energy dispersive spectroscopy (Fig. 2.25a, b) mapping.

Carrier gasses are interestingly participating to control the film thickness into CVD chamber. Remarkably the reported data has showed that under Ar flow from 500 to 100 sccm the thickness of synthesized VSe_2 film was decreased with increasing the gas flow rate (Fig. 2.25e). Figure 2.25c shows optical microscopy image of VSe_2 of different types of polygonal shapes like triangles, hexagons as well as hexagrams. This type of well-defined shape confirmed the high crystallinity of the material. Moreover atomic force microscopy showed a well-defined morphology of CVD grown VSe_2 nanosheet of thickness about 4.9 nm (Fig. 2.25d). In another example, Wang et al. [61] reported VSe_2 growth on mica substrate followed by same growth conditions under same precursors. In both cases, deposition temperature was kept around 600–650 °C.

High-quality growth of $NbSe_2$ monolayer was also conducted under same carrier gas treatment and metal oxide reduction at 795 °C for 16 min as per report [62]. So

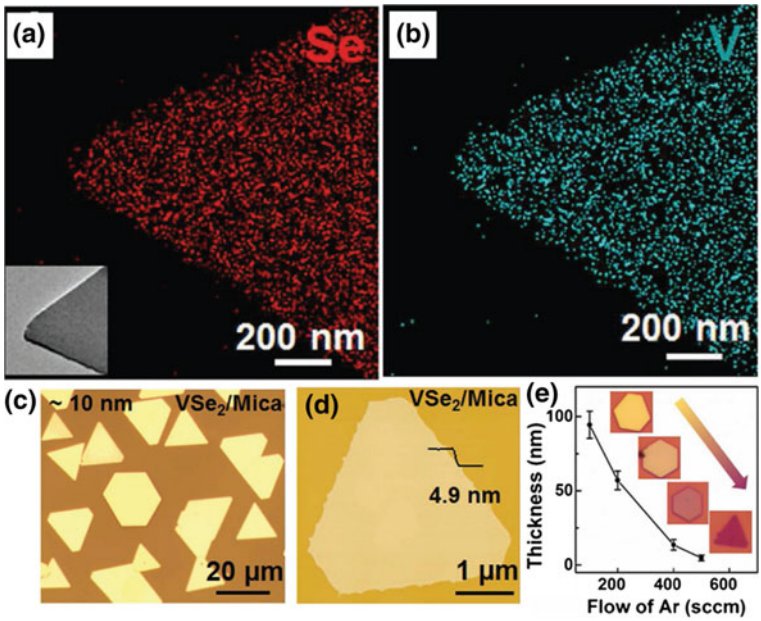

Fig. 2.25 Direct synthesis of VSe_2 polygons on mica via an atmospheric-pressure CVD method. **a**, **b** EDS mapping images of Se and V for a corner of a triangular VSe_2 nanosheet, respectively. **c** OM image of typical VSe_2 triangles and hexagons achieved directly on the mica substrate (400 sccm Ar and 2 sccm H_2 as carrier gases, growth time of 2 min). **d** AFM image and corresponding height profile of an ultrathin VSe_2 nanosheet with a thickness of ≈4.9 nm. **e** Average thickness of VSe_2 nanosheets plotted as a function of Ar flow rate. Insets are optical images of transferred VSe_2 nanosheets on 300 nm SiO_2/Si, showing contrast evolutions from yellow to red when decreasing their thicknesses [60]. Copyright 2017. Reproduced with permission from Wiley-VCH Verlag GmbH

the above-mentioned CVD processes lead to form different types of TMDs with varying crystal structure and morphological orientation with controllable layer numbers under growth parameters variations (Table 2.2).

2.3.3 Electrodeposition

Electrodeposition is a well handy technique to produce metallic or semiconducting thin film on base material (substrate) through electrochemical reduction of metallic ions from electrolytes. Currently, electrodeposition is emerging as a versatile technique for the preparation of thin film with reduced grain size. To begin electrodeposition cathode (working electrode) and anode (counter electrode) are taken and immersed into an electrolyte contained cell/bath. The electrodeposition occurs by charge transfer reaction when external potential is applied across substrate/electrolyte interface. The schematic diagram of an electrochemical cell setup for electrodeposi-

Table 2.2 TMD preparation through CVD and their corresponding growth criteria with structural view of grown materials

MDs	Precursors	Synthesis temperature	Substrate	Grown structure	References
MoS_2	Mo-coated SiO_2 and Sulfur	750 °C	Oxide-coated SiO_2	Monolayer(Hexagonal lattice structure)	[47]
	$(NH4)_2MoS_4$	1000 °C	Sapphire	Trilayer(Polycrystalline)	[48]
	Ammonium thiomolybdate	400 °C	Graphene-coated Cu foil	Single crystalline hexagonal flakes	[49]
WS_2	WO_x-coated Si/SiO_2 substrate and Sulfur	750–950 °C	Oxide-coated Si/SiO_2 substrate	Monolayer and multilayer-stacked structure	[50]
VS_2	VCl_3 and sulfur	500–600 °C	SiO_2/Si substrate	Nanosheets (single crystalline hexagonal 1T structure)	[52, 53]
WSe_2	WO_3 and selenium powder	850 °C	Sapphire	Monolayer flakes	[54]
$MoSe_2$	MoO_3 and Selenium pellets	850 °C	SiO_2/Si substrate	Monolayer in single crystalline island of triangular geometry	[59]
VSe_2	VCl_3 and Se powder	500–600 °C	Mica, sapphire	Single crystalline VSe_2 nanosheets in triangular or hexagonal form	[60, 61]

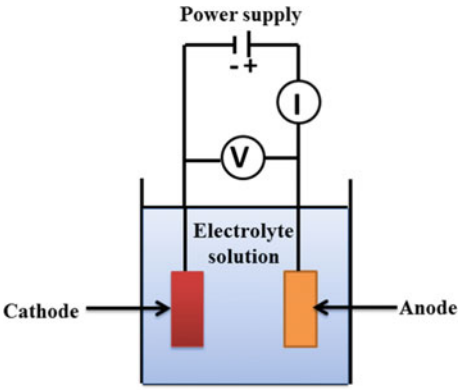

Fig. 2.26 Schematic view of electrode deposition bath

tion set up consists of working electrode/cathode, anode, electrolyte containing bath, current source and ampere/voltmeter is shown in Fig. 2.26.

Among the above-discussed processes, the electrodeposition method is a unique, fast, simple, and inexpensive process for the synthesis of various nanostructured materials, e.g., thin film, nanoparticles, nanowires, nanocrystalline material, and nanocomposites with controlled characteristics, likely, composition, geometry, and morphology [63]. Electrodeposition is occurred through pure metal deposition or co-deposition of alloy from electrolyte by applying external current. In this method, 2D and 3D nanostructures are successfully deposited on targeting substrate. The key advantage of this electrochemical deposition is its controllable synthesis process for nanostructured materials of desired geometry, morphology, and crystallographic orientation by the direct growth on substrates with control of operating conditions and bath chemistry. This method also elucidates the influence of electrochemistry on nanoparticle properties. [64].

This highly controllable, repeatable, and scalable nature of electrodeposition could pave a great attention for fabrication of TMD nanostructures with various exciting characteristics and device functionality through a low cost effective and efficient way.

Nanostructured MoS_2 has been prepared by various types of electrochemical methods based on aqueous and non-aqueous cathodic electrodeposition [65–71]. Albu-Yaron et al. [65] reported MoS_2 synthesis through both aqueous (water) and non-aqueous (ethylene glycol) route by using sodium tetrathiomolybdate ion at different temperatures on conductive glass substrate. The two-electron reduction of tetrathiomolybdate ions (MoS_4^{2-}) produced MoS_2 followed by the reaction.

$$MoS_4^{2-} + 2e^- + 4H^+ \rightarrow MoS_2 + 2H_2S \tag{2.6}$$

Potassium chloride and ammonium chloride were used as supporting electrolyte and proton donor for ethylene glycol-based electrolyte respectively. This report showed the formation of amorphous MoS_2 matrix embedded by nanocrystallites

and nanoclusters MoS_2 under aqueous and non-aqueous electrolyte mode. The electrodeposition process greatly influences the formation of crystalline embryo by varying temperature electrolytic medium, substrate and operating voltage. It was shown by HRTEM image, the densely scattered crystalline embryo with disordered structure throughout the MoS_2 matrix. During electrodeposition when temperature was increased, i.e., 98 °C for aqueous and 165 °C for ethylene glycol, the smaller sizes nanoparticles were found into amorphous MoS_2 matrix. For the ethylene glycol-based electrochemical synthesis, single or double (0002) plane MoS_2 nanoplatelets were formed throughout the matrix. Importantly it was also noted that after increasing the temperature structural quality might be deteriorated due to enhancement of various types of defects. So it is essential to control structural morphology with increasing temperature to get high-quality defect-free structure and exciting characteristics for device potential applications.

Another report showed MoS_2 synthesis by electrolyzing the aqueous solution of $(NH_4)_2[MoS_4]$ and the same amorphous MoS_2 formation was occurred with mixed phases of MoS_2 and MoS_3 [68]. To overcome this type of amorphous material formation and to get pure crystalline structure, a non-aqueous-based electrodeposition method was proposed by using room temperature ionic liquids (RTILs) where precursors were taken as 1:1 molar ratio. This electrodeposition method was performed on glassy carbon substrate into electrochemical bath containing Pt as a reference electrode followed by potentiodynamic depositions (scan rate 100 mV/s, temperature varying from room temperature to 100 °C) and chronoamperometric deposition(at constant temperature, varying potential from 2.7 to 1 V). Murugesan et al. [69] reported temperature-dependent morphology evolution where room temperature synthesized MoS_2 showed amorphous nature and after increasing the temperature nanoparticles were agglomerated and form nanoclustered material. Afterward by a further increase of temperature at 100 °C the fused nanoparticles of cluster form a thin crystalline film of pure phase via Oswald ripening where smaller nanoparticles coalesce and form larger particles in crystalline form. In Potentiodynamic depositions, morphological evolution with increase temperature was happened as discussed above.

Figure 2.27 shows the SEM image of potentiodynamic depositions of MoS_x at various temperatures. At room temperature (Fig. 2.27a), amorphous MoS_x nanoparticles were formed and with increasing temperature nanoparticles agglomerate to form MoS_x cluster structure (Fig. 2.27b). Furthermore, increasing temperature at 75 and 100 °C (Fig. 2.27c, d) a uniform-layered MoS_x structure was formed through coalescence of small crystalline particles to larger crystalline structure via Oswald ripening [72].

Moreover the chronoamperometric deposition at −2.7 V Vs Pt at 100 °C has shown the flowerlike morphology (Fig. 2.28) of MoS_x that was confirmed by irregular current response due to heterogeneous nucleation of MoS_x growth on glassy carbon substrate by ionic liquid electrolyte. The uniform flowerlike morphology of electrodeposited MoS_x was shown in SEM image (Fig. 2.28a) and the enlarged image showed small spherical flowerlike particles (Fig. 2.28b, c).

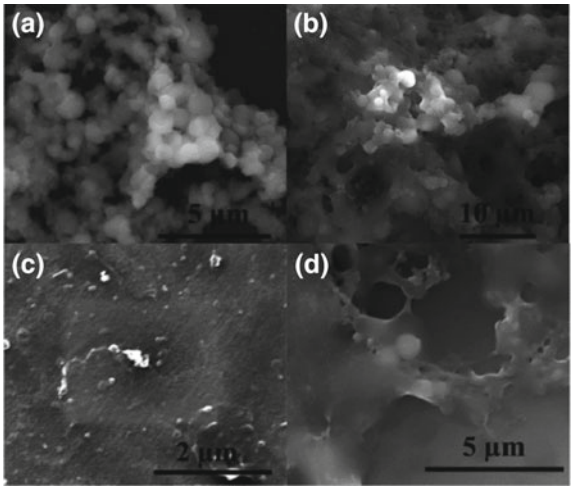

Fig. 2.27 SEM images of potentiodynamically electrodeposited MoS_2 at various temperatures. **a** RT, **b** 50, **c** 75, and **d** 100 °C [69]. Copyright 2013. Reproduced with permission from American Chemical Society

Electrodeposition of WS_2 on conducting glass plate was reported into the electrolyte of 1:1 mixture of tungstic acid and aqueous solution of Na_2SO_3. Devadasan et al. [73] studied the variation of film quality with current density and temperature under specific pH value of the electrolyte. The study reported that at current density 30 mA/cm^2 and bath temperature 40 °C the electrodeposited film was of high thickness and exceedingly opaque to light. But after increasing the current density, the film quality was degraded and also with increasing temperature, i.e., above 40 °C diffusion takes place that give rise to increase pin hole formation into the film. So to get high-quality film, the temperature and current density should be optimized under specific pH value.

Interestingly nanowire formation was also conducted through electrodeposition which actively plays for hydrogen evolution. Jana et al. [74] reported polycrystalline WS_2 formation on ITO-coated glass substrate using three electrode configuration into an aqueous electrolyte solution mixed of sodium tungstate ($Na_2WO_4{\cdot}2H_2O$) and thioacetamide ($CH_3C(S)NH_2$). But in that process due to use of $Na_2WO_4{\cdot}2H_2O$ as a source of metal a mixed phase of WS_2/WO_3 thin film was formed rather to formation of pure phase WS_2. Figure 2.29 shows the FESEM images of WS_2 thin film and WS_2/WO_3 thin films.

As the electrode potential of metal is more negative than hydrogen discharge potential, metal cannot be easily electrodeposited from aqueous solution. Generally the electrolysis reaction can be written as [75],

$$H_2MoO_4(\text{aqueous}) + 6H^+ + 6e^- \overset{\text{Electrolysis}}{\Leftrightarrow} Mo + 4H_2O \tag{2.7}$$

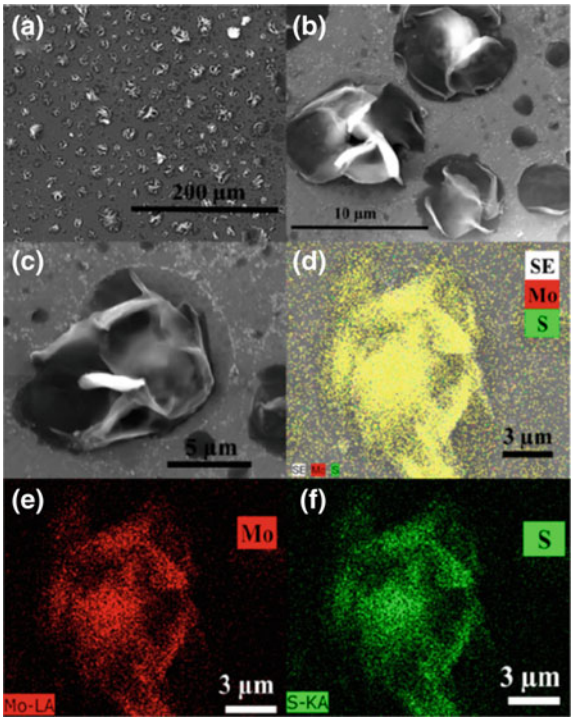

Fig. 2.28 **a** SEM-EDS analysis of chronoamperometrically at −2.7 V versus Pt electrodeposited MoS_2 over glassy carbon electrodes showing the formation of flower morphology. **b**, **c** Enlarged and closer view of MoS_2 flower morphology. **d** Elemental analysis of MoS_2 showing the presence of Mo and S in the secondary electron (SE) image. **e** Elemental analysis of showing the presence of Mo. **f** Elemental analysis showing the presence of S [69]. Copyright 2015. Reproduced with permission from American Chemical Society

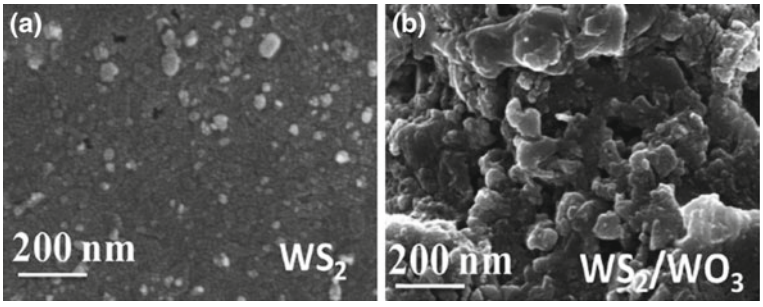

Fig. 2.29 **a** FESEM images of (**a**) WS_2 thin film; **b** WS_2/WO_3 thin film [74]. Copyright 2015. Reproduced with permission from Elsevier

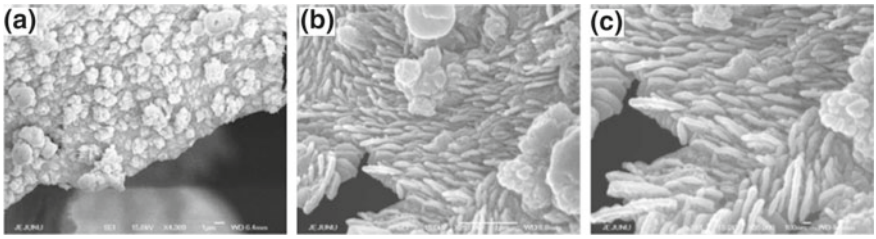

Fig. 2.30 Field emission scanning electron microscopy (**a**–**c**) shows the low resolution and high-resolution images of 10 min electrochemically deposited $MoSe_2$/Ni [77]. Copyright 2017. Reproduced with permission from Elsevier

But at the intermediate stage, MoO_4^{-2} is formed which is highly thermodynamically stable anion (high energy formation, i.e., −218.8 kcal/mol)) and cannot be easily separated into Mo and O. So for breaking this type of strong hybridization bond of MoO_4^{-2} more potential energy is required than the cathodic potential for hydrogen discharge. So it is not easy to achieve a cathodic deposition of metal under normal bath condition. But it would be possible under critical controlling of growth kinetics and bath condition. For deposition, equilibrium electrode potential of selenium is more positive than molybdenum. It is theoretically recommended that high concentration of Mo shifts the deposition potential toward positive value and low concentration of Se shifts the potential toward negative value that are essentially required for $MoSe_2$ deposition under diffusion-controlled growth kinetics.

The polycrystalline $MoSe_2$ synthesis was reported by electrolysis of ammoniacal solution (mixture of molybdic acid(H_2MoO_4) and aqueous solution of SeO_2) under galvanostatic conditions on titanium and conducting glass substrate [76]. In an another report, Mariappan et al. [77] reported electrodeposition of $MoSe_2$ via three electrode configuration (Ni foam as a working electrode, Ag/AgCl as a reference, and platinum as a counter electrode) on Nickel foam under electrolyte solution mixed of ammonium molybdate tetrahydrate ($(NH_4)_6Mo_7O_{24}{\cdot}4H_2O$) and selenium dioxide ($SeO_2$). The electrodeposition was performed by applying chronoamperometry voltage at −1.1 V (vs. Ag/AgCl) and during synthesis a slightly high temperature (60 °C) was maintained to improve ion diffusion toward the electrode surface. Remarkably with increasing deposition time from 5 to 10 min, the number of sheet formation of $MoSe_2$ was increased in electrolysis technique (see Fig. 2.30; Table 2.3).

WSe_2 thin films are grown in the same way as discussed above as like $MoSe_2$. Gawale et al. [78] reported WSe_2 synthesis from aqueous ammoniacal electrolyte solution of H_2WO_4 and SeO_2 at the same deposition temperature 60 °C as discussed for $MoSe_2$. The electrodeposition of WSe_2 was performed on stainless steel and fluorine-doped tin oxide-coated glass substrates. Delphine et al. [79] reported the same synthesis procedure of WSe_2 under galvanometric mode and confirmed the formation of polycrystalline WSe_2 with hexagonal structure using aqueous electrolytic bath. The electrodeposited WSe_2 shows n-type semiconducting nature with indirect band gap of $\approx$ 1.0 eV.

Table 2.3 The preparation of TMD through electrodeposition mode and their corresponding growth criteria and structural view

TMDs	Precursors	Substrate and bath conditions	Grown structure	References
MoS_2	Sodium tetrathiomolybdate ion (aqueous and non-aqueous(ethylene glycol) route)	Conductive glass substrate, 98 °C for aqueous and 165 °C for non-aqueous route	Amorphous MoS_2 nanoplatelets	[65]
	Molybdenum glycolate and 1,4-butanedithiol (*N*-methyl-N-propylpiperidinium cation and bis(trifluoromethanesulfonyl)imide anion used as room temperature ionic liquids (RTIL) electrolyte)	Glassy carbon (GC) electrode	Nanoflower crystal structure	[69]
WS_2	1:1 mixture of tungstic acid and aqueous solution of Na_2SO_3	Conducting glass substrate, 40 °C	Polycrystalline thin film	[73]
	Sodium tungstate ($Na_2WO_4{\cdot}2H_2O$) and thioacetamide ($CH_3C(S)NH_2$)	ITO-coated glass	Nanoparticles	[74]
$MoSe_2$	Ammoniacal solution (mixture of molybdic acid(H_2MoO_4) and aqueous solution of SeO_2)/ammonium molybdate tetrahydrate ($(NH_4)_6Mo_7O_{24}{\cdot}4H_2O$) and selenium dioxide ($SeO_2$)	Titanium and conducting glass substrate/Ni foam, 60 °C	Lamellar nanostructures, 2D nanosheets	[76, 77]
WSe_2	Aqueous ammoniacal electrolyte solution of H_2WO_4 and SeO_2	Stainless steel, conducting glass and titanium substrates, 60 °C	Polycrystalline, hexagonal structure	[78, 79]

2.4 Conclusion

In summary, we have discussed various synthesis routes from top-down to bottom-up approaches over various TMD materials with their exciting structural-morphological orientation. As a top-down approach, exfoliation technique has been devoted as a gateway to prepare layered material in large scale but it is not well suited for electronics and optoelectronics application due to lack of fine-tuning controllability over growth techniques. The poor electronic properties of liquid-exfoliated TMDs might be improved after annealing treatment. Bottom-up approach in contrary to top-down approach has been developed through various process technologies to synthesize high quality and uniform film with comparatively low defect density and various morphological evolutions such as nanoparticles, nanosheets, nanowire, nanoflower, hexagonal, half hexagonal, solid block structure. As a bottom-up approach, wet chemical synthesis offers a powerful alternative method to exfoliation route that yields various forms of nanostructures with interesting properties in nanoscale. Wet chemical synthesis has been reported by a number of processes to grow various TMDs at low synthesis temperature with various exciting morphology from nanoparticles to nanoflowers with flake sizes typically from hundreds of nanometers to few micrometers. Among different bottom-up methods, importantly CVD offers a high crystalline epitaxial growth with low defect density and various crystal structures in monolayer to multilayer-stacked formation of different geometry under controlling the process parameters. In CVD technique, carrier gasses perform a great role to conduct reaction process upon the substrate under specific flow rate. Importantly different CVD synthesis routes perform in wafer-scale fabrication of electronic and opto-electronic devices. The electrochemical synthesis as a bottom-up approach is being explored as a green synthesis technology in both aqueous and non-aqueous electrolytes bath under galvanostatic condition and also the technique endorses multiple advantages like versatility of substrate choice, very fast deposition rate, and growth scalability. It has been also noticed that non-aqueous bath rather than aqueous provides better quality film by using ionic liquid electrolyte at room temperature. Typically electrodeposition is utilized for metallic coating or hybrid formation for the purpose of good appearance, special surface and engineering properties.

Moreover, the preparations of layered TMDs are still remained a challenge to control the desired morphology and crystal structure under specific treatment for the purpose of rational-technological development. We predict and demonstrate the growing research interest of various controlled synthesis routes for the development of more powerful and exciting characteristics of the materials for the real applications.

References

1. Chia X, Eng AYS, Ambrosi A et al (2015) Electrochemistry of nanostructured layered transition-metal dichalcogenides. Chem Rev 115:11941–11966
2. Choi W, Choudhary N, Han GH, Park J, Akinwande D, Lee YH (2017) Recent development of two-dimensional transition metal dichalcogenides and their applications. Mater Today 20:116–130
3. Lv R, Robinson JA, Schaak RE, Sun D, Sun Y, Mallouk TE, Terrones M (2014) Transition metal dichalcogenides and beyond: synthesis, properties, and applications of single-and few-layer nanosheets. Acc Chem Res 48:56–64
4. Wang QH, Kalantar-Zadeh K, Kis A, Coleman JN, Strano MS (2012) Electronics and optoelectronics of two-dimensional transition metal dichalcogenides. Nat Nanotechnol 7:699
5. Bernal MM, Milano D (2014) Two-dimensional nanomaterials via liquid-phase exfoliation: synthesis, properties and applications. Carbon Nanotechnol 159
6. Lee C, Yan H, Brus LE, Heinz TF, Hone J, Ryu S (2010) Anomalous lattice vibrations of single-and few-layer MoS_2. ACS Nano 4:2695–2700
7. Mak KF, Lee C, Hone J, Shan J, Heinz TF (2010) Atomically thin MoS_2: a new direct-gap semiconductor. Phys Rev Lett 105:136805
8. Splendiani A, Sun L, Zhang Y, Li T, Kim J, Chim CY et al (2010) Emerging photoluminescence in monolayer MoS_2. Nano Lett 10:1271–1275
9. Bertolazzi S, Brivio J, Kis A (2011) Stretching and breaking of ultrathin MoS_2. ACS Nano 5:9703–9709
10. Li H, Wu J, Yin Z, Zhang H (2014) Preparation and applications of mechanically exfoliated single-layer and multilayer MoS_2 and WSe_2 nanosheets. Acc Chem Res 47:1067–1075
11. Yuan L, Ge J, Peng X, Zhang Q, Wu Z, Jian Y et al (2016) A reliable way of mechanical exfoliation of large scale two dimensional materials with high quality. AIP Adv 6:125201
12. Li H, Yin Z, He Q, Li H, Huang X, Lu G et al (2012) Fabrication of single- and multilayer MoS_2 film-based field-effect transistors for sensing NO at room temperature. small 8:63–67
13. Li H, Wu J, Huang X, Lu G, Yang J, Lu X et al (2013) Rapid and reliable thickness identification of two-dimensional nanosheets using optical microscopy. ACS Nano 7:10344–10353
14. Coleman JN, Lotya M, O'Neill A, Bergin SD, King PJ, Khan U et al (2011) Two-dimensional nanosheets produced by liquid exfoliation of layered materials. Science 331:568–571
15. Smith RJ, King PJ, Lotya M, Wirtz C, Khan U, De S et al (2011) Large-scale exfoliation of inorganic layered compounds in aqueous surfactant solutions. Adv Mater 23:3944–3948
16. Dines MB (1975) Lithium intercalation via n-butyllithium of the layered transition metal dichalcogenides. Mater Res Bull 10:287–291
17. Gordon RA, Yang D, Crozier ED, Jiang DT, Frindt RF (2002) Structures of exfoliated single layers of WS_2, MoS_2, and $MoSe_2$ in aqueous suspension. Phys Rev B 65:125407
18. Zeng Z, Yin Z, Huang X, Li H, He Q et al (2011) Single-layer semiconducting nanosheets: high-yield preparation and device fabrication. Angew Chem 123:11289–11293
19. Eda G, Yamaguchi H, Voiry D, Fujita T, Chen M, Chhowalla M (2011) Photoluminescence from chemically exfoliated MoS_2. Nano Lett 11:5111–5116
20. Frey GL, Reynolds KJ, Friend RH, Cohen H, Feldman Y (2003) Solution-processed anodes from layer-structure materials for high-efficiency polymer light-emitting diodes. J Am Chem Soc 125:5998–6007
21. Bissessur R, Kanatzidis MG, Schindler JL, Kannewurf CR (1993) Encapsulation of polymers into MoS_2 and metal to insulator transition in metastable MoS_2. J Chem Soc Chem Commun 20:1582–1585
22. Xu K, Chen P, Li X, Wu C, Guo Y, Zhao J et al (2013) Ultrathin nanosheets of vanadium diselenide: a metallic two-dimensional material with ferromagnetic charge-density-wave behavior. Angew Chem Int Ed 52:10477–10481
23. Jang JT, Jeong S, Seo JW, Kim MC, Sim E, Oh Y et al (2011) Ultrathin zirconium disulfide nanodiscs. J Am Chem Soc 133:7636–7639

24. Jeong S, Yoo D, Jang JT, Kim M, Cheon J (2012) Well-defined colloidal 2-D layered transition-metal chalcogenide nanocrystals via generalized synthetic protocols. J Am Chem Soc 134(44):18233–18236
25. Lv R, Robinson JA, Schaak RE, Sun D, Sun Y, Mallouk TE, Terrones M (2014) Transition metal dichalcogenides and beyond: synthesis, properties, and applications of single-and few-layer nanosheets. Acc Chem Res 48:56–64
26. Chen X, Fan R (2001) Low-temperature hydrothermal synthesis of transition metal dichalcogenides. Chem Mater 13:802–805
27. Splendiani A, Sun L, Zhang Y, Li T, Kim J, Chim CY et al (2010) Emerging photoluminescence in monolayer MoS_2. Nano Lett 10:1271–1275
28. Ye L, Xu H, Zhang D, Chen S (2014) Synthesis of bilayer MoS_2 nanosheets by a facile hydrothermal method and their methyl orange adsorption capacity. Mater Res Bull 55:221–228
29. Javed MS, Dai S, Wang M, Guo D, Chen L, Wang X et al (2015) High performance solid state flexible supercapacitor based on molybdenum sulfide hierarchical nanospheres. J Power Sources 285:63–69
30. Shelke NT, Karche BR (2015) Hydrothermal synthesis of WS_2/RGO sheet and their application in UV photodetector. J Alloys Compd 653:298–303
31. Piao M, Chu J, Wang X, Chi Y, Zhang H, Li C et al (2017) Hydrothermal synthesis of stable metallic 1T phase WS_2 nanosheets for thermoelectric application. Nanotechnology 29:025705
32. Cao S, Liu T, Zeng W, Hussain S, Peng X, Pan F (2014) Synthesis and characterization of flower-like WS_2 nanospheres via a facile hydrothermal route. J Mater Sci Mater Elect 25:4300–4305
33. Feng J, Sun X, Wu C, Peng L, Lin C, Hu S et al (2011) Metallic few-layered VS_2 ultrathin nanosheets: high two-dimensional conductivity for in-plane supercapacitors. J Am Chem Soc 133:17832–17838
34. Liu X, Yue G, Zheng H (2017) A promising vanadium sulfide counter electrode for efficient dye-sensitized solar cells. RSC Adv 7:12474–12478
35. Emadi H, Salavati-Niasari M, Davar F (2012) Synthesis and characterization of cobalt sulfide nanocrystals in the presence of thioglycolic acid via a simple hydrothermal method. Polyhedron 31:438–442
36. Zhan JH, Xie Y, Yang XG, Zhang WX, Qian YT (1999) Hydrazine-assisted low-temperature hydrothermal preparation of nanocrystalline Jaipurite. J Solid State Chem 146:36–38
37. Liu L, Rong H, Li J, Tong X, Wang Z (2017) Synthesis of a hierarchical cobalt sulfide/cobalt basic salt nanocomposite via a vapor-phase hydrothermal method as an electrode material for supercapacitor. New J Chem 41:12147–12152
38. Chen H, Jiang J, Zhang L, Xia D, Zhao Y, Guo D et al (2014) In situ growth of $NiCo_2S_4$ nanotube arrays on Ni foam for supercapacitors: maximizing utilization efficiency at high mass loading to achieve ultrahigh areal pseudocapacitance. J Power Sources 254:249–257
39. Cai X, Shen X, Ma L, Ji Z (2015) Facile synthesis of nickel–cobalt sulfide/reduced graphene oxide hybrid with enhanced capacitive performance. RSC Adv 5:58777–58783
40. Wu J, Dou S, Shen A, Wang X, Ma Z, Ouyang C, Wang S (2014) One-step hydrothermal synthesis of $NiCo_2$ S_4–rGO as an efficient electrocatalyst for the oxygen reduction reaction. J Mater Chem A 2:20990–20995
41. Chen Z, Wan Z, Yang T, Zhao M, Lv X, Wang H et al (2016) Preparation of nickel cobalt sulfide hollow nanocolloids with enhanced electrochemical property for supercapacitors application. Sci Rep 6:25151
42. Tang H, Dou K, Kaun CC, Kuang Q, Yang S (2014) $MoSe_2$ nanosheets and their graphene hybrids: synthesis, characterization and hydrogen evolution reaction studies. J Mater Chem A 2:360–364
43. Tang H, Huang H, Wang X, Wu K, Tang G, Li C (2016) Hydrothermal synthesis of 3D hierarchical flower-like $MoSe_2$ microspheres and their adsorption performances for methyl orange. Appl Surf Sci 379:296–303
44. Chakravarty D, Late DJ (2015) Microwave and hydrothermal syntheses of WSe_2 micro/nanorods and their application in supercapacitors. RSC Adv 5:21700–21709

45. Ali A, Oh WC (2017) Preparation of nanowire like WSe_2-graphene nanocomposite for photocatalytic reduction of CO_2 into CH_3OH with the presence of sacrificial agents. Sci Rep 7:1867
46. Ratha S, Bankar P, Gangan AS, More MA, Late DJ, Behera JN et al (2018) VSe_2-reduced graphene oxide as efficient cathode material for field emission. J Phy Chem Solids. https://doi.org/10.1016/j.jpcs.2018.02.020
47. Zhan Y, Liu Z, Najmaei S, Ajayan PM, Lou J (2012) Large-area vapor-phase growth and characterization of MoS_2 atomic layers on a SiO_2 substrate. Small 8:966–971
48. Liu KK, Zhang W, Lee YH, Lin YC, Chang MT, Su CY et al (2012) Growth of large-area and highly crystalline MoS_2 thin layers on insulating substrates. Nano Lett 12:1538–1544
49. Shi Y, Zhou W, Lu AY, Fang W, Lee YH, Hsu AL et al (2012) van der Waals epitaxy of MoS_2 layers using graphene as growth templates. Nano Lett 12:2784–2791
50. Elías AL, Perea-Lopez N, Castro-Beltran A, Berkdemir A, Lv R, Feng S et al (2013) Controlled synthesis and transfer of large-area WS_2 sheets: from single layer to few layers. ACS Nano 7:5235–5242
51. Li C, Yamaguchi Y, Kaneko T, Kato T (2017) Large single-domain growth of monolayer WS_2 by rapid-cooling chemical vapor deposition. Appl Phy Exp 10:075201
52. Yuan J, Wu J, Hardy WJ, Loya P, Lou M, Yang Y et al (2015) Facile synthesis of single crystal vanadium disulfide nanosheets by chemical vapor deposition for efficient hydrogen evolution reaction. Adv Mater 27:5605–5609
53. Ji Q, Li C, Wang J, Niu J, Gong Y, Zhang Z et al (2017) Metallic vanadium disulfide nanosheets as a platform material for multifunctional electrode applications. Nano Lett 17:4908–4916
54. Huang JK, Pu J, Hsu CL, Chiu MH, Juang ZY, Chang YH et al (2013) Large-area synthesis of highly crystalline WSe_2 monolayers and device applications. ACS Nano 8:923–930
55. Liu B, Fathi M, Chen L, Abbas A, Ma Y, Zhou C (2015) Chemical vapor deposition growth of monolayer WSe_2 with tunable device characteristics and growth mechanism study. ACS Nano 9:6119–6127
56. Chen J, Zhao X, Tan SJ, Xu H, Wu B, Liu B et al (2017) Chemical vapor deposition of large-size monolayer $MoSe_2$ crystals on molten glass. J Am Chem Soc 139:1073–1076
57. Zheng B, Chen Y (2017) Controllable growth of monolayer MoS_2 and $MoSe_2$ crystals using three-temperature-zone furnace. In: IOP conference series: materials science and engineering, vol 274. IOP Publishing, pp 012085
58. Shaw JC, Zhou H, Chen Y, Weiss NO, Liu Y, Huang Y, Duan X (2014) Chemical vapor deposition growth of monolayer $MoSe_2$ nanosheets. Nano Res 7:511–517
59. Wang X, Gong Y, Shi G, Chow WL, Keyshar K, Ye G et al (2014) Chemical vapor deposition growth of crystalline monolayer $MoSe_2$ ACS Nano 8:5125–5131
60. Zhang Z, Niu J, Yang P, Gong Y, Ji Q, Shi J et al (2017) Van der Waals epitaxial growth of 2D metallic vanadium diselenide single crystals and their extra-high electrical conductivity. Adv Mater 29:1702359
61. Wang C, Wu X, Ma Y, Mu G, Li Y, Luo C et al (2018) Metallic few-layered VSe_2 nanosheets: high two-dimensional conductivity for flexible in-plane solid-state supercapacitors. J Mater Chem A 6:8299–8306
62. Wang H, Huang X, Lin J, Cui J, Chen Y, Zhu C et al (2017) High-quality monolayer superconductor $NbSe_2$ grown by chemical vapour deposition. Nat commun 8:394
63. Mohanty US (2011) Electrodeposition: a versatile and inexpensive tool for the synthesis of nanoparticles, nanorods, nanowires, and nanoclusters of metals. J Appl Electrochem 41:257–270
64. Nasirpouri F (2017) Electrodeposition of nanostructured materials. Springer International Publishing
65. Albu-Yaron A, Levy-Clement C, Hutchison JL (1999) A study on MoS_2 thin films electrochemically deposited in ethylene glycol at 165 C. Electrochem Solid-State Lett 2:627–630
66. Albu-Yaron A, Lévy-Clément C, Katty A, Bastide S, Tenne R (2000) Influence of the electrochemical deposition parameters on the microstructure of MoS_2 thin films. Thin Solid Films 361:223–228

67. Falola BD, Wiltowski T, Suni II (2016) Electrodeposition of MoS_2 for charge storage in electrochemical supercapacitors. J Electrochem Soc 163:D568–D574
68. Merki D, Fierro S, Vrubel H, Hu X (2011) Amorphous molybdenum sulfide films as catalysts for electrochemical hydrogen production in water. Chem Sci 2:1262–1267
69. Murugesan S, Akkineni A, Chou BP, Glaz MS, Vanden Bout DA, Stevenson KJ (2013) Room temperature electrodeposition of molybdenum sulfide for catalytic and photoluminescence applications. ACS Nano 7:8199–8205
70. Ponomarev EA, Neumann-Spallart M, Hodes G, Levy-Clement C (1996) Electrochemical deposition of MoS_2 thin films by reduction of tetrathiomolybdate. Thin Solid Films 280:86–89
71. Wan X, Chen K, Chen Z, Xie F, Zeng X, Xie W et al (2017) controlled electrochemical deposition of large-area MoS_2 on graphene for high-responsivity photodetectors. Adv Funct Mater 27:1603998
72. Murugesan S, Kearns P, Stevenson KJ (2012) Electrochemical deposition of germanium sulfide from room-temperature ionic liquids and subsequent Ag doping in an aqueous solution. Langmuir 28:5513–5517
73. Devadasan JJ, Sanjeeviraja C, Jayachandran M (2001) Electrodeposition of p-WS_2 thin film and characterisation. J Cryst Growth 226:67–72
74. Jana S, Bera P, Chakraborty B, Mitra BC, Mondal A (2014) Impact of annealing on the electrodeposited WS_2 thin films: enhanced photodegradation of coupled semiconductor. Appl Surf Sci 317:154–159
75. Delphine SM, Jayachandran M, Sanjeeviraja C (2005) Pulsed electrodeposition and characterization of molybdenum diselenide thin film. Mater Res Bull 40:135–147
76. Chandra S, Sahu SN (1984) Electrodeposited semiconducting molybdenum selenide films. I. Preparatory technique and structural characterisation. J Phy D Appl Phy 17:2115
77. Mariappan VK, Krishnamoorthy K, Pazhamalai P, Sahoo S, Kim SJ (2018) Electrodeposited molybdenum selenide sheets on nickel foam as a binder-free electrode for supercapacitor application. Electrochimi Acta 265:514–522
78. Gawale SN, Mane RM, Sargar AM, Mane SR, Kharade RR, Bhosale PN (2010) Electrosynthesis and characterisation of WSe_2 thin films. J Archi Appl Sci Res 2:218–224
79. Delphine SM, Jayachandran M, Sanjeeviraja C (2003) Pulsed electrodeposition and characterisation of tungsten diselenide thin films. Mater Chem Phy 81:78–83

Chapter 3
Properties of Transition Metal Dichalcogenides

James T. Gibbon and Vinod R. Dhanak

Abstract Much of the interest in the two-dimensional transition metal dichalcogenides (2D TMDs) is due to their varied optical, electronic, magnetic and electrical properties, particularly how these properties vary as the number of layers is reduced. In this chapter, we will consider these properties in detail and comment upon how these are useful for various applications.

3.1 Introduction

Numerous crystal structures have been reported for the 2D TMDs, including the 2H, 1T and the (distorted) 1T′ structures. Such a range of crystal structures inevitably results in many varied electronic phases. Figure 3.1 shows a 'periodic table' of the 2D TMDs, indicating the structural and electronic phases observed for each.

In the case of the Pd-based TMDs, the unit cell of the bulk material is orthorhombic [2, 3], with neighbouring sheets bonded via van der Waals forces. Recent density functional theory (DFT) results suggest that the most stable phase of PdS_2 has the corresponding 2D rectangular unit cell, with a pentagonal configuration of atoms [4], and similar results have been shown experimentally for $PdSe_2$ [5]. Experimental verification of the properties of monolayer PdX_2 is rendered difficult as competing Pd_2X_3 phases are frequently formed upon exfoliation [6]. Top and side views of the 2H, 1T and PdX_2 structures are presented in Fig. 3.2. The crystallographic information presented in Fig. 3.2 was obtained from [7] for the 2H structure, [8] for the 1T structure and [3] for the PdX_2-type structure. A final phase of note is the Haeckelite phase predicted for numerous TMDs. In the case of the group VI TMD monolayers, the Haeckelite phases exhibit semi-metallic behaviour, whilst for group V TMD monolayers, a band gap opens resulting in semiconducting behaviour [9].

J. T. Gibbon · V. R. Dhanak (✉)
Department of Physics, University of Liverpool, Liverpool L69 7ZE, UK
e-mail: vin@liverpool.ac.uk

N. S. Arul and V. D. Nithya (eds.), *Two Dimensional Transition Metal Dichalcogenides*,
https://doi.org/10.1007/978-981-13-9045-6_3

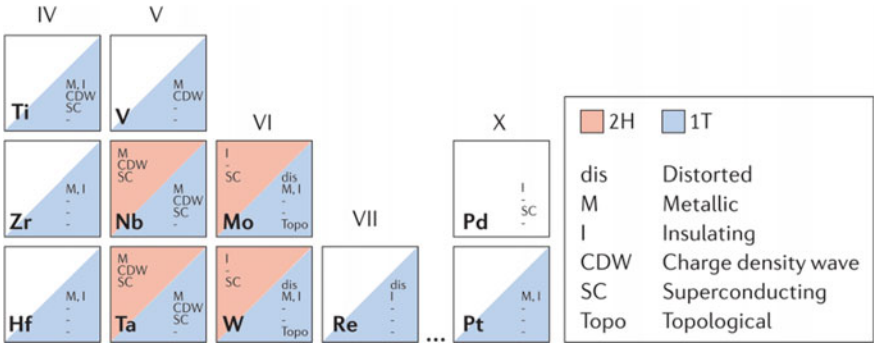

Fig. 3.1 A 'periodic table' of the 2D TMDs showing the many varied structural and electronic phases that the TMDs exhibit [1]. Copyright 2017. Reproduced with permission from Macmillan Publishers Limited

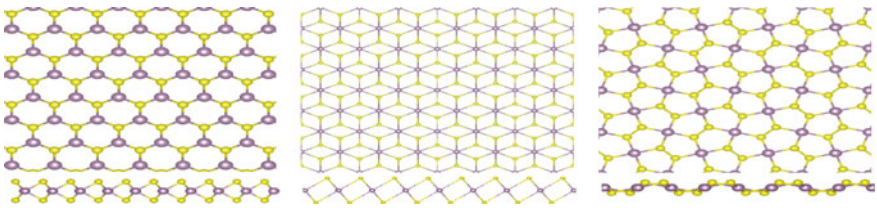

Fig. 3.2 Common crystal structures of the TMDs. Metal atoms are purple, and chalcogen atoms are in yellow. Left shows the top and side views of the 2H structure [7]. Centre shows the top and side views of the 1T structure [8]. Right shows the PdX_2-type structure [3]. This structure is unusual as it is pentagonal as can be seen in the top view. In the side view, it is clear that the structure follows a puckered-type structure

3.2 Optical Properties of the TMDs

Generally, the semiconducting group VI TMDs, MX_2 (M = Mo, W), have an indirect band gap when in the bulk phase. As the number of layers is reduced, there exists a point at which the band gap transitions from an indirect to a direct gap. The transition of the band gap has been studied theoretically and experimentally in the archetypal TMD, MoS_2, by DFT [10, 11] and angle-resolved photoelectron spectroscopy (ARPES) [12], respectively. Early experimental evidence of the transition from an indirect to a direct gap came from observing the increased photoluminescence yield, as the number of layers decreased [13, 14]. Direct observation of the changing value of the band gap with the number of layers has also been made by spatially resolved optical absorption spectroscopy of MoS_2 flakes [15].

Figure 3.3 shows the ARPES band structure for monolayer, bilayer, trilayer and bulk-like MoS_2. For the bulk-like MoS_2 layer, the valence band maximum is at $\overline{\Gamma}$, whilst the conduction band minimum is known to be at $\overline{K}$. As the number of layers is

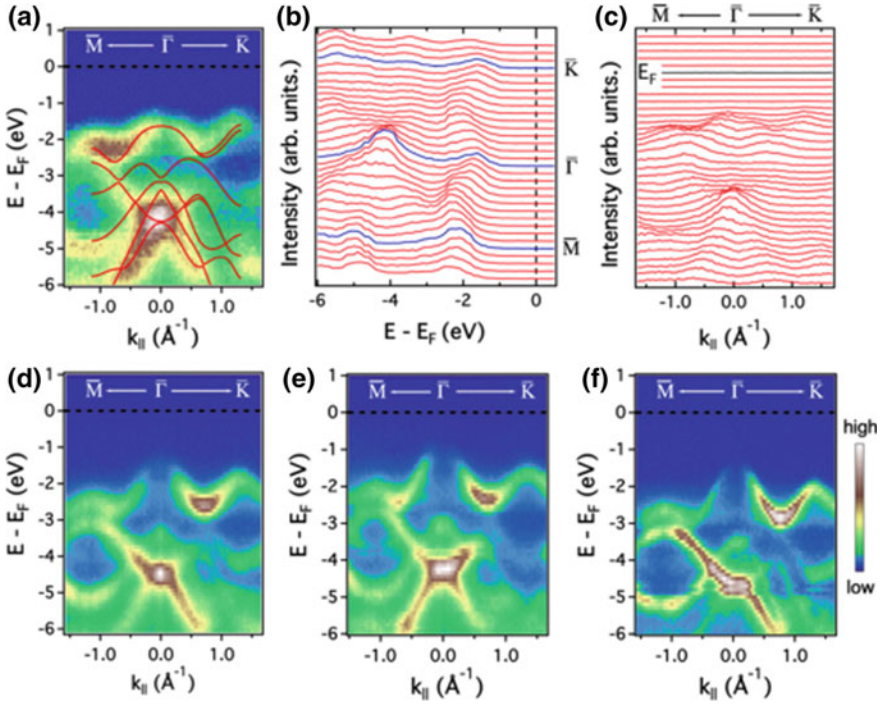

Fig. 3.3 ARPES valence band structure of MoS_2 for varying numbers of layers. **a** Monolayer MoS_2 ARPES valence band spectra overlaid with DFT calculated band structure. **b**, **c** are the corresponding energy and momentum distribution curves, respectively. **d**–**f** ARPES band structure of bilayer, trilayer and bulk-like MoS_2 [12]. Copyright 2013. Reproduced with permission from the American Physical Society

reduced, the states at $\overline{K}$ move upwards in energy towards the VBM at $\overline{\Gamma}$ and finally move above the states at $\overline{\Gamma}$ when the MoS_2 is monolayer in nature. The evolution of the band structure in this way is explained by considering the quantum confinement of the electrons at $\overline{K}$ and $\overline{\Gamma}$. The electrons at $\overline{K}$ are derived from in-plane Mo $d_{x^2-y^2}/d_{xy}$ orbitals, which are unaffected by the confinement in the z-direction [12]. In contrast, the states at $\overline{\Gamma}$ are derived from Mo d_{z^2} and S p_z contributions [12]. As the number of layers is reduced, the interplanar contributions at $\overline{\Gamma}$ are necessarily reduced.

Thus, the energy of the VBM at $\overline{\Gamma}$ is reduced relative to $\overline{K}$ as the number of layers is reduced. Similar behaviour is predicted for many other TMDs including $MoSe_2$, $MoTe_2$ and the tungsten dichalcogenides [10, 11] and has been confirmed experimentally in $MoSe_2$ [16], WS_2 [17] and WSe_2 [17]. Similar behaviour has been seen for $MoTe_2$ [18]; however, verification of this behaviour in WTe_2 has been complicated by the existence of a thermodynamically preferred type II Weyl semimetallic phase [19, 20]. As the increasing band gap with reduced layer number is due to the reduced interactions between neighbouring atomic layers, it is likely that this

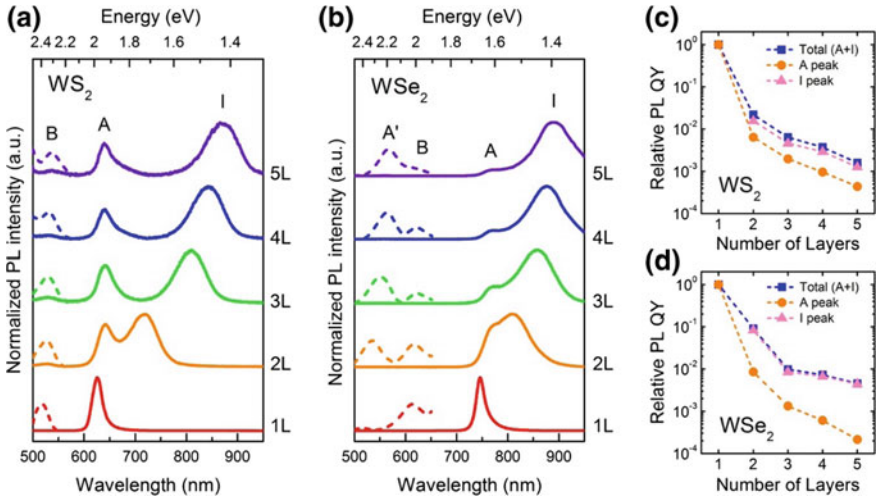

Fig. 3.4 **a**, **b** Normalised photoluminescence of WS_2 and WSe_2 layers, respectively. **c**, **d** The relative photoluminescence quantum yield as a function of layer number for the direct and indirect transition of the WS_2 and WSe_2, respectively [17]. Copyright 2012. Reprinted with permission from the American Chemical Society

behaviour, in fact, holds for all of the semiconducting 2D TMDs in the 2H crystal structure.

Figure 3.4a, b shows the photoluminescent behaviour of monolayers, bilayers and multilayers of WS_2 and WSe_2, after normalisation [17]. In the multilayer regime, a small feature is seen due to photoluminescence across the direct gap (A), with a larger feature occurring for the indirect gap (I).

Also present are hot electron peaks A' and B, corresponding to direct transitions from excited states in the conduction band. As the layer number is reduced, the indirect PL peak moves to higher energy (i.e. lower wavelength), indicating the increasing band gap, whilst the direct gap does not change [17]. The direct PL peak also becomes more intense with decreasing layer number [17] as can be seen in Fig. 3.4c, d, which show the relative PL quantum yield. Similar behaviour is observed in other group VI TMDs [13, 14].

Generally, the absorption spectrum of a 2D material within the infrared–visible part of the electromagnetic spectrum is dominated by a step function-like spectrum resulting from the joint density of states and the matrix elements close to the band edges. In practice, the 2D TMDs actually exhibit strong resonance features close to the absorption edge due to excitonic effects. Doped TMD monolayers have also been observed to exhibit trion quasiparticles [21–26] (i.e. two-hole, one-electron or one-hole, two-electron quasiparticles, analogous to H_2^+ and H^- ions, respectively [27–29]), and there is evidence of bi-excitons [30–38] (bound states of two holes, two electrons) in monolayer TMDs. The binding energy of these excitons is approximately an order of magnitude larger [39–46] than can be obtained from quantum

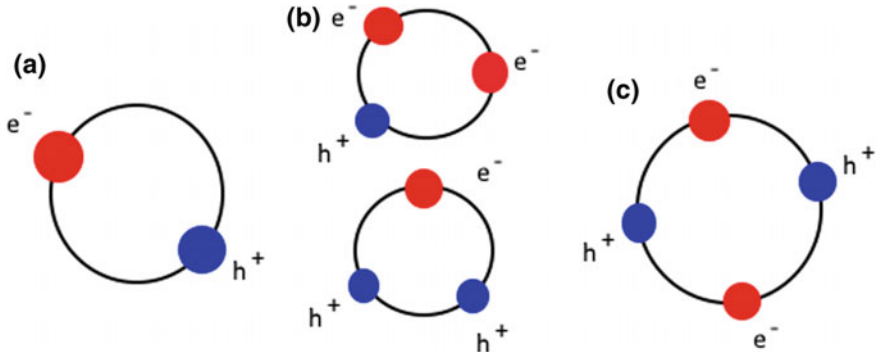

Fig. 3.5 A schematic diagram showing **a** an exciton, **b** negatively and positively charged trions and **c** bi-excitons

well-type structures [47–49] and would thus allow for high-temperature excitonic devices. A schematic diagram showing excitons, trions and bi-excitons can be found in Fig. 3.5. A tuneable excitonic LED has already been demonstrated using monolayer WSe_2 p–n junctions [50]. Manipulation of the excitons can also allow for the nonlinear generation of light [51], by second-harmonic generation, which can be controlled electrically using a FET-like device structure [52] as shown in Fig. 3.6.

Strongly bound excitons have been reported in other layered materials including black phosphorous [53]. Relatively strongly bound excitons have also been reported recently in the layered chalcostibite material, $CuSbS_2$, where an excitonic state with a binding energy of 27 meV was observed in bulk polycrystalline films [54], as shown in Fig. 3.7. By comparison with MoS_2, where the bulk exciton binding energy is reported to be 84 meV [55], it is highly likely that the exciton binding energy of $CuSbS_2$ will similarly increase with reducing layer numbers, as a reduced number of layers result in reduced dielectric screening and greater spatial confinement.

The excitonic properties of the TMDs can also enhance the absorbance of monolayers, resulting in enhanced absorbance in the visible part of the electromagnetic spectrum, as shown in Fig. 3.8 [56]. Photovoltaics devices built on a graphene/MoS_2 monolayer architecture are predicted to have power conversion efficiency (PCE) of only 0.1–1%, whilst WS_2/MoS_2 heterojunctions are expected to exhibit PCEs of 0.4–1.5%, both of which are considerably less than that of commercial Si-based photovoltaics [56]; however, multilayer stacks could be used to increase the PCE further [56].

Alternatively, devices based on these structures could be grown on architectural glass, as a semi-transparent photovoltaic device [57, 58].

The nonlinear optical properties of the semiconducting monolayer TMDs are likely also of interest as they naturally break inversion symmetry due to the reduced dimensionality; however reports on these properties have been limited. The second-order nonlinear susceptibility of WS_2 has been reported to be approximately three orders of magnitude larger than other common nonlinear materials [59]. Results

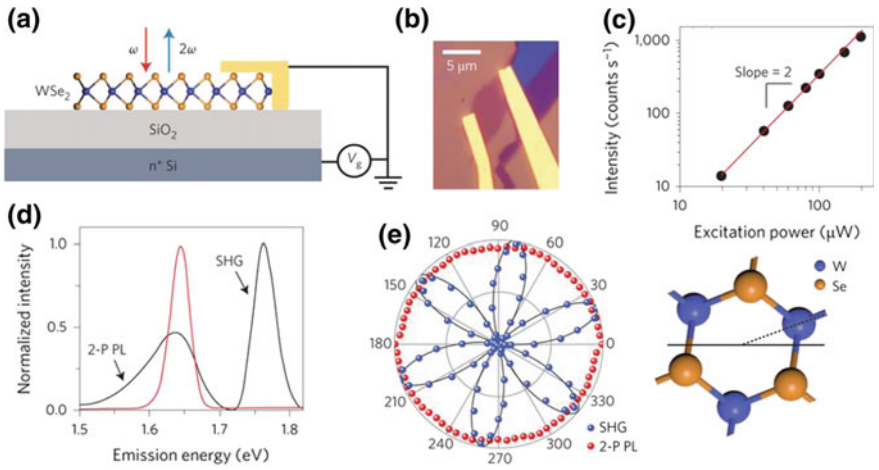

Fig. 3.6 Characterisation of second-harmonic generation (SHG) in a WSe_2 monolayer transistor. **a** A schematic diagram of the WSe_2 monolayer transistor. Excitation with a frequency ω generates second-harmonic radiation at 2ω. **b** A microscope image of the transistor. The shaded area between the contacts is the WSe_2 monolayer. **c** The power dependence of the SHG peak intensity for two-photon resonant excitation of the A exciton. The red line indicates a quadratic fit of the data as would be expected. **d** The emission spectrum for excitation with a 0.83 eV source (red), which is dominated by the SHG and excitation with a 0.88 eV source (black), which shows SHG and two-photon-induced photoluminescence (2P-PL) from the exciton. **e** The left figure shows the SHG and 2-P PL intensity under 0.88 eV excitation parallel to the source polarisation, as a function of crystal angle. The right figure shows the WSe_2 crystal structure with the corresponding orientation. The armchair axis is offset from the horizontal by approximately 20° [52]. Copyright 2015. Reprinted with the permission from Macmillan Publishers Limited

have shown that the nonlinear refractive index of these materials is tuneable [60]. The nonlinear absorption (i.e. two-photon absorption processes, etc.) has also been shown to be size dependent [61] and layer number dependent [62], allowing for further tuning of the optical properties.

Figure 3.9 shows an example of the layer number dependence of the nonlinear optical properties. These materials are, thus, of interest for all-optical switches and other ultrafast photonics applications [63–65]; however, the nonlinear properties and surface passivation need to be further investigated [66]. MoS_2 has also been used to produce nanoscale optical components, including micro-lenses and gratings, allowing for the control of light with considerably higher accuracy than traditional bulk materials [67]. In contrast to the group VI TMDs, the group V TMDs (M = V, Nb, Ta) are not semiconductors, but rather metallic in most cases [68–73], as such the optical properties are relatively limited.

A lesser studied material, TiS_2, is semi-metallic in the bulk; however, some recent research has shown that for 2D sheets, the band gap opens to a direct gap of 2.87 eV, as determined by photoluminescence [74]. In the same work, the TiS_2 sheets also showed comparable transmittance to graphene [74] as shown in Fig. 3.10.

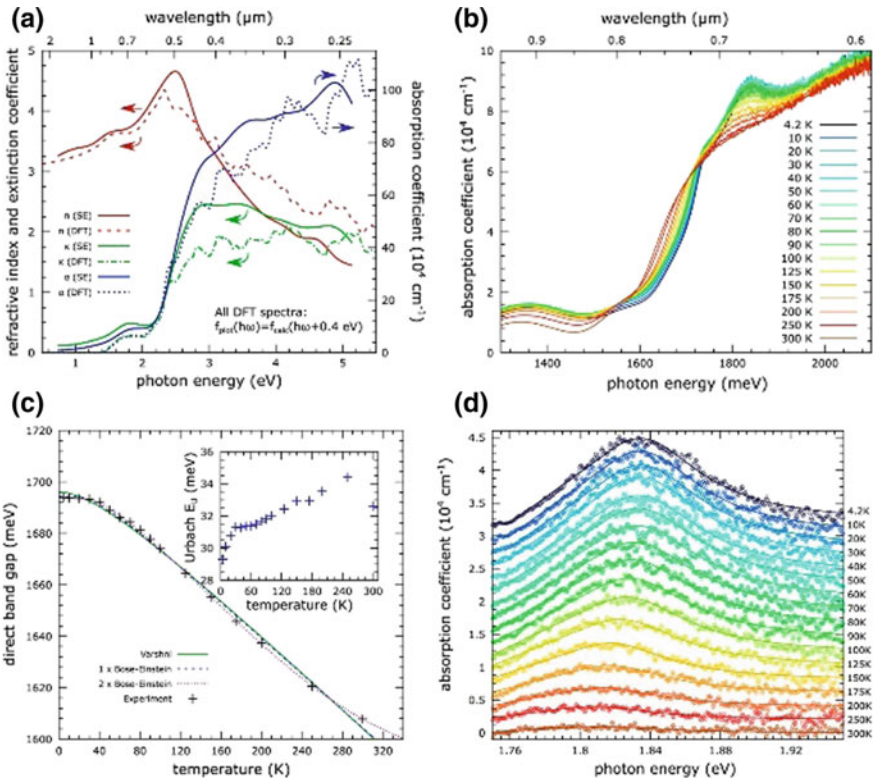

Fig. 3.7 **a** Complex refractive index and absorption spectra obtained from DFT (HSE06) and spectroscopic ellipsometry at 300 K. The DFT spectra are a good match to the experimental spectra. **b** The absorption spectra of the $CuSbS_2$ films as measured by FTIR at temperatures from 4.2 to 300 K. An exciton-like feature is observed to occur at approximately 1.83 eV. **c** The temperature dependence of the optical gap, fitted with the Varshni relation. At high temperatures, an Urbach tail is observed, the size of which can be seen in the inset figure. **d** The temperature-dependent absorption feature after subtraction of the absorption edge [54]. Reproduced with the permission under a CC BY 4.0 License

As such, TiS_2 may be of interest for applications where optically transparent layers are required, such as optoelectronics and photovoltaics, where it has recently been deployed as the n-type layer in a perovskite *n-i-p* solar cell [75], the characteristics of which are shown in Fig. 3.11. Although Sn is not formally a transition metal, it is worth noting that the SnX_2 ($X = S, Se, Te$) compounds also exhibit layered structures and have similar properties to the group VI TMDs.

The bulk band gap of SnS_2 is known to be 2.2 eV [76–80], whilst the monolayer band gap is approximately 2.6–2.7 eV [81]. In contrast to the group VI TMDs, the band gap of SnX_2 remains indirect, even at the monolayer scale [78, 81, 82]. Thus far, reports of high-quality 2D SnX_2 are somewhat limited; however, recent advances have been made by numerous techniques, including atmospheric pressure vapour

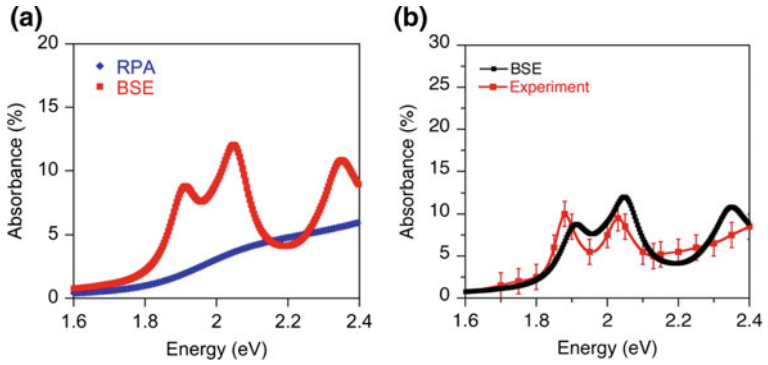

Fig. 3.8 **a** Two different models for the absorption spectra of a MoS_2 monolayer under the DFT-random phase approximation (RPA) and the Bethe–Salpeter equation (BSE) models, which considers excitons. **b** The absorbance of the BSE model compared with experimentally determined absorbance [56]. Copyright 2013. Reproduced and adapted with permission from the American Chemical Society

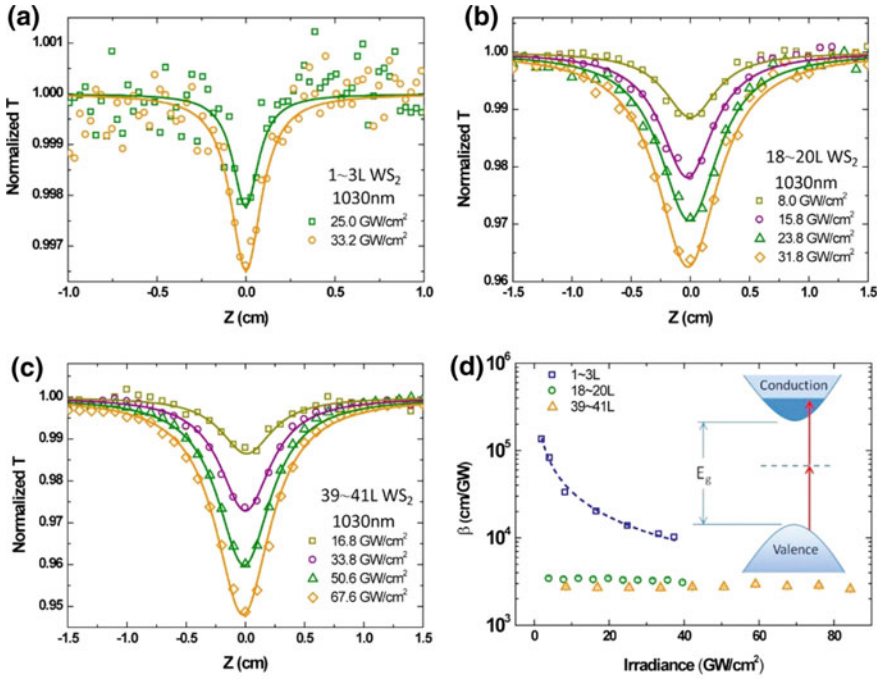

Fig. 3.9 **a–c** Normalised z-scan results for 1–3 layer, 18–20 layer and 39–41 layer WS_2 films with a source wavelength of 1030 nm and a pulse duration of 340 fs. **d** The resulting nonlinear parameter for each set of measurements. The insert of **d** shows a schematic of a two-photon absorption process and also indicates how such processes are saturated [62]. Copyright 2015. Reprinted with permission from the American Chemical Society

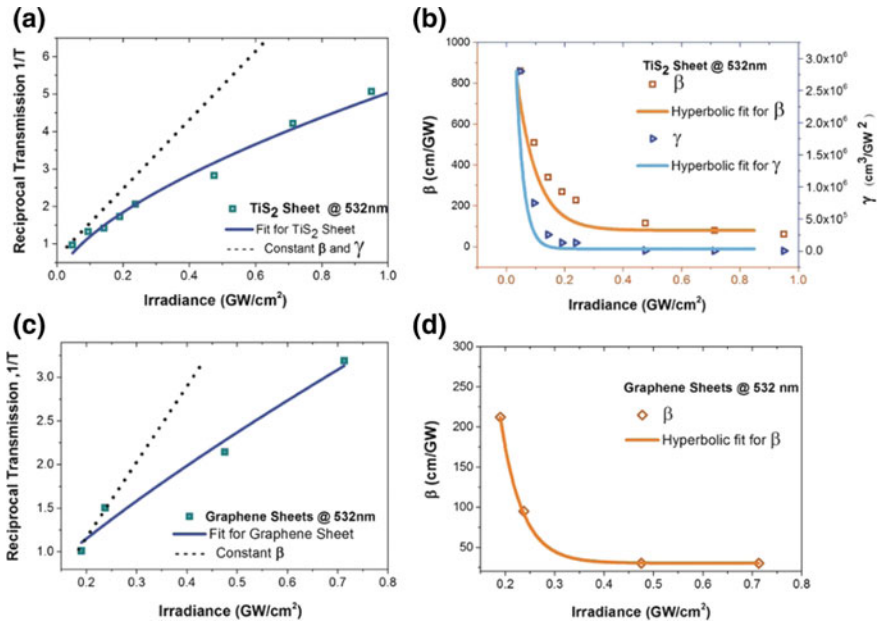

Fig. 3.10 **a**, **c** Reciprocal transmittance for TiS_2 and graphene sheets, respectively. The transmittance for the TiS_2 is comparable to that graphene. **b** and **d** The fits for the nonlinear parameter, β, for TiS_2 and graphene, respectively. Also shown in (**b**) is a fit for the second-order nonlinear parameter, γ [74]. Copyright 2017. Reprinted with permission from Wiley-VCH Verlag GmbH & Co.

deposition [83], chemical vapour deposition [81, 84, 85] and atomic layer deposition [86, 87]. Figure 3.12 shows the characterisation of SnS_2 multilayers, grown by atomic layer deposition on Si substrates. With the band gap being comparatively large, SnS_2 may be of interest for applications where optically transparent layers are required. Two-dimensional SnS_2/MoS_2 heterostructures have already been demonstrated [88].

3.3 Electronic Properties of the TMDs

Many of the 2D TMDs show a number of interesting phases with unusual electronic properties including charge density wave (CDW) phases [89], superconducting phases [90–92], Mott insulating phases and topological insulating phases [93]. Predictions of interesting topological phases [94, 95] have also been made for TMDs in the distorted 1T crystal structure [96, 97], the 1S crystal structure [98] and for nanoribbons [99, 100]. Several possible room temperature topological phases have similarly been predicted from first principles [101, 102]. Despite the many theoret-

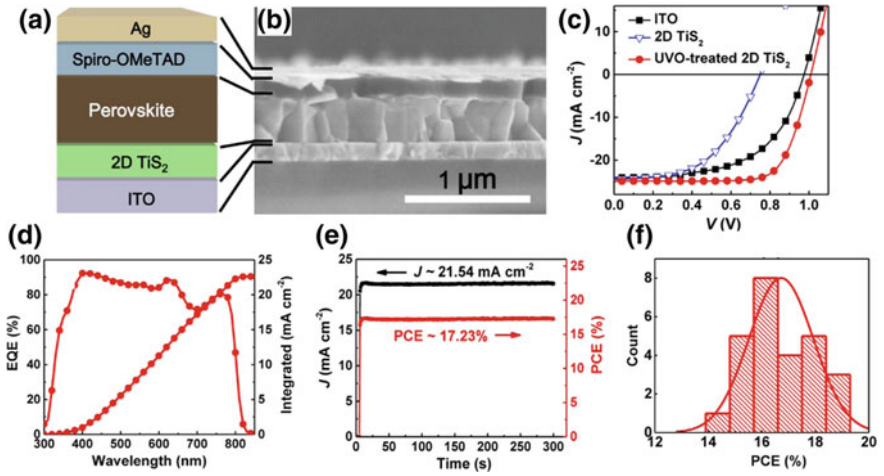

Fig. 3.11 Characteristics of a p-i-n perovskite solar cell, where 2D TiS_2 is used as the n-type layer. **a** A schematic diagram of the device architecture, with **b** showing a corresponding cross-sectional SEM image. **c** The J–V curves of typical cells with different n-type layers under AM 1.5G, 100 mW cm^{-2} illumination. **d** The external quantum efficiency and the integrated current density of the cell with a UVO-treated 2D TiS_2 layer. **e** The steady-state efficiency of devices with a UVO-treated TiS_2 layer. **f** A histogram representing 26 devices with a UVO-treated TiS_2 layer [75]. Copyright 2018. Reprinted with permission from the American Chemical Society

ical predictions of 2D topological phases, experimentalists are yet to demonstrate these phases convincingly.

The monolayers of the group VI TMDs have a direct band gap at $\overline{K}$, as outlined in the previous section. However, there are two points at which $\overline{K}$ occurs, namely K and K'. This results in two degenerate valleys, one at K and the other at K'. The degeneracy of the two valleys can be broken by the application of an external field, such as a strain or magnetic field [103]. This can be seen in Fig. 3.13, where in Fig. 3.13d, e, the energies of the valence band maxima at K and K' are clearly at different energies. Experimental breaking of the valley degeneracy has been reported in several cases [104–106].

The separation of charge carriers in reciprocal space can also lead to the formation of numerous quasiparticles including Dirac fermions [107], polaritons [108] and intervalley (bi)excitons [31, 33, 37]. The electrons in the different valleys are also subject to opposite effective Zeeman fields, known as the Ising spin–orbit coupling (SOC) [92]. If a half-metallic layer is placed on top of a monolayer TMD, spin triplet Cooper pairs in the TMD can induce topological superconducting behaviour in the half-metallic layer [92].

Superconductivity has been demonstrated in numerous TMDs, including the Nb- [109], [110] and Ta-based [111], [112] dichalcogenides, WTe_2 [90], $MoTe_2$ [91], MoS_2 [113] and WS_2 [113]. In the case of the Nb- and Ta-based TMDs, a CDW phase is also observed. Castro Neto [114] provided a unified microscopic theory to

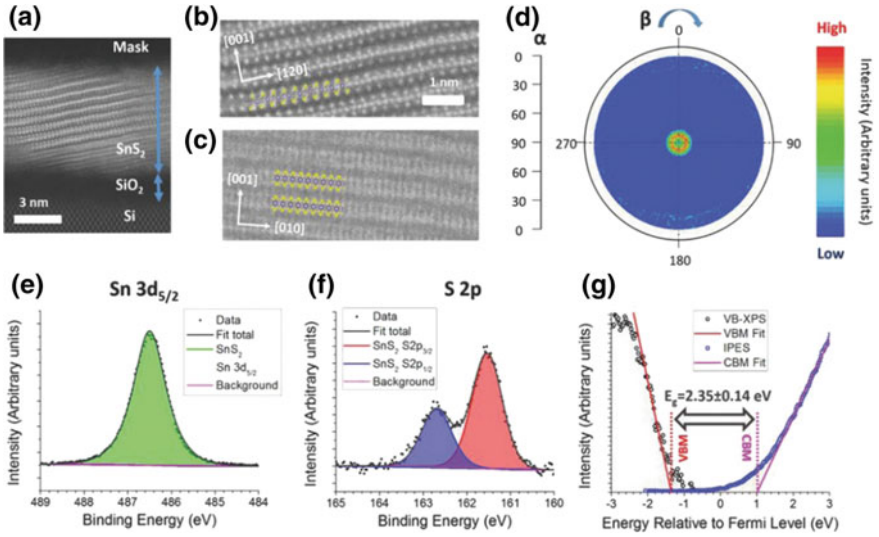

Fig. 3.12 Characterisation of SnS_2 multilayer films. **a** A cross-sectional HAADF-STEM image deposited on Si substrates. **b** and **c** Enlarged HAADF-STEM images with the SnS_2 crystal structure superimposed along the [100] and [210] directions, respectively. **d** The SnS_2 (001) in-plane pole figure, which indicates that the (001) plane is tilted by about 10° with respect to the substrate surface. **e** and **f** The Sn $3d_{5/2}$ and S 2p core levels as measured by XPS, the fact that only one set of spin–orbit split components suggests that the multilayers are phase-pure. **g** The valence band maximum and conduction band minimum of the multilayer as measured by XPS and IPES, respectively. By combining the band edge positions, the band gap of the multilayers can be obtained [87]. Copyright 2018. Figure reproduced with permission Wiley-VCH Verlag GmbH & Co.

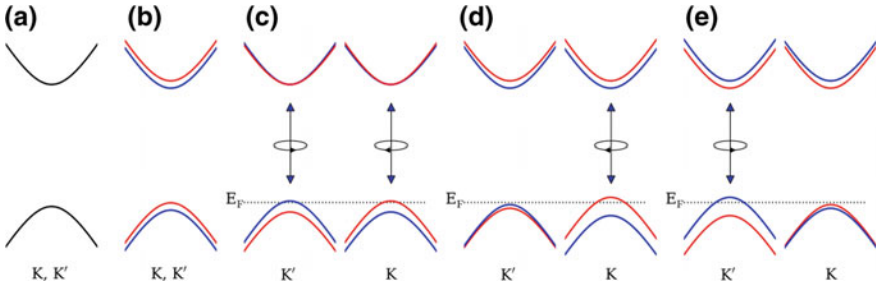

Fig. 3.13 Band structure of monolayer MoS_2 close to the K and K' points. **a** pristine, without spin–orbit coupling (SOC), **b** with exchange field, but no SOC, **c** pristine with SOC, **d** with exchange field and SOC and **e** with exchange field and SOC but with inverted spin polarisation to (**d**), and red and blue indicate spin-up and spin-down state, respectively [103]. Copyright 2014. Reprinted figure with permission from the American Physical Society

explain both the CDW and the superconducting phases of these materials. In this theory, the primary excitations in the CDW phase are the Dirac electrons. The host materials thus remain good metals whilst in the CDW phase. The Dirac electrons are then coupled to the acoustic phonons due to the loss of the lattice inversion symmetry, resulting in a damping of the electrons. These same phonons then drive the system to a superconducting state via a Kosterlitz–Thouless phase transition, where the Cooper pairs consist of Dirac fermions with momenta opposite to that of the Dirac points.

No CDW phase has been reported for the Mo- or W-based TMDs, suggesting a different origin of the superconducting behaviour. Several explanations have been proposed for origin of superconductivity in MoS_2, namely electron–phonon interactions (or quasiparticle–boson interactions) [115, 116], Ising SOC [92] and electron–electron interactions [117].

In the case of electron–electron interactions as the origin of superconductivity in MoS_2, the short-range repulsive forces between carriers at the conduction band induce the superconducting phase, with a gap of opposite sign at the inequivalent pockets of the conduction band [117]. $MoSe_2$, WS_2 and WSe_2 will likely share the same origin of superconductivity as MoS_2. In contrast, the electron–phonon interaction is heavily dependent on the occupation of valleys in the conduction band [115]; however when electron–electron interactions are neglected, the critical temperatures T_C are consistently overestimated [116]. CDW phases have, in fact, been predicted for MoS_2 at high doping levels [118], which may aid in unifying the origin of the superconductivity of the Mo- and W-based dichalcogenides, with the Ta and Nb chalcogenides. By considering Rashba SOC and the electron–electron interactions, MoS_2 has been predicted to support numerous superconducting phases [100]. Defects also play a key role in determining the electronic properties of the TMDs. MoS_2 has been shown to exhibit both n-type [119–122] and p-type behaviours [122–126]. Different conductivity behaviours have, in fact, been observed within the same sample, over the scale of nanometres, and appear to be heavily dependent on the local defect density [127], as can be seen in Fig. 3.14.

The presence of defects has also been shown to significantly affect the height of the Schottky barrier between the TMDs and the metallic contacts [128–130]. Considerations of the defects in TMDs are therefore critical for applications in electronic devices. It is reasonable to assume that this behaviour will likely extend to further TMDs, and in fact, both n-type and p-type conductivities have also been demonstrated in other TMDs [131–133].

In both WSe_2 and MoS_2 single crystals, irradiation with Ar^+ results in chalcogen vacancies and causes the Fermi level of the crystal to move towards the valence band edge [130, 134], suggesting that the crystal surface becomes more p-type in nature or alternatively that the bands are bent upwards by the surface defects. In contrast, when polycrystalline films or naturally occurring molybdenite is etched in the same manner, chalcogen vacancies are still produced, but the Fermi level of the sample is not observed to change, presumably due to pinning of the Fermi level by surface defects [126, 134, 135].

In the work of Santoni et al. [126], polycrystalline thin films of MoS_2, formed by the sulphurisation of Mo films on glass, are exposed to Ar^+ ion irradiation with

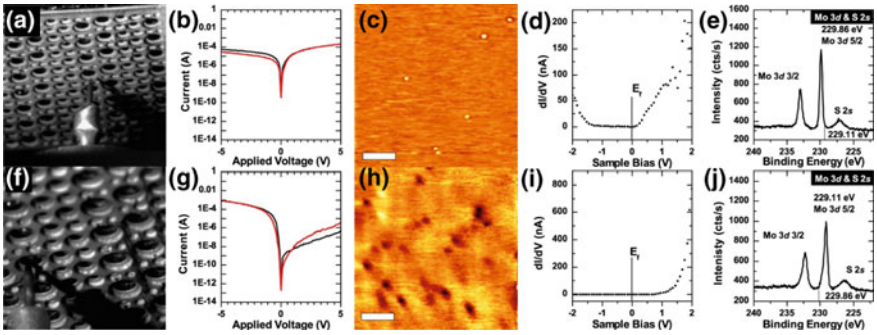

Fig. 3.14 Correlated I–V characteristics of MoS_2 crystals with STM, STS and XPS **a** STM tip position above an aperture in a shadow mask. **b** I–V characteristics of the MoS_2 crystal measured from a particular aperture, indicative of n-type behaviour. Measurements shown in **c**–**f** were made on the same aperture as (**b**). **c** STM image showing light and dark defects. **d** STS from the aperture used for (**b**), showing the Fermi level close to the conduction band, indicating n-type behaviour. **e** XPS spectrum of the Mo 3d and S 2s core levels, consistent with n-type MoS_2. **f** A different aperture in the shadow mask. **g** I–V characteristics from the second aperture. The asymmetry on the positive voltage side is indicative of p-type behaviour. **h**–**j** Measured from the same aperture. **h** STM image showing a high concentration of dark defects. **i** STS results showing that the Fermi level is much further away from the conduction band than for (**d**), suggesting p-type behaviour (**j**) XPS spectrum of the Mo 3d and S 2s regions. The shift in the core levels relative to those in (**e**) is indicative of p-type behaviour [127]. Copyright 2014. Reprinted with permission from the American Chemical Society

increasing ion dosage and the changes in the chemical and electronic structures are observed using XPS and IPES. The XPS spectra of the Mo 3d regions are shown in Fig. 3.15. In this work, it is found that the surface region can become heavily depleted of sulphur, with the Mo 3d component due to the MoS_2 having much less area than the area of the metallic Mo^0 species; i.e. the metal: sulphide ratio reaches a value of greater than 1.5:1. An equilibrium state is found to occur at 2.49×10^{17} ions/cm^2.

Unpublished work by the authors of this chapter considers Ar^+ ion bombardment of MoS_2 multilayers exfoliated by carbon tape from a bulk synthetic single crystal (2D semiconductors). The multilayers reach an equilibrium state at considerably lower dosages (6.0×10^{15} ions/cm^2) than in the work of Santoni et al. [126] and have a much smaller metal: sulphide ratio (0.74:1) than reported elsewhere, as can be seen by comparing Fig. 3.16f and Fig. 3.16e. This is likely due to the reduced dimensionality of the multilayer system, as in bulk-like systems, both preferential sputtering and ion implantation can occur. Implantation of lighter ions from the surface region into the bulk is known to occur, even at low ion energies. Clearly, this process cannot happen in a multilayer system such as that investigated, due to the reduced dimensionality of the system; as such, this may explain the different ratios at which the steady state occurs. Similarly, the reduced dimensionality is likely the reason for the equilibrium state occurring at reduced dosage in the case of MoS_2 multilayers.

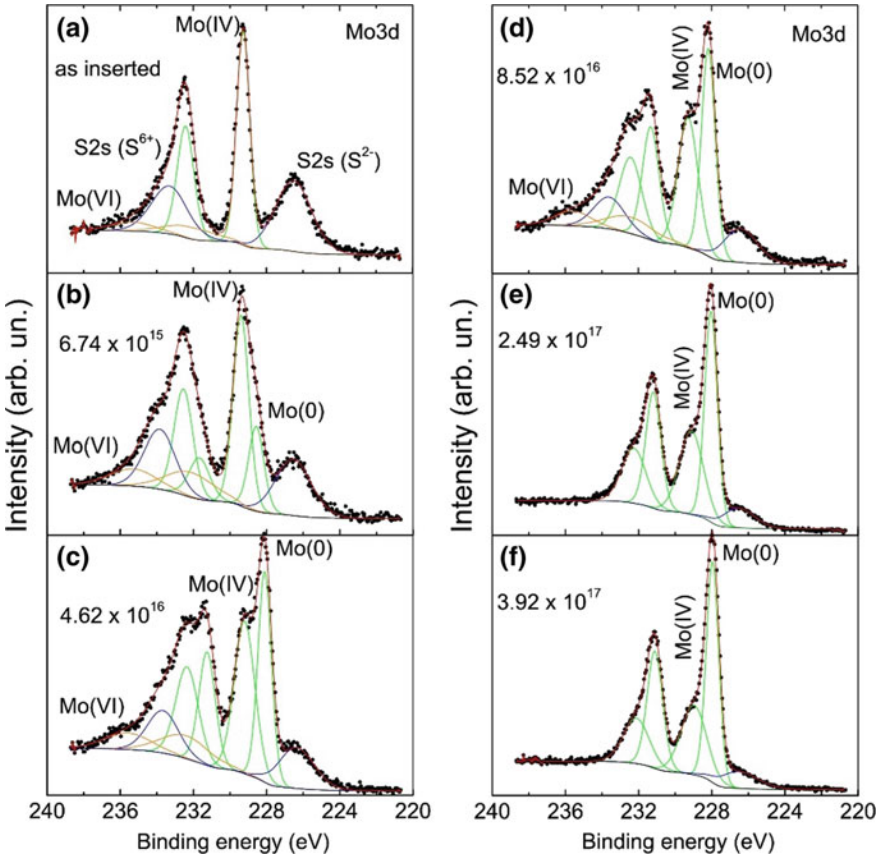

Fig. 3.15 Mo 3d X-ray photoelectron spectra from polycrystalline MoS_2 thin films grown on glass at increasing Ar^+ ion doses. Ion doses are indicated on the graphs, in units of ions/cm^2 [126]. Copyright 2017. Reprinted with permission from Elsevier

Table 3.1 shows the binding energies of the features shown in Fig. 3.16. The binding energy position of the low ion dose sample is consistent with the exfoliated layers being p-type in nature [126, 127, 136]. With increasing ion dose, the binding energies of the core levels due to the stoichiometric MoS_2 are shifted to lower binding energy by 0.10 ± 0.05 eV. In contrast, metallic Mo^0 species starts at 0.70 eV below the MoS_2 peak, but moves to be approximately 0.90 eV below the stoichiometric species. This is consistent with Santoni et al. [126], who found that the metallic species was initially 0.70 eV below the MoS_2 species, before moving to approximately 1.00 eV below the MoS_2 species once the sample was equilibrated.

Figure 3.16d, h shows the valence bands of the dosed material. At low ion dose, the valence band maximum occurs at 0.56 eV from the Fermi level. With increasing ion dose, the valence band maximum approaches the Fermi level, until a steady state is reached, at which point the valence band maximum is only 0.24 eV away from

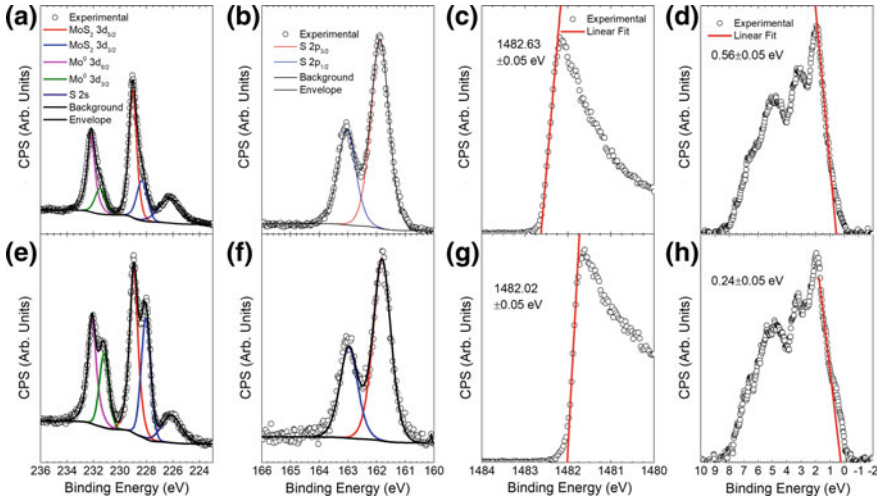

Fig. 3.16 XPS spectra of MoS_2 multilayers after Ar^+ ion etching. **a** and **e** The Mo 3d regions after receiving an ion dosage of 6×10^{14} and 6×10^{15} ions/cm^2. **b** and **f** The S 2p at the same dosage. **c** and **g** The secondary electron cut-off (SEC), whilst **d** and **h** the valence bands for the same ion doses

Table 3.1 A summary of the binding energies of features shown in Fig. 3.16

Ion dose (ions/cm^2)	Binding energy (eV)						Mo^0/MoS_2
	MoS_2 $3d_{5/2}$	Mo^0 $3d_{5/2}$	S 2 s	S $2p_{3/2}$	SEC	VBM, ξ	
6×10^{14}	229.05	228.35	226.21	161.88	1482.63	0.56	0.40
6×10^{15}	228.97	228.05	226.10	161.81	1482.02	0.24	0.74

Also given is the area ratio of the metallic Mo^0 species to that of the MoS_2 species

the Fermi level. Intriguingly, there is a little variation in the relative intensities of the features in the valence band, suggesting that at the photon energy used ($h\omega =$ 1486.6 eV), the valence band is dominated by Mo states. Also present in (d) and (h) are intensities at the Fermi level. This is due to the presence of the metallic Mo^0 states. Also of interest is the secondary electron cut-off, which moves to lower binding energy (0.61 eV). This is of interest as the ionisation potential is given by the relation $V_{IP} = h\omega$-(SEC $- \xi$); thus as the relative shifts of the VBM and the SEC differ, there appears to be some tunability in the ionisation potential and electron affinity of the material.

In contrast to MoS_2, $MoSe_2$ single crystals were found to require a considerably larger ion dose of 18×10^{16} ions cm^2 to reach a steady state. Figure 3.17 shows the Mo 3d core levels for various ion dosages, the binding energies of which are presented in Table 3.2. It should be noted that as these results are from a bulk single crystal the sputtered atoms can be implanted into the bulk material, allowing for a

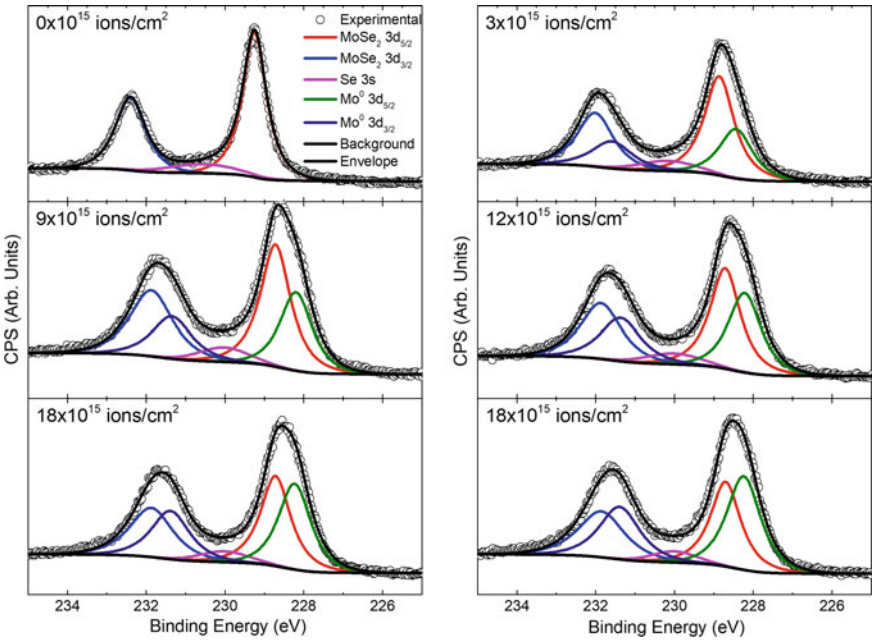

Fig. 3.17 Mo 3d core levels for a $MoSe_2$ multilayer exposed to increasing Ar^+ ion doses. As the dosage increases, the area of the Mo^0 component increases up to a dosage of 15×10^{15} ions/cm^2, at which point a steady state is reached

Table 3.2 A summary of the binding energies of core levels in the Ar^+ ion-dosed $MoSe_2$ single crystal at different dosages

Ion dosage ($\times 10^{15}$ ions/cm^2)	Binding energy (eV)			$Mo^0/MoSe_2$	Se/Mo
	$MoSe_2$ $3d_{5/2}$	Mo^0 $3d_{5/2}$	Se 3s		
0	229.25	N/A	230.55	0.00	2.00
3	228.86	228.43	230.16	0.52	1.43
9	228.72	228.20	230.02	0.64	1.28
12	228.71	228.22	230.01	0.81	1.16
15	228.72	228.23	230.02	0.96	1.03
18	228.72	228.24	230.00	1.17	0.96

Also given is the ratio of the area of the metallic Mo^0 species to that of the $MoSe_2$ species

larger Mo^0/MoX_2 ratio than was possible for the MoS_2 above. However, the final Mo^0/MoX_2 ratio is smaller than that obtained for bulk MoS_2 by Santoni et al. [126]. This is reasonable, as the atomic mass of Se is much closer to that of Mo than the atomic mass of S is. As such, preferential sputtering processes are considerably less likely, resulting in a higher X/Mo ratio and hence a smaller $Mo^0/MoSe_2$ ratio.

The binding energies presented in Table 3.2 are consistent with those of Abdallah et al. [137] both before and after Ar^+ ion etching. Similarly, the final Se/Mo ratio obtained is consistent with that found by Bernede [138].

As outlined previously, the TMDs have unusually strongly bound excitons, allowing for their existence and application at high temperatures. Another intriguing property of excitons is that due to their bosonic nature, they can, in principle, Bose condense. Excitonic condensates have been observed in semiconductor quantum well structures and in quantum Hall bilayers previously; however, recent work by Kogar et al. [139] described the observation of an excitonic condensate in $TiSe_2$. These excitonic condensates have a considerable advantage over traditional condensates, namely that they should be observable at much higher temperatures than would normally be the case, allowing their fundamental properties to be investigated much more effectively. This is particularly important for the long-standing metal–insulator problem, where exciton condensates have long been theorised to play a fundamental role. Such a system would also help facilitate the study of macroscopic, coherent quantum systems.

3.4 Magnetic Properties of the TMDs

The VX_2 compounds are expected to be ferromagnetic from the bulk [140], down to the monolayer regimes [89, 140–142]. Room temperature ferromagnetic behaviour has been observed in VSe_2 chemically exfoliated nanosheets [89] and monolayers [143] as well as in few-layered VS_2 [144]. Results from DFT suggest that the ferromagnetic behaviour is primarily due to the V^{4+} ions in the lattice, with electronic structure $[A]3d^1$, resulting in an unpaired electron and through-bond spin polarisation [141]. Interestingly, for VS_2, the most stable phase exhibits the 1T-VS_2 structure, which when reduced to a monolayer remains metallic. However, the H-VS_2 structure is more stable at the monolayer level [145]. An energy level diagram for the T-VS_2 and H-VS_2 structures in different magnetic phases is shown in Fig. 3.18, the energy scale of which is referenced to the T-VS_2 ferromagnetic ground state [145].

In both theoretical [145–150] and experimental works [144, 151], a band gap opens for few-layered H-VS_2, resulting in a magnetic semiconductor (Fig. 3.19), with a magnetic moment of 1.0 μ_B per unit cell [145, 146, 148–150, 152]. Similar predictions have also been made for VSe_2 and VTe_2 [140, 150, 152].

Room temperature ferromagnetic behaviour has also been demonstrated in T-VSe_2 monolayers grown on HOPG and MoS_2 substrates [143], where it is found that the temperature dependence of the magnetic properties is enhanced, when VSe_2 is grown on MoS_2 compared to HOPG. In contrast, a recently accepted work concerning VSe_2 monolayers grown by molecular beam epitaxy on bilayer graphene and HOPG finds no ferromagnetic ordering down to 10 K [153]. X-ray magnetic circular dichroism (XMCD) measurements of the V $L_{2,3}$ edge showed no dichroism down to 100 K, in a magnetic field of 9 T, indicating a lack of ferromagnetic behaviour. ARPES measurements show only a single V *d*-band in contrast to the split minority and

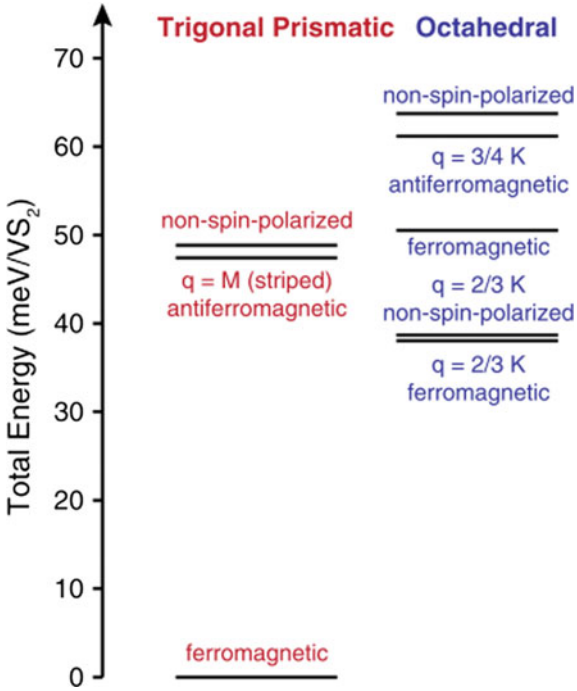

Fig. 3.18 DFT energy level diagrams for the T-VS_2 and H-VS_2 in different magnetic phases. The energy scale is referenced to the T-VS_2 ferromagnetic ground state [145]. Copyright 2016. Reprinted figure with permission from the American Physical Society

majority spin bands predicted by magnetic calculations, as can be seen in Fig. 3.19 [153]. The single V *d*-band is observed down to temperatures of 10 K, suggesting no magnetic ordering to this temperature.

The authors speculate that their work contrasts with that phase fluctuations may play an important role in determining the magnetic properties of the system, suggesting that these may cause renormalisation of the energy scale of the ferromagnetic phase to below that at which the CDW is dominant [153]; however, further research is required to fully understand the competition between the magnetic and the non-magnetic states in VSe_2 monolayers.

An intriguing observation in the same work [153] is the presence of a Van Hove singularity (i.e. a point in the density of states [DOS] where the DOS is not differentiable [154]), close to the Fermi edge (Fig. 3.20). The presence of such a singularity at a small energy separation from the Fermi level suggests that by controlled doping of the VSe_2 monolayer, it may be possible to drive a Lifshitz transition [155, 156]. At low temperatures, extra features are seen in the low-energy electron diffraction (LEED) pattern, which are suggested to be due to the $\overline{\Gamma}_{(11)}$ family of charge order spots with an ordering wavevector $\boldsymbol{q}_{CDW} = (1/4, 1/4)$ [153].

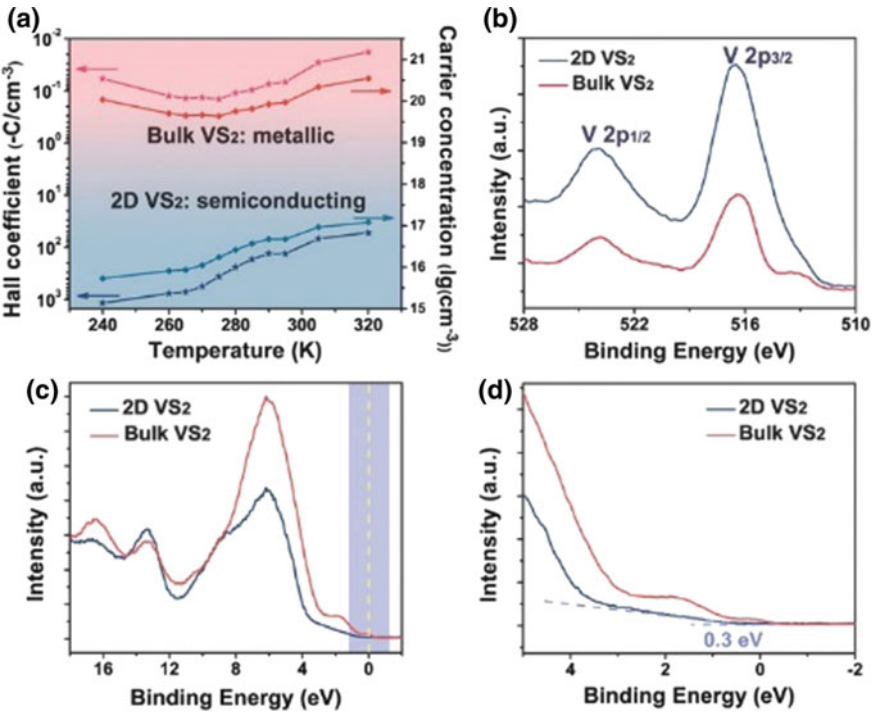

Fig. 3.19 **a** Hall coefficient and carrier densities for bulk, metallic VS_2 and few-layered, semiconducting VS_2. **b** The V 2p core level as measured by XPS. **c** The valence band of bulk and few-layered VS_2 as measured by UPS. **d** The region close to the Fermi level for bulk and few-layered VS_2. For the bulk VS_2, there is intensity at the Fermi level, indicative of metallic behaviour; however for the few-layered VS_2, the valence band edge occurs at 0.3 eV below the Fermi level, indicating that the few-layered VS_2 is a semiconductor [144]. Copyright 2017. Figure adapted with permission from Wiley-VCH Verlag GmbH & Co.

Low layer number VX_2 is therefore highly interesting material for optomagnetic and spintronic applications, although further work is required to fully understand their properties. Although not expected to natively exhibit magnetic properties, ferromagnetism (Fig. 3.21) is exhibited in both bulk, nanosheet and exfoliated MoS_2 and WS_2 [157–159]. Theoretical models based on MoS_2 nanoribbons suggest that these are due to the presence of zigzag edges, which are (half-)metallic, and have a nonzero magnetic moment, in contrast to armchair edges, which are semiconducting and non-magnetic [160–163]. The zigzag edges are more chemically stable, are energetically favourable and hence would be expected at the edges of crystals and atomic-scale layers [158, 160, 163, 164].

In nanosheets and exfoliated MoS_2 and WS_2, the layers exhibiting ferromagnetism are found to have a high density of point defects [157], [159]. Theoretical modelling suggests that molybdenum and sulphur vacancies can both produce magnetic moments comparable to μ_B [157, 162, 164]. An alternative explanation is that

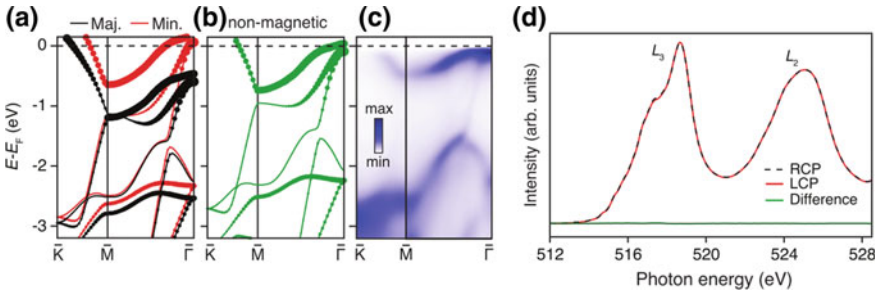

Fig. 3.20 Electronic structure of VSe_2 monolayers resulting from **a** spin-polarised **b** non-magnetic DFT calculations. The calculations are projected onto the V 3d orbital characters, which is signified by the size of the data points. **c** The equivalent ARPES spectrum which is consistent with the non-magnetic calculations only. **d** The X-ray absorption spectra close to the V $L_{2,3}$-edge using left circularly polarised (LCP) and right circularly polarised light in a 9 T magnetic field at 100 K. The green line shows the difference spectrum, which shows the negligible difference, indicating the absence of XMCD and hence a lack of ferromagnetic ordering [153]. Copyright 2018. Reprinted with permission from the American Chemical Society

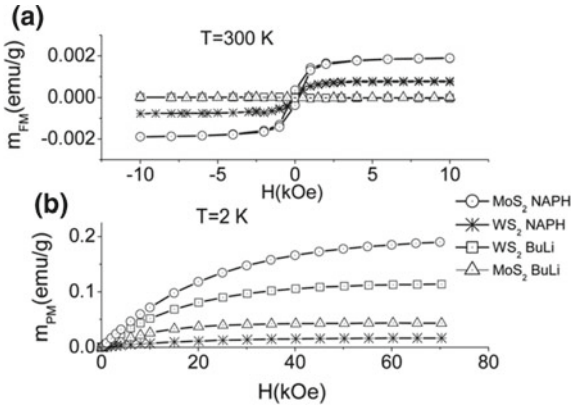

Fig. 3.21 **a** Ferromagnetic hysteresis loops of monolayers of MoS_2 and WS_2 exfoliated by two different chemical methods, measured at room temperature. **b** The magnetisation curves for the same samples measured at 2 K [159]. Figure reprinted with permission from the Royal Society of Chemistry, under a Creative Commons Attribution 3.0 Unported Licence

wrinkles are observed by TEM in exfoliated samples [159], which has also been seen in ferromagnetic $ReSe_2$ nanosheets [165]. Finally, unsaturated bonds at the edges of the sample may be responsible [157]. Intriguingly, the Curie temperature observed for nanosheet MoS_2 is 685 K, higher than that of other magnetic semiconductors [157]. An alternative approach to inducing magnetism in the 2D TMDs is to introduce magnetic defects by doping the material with metals [166–169] or other elements, introducing defects [170, 171], applying strain [170–172] or irradiation by charged particles [173].

There are two main approaches to doping the TMD with metallic atoms. Firstly, the dopant atom can replace the metal atom in the TMD, and secondly the dopant atom can replace the chalcogen. Typically, the dopant will be more likely to occupy a metal lattice site, rather than a chalcogen lattice site, due to the larger difference in the electron affinity and ionic radius of the chalcogen. However, to confirm this X-ray photoelectron spectroscopy should be used to confirm the chemical state of the dopant. Theoretical methods have identified numerous potential dopants for the metal site that could induce magnetic behaviour, namely Mn [166, 168, 174–181], Ni [174, 182, 183, Fe [166, 174, 176–181], Co [166, 174, 176–182], Zn [177], Cd [177], Cr [166, 176, 179–181], V [166, 178–180], Cu [166, 178, 184] and Hg [177] and others [182, 185–190]. Co doping of transition metal pairs has also been suggested to produce enhanced ferromagnetic coupling [191].

Experimental verification of this behaviour is still ongoing, with ferromagnetic behaviour having been observed in Mn- [169, 174, 192], Fe- [174], Ni- [174], Co- [174] and Cu [193] -doped MoS_2. In the case of Cu-doped MoS_2, the ferromagnetic behaviour originates from the strong hybridisation of the Cu 3d bands, the Mo 4d bands and the S 3p bands [193], with a similar origin also being proposed for Ni-doped MoS_2 [183]. A key requirement for the development of spintronic devices is that the ferromagnetic behaviour is observed at high temperature. In Cu-doped MoS_2, the Curie temperature is found to occur at approximately 930 K [193]; thus, Cu-doped MoS_2 is of interest for spintronic applications.

Room temperature ferromagnetism has also been realised in the Fe-doped MoS_2 [194] and Fe-doped ZrS_2 [195] systems, with Curie temperatures of > 930 K and 385 K, respectively. Also of importance for the development of spintronics is the ability to switch magnetic states. Recent results of first principles calculations indicate that the ferromagnetic response of transition metal-doped MoS_2 can be switched to an antiferromagnetic response by current injection [196], which is a key result for the development of spintronic devices based on these materials.

An alternative method is to use a different number of layers, as first principles calculations have shown that for the Fe-doped MoS_2 system, monolayers are ferromagnetic, whilst bilayers and multilayers are antiferromagnetic due to the competition between the double-exchange and super-exchange couplings [197]. The spin densities of Fe-doped MoS_2 monolayers and bilayer are shown in Fig. 3.22.

Numerous theoretical works have considered both transition metal [167] and non-metal dopants on the chalcogen lattice sites [167, 179, 198, 199]. Caution must, however, be taken when doping the 2D TMDs as numerous theoretical works have shown that the dopants can have significant effects on the band structure of the host material [200], by reducing the band gap [199] or changing the host from a semiconducting to a semi-metallic material [179, 198, 201].

A particularly novel magnetic system in the TMDs is the case of Cr doping of $TiSe_2$ [202]. The HAADF-STEM image of $TiSe_2$ with model crystal structures and Curie–Weiss plot are shown in Fig. 3.23. At Cr concentrations up to 20%, the Cr ions primarily occupy the interstitial sites between octahedral layers. However, at higher concentrations, the Cr ions start to substitute Ti, which is displaced to the interstitial

sites, resulting in considerable lattice disorder. The disorder causes frustration of the magnetic ordering, resulting in the formation of a spin glass [201–204].

However, the Cr concentrations at which the phase changes to and from the spin glass state are inconsistent in the reports to date, suggesting that it is dependent on the growth and intercalation methods [202–204].

3.5 Electrical Properties of the TMDs

Probably, the most important application of semiconductors is in digital electronics, which is fundamentally based on the transistor. By Moore's law, the number of transistors in an integrated circuit doubles every two years; however, modern state-of-the-art silicon-based metal-oxide-semiconductor field-effect transistors (MOSFETs) are approaching sizes where quantum effects (i.e. quantum tunnelling) are no longer negligible and heat dissipation becomes an issue. Recently, IBM announced the development of 5-nm transistors based on Si nanosheets [205]; however, reducing the size beyond this is likely to prove difficult for the aforementioned reasons.

One of the key developments that has enabled nanoscale devices is the development of high-κ dielectrics (i.e. a dielectric layer with a dielectric constant much larger than that of SiO_2.) such as HfO_2, Ta_2O_5 and ZrO_2. The use of a high-κ dielectric results in a much reduced leakage current compared to a SiO_2 layer of the same thickness. However, the dielectric constant is inversely related to the band gap [206] as can be seen in Fig. 3.24. This is problematic as the conduction band offset between the channel and the dielectric is required to be greater than 1 eV to prevent current leak-

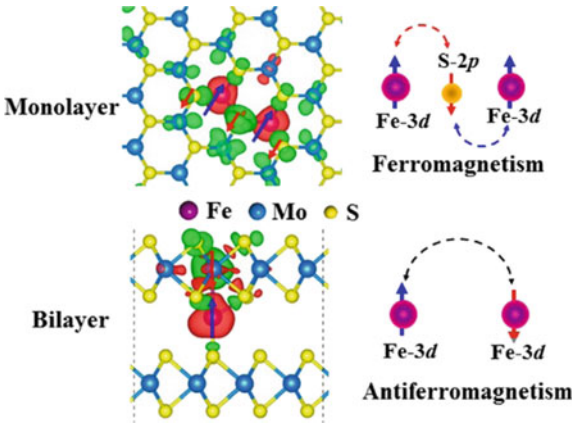

Fig. 3.22 Spin densities of Fe-doped MoS_2 monolayers and bilayers. Red and green isosurfaces denote positive and negative spin densities. Blue and red arrows denote opposite spin polarisation. Also shown are the exchanges explaining the ferromagnetic and antiferromagnetic ordering [197]. Copyright 2015. Reprinted with permission from the American Chemical Society

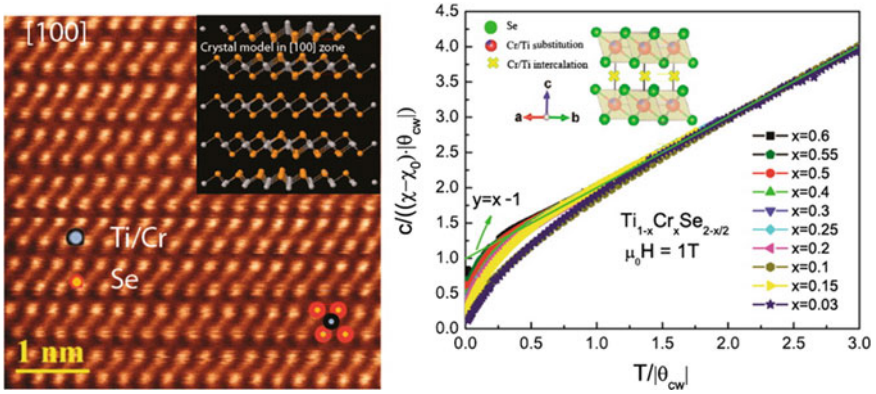

Fig. 3.23 Left figure shows a HAADF-STEM image of the [100] lattice plane. Inset is a model showing the crystal structure of $TiSe_2$ in the [100] plane. On the right is a Curie–Weiss plot, which shows that the compounds exhibit Curie behaviour at high temperature across the entire concentration range. Inset is a figure showing the crystal structure, with the interstitial sites also shown [202]. Copyright 2015. Reprinted with permission from the American Chemical Society

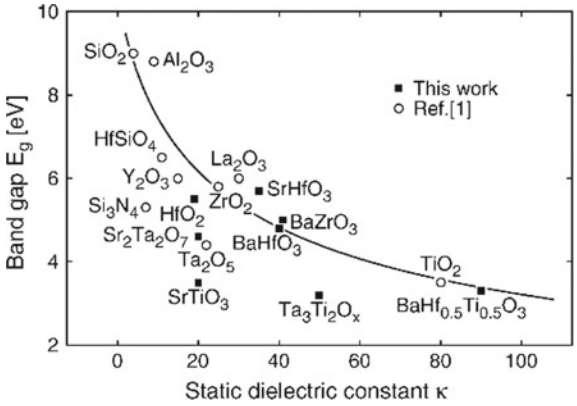

Fig. 3.24 A plot of band gap against the static dielectric constant for numerous dielectric materials [206]. Copyright 2012. Reprinted with permission from Elsevier

age by thermionic emission. As such, the band gap of the dielectric typically needs to be considerably larger than that of the channel material, which places further limits on the materials that can be used.

Due to the interesting electronic and mechanical properties of the TMDs, there is considerable interest in replacing the Si MOSFET with a TMD-based field-effect transistor (FET), a schematic of which is shown in Fig. 3.25. FET operation is characterised by applying a voltage between the source and the drain through the semiconducting channel to produce a current. By applying a potential to the top gate, the channel can be partly depleted of charge carriers, resulting in a narrower effective channel width and hence a reduced current, and this corresponds to the off state. The

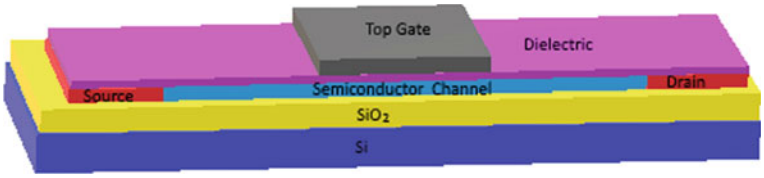

Fig. 3.25 A schematic diagram of a TMD-based field-effect transistor (FET). The current between the source and the drain is controlled by applying a voltage to the top gate

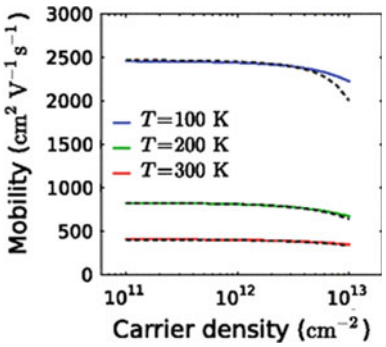

Fig. 3.26 A plot of the electron mobility against the carrier density for intrinsic, n-type monolayer MoS_2 [207]. Copyright 2012. Reprinted figure with permission from the American Physical Society

case where no potential is applied to the top gate corresponds to the on state of the transistor.

The ratio between the on and off currents is typically required to be in the range of 10^4–10^7 for application as a switch in digital logic applications. To obtain a high on/off ratio, a high conductance is required, which requires a high carrier density and a high mobility. Usually, a high carrier density can be obtained by doping the material; however, doping can result in scattering due to the ionised impurities, resulting in a decrease in the mobility. At high carrier densities, scattering is typically dominated by ionised impurity, whereas at low carrier densities, scattering processes are usually phonon-related. An example of the mobility limits in different carrier density regimes for MoS_2 [207] is given in Fig. 3.26.

At impurity concentrations greater than approximately 5×10^{11} cm^{-2}, the mobility is limited primarily by ionised impurity scattering, and this corresponds to a high dopant density, far beyond what would typically be required for a device [207]. The decrease in mobility with temperature shown in Fig. 3.26 is due to the increased phonon scattering, primarily due to a greater number of excited optical phonons [207, 208]. Similar results can also be seen in Fig. 3.27. A carrier density of 8×10^{12} cm^{-2} is required to produce a degenerately doped material, where the Fermi level sits above the conduction band minimum. Hence for most useful doping regimes, the mobility of MoS_2 and likely the other semiconducting TMDs will be limited only by phonon scattering [207].

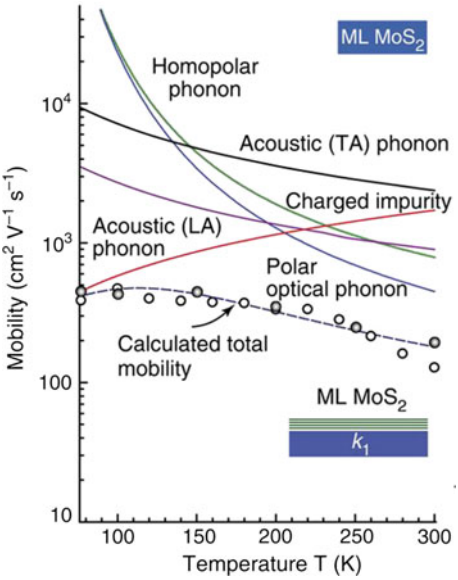

Fig. 3.27 Temperature-dependent mobility limits for an intrinsic n-type MoS_2 monolayer [208]. Copyright 2012. Reproduced with permission from Macmillan Publishers Limited

Hafnium-based and zirconium-based TMDs are likely to be particularly interesting for electronic applications. $HfSe_2$ and HfS_2 have band gaps of 1.1 eV [209, 210] and 2.0 eV [211], respectively, whilst $ZrSe_2$ and ZrS_2 have band gaps of 0.95 eV [210] and 2.16 eV [212], which are comparable to Si and hence would be suitable for high-speed, low-power electronic and optoelectronic applications. Several of these TMDs are expected to have considerably higher electron mobilities ($\mu_e > 1000 \text{cm}^2\text{V}^{-1}\text{s}^{-1}$ than Si [213, 214]. The reported electron mobilities of several commonly used semiconducting materials, and the calculated mobilities the Zr and Hf-based TMDs are presented in Table 3.3. The mobilities of each of the TMDs presented are at least comparable to that of Si, and in the case of $HfSe_2$, the mobility is comparable to that of Ge. Thus, Zr- and Hf-based TMDs may be useful for high-speed, low-power electronics, where Ge and Si-Ge alloys are currently used.

Arguably, more importantly, the native oxides of both the Zr-TMDs and the Hf-TMDs are high-K dielectrics [215–217], which reduce the number of defects at the interface of the dielectric and channel layers [210], thus facilitating the growth of high-quality gate dielectric layers. Both dielectrics have a band gap considerably larger than their respective TMDs as can be seen in Fig. 3.24, suggesting that the CBO would be sufficiently large to facilitate their use in electronics.

High-efficiency ZrS_2 nanobelt-based FETs and photodetectors have already been demonstrated, showing high responsivity, quantum efficiency and fast response times [221], as can be seen in Fig. 3.28. $HfSe_2$ FETs have also been demonstrated [222]. HfS_2 FETs have similarly been demonstrated and have shown field-effect responses

Table 3.3 Electron mobilities for Si, Ge and GaAs and the calculated acoustic phonon-limited electron mobilities for several promising TMDs

Material	$\mu_e\left(\mathrm{cm}^2\,\mathrm{V}^{-1}\,\mathrm{s}^{-1}\right)$
Si	1200 [218]
Ge	3900 [219]
GaAs	9400 [220]
HfS_2	1833 [213]
$HfSe_2$	3579 [213]
ZrS_2	1247 [213] 1045 [214]
$ZrSe_2$	2316 [213]

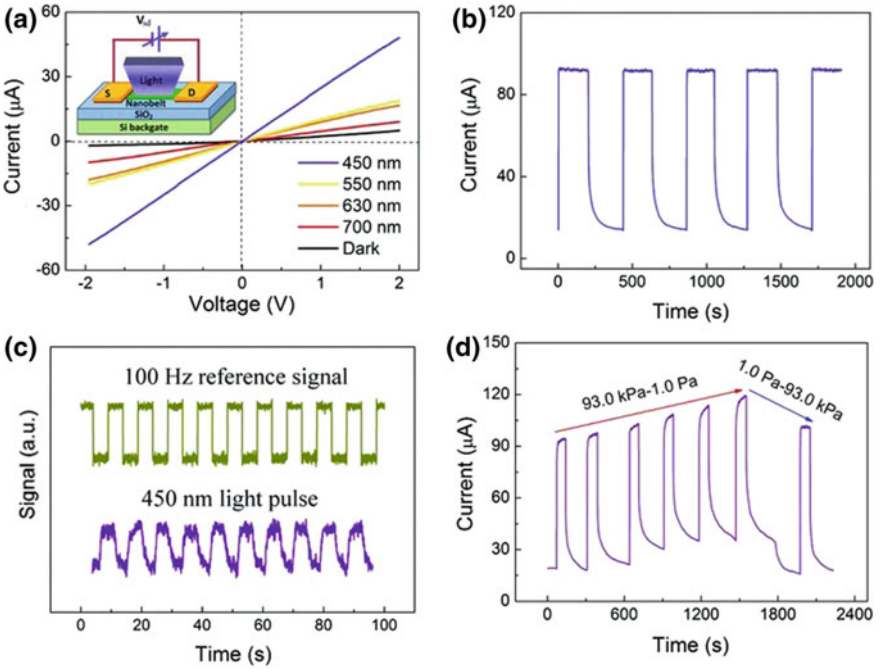

Fig. 3.28 **a** I–V characteristics of the photodetector illuminated under different wavelengths; the insert shows a schematic diagram of the experimental set-up. **b** The reproducible on/off switching behaviour of the photodetector under illumination from a 450-nm source. **c** The transient response of the photodetector under illumination with a 450-nm light source, chopped at a frequency of 100 Hz. **d** The response of the photodetectors under different pressures [221]. Copyright 2010. Reproduced with permission from Wiley-VCH Verlag GmbH & Co.

of $\mu_e > 1000\,\mathrm{cm}^2\,\mathrm{V}^{-1}\,\mathrm{s}^{-1}$, despite the mobility being considerably lower than the theoretical maximum [223]. The photoemission results shown in Fig. 3.29 suggest that $TaSe_2$ would make an Ohmic contact with $HfSe_2$ [224].

Memristors and memcaps are attractive propositions for the development of computing beyond current limitations as these phases can be used to mimic biological

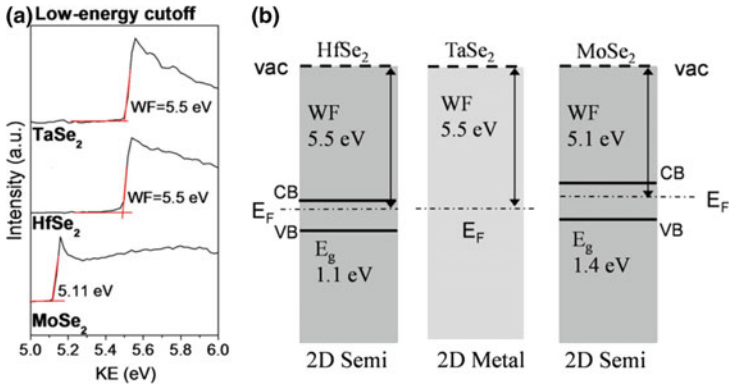

Fig. 3.29 **a** Secondary electron cut-offs for $TaSe_2$, $HfSe_2$ and $MoSe_2$ as measured by UPS. **b** The alignments of each material with the vacuum level and hence the natural band alignments by the Anderson electron affinity rule between the materials. From this, it can be seen that $TaSe_2$ would be expected to for an Ohmic contact with $HfSe_2$, whereas for $MoSe_2$ a small barrier of approximately 0.4 eV is expected [224]. Copyright 2016. Reprinted with permission from the American Chemical Society

neural systems, enabling lower power consumption and potentially enhanced cognitive advantages over traditional computing systems [225].

The reduced dimensionality of the 2D TMDs results in a further reduced power consumption over more traditional 3D materials [226]. Memristive phase switching has been demonstrated in 2D 1T-TaS_2, where the thickness of the crystal controls the kinetics of the first-order CDW phase change [61]. Memristive behaviour has also been observed in the MoS_2 [225, 227–229], as has memcapactive behaviour [225]. Device characteristics of MoO_x/MoS_2 memristors and memcaps can be seen in Fig. 3.30. WS_2 has also been used to form memristors and memcaps [225].

3.6 Conclusions

In this chapter, electronic, optical and magnetic properties of TMDs are addressed. The most studied TMDs from group IV to group X are included in terms of their atomic arrangement, and electronic and magnetic properties. Furthermore, the effects of layered TMDs on their optoelectronic and magnetic properties are discussed throughout this chapter.

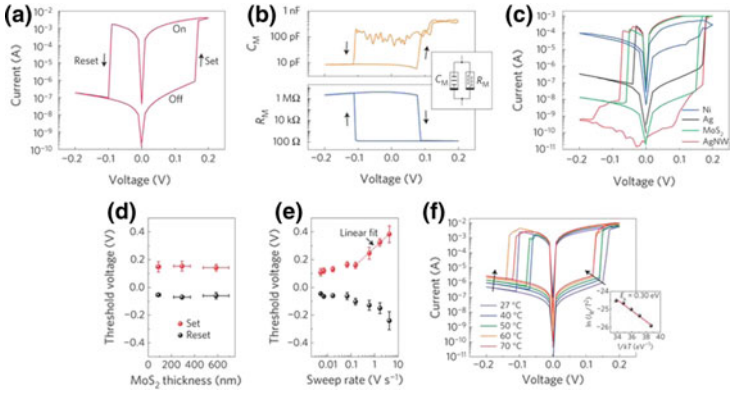

Fig. 3.30 Performance and statistics of MoO_x/MoS_2 memristors and memcaps. **a** A typical I–V curve for a MoO_x/MoS_2 memristor operated under forward bias and with a negatively biased top electrode. **b** The capacitive and resistive components of the memory device. When the device is set from off to on, the resistance decreases by 10^4, whilst the capacitance increases by a factor. **c** The I–V behaviour with various top electrodes at a constant compliance current of 1 mA. **d** The set and reset voltages as a function of MoS_2 thickness. As the voltage does not vary with thickness, it is implied that the resistance switching is entirely due to the MoO_x layer. **e** The threshold voltage for the set and reset state as a function of sweep rate. For low sweep rates, the set and reset voltages approach a critical value as oxygen vacancies can diffuse to the depletion region, whilst at high sweep rates, the behaviour is exponential in nature. **f** The temperature dependence of the set threshold voltage and the off current. Inset is a figure allowing for the determination of the activation energy [225]. Copyright 2015. Reprinted with permission from Macmillan Publishers Ltd.

References

1. Manzeli S, Ovchinnikov D, Pasquier D, Yazyev OV, Kis A (2017) 2D transition metal dichalcogenides. Nat Rev Mater 2:17033
2. Grønvold F, Røst E (1957) The crystal structure of $PdSe_2$ and PdS_2. Acta Crystallogr 10:329–331
3. Soulard C, Rocquefelte X, Petit PE, Evain M, Jobic S, Itié JP et al (2004) Experimental and theoretical investigation on the relative stability of the PdS_2- and pyrite-type structures of $PdSe_2$. Inorg Chem 43:1943–1949
4. Wang Y, Li Y, Chen Z (2015) Not your familiar two dimensional transition metal disulfide: structural and electronic properties of the PdS_2 monolayer. J Mater Chem C 3:9603–9608
5. Oyedele AD, Yang S, Liang L, Puretzky AA, Wang K, Zhang J et al (2017) $PdSe_2$: pentagonal two-dimensional layers with high air stability for electronics. J Am Chem Soc 139:14090–14097
6. Lin J, Zuluaga S, Yu P, Liu Z, Pantelides ST, Suenaga K (2017) Novel Pd_2Se_3 Two-dimensional phase driven by interlayer fusion in layered $PdSe_2$. Phys Rev Lett 119:1–6
7. Schönfeld B, Huang JJ, Moss SC (1983) Anisotropic mean-square displacements (MSD) in single-crystals of 2H- and 3R-MoS_2. Acta Crystallogr Sect B 39:404–407
8. Chou SS, Sai N, Lu P, Coker EN, Liu S, Artyushkova K, Luk TS, Kaehr B, Brinker CJ (2015) Understanding catalysis in a multiphasic two-dimensional transition metal dichalcogenide. Nat Commun 6:1–8
9. Terrones H, Terrones M (2014) Electronic and vibrational properties of defective transition metal dichalcogenide Haeckelites: New 2D semi-metallic systems. 2D Mater 1:1

10. Zhu ZY, Cheng YC, Schwingenschlogl U (2011) Giant spin-orbit-induced spin splitting in two-dimensional transition-metal dichalcogenide semiconductors. Phys Rev B: Condens Matter Mater Phys 84:1–5
11. Yun WS, Han SW, Hong SC, Kim IG, Lee JD (2012) Thickness and strain effects on electronic structures of transition metal dichalcogenides: 2H-. Phys Rev B 85:033305
12. Jin W, Yeh PC, Zaki N, Zhang D, Sadowski JT, Al-Mahboob A et al (2013) Direct measurement of the thickness-dependent electronic band structure of MoS_2 using angle-resolved photoemission spectroscopy. Phys Rev Lett 111:1–5
13. Splendiani A, Sun L, Zhang Y, Li T, Kim J, Chim CY et al (2010) Emerging photoluminescence in monolayer MoS_2. Nano Lett 10:1271–1275
14. Mak KF, Lee C, Hone J, Shan J, Heinz TF (2010) Atomically thin MoS_2: a new direct-gap semiconductor. Phys Rev Lett 105:2–5
15. Castellanos-Gomez A, Quereda J, van der Meulen HP, Agraït N, Rubio-Bollinger G (2016) Spatially resolved optical absorption spectroscopy of single- and few-layer MoS_2 by hyperspectral imaging. Nanotechnology 27:115705
16. Zhang Y, Chang TR, Zhou B, Cui YT, Yan H, Liu Z et al (2014) Direct observation of the transition from indirect to direct bandgap in atomically thin epitaxial $MoSe_2$. Nat Nanotechnol 9:111–115
17. Zhao W, Ghorannevis Z, Chu L, Toh M, Kloc C, Tan PH, Eda G (2013) Evolution of electronic structure in atomically thin sheets of WS_2 and WSe_2. ACS Nano 7:791–797
18. Lezama IG, Arora A, Ubaldini A, Barreteau C, Giannini E, Potemski M, Morpurgo AF (2015) Indirect-to-direct band gap crossover in few-layer $MoTe_2$. Nano Lett 15:2336–2342
19. Lee CH, Silva EC, Calderin L, Nguyen MAT, Hollander MJ, Bersch B, Mallouk TE, Robinson JA (2015) Tungsten ditelluride: a layered semimetal. Sci Rep 5:1–8
20. Di Sante D, Das PK, Bigi C, Ergönenc Z, Gürtler N, Krieger JA et al (2017) Three-dimensional electronic structure of the type-II Weyl semimetal WTe_2. Phys Rev Lett 119:1–6
21. Lui CH, Frenzel AJ, Pilon DV, Lee YH, Ling X, Akselrod GM, Kong J, Gedik N (2014) Trion-induced negative photoconductivity in monolayer MoS_2. Phys Rev Lett 113:1–5
22. Lin JD, Han C, Wang F, Wang R, Xiang D, Qin S (2014) Electron-doping-enhanced trion formation in monolayer molybdenum disulfide functionalized with cesium carbonate. ACS Nano 8:5323–5329
23. Wang H, Zhang C, Chan W, Manolatou C, Tiwari S, Rana F (2016) Radiative lifetimes of excitons and trions in monolayers of the metal dichalcogenide MoS_2. Phys Rev B 93:1–11
24. Singh A, Moody G, Tran K, Scott ME, Overbeck V, Berghäuser G (2016) Trion formation dynamics in monolayer transition metal dichalcogenides. Phys Rev B 93:1–5
25. Rezk AR, Carey B, Chrimes AF, Lau DWM, Gibson BC, Zheng et al (2016) Acoustically-driven trion and exciton modulation in piezoelectric two-dimensional MoS_2. Nano Lett 16:849–855
26. Christopher JW, Goldberg BB, Swan AK (2017) Long tailed trions in monolayer MoS_2: Temperature dependent asymmetry and resulting red-shift of trion photoluminescence spectra. Sci Rep 7:1–8
27. Lampert MA (1958) Mobile and immobile effective-mass-particle complexes in nonmetallic solids. Phys Rev Lett 1:450–453
28. Sanvitto D, Pulizzi F, Shields AJ, Christiansen PCM, Holmes SN, Simmons MY et al (2001) Observation of charge transport by negatively charged excitons. Science 294:837–839
29. Pulizzi F, Sanvitto D, Christianen PCM, Shields AJ, Holmes SN, Simmons MY et al (2003) Optical imaging of trion diffusion and drift in GaAs quantum wells. Phys Rev B Condens Matter Mater Phys 68:1–9
30. You Y, Zhang XX, Berkelbach TC, Hybertsen MS, Reichman DR, Heinz TF (2015) Observation of biexcitons in monolayer WSe_2. Nat Phys 11:477–481
31. Sie EJ, Frenzel AJ, Lee YH, Kong J, Gedik N (2015) Intervalley biexcitons and many-body effects in monolayer MoS_2. Phys Rev B Condens Matter Mater Phys 92:1–8
32. Zhang DK, Kidd DW, Varga K (2015) Excited biexcitons in transition metal dichalcogenides. Nano Lett 15:7002–7005

33. Sie EJ, Lui CH, Lee YH, Kong J, Gedik N (2016) Observation of intervalley biexcitonic optical stark effect in monolayer WS_2. Nano Lett 16:7421–7426
34. Lee HS, Kim MS, Kim H, Lee YH (2016) Identifying multiexcitons in MoS_2 monolayers at room temperature. Phys Rev B 93:1–6
35. Kim MS, Yun SJ, Lee Y, Seo C, Han GH, Kim KK et al (2016) Biexciton emission from edges and grain boundaries of triangular WS_2 monolayers. ACS Nano 10:2399–2405
36. He Z, Xu W, Zhou Y, Wang X, Sheng Y, Rong Y et al (2016) Biexciton formation in bilayer tungsten disulfide. ACS Nano 10:2176–2183
37. Hao K, Specht JF, Nagler P, Xu L, Tran K, Singh A et al (2017) Neutral and charged inter-valley biexcitons in monolayer $MoSe_2$. Nat Commun 8:1–7
38. Paradisanos I, Germanis S, Pelekanos NT, Fotakis C, Kymakis E, Kioseoglou G et al (2017) Room temperature observation of biexcitons in exfoliated WS_2 monolayers. Appl Phys Lett 110:19
39. Chernikov A, Berkelbach TC, Hill HM, Rigosi A, Li Y, Aslan OB (2014) Exciton binding energy and nonhydrogenic Rydberg series in monolayer WS_2. Phys Rev Lett 113:1–5
40. He K, Kumar N, Zhao L, Wang Z, Mak KF, Zhao H, Shan J (2014) Tightly bound excitons in monolayer WSe_2. Phys Rev Lett 113:1–5
41. Hanbicki AT, Currie M, Kioseoglou G, Friedman AL, Jonker BT (2015) Measurement of high exciton binding energy in the monolayer transition-metal dichalcogenides WS_2 and WSe_2. Solid State Commun 203:16–20
42. Liu HJ, Jiao L, Xie L, Yang F, Chen JL, Ho WK et al (2015) Molecular-beam epitaxy of monolayer and bilayer WSe_2: a scanning tunneling microscopy/spectroscopy study and deduction of exciton binding energy. 2D Mater 2:3
43. Zhu B, Chen X, Cui X (2015) Exciton binding energy of monolayer WS_2. Sci Rep 5:9218
44. Ramasubramaniam A (2012) Large excitonic effects in monolayers of molybdenum and tungsten dichalcogenides. Phys Rev B Condens Matter Mater Phys 86:1–6
45. Qiu DY, Da Jornada FH, Louie SG (2013) Optical spectrum of MoS_2: many-body effects and diversity of exciton states. Phys Rev Lett 111:1–5
46. Zhang C, Johnson A, Hsu CL, Li LJ, Shih CK (2014) Direct imaging of band profile in single layer MoS_2on graphite: Quasiparticle energy gap, metallic edge states, and edge band bending. Nano Lett 14:2443–2447
47. Tran Thoai DB (1990) Exciton binding energy in semiconductor quantum wells and in heterostructures. Phys B 164:295–299
48. Hrivnák L (1992) Exciton binding energy as a function of the well width. J Appl Phys 72:3218
49. Belov PA, Khramtsov ES (2017) The binding energy of excitons in narrow quantum wells. J Phys: Conf Ser 816:012018
50. Ross JS, Klement P, Jones AM, Ghimire NJ, Yan J, Mandrus DG et al (2014) Electrically tunable excitonic light-emitting diodes based on monolayer WSe_2 p–n junctions. Nat Nanotechnol 9:268–272
51. Rodrigues SP, Cai W (2015) Nonlinear optics: tuning harmonics with excitons. Nat Nanotechnol 10:387–388
52. Seyler KL, Schaibley JR, Gong P, Rivera P, Jones AM, Wu S et al (2015) Electrical control of second-harmonic generation in a WSe_2 monolayer transistor. Nat Nanotechnol 10:407–411
53. Zhang G, Chaves A, Huang S, Wang F, Xing Q, Low T. Yan H (2018) Determination of layer-dependent exciton binding energies in few-layer black phosphorus. Sci Adv 4:1–7
54. Birkett M, Savory CN, Rajpalke MK, Linhart WM, Whittles TJ, Gibbon JT et al (2018) Band gap temperature-dependence and exciton-like state in copper antimony sulphide, $CuSbS_2$. APL Mater 6:084904
55. Saigal N, Sugunakar V, Ghosh S (2016) Exciton binding energy in bulk MoS2: a reassessment. Appl Phys Lett 108:132105
56. Bernardi M, Palummo M, Grossman JC (2013) Extraordinary sunlight absorption and one nanometer thick photovoltaics using two-dimensional monolayer materials. Nano Lett 13:3664–3670

57. Akama T, Okita W, Nagai R, Li C, Kaneko T, Kato T (2017) Schottky solar cell using few-layered transition metal dichalcogenides toward large-scale fabrication of semitransparent and flexible power generator. Sci Rep 7:1–10
58. Furchi MM, Zechmeister AA, Hoeller F, Wachter S, Pospischil A, Mueller T (2017) Photovoltaics in Van der Waals Heterostructures. IEEE J Sel Top Quantum Electron 23:4100111
59. Janisch C, Wang Y, Ma D, Mehta N, Elías AL, Perea-López N et al (2014) Extraordinary second harmonic generation in Tungsten disulfide monolayers. Sci Rep 4:1–5
60. Wang G, Zhang S, Zhang X, Zhang L, Cheng Y, Fox D et al (2015) Tunable nonlinear refractive index of two-dimensional MoS_2, WS_2, and $MoSe_2$ nanosheet dispersions [Invited]. Photonics Res 3:A51
61. Zhou KG, Zhao M, Chang MJ, Wang Q, Wu XZ, Song Y, Zhang HL (2015) Size-dependent nonlinear optical properties of atomically thin transition metal dichalcogenide nanosheets. Small 11:694–701
62. Zhang S, Dong N, McEvoy N, OBrien M, Winters S, Berner NC et al (2015) Direct observation of degenerate two-photon absorption and its saturation in WS_2 and MoS_2 monolayer and few-layer films. ACS Nano 9:7142–7150
63. Luo Z, Li Y, Zhong M, Huang Y, Wan X, Peng J, Weng J (2015) Nonlinear optical absorption of few-layer molybdenum diselenide ($MoSe_2$) for passively mode-locked soliton fiber laser [Invited]. Photonics Res 3:A79
64. Wang W, Wu Y, Wu Q, Hua J, Zhao J (2016) Coherent nonlinear optical response spatial self-phase modulation in $MoSe_2$ nano-sheets. Sci Rep 6:1–6
65. Woodward RI, Kelleher EJR, Howe RCT, Hu G, Torrisi F, Hasan T et al (2014) Tunable Q-switched fiber laser based on saturable edge-state absorption in few-layer molybdenum disulfide (MoS_2). Opt Express 22:31113
66. Liu X, Guo Q, Qiu J (2017) Emerging low-dimensional materials for nonlinear optics and ultrafast photonics. Adv Mater 29:14
67. Yang J, Wang Z, Wang F, Xu R, Tao J, Zhang S et al (2016) Atomically thin optical lenses and gratings. Light Sci Appl 5:e16046
68. Hughes HP, Webb C, Williams PM (1980) Angle resolved photoemission from VSe_2. J Phys C: Solid State Phys 13:1125–1138
69. Feng J, Sun X, Wu C, Peng L, Lin C, Hu S, Yang J, Xie Y (2011) Metallic few-layered VS_2 ultrathin nanosheets: high two-dimensional conductivity for in-plane supercapacitors. J Am Chem Soc 133:17832–17838
70. Jing Y, Zhou Z, Cabrera CR, Chen Z (2013) Metallic VS_2 monolayer: a promising 2D anode material for lithium ion batteries. J Phys Chem C 117:25409–25413
71. Güller F, Helman C, Llois AM (2012) Electronic structure and properties of NbS_2 and TiS_2 low dimensional structures. Phys B Condens Matter 407:3188–3191
72. Wang Z, Su Q, Yin GQ, Shi J, Deng H, Guan J et al (2014) Structure and electronic properties of transition metal dichalcogenide MX_2(M = Mo, W, Nb; X = S, Se) monolayers with grain boundaries. Mater Chem Phys 147:1068–1073
73. Laulhé C, Cario L, Corraze B, Janod E, Huber T, Lantz G et al (2015) X-ray study of femtosecond structural dynamics in the 2D charge density wave compound 1T-TaS_2. Phys B Condens Matter 460:100–104
74. Varma SJ, Kumar J, Liu Y, Layne K, Wu J, Liang C et al (2017) 2D TiS_2 layers: a superior nonlinear optical limiting material. Adv Opt Mater 5:1700713
75. Huang P, Yuan L, Zhang K, Chen Q, Zhou Y, Song B, Li Y (2018) Room-temperature and aqueous solution-processed two-dimensional TiS_2 as an electron transport layer for highly efficient and stable planar n-i-p perovskite solar cells. ACS Appl Mater Interfaces 10:14796–14802
76. Greenaway DL, Nitsche R (1965) Preparation and optical properties of group IV–VI2 chalcogenides having the CdI2 structure. J Phys Chem Solids 26:1445
77. Burton LA, Colombara D, Abellon RD, Grozema C, Peter LM, Savenije TJ (2013) Synthesis, characterization, and electronic structure of single-crystal SnS, Sn_2S_3, and SnS_2 Chem Mater 25:4908–4916

78. Gonzalez JM, Oleynik II (2016) Layer-dependent properties of SnS_2 and $SnSe_2$ two-dimensional materials Phys Rev B 94:1–10
79. Burton LA, Whittles TJ, Hesp D, Linhart WM, Skelton JM, Hou B (2016) Electronic and optical properties of single crystal SnS_2: an earth-abundant disulfide photocatalyst. J Mater Chem A 4:1312–1318
80. Whittles TJ, Burton LA, Skelton JM, Walsh A, Veal TD, Dhanak VR (2016) Band alignments, valence bands and core levels in the tin sulfides SnS, SnS_2 and Sn_2S_3: experiment and theory. Chem Mater 28:3718
81. Ye G, Gong Y, Lei S, He Y, Li B, Zhang X (2017) Synthesis of large-scale atomic-layer SnS_2 through chemical vapor deposition. Nano Res 10:2386–2394
82. Huang Y, Sutter E, Sadowski JT, Cotlet M, Monti OLA, Racke DA et al (2014) Tin disulfide-an emerging layered metal dichalcogenide semiconductor: materials properties and device characteristics. ACS Nano 8:10743–10755
83. Xia J, Zhu D, Wang L, Huang B, Huang X, Meng XM (2015) Large-scale growth of two-dimensional SnS_2 crystals driven by screw dislocations and application to photodetectors. Adv Funct Mater 25:4255–4261
84. Zhang H, Balaji Y, Nalin Mehta A, Heyns MM, Caymax M, Radu W (2018) Formation mechanism of 2D SnS_2 and SnS by chemical vapor deposition using $SnCl_4$ and H_2S. J Mater Chem C 6:6172–6178
85. Zhang H, van Pelt T, Mehta AN, Bender H, Radu I, Caymax M (2018) Nucleation and growth mechanism of 2D SnS_2 by chemical vapor deposition: initial 3D growth followed by 2D lateral growth. 2D Mater 5:035006
86. Seo W, Shin S, Ham G, Lee J, Lee S, Choi H (2017) Thickness-dependent structure and properties of SnS_2 thin films prepared by atomic layer deposition. Jpn J Appl Phys 56:031201
87. Mattinen M, King PJ, Khriachtchev L, Meinander K, Gibbon JT, Dhanak VR (2018) Low-Temperature wafer-scale deposition of continuous 2D SnS_2 films. Small 14:1800547
88. Bo L, Le H, Mianzeng Z, Yan L, Yan W, Jingbo L, Zhongming W (2016) direct vapor phase growth and optoelectronic application of large band offset SnS_2/MoS_2 vertical bilayer heterostructures with high lattice mismatch. Adv Electron Mater 2:1600298
89. Xu K, Chen P, Li X, Wu C, Guo Y, Zhao J (2013) Ultrathin nanosheets of vanadium diselenide: a metallic two-dimensional material with ferromagnetic charge-density-wave behavior. Angew Chemie Int Ed 52:10477–10481
90. Pan XC, Chen X, Liu H, Feng Y, Wei Z, Zhou Y (2015) Pressure-driven dome-shaped superconductivity and electronic structural evolution in tungsten ditelluride. Nat Commun 6:3–8
91. Qi Y, Naumov PG, Ali MN, Rajamathi CR, Schnelle W, Barkalov O (2016) Superconductivity in Weyl semimetal candidate $MoTe_2$. Nat Commun 7:1–7
92. Zhou BR, Yuan NFQ, Jiang HL, Law KT (2016) Ising superconductivity and Majorana fermions in transition-metal dichalcogenides. Phys Rev B 93:1–5
93. Nie SM, Song Z, Weng H, Fang Z (2015) Quantum spin Hall effect in two-dimensional transition-metal dichalcogenide haeckelites. Phys Rev B 91:235434
94. Hasan MZ, Kane CL (2010) Colloquium: topological insulators. Rev Mod Phys 82:3045–3067
95. Qi XL, Zhang SC (2011) Topological insulators and superconductors. Rev Mod Phys 83:4
96. Qian X, Liu J, Fu L, Li J (2014) Quantum spin Hall effect in two-dimensional transition metal dichalcogenides. Science 344:8–13
97. Choe DH, Sung HJ, Chang KJ (2016) Understanding topological phase transition in monolayer transition metal dichalcogenides. Phys Rev B 93:125109
98. Ma Y, Kou L, Li X, Dai Y, Smith SC, Heine T (2015) Quantum spin Hall effect and topological phase transition in two-dimensional square transition-metal dichalcogenides. Phys Rev B 92:085427
99. Xu G, Wang J, Yan B, Qi XL (2014) Topological superconductivity at the edge of transition-metal dichalcogenides. Phys Rev B Condens Matter Mater Phys 90:1–5
100. Yuan NFQ, Mak KF, Law KT (2014) Possible topological superconducting phases of MoS_2. Phys Rev Lett 113:1–5

101. Ma F, Gao G, Jiao Y, Gu Y, Bilic A, Zhang H et al (2016) Predicting a new phase (T′′) of two-dimensional transition metal di-chalcogenides and strain-controlled topological phase transition. Nanoscale 8:4969–4975
102. Ma Y, Kou L, Li X, Dai Y, Heine T (2016) Two-dimensional transition metal dichalcogenides with a hexagonal lattice: Room-temperature quantum spin Hall insulators. Phys Rev B 93:1–7
103. Cheng YC, Zhang QY, Schwingenschlögl U (2014) Valley polarization in magnetically doped single-layer transition-metal dichalcogenides. Phys Rev B-Condens Matter Mater Phys 89:2–6
104. Macneill D, Heikes C, Mak KF, Anderson Z, Kormányos A, Zólyomi V et al (2015) Breaking of valley degeneracy by magnetic field in monolayer $MoSe_2$. Phys Rev Lett 114:1–5
105. Aivazian G, Gong Z, Jones AM, Chu RL, Yan J, Mandrus DG et al (2015) Magnetic control of valley pseudospin in monolayer WSe_2. Nat Phys 11:148–152
106. Song Y, Zhang Q, Mi W, Wang X (2016) Valley polarization and p-/n-type doping of monolayer WTe_2 on top of Fe_3O_4 (111). Phys Chem Chem Phys 18:15039–15045
107. Cai T, Yang SA, Li X, Zhang F, Shi J, Yao W, Niu Q (2013) Magnetic control of the valley degree of freedom of massive Dirac fermions with application to transition metal dichalcogenides. Phys Rev B Condens Matter Mater Phys 88:1–8
108. Dufferwiel S, Lyons TP, Solnyshkov DD, Trichet AAP, Withers F, Schwarz S et al (2017) Valley-addressable polaritons in atomically thin semiconductors. Nat Photonics 11:497–501
109. Guillamón I, Suderow H, Vieira S, Cario L, Diener P, Rodière P (2008) Superconducting density of states and vortex cores of 2H-NbS_2. Phys Rev Lett 101:2–5
110. Wang H, Huang X, Lin J, Cui J, Chen Y, Zhu C (2017) High-quality monolayer superconductor $NbSe_2$ grown by chemical vapour deposition. Nat Commun 8:1–8
111. Coronado E, Martí-Gastaldo C, Navarro-Moratalla E, Burzurí E, Camõn A, Luis F (2011) Hybrid magnetic/superconducting materials obtained by insertion of a single-molecule magnet into TaS_2 layers. Adv Mater 23:5021–5026
112. Navarro-Moratalla E, Island JO, Manãs-Valero S, Pinilla-Cienfuegos E, Castellanos-Gomez A, Quereda J (2016) Enhanced superconductivity in atomically thin TaS_2. Nat Commun 7:1–7
113. Roldan R, Silva-Guillén JA, López-Sancho MP, Guinea F, Cappelluti E, Ordejón P (2014) Electronic properties of single-layer and multilayer transition metal dichalcogenides MX_2 (M = Mo, W and X = S, Se). Ann Phys 526:347–357
114. Castro Neto AH (2001) Charge density wave, superconductivity, and anomalous metallic behavior in 2D transition metal dichalcogenides. Phys Rev Lett 86:4382–4385
115. Ge Y, Liu AY (2013) Phonon-mediated superconductivity in electron-doped single-layer MoS_2: a first-principles prediction. Phys Rev B-Condens Matter Mater Phys 87:1–5
116. Das T, Dolui K (2015) Superconducting dome in MoS_2 and $TiSe_2$ generated by quasiparticle-phonon coupling. Phys Rev B-Condens Matter Mater Phys 91:1–9
117. Roldán R, Cappelluti E, Guinea F (2013) Interactions and superconductivity in heavily doped MoS_2. Phys Rev B Condens Matter Mater Phys 88:1–5
118. Rösner M, Haas S, Wehling TO (2014) Phase diagram of electron-doped dichalcogenides. Phys Rev B Condens Matter Mater Phys 90:1–6
119. Schneemeyer LF, Wrighton MS (1979) Flat-band potential of n-type semiconducting molybdenum disulfide by cyclic voltammetry of two-electron reductants: interface energetics and the sustained photooxidation of chloride. J Am Chem Soc 101:6496–6500
120. Kautek W, Gerischer H (1980) Photoelectrochemical reactions and formation of inversion layers at n-Type MoS_2-, $MoSe_2$-, and WSe_2-electrodes in aprotic solvents. Berichte der Bunsengesellschaft für Phys Chemie 84:645–653
121. Kautek W, Gerischer H (1982) Anisotropic photocorrosion of n-type MoS_2, $MoSe_2$, and WSe_2 single crystal surfaces: the role 0f cleavage steps, line and screw dislocations. Surf Sci 119:46–60
122. Dolui K, Rungger I, Sanvito S (2013) Origin of the n-type and p-type conductivity of MoS_2 monolayers on a SiO_2 substrate. Phys Rev B-Condens Matter Mater Phys 87:1–7
123. Meng F, Li J, Cushing SK, Zhi M, Wu N (2013) Solar hydrogen generation by nanoscale p-n junction of p-type molybdenum disulfide/n-type nitrogen-doped reduced graphene oxide. J Am Chem Soc 135:10286–10289

124. Chuang S, Battaglia C, Azcatl A, McDonnell S, Kang JS, Yin X et al (2014) MoS_2 P-type transistors and diodes enabled by high work function MoOx contacts. Nano Lett 14:1337–1342
125. Xue F, Chen L, Chen J, Liu J, Wang L, Chen M et al (2016) P-Type MoS_2 and n-Type ZnO diode and its performance enhancement by the piezophototronic effect. Adv Mater 28(17):3391–3398
126. Santoni A, Rondino F, Malerba C, Valentini M, Mittiga A (2017) Electronic structure of Ar+ ion-sputtered thin-film MoS_2: A XPS and IPES study. Appl Surf Sci 392:795–800
127. McDonnell S, Addou R, Buie C, Wallace RM, Hinkle CL (2014) Defect-dominated doping and contact resistance in MoS_2. ACS Nano 8:2880–2888
128. Su J, Li N, Zhang Y, Feng L, Liu Z (2015) Role of vacancies in tuning the electronic properties of Au-MoS_2 contact. AIP Adv 5:077182
129. Feng L, Su J, Liu Z (2015) Effect of vacancies in monolayer MoS_2 on electronic properties of Mo–MoS_2 contacts. RSC Adv 5:20538–20544
130. Kim DH, Du H, Kim T, Shin S, Kim S, Song M et al (2016) The enhanced low resistance contacts and boosted mobility in two-dimensional p-type WSe_2 transistors through Ar+ ion-beam generated surface defects. AIP Adv 6:105307
131. Chuang HJ, Tan X, Ghimire NJ, Perera MM, Chamlagain B, Cheng MMC et al (2014) High mobility WSe_2 p- And n-Field-effect transistors contacted by highly doped graphene for low-resistance contacts. Nano Lett 14:3594–3601
132. Baglio JA, Calabrese GS, Kamieniecki E, Kershaw R, Kubiak CP, Ricco AJ (1982) Characterization of n-type semiconducting tungsten disulfide photoanodes in aqueous and nonaqueous electrolyte solutions: photo-oxidation of halides with high efficiency. J Electrochem Soc 129:1461–1472
133. Baglio JA, Calabrese GS, Harrison DJ, Kamieniecki E, Ricco AJ, Wrighton MS et al (1983) Electrochemical characterization of p-Type semiconducting tungsten disulfide photocathodes: efficient photoreduction processes at semiconductor/liquid electrolyte interfaces. J Am Chem Soc 105:2246–2256
134. McIntyre NS, Spevack PA, Beamson G, Briggs D (1990) Effects of argon ion bombardment on basal plane and polycrystalline MoS_2. Surf Sci 237:1–3
135. Lince JR, Fleischauer PD, Hills MM (1989) Chemical effects of Ne+ bombardmenton the MoS_2 (0001) surface studied by HR photoelectron spectroscopy. Surf Sci 210:387–405
136. Suryawanshi MP, Shin SW, Ghorpade UV, Gurav KV, Hong CW, Patil PS (2016) Improved solar cell performance of Cu_2ZnSnS_4(CZTS) thin films prepared by sulfurizing stacked precursor thin films via SILAR method. J Alloys Compd 671:509–516
137. Abdallah WA, Nelson AE (2005) Characterization of $MoSe_2$ (0001) and ion-sputtered $MoSe_2$ by XPS. J Mater Sci 40:2679–2681
138. Bernede JC (2001) About the preferential sputtering of chalcogen from transition metal dichalcogenide compounds and the determination of compound stoichiometry from XPS peak positions. Appl Surf Sci 171:15–20
139. Kogar A, Rak MS, Vig S, Husain AA, Flicker F, Il Joe Y et al (2017) Signatures of exciton condensation in a transition metal dichalcogenide. Science 358:1314–1317
140. Li F, Tu K, Chen Z (2014) Versatile electronic properties of VSe_2 bulk, few-layers, monolayer, nanoribbons, and nanotubes: a computational exploration. J Phys Chem C 118(36):21264–21274
141. Ma Y, Dai Y, Guo M, Niu C, Zhu Y, Huang B (2012) Evidence of the existence of magnetism in pristine VX 2 monolayers (X = S, Se) and their strain-induced tunable magnetic properties. ACS Nano 6:1695–1701
142. Gao D, Xue Q, Mao X, Wang W, Xu Q, Xue D (2013) Ferromagnetism in ultrathin VS_2 nanosheets. J Mater Chem C 1:5909–5916
143. Bonilla M, Kolekar S, Ma Y, Diaz HC, Kalappattil V, Das R et al (2018) Strong room-temperature ferromagnetism in VSe_2 monolayers on van der Waals substrates. Nat Nanotechnol 13:289–294
144. Guo Y, Deng H, Sun X, Li X, Zhao J, Wu J et al (2017) Modulation of metal and insulator states in 2D ferromagnetic VS_2 by van der Waals interaction engineering. Adv Mater 29:1–7

145. Isaacs EB, Marianetti CA (2016) Electronic correlations in monolayer VS_2. Phys Rev B 94:1–11
146. Zhuang HL, Hennig RG (2016) Stability and magnetism of strongly correlated single-layer VS_2. Phys Rev B 93:1–7
147. Zhang Y, Wu X (2013) Vanadium sulfide nanoribbons: electronic and magnetic properties. Phys Lett Sect A Gen At Solid State Phys 377:3154–3157
148. Zhang H, Liu LM (2013) Lau WM (2013) Dimension-dependent phase transition and magnetic properties of VS_2. J Mater Chem A 1:10821
149. Kan M, Wang B, Lee YH, Sun Q (2015) A density functional theory study of the tunable structure, magnetism and metal-insulator phase transition in VS_2 monolayers induced by in-plane biaxial strain. Nano Res 8:1348–1356
150. Fuh HR, Chang CR, Wang YK, Evans RFL, Chantrell RW, Jeng HT (2016) Newtype single-layer magnetic semiconductor in transition-metal dichalcogenides VX2 (X = S, Se and Te). Sci Rep 6:32625
151. Ghobadi A, Gamze T, Ghobadi U, Okyay AK, Ozbay E (2018) Emerging photoluminescence from defective vanadium diselenide nanosheets. Photonic Res 6:244–253
152. Pan H (2014) Electronic and magnetic properties of vanadium dichalcogenides monolayers tuned by hydrogenation. J Phys Chem C 118:13248–13253
153. Feng J, Biswas D, Rajan A, Watson MD, Mazzola F, Clark OJ, Underwood K et al (2018) Electronic structure and enhanced charge- density wave order of monolayer VSe_2. Nanoletters 18:4493–4499
154. Van Hove L (1953) The occurrence of singularities in the elastic frequency distribution of a crystal. Phys Rev 89:1189–1193
155. Lifshitz IM (1960) Anomalies of electron characteristics of a metal in the high pressure region. Sov Phys JETP 11:1130–1135
156. Volovik GE (2017) Topological Lifshitz transitions. Low Temp Phys 43:47–55
157. Zhang J, Soon JM, Loh KP, Yin J, Ding J, Sullivian MB, Wu P (2007) Magnetic molybdenum disulfide nanosheet films. Nano Lett 7:2370–2376
158. Tongay S, Varnoosfaderani SS, Appleton BR, Wu J, Hebard AF (2012) Magnetic properties of MoS_2: existence of ferromagnetism. Appl Phys Lett 101:123105
159. Luxa J, Jankovsky O, Sedmidubský D, Medlín R, Maryško M, Pumera M, Sofer S (2016) Origin of exotic ferromagnetic behavior in exfoliated layered transition metal dichalcogenides MoS_2 and WS_2. Nanoscale 8:1960–1967
160. Li Y, Zhou Z, Zhang Z, Chen Z (2008) MoS_2 nanoribbons: high stability and unusual electronic and magnetic properties. J Am Chem Soc 130:16739–16744
161. Botello-Méndez AR, López-Urías F, Terrones M, Terrones H (2009) Metallic and ferromagnetic edges in molybdenum disulfide nanoribbons. Nanotechnology 20:325703
162. Shidpour R, Manteghian M (2010) A density functional study of strong local magnetism creation on MoS_2 nanoribbon by sulfur vacancy. Nanoscale 2:1429–35
163. Ataca C, Şahin H, Aktuörk E, Ciraci S (2011) Mechanical and electronic properties of MoS_2 nanoribbons and their defects. J Phys Chem C 115:3934–3941
164. Zhou Y, Yang P, Zu H, Gao F, Zu X (2013) Electronic structures and magnetic properties of MoS_2 nanostructures: atomic defects, nanoholes, nanodots and antidots. Phys Chem Chem Phys 15:10385–10394
165. Yang S, Wang C, Sahin H, Chen H, Li Y, Li SS et al (2015) Tuning the optical, magnetic, and electrical properties of $ReSe_2$ by nanoscale strain engineering. Nano Lett 15:1660–1666
166. Zhao X, Wang T, Wang G, Dai X, Xia C, Yang L (2016) Electronic and magnetic properties of 1T-HfS_2 by doping transition-metal atoms. Appl Surf Sci 383:151–158
167. Zhao C, Jin C, Wu J, Ji W (2016) Magnetism in molybdenum disulphide monolayer with sulfur substituted by 3 d transition metals. J Appl Phys 120:1–8
168. Lin X, Ni J (2014) Charge and magnetic states of Mn-, Fe-, and Co-doped monolayer MoS_2. J Appl Phys 116:044311
169. Wang J, Sun F, Yang S, Li Y, Zhao C, Xu M, Zhang Y, Zeng H (2016) Robust ferromagnetism in Mn-doped MoS_2 nanostructures. Appl Phys Lett 109:1–6

170. Tao P, Guo H, Yang T, Zhang Z (2014) Strain-induced magnetism in MoS_2 monolayer with defects. J Appl Phys 115:054305
171. Zheng H, Yang B, Wang D, Han R, Du X, Yan Y (2014) Tuning magnetism of monolayer MoS_2 by doping vacancy and applying strain. Appl Phys Lett 104:1–6
172. Yun WS, Lee JD (2015) Strain-induced magnetism in single-layer MoS_2: Origin and manipulation. J Phys Chem C 119:2822–2827
173. Mathew S, Gopinadhan K, Chan TK, Yu XJ, Zhan D, Cao L et al (2012) Magnetism in MoS_2 induced by proton irradiation. Appl Phys Lett 101:102103
174. Wang Y, Tseng LT, Murmu PP, Bao N, Kennedy J, Ionesc M et al (2017) Defects engineering induced room temperature ferromagnetism in transition metal doped MoS_2. Mater Des 121:77–84
175. Ramasubramaniam A, Naveh D (2013) Mn-doped monolayer MoS_2: An atomically thin dilute magnetic semiconductor. Phys Rev B Condens Matter Mater Phys 87:1–7
176. Huang Z, Peng X, Yang H, He C, Xue L, Hao G (2013) The structural, electronic and magnetic properties of bi-layered MoS_2 with transition-metals doped in the interlayer. RSC Adv 3:12939–12944
177. Cheng YC, Zhu ZY, Mi WB, Guo ZB, Schwingenschlögl U (2013) Prediction of two-dimensional diluted magnetic semiconductors: doped monolayer MoS_2 systems. Phys Rev B Condens Matter Mater Phys 87:2–5
178. Fan XL, An YR, Guo WJ (2016) Ferromagnetism in transitional metal-doped MoS_2 monolayer. Nanoscale Res Lett 11:154
179. Yue Q, Chang S, Qin S, Li J (2013) Functionalization of monolayer MoS2 by substitutional doping: a first-principles study. Phys Lett Sect A Gen At Solid State Phys 377:1362–1367
180. Kanoun MB (2018) Tuning magnetic properties of two-dimensional $MoTe_2$ monolayer by doping 3d transition metals: insights from first principles calculations. J Alloys Compd 748:938–942
181. Yang G, Yang Y, Ma H, Mao X, Li C, Li J et al (2018) Realization of a half-metallic state on bilayer WSe2 using doping transition metals (Cr, Mn, Fe Co, Ni) in its interlayer. Nanotechnology 29:115201
182. Ma D, Ju W, Li T, Zhang X, He C, Ma B et al (2016) Modulating electronic, magnetic and chemical properties of MoS_2 monolayer sheets by substitutional doping with transition metals. Appl Surf Sci 364:181–189
183. Luo M, Shen YH, Chu JH (2016) First-principles study of the magnetism of Ni- doped MoS_2 monolayer. Jpn J Appl Phys 55:093001
184. Zhao X, Dai X, Xia C (2015) Magnetic properties of two nearest Cu-doped monolayer WS_2: a first-principles study. Solid State Commun 217:66–69
185. Zhang XJ, Wang XC, Mi WB (2015) Density functional theory prediction on magnetism in Gd-doped monolayer MoS_2. Solid State Commun 212:35–40
186. Luo M, Yin HH, Chu JH (2017) Magnetic properties of a Na-Doped WS_2 monolayer in the presence of an isotropic strain 1. JETP Lett 106:672–676
187. Majid A, Imtiaz A, Yoshiya M (2016) A density functional theory study of electronic and magnetic properties of rare earth doped monolayered molybdenum disulphide. J Appl Phys 120:142124
188. Luo M, Xu YE (2017) A first principle study on the magnetic properties of Ag, Al, Li, Mg, and Na Doped ReS_2 monolayers. J Supercond Nov Magn 31:2431–2436
189. Xhao Z, Xia C, Wang T, Dai X (2016) Electronic and magnetic properties of X-doped (X = Ti, Zr, Hf) tungsten disulphide monolayer. J Alloys Compd 654:574–579
190. Yang B, Zheng H, Han R, Du X, Yan Y (2014) Tuning the magnetism of a ZrS_2 monolayer by substitutional doping. RSC Adv 97:54335–54343
191. Andriotis AN, Menon M (2014) Tunable magnetic properties of transition metal doped MoS_2. Phys Rev B 90:125304
192. Zhang K, Feng S, Wang J, Azcatl A, Lu N, Addou R et al (2015) Manganese doping of Monolayer MoS_2: the substrate is critical. Nano Lett 15:6586–6591

193. Xia B, Guo Q, Gao D, Shi S, Tao K (2016) High temperature ferromagnetism in Cu-doped MoS_2 nanosheets. J Phys D Appl Phys 49:165003
194. Xia B, Yang Y, Ma J, Tao K, Gao D (2017) Adjustable ferromagnetic behavior in iron-doped two-dimensional MoS_2 multilayer nanosheets. Appl Phys Exp 10:093002
195. Muhammad Z, Lv H, Wu C, Habib M, Rehman Z, Khan R (2018) Room temperature ferromagnetism in Fe-doped semiconductor ZrS_2 single crystals Room temperature ferromagnetism in Fe-doped semiconductor ZrS_2 single crystals. Mater. Res. Exp. 5:046110
196. Song C, Pan J, Wu X, Cui C, Li C, Wang J (2017) Charge injection driven switching between ferromagnetism and antiferromagnetism in transitional metal-doped MoS_2 materials. J Phys D Appl Phys 50:465006
197. Shu H, Luo P, Liang P, Cao D, Chen X (2015) Layer-dependent dopant stability and magnetic exchange coupling of iron-doped MoS_2 nanosheets. ACS Appl Mater Interfaces 7:7534–7541
198. Hu AM, Wang LL, Xiao WZ, Xiao G, Rong QY (2015) Electronic structures and magnetic properties in nonmetallic element substituted MoS_2 monolayer. Comput Mater Sci 107:72–78
199. Zhang L, Liu T, Li T, Hussain Z (2017) A study on monolayer MoS_2 doping at the S site via the first principle calculations. Phys E Low-Dimensional Syst Nanostructures 94:47–52
200. Eshun K, Xiong HD, Yu S, Li Q (2015) Doping induces large variation in the electrical properties of MoS_2 monolayers. Solid State Electron 106:44–49
201. Zhao X, Chen P, Xia C, Wang T, Dai X (2016) Electronic and magnetic properties of n-type and p-doped MoS_2 monolayers. RSC Adv 6:16772–16778
202. Luo H, Krizan JW, Seibel EM, Xie W, Sahasrabudhe GS, Bergman SL et al (2015) Cr-doped $TiSe_2$—a layered dichalcogenide spin glass. Chem Mater 27:6810–6817
203. Shkvarin AS, Merentsov AI, Yarmoshenko YM, Skorikov NA, Titov AN (2011) Electronic structure and magnetic state of $TiSe_2$ doped with Cr by means of intercalation or substitution of Ti. Solid State Phenom 168–169:380–383
204. Pleschov VG, Baranov NV, Titov AN, Inoue K, Bartashevich MI, Goto T (2001) Magnetic properties of Cr-intercalated $TiSe_2$. J Alloys Compd 320:13–17
205. IBM, IBM Research Alliance Builds New Transistor for 5 nm Technology (2018) Available: https://www-03.ibm.com/press/us/en/pressrelease/52531.wss#feeds
206. Fursenko O, Bauer J, Lupina G, Dudek P, Lukosius M, Wenger C, Zaumseil P (2012) Optical properties and band gap characterization of high dielectric constant oxides. Thin Solid Films 520:4532–4535
207. Kaasbjerg K, Thygesen KS, Jacobsen KW (2012) Phonon-limited mobility in n-type single-layer MoS_2 from first principles. Phys Rev B Condens Matter Mater Phys 85:1–16
208. Kim S, Konar A, Hwang WS, Lee JH, Lee J, Yang J et al (2012) High-mobility and low-power thin-film transistors based on multilayer MoS_2 crystals. Nat Commun 3:1011
209. Yue R, Barton AT, Zhu H, Azcatl A, Pena LF, Wang J et al (2015) $HfSe_2$ thin films: 2D transition metal dichalcogenides grown by molecular beam epitaxy. ACS Nano 9:474–480
210. Mleczko MJ, Zhang C, Lee HR, Kuo HH, Magyari-Köpe B, Moore RG et al (2017) HfSe2 and ZrSe2: two-dimensional semiconductors with native high-k oxides. Sci Adv 3:e1700481
211. Yan C, Gan L, Zhou X, Guo J, Huang W, Huang J et al (2017) Space-confined chemical vapor deposition synthesis of ultrathin HfS_2 flakes for optoelectronic application. Adv Funct Mater 27:1–9
212. Zhao Q, Guo Y, Si K, Ren Z, Bai J, Xu X (2017) Elastic, electronic, and dielectric properties of bulk and monolayer ZrS_2, $ZrSe_2$, HfS_2, $HfSe_2$ from van der Waals density-functional theory. Phys Status Solidi Basic Res 254:1700033
213. Zhang W, Huang Z, Zhang W, Li Y (2014) Two-dimensional semiconductors with possible high room temperature mobility. Nano Res 7:1731–1737
214. Lv HY, Lu WJ, Shao DF, Lu HY, Sun YP (2016) Strain-induced enhancement in the thermoelectric performance of a ZrS_2 monolayer. J Mater Chem C 4:4538–4545
215. Althobaiti M, Mather S, Sedghi N, Dhanak VR, Mitrovic IZ, Hall S et al (2015) "Hafnia and alumina on sulphur passivated germanium. Vacuum 122:306–309
216. Adamopoulos G, Thomas S, Wöbkenberg PH, Bradley DDC, McLachlan MA, Anthopoulos TD (2011) High-mobility low-voltage ZnO and Li-doped ZnO transistors based on ZrO_2 high-k dielectric grown by spray pyrolysis in ambient air. Adv Mater 23:1894–1898

217. Mirabelli G, McGeough C, Schmidt M, McCarthy EK, Monaghan S, Povey IM et al (2016) Air sensitivity of MoS_2, $MoSe_2$, $MoTe_2$, HfS_2, and $HfSe_2$. J Appl Phys 120:125102
218. Prince MB (1953) Drift mobilities in semiconductors. II. Silicon. Phys Rev 93:1204–1206
219. Prince MB (1953) Drift mobilities in semiconductors. I. Germanium. Phys Rev 92:681–687
220. Blakemore JS (1982) Semiconducting and other major properties of gallium arsenide. J Appl Phys 53:R123
221. Li L, Fang X, Zhai T, Liao M, Gautam UK, Wu X et al (2010) Electrical transport and high-Performance photoconductivity in individual ZrS_2 nanobelts. Adv Mater 22:4151–4156
222. Kang M, Rathi S, Lee I, Lim D, Wang J, Li L, Khan MA, Kim GH (2015) Electrical characterization of multilayer $HfSe_2$ field-effect transistors on SiO_2 substrate. Appl Phys Lett 106:143108
223. Chae SH, Jin Y, Kim TS, Chung DS, Na H, Nam H et al (2016) Oxidation effect in octahedral hafnium disulfide thin film. ACS Nano 10:1309–1316
224. Tsoutsou D, Aretouli KE, Tsipas P, Marquez-Velasco Xenogiannopoulou E, Kelaidis N et al (2016) Epitaxial 2D $MoSe_2$ ($HfSe_2$) semiconductor/2D $TaSe_2$ metal van der Waals heterostructures. ACS Appl Mater Interfaces 8:1836–1841
225. Bessonov AA, Kirikova MN, Petukhov DI, Allen M, Ryhänen T, Bailey MJA (2015) Layered memristive and memcapacitive switches for printable electronics. Nat Mater 14:199–204
226. Yuan J, Lou J (2015) 2D materials: memristor goes two-dimensional. Nat Nanotechnol 10:389–390
227. Sangwan VK, Jariwala D, Kim IS, Chen KS, Marks TJ, Lauhon LJ et al (2015) Gate-tunable memristive phenomena mediated by grain boundaries in single-layer MoS_2. Nat Nanotechnol 10:403–406
228. Cheng P, Sun K, Hu YH (2016) Mechanically-induced reverse phase transformation of MoS_2 from stable 2H to metastable 1T and its memristive behavior. RSC Adv 6:65691–65697
229. Cheng P, Sun K, Hu YH (2016) Memristive Behavior and Ideal Memristor of 1T Phase MoS_2 nanosheets. Nano Lett 16:572–576

Chapter 4
Transition Metal Dichalcogenides in Photocatalysts

Ting Huang, Min Zhang, Hongfei Yin and Xiaoheng Liu

Abstract Photocatalysis is widely recognized as one of the most promising methods for tackling many environmental and energy problems. Recently, transition metal dichalcogenides (TMD) have attracted tremendous research interest owing to their unique properties and great potential in a wide range of applications. TMDs are normally applied as cocatalysts loaded on semiconductors, and the formed junctions between them will facilitate charge transfer of the photogenerated electrons and holes. Besides, the exposed edges of TMDs will function as active sites for catalytic process. Till now, enormous research work has been focused on TMD-based photocatalyst for use in pollutants degradation and hydrogen evolution. In this chapter, we will focus on the recent progress about TMD-based photocatalysts especially currently most studied MoS_2-based photocatalysts. At the end of the chapter, we will also give some perspectives on the challenges and opportunities in this promising research area.

4.1 Introduction

Environmental pollution and energy crisis are two serious problems facing our planet. Photocatalysis might be a promising way to tackle these problems. Sunlight can be harvested by semiconductor photocatalysts, which provide the driving force for pollutant degradation and energy production. As early as 1972, Fujishima and Honda successfully generated H_2 on a TiO_2-based photoelectrode [1]. Their pioneering work sparked a worldwide research interest toward semiconductor-based photocatalysis. Numerous semiconductors, such as TiO_2 [2–6], ZnO [7–9], and CdS [10, 11], have been exploited and used for photocatalysis. However, their real application is still limited due to their low efficiency caused by the rapid electron–hole recombination [12]. Noble metals are widely used as cocatalyst to enhance the activity of the semiconductor photocatalysts [13–15]. However, the high cost and low abundance

T. Huang · M. Zhang · H. Yin · X. Liu (✉)
Key Laboratory for Soft Chemistry and Functional Materials of Ministry of Education, School of Chemical Engineering, Nanjing University of Science and Technology, Nanjing, China
e-mail: xhliu@njust.edu.cn

N. S. Arul and V. D. Nithya (eds.), *Two Dimensional Transition Metal Dichalcogenides*,
https://doi.org/10.1007/978-981-13-9045-6_4

hindered their application. Enormous efforts have been made in the search of their low-cost alternatives composed of earth-abundant elements.

In recent years, transition metal dichalcogenides (TMDs) have attracted tremendous research enthusiasm. Bulk TMD crystals can be exfoliated to layer-structured nanosheets due to the weak van der Waals interaction between layers. Each individual layer of the TMDs consists of three atomic layers in which the transition metal is sandwiched by two chalcogen [16]. Benefit from the high anisotropy and unique crystal structures, TMDs can be utilized in various fields, including energy conversion and storage [17–19], electronics/optoelectronics [20, 21], catalysis [22, 23], as well as sensing [24].

The application of TMDs in photocatalysis is an attractive research topic. The last few years have witnessed a growing research enthusiasm toward TMDs-based photocatalysts. The layer-structured TMDs can be used as effective supports for anchor of semiconductor nanoparticles. A more efficient charge transport will be achieved through the formed heterojunctions between TMD nanosheets and semiconductors. Besides, density functional theory calculations and pioneer experimental works found that the catalytic activity stems from the active sites anchored in the exposed and under-coordinated edge sites [25]. Thus, transition metal dichalcogenides are widely accepted as a promising cocatalyst for semiconductor photocatalysts and show great potential as substitute of noble metal cocatalysts.

The family of transition metal dichalcogenides materials encompasses a wide selection of compositions. Among them, MoS_2 and WS_2 are the most widely synthesized and studied material to date. In this chapter, we will focus on the recent progress in hybrid nanoarchitectures based on 2D TMD nanosheets, with an emphasis on their useful environmental applications for hazardous pollutants degradation and sustainable hydrogen evolution. The synthetic strategies, properties, and applications will be summarized and discussed.

4.2 TMD-Based Binary Photocatalysts

4.2.1 MoS_2-Based Photocatalysts

Among all kinds of transition metal dichalcogenides, MoS_2 is one of the most studied materials. As a typical TMD compound, the layer of MoS_2 is composed of covalent Mo–S bonding, while interactions between the layers are weak van der Waals forces. Compared to their bulk counterparts, few-layer-structured MoS_2 has exploded extensive research enthusiasm in the past decade due to their thickness-dependent electronic structures. When it was exfoliated from bulk to monolayer, it will change from an indirect bandgap semiconductor to a direct bandgap semiconductor. Since Novoselov et al. successfully obtained monolayer graphene by mechanical exfoliation of natural bulk graphite [26], numerous research work has been devoted to the exploration of two-dimensional layer-structured materials. The non-covalent bonded

interaction between the individual layers of TMDs allows them to be exfoliated from bulk to a single layer and exfoliation of the bulk structures will create more edge sites and expose more active sites and consequently to enhance the catalytic performances of TMDs.

The application of layer-structured MoS_2 in photocatalysis is a quite appealing research topic benefit from its unique structure and properties. Hybridizing MoS_2 nanosheets with other semiconductors is a research focus during the past few years. Here, we will discuss different MoS_2-based photocatalysts with their different applications in photocatalysis, including their use in photocatalytic H_2 evolution and pollutant degradation. The mechanism of photocatalytic reactions will also be clarified through several examples.

4.2.1.1 MoS_2-Based Photocatalysts for Photocatalytic H_2 Evolution

Nowadays, hydrogen has been recognized as a clean and sustainable fuel to replace traditional fossil fuels. Hydrogen generation via photocatalytic water splitting holds great promise for solar energy conversion in view of the abundance of both solar energy and water. Since the combustion product of H_2 is water, it will be an ideal solution to the current environmental and energy problem if we can generate H_2 from water using solar light as driving force.

Figure 4.1 shows the main process in photocatalytic water splitting. Semiconductors have a band structure in which the conduction band is separated from the valence band by a bandgap with a suitable width [27]. Under visible light and/or UV light irradiation, the electrons in the valence band of the semiconductors will be excited to the conduction band, while the holes are left in the valence band. The photogenerated electrons and holes might diffuse to the surface of the photocatalyst and give rise to the reduction or oxidation reactions. Water molecules are reduced by the electrons to form H_2 and are oxidized by the holes to form O_2 for overall water splitting. In this process, the band position of the semiconductor photocatalyst is quite important. For semiconductor photocatalysts, to realize photocatalytic H_2 evolution from water, the bottom level of the conduction band must be more negative than the reduction potential of H^+/H_2 (0 V vs. NHE, pH = 0) [28]. An appropriate bandgap is also necessary so that it can absorb UV and/or visible light [29]. Normally, the minimum bandgap for water splitting is 1.23 eV. To utilize visible light, that bandgap energy should be <3.0 eV (>400 nm).

Considering the fast recombination of photogenerated electrons and holes, cocatalysts are usually applied for the modification of semiconductor photocatalysts. Loading MoS_2 on semiconductor photocatalysts can promote or accelerate the photocatalytic courses because they can accept photogenerated charge carriers and provide active sites for photocatalytic process.

The rational design and fabrication of MoS_2-based photocatalysts are quite important. Table 4.1 summarizes the recent development of MoS_2-based nanocomposite photocatalysts for H_2 evolution, including their synthesis approach, photocatalytic activity, and morphology. From the table, we can see that various semiconduc-

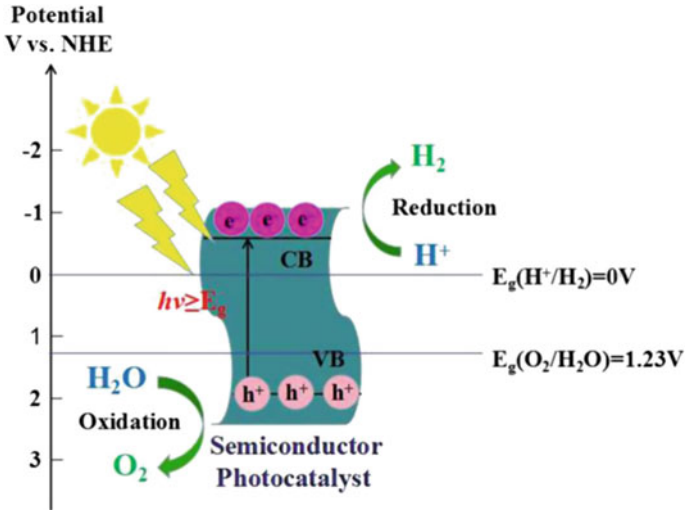

Fig. 4.1 Schematic illustration of photocatalytic water splitting

tors have been coupled with MoS_2 for use in photocatalytic H_2 evolution. Some of them have achieved considerable improvement in photocatalytic activity compared with pristine semiconductor photocatalyst. Among them, TiO_2 has been the most widely studied photocatalyst benefiting from its low-cost, nontoxic, and good anti-photocorrosion properties [30, 31].

Yuan et al. [37] reported the fabrication of layer-by-layer-structured MoS_2/TiO_2 composite via a two-step hydrothermal method. TiO_2 nanosheets with exposed (001) facets were coupled with MoS_2 layers and the resulting product exhibited obviously enhanced photocatalytic hydrogen evolution rate (Fig. 4.2a–c). Under the irradiation of a 300 W Xe-arc lamp, the highest H_2 evolution rate of 2145 $\mu mol\ h^{-1}\ g^{-1}$ was obtained with an optimal ratio of 0.50 wt% MoS_2 (Fig. 4.2d). The authors attributed the enhanced activity to the intimate 2D nanojunction between TiO_2 and MoS_2, which provides an efficient transport channel for charge carrier. Besides, the lower CB position of MoS_2 than TiO_2 provides a strong thermodynamic driving force for electron transfer from excited TiO_2 to MoS_2 (Fig. 4.2e). The electron on the surface of MoS_2 can react with the absorbed protons to evolve H_2 efficiently, while the holes in the VB of TiO_2 are consumed by methanol sacrificial reagent.

In the above-mentioned work, MoS_2 acts as cocatalysts, whereas TiO_2 acts as active component for light harvesting. But Zhou and his coworkers proposed a quite different mechanism for their constructed TiO_2@MoS_2 heterostructure [44]. In this system, MoS_2 can function as active component for light absorption and utilization. They successfully prepared TiO_2@MoS_2 heterostructure which consists of a core of TiO_2 nanobelt and shell of MoS_2 nanosheets. An acid treatment was applied to TiO_2 nanobelts and the obtained TiO_2 nanobelts with rough surface provided high-energy nucleation sites for the nucleation and growth of MoS_2 nanosheets.

Table 4.1 Summary of MoS_2-based nanocomposite photocatalysts for H_2 evolution

Catalyst	Light source	Sacrificial reagent	Activity	Morphology	Refs.
MoS_2/ Cu–$ZnIn_2S_4$	300 W Xe lamp $\lambda > 420$ nm	0.1 M ascorbic acid	5463 $\mu mol\ g^{-1}\ h^{-1}$	Sheet/quantum dots	[32]
MoS_2/ CdS	300 W Xe lamp $\lambda > 420$ nm	20 vol.% lactic acid	775 $\mu mol\ h^{-1}$	Core/shell	[33]
MoS_2/CdS	500 W Xe lamp $\lambda > 420$ nm	10 vol.% of lactic acid	5.24 $mmol\ g^{-1}\ h^{-1}$	Sheet/particle	[34]
MoS_2/g-C_3N_4	300 W Xe lamp $\lambda > 420$ nm	10 vol.% of lactic acid	26.8 $\mu mol\ h^{-1}$	Sheet/hollow spheres	[35]
MoS_2–$Cd_{0.5}Zn_{0.5}S$	500 W Xe lamp $\lambda > 420$ nm	10 vol.% of lactic acid	12.30 $mmol\ g^{-1}\ h^{-1}$	Sheet/particle	[36]
MoS_2/TiO_2	300 W Xe lamp	10 vol.% methanol	2145 $\mu mol\ g^{-1}\ h^{-1}$	Sheet/sheet	[37]
MoS_2/CdS	300 W Xe lamp $\lambda > 420$ nm	10 vol.% of lactic acid	49.80 $mmol\ g^{-1}\ h^{-1}$	Sheet/nanorod	[38]
MoS_2/CdS	300 W Xe lamp $\lambda > 400$ nm	20 vol.% lactic acid	1914 $\mu mol\ g^{-1}\ h^{-1}$	Sheet/nanowire	[39]
MoS_2/TiO_2	300 W Xe lamp	0.35 M Na_2S and 0.25 M Na_2SO_3	1.68 $mmol\ g^{-1}\ h^{-1}$	Sheet/nanofiber	[40]
MoS_2/$ZnIn_2S_4$	300 W Xe lamp $\lambda > 420$ nm	0.5 M Na_2SO_3 and 0.43 M Na_2S	153 $\mu mol\ h^{-1}$	Sheet/ nanoflower	[41]
MoS_2/$SrZrO_3$	100 W mercury lamp	Na_2S (0.35 M) and Na_2SO_3 (0.25 M)	5.31 $mmol\ h^{-1}$	Sheet/cube	[42]
$Zn_xCd_{1-x}S$/ MoS_2	150 W Xe lamp $\lambda > 420$ nm	10 vol.% lactic acid	7806.0 $\mu mol\ g^{-1}$	Sheet/particle	[43]
MoS_2/TiO_2	300 W xenon arc lamp	0.35 M Na_2S and 0.25 M Na_2SO_3	1.6 $mmol\ h^{-1}g^{-1}$	Sheet/belt	[44]
MoS_2/CdS	300 W Xe lamp $\lambda > 420$ nm	10 vol.% lactic acid	532 $\mu mol\ h^{-1}$	Sheet/particle	[45]

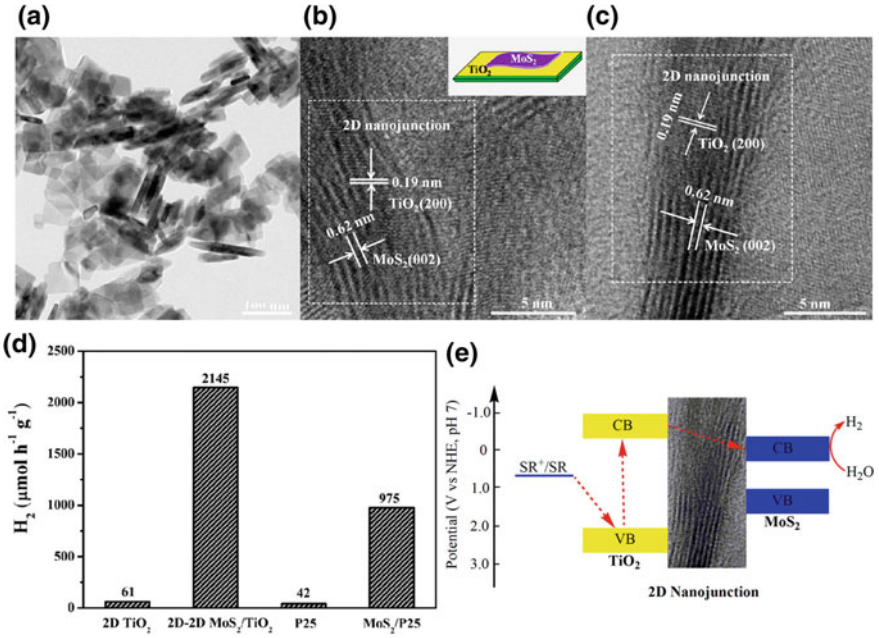

Fig. 4.2 **a** TEM images of 2.00 wt% 2D-2D MoS_2/TiO_2 photocatalyst. **b**, **c** HRTEM images of 2.00 wt% 2D-2D MoS_2/TiO_2. The inset of (**b**) is a schematic diagram of the 2D-2D MoS_2/TiO_2 photocatalyst. **d** Rate of H_2 production on TiO_2 nanosheets, 2D-2D MoS_2/TiO_2, P25, and MoS_2/P25 under irradiation from a 300 W Xe lamp in 100 mL of 10 vol.% aqueous methanol solution. **e** Illustration and energy diagram of charge transfer and photocatalytic processes for efficient solar-to-H_2 conversion system using 2D-2D MoS_2/TiO_2 as the photocatalyst. Reprinted with permission [37]. Copyright 2015 American Chemical Society

The photocatalytic hydrogen production activities of aforementioned samples were measured and compared as well. When the loading amount of MoS_2 was 50 wt%, the highest hydrogen production rate reaches 1.6 mmol h^{-1} g^{-1} (Fig. 4.3). They proposed a different mechanism for the photocatalytic hydrogen evolution process. Bare TiO_2 nanobelts show negligible photocatalytic hydrogen production activity, although it can absorb the UV light. While the introduction of MoS_2 can obviously enhance the visible light absorption due to the apporpriate bandgap of MoS_2 (1.9 eV). Due to the quantum confinement effect of the thin MoS_2 nanosheets, the redox potentials and bandgap of MoS_2 also changed. In this case, the conduction band (CB) and valence band (VB) positions of MoS_2 are higher than those of TiO_2 nanobelts. Under light irradiation, the photoexcited electrons from the VB of MoS_2 nanosheets are directly transferred to CB of MoS_2 and then transmitted to CB of TiO_2 nanobelts driven by the built-in potential in the heterojunction and eventually to produce hydrogen. The left hole was consumed by sacrificial agents.

Although TiO_2 is an active and stable photocatalyst for H_2 evolution, the practical application of TiO_2 is still limited by its poor response to visible light [46]. So

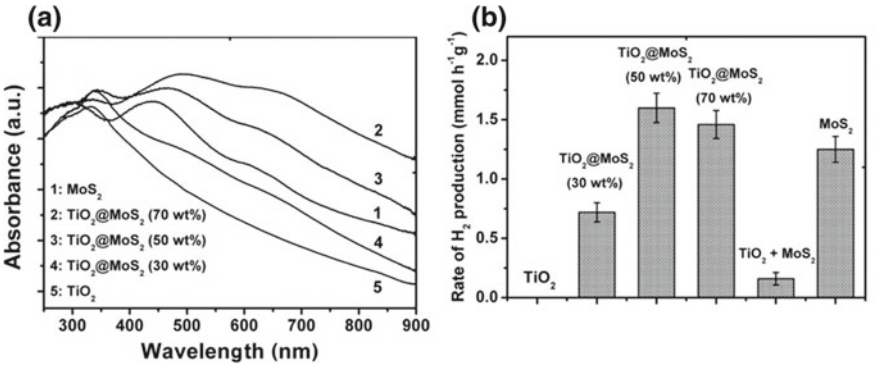

Fig. 4.3 **a** UV-Vis absorption spectra of pure TiO_2 nanobelts, TiO_2@MoS_2 heterostructures and pure MoS_2 nanosheets. **b** Comparison of the photocatalytic hydrogen production activities of different samples under the illumination with the same lighting source in the mixed aqueous solution containing 0.35 M Na_2S and 0.25 M Na_2SO_3 as sacrificial agents. Reprinted with permission [44]. Copyright 2015 Wiley-VCH

tremendous efforts have been devoted to exploring semiconductor photocatalyst with visible-light response [47, 48]. The appropriate bandgap and band alignment of CdS make it a promising candidate for photocatalytic H_2 evolution under visible-light irradiation [49]. During the past few years, the coupling of MoS_2 and CdS is another research hotspot for TMD-based photocatalysis.

As early as 2008, Zong et al. [45] first reported the fabrication of MoS_2/CdS nanocomposite for photocatalytic H_2 evolution. CdS was first prepared and then impregnated with an aqueous solution of $(NH_4)_2MoS_4$, followed by a treatment in H_2S flow at high temperatures for 2 h (Fig. 4.4a, b). The as-obtained MoS_2/CdS catalysts exhibited superior H_2 evolution activity. The activity is increased by up to 36 times when loaded with only 0.2 wt% of MoS_2 (Fig. 4.4c). The loading of MoS_2 can offer the low activation potentials for H_2 evolution and are often served as the active sites for H_2 generation.

Theoretical studies indicate that the edges of MoS_2 have strong bonds to H^+ in the solution, which are easily reduced to H_2 by electrons. Thus, the H_2 evolution rate is obviously enhanced after the loading of MoS_2. A parallel experiment was also conducted. Noble metal Pt was used as a cocatalyst for CdS as well. But the result demonstrated that activity of 0.2 wt% MoS_2/CdS is even higher than that of 0.2 wt% Pt/CdS under the same reaction conditions (Fig. 4.4d). So we come to this conclusion that MoS_2 might replace the currently widely used noble metals such as Pt, Pd, Rh, Ru, and Au and function as efficient H_2 evolution promoters for photocatalysts.

Wu et al. [33] successfully synthesized core-shell structured MoS_2–CdS via a sequential two-step hydrothermal growth method. Flower-like MoS_2 was first formed by the hydrothermal method. After that, certain amount of Cd source was added directly to the above reaction system and sealed in the autoclave again (Fig. 4.5). By varying the amounts of Cd source, the composites with different ratio of MoS_2

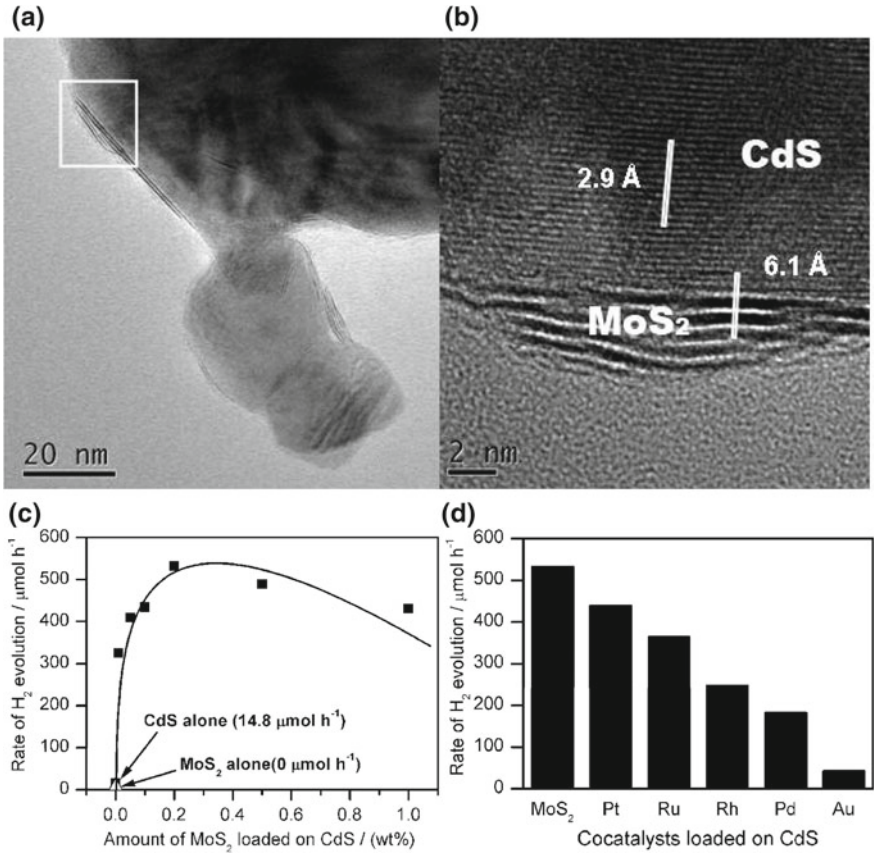

Fig. 4.4 **a** HRTEM image of 1 wt% MoS_2/CdS prepared at 773 K. **b** Magnified HRTEM image of the selected frame from image (**a**). **c** Rate of H_2 evolution on MoS_2/CdS photocatalysts loaded with different amounts of MoS_2 under visible light ($\lambda > 420$ nm). Catalyst (0.1 g); 10 vol.% lactic solution (200 mL); light source, Xe lamp (300 W). **d** Rate of H_2 evolution on CdS loaded with 0.2 wt% of different cocatalysts. Catalyst (0.1 g); 10 vol.% lactic solution (200 mL); light source, Xe lamp (300 W). Reprinted with permission [45]. Copyright 2008 American Chemical Society

and CdS were prepared. In this constructed system, MoS_2 flower served as the core while CdS nanoparticles were placed on outside surface of MoS_2.

Photocatalytic H_2 evolution performance was evaluated under visible-light irradiation (>420 nm) with lactic acid as sacrificial agents. Blank MoS_2 has no obvious PHE activity. But the introduction of MoS_2 can significantly enhance the photocatalytic performance of CdS, indicating the cocatalyst role of MoS_2. The optimal photocatalytic activity was achieved at Mo:Cd = 1:6. The H_2 evolution rate could reach to 775 μmol h^{-1}, which is 64 times as high as the pure CdS. The authors ascribed the enhanced photocatalytic performance to the intimate contacts between MoS_2 and CdS. The formed heterojunction between them may facilitate the charge

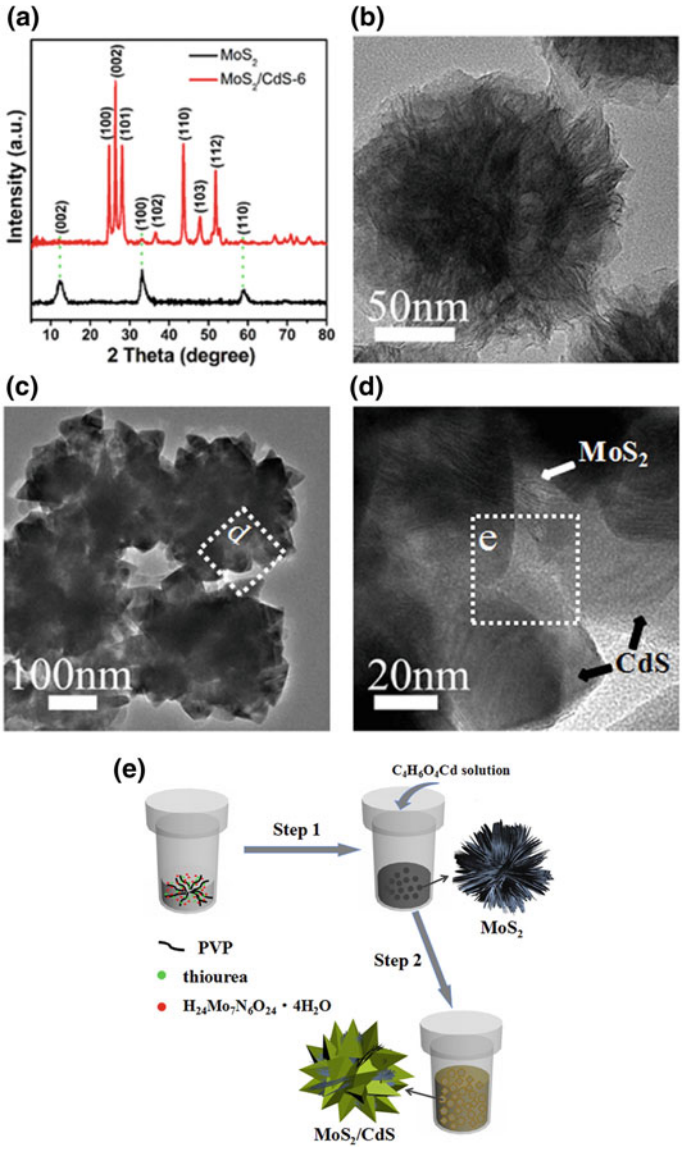

Fig. 4.5 **a** XRD patterns and TEM images of (**b**) MoS_2 spheres. **c**, **d** MoS_2/CdS-6 and **e** schematic for the formation of MoS_2/CdS composites. Reprinted with permission [33]. Copyright 2017 Elsevier

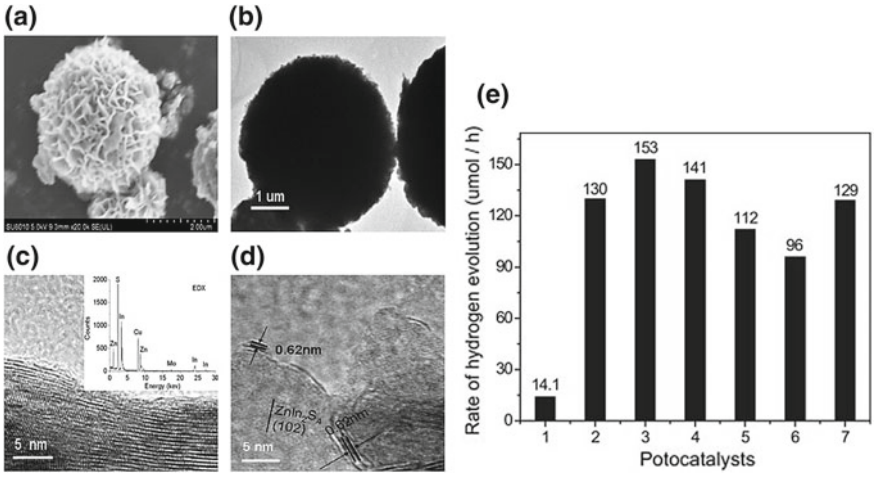

Fig. 4.6 MoS_2–$ZnIn_2S_4$-623 K. **a** SEM image. **b** TEM image. **c** HRTEM image (inset: EDS); MoS_2/$ZnIn_2S_4$-723 K. **d** HRTEM image. **e** Photocatalytic hydrogen evolution rate over (1) pure $ZnIn_2S_4$; $ZnIn_2S_4$ with different amounts of MoS_2 (2) 0.3 wt%; (3) 0.6 wt%; (4) 1.0 wt%; (5) 3.0 wt%; (6) 5.0 wt%; and (7) 1.0 wt% Pt/$ZnIn_2S_4$ (reaction conditions: catalyst, 0.05 g; 100 ml H_2O containing 0.43 M Na_2S and 0.5 M Na_2SO_3). Reprinted with permission [41]. Copyright 2014 Elsevier

transfer and reduce the recombination rate of photogenerated electrons and holes. Finally, the electrons trapped by MoS_2 can react with adsorbed H^+ to produce H_2 due to the like-Pt activity of MoS_2.

Recently, $ZnIn_2S_4$, a ternary chalcogenide which has a suitable bandgap (2.34–2.48 eV), has sparked much research enthusiasm. Previous studies have revealed that $ZnIn_2S_4$ are active for photocatalytic H_2 generation due to its suitable bandgap alignment. However, the short lifetimes of the photogenerated electron–hole pairs still limited its application. The coupling of $ZnIn_2S_4$ and MoS_2 might be an effective way to enhance the photocatalytic H_2 production activity of $ZnIn_2S_4$. Wei et al. [41] reported the preparation of MoS_2/$ZnIn_2S_4$ nanocomposites by calcinating $(NH_4)_2MoS_4$/$ZnIn_2S_4$ precursors in H_2S–H_2 mixed gas atmosphere. A maximum H_2 evolution rate of 153 μmol/h was obtained when the loading amount of MoS_2 was at 0.6 wt%. Excess loading amount of MoS_2 will block the absorption of the incident light by $ZnIn_2S_4$ (Fig. 4.6).

4.2.1.2 MoS_2-Based Photocatalysts for Pollutants Degradation

The application of MoS_2 to the degradation of pollutants in water is also an attractive research topic. Table 4.2 listed some representative MoS_2-based photocatalyst for use in pollutant degradation. As can be seen from that, a variety of semiconductors,

including Ag_3PO_4 [50], C_3N_4 [51], and BiOBr [52], have been coupled with MoS_2 for pollutant degradation.

Wang et al. [62] fabricated the nanocomposite Ag_3PO_4/MoS_2 through a hydrothermal-in situ precipitation method. Ag_3PO_4 nanoparticles were in situ grown on the surface of three-dimensional spherical MoS_2. The coupling of MoS_2 could significantly enhance the photocatalytic performance of RhB degradation compared with pure Ag_3PO_4 under visible-light irradiation. When the loading amount of MoS_2 was at 15 wt%, the nanocomposite showed the optimal photoactivity for the degradation of RhB. A possible Z-scheme photocatalytic mechanism was proposed for the hierarchical Ag_3PO_4/MoS_2 composite. The main reaction steps were depicted as follows:

$$Ag_3PO_4/MoS_2 + h\nu\,(\text{visible light}) \rightarrow Ag_3PO_4/MoS_2\left(h^+ + e^-\right)$$
$$Ag_3PO_4\left(e^-\right) + MoS_2\left(h^+\right) \rightarrow Ag_3PO_4 + MoS_2$$
$$MoS_2 + Ag_3PO_4\left(e^-\right) \rightarrow MoS_2\left(e^-\right) + Ag_3PO_4$$
$$O_2 + MoS_2\left(e^-\right) \rightarrow \bullet O_2^- + MoS_2$$
$$RhB + \bullet O_2^- \rightarrow CO_2 + H_2O + \text{other products}$$
$$RhB + Ag_3PO_4\left(h^+\right) \rightarrow CO_2 + H_2O + \text{other products}$$

Because the conduction band (CB) position and the valance band (VB) position of MoS_2 are all higher than that of Ag_3PO_4, the photogenerated electrons in the CB of Ag_3PO_4 go to the VB of MoS_2 and combine with holes there. And the photogenerated holes in the VB of Ag_3PO_4 could directly react with the organic compounds.

$BiVO_4$ is a promising visible-light-driven photocatalyst with a bandgap of ~2.4 eV. Li et al. [57] reported the fabrication of flower-like $MoS_2/BiVO_4$ composite via a two-step approach (Fig. 4.7a, b). The photodegradation of methylene blue (MB) was adopted to assess the photocatalytic ability of the synthesized nanocomposite. An enhanced photodegradation ability of $MoS_2/BiVO_4$ heteronanostructure was observed (Fig. 4.7c, d). A specific charge-transfer mechanism may account for that phenomenon. Because the CB and the VB of $BiVO_4$ both lie below the corresponding energy bands of MoS_2, the photoexcited electrons tend to transfer to the CB of $BiVO_4$ and while the holes to the VB of MoS_2. The efficient separation of photogenerated electrons and holes lead to the advancement of photocatalytic performance.

Di et al. [52] successfully synthesized the few-layer MoS_2 coupled BiOBr microspheres via a facile hydrothermal method. Ionic liquid [C_{16}mim] Br functioned as the source of Br and acted as a reactant to generate BiOBr. Besides, it can improve the dispersity of MoS_2 on the surface of the BiOBr microspheres. The obtained composite was found to be an effective catalyst for degradation of RhB under visible-light irradiation (Fig. 4.8a, b).

Because the CB and VB positions of MoS_2 are both more negative than those of BiOBr microspheres, the photogenerated electrons can be effectively collected by BiOBr, and the holes can be effectively collected by MoS_2 (Fig. 4.8c). A trapping experiment was also conducted and verified that holes are the main active species

Table 4.2 Summary of some representative MoS_2-based photocatalyst for use in pollutant degradation

Catalyst	Synthesis method	Application	Light source	Morphology	Refs.
Ag_3PO_4/MoS_2	Precipitation method	MB degradation 20 mg L^{-1}	35 W Xe lamp $\lambda > 420$ nm	Sheet/ nanoparticle	[50]
$MoS_2/g\text{-}C_3N_4$	Hydrothermal method	MO degradation 20 mg L^{-1}	500 W Xe lamp	Sheet/sheet	[51]
$MoS_2/BiOBr$	Hydrothermal method	RhB degradation 10 mg L^{-1}	300 W Xe lamp $\lambda > 400$ nm	Sheet/ nanosphere	[52]
MoS_2/Bi_2WO_6	Hydrothermal method	MB degradation 10^{-5} mol L^{-1}	250 W mercury lamp	Core-shell heterostructure	[53]
MoS_2/SnO_2	Solvothermal method	RhB degradation 10 mg L^{-1}	150 W mercury lamp	Sheet/ nanoparticle	[54]
MoS_2/Ag_3PO_4	Precipitation method	RhB degradation 10 mg L^{-1} BPA degradation 20 mg L^{-1}	300 W Xe lamp $\lambda > 400$ nm	Sheet/ nanoparticle	[55]
MoS_2/TiO_2	Hydrothermal method	RhB degradation 10 mg L^{-1}	500 W Xe lamp	Sheet/nanobelts	[56]
$MoS_2/BiVO_4$	Hydrothermal method	MB degradation 40 mg L^{-1}	500 W Xe lamp $\lambda > 400$ nm	Nanoflower	[57]
MoS_2/Bi_2MoO_6	Solvothermal	RhB degradation 10 mg L^{-1}	150 W Xe lamp $\lambda > 420$ nm	Nanoslice/ nanoflake	[58]
MoS_2/CdS	Hydrothermal method	MB RhB degradation 2×10^{-5} mol L^{-1}	300 W Xe lamp $\lambda > 420$ nm	Sheet/branched-like structure	[59]
$MoS_2/SrTiO_3$	Hydrothermal method	MO degradation 30 mg L^{-1}	GGZ 100-1, 100 W	Sheet/ nanoparticle	[60]
MoS_2/C_3N_4	Hydrothermal method	RhB MO degradation 5 mg L^{-1}	300 W Xe lamp $\lambda > 420$ nm	Sheet/sheet	[61]

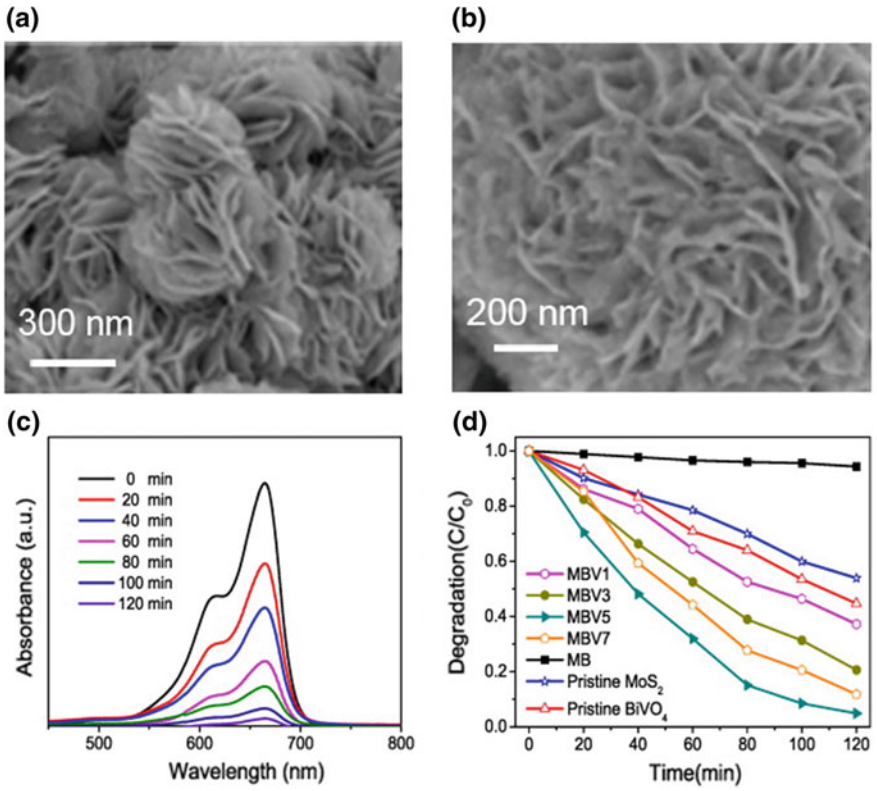

Fig. 4.7 **a** High-magnification SEM images of the pristine MoS_2 nanoflowers. **b** High magnification of a MBV5 sphere. **c** Absorption spectra of MB solution after 120 min irradiation at room temperature in the presence of MBV5 heteronanostructure. **d** Normalized decrease concentration C/C_0 of the MB solution containing different catalysts. Reprinted with permission [57]. Copyright 2015 American Chemical Society

in RhB photodegradation. Thus, the holes accumulated in the VB of MoS_2 could react with the pollutant and exhibit admirable photocatalytic activity for pollutant degradation.

4.2.2 WS_2-Based Photocatalysts

WS_2 is another frequently used TMD cocatalyst for the modification of semiconductors. WS_2 possess extremely similar crystal structure and chemical property of MoS_2 [63, 64]. The planes of W atoms are sandwiched between two atomic layers of S with strong in-plane bonding; while layers are stacked together via weak van der Waals interaction. They can also act as an efficient cocatalyst to enhance the activity of

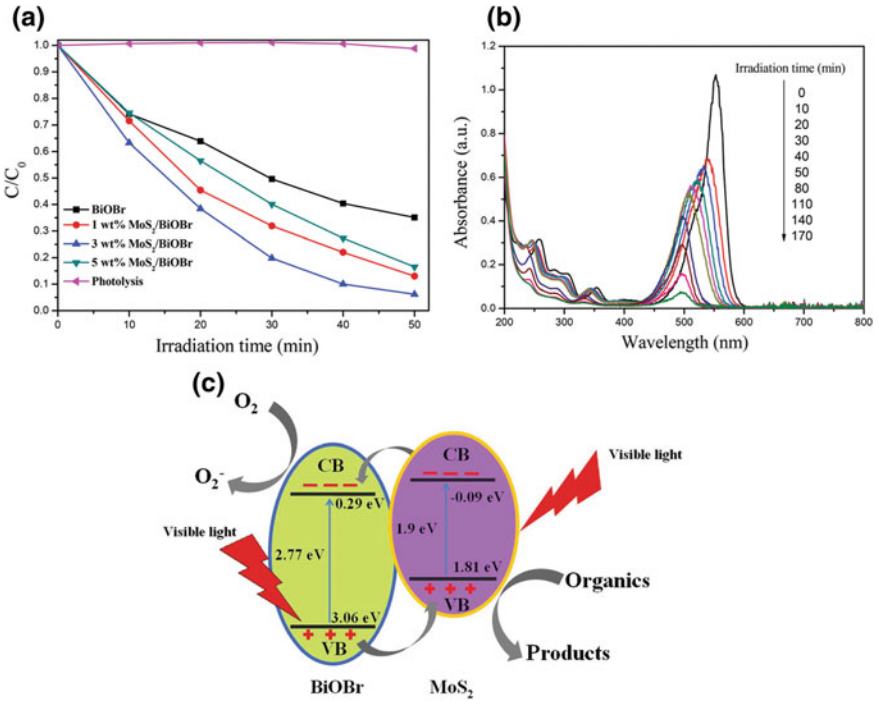

Fig. 4.8 **a** Photocatalytic degradation of RhB in the presence of pure BiOBr and MoS_2/BiOBr and photolysis of RhB under visible-light irradiation. **b** Temporal UV-Vis absorption spectral changes during the photocatalytic degradation of RhB in aqueous solution in the presence of 3 wt% MoS_2/BiOBr. **c** Proposed photocatalytic charge-transfer mechanism in the MoS_2/BiOBr materials under visible-light irradiation. Reprinted with permission [52]. Copyright 2014 Royal Society of Chemistry

semiconductor photocatalysts. But compared with the currently most studied MoS_2, their application in photocatalysis is rarely discussed.

4.2.2.1 WS_2-Based Photocatalysts for Photocatalytic H_2 Evolution

Zong et al. [65] successfully loaded WS_2 onto commercial CdS powder by an impregnation method. In brief, $(NH_4)_2WS_4$/CdS precursor was first prepared by immersing CdS nanoparticles into ammonia solution containing different amounts of $(NH4)_2WS_4$. Then the obtained precursor was heated in H_2S flow to obtain the WS_2/CdS catalyst. The result demonstrated that H_2 evolution rate of CdS loaded with only 1 wt% of WS_2 increased up to 28 times in comparison with that of pristine CdS (Fig. 4.9a). CdS loaded with different noble metals, including Pt, Ru, Rh, and Au, were also prepared for a comparison (Fig. 4.9b). The obviously enhanced photocatalytic performance could be ascribed to the intimate junctions formed between WS_2

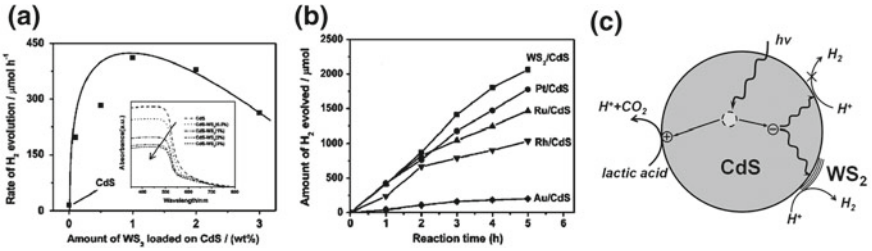

Fig. 4.9 **a** Rate of H_2 evolution on CdS photocatalysts under visible light ($\lambda > 420$ nm) loaded with different amounts of WS_2. **b** Time courses of photocatalytic H_2 evolution on CdS loaded with 1 wt% of different cocatalysts under visible light ($\lambda > 420$ nm). **c** Proposed reaction mechanism for photocatalytic H_2 production on WS_2/CdS catalyst. Reprinted with permission [65]. Copyright 2011 American Chemical Society

and CdS. Besides, the introduction of WS_2 also produces active sites for hydrogen evolution process (Fig. 4.9c).

As we know, WS_2 possesses two main typical types of structure, 1T structure and 2H structure. The 1T structure exhibits metallic properties and the 2H structure own semiconducting nature. Benoit Mahler and his coworkers [66] first described a novel colloidal synthesis method for both 1T–WS_2 and 2H–MoS_2. They compared the photocatalytic water splitting properties of the two different structures by coupling them with TiO_2 nanoparticles. The results demonstrated that 1T–WS_2 structure was an efficient hydrogen evolution cocatalyst, while the nanocomposite of 2H–WS_2 and TiO_2 exhibits low photoactivity. This might because the introduction of 2H–WS_2 will provide recombination centers for the photogenerated electrons and holes.

Chen et al. [67] developed a novel one-pot synthesis method for MS_2–CdS (M=Mo, W). The MS_2–CdS nanohybrids were synthesized through a hot-injection method. In brief, Cd source was injected into the solution containing sulfur donors, such as WS_4^{2-}, Et_2NCS_2. In the obtained nanohybrids, single-layer MS_2 sheets selectively grew on the Cd-rich (0001) surface of wurtzite CdS nanocrystals (Fig. 4.10). The photocatalytic hydrogen evolution activities were evaluated under visible-light irradiation. Compared with pure CdS, the hydrogen evolution rates of WS_2/CdS enhanced nearly 16 times. The authors ascribed the obviously enhanced photocatalytic performance to the large number of active sites of single-layer WS_2 and the formed p/n heterojunction between WS_2 and CdS.

4.2.2.2 WS_2-Based Photocatalysts for Pollutant Degradation

Yu et al. [68] exfoliated bulk WS_2 to few-layer by a mechanical exfoliation method. The obtained WS_2 nanosheet served as supports for the growth of Ag_3PO_4 nanoparticles. The Ag_3PO_4/WS_2 heterostructure was found with superior photocatalytic activity for the degradation of RhB under visible-light irradiation (Fig. 4.11a–d). Several factors may account for the improved photocatalytic performance. As can be seen

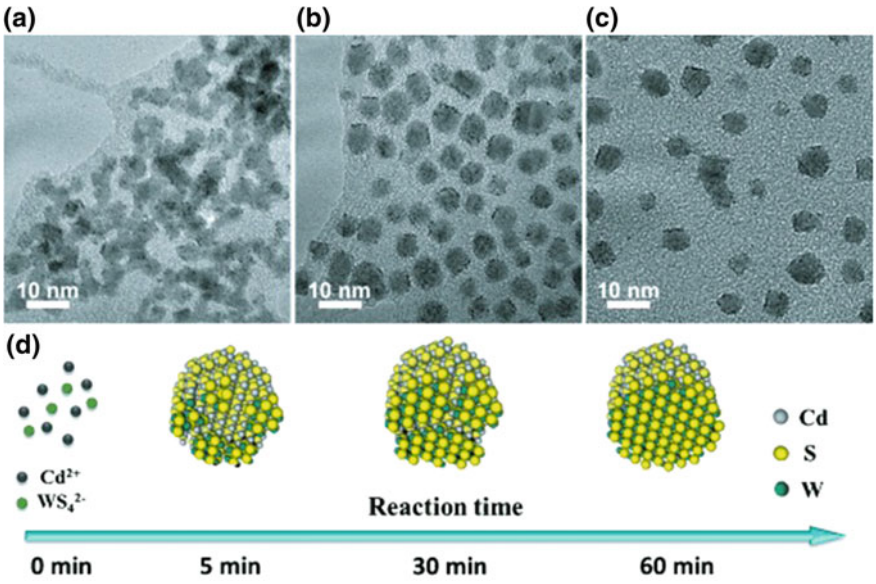

Fig. 4.10 TEM images of WS_2–CdS nanohybrids obtained at different reaction time. The reaction time is **a** 5, **b** 30, **c** 60 min. **d** Schematic illustration of the shape evolution of WS_2–CdS nanohybrids. Reprinted with permission [67]. Copyright 2015 Wiley-VCH

from Fig. 4.11e, because of the energy level match between Ag_3PO_4 and WS_2, the electrons tend to transfer from WS_2 to Ag_3PO_4 while the holes located in the valance band of Ag_3PO_4 are prone to migrate to the valance band of WS_2. A more efficient separation of photogenerated electrons and holes contributes to the enhancement of photocatalytic performance. Besides, the high interface area and abundant active sites also play a vital role in the catalytic process.

Atkin et al. [69] synthesized WS_2 nanoflakes hybridized with carbon dots by a facile two-step method. 2D WS_2 suspension was produced by a modified two-solvent grinding/sonication method. The as-produced suspension was added to citric acid solution and exposed to microwave irradiation for few minutes. To evaluate its photocatalytic performance, Congo Red (CR) was selected as a model dye. Compared with pure WS_2 nanoflakes, carbon dot anchored WS_2 exhibited obviously enhanced photocatalytic performance. The authors ascribed the enhancement of photocatalytic performance to the increased affinity of CR molecules onto the surface of the flakes rather than a 2D WS_2/CD heterostructuring effect.

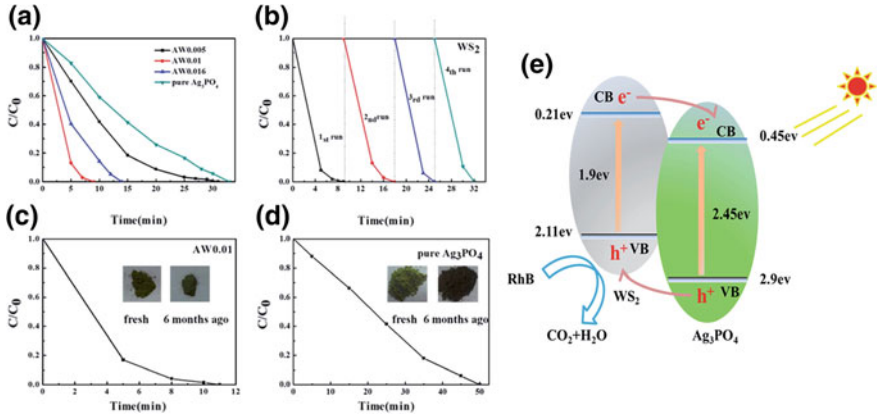

Fig. 4.11 **a** Photocatalytic degradation of RhB solution over the as-prepared Ag_3PO_4/WS_2 composite, bare WS_2 sheets and pure Ag_3PO_4. **b** Repeated degradation of RhB solution over the recycled AW0.01 photocatalyst under visible light. **c** Photocatalytic degradation of RhB solution over AW0.01 and pure Ag_3PO_4 prepared six months earlier, respectively. Insets in (**c**) and (**d**) are pictures of catalyst powder. **e** Schematic of the band structure and expected charge separation of Ag_3PO_4/WS_2 composites under visible-light irradiation. Reprinted with permission [68]. Copyright 2015 Royal Society of Chemistry

4.2.3 Other TMD-Based Photocatalysts

The layered transition metal dichalcogenides constitute a broad family of materials. Except from the above-mentioned MoS_2, WS_2, a variety of TMDs can be used in photocatalysis application. For example, Zhu et al. [70] reported the synthesis of NiS_2/g-C_3N_4 hybrid photocatalysts by a facile hydrothermal method. The nanocomposite exhibited enhanced photocatalytic performance toward the degradation of RhB. A possible mechanism was proposed for this photocatalytic process. The g-C_3N_4 sheets provide a support for dispersing small NiS_2 on its nanosheet surface, and the intimate contact between NiS_2 and g-C_3N_4 can facilitate the charge transfer and decrease the charge recombination rate, which is beneficial for the enhancement of photocatalytic performance.

Meng et al. [71] synthesized novel BiOCl/SnS_2 hollow spheres via a facile one-pot hydrothermal method. The photocatalytic activity was evaluated by the photodegradation of RhB, and a remarkable improvement in the photocatalytic performance was observed in the BiOCl/SnS_2 hollow sphere. Because the valence band and conduction band potentials of SnS_2 are more negative than those of BiOCl, the photogenerated electron can transfer from the conduction band of SnS_2 to the conduction band of BiOCl, which can enhance the separation of photogenerated electrons and holes. Besides, the authors think the hierarchical assembly of nanoflakes greatly increases the surface area and enhances light-harvesting efficiency.

4.3 TMD/GR-Based Ternary Photocatalysts

Although MoS_2 is an efficient cocatalyst for photocatalysis, the further advancement of their photocatalytic performance is still limited by their poor electrical conductivity [72]. Graphene, featured by its single-layer sp^2-hybridized carbon atoms, has been widely accepted as an efficient charge transporter [73]. To couple graphene with MoS_2 can significantly improve the electrical conductivity and overcome such drawback. Till now extensive research works about this topic have been published. We summarized some representative work in Table 4.3.

4.3.1 TMD/GR-Based Ternary Photocatalysts for Photocatalytic H_2 Evolution

The coupling of MoS_2 and graphene can form a new cocatalyst for photocatalytic H_2 evolution. As early as 2012, Xiang et al. [82] first reported the synthesis of TiO_2 NPs on a layered MoS_2/graphene

hybrid for use in photocatalytic H_2 production. Layer-structured MoS_2/graphene was first prepared via a hydrothermal method and then served as a support for the growth of TiO_2 nanoparticles (Fig. 4.12a–d). The photocatalytic H_2 production activity was evaluated under xenon arc lamp irradiation using ethanol as a scavenger. Significantly enhanced photocatalytic performance was observed, and the highest H_2 evolution rate was obtained when the cocatalyst 95M5.0G (the composite photocatalyst containing 95% MoS_2 and 5% graphene in the cocatalyst) was introduced to this system. The authors claimed that MoS_2 and graphene play a synergetic effect on the improvement of the photocatalytic H_2 production activity. Graphene sheet can improve the mobility of the photogenerated electrons while MoS_2 can act as active sites for H_2 evolution (Fig. 4.12e).

Since MoS_2-graphene/TiO_2 photocatalyst was inactive under visible-light irradiation, much research work was focused on visible-light-responsive photocatalyst. For example, Yuan and his coworkers [77] successfully synthesized MoS_2-graphene/$ZnIn_2S_4$ nanocomposite and evaluated their photocatalytic H_2 generation performance in Na_2S–Na_2SO_3 solution under visible-light irradiation. As can be seen from Fig. 4.13a–d, the synthesized $ZnIn_2S_2$ possessed a flower-like morphology. The photocatalytic results demonstrated that the optimum H_2 production rate was 22.8 times higher than that of pure $ZnIn_2S_4$ when the content of MoS_2-graphene is 1.2 wt%. The superior catalytic activity was ascribed to the positive synergistic effect between MoS_2 and graphene, which act as a hydrogen evolution reaction catalyst and an electron transport bridge (Fig. 4.13e, f).

Table 4.3 Representative work of MoS_2/GR-based photocatalysts and their different application

Catalyst	Synthesis method	Application	Light source	Morphology	Refs.
CuInZnS/ MoS_2–GO	Hydrothermal	H_2 evolution	300 W Xe lamp $\lambda > 420$ nm	Nanoparticle/ sheet	[74]
g-C_3N_4/ MoS_2–GO	Two-step method	H_2 evolution	450 W Xe lamp with an AM 1.5G filter	Quantum dot/sheet	[75]
ZnO/MoS_2–GO	Hydrothermal	H_2 evolution	Natural sunlight, a	Nanoparticle/ sheet	[76]
$ZnIn_2S_4$/ MoS_2–GO	Hydrothermal	H_2 evolution	300 W Xe lamp $\lambda > 420$ nm	Microspheres/ sheet	[77]
CdS/MoS_2–GO	Hydrothermal	H_2 evolution	300 W Xe lamp $\lambda > 400$ nm	Hollow spheres/sheet	[78]
CdS/MoS_2–GO	Hydrothermal	H_2 evolution	350 W Xe lamp $\lambda > 420$ nm	Nanorods/sheet	[79]
ZnS/MoS_2–GO	Hydrothermal	H_2 evolution	300 W Xe lamp	Nanoparticle/ sheet	[80]
CdS/MoS_2–GO	Photodeposition method	H_2 evolution	350 W Xe lamp $\lambda > 420$ nm	Nanoparticle/ sheet	[81]
TiO_2/MoS_2–GO	Hydrothermal	H_2 evolution	350 W Xe lamp	Nanoparticle/ sheet	[82]
CdS/WS_2–GO	Solvothermal	H_2 evolution	500 W Xe lamp $\lambda > 420$ nm	Nanorod/sheet	[83]
Bi_2WO_6/ MoS_2–GO	Hydrothermal	RhB degradation	300 W Xe lamp $\lambda > 400$ nm	Nanoplates/ nanosheet	[84]
Cu_2O/ MoS_2–GO	In situ deposition	Acid Blue 92 degradation	$\lambda > 420$ nm	Cube/sheet	[85]
Ag_3PO_4 /MoS_2–GO	Hydrothermal	phenol degradation	500 W Xe lamp $\lambda > 420$ nm	Particle/sheet	[86]

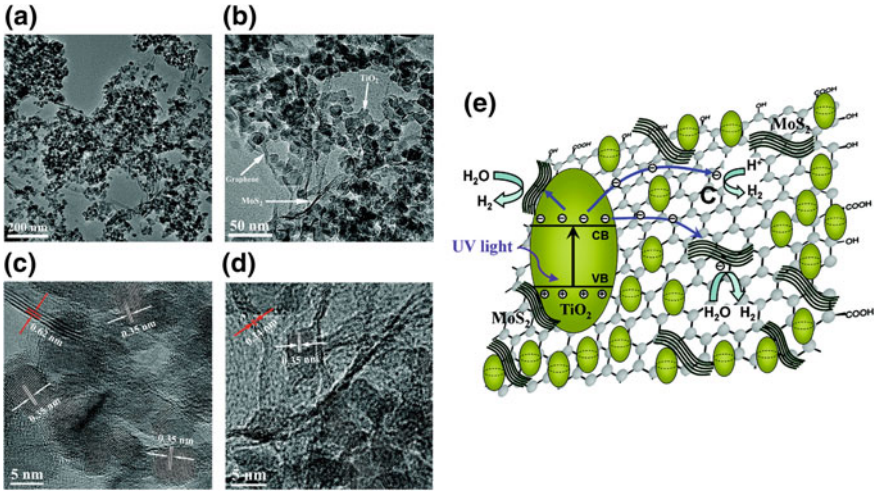

Fig. 4.12 Structural analysis of the T/95M5.0G composite. **a**, **b** TEM images of TiO_2 NPs combined with layered MG hybrids. **c**, **d** High-resolution TEM images of TiO_2 nanocrystals grown on layered MG hybrids. The MG sheets can be considered as a support and interconnecting medium for the TiO_2 NPs. **e** Schematic illustration of the charge transfer in TiO_2/MG composites. The proposed mechanism for the enhanced electron transfer in the TiO_2/MG system under irradiation assumes that the photoexcited electrons are transferred from the CB of TiO_2 not only to the MoS_2 nanosheets but also to the C atoms in the graphene sheets, which can effectively reduce H^+ to produce H_2. Reprinted with permission [82]. Copyright 2012 American Chemical Society

4.3.2 TMD/GR-Based Ternary Photocatalysts for Pollutants Degradation

Using TMD/GR hybrid for degradation of pollutants in water is also an attractive technology. Here, we give some examples in this area. Liu et al. [84] synthesized a ternary Bi_2WO_6@MoS_2/graphene (BWO/MG) nanocomposite by a facile two-step hydrothermal method (Fig. 4.14a–d). The ternary nanocomposite exhibited superior photocatalytic performance for the degradation of RhB under visible-light irradiation, which might be contributed to an enhanced charge carrier separation via gradual charge transferred pathway. The loading of cocatalyst MoS_2/graphene can provide large specific surface area and a mass of active adsorption sites. Besides, a more efficient charge transfer can be achieved in the constructed ternary composite (Fig. 4.14e, f).

Peng et al. [86] prepared Ag_3PO_4 coupled with MoS_2/graphene hybrid via a simple two-step hydrothermal method. The photocatalytic performance was evaluated by degradation of 2,4-dichlorophenol (DCP) under visible-light irradiation. With the optimized composition (2% cocatalyst), DCP degradation exhibited best photocatalytic performance. It is worth noted that the photocatalytic performance of pure MoS_2/graphene was also tested and no degradation was observed. So MoS_2/graphene

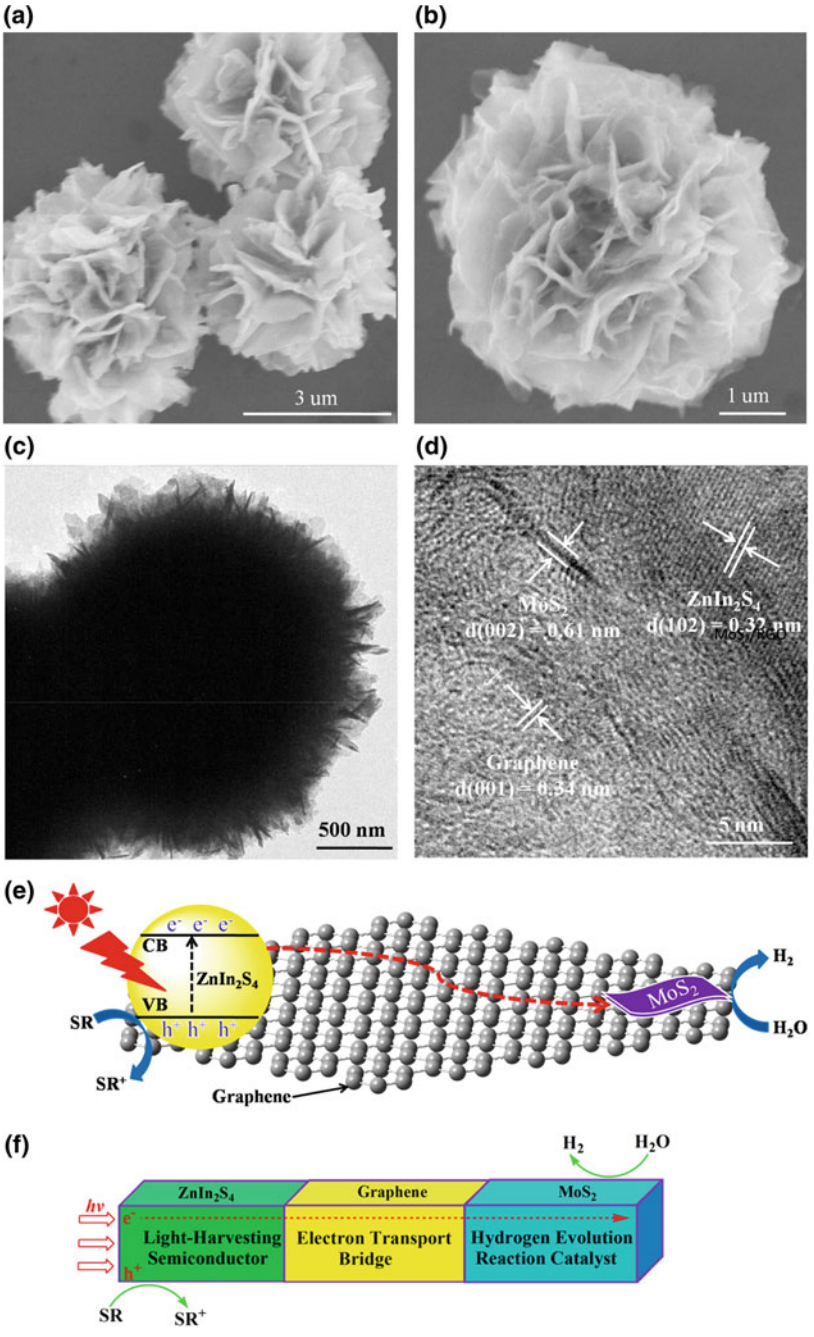
(a)
3 um
(b)
1 um
(c)
500 nm
(d)
MoS2
d(002) = 0.61 nm
ZnIn2S4
d(102) = 0.32 nm
Graphene
d(001) = 0.34 nm
5 nm
(e)
CB
VB
ZnIn2S4
e- e- e-
h+ h+ h+
SR
SR+
Graphene
MoS2
H2
H2O
(f)
H2
H2O
ZnIn2S4
Graphene
MoS2
hv
e-
h+
Light-Harvesting Semiconductor
Electron Transport Bridge
Hydrogen Evolution Reaction Catalyst
SR
SR+

◀**Fig. 4.13** **a**, **b** SEM images of 1.2 wt% Mo10G1/$ZnIn_2S_4$ composites. **c** TEM and **d** HRTEM images of 1.2 wt% Mo10G1/$ZnIn_2S_4$ composite. **e** Schematic illustration for photocatalytic hydrogen generation over MoS_2-graphene/$ZnIn_2S_4$ under visible-light irradiation. **f** Schematic illustration for charge carriers in MoS_2-graphene/$ZnIn_2S_4$ photocatalyst, $ZnIn_2S_4$: light-harvesting semiconductor, graphene: electron transport bridge, MoS_2: hydrogen evolution reaction catalyst. Reprinted with permission [77]. Copyright 2016 Elsevier

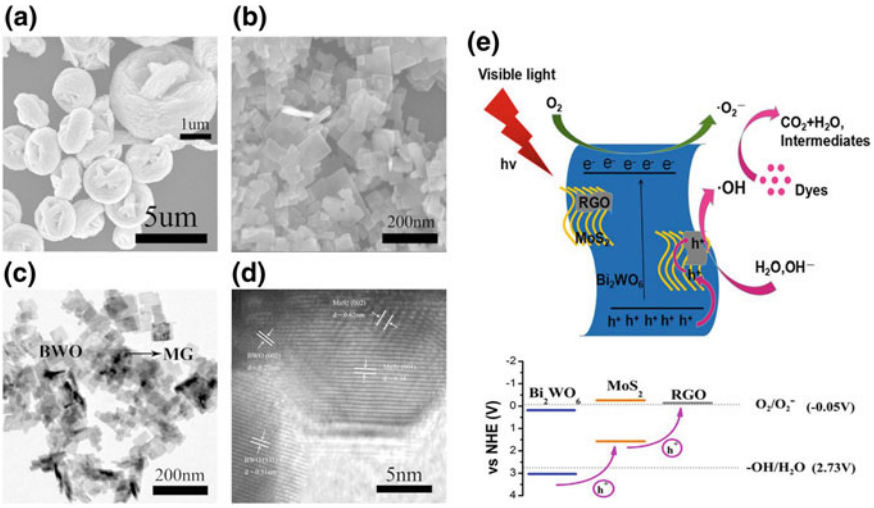

Fig. 4.14 SEM images of **a** BWO and **b** BWO/MG, **c** TEM image of BWO/MG and **d** HRTEM image of BWO/MG. **e** Schematic diagram for photocatalytic mechanism of BWO/MG hybrids. **f** Band structure, RGO, CB and VB levels of MoS_2 and BWO. Reprinted with permission [84]. Copyright 2017 Springer

can only function as cocatalyst. In the constructed system, MoS_2/GR nanosheets will function as electron collectors for the interfacial electron transfer, which enhanced the separation of the photogenerated electrons and holes. Besides, the MoS_2/GR hybrid can provide more active adsorption sites and allow for the activation of dissolved O_2 for organic degradation (Fig. 4.15).

4.4 Summary and Outlook

As a kind of novel nanomaterials, TMDs have great potential in photocatalytic environmental remediation and renewable energy production. It is worthy of mention that the development of novel TMDs materials might open up a way for future energy conversion as well as environmental remediation. Recently, huge advances in the design and controlled synthesis of novel TMD nanosheets-based photocatalysts have been achieved. However, MoS_2-based photocatalyst is most explored in the past few years. The variations in the composition of TMDs might lead to significant differences in

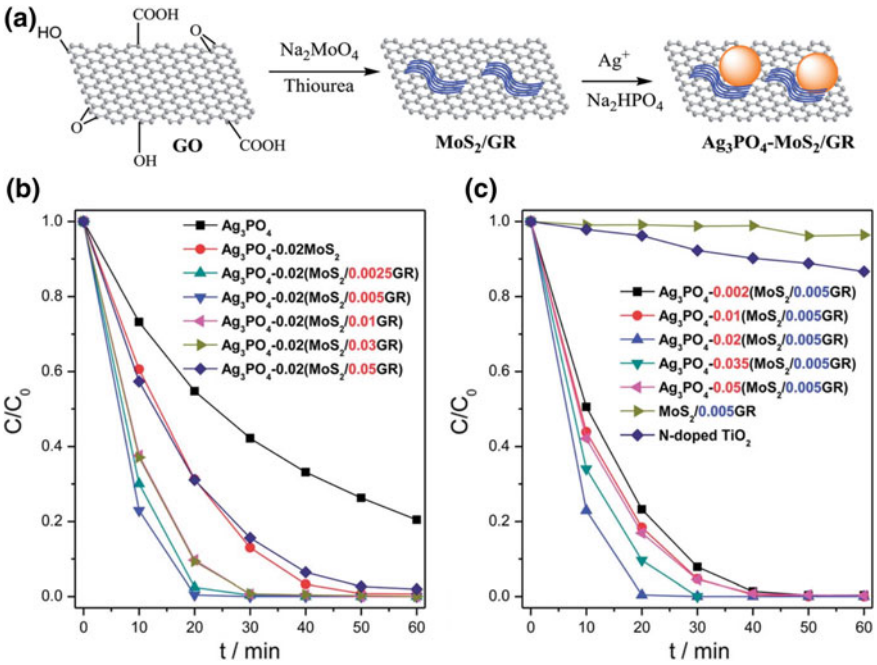

Fig. 4.15 **a** Illustration of the Ag_3PO_4–MoS_2/GR photocatalyst synthesis. Photocatalytic DCP degradation by the photocatalysts under SS light. **b** With different GR contents and **c** with different MoS_2/0.005GR percentages. Reprinted with permission [86]. Copyright 2014 Royal Society of Chemistry

their catalytic activity. So the research toward other rarely studied members in TMDs or their combination alloys could be an interesting ground and allow new possibilities for efficient photocatalysts. Although some key advances have been achieved at the laboratory scale, it is still a long way to go to achieve practical efficiencies.

References

1. Fujishima A, Honda K (1972) Electrochemical photolysis of water at a semiconductor electrode. Nature 238:37–38
2. Yang Y, Liu G, Irvine JT, Cheng HM (2016) Enhanced photocatalytic H_2 production in core-shell engineered rutile TiO_2. Adv Mater 28:5850–5856
3. Khan SU, Al-Shahry M, Ingler-Jr WB (2002) Efficient photochemical water splitting by a chemically modified n-TiO_2. Science 297:2243–2245
4. Yang J, Jiang YL, Li LJ, Muhire E, Gao MZ (2016) High-performance photodetectors and enhanced photocatalysts of two-dimensional TiO_2 nanosheets under UV light excitation. Nanoscale 8:8170–8177
5. Wang W, Dong J, Ye X, Li Y, Ma Y, Qi L (2016) Heterostructured TiO_2 nanorod@nanobowl arrays for efficient photoelectrochemical water splitting. Small 12:1469–1478

6. Nolan M, Iwaszuk A, Lucid AK, Carey JJ, Fronzi M (2016) Design of Novel visible light active photocatalyst materials: surface modified TiO_2. Adv Mater 28:5425–5446
7. Wang X, Zhang Y, Hao C, Feng F, Yin H, Si N (2014) Solid-phase synthesis of mesoporous ZnO using lignin-Amine template and its photocatalytic properties. Ind Eng Chem Res 53:6585–6592
8. Ren X, Hou H, Liu Z, Gao F, Zheng J, Wang L, Li W, Ying P, Yang W, Wu T (2016) Shape-enhanced photocatalytic activities of thoroughly mesoporous ZnO nanofibers. Small 12:4007–4017
9. Chen D, Wang Z, Ren T, Ding H, Yao W, Zong R, Zhu Y (2014) Influence of defects on the photocatalytic activity of ZnO. J Phy Chem C 118:15300–15307
10. Zhai T, Fang X, Li L, Bando Y, Golberg D (2010) One-dimensional CdS nanostructures: synthesis, properties, and applications. Nanoscale 2:168–187
11. Li Q, Guo B, Yu J, Ran J, Zhang B, Yan H, Gong JR (2011) Highly efficient visible-light-driven photocatalytic hydrogen production of CdS-cluster-decorated graphene nanosheets. J Am Chem Soc 133:10878–10884
12. Qu Y, Duan X (2013) Progress, challenge and perspective of heterogeneous photocatalysts. Chem Soc Rev 42:2568–2580
13. Zhang L, Fu X, Meng S, Jiang X, Wang J, Chen S (2015) Ultra-low content of Pt modified CdS nanorods: one-pot synthesis and high photocatalytic activity for H_2 production under visible light. J Mater Chem A 3:23732–23742
14. Seh ZW, Liu S, Low M, Zhang SY, Liu Z, Mlayah A, Han MY (2012) Janus Au–TiO_2 photocatalysts with strong localization of plasmonic near-fields for efficient visible-light hydrogen generation. Adv Mater 24:2310–2314
15. Vaiano V, Matarangolo M, Murcia JJ, Rojas H, Navío JA, Hidalgo MC (2018) Enhanced photocatalytic removal of phenol from aqueous solutions using ZnO modified with Ag. Appl Catal B: Environ 225:197–206
16. Chhowalla M, Liu Z, Zhang H (2015) Two-dimensional transition metal dichalcogenide (TMD) nanosheets. Chem Soc Rev 44:2584–2586
17. Gao J, Li L, Tan J, Sun H, Li B, Idrobo JC, Singh CV, Lu TM, Koratkar N (2016) Vertically oriented arrays of ReS_2 nanosheets for electrochemical energy storage and electrocatalysis. Nano Lett 16:3780–3787
18. Acerce M, Voiry D, Chhowalla M (2015) Metallic 1T phase MoS_2 nanosheets as supercapacitor electrode materials. Nat Nanotechnol 10:313–318
19. Zhang Y, Zhou Q, Zhu J, Yan Q, Dou SX, Sun W (2017) Nanostructured metal chalcogenides for energy storage and electrocatalysis. Adv Funct Mater 27:1702317
20. Fu L, Wang F, Wu B, Wu N, Huang W, Wang H, Jin C, Zhuang L, He J, Fu L, Liu Y (2017) Van der Waals epitaxial growth of atomic layered HfS_2 crystals for ultrasensitive near-Infrared phototransistors. Adv Mater 29:1700439
21. Kappera R, Voiry D, Yalcin SE, Branch B, Gupta G, Mohite AD, Chhowalla M (2014) Phase-engineered low-resistance contacts for ultrathin MoS_2 transistors. Nat Mater 13:1128–1134
22. Lee CP, Chen W-F, Billo T, Lin YG, Fu FY, Samireddi S, Lee CH, Hwang JS, Chen KH, Chen LC (2016) Beaded stream-like $CoSe_2$ nanoneedle array for efficient hydrogen evolution electrocatalysis. J Mater Chem A 4:4553–4561
23. Li H, Tan Y, Liu P, Guo C, Luo M, Han J, Lin T, Huang F, Chen M (2016) Atomic-sized pores enhanced electrocatalysis of TaS_2 nanosheets for hydrogen Evolution. Adv Mater 28:8945–8949
24. Chen X, Yu K, Shen Y, Feng Y, Zhu Z (2017) Synergistic Effect of MoS_2 nanosheets and VS_2 for the hydrogen evolution reaction with enhanced humidity-sensing performance. ACS Appl Mater Interfaces 9:42139–42148
25. Karunadasa HI, Montalvo E, Sun Y, Majda M, Long J-R, Chang CJ (2012) A molecular MoS_2 edge site mimic for catalytic hydrogen generation. Science 335:698–702
26. Novoselov KS, Geim AK, Morozov SV, Jiang D, Zhang Y, Dubonos SV, Grigorieva IV, Firsov AA (2004) Electric field effect in atomically thin carbon films. Science 306:666–669

27. Kudo A, Miseki Y (2009) Heterogeneous photocatalyst materials for water splitting. Chem Soc Rev 38:253–278
28. Su T, Shao Q, Qin Z, Guo Z, Wu Z (2018) Role of interfaces in two-dimensional photocatalyst for water splitting. ACS Catal 8:2253–2276
29. Chen X, Shen S, Guo L, Mao SS (2010) Semiconductor-based photocatalytic hydrogen generation. Chem Rev 110:6503–6570
30. Liu C, Zhou W, Song J, Liu H, Qu J, Guo L, Song G, Huang C-P (2017) Nanostructure-induced colored TiO_2 array photoelectrodes with full solar spectrum harvesting. J Mater Chem A 5:3145–3151
31. Zhou X, Haublein V, Liu N, Nguyen NT, Zolnhofer EM, Tsuchiya H, Killian MS, Meyer K, Frey L, Schmuki P (2016) TiO_2 Nanotubes: Nitrogen-Ion implantation at low dose provides noble-metal-free photocatalytic H_2-evolution activity. Angew Chem 55:3763–3767
32. Yuan YJ, Chen D, Zhong J, Yang LX, Wang J, Liu MJ, Tu WG, Yu ZT, Zou Z-G (2017) Interface engineering of a noble-metal-free 2D–2D MoS_2/Cu–$ZnIn_2S_4$ photocatalyst for enhanced photocatalytic H_2 production. J Mater Chem A 5:15771–15779
33. Wu A, Tian C, Jiao Y, Yan Q, Yang G, Fu H (2017) Sequential two-step hydrothermal growth of MoS_2/CdS core-shell heterojunctions for efficient visible light-driven photocatalytic H_2 evolution. Appl Catal B: Environ 203:955–963
34. Zhou X, Huang J, Zhang H, Sun H, Tu W (2016) Controlled synthesis of CdS nanoparticles and their surface loading with MoS_2 for hydrogen evolution under visible light. Int J Hydrogen Energy 41:14758–14767
35. Zheng D, Zhang G, Hou Y, Wang X (2016) Layering MoS_2 on soft hollow g-C_3N_4 nanostructures for photocatalytic hydrogen evolution. Appl Catal A: Gen 521:2–8
36. Zhao S, Huang J, Huo Q, Zhou X, Tu W (2016) A non-noble metal MoS_2–$Cd_{0.5}Zn_{0.5}S$ photocatalyst with efficient activity for high H_2 evolution under visible light irradiation. J Mater Chem A 4:193–199
37. Yuan YJ, Ye ZJ, Lu HW, Hu B, Li YH, Chen DQ, Zhong JS, Yu ZT, Zou ZG (2016) Constructing anatase TiO_2 nanosheets with exposed (001) facets/layered MoS_2 two-dimensional nanojunctions for enhanced solar hydrogen generation. ACS Catal 6:532–541
38. Yin X-L, Li L-L, Jiang W-J, Zhang Y, Zhang X, Wan L-J, Hu J-S (2016) MoS_2/CdS nanosheets-on-nanorod heterostructure for highly efficient photocatalytic H_2 generation under visible light irradiation. ACS Appl Mater Interfaces 8:15258–15266
39. He J, Chen L, Wang F, Liu Y, Chen P, Au CT, Yin SF (2016) CdS nanowires decorated with ultrathin MoS_2 nanosheets as an efficient photocatalyst for hydrogen evolution. Chemsuschem 9:624–630
40. Liu C, Wang L, Tang Y, Luo S, Liu Y, Zhang S, Zeng Y, Xu Y (2015) Vertical single or few-layer MoS_2 nanosheets rooting into TiO_2 nanofibers for highly efficient photocatalytic hydrogen evolution. Appl Catal B: Environ 164:1–9
41. Wei L, Chen Y, Lin Y, Wu H, Yuan R, Li Z (2014) MoS_2 as non-noble-metal co-catalyst for photocatalytic hydrogen evolution over hexagonal $ZnIn_2S_4$ under visible light irradiations. Appl Catal B: Environ 144:521–527
42. Tian Q, Zhang L, Liu J, Li N, Ma Q, Zhou J, Sun Y (2014) Synthesis of MoS_2/$SrZrO_3$ heterostructures and their photocatalytic H_2 evolution under UV irradiation. RSC Adv 5:734–739
43. Lu Y, Wang D, Yang P, Du Y, Lu C (2014) Coupling $Zn_xCd_{1-x}S$ nanoparticles with graphene-like MoS_2: superior interfacial contact, low overpotential and enhanced photocatalytic activity under visible-light irradiation. Catal Sci Tech 4:2650
44. Zhou W, Yin Z, Du Y, Huang X, Zeng Z, Fan Z, Liu H, Wang J, Zhang H (2013) Synthesis of few-layer MoS_2 nanosheet-coated TiO_2 nanobelt heterostructures for enhanced photocatalytic activities. Small 9:140–147
45. Zong X, Yan H, Wu G, Ma G, Wen F, Wang L, Li C (2008) Enhancement of photocatalytic H_2 evolution on CdS by loading MoS_2 as cocatalyst under visible light irradiation. J Am Chem So 130:7176–7177
46. Liu Y, Yao Q, Wu X, Chen T, Ma Y, Ong CN, Xie J (2016) Gold nanocluster sensitized TiO_2 nanotube arrays for visible-light driven photoelectrocatalytic removal of antibiotic tetracycline. Nanoscale 8:10145–10151

47. Qiu P, Chen H, Xu C, Zhou N, Jiang F, Wang X, Fu Y (2015) Fabrication of an exfoliated graphitic carbon nitride as a highly active visible light photocatalyst. J Mater Chem A 3:24237–24244
48. Schultz DM, Yoon TP (2014) Solar synthesis: prospects in visible light photocatalysis. Science 343:1239176
49. Garg P, Kumar S, Choudhuri I, Mahata A, Pathak B (2016) Hexagonal planar CdS monolayer sheet for visible light photocatalysis. J Phy Chem C 120:7052–7060
50. Zhu C, Zhang L, Jiang B, Zheng J, Hu P, Li S, Wu M, Wu W (2016) Fabrication of Z-scheme Ag_3PO_4/MoS_2 composites with enhanced photocatalytic activity and stability for organic pollutant degradation. Appl Surf Sci 377:99–108
51. Peng WC, Li XY (2014) Synthesis of MoS_2/g-C_3N_4 as a solar light-responsive photocatalyst for organic degradation. Catal Commun 49:63–67
52. Di J, Xia J, Ge Y, Xu L, Xu H, Chen J, He M, Li H (2014) Facile fabrication and enhanced visible light photocatalytic activity of few-layer MoS_2 coupled BiOBr microspheres. Dalton Trans 43:15429–15438
53. Zhang J, Huang L, Jin H, Sun Y, Ma X, Zhang E, Wang H, Kong Z, Xi J, Ji Z (2017) Constructing two-dimension MoS_2/Bi_2WO_6 core-shell heterostructure as carriers transfer channel for enhancing photocatalytic activity. Mater Res Bull 85:140–146
54. Vattikuti SVP, Byon C, Reddy CV, Ravikumar RVSSN (2015) Improved photocatalytic activity of MoS_2 nanosheets decorated with SnO_2 nanoparticles. RSC Adv 5:86675–86684
55. Song Y, Lei Y, Xu H, Wang C, Yan J, Zhao H, Xu Y, Xia J, Yin S, Li H (2015) Synthesis of few-layer MoS_2 nanosheet-loaded Ag_3PO_4 for enhanced photocatalytic activity. Dalton Trans 44:3057–3066
56. Liu H, Lv T, Zhu C, Su X, Zhu Z (2015) Efficient synthesis of MoS_2 nanoparticles modified TiO_2 nanobelts with enhanced visible-light-driven photocatalytic activity. J Mol Catal A: Chem 396:136–142
57. Li H, Yu K, Lei X, Guo B, Fu H, Zhu Z (2015) Hydrothermal synthesis of novel $MoS_2/BiVO_4$ hetero-nanoflowers with enhanced photocatalytic activity and a mechanism investigation. J Phy Chem C 119:22681–22689
58. Chen Y, Tian G, Shi Y, Xiao Y, Fu H (2015) Hierarchical MoS_2/Bi_2MoO_6 composites with synergistic effect for enhanced visible photocatalytic activity. Appl Catal B: Environ 164:40–47
59. Min Y, He G, Xu Q, Chen Y (2014) Dual-functional MoS_2 sheet-modified CdS branch-like heterostructures with enhanced photostability and photocatalytic activity. J Mater Chem A 2:2578
60. Liu J, Zhang L, Li N, Tian Q, Zhou J, Sun Y (2015) Synthesis of $MoS_2/SrTiO_3$ composite materials for enhanced photocatalytic activity under UV irradiation. J Mater Chem A 3:706–712
61. Li Q, Zhang N, Yang Y, Wang G, Ng DH (2014) High efficiency photocatalysis for pollutant degradation with MoS_2/C_3N_4 heterostructures. Langmuir 30:8965–8972
62. Wang L, Chai Y, Ren J, Ding J, Liu Q, Dai WL (2015) Ag_3PO_4 nanoparticles loaded on 3D flower-like spherical MoS_2: a highly efficient hierarchical heterojunction photocatalyst. Dalton Trans 44:14625–14634
63. Zhao X, Ma X, Sun J, Li D, Yang X (2016) Enhanced catalytic activities of surfactant-assisted exfoliated WS_2 nanodots for hydrogen evolution. ACS Nano 10:2159–2166
64. Pesci FM, Sokolikova MS, Grotta C, Sherrell PC, Reale F, Sharda K, Ni N, Palczynski P, Mattevi C (2017) MoS_2/WS_2 heterojunction for photoelectro-chemical water oxidation. ACS Catal 7:4990–4998
65. Zong X, Han J, Ma G, Yan H, Wu G, Li C (2011) Photocatalytic H_2 evolution on CdS loaded with WS_2 as cocatalyst under visible light irradiation. J Phy Chem C 115:12202–12208
66. Mahler B, Hoepfner V, Liao K, Ozin GA (2014) Colloidal synthesis of 1T-WS_2 and 2H-WS_2 nanosheets: applications for photocatalytic hydrogen evolution. J Am Chem Soc 136:14121–14127
67. Chen J, Wu XJ, Yin L, Li B, Hong X, Fan Z, Chen B, Xue C, Zhang H (2015) One-pot synthesis of CdS nanocrystals hybridized with single-layer transition-metal dichalcogenide nanosheets for efficient photocatalytic hydrogen evolution. Angew Chem 54:1210–1214

68. Yu HJ, Yu Y, Liu JH, Ma P-Y, Wang YC, Zhang F, Fu ZY (2015) Space-confined growth of Ag_3PO_4 nanoparticles within WS_2 sheets: Ag_3PO_4/WS_2 composites as visible-light-driven photocatalysts for decomposing dyes. J Mater Chem A 3:19439–19444
69. Atkin P, Daeneke T, Wang Y, Carey BJ, Berean KJ, Clark R-M, Ou JZ, Trinchi A, Cole IS, Kalantar-zadeh K (2016) 2D WS_2/carbon dot hybrids with enhanced photocatalytic activity. J Mater Chem A 4:13563–13571
70. Zhu C, Jiang Z, Wei W, Chen L, Liu D, Qian K, Lü X, Xie J (2016) Fabrication of noble-metal-free $NiS_2/g\text{-}C_3N_4$ hybrid photocatalysts with visible light-responsive photocatalytic activities. Res Chem Inter 42:6483–6499
71. Meng H, Wang T, Yu X, Zhu Y, Zhang Y (2015) $BiOCl/SnS_2$ hollow spheres for the photocatalytic degradation of waste water. RSC Adv 5:107088–107097
72. Xie J, Zhang J, Li S, Grote F, Zhang X, Zhang H, Wang R, Lei Y, Pan B, Xie Y (2013) Controllable disorder engineering in oxygen-incorporated MoS_2 ultrathin nanosheets for efficient hydrogen evolution. J Am Chem Soc 135:17881–17888
73. Liu X, Yang J, Zhao W, Wang Y, Li Z, Lin Z (2016) A simple route to reduced graphene oxide-draped nanocomposites with markedly enhanced visible-light photocatalytic performance. Small 12:4077–4085
74. Huang T, Luo Y, Chen W, Yao J, Liu X (2018) Self-assembled MoS_2–GO framework as an efficient cocatalyst of CuInZnS for visible-light driven hydrogen evolution. ACS Sustain Chem Engg 6:4671–4679
75. Wang M, Ju P, Li J, Zhao Y, Han X, Hao Z (2017) Facile synthesis of $MoS_2/g\text{–}C_3N_4$/GO ternary heterojunction with enhanced photocatalytic activity for water splitting. ACS Sustain Chem Eng 5:7878–7886
76. Kumar S, Reddy NL, Kushwaha HS, Kumar A, Shankar MV, Bhattacharyya K, Halder A, Krishnan V (2017) Efficient electron transfer across a ZnO–MoS_2-reduced graphene Oxide heterojunction for enhanced sun light-driven photocatalytic hydrogen evolution. Chemsuschem 10(3588):3603
77. Yuan Y-J, Tu J-R, Ye Z-J, Chen D-Q, Hu B, Huang Y-W, Chen T-T, Cao D-P, Yu Z-T, Zou Z-G (2016) MoS_2-graphene/$ZnIn_2S_4$ hierarchical microarchitectures with an electron transport bridge between light-harvesting semiconductor and cocatalyst: a highly efficient photocatalyst for solar hydrogen generation. Appl Catal B: Environ 188:13–22
78. Yu X, Du R, Li B, Zhang Y, Liu H, Qu J, An X (2016) Biomolecule-assisted self-assembly of CdS/MoS_2/graphene hollow spheres as high-efficiency photocatalysts for hydrogen evolution without noble metals. Appl Catal B: Environ 182:504–512
79. Lang D, Shen T, Xiang Q (2015) Roles of MoS_2 and graphene as cocatalysts in the enhanced visible-light photocatalytic H_2 production activity of multiarmed CdS nanorods. ChemCatChem 7:943–951
80. Zhu B, Lin B, Zhou Y, Sun P, Yao Q, Chen Y, Gao B (2014) Enhanced photocatalytic H_2 evolution on ZnS loaded with graphene and MoS_2 nanosheets as cocatalysts. J Mater Chem A 2:3819
81. Li Y, Wang H, Peng S (2014) Tunable photodeposition of MoS_2 onto a composite of reduced graphene oxide and CdS for synergic photocatalytic hydrogen generation. J Phy Chem C 118:19842–19848
82. Xiang Q, Yu J, Jaroniec M (2012) Synergetic effect of MoS_2 and graphene as cocatalysts for enhanced photocatalytic H_2 production activity of TiO_2 nanoparticles. J Am Chem Soc 134:6575–6578
83. Xiang Q, Cheng F, Lang D (2016) Hierarchical layered WS_2/graphene-modified CdS nanorods for efficient photocatalytic hydrogen evolution. Chemsuschem 9:996–1002
84. Liu M, Xue X, Yu S, Wang X, Hu X, Tian H, Chen H, Zheng W (2017) Improving photocatalytic performance from Bi_2WO_6@MoS_2/graphene hybrids via gradual charge transferred pathway. Sci Rep 7:3637
85. Akbarzadeh E, Rahman Setayesh S, Gholami M-R (2017) Investigating the role of MoS_2/reduced graphene oxide as cocatalyst on Cu_2O activity in catalytic and photocatalytic reactions. New J Chem 41:7998–8005

86. Peng WC, Wang X, Li XY (2014) The synergetic effect of MoS_2 and graphene on Ag_3PO_4 for its ultra-enhanced photocatalytic activity in phenol degradation under visible light. Nanoscale 6:8311–8317

Chapter 5
Simulation of Transition Metal Dichalcogenides

Mohammad Rezwan Habib, Wenchao Chen, Wen-Yan Yin, Huanxing Su and Mingsheng Xu

Abstract The discovery of graphene in 2004 by Konstantin Novoselov and Andre Geim opened a new scientific arena: "2D materials". The finding of new layered and non-layered materials and their potential applications in various fields has been taken a great attention in recent years. A wide variety of 2D materials such as transition metal dichalcogenides (TMDs), transition metal trichalogenides (Bi_2Se_3, Bi_2Te_3, etc.), transition metal monochalcogenide (GaSe, GaS, etc.), transition metal thiophosphides ($MnPS_3$, $FePS_3$, etc.), silicene, phosphorene and hexagonal boron nitride have been found to possess many fascinating and unique properties that are promising for various potential applications such as in optoelectronics, sensors, spintronics, valleytronics, energy storage and catalysis. Among the 2D family, the TMDs grasp diverse properties, ranging from insulator, semimetal, metal, semiconductor and superconductor and make them most interesting 2D materials in both academic and industrial perspectives. The TMDs are usually abbreviated by the chemical formula of MX_2, where M is a transition metal such as Cr, Mo, W, Re, Ta, Zr and Pd, and X is a chalcogen of S, Se and Te. The different filling states of the *d* orbitals in this wide range of transition metals gives rise to TMDs with versatile properties. Among TMDs, group 6 TMDs such as MoS_2, WS_2, $MoSe_2$ and WSe_2 are attracting great attention due to their semiconducting nature, layer-dependent bandgap and strong light–matter interaction. The finite and tunable bandgap of group 6 TMDs compensate the lack in microelectronic application of graphene which arises due to its gapless feature. Herein we address different phases of TMDs including hexago-

M. R. Habib · M. Xu (✉)
State Key Laboratory of Silicon Materials, College of Information Science and Electronic Engineering, Zhejiang University, Hangzhou 310027, People's Republic of China
e-mail: msxu@zju.edu.cn

W. Chen · W.-Y. Yin
College of Information Science and Electronic Engineering, Zhejiang University, Hangzhou 310027, People's Republic of China
e-mail: wyyin@zju.edu.cn

H. Su
State Key Laboratory of Quality Research in Chinese Medicine and Institute of Chinese Medical Sciences, University of Macau, Macau SAR, People's Republic of China
e-mail: huanxingsu@umac.mo

N. S. Arul and V. D. Nithya (eds.), *Two Dimensional Transition Metal Dichalcogenides*,
https://doi.org/10.1007/978-981-13-9045-6_5

nal (H), trigonal (T) and rhombohedral (R). We reviewed the optical and electronic properties such as thickness-dependent band structure, spin–orbit coupling, excitonic properties, Berry-phase-related properties and valley Hall effect of semiconducting TMDs. The modulation of electronic properties by external stimuli such as electric field and strain is also discussed in this chapter. The metallic TMDs such as 1T phase of group 6 TMDs, Ti-, V-, Nb-based TMD and 2H phase of NbS_2, $NbSe_2$, TaS_2 and $TaSe_2$ are discussed. The magnetism, strain and doping-induced magnetism in both metallic and semiconducting TMDs are addressed in this chapter.

5.1 Introduction

The discovery of graphene through mechanical exfoliation from graphite [1] leads us in pursuit a new class of materials known as "2D materials". The finding of alternative layered and non-layered 2D materials has emerged as an active field of scientific research. This kind of layered material has attracted a significant attention compared to their bulk counterpart due to their unique physical, chemical and optoelectronic properties. However, the gapless feature of pristine graphene limits its microelectronic applications. The diverse properties of transition metal dichalcogenides (TMDs), ranging from insulators such as HfS_2, semiconductors such as MoS_2, WS_2 and PdS_2, semimetal such as WTe_2, metal such as NbS_2 and VS_2, make them a unique and wide field of research interest [2, 3]. Furthermore, the fascinating physical, chemical, electronic, optical and magnetic properties of TMDs are rendering them for potential candidate for applications in the field of optoelectronics, catalysis, sensors, spintronics and valleytronics. In this chapter, we address the theoretical perspective of the electronic, optical and magnetic properties of TMDs and their modulation by external strain and electric fields.

5.1.1 Structure of Transition Metal Dichalcogenides

5.1.1.1 Atomic Structure

The transition metal chalcogenides are usually abbreviated by the chemical formula of MX_2 (M = transition metal and X = chalcogen). The position of the constitute atoms M and X is indicated in the periodic table as shown in Fig. 5.1a. TMDs form a very large and rich family of crystals, whose members present several kinds of lattice structures and many different physical properties. An MX_2 single layer is a sandwich structure in which the M atoms are ordered in a triangular lattice, each of them bonded covalently to six X atoms, of which there are three of them in the top and three in the bottom layer.

In the bulk, the monolayers (MLs) are held together by weak interlayer interactions, i.e. van der Waals (vdW) force, thus allowing the crystal to readily cleave along

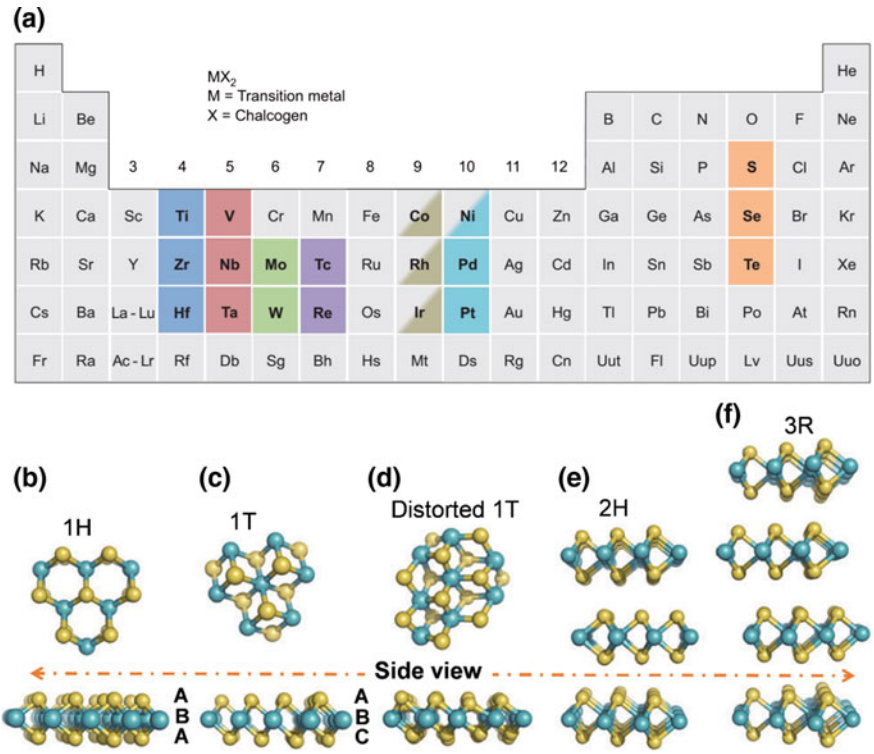

Fig. 5.1 **a** Transition metals and the three chalcogen elements that form layered structure are highlighted in the periodic table. Reprinted with permission from Ref. [2], Copyright 2013, Nature Publishing Group. **b–f** Different polymorphs or phases of single-layer and stacked single-layer TMDs: **b** 1H phase, **c** 1T phase, **d** distorted 1T phase, **e** 2H phase and **f** 3R phase. Reproduced from Ref. [4] with permission, Copyright 2015, from The Royal Society of Chemistry

the layer surface. It is noted that group 4–7 TMDs are predominantly layered structure like graphite, whereas group 8–10 TMDs are commonly found in non-layered form.

5.1.1.2 Polymorphs

In contrast to graphite, bulk TMDs exhibit a wide variety of polymorphs and stacking polytypes (a specific case of polymorphism) due to the presence of three atomic layers (X–M–X) in one individual MX_2 layer. 1T, 2H and 3R are the commonly observed polymorphs [4], where the letters "T", "H" and "R" denote trigonal, hexagonal and rhombohedral, respectively, and the number before the aforementioned three letters specifies the number of X–M–X units in the unit cell, which implies the number of layers in the stacking sequence as shown in Fig. 5.1b. The monolayer TMDs itself

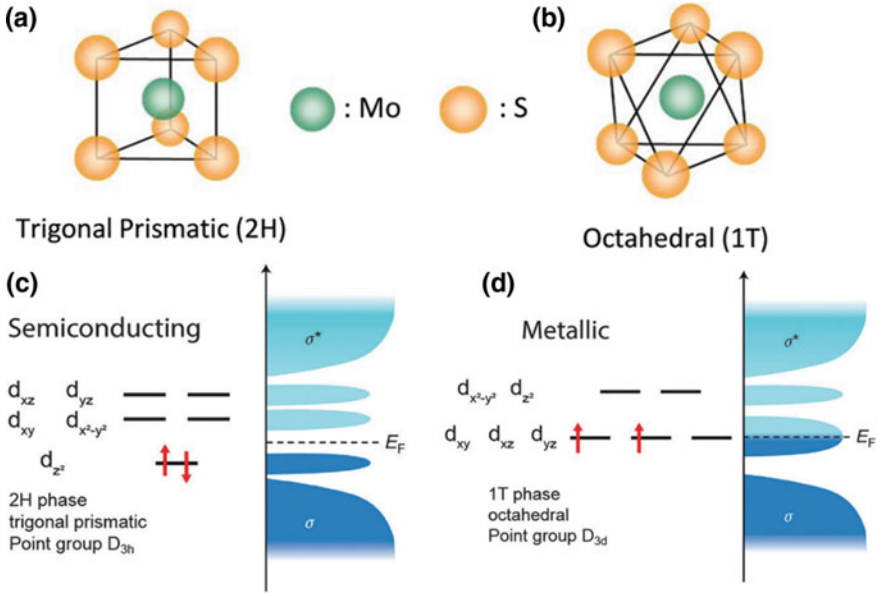

Fig. 5.2 **a**, **b** Structures of 2H- and 1T-MoS_2. Reproduced with permission from Ref. [11], Copyright 2011, American Chemical Society. **c**, **d** Filling of the non-bonding *d* orbitals for a typical d2 TMD along with the band structure and the representative position of the Fermi level for **c** 2H phase and **d** 1T phase. Reprinted with permission from Ref. [2], Copyright 2013, Nature Publishing Group

exhibit two polymorphs [4–6]: trigonal prismatic (2H) and octahedral (1T) phases (Fig. 5.2a). The 1T TMDs belong to the D_{3d} group, and the 2H TMDs belong to the D_{3h} Point Group. These structural phases can also be viewed in terms of different stacking orders of the three atomic planes (X–M–X) forming the individual layers of these materials. The 2H phase corresponds to an ABA stacking, in which chalcogen atoms in different atomic planes occupy the same position A and are located on top of each other in the direction perpendicular to the layer. By contrast, the 1T phase is characterized by an ABC stacking order (Fig. 5.1b). Along with the 2H and 1T phases, a metastable phase also exists in TMDs due to the formation of M–M bond which is originated from distortions. For example, 1T′ structural phase is formed due to the dimerization of the 1T phase of group 6 TMDs. In addition, ReX_2 (X = S, Se) exhibits a distorted 1T structure originated from the Peierls distortion [7, 8]. And due to periodic weaker lattice distortions, charge density wave (CDW) phase is formed in $NbSe_2$ and $TaSe_2$ at low temperature [9, 10]. Different structural phases of TMDs exhibit different basic properties. For example, the 1T phase of MoS_2 is metallic, while the 2H phase is semiconducting [5, 11].

According to the ligand field theory, the metallic nature of the 1T phase is caused by the partially filled t_{2g} band (d_{xy}, d_{xz}, d_{yz}), while the semiconducting behaviour of the 2H phase is due to the completely filled d_{z^2} and empty d_{xy} and $d_{x^2-y^2}$ orbitals

(Fig. 5.2b). The type of symmetry adopted by a TMD depends primarily on *d* orbital filling, i.e. the *d* electron count of the transition metal (TM). Group 4 TMDs (defined as $d0$ transition metal) are preferred to be in the 1T phase, whereas both octahedral and trigonal prismatic phases are seen in group 5 TMDs ($d1$). Group 6 TMDs ($d2$) are primarily found in 2H geometry, and group 7 TMDs ($d3$) are typically in a distorted octahedral structure. Group 10 TMDs ($d6$) are all in an octahedral structure.

5.1.2 Electronic and Optical Properties

Unlike graphene, where the optoelectronic properties are based on *s* and *p* hybridization, the optoelectronic properties of TMDs depend on the *d* electron count, i.e. filling of the *d* orbitals of TM and its coordination environment. The number of *d* electron in TM varies between 0 and 6 for group 4 to group 10 TMDs, respectively. This thus provides diverse optoelectronic and magnetic properties in TMDs. The completely filled *d* orbitals, as in the case of 2H-MoS_2 (group 6) and 1T-PtS_2 (group 10), give rise to semiconducting nature, while partially filled, as in the case of 2H-$NbSe_2$ (group 5) and 1T-ReS_2 (group 7), exhibit metallic conductivity.

5.1.2.1 Semiconducting TMDs

In general, group 6 and 10 TMDs show semiconducting behaviour due to the reasons mentioned above. Among all semiconducting TMDs, the group 6 TMDs have been intensively studied due to their extraordinary electronic, optical properties and air stability at room temperature. In this section, we discuss the electronic and optical properties of semiconducting TMDs.

DFT-Predicted Bandgap

The bandgap is generally defined as the energy difference between conduction band minimum (CBM) and valance band maximum (VBM). Experimentally, this gap can be measured either by transport or by optical measurement. Photoluminescence (PL) measurement gives the information about exciton and measures optical bandgap, whereas the gap which is measured by scanning tunnelling spectroscopy (STS) and angle-resolved photoemission (ARPES) is called electronic bandgap. There are mainly three approaches to predict the band structure of TMDs in DFT calculations: (a) DFT with local density approximation (LDA) or generalized gradient approximation (GGA), (b) Heyd–Scuseria–Ernzerhof (HSE) hybrid functional and (c) GW method. DFT calculation based on the LDA or GGA approximation underestimates the bandgap of TMDs compared to the experimental bandgap. The most commonly used hybrid functional HSE06 incorporates a portion of the short-range Hartree–Fock exchange energy of Kohn–Sham orbitals and rest of the potential

energy of exchange-correlation, while long-range Hartree–Fock exchange energy is derived from the exchange-hole formalism of PBE. The GW method which is based on many-body perturbation theory is a potential method to describe the band structure of TMDs accurately. However, the application of GW method is significantly restricted by the huge consumption of computational resources. Pure and hybrid DFT methods underestimate the bandgap of TMDs at certain level if we compare with experimental result. However, in general all the above-mentioned three methods provide an identical physical picture of TMDs.

Thickness-Dependent Bandgap

The most interesting feature of semiconducting TMDs is thickness-dependent band structure tunability. The bulk group 6 TMDs are indirect bandgap material. For example, bulk MoS_2 has indirect bandgap of 1.2 eV since the VBM and CBM are located at Γ point and Q point (middle of the Γ and K points), respectively. As the thickness decreases to monolayer, the bandgap of group 6 TMDs increases due to quantum confinement and more interestingly they become direct bandgap material [12]. The variation of band structure and bandgap with layer numbers is shown in Fig. 5.3. All the bandgaps of different layered MoS_2 decrease monotonically with increasing the number of layers and converge rapidly to the bulk value [13]. Monolayer MoS_2 shows a direct bandgap where VBM and CBM are lying at K and −K points in the hexagonal Brillouin zone. Other group 6 TMDs such as WX_2 (X = S, Se, Te) exhibit similar band structure evolution with layer numbers [12].

Unlike group 6 TMDs, the group 4 TMDs show a wide range of electronic properties such as monolayer 1T-ZrS_2 which is a semiconductor with large bandgap [14], 1T-TiS_2 is semimetallic in nature [15], and 1T-HfS_2 is a wide bandgap semiconductor [16] (Fig. 5.4a, b). 1T-MX_2 (M = Zr, Hf; X = S, Se) shows same layer-dependent bandgap as group 6 TMDs, but the indirect nature of bandgap remains intact as in its bulk form. The layer-dependent band structure of ZrS_2 is shown in Fig. 5.4c [17]. The 1T-ZrS_2 and 1T-$ZrSe_2$ monolayers are semiconductors with indirect bandgap of 1.10 and 0.45 eV, respectively. In contrast, the monolayer of 1T-$ZrTe_2$ shows metallic characteristics [14]. Hence, for monolayer ZrX_2, the variation of bandgap due to the change in the chalcogen anions is more significant than that for group 6 TMDs, i.e. the bandgap of ZrX_2 ranges from 1.1 eV (1T-ZrS_2) to 0 eV (1T-$ZrTe_2$) as compared to the variation from 1.8 eV for H-MoS_2 to 0.60 eV for H-$CrTe_2$.

DFT calculations show that, unlike group 6 TMDs, ReX_2 (X = S, Se) exhibits a distorted 1T structure which arises from the Peierls distortion [7]. This kind of distortion prevents ordered interlayer stacking and minimizes the wave functions overlap. As a result, the ReX_2 shows weaker interlayer interaction than that in MoS_2 (18 meV vs. 460 meV per unit MX_2) as predicted by DFT calculation as shown in Fig. 5.5. Due to this weak interlayer interaction, the band structure of ReX_2 is barely influenced by the layer numbers. DFT-calculated band structure of monolayer, trilayer and pentalayer of ReS_2 is shown in Fig. 5.5b. The bandgap varies slightly

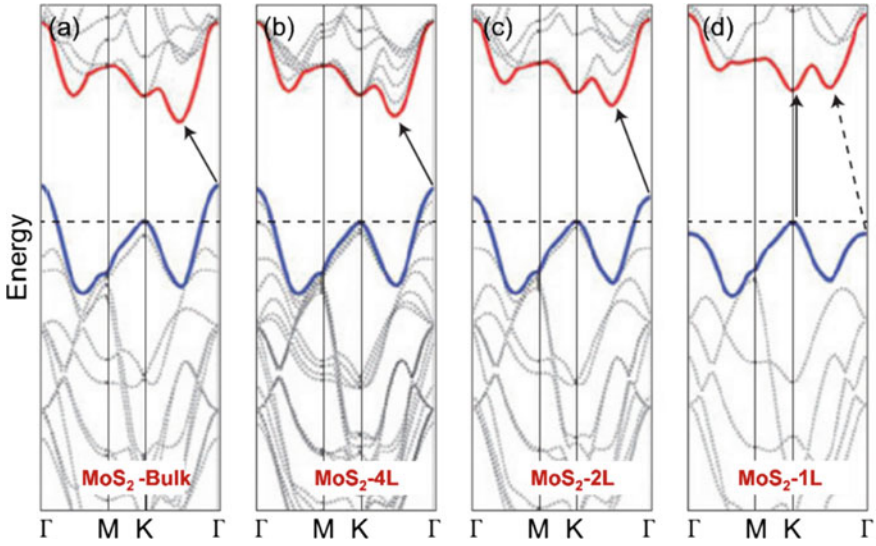

Fig. 5.3 Layer-dependent band structure of MoS_2. The red and blue lines represent the conduction and valence band edges, respectively. The lowest energy transition (indicated by the solid arrows) is direct (vertical) only in the case of a single layer. Indirect transition in monolayer (dashed arrow in 1L plot) is greater in energy than the direct band edge transition (solid arrow). Reproduced with permission from Ref. [13], Copyright 2010, American Chemical society

from monolayer to the pentalayer ReS_2, and the values of monolayer, trilayer and five-layer ReS_2 are 1.44, 1.40 and 1.35 eV, respectively [18].

More interestingly, all of the mentioned bandgaps are direct in nature. Similarly, the bulk ReS_2 also exhibits a direct bandgap of 1.35 eV as predicted by GGA. In the case of PL of ReS_2 layers except the intensity enhancement, no significant peak shift is observed as the layer number increases due to the similar bandgap [7]. Other members of group 7 TMDs such as monolayer TcX_2 (X = S, Se) have indirect bandgap of 1.91 and 1.69 eV for S and Se, respectively [19], as predicted by hybrid DFT functional (Fig. 5.6a, b). The layer-dependent behaviour of TcS_2 and $TcSe_2$ is different from each other. As the thickness increases, the bandgap of both TcS_2 and $TcSe_2$ decreases. However, an indirect-to-direct bandgap transition is revealed in TcS_2 as its layer number increases from one to two (Fig. 5.6) [19].

The strong interlayer interaction in MX_2 (M = Ni, Pt, Pd; X = S, Se) resulting from the overlapping of p_z orbital of X atom, as compared to the weak interlayer interaction in group 7 TMDs and moderate interlayer interaction in group 6 TMDs, is responsible for unique and interesting features such as layer-dependent semiconducting-to-metallic transition. The band structure of MX_2 (M = Ni, Pt, Pd; X = S, Se) changes dramatically with the change of layer number. Monolayer MS_2 (M = Ni, Pt, Pd) are semiconductors with indirect bandgaps of 0.51, 1.11 and 1.75 eV for NiS_2, PdS_2 and PtS_2, respectively [20]. Furthermore, the bilayer NiS_2 and PdS_2

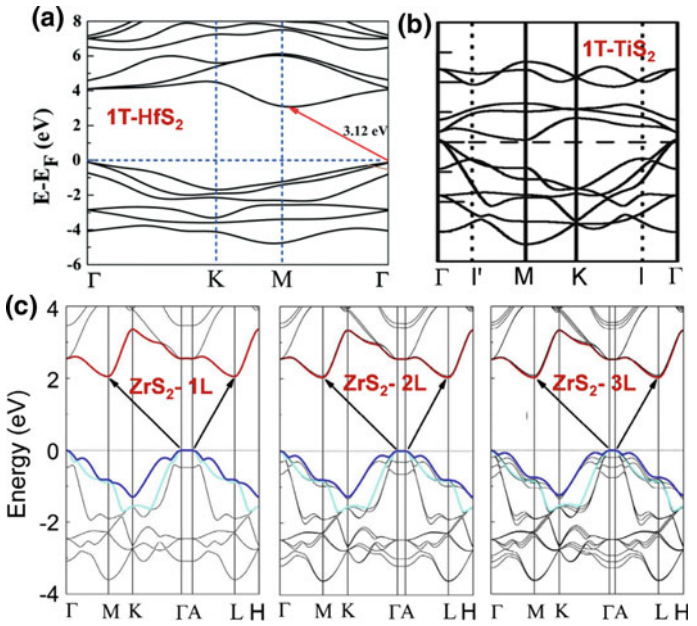

Fig. 5.4 **a** Band structure of monolayer 1T-HfS_2. Reproduced with permission from Ref. [16], Copyright 2016, The Royal Society of Chemistry. **b** Band structure of monolayer 1T-TiS_2. Reproduced with permission from Ref. [15], Copyright 2015, The Royal Society of Chemistry. **c** Layer-dependent band structure of 1T-ZrS_2. The figure reproduced with permission from Ref [17], copyright 2015, Elsevier Ltd

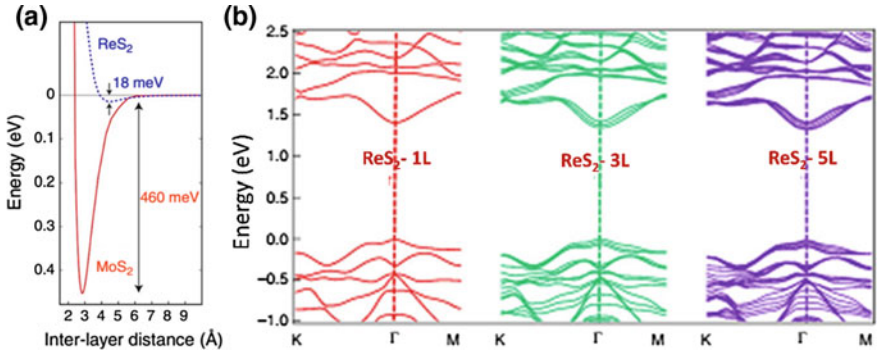

Fig. 5.5 **a** Calculated total energy of the MoS_2 and ReS_2 as a function of interlayer separation. The significantly shallower depth of the well in ReS_2 implies much weaker interlayer coupling energy in ReS_2 as compared with MoS_2. Reproduced with permission from Ref. [7], Copyright 2014, Nature Publishing Group. **b** Band structure of monolayer, trilayer and five-layer ReS_2 by ab initio calculations, indicating bandgaps of 1.44, 1.40 and 1.35 eV, respectively. Reproduced with permission from Ref. [18], Copyright 2015, Nature Publishing Group

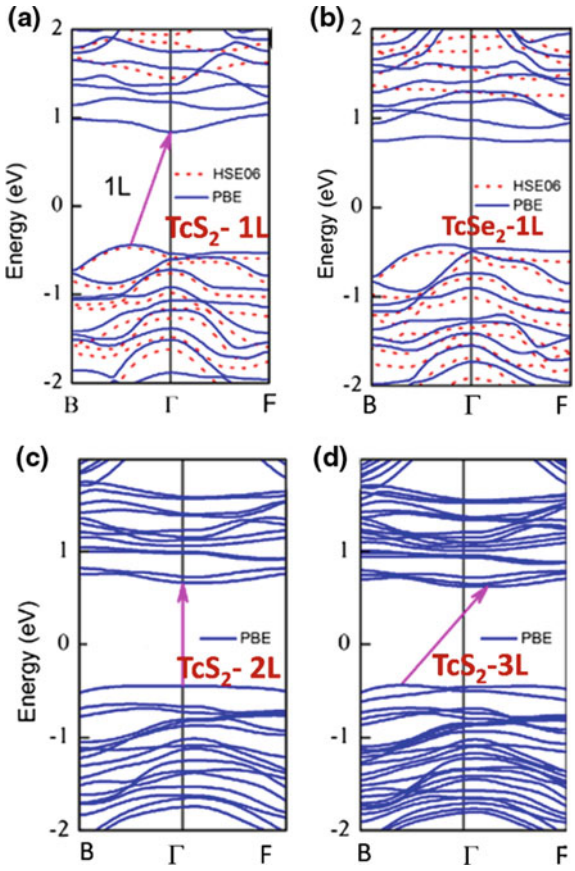

Fig. 5.6 **a**, **b** Band structure of monolayer TcS_2 (**a**) and $TcSe_2$ (**b**). Bilayer (**c**) and trilayer (**d**) band structures of TcS_2. Zero defines the Fermi level. Reproduced with permission from Ref. [19], Copyright 2016, American Chemical Society

become metallic as predicted by first-principles calculation at DFT/PBE-D level of theory (Fig. 5.7).

The experimentally verified and DFT-calculated layer-dependent bandgaps of PtS_2 are compared [21] as shown in Fig. 5.8d. Similar to PtS_2, monolayer $PtSe_2$ is also an indirect bandgap semiconductor. First-principles calculation shows that the bandgap of PtS_2 becomes narrow in bilayer and turns to zero in trilayer which basically implies metallic character [22]. This theoretical result has also been experimentally verified [23–25] (Fig. 5.8a–c).

Mobility

Computationally, the carrier mobility of TMD semiconductors can be evaluated by deformation potential (DP) theory, which was first proposed by Barden and Shockley [26]. According to the DP theory, the respective energies of the CBM and VBM have

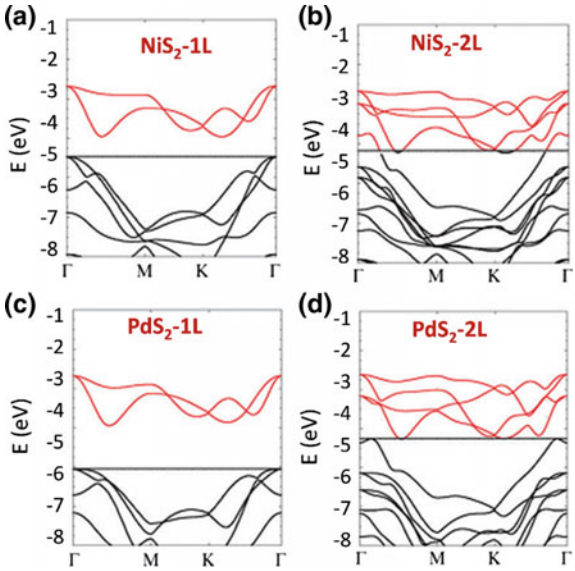

Fig. 5.7 Band structure of monolayer and bilayer NiS_2 (**a**, **b**) and PdS_2 (**c**, **d**). Reproduced with permission from Ref. [20], Copyright 2014, WILEY-VCH Verlag GmbH & Co. KGaA

a linear relationship with the lattice dilation or compression. The carrier mobility (μ) of TMDs can be expressed by the following formula [23, 27, 28]:

$$\mu = \frac{2e\hbar^3 C}{3k_b T m^* m_d (E_1^i)^2} \tag{5.1}$$

where $\hbar$ is reduced Planck's constant, k_b is Boltzmann's constant and T is the temperature. m^* and C are the effective mass along transport direction and in-plane stiffness of the studied TMDs, respectively. m_d is the density of mass determined by $m_d = \sqrt{m_x m_y}$. Term E_1^i represents the deformation potential constant of the VBM (hole) or CBM (electron) along the transport direction which is defined as $E_1^i = \frac{\Delta V_i}{(\Delta l/l_0)}$, where ΔV_i is the energy change of the ith band under proper cell compression and dilatation, l_0 is the lattice constant along the transport direction and Δl is the length of deformation on l_0. Phonon-limited electron mobility along both x (μ_x) and y (μ_y) directions in MoS_2 is almost same ($\mu_x = 410$ cm^2/Vs and $\mu_y = 430$ cm^2/Vs) and provides mobility transport isotropy in MoS_2. However, PdS_2 and $PtSe_2$ show anisotropic mobility transport along x- and y-direction due to the different wave-function overlap along the directions [23, 29]. In TMDs, the charge carriers are confined within the layer, and that can potentially offer an improved mobility. However, this charge carrier mobility in TMDs is influenced and reduced by various charge scattering mechanisms such as Coulombic scattering, polar optical phonon scattering, acoustic phonon scattering and surface roughness scattering [30]. The overall carrier mobility can then be obtained using Matthiessen's rule [31]:

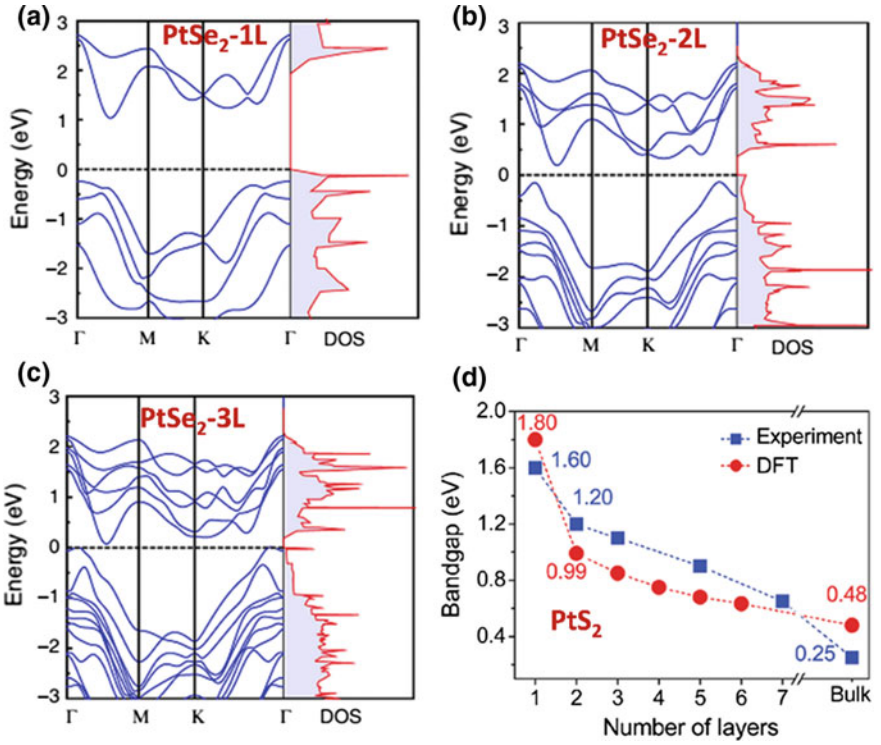

Fig. 5.8 Density of states and band structure of **a** monolayer, **b** bilayer and **c** trilayer $PtSe_2$. Reproduced with permission from Ref. [22], Copyright 2018, Nature Publishing Group. **d** Layer-dependent bandgap of PtS_2 predicted from both experimentally and theoretically. Reproduced with permission from Ref. [21], Copyright 2016, WILEY-VCH Verlag GmbH & Co. KGaA

$$\frac{1}{\mu_{\text{TOTAL}}} = \frac{1}{\mu_{\text{C}}} + \frac{1}{\mu_{\text{PO}}} + \frac{1}{\mu_{\text{A}}} + \frac{1}{\mu_{\text{SR}}} \tag{5.2}$$

where μ_{TOTAL} is the overall mobility and μ_{C}, μ_{PO}, μ_{A} and μ_{SR} are the effective carrier mobilities limited by Coulombic, polar optical phonon, acoustic phonon and surface roughness scattering effects, respectively. In addition to the impact of the above-mentioned scattering mechanisms, charge carrier mobility of TMDs is also influenced by layer number, carrier density and temperature [32]. As temperature increases, carrier mobility is increasingly affected by phonon scattering. The temperature dependence of electron mobility in MoS_2 is calculated using DFT as shown in Fig. 5.9.

At low temperatures ($T < 100$ K), the acoustic component dominates, but at elevated temperatures the optical component dominates. So, the room temperature mobility in MoS_2 is mainly due to optical phonons [32, 33]. Coulomb scattering is caused by charge impurity located within or on the surface of 2D materials. It is the dominant mechanism in reducing the overall charge carrier mobility at or below

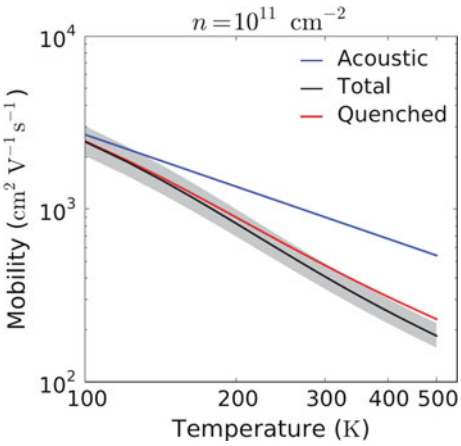

Fig. 5.9 DFT-calculated temperature-dependent mobility of monolayer MoS_2. Reproduced with permission from Ref. [32], Copyright 2012, American Physical Society

the room temperature. Therefore, the increase in the dielectric constant of either the surrounding environment or the 2D materials reduces the Coulombic effect, and it has proven to be effective in enhancing the charge carrier mobility of 2D materials such as graphene and MoS_2 [31, 34–36].

Critical Points in Band Structure and Valley

Critical points refer to extrema or saddle points in the band structure. The critical points play a crucial role in determining the electronic and optical properties of TMDs. In monolayer group 6 TMDs, the six corners in the first Brillouin zone are grouped by inequivalent K and −K points, respectively, where each group has three corners connected by reciprocal vector [37]. The energetically degenerated but inequivalent band extrema at K and −K make another degrees of freedom for charge carriers, which is known as valley index or pseudospin [38]. Therefore, in addition to spin, low-energy electron or hole has this extra valley degrees of freedom. The K and −K are related by time reversal operation, and these points are denoted by K_c and K_v for CBM and VBM, respectively [39]. Conduction band (CB) also possesses six local minima denoted by Q_c, and valance band (VB) has local maximum at Γ referred by Γ_v [40]. Q_c and Γ_v are important extrema because they are energetically close to K_c and K_v, respectively. And in certain cases such as in multilayers, they become global energy extrema under strain [41]. Similar to K point, six Q_c points can be divided into two groups: Q and −Q, and they are related by time reversal operation. K and Γ are high-symmetry points, and they remain invariant under C_3 operation (the rotation by $2\pi/3$ around *Z*-axis).

Valley Optical Selection Rule

One of the most intriguing properties of group 6 TMD monolayer is the valley-dependent circularly polarized selection rules for the optical direct bandgap transitions at the ±K points. This valley optical selection rule is analogous to the spin optical selection rule in III–V semiconductors. According to the selection rules, the direct bandgap optical transition at K (−K) couples only to $\sigma+$ ($\sigma-$) circularly polarized light. The inversion operation changes the K and −K to one another leaving unchanged the circular polarization of light. Thus, the valley-dependent selection rule conflicts the inversion symmetry. Hence, the broken inversion symmetry is the necessary condition for having optical selection rule. This valley selection rule is not only applicable near ±K points but also can be applied within a large surrounding region in the Brillouin zone of monolayer MoS_2 [42].

Spin–Orbit Coupling and Spin–Valley Locking

The 2D TMDs also provide a unique system to explore the interplay between spin and pseudospins. TMDs have a strong spin–orbit coupling (SOC) which is originated from the *d* orbitals of the heavy metal atoms. The SOC takes an unusual form in the multivalley band structure. The SOC is included to the Hamiltonian through the term [43, 44]:

$$H_{\mathrm{SO}} = \frac{1}{2m^2c^2}\frac{1}{r}\frac{\partial V(r)}{\partial r}\mathbf{L}\cdot\mathbf{S} \tag{5.3}$$

where c is the speed of light, m the electron mass, V the electron potential, $\mathbf{S}$ the spin angular momentum and $\mathbf{L}$ the angular momentum operator of an electron. To compute the spin–orbit (SO) splitting in the bands, the single-particle Hamiltonian (including the H_{SO} term) must be diagonalized within the space of up-spin and down-spin eigenstates. The nature of SOC induced spin splitting of bands in monolayers can be fully determined by symmetry elements, i.e. (a) mirror reflection symmetry (σ_{h}) about the metal atom plane and (b) time reversal symmetry. The former one dictates that the Bloch state and its mirror reflection have identical energy. The σ_{h} mirror reflection of an in-plane spin vector is its opposite, while the mirror reflection of an out-of-plane spin vector is itself. Thus, spin splitting is allowed in the out-of-plane (z) direction only where the spin expectation value of the Bloch states is either along the $+s$ or $-z$ direction. The later one dictates the spin splitting at an arbitrary pair of momentum space points K and −K to have identical magnitude but opposite in sign [41, 45].

As a result of this strong SOC, the VBM in monolayer TMDs has the spin index locked with the valley index, i.e. valley K (−K) has only the up-spin (down-spin) holes (Fig. 5.10a). The important consequence of this spin-valley locking is that the valley-dependent optical selection rule becomes a spin-dependent as well [46]. For example, $\sigma+$ polarized light excites only the K valley with the carriers of either

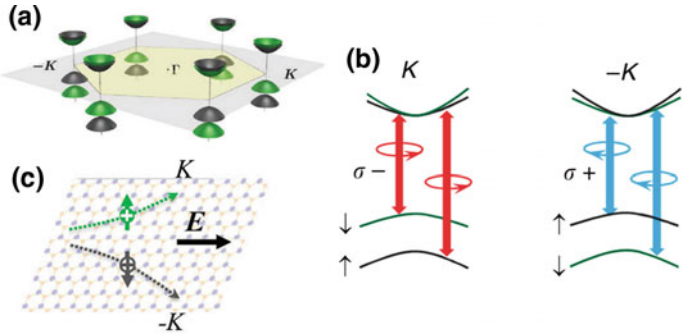

Fig. 5.10 Spin and valley physics in monolayer MoX_2. **a** Schematics of the spin–valley-coupled band edges in monolayer MoX_2. Black (green) colour denotes spin-up (-down) bands. **c** Schematics of valley Hall effect. Reproduced with permission from Ref. [41], Copyright 2015, Royal Society of Chemistry. **b** Valley- and spin-dependent optical transition selection rules in monolayers. Reproduced with permission from Ref. [45], Copyright 2013, Nature Publishing Group

up-spin or down-spin depending on the light frequency as shown in Fig. 5.10b. Although the CB splits akin to the VB as a consequence of the spin-orbit coupling, the magnitude of splitting is smaller than that of VB. SO-induced splitting of valance band at K and −K points leads to a splitting of the lowest exciton into two excitons with opposite spin (A and B excitons of monolayer MoS_2 as discussed later).

Berry-Phase-Related Properties

The dependence of the internal structure of a particle on the dynamical parameter can give rise to anomalous transport properties, in particular the Berry-phase effect [47]. The Berry curvature ($\mathbf{\Omega}$) and orbital magnetic moment ($\mathbf{m}$) are two physical quantities that characterize the effect of Berry phase of electrons in the Bloch bands. $\mathbf{\Omega}$ and $\mathbf{m}$ both have odd parity under time reversal operation which makes them good candidates to distinguish the valley pseudospin states. The Berry curvature, behaving like magnetic field in the momentum space, is originated from the dependence of the periodic part of the Bloch function, $u_{n,\mathbf{k}}$, on the wave vector $\mathbf{k}$. The orbital magnetic moment arises from the self-rotating motion of electron wave packet. For 2D crystal, Berry curvature and orbital magnetic moment are defined by [38, 48, 49]:

$$\Omega_n(\mathbf{k}) = \mathrm{i}\frac{\hbar^2}{m^2}\sum_{i\neq n}\frac{\mathbf{P}_{n,i}(\mathbf{k})\times\mathbf{P}_{i,n}(\mathbf{k})}{\left[E_n^0(\mathbf{k})-E_i^0(\mathbf{k})\right]^2} \tag{5.4}$$

$$\mathbf{m}_n(\mathbf{k}) = -\mathrm{i}\frac{e\hbar}{2m^2}\sum_{i\neq n}\frac{\mathbf{P}_{n,i}(\mathbf{k})\times\mathbf{P}_{i,n}(\mathbf{k})}{E_n^0(\mathbf{k})-E_i^0(\mathbf{k})} \tag{5.5}$$

here $\mathbf{P}_{n,i}(\mathbf{k}) \equiv \langle u_{n,k}|\hat{\mathbf{p}}|u_{i,k}\rangle$ is the interband matrix element of the momentum operator $\hat{\mathbf{p}}$. $E_n^0(\mathbf{k})$ is the dispersion of nth band.

As both $\boldsymbol{\Omega}$ and $\mathbf{m}$ are pseudovectors, the $\pm$K valleys are allowed to have opposite values of these quantities. A dilemma arises when spatial inversion symmetry is present. Both the pseudovectors $\boldsymbol{\Omega}$ and $\mathbf{m}$ remain invariant under spatial inversion that also transforms K and $-$K valleys into one another. Therefore, inversion symmetry breaking is the necessary condition for the $\pm$K valleys to exhibit valley contrast for $\boldsymbol{\Omega}$ and $\mathbf{m}$.

In monolayer group 6 TMDs, the conduction and valance band edges at the $\pm$K valleys can be described by a massive Dirac fermion model [46]:

$$\hat{H} = \mathrm{at}\left(\tau_z k_x \widehat{\sigma_x} + k_y \widehat{\sigma_y}\right) + \frac{\Delta}{2}\widehat{\sigma_z} \tag{5.6}$$

where $\tau_z = \pm 1$ is the valley index, a is the lattice constant, t is the effective nearest-neighbour hopping integral and Δ is the bandgap. The Pauli matrix $\hat{\sigma}$ is defined in a basis consisting of the two d orbitals of the metal atom with magnetic quantum numbers of $m = 0$ and $m = 2\tau_z$, respectively. The Berry curvature in the conduction band (opposite signed for valance band) is given by [38]:

$$\boldsymbol{\Omega}_c(\boldsymbol{k}) = -\hat{z}\frac{2a^2t^2\Delta}{\left(4a^2t^2k^2 + \Delta^2\right)^{3/2}}\tau_z \tag{5.7}$$

From theoretical modelling and DFT calculations, a sizable Berry curvature is found in the neighbourhood of the K points of ML TMDs [38, 42, 46, 50]. The calculated Berry curvature of MoS_2 along high-symmetry lines and along 2D k plane is presented in Fig. 5.11. The orbital magnetic moment has identical values in the conduction and valence band and is expressed by:

$$\boldsymbol{m}(\boldsymbol{k}) = -\hat{z}\frac{2a^2t^2\Delta}{4a^2t^2k^2 + \Delta^2}\frac{e}{2\hbar}\tau_z \tag{5.8}$$

Moreover, orbital magnetic moment and Berry curvature are related to optical circular dichroism, and their ratio defines the degree of circular polarization for interband transition [38].

Valley Hall Effect

The valley Hall effect refers to the opposite Hall currents for carriers located in opposite valleys as shown in Fig. 5.9c. Briefly, in an electric field, the valley contrasting Berry curvature (Eq. 5.7) serves as an effective magnetic field in momentum space and can drive carriers at the K and $-$K valleys to the opposite transverse edges. This valley-dependent Hall effect is analogue to spin Hall effect, but valley pseudovector acts as spin. Like graphene [51–53], valley Hall effect has been also observed in TMD

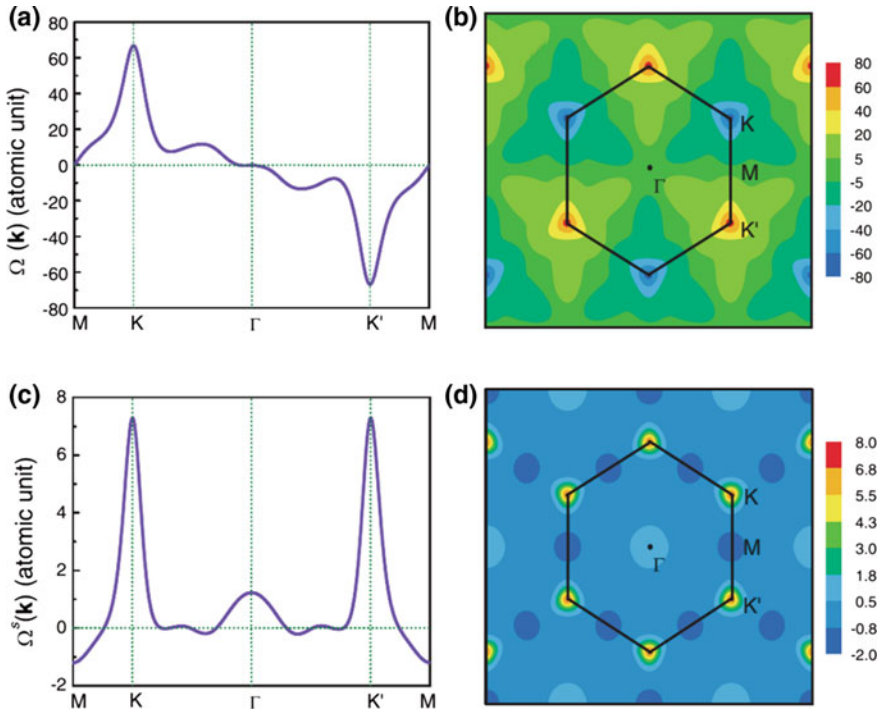

Fig. 5.11 Berry curvatures of monolayer MoS_2 along the high-symmetry lines (**a**) and in the 2D k plane (**b**). The spin Berry curvatures of monolayer MoS_2 along the high-symmetry lines (**c**) and in the 2D k plane (**d**). All of the Berry curvatures are in the atomic unit (bohrs^2). Reproduced with permission from Ref. [50], Copyright 2013, American Physical Society

system [54, 55]. Furthermore, a tunable valley Hall effect in bilayer TMDs has been reported [55]. As the 2H-stacked unperturbed bilayer MoS_2 is centrosymmetric, the valley current is forbidden, but the introduction of applied electric field breaks the inversion symmetry. The broken inversion symmetry again gives rise to finite Berry curvatures at the $\pm$K valleys, resulting in a finite valley Hall conductivity.

Tuning of Electronic Properties of TMDs

Various methods have been widely used to tune the properties of TMDs, including external elastic strain and external electric field.

By external strain: Owing to the mechanical flexibility and anisotropy of TMDs, elastic strain can intensely tune the properties of TMDs. The band structure of ML TMDs is strongly affected by the external elastic strain. As reported by various theoretical calculations, strain can cause a direct-to-indirect gap transition as well as semiconducting-to-metallic transition. Using first-principles calculation, Chang

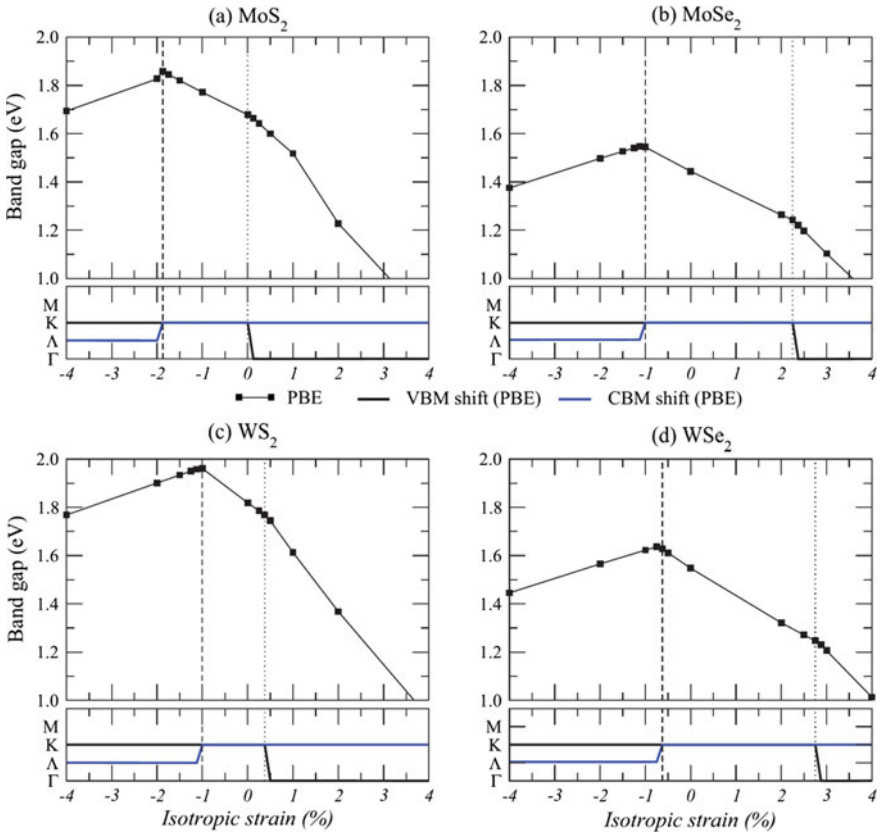

Fig. 5.12 Bandgap variations of MX_2 with compressive and tensile biaxial strains. The VBM (black line) and CBM (blue line) positions under strains are extracted in the lower panels. When the black and blue lines overlap, the gap is direct (VBM and CBM are at the same k point). Reproduced with permission from Ref. [56], Copyright 2013, American Physical Society

et al. [56] systematically studied the band structure of MX_2 (M = Mo, W; X = S, Se) under both tensile and compressive strains. As shown in Fig, 5.12, direct-to-indirect band transition occurred under both applied tensile and compressive strains for MX_2.

It is observed that within 2% of compressive strain, it is possible to widen the direct bandgaps by up to 10.7, 7.8, 6.9 and 5.2% for MoS_2, WS_2, $MoSe_2$ and WSe_2, respectively. In addition, bilayer MoS_2 is found to behave similarly to its monolayer counterpart under in-plane biaxial strain: (i) bandgap decreases with the increase of tensile strain; (ii) under compressive strain, the gap first increases and then decreases gradually; (iii) under large stain which may be either tensile or compressive, the bilayer can become metallic [57]. Similarly, the bilayer TMDs can also exhibit semiconducting-to-metallic transition under out-of-plane compressive strain [58].

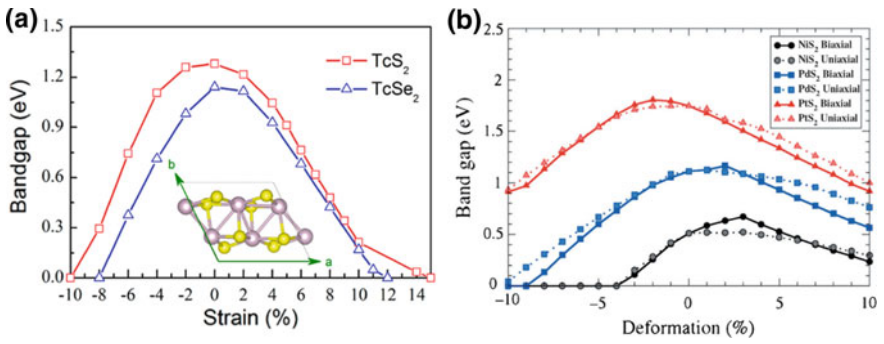

Fig. 5.13 **a** Bandgap as a function of biaxial strain calculated with the PBE functional for TcS_2 (red line) and $TcSe_2$ (blue line) monolayers. Reproduced with permission from Ref. [19], Copyright 2016, American Chemical Society. **b** Bandgap at PBE levels of theory of NiS_2, PdS_2 and PtS_2 at different uniaxial (dashed lines) and biaxial (solid lines) compression or strain percentages. Reproduced with permission from Ref. [20], Copyright 2014, WILEY-VCH Verlag GmbH & Co. KGaA

In case of monolayer TcS_2 and $TcSe_2$, the semiconducting-to-metal transition can be triggered by tensile or compressive strain as predicted by DFT [19] (Fig. 5.13a).

The uniaxial compression or elongation on MS_2 (M = Ni, Pd, Pt) leads to the reduction of bandgap, whereas under biaxial stretch, deformations of the bandgap of NiS_2 and PdS_2 monolayers increase up to 2–3% strain before decreasing, and the bandgap of PtS_2 always decreases proportionally to the strain (Fig. 5.13b) [20]. Similarly, semiconducting-to-metallic or semimetallic transition is also predicted by first principles in other TMDs such as TiS_2 [15] and ZrS_2 [59].

By electric field: The response of the electronic structure of 2D TMDs towards an external perpendicular electric field ($E_\perp$) crucially depends on the number of layers [43, 60–62]. The electronic structures of TMD MLs are not affected by $E_\perp$ within field strengths that are common in electronic devices. In contrast, $E_\perp$ significantly changes the electronic structure of bilayers (BLs) of TMDs. $E_\perp$ polarizes the electron density and introduces an anisotropy into the system. This anisotropy breaks the inversion symmetry which creates SO splitting in the valence and conduction bands due to the so-called Stark effect [43] (Fig. 5.14b). Figure 5.14c shows that the bandgap of BLs reduces nearly linearly with the applied $E_\perp$ and undergoing the semiconductor to metal transition for field strengths of about 1.2 V $Å^{-1}$ [61]. In addition, a weaker $E_\perp$ fields can easily modify the band structure of bilayer WX_2 (X = S, Se) as compared to that of ML MoX_2 (X = S, Se) (Fig. 5.14c).

As a consequence of the Stark effect which causes band splitting and energy shift under electric field, the monolayer and bilayer MX_2 (M = Mo, W; X = S, Se) become indirect at smaller applied $E_\perp$ field. Furthermore, electric field causes another interesting phenomenon at the high-symmetry Γ point, which is known as Rashba spin splitting [60]. The Rashba effect leads to the shift of spin-splitting band in the reverse directions in the momentum space as demonstrated in Fig. 5.14d.

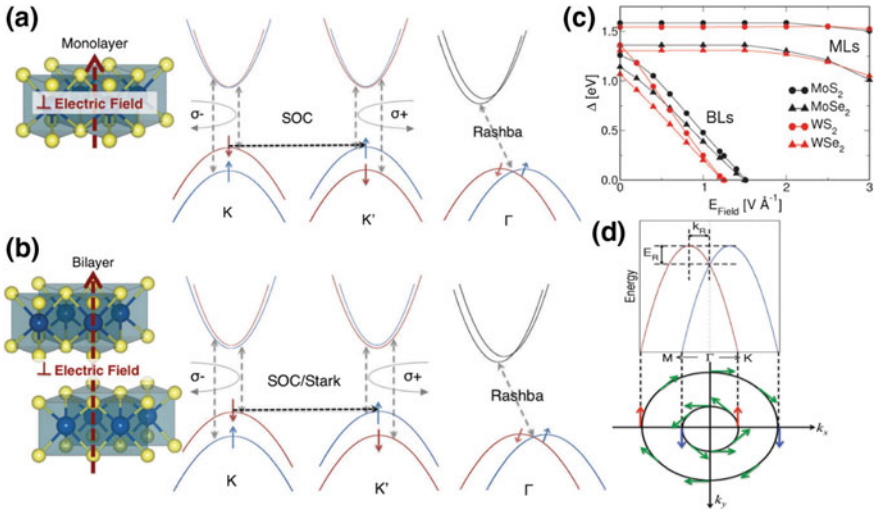

Fig. 5.14 Schematic representation of 2H TMD monolayer **a** and bilayer **b** together with the VBM and CBM in the presence of an external electric field perpendicular to the basal planes. The electric field polarizes the planes and breaks the inversion and mirror symmetries. Spin–orbit coupling (SOC) at the K points occurs in the BLs, while it stays intact in the MLs. **d** Schematic representation of Rashba spin splitting in the momentum space at the Γ point. E_R and k_R denote the Rashba energy of the split states and the momentum, respectively. Reproduced with permission from Ref. [43], Copyright 2015, The Royal Society of Chemistry. **c** Effect of an external electric field ($E_\perp$) perpendicular to the basal planes of TMC MLs and BLs. Reproduced with permission from Ref. [61], Copyright 2012, The Royal Society of Chemistry

Rashba energy (E_R) and Rashba coupling parameter (α_R) describe the spin-induced splitting in the momentum space, and these two physical quantities are related by the equation $\alpha_R = \frac{2E_R}{k_R}$, where, k_R is the shift of bands in the momentum space. It is to be noted that under an applied electric field, the heavier TMD materials exhibit more pronounced Rashba effect and it increases with the field strength [43].

Dielectric Screening and Excitonic Properties

Similar to zero-dimensional (0D) and one-dimensional (1D) nanomaterials, 2D materials show different electronic screening compared to the bulk materials. In the general description of screening, a test charge placed in the material polarizes the surrounding medium by applying forces on the electrons and nuclei [63, 64]. In a bulk metallic system, the additional charge is completely screened within a Thomas–Fermi length of a few angstroms, and the macroscopic field vanishes within the metal, whereas in a bulk semiconductor or insulator, a test charge Q is partially screened by a polarization charge, $-Q(1 - 1/\varepsilon)$, where ε is the static dielectric constant [63]. However, in 2D materials, these simple models break down since the field lines from

the test charge extend outside the material into the vacuum where no screening is possible. Therefore, a 2D metal may not screen a test charge completely, while in 2D semiconductors, screening is reduced by the presence of vacuum [65]. Similar to other 2D materials, the dielectric function of TMDs is strongly $\mathbf{q}$ (wave vector) dependent. In an approximation, the TMDs can be modelled by an infinite thin isotropic slab and according to this approximation, the dielectric function becomes [44, 66]:

$$\varepsilon_{2D}(\mathbf{q}, \omega) = 1 + 2\pi\alpha(\omega)q \tag{5.9}$$

where α is the 2D polarizability of the layer, which can be computed from the first principles. The screened interaction can be written as [44]:

$$W_{2D}(\mathbf{q}, \omega) = \frac{2\pi}{q\varepsilon_{2D}(\mathbf{q}, \omega)} \tag{5.10}$$

where $2\pi/q$ is the 2D Fourier transformation of $1/r$ in the Coulomb interaction. This simplest screened interaction has been extensively used to study the excitons and excitonic properties of 2D materials [67, 68].

Excitons: One of the most important characteristics of the 2D semiconductors and insulators is the existence of excitons. An exciton is a bound electron–hole pair. Similar to graphene [68] and *h*-BN [69], exciton with large binding energy is also observed in TMD monolayers [70, 71] due to the combination of reduced dielectric screening [66, 68, 72] and geometric confinement [73]. These excitons strongly couple to the light and lead to peculiar optical properties which can be studied by treating them as a hydrogen-like problem or computationally by solving Bathe–Salpeter equation (BSE). The exciton is equivalent to a hydrogen-like problem; thus, the energy of the nth level corresponds to the nth excitonic energy level:

$$E_n^{2D} = -\frac{\mu e^4}{2\varepsilon^2\hbar^2}\frac{1}{n^2} = -R_X\frac{1}{n^2} \tag{5.11}$$

where integers $n = 1, 2, 3 \ldots$, $R_X = \frac{\mu e^4}{2\varepsilon^2\hbar^2}$ is the exciton Rydberg energy and $\mu = m_e m_h/m_e + m_h$ is the reduced electron–hole mass. Equation (5.11) gives the exciton binding energy. In 2D materials, due to spatial confinement, the binding energy of exciton is enhanced and is given by [74]:

$$E_n^{2D} = -\frac{\mu e^4}{2\varepsilon^2\hbar^2}\frac{1}{\left(n-\frac{1}{2}\right)^2} = -R_X\frac{1}{\left(n-\frac{1}{2}\right)^2} \tag{5.12}$$

The spectrum of exciton is series of discrete levels and for monolayer TMD is given by:

$$E_x(n) = E_g - R_X \frac{1}{\left(n - \frac{1}{2}\right)^2} \tag{5.13}$$

where E_g is the quasiparticle bandgap and the equation describes that the exciton resonances occur within the forbidden bandgap. Under excitonic effects, strong peaks at energies equal to E_n and just below the band edge are expected to appear in absorption and emission spectra [75].

Computationally, the most used approach for addressing the excitonic properties of TMDs is the GW plus Bethe–Salpeter equation (GW-BSE). The GW approximation is an approximation made to calculate self-energy of a many-body system in terms of the single-particle Green function "G" and the screened Coulomb interaction "W". By solving the Bethe–Salpeter equation (BSE) for the basis set of quasi-electron and quasihole states, the electron–hole interaction and optical absorption spectra can be obtained as follows [76]:

$$(\varepsilon_c^{QP} - \varepsilon_v^{QP})A_{vc} + \sum_{v'c'} \langle vc \left| K^{eh} \right| v'c' \rangle A_{v'c'} = \Omega A_{vc} \tag{5.14}$$

where Ω is the resulting *e–h* excitation energies, A_{vc} is the corresponding eigenvectors, ε^{QP} is the single quasiparticle energies obtained at the GW level and K^{eh} is the CB electron-VB hole interaction kernel. This term K^{eh} consists of K_x and K_d, of which K_x is the exchange term containing the bare Coulomb interaction and determines the excitation spectrum [77], while K_d is the direct interaction term involving the screened Coulomb interaction which is responsible for the attractive interactions of the electrons and holes and the formation of excitons [76].

Unlike the conventional semiconductors [78], the binding energies of excitons in bulk TMDs are higher (~100 meV) than the thermal energy at room temperature (26 meV). Hence, a prominent excitonic effect in optical transitions at room temperature can be observed [79]. The strong binding energy of neutral exciton in bulk TMDs is attributed to weak van der Waals layered structure and the heavy effective mass of valence or conduction bands [80]. The excitonic effects are more clearly manifested in monolayer or a few layer TMDs, which arises from the combination of reduced dielectric screening and geometric confinement. Figure 5.15 shows the absorption spectra of monolayer Mo- and WX_2 (X = S, Se, Te) calculated from BSE [81].

As mentioned in the previous section, in the TMD monolayer the spin–orbit coupling induces large VB splitting, whereas its effect in CB is negligible. Therefore, two possible vertical transitions from two spin–orbit split VBs to a doubly degenerated CB contribute to two distinct low-energy features in absorption spectra that commonly referred to as A and B exciton peaks. The energy difference between A and B exciton peaks carries the information about valance band splitting, and it was found to be larger in WX_2 compounds than that in their MoX_2 counterparts [81]. Similar to group 6 TMD, PtS_2 and $PtSe_2$ also show large exciton binding energy of 0.78 and 0.6 eV, respectively [82].

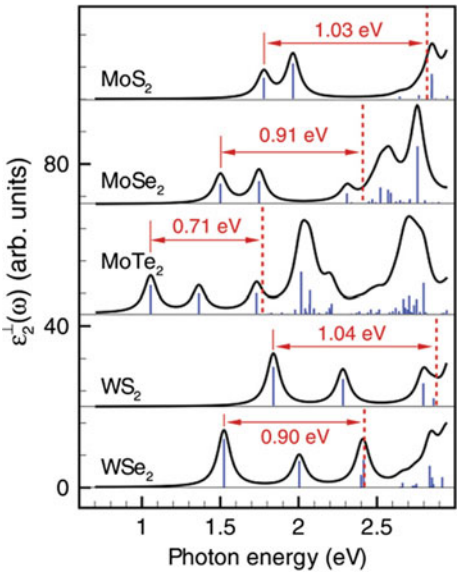

Fig. 5.15 Imaginary part of the transverse dielectric constant $\varepsilon_2^{\perp}(\omega)$ as a function of photon energy for MoX_2 and WX_2 monolayers. Vertical (blue) bars represent the relative oscillator strengths for the optical transitions. Red dashed lines indicate the G_0W_0 bandgap. The binding energies of the A exciton are indicated in each case. Reproduced with permission from Ref. [81], Copyright 2012, American Physical Society

Dark, Bright Exciton and Other Quasiparticles: Beyond neutral or two-particle (electron and hole) complex, the strong geometric and dielectric confinement also allow the formation of more complex quasiparticles such as charged exciton named as trion and bi-exciton in TMDs [44, 83, 84] (Fig. 5.16a, b). In doped TMDs, free electrons (in *n*-doped regions) or holes (in *p*-doped regions) can interact with the neutral excitons forming three-particle complexes known as trions. The non-equivalent valleys in the band structure are responsible for the formation of trions, which may form optically bright states using carriers located within one valley known as intravalley trion or in different valleys named as intervalley trion [85] (Fig. 5.16c, d). For intravalley trions, the Pauli exclusion principle dictates that the two electrons must occupy different spin states and therefore reside at the top and bottom spin-split conduction bands, respectively, forming a spin singlet, whereas in case intervalley trions, the two electrons may have the same spin as they have different valley index, and thus form a triplet state [85, 86]. At higher concentration of exciton, two excitons can bind together and form a four-particle complex called bi-exciton. Bi-exciton with binding energy ranging from about 30–70 meV is observed in TMDs [87, 88].

The excitonic properties of MoX_2 and WX_2 are different due to the presence of dark excitonic states as evidenced by temperature-dependent PL (Fig. 5.17a). The spin–orbit-induced CB splitting and both sign and amplitude of the electron–hole short-range Coulomb exchange within the exciton are responsible for the evolution and splitting of dark excitonic states [89, 90]. The sign and amplitude of the spin–orbit-induced CB splitting differ among the different TMDs. For WX_2 (X = S, Se, Te), electrons in the CBM are expected to have spin polarization opposite to those in the VBM, leading to the lowest energy state of dark exciton [91]. In contrast,

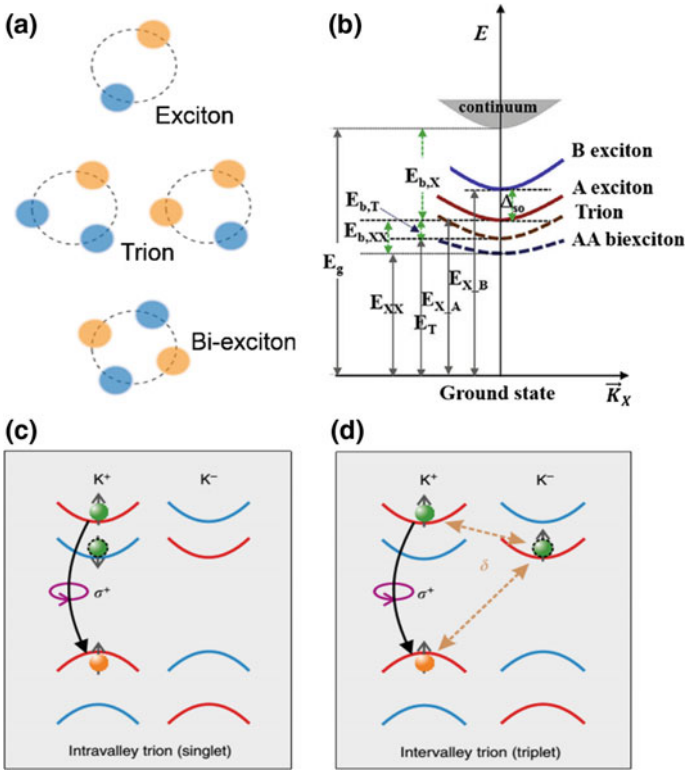

Fig. 5.16 **a** Illustration of exciton and higher-order excitonic complexes: a two-particle charge-neutral exciton, a three-particle charged exciton (trion) and a four-particle bi-exciton. Reproduced with permission from Ref. [84], Copyright 2015, Nature Publishing Group. **b** Dispersion relation diagram of exciton, trion and bi-exciton. Different parabolas correspond to the dispersion relation curves of trion, A, B exciton and bi-exciton. E_{X_A}, E_{X_B}, E_{XX}, E_T are emission energies of A, B exciton, AA bi-exciton and trion, respectively. $E_{b,X}$, $E_{b,XX}$, $E_{b,T}$ are binding energies of A exciton, AA bi-exciton and trion. Reproduced with permission from Ref. [75], Copyright 2016, Elsevier B.V. Schematic illustration of singlet (**c**) and triplet (**d**) trion configurations for WS_2 in the K^+ (K and K^+ denote the same) valley. Electrons in the conduction (valence) band are represented by green (orange) spheres. Spin-up (-down) bands appear in red (blue) colour. The curved arrows indicate the interband recombination. The final state of the remaining conduction band electron after trion recombination is marked by the dashed black outline. The intervalley electron–hole exchange interaction leading to an energetic splitting δ is indicated by the dashed arrows. Reproduced with permission from Ref. [85], Copyright 2016, Nature Publishing Group

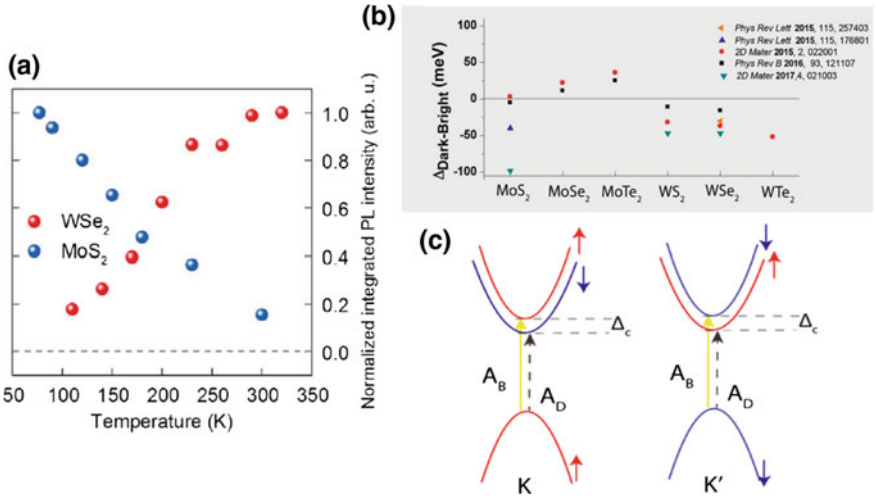

Fig. 5.17 **a** Comparison of temperature dependence of the time-integrated PL intensity of WSe_2 and MoS_2. Reproduced with permission from Ref. [90], Copyright 2015, American Physical Society. **b** Summary of literature-reported bright–dark exciton energy splitting for TMD monolayers. **c** Schematic illustration of the spin-allowed bright exciton (A_B) and spin-forbidden dark exciton (A_D) in W-based TMDs at the K and K′ valleys. Δc is the bright–dark exciton energy splitting. Reproduced with permission from Ref. [94], Copyright 2017, American Chemical Society

for MoX_2 (X = Se, Te) electron in the CBM is expected to have the same spin polarization as holes in the VBM, leading to a bright state as lowest exciton energy level [92, 93]. The case for MoS_2 is in under debate [94]. Kormányos et al. [95] concluded that lowest exciton energy level is bright exciton, while Molas et al. [96] inferred lowest dark exciton with energy as much as ~100 meV below the bright exciton. The splitting of dark and bright excitons for Mo- and W-based TMDs is summarized in Fig. 5.17b. Because of the spin–orbit-induced splitting in the conduction band, there are two intravalley bright (singlet-like) excitons (A_B) denoted by $\left|K_{e\uparrow}K_{h\uparrow}\right\rangle$ and $\left|K'_{e\uparrow}K'_{h\downarrow}\right\rangle$ and two intravalley spin-forbidden (triplet-like) dark excitons (A_D) represented by $\left|K_{e\downarrow}K_{h\uparrow}\right\rangle$ and $\left|K'_{e\uparrow}K'_{h\downarrow}\right\rangle$ formed in W-based TMDs, as schematically depicted in Fig. 5.17c. Four possible dark intervalley exciton states are also possible and for W-based system those represented by $\left|K_{e\downarrow}K'_{h\downarrow}\right\rangle$, $\left|K_{e\uparrow}K'_{h\downarrow}\right\rangle$, $\left|K'_{e\uparrow}K_{h\uparrow}\right\rangle$ and $\left|K'_{e\downarrow}K_{h\uparrow}\right\rangle$.

5.1.3 Magnetism in TMDs

The absence of 2D magnetic material has been predicted from the 2D isotropic Heisenberg model by Mermin–Wagner theorem [97]. However, magnetically ordered states such as ferromagnetism (FM) and antiferromagnetism (AFM) have recently

been discovered in monolayer 2D materials such as semiconducting FM CrI_3 [98] and $CrSiTe_3$ [99], semiconducting AFM MPS_3 family (M = Ni, Fe, Mn) [100]. Few metallic TMDs such as VX_2 (X = S, Se), T phase of CrX_2 (X = S, Se, Te) [101, 102] and semiconducting MnX_2 (X = S, Se) also exhibit magnetism. Furthermore, doping, vacancy and strain can induce and manipulate the magnetic properties of TMDs. In this section, we address the magnetic properties of metallic TMDs as well as the induced magnetism by external stimuli in both semiconducting and metallic TMDs.

5.1.3.1 Metallic TMDs

Beside semiconducting TMDs, several TMDs exhibit metallic behaviour. For example, the 1T phase of TMDs such as ReS_2, and Ti-, Nb-, V-, Mo-,W- and Cr-X_2 (X = S, Se, Te) show metallic properties [103, 104]. Beside the 1T phase of these TMDs, 2H phase of TMDs such as NbS_2, $NbSe_2$, TaS_2 and $TaSe_2$ is also metallic in nature [102], and the phenomenon can be explained by nature of the *d* orbital of transition metals. So, 2H and 1T phases do not give the guarantee of the material property as semiconducting or metallic, respectively.

5.1.3.2 Magnetism in Metallic and Semiconducting TMDs

T phase of VX_2 and CrX_2 (X = S, Se, Te) are metallic, and more interestingly, they exhibit magnetic ordering. In contrast, MnX_2 (X = S, Se) has been predicted as low bandgap semiconductor with long-range ferromagnetic order, which has been shown by first-principles calculation [105]. The calculated band structure (Fig. 5.18) of MnX_2 using hybrid functional implies that both MnS_2 and $MnSe_2$ are indirect bandgap semiconductor with bandgap of 0.69 and 0.01 eV, respectively.

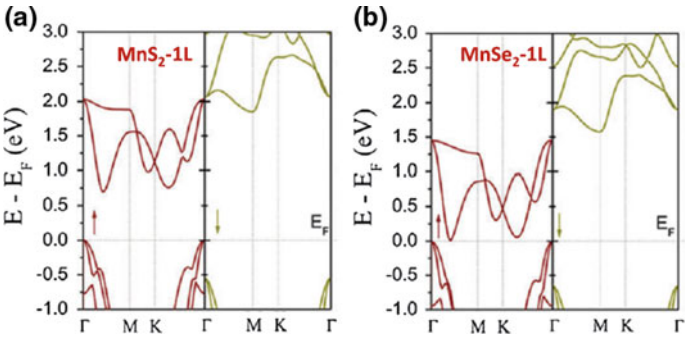

Fig. 5.18 Band structure of monolayer **a** MnS_2 and **b** $MnSe_2$ calculated at HSE06 level. Reproduced with permission from Ref. [105], Copyright 2014, The Royal Society of Chemistry

Table 5.1 Experimentally or theoretically reported magnetic TMDs in bulk and monolayer form

TMDs	Magnetic ordering of 1T-ML (bulk) TMDs	Curie or Neel temp in K	Magnetic moment
VS_2	FM (FM) [FM-thin flake]	309 [RT]	~0.486–0.858 μ_B/V atom ~−0.026–0.047 μ_B/S atom [0.51 μ_B/V atom]
VSe_2	FM (FM/paramagnetic) [FM-ML and thin film]	541 [RT]	0.680, 0.951 μ_B/V atom 0.048, 0.062 μ_B/Se atom
VTe_2	FM (FM)	618	0.986 μ_B/V atom 0.096 μ_B/Te atom
CrS_2	sAFM (AFM) 1H phase-NM		
$CrSe_2$	AFM (FM) 1H phase NM	363 (at 4% strain) Bulk ~550	
$CrTe_2$	FM (FM) 1H phase NM [FM-monolayer]	219 721 (at 4% strain) [310]	
MnS_2	FM	225	3 μ_B/unit cell
$MnSe_2$	FM	250	3 μ_B/unit cell

Magnetic ordering, magnetic moment, Curie or Neel temperature are summarized. *FM* ferromagnetic, *AFM* antiferromagnetic, *sAFM* striped antiferromagnetic, *NM* non-magnetic. Inside [] represent experimental result. The data taken from Refs. [101, 103–107, 109, 110, 112, 113]

In Table 5.1, type of magnetism, Curie (Neel) temperature, and magnetic moment of theoretically and experimentally reported bulk and monolayer magnetic materials are summarized. Ma et al. [106] reported that monolayer VX_2 (X = S, Se) has both stable FM and AFM ordering states while both the monolayers exhibit FM ordering in their ground state. Figure 5.19 shows the density of states and the atomic site projected density of states of VX_2 (X = S, Se). The difference between the up- and down-spin states of VX_2 indicates that monolayer VX_2 is a ferromagnetic material. The V-*d* states are highly delocalized and hybridized with the X-*p* states indicating covalent bonding between the V and X atoms. The total magnetic moment of VX_2 and their atomic contribution have been predicted using first-principles calculation and mentioned in Table 5.1 [106–108].

The total magnetic moment in VX_2 is mainly contributed by V atom. Spin ordering in magnetic TMDs can be realized by the competition between through-bond spin polarization (defined as, an A atom with an up-spin (down-spin) density induces a down-spin (up-spin) density on the adjacent B atom that is directly bonded to A atom) and through-space spin polarization (defined as, an A atom with an up-spin (down-spin) density induces a down-spin (up-spin) density on the nearest-neighbour A atom without any mediation of a B atom.). The FM state in monolayer VX_2 (X = S, Se) can originate from through-bond spin polarization; the up-spin of a V atom

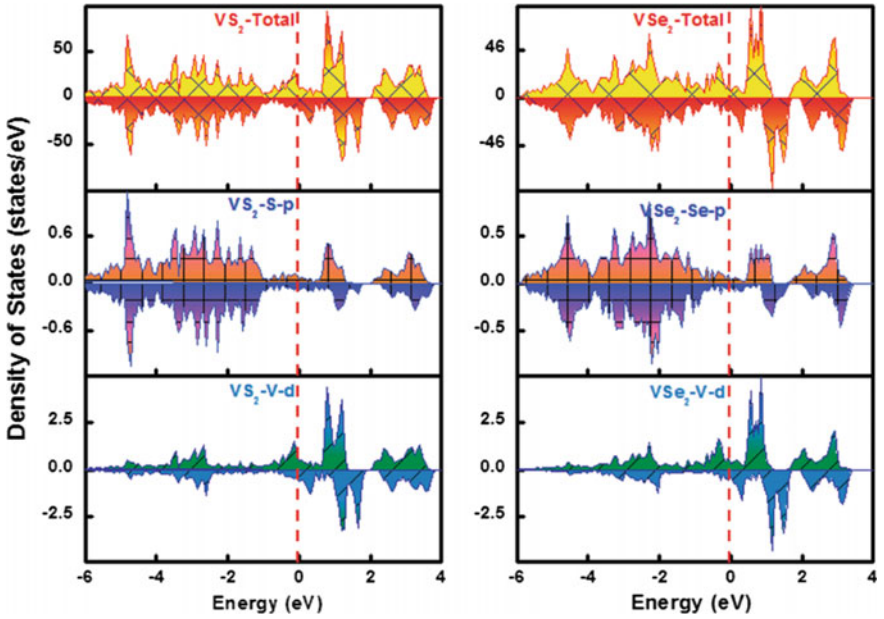

Fig. 5.19 Total density of states and corresponding projected density of states of VX_2. The vertical dashed line represents the Fermi level. Reproduced with permission from Ref. [106], Copyright 2012, American Chemical Society

induces down-spin to X atom. Furthermore, the down-spin X atom again induces up-spin to another V atom, leading to long-range magnetic ordering. Because the magnetic moment of V atoms is greater than that of X atoms, the total magnetic moment is nonzero and leads to long-range FM ordering.

Bulk CrX_2 (X = S, Se, Te) exhibits magnetic ordering, while by first-principles calculation, Ataca et al. [103] revealed that monolayer CrX_2 in H phase is non-magnetic. In contrast, the T phase of CrX_2 (X = Se, Te) is AFM and FM at their ground state, respectively; and they show strain-induced interplay between AFM and FM [109]. Similarly, T phase of monolayer CrS_2 is reported as magnetic material with striped AFM ordering. Moreover, T phase of CrS_2 exhibits a striped AFM to FM transition undergoing from monolayer to bilayer or multilayer CrS_2 [110]. The Curie or Neel temperature characteristics of ferromagnetic or antiferromagnetic material can be estimated based on mean field theory and Heisenberg model by using the following equation [108, 111, 112]: $k_B T_C = \frac{2}{3}\Delta E$. The Monte Carlo simulation based on Ising model can also predict these critical temperatures [105]. The estimated Curie temperatures for VS_2, VSe_2 and VTe_2 are 309, 541 and 618 K, respectively, which are higher than room temperature, making them attractive materials for spintronics applications [108]. Recently, monolayer and few layered VS_2 and VSe_2 have been synthesized experimentally, and ferromagnetism has been observed in these materials [107, 113].

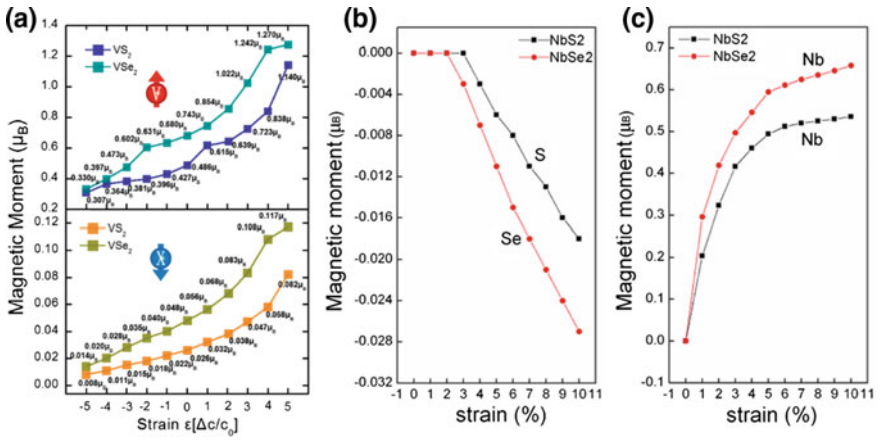

Fig. 5.20 Strain dependence of the magnetic moment of transition metal and chalcogen of **a** monolayer VX_2. Reproduced with permission from Ref. [106], Copyright 2017, American Chemical Society. **b**, **c** Monolayer NbX_2 monolayers. Reproduced with permission from Ref. [114], Copyright 2017, American Chemical Society

5.1.3.3 Induced Magnetism

Strain-Induced Tunable Magnetism

Magnetism can be induced and modulated by external strain in TMDs. Both magnetic moment and spin ordering in 2D magnetic TMDs are strongly affected by the external strain. In monolayer VX_2 (X = S, Se), tensile strain enhances both magnetic moment of metal and magnetic moment of chalcogen, whereas compressive strain quenches the magnetic moments (Fig. 5.20a). This modulation of magnetic moment with strain can be understood from the competition of ionic and covalent bonding interactions between V and X atoms. For example, the distance between V and X atoms becomes elongated under tensile strain that results in the reduction of covalent bonding interaction and enhancement of the ionic bonding interaction. Consequently, the enhanced ionic bonding interaction leads to an increase in the population of unpaired electrons on V and X atoms, giving rise to a strain-dependent magnetic moment variation [106]. More interestingly, the external strain can induce magnetism in non-magnetic NbX_2 (X = S, Se) [114]. The external tensile strain generates a finite magnetic moment in NbX_2 (X = S, Se), which is further enhanced with higher tensile strain (Fig. 5.20b, c).

The through-space and through-bond interactions, responsible for generating magnetization as mentioned above, are affected by external strain. The through-space interaction compared to the through-bond interaction is greatly reduced with increasing tensile strain (or decreasing compression strain) which results in the relative increase of the through-bond interaction. This phenomena can explain the monotonous increasing behaviour of ΔE ($\Delta E = E_{AFM} - E_{FM}$) with strain ranging

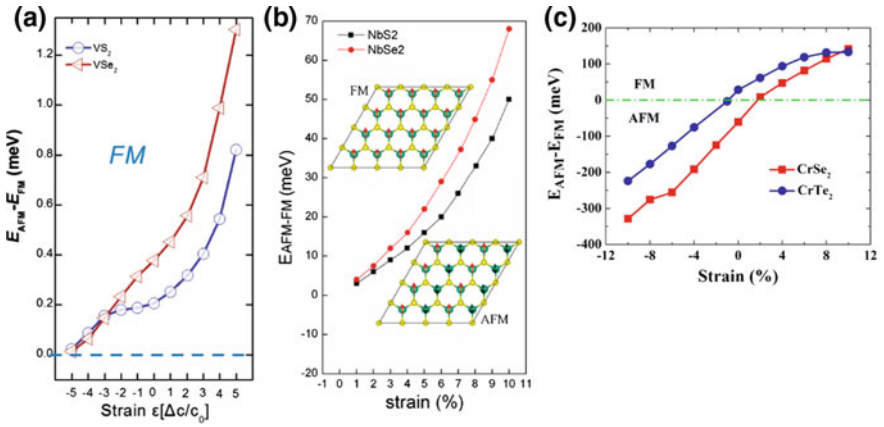

Fig. 5.21 Strain-tunable magnetism in monolayer TMDs. The energy difference between FM and AFM order of **a** VX_2 (X = S, Se). Reproduced with permission from Ref. [106], Copyright 2017, American Chemical Society. **b** NbX_2 (X = S, Se). Reproduced with permission from Ref. [114], Copyright 2017, American Chemical Society. **c** CrX_2 (X = Se, Te). Reproduced with permission from Ref. [109], Copyright 2015, American Physical Society

from −5 to 5% [106] (Fig. 5.21a). The 2D NbX_2 (X = S, Se) also exhibits similar behaviour as reflected in Fig. 5.21b. Furthermore, first-principles study showed that the ground state of 1T-CrS_2 can be switched from AFM to FM at 2% tensile strain, while 1T-$CrTe_2$ shows opposite transition, i.e. FM to AFM at 1% compressive strain (Fig. 5.21c). A biaxial strain over 6% changes the ground state of 2D TaS_2 and $TaSe_2$ from Pauli-paramagnetic to ferromagnetic [115].

Doping-Induced Magnetism in TMDs

Doping or alloying has been used to induce magnetism in 2D materials. Numerous first-principles calculations have been carried out to investigate the doping-induced magnetism in TMDs. There are mainly three approaches for doping to generate magnetism in TMDs: (a) vacancy creation, (b) surface hydrogenation or halogenation, and (c) substitution by dopants.

Vacancy-Induced Magnetism: Like other 2D materials, vacancy provides an effective approach to modulate the magnetic properties of TMDs. Using DFT-based first-principles calculations, Zheng et al. [116] investigated the magnetism of monolayer MoS_2 with various types of vacancies and effect of strain. They found that in the absence of strain, only V_{MoS_6} (vacancy constructed by a Mo atom and nearby three disulphur pairs) is magnetic and the magnetic moment is contributed by the six Mo atoms around the vacancy. In contrast, single S vacancy (V_S), double S vacancy (V_{S_2}) and V_{MoS_3} (vacancy introduced by removing Mo atom and nearby three S atoms on a S layer) are non-magnetic [116]. In addition, V_S, V_{S_2} and V_{MoS_3} can be made mag-

netic by applying an external biaxial tensile strain which breaks the Mo–Mo bonds. Furthermore, chalcogen vacancies have an influence on the magnetic properties of magnetic material. For example, in the case VS_2, the magnetic moment of V atoms near the S vacancy is gradually increased with more S vacancies (1.17, 1.67, 2.32 and 2.74 μ_B for V_{no} (no vacancy), V_S, V_{S_2} and V_{S_3} (triple S vacancy), respectively) [117]. More interestingly, the S vacancy changes the magnetic ordering. For instance, VS_2 with no vacancies is stable at FM ordering, whereas in the presence of S vacancies, AFM ordering is stable [117].

Dopant-Induced Magnetism: Magnetic properties of TM atom-doped TMDs have been studied rigorously using first-principles calculations. Magnetic atom (Fe, Co, Ni)-doped MoS_2 is predicted to be magnetic [118–121]. In addition to the above TM, Cd-, Hg- or Zn-doped monolayer MoS_2 exhibits ferromagnetism. First-principles calculation revealed that the magnetism induced by group 8 to group 12 TM atom dopants is suppressed by Jahn–Teller distortions [119]. Furthermore, doping of TM atoms from the group 3 to group 6 results in non-magnetic states, because the number of valance electrons is smaller than Mo. Moreover, like MoS_2, Mn, Fe, Co, Ni, Cu and Zn can induce magnetism in WS_2 monolayer. Interestingly, using first-principles calculation, Manchanda et al. [122] revealed that addition of V into WSe_2 leads to a transition from a non-magnetic semiconductor to a ferromagnetic metal, with a magnetic moment of about 1.0 μ_B per V atom. In addition, Shu et al. [123] revealed the layer number and chemical potential-dependent magnetic exchange coupling of Fe-doped MoS_2. The substitution Fe dopant atoms at the Mo sites (Fe_{Mo}) are energetically favourable in monolayer MoS_2, whereas the formation of intercalated and substitutional Fe complex ($Fe_{Mo}Fe_i$) is preferred in bilayer or in multilayer MoS_2 at S-rich regime (Figs. 5.22 and 5.23).

Furthermore, in monolayer MoS_2, the substitutional Fe dopants at Mo sites are coupled ferromagnetically via the double-exchange mechanism with the FM cou-

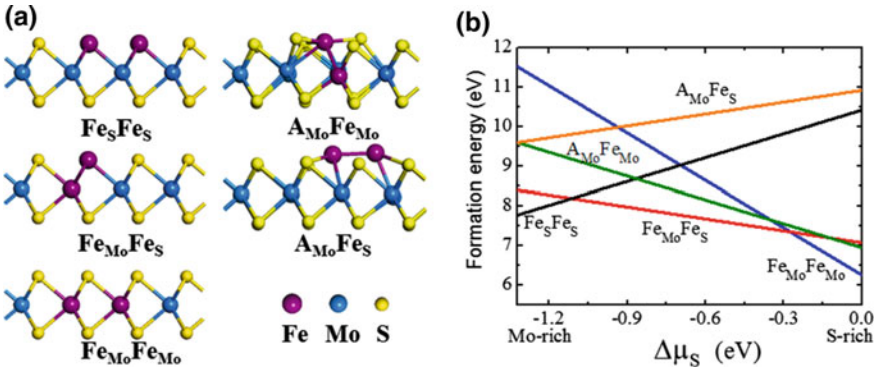

Fig. 5.22 **a** Optimized doping atomic configurations (side view) and **b** formation energies of two Fe impurities in monolayer MoS_2. Five potential doping configurations are $Fe_{Mo}Fe_{Mo}$, $Fe_{Mo}Fe_S$ and Fe_SFe_S, respectively. Mo, S and Fe atoms are coloured by blue, yellow and purple balls, respectively. Reproduced with permission from Ref. [123], Copyright 2017, American Chemical Society

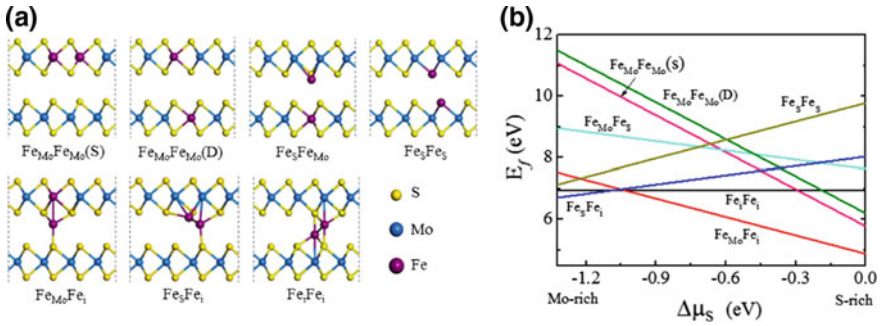

Fig. 5.23 **a** Optimized doping atomic configurations (side view) and **b** formation energies of two Fe impurities in bilayer MoS_2. Reproduced with permission from Ref. [123], Copyright 2015, American Chemical Society

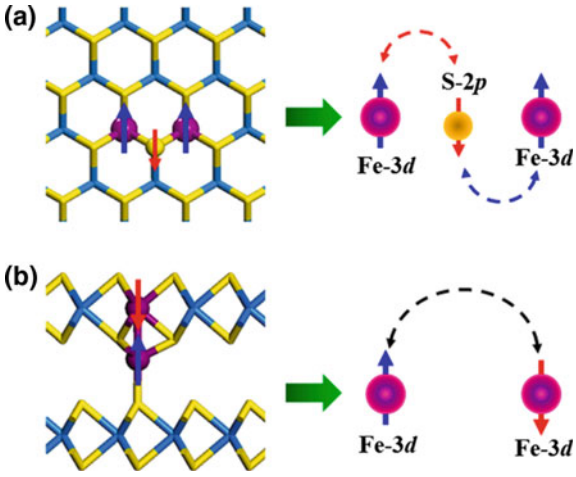

Fig. 5.24 Schematic models of **a** double-exchange mechanism and **b** superexchange mechanism in Fe-doped MoS_2 nanosheets. Reproduced with permission from Ref. [123], Copyright 2015, American Chemical Society

pling being mediated by the hybridization between Fe 3*d* states and S 2*p* states, which results in the AFM coupling between the Fe dopants and the nearest-neighbour S atoms. For Fe-doped bilayer or multilayer MoS_2, the formation of $Fe_{Mo}Fe_i$ structures leads to a direct and mediated bonding interaction between dopants which follows superexchange mechanism, resulting in an antiparallel spin polarization among neighbouring Fe dopants (Fig. 5.24). Hence, AFM coupling is favoured in bilayer or multilayer Fe-doped MoS_2 [123].

Furthermore, Mishra et al. [124] pointed out that Mn-doped MX_2 (M = Mo, W; X = S, Se, Te) is more promising two-dimensional dilute magnetic semiconductors (DMSCs) than TMDs doped by other TM. This is because the long-range FM of Mn

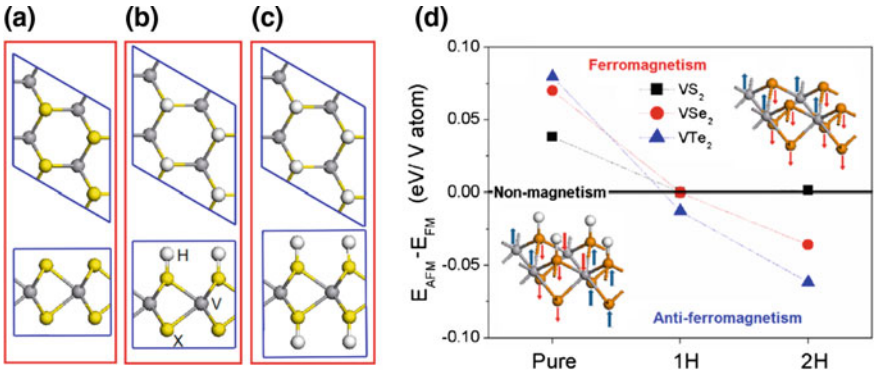

Fig. 5.25 Effect of hydrogenation on magnetism. Representative structures of **a** VX_2 monolayer, **b** VX_2 monolayer with one side fully covered by hydrogen atoms and **c** VX_2 monolayer with two sides fully covered by hydrogen atoms. **d** Calculated energy difference between antiferromagnetic and ferromagnetic states of VX_2 monolayer with and without hydrogenation. Reproduced with permission from Ref. [108], Copyright 2014, American Chemical Society

spins is mediated by an anti-FM exchange between the localized Mn *d* states and the delocalized *p* states of the S, Se and Te atoms. In contrast, TM like Fe, Co and Ni showed a FM exchange with the S, Se and Te atoms, resulting in a very weak FM (even slightly AFM) coupling for transition metal dopants with large separations.

Surface Hydrogenation or Halogenation: Hydrogenation or halogenation of 2D materials can modify their magnetism and induce FM from non-magnetic materials. He et al. [125] studied the magnetic properties of H-, B-, C-, N-, O- and F-adsorbed MoS_2 by first-principles calculations. The contributions of the adatoms H, B, C, N and F to the total magnetic moments are 12.6, 0.3, 1.7, 56.4 and 28.1%, respectively, indicating non-magnetic atom can induce magnetism in non-magnetic TMDs. Furthermore, using DFT calculation, Pan et al. [108] anticipated the effect of hydrogenation on the magnetism of VS_2 and revealed interesting features as shown in Fig. 5.25.

The observed features are: (i) the exchange energy (E_{ex}), where $E_{ex} = (E_{AFM} - E_{FM})$ of monolayer VX_2 increases as the chalcogen is varied from S to Te, indicating a higher Curie temperature; and (ii) spin ordering and magnetic moment are strongly affected by the coverage of hydrogen. For example, the half side H covered VX_2 (VX_2-1H) (Fig. 5.25b) loses its magnetic properties and further hydrogenation to VX_2-2H gives rise to AFM order in VX_2 (Fig. 5.25d).

5.2 Conclusion

In this chapter, electronic, optical and magnetic properties of TMDs are addressed in theoretical point of view. The most studied TMDs from group 4 to group 10 are

included in terms of their atomic arrangement, electronic and magnetic properties. Furthermore, the effects of external stimuli such as elastic strain, external electric field on their optoelectronic and magnetic properties are discussed throughout this chapter.

Acknowledgements Xu thanks the financial support of the National Natural Science Foundation of China (Grant 51872257, 51472219 and 51672244). Chen and Yin appreciate the financial support of the National Natural Science Foundation of China under Grant of 61431014, and Su is financially supported by the Macao Science and Technology Development Fund (020/2017/A1) and multiple-year research grant, University of Macau, MYRG2016-00184-ICMS-QRCM.

References

1. Novoselov KS, Geim AK, Morozov SV, Jiang D, Zhang Y, Dubonos SV et al (2004) Electric field effect in atomically thin carbon films. Science 306:666–669
2. Chhowalla M, Shin HS, Eda G, Li LJ, Loh KP, Zhang H (2013) The chemistry of two-dimensional layered transition metal dichalcogenide nanosheets. Nat Chem 5:263
3. Xu M, Liang T, Shi M, Chen H (2013) Graphene-like two-dimensional materials. Chem Rev 113:3766–3798
4. Voiry D, Mohite A, Chhowalla M (2015) Phase engineering of transition metal dichalcogenides. Chem Soc Rev 44:2702–2712
5. Shirodkar SN, Waghmare UV (2014) Emergence of ferroelectricity at a metal-semiconductor transition in a 1T monolayer of MoS_2. Phys Rev Lett 112:157601
6. Ruppert C, Aslan OB, Heinz TF (2014) Optical properties and band gap of single- and few-layer $MoTe_2$ crystals. Nano Lett 14:6231–6236
7. Tongay S, Sahin H, Ko C, Luce A, Fan W, Liu K et al (2014) Monolayer behaviour in bulk ReS_2 due to electronic and vibrational decoupling. Nat Commun 5:3252
8. Arora A, Noky J, Drüppel M, Jariwala B, Deilmann T, Schneider R et al (2017) Highly anisotropic in-plane excitons in atomically thin and bulklike 1T′-$ReSe_2$. Nano Lett 17:3202–3207
9. Castro Neto AH (2001) Charge density wave, superconductivity, and anomalous metallic behavior in 2D transition metal dichalcogenides. Phys Rev Lett 86:4382–4385
10. Ishioka J, Liu YH, Shimatake K, Kurosawa T, Ichimura K, Toda Y, Oda M, Tanda S (2010) Chiral charge-density waves. Phys Rev Lett 105:176401
11. Eda G, Yamaguchi H, Voiry D, Fujita T, Chen M, Chhowalla M (2011) Photoluminescence from chemically exfoliated MoS_2. Nano Lett 11:5111–5116
12. Kuc A, Zibouche N, Heine T (2011) Influence of quantum confinement on the electronic structure of the transition metal sulfide TS_2. Phys Rev B 83:245213
13. Splendiani A, Sun L, Zhang Y, Li T, Kim J, Chim CY et al (2010) Emerging photoluminescence in monolayer MoS_2. Nano Lett 10:1271–1275
14. Guo H, Lu N, Wang L, Wu X, Zeng XC (2014) Tuning electronic and magnetic properties of early transition-metal dichalcogenides via tensile strain. J Phys Chem C 118:7242–7249
15. Xu C, Brown PA, Shuford KL (2015) Strain-induced semimetal-to-semiconductor transition and indirect-to-direct band gap transition in monolayer 1T-TiS^2. RSC Adv 5:83876–83879
16. Singh D, Gupta SK, Sonvane Y, Kumar A, Ahuja R (2016) 2D-HfS_2 as an efficient photocatalyst for water splitting. Cata Sci Technol 6:6605–6614
17. Li S, Wang C, Qiu H (2015) Single- and few-layer ZrS^2 as efficient photocatalysts for hydrogen production under visible light. Int J Hydrog Energy 40:15503–15509
18. Liu E, Fu Y, Wang Y, Feng Y, Liu H, Wan X et al (2015) Integrated digital inverters based on two-dimensional anisotropic ReS_2 field-effect transistors. Nat Commun 6:6991

19. Jiao Y, Zhou L, Ma F, Gao G, Kou L, Bell J (2016) Predicting single-layer technetium dichalcogenides (TcX_2, X = S, Se) with promising applications in photovoltaics and photocatalysis. ACS Appl Mater Interfaces 8:5385–5392
20. Pere M, Mahdi GA, Thomas H (2014) Two dimensional materials beyond MoS_2: noble-transition-metal dichalcogenides. Angew Chem Inter Edit 53:3015–3018
21. Yuda Z, Jingsi Q, Peng Y, Zhixin H, Ziyuan L, Ping LS et al (2016) Extraordinarily strong interlayer interaction in 2D layered PtS_2. Adv Mater 28:2399–2407
22. Yu X, Yu P, Wu D, Singh B, Zeng Q, Lin H et al (2018) Atomically thin noble metal dichalcogenide: a broadband mid-infrared semiconductor. Nat Commun 9:1545
23. Yuda Z, Jingsi Q, Zhihao Y, Peng Y, Kang X, Ping LS et al (2017) High-electron-mobility and air-stable 2D layered $PtSe_2$ FETs. Adv Mater 29:1604230
24. Mingzhe Y, Eryin W, Xue Z, Guangqi Z, Hongyun Z, Kenan Z et al (2017) High quality atomically thin $PtSe_2$ films grown by molecular beam epitaxy. 2D Mater 4:045015
25. Wang Y, Li L, Yao W, Song S, Sun JT, Pan J et al (2015) Monolayer $PtSe_2$, a new semiconducting transition-metal-dichalcogenide, epitaxially grown by direct selenization of Pt. Nano Lett 15:4013–4018
26. Bardeen J, Shockley W (1950) Deformation potentials and mobilities in non-polar crystals. Phys Rev 80:72–80
27. Qiao J, Kong X, Hu ZX, Yang F, Ji W (2014) High-mobility transport anisotropy and linear dichroism in few-layer black phosphorus. Nat Commun 5:4475
28. Hong J, Hu Z, Probert M, Li K, Lv D, Yang X et al (2015) Exploring atomic defects in molybdenum disulphide monolayers. Nat Commun 6:6293
29. Wang Y, Li Y, Chen Z (2015) Not your familiar two dimensional transition metal disulfide: structural and electronic properties of the PdS_2 monolayer. J Mater Chem C 3:9603–9608
30. Ando T, Fowler AB, Stern F (1982) Electronic properties of two-dimensional systems. Rev Mod Phys 54:437–672
31. Sivacarendran B, Sumeet W, Hussein N, Zhen OJ, Serge ZB, Sharath KR et al (2013) Two-dimensional molybdenum trioxide and dichalcogenides. Adv Func Mater 23:3952–3970
32. Kaasbjerg K, Thygesen KS, Jacobsen KW (2012) Phonon-limited mobility in n-type single-layer MoS_2 from first principles. Phys Rev B 85:115317
33. Wang QH, Kalantar-Zadeh K, Kis A, Coleman JN, Strano MS (2012) Electronics and optoelectronics of two-dimensional transition metal dichalcogenides. Nat Nanotechnol 7:699
34. Radisavljevic B, Radenovic A, Brivio J, Giacometti V, Kis A (2011) Single-layer MoS_2 transistors. Nat Nanotechnol 6:147–150
35. Sivacarendran B, Junkai D, Zhen OJ, Sumeet W, James S, Jianshi TL et al (2013) Enhanced charge carrier mobility in two-dimensional high dielectric molybdenum oxide. Adv Mater 25:109–114
36. Jena D, Konar A (2007) Enhancement of carrier mobility in semiconductor nanostructures by dielectric engineering. Phys Rev Lett 98:136805
37. Padilha JE, Peelaers H, Janotti A, Van de Walle CG (2014) Nature and evolution of the band-edge states in MoS_2: From monolayer to bulk. Phys Rev B 90:205420
38. Xu X, Yao W, Xiao D, Heinz TF (2014) Spin and pseudospins in layered transition metal dichalcogenides. Nat Phys 10:343
39. Zhao W, Ribeiro RM, Toh M, Carvalho A, Kloc C, Castro Neto AH et al (2013) Origin of indirect optical transitions in few-layer MoS_2, WS_2, and WSe_2. Nano Lett 13:5627–5634
40. Debbichi L, Eriksson O, Lebègue S (2014) Electronic structure of two-dimensional transition metal dichalcogenide bilayers from ab initio theory. Phys Rev B 89:205311
41. Liu GB, Xiao D, Yao Y, Xu X, Yao W (2015) Electronic structures and theoretical modelling of two-dimensional group-VIB transition metal dichalcogenides. Chem Soc Rev 44:2643–2663
42. Cao T, Wang G, Han W, Ye H, Zhu C, Shi J (2012) Valley-selective circular dichroism of monolayer molybdenum disulphide. Nat Commun 3:887
43. Kuc A, Heine T (2015) The electronic structure calculations of two-dimensional transition-metal dichalcogenides in the presence of external electric and magnetic fields. Chem Soc Rev 44:2603–2614

44. Kristian Sommer T (2017) Calculating excitons, plasmons, and quasiparticles in 2D materials and van der Waals heterostructures. 2D Mater 4:022004
45. Gong Z, Liu GB, Yu H, Xiao D, Cui X, Xu X, Yao W (2013) Magnetoelectric effects and valley-controlled spin quantum gates in transition metal dichalcogenide bilayers. Nat Commun 4:2053
46. Xiao D, Liu GB, Feng W, Xu X, Yao W (2012) Coupled spin and valley physics in monolayers of MoS_2 and other group-VI dichalcogenides. Phys Rev Lett 108:196802
47. Xiao D, Chang MC, Niu Q (2010) Berry phase effects on electronic properties. Rev Mod Phys 82:1959–2007
48. Yu H, Cui X, Xu X, Yao W (2015) Valley excitons in two-dimensional semiconductors. Natl Sci Rev 2:57–70
49. Schaibley JR, Yu H, Clark G, Rivera P, Ross JS, Seyler KL (2016) Valleytronics in 2D materials. Nat Rev Mater 1:16055
50. Feng W, Yao Y, Zhu W, Zhou J, Yao W, Xiao D (2012) Intrinsic spin Hall effect in monolayers of group-VI dichalcogenides: a first-principles study. Phys Rev B 86:165108
51. Gorbachev RV, Song JCW, Yu GL, Kretinin AV, Withers F, Cao Y (2014) Detecting topological currents in graphene superlattices. Science 346:448–451
52. Sui M, Chen G, Ma L, Shan WY, Tian D, Watanabe K et al (2015) Gate-tunable topological valley transport in bilayer graphene. Nat Phys 11:1027
53. Shimazaki Y, Yamamoto M, Borzenets IV, Watanabe K, Taniguchi T, Tarucha S (2015) Generation and detection of pure valley current by electrically induced Berry curvature in bilayer graphene. Nat Phys 11:1032
54. Mak KF, McGill KL, Park J, McEuen PL (2014) The valley Hall effect in MoS_2 transistors. Science 344:1489–1492
55. Lee J, Mak KF, Shan J (2016) Electrical control of the valley Hall effect in bilayer MoS_2 transistors. Nat Nanotechnol 11:421
56. Chang CH, Fan X, Lin SH, Kuo JL (2013) Orbital analysis of electronic structure and phonon dispersion in MoS_2, $MoSe_2$, WS_2, and WSe_2 monolayers under strain. Phys Rev B 88:195420
57. Lu P, Wu X, Guo W, Zeng XC (2012) Strain-dependent electronic and magnetic properties of MoS_2 monolayer, bilayer, nanoribbons and nanotubes. Phys Chem Chem Phys 14:13035–13040
58. Johari P, Shenoy VB (2012) Tuning the electronic properties of semiconducting transition metal dichalcogenides by applying mechanical strains. ACS Nano 6:5449–5456
59. Lv HY, Lu WJ, Shao DF, Lu HY, Sun YP (2016) Strain-induced enhancement in the thermoelectric performance of a ZrS_2 monolayer. J Mater Chem C 4:4538–4545
60. Liu Q, Li L, Li Y, Gao Z, Chen Z, Lu J (2012) Tuning electronic structure of bilayer MoS_2 by vertical electric field: a first-principles investigation. J Phys Chem C 116:21556–21562
61. Zibouche N, Philipsen P, Heine T, Kuc A (2014) Electron transport in MoWSeS monolayers in the presence of an external electric field. Phys Chem Chem Phys 16:11251–11255
62. Zibouche N, Philipsen P, Kuc A, Heine T (2014) Transition-metal dichalcogenide bilayers: switching materials for spintronic and valleytronic applications. Phys Rev B 90:125440
63. Ashcroft NW, Mermin ND (1976) Solid state physics. Saunders, Philadelphia
64. Kittel C (2004) Introduction to solid state physics, 8th edn. Wiley, USA
65. Bernardi M, Ataca C, Palummo M, Grossman Jeffrey C (2017) Optical and electronic properties of two-dimensional layered materials. Nanophotonics 6:479
66. Hüser F, Olsen T, Thygesen KS (2013) How dielectric screening in two-dimensional crystals affects the convergence of excited-state calculations: monolayer MoS_2. Phys Rev B 88:245309
67. Berkelbach TC, Hybertsen MS, Reichman DR (2013) Theory of neutral and charged excitons in monolayer transition metal dichalcogenides. Phys Rev B 88:045318
68. Cudazzo P, Tokatly IV, Rubio A (2011) Dielectric screening in two-dimensional insulators: Implications for excitonic and impurity states in graphane. Phys Rev B 84:085406
69. Wirtz L, Marini A, Rubio A (2006) Excitons in boron nitride nanotubes: dimensionality effects. Phys Rev Lett 96:126104

70. Komsa HP, Krasheninnikov AV (2012) Effects of confinement and environment on the electronic structure and exciton binding energy of MoS_2 from first principles. Phys Rev B 86:241201
71. Qiu DY, da Jornada FH, Louie SG (2013) Optical spectrum of MoS_2: many-body effects and diversity of exciton states. Phys Rev Lett 111:216805
72. Latini S, Olsen T, Thygesen KS (2015) Excitons in van der Waals heterostructures: the important role of dielectric screening. Phys Rev B 92:245123
73. Yang XL, Guo SH, Chan FT, Wong KW, Ching WY (1991) Analytic solution of a two-dimensional hydrogen atom. I. Nonrelativistic theory. Phys Rev A 43:1186–1196
74. Chernikov A, Berkelbach TC, Hill HM, Rigosi A, Li Y, Aslan OB et al (2014) Exciton binding energy and nonhydrogenic rydberg series in monolayer WS_2. Phys Rev Lett 113:076802
75. Tran MD, Kim JH, Lee YH (2016) Tailoring photoluminescence of monolayer transition metal dichalcogenides. Curr Appl Phys 16:1159–1174
76. Wang M, Li CM (2012) Excitonic properties of graphene-based materials. Nanoscale 4:1044–1050
77. Rohlfing M, Louie SG (2000) Electron-hole excitations and optical spectra from first principles. Phys Rev B 62:4927–4944
78. Fox M (2001) Optical properties of solids, 1st edn. Oxford University Press, New York
79. Beal AR, Knights JC, Liang WY (1972) Transmission spectra of some transition metal dichalcogenides. II. Group VIA: trigonal prismatic coordination. J Phys C Solid State Phys 5:3540
80. Zeng H, Cui X (2015) An optical spectroscopic study on two-dimensional group-VI transition metal dichalcogenides. Chem Soc Rev 44:2629–2642
81. Ramasubramaniam A (2012) Large excitonic effects in monolayers of molybdenum and tungsten dichalcogenides. Phys Rev B 86:115409
82. Sajjad M, Singh N, Schwingenschlögl U (2018) Strongly bound excitons in monolayer PtS_2 and $PtSe_2$. Appl Phys Lett 112:043101
83. Mak KF, He K, Lee C, Lee GH, Hone J, Heinz TF, Shan J (2013) Tightly bound trions in monolayer MoS_2. Nat Mater 12:207–211
84. Mak KF, Shan J (2016) Photonics and optoelectronics of 2D semiconductor transition metal dichalcogenides. Nat Photonics 10:216
85. Plechinger G, Nagler P, Arora A, Schmidt R, Chernikov A, del Águila AG et al (2016) Trion fine structure and coupled spin–valley dynamics in monolayer tungsten disulfide. Nat Commun 7:12715
86. Yu H, Liu GB, Gong P, Xu X, Yao W (2014) Dirac cones and Dirac saddle points of bright excitons in monolayer transition metal dichalcogenides. Nat Commun 5:3876
87. You Y, Zhang XX, Berkelbach TC, Hybertsen MS, Reichman DR, Heinz TF (2015) Observation of biexcitons in monolayer WSe_2. Nat Phys 11:477
88. Sie EJ, Frenzel AJ, Lee YH, Kong J, Gedik N (2015) Intervalley biexcitons and many-body effects in monolayer MoS_2. Phys Rev B 92:125417
89. Echeverry JP, Urbaszek B, Amand T, Marie X, Gerber IC (2016) Splitting between bright and dark excitons in transition metal dichalcogenide monolayers. Phys Rev B 93:121107
90. Zhang XX, You Y, Zhao SYF, Heinz TF (2015) Experimental evidence for dark excitons in monolayer WSe_2. Phys Rev Lett 115:257403
91. Arora A, Koperski M, Nogajewski K, Marcus J, Faugeras C, Potemski M (2015) Excitonic resonances in thin films of WSe_2: from monolayer to bulk material. Nanoscale 7:10421–10429
92. Arora A, Nogajewski K, Molas M, Koperski M, Potemski M (2015) Exciton band structure in layered $MoSe_2$: from a monolayer to the bulk limit. Nanoscale 7:20769–20775
93. Baranowski M, Surrente A, Maude DK, Ballottin M, Mitioglu AA, Christianen PCM et al (2017) Dark excitons and the elusive valley polarization in transition metal dichalcogenides. 2D Mater 4:025016
94. Yuan L, Wang T, Zhu T, Zhou M, Huang L (2017) Exciton dynamics, transport, and annihilation in atomically thin two-dimensional semiconductors. J Phys Chem Lett 8:3371–3379

95. Kormányos A, Burkard G, Gmitra M, Fabian J, Zólyomi V, Drummond ND et al (2015) k · p theory for two-dimensional transition metal dichalcogenide semiconductors. 2D Mater 2:022001
96. Molas MR, Faugeras C, Slobodeniuk AO, Nogajewski K, Bartos M, Basko DM, Potemski M (2017) Brightening of dark excitons in monolayers of semiconducting transition metal dichalcogenides. 2D Mater 4:021003
97. Mermin ND, Wagner H (1966) Absence of ferromagnetism or antiferromagnetism in one-or two-dimensional isotropic heisenberg models. Phys Rev Lett 17:1133–1136
98. Huang B, Clark G, Navarro-Moratalla E, Klein DR, Cheng R, Seyler KL et al (2017) Layer-dependent ferromagnetism in a van der Waals crystal down to the monolayer limit. Nature 546:270
99. Lin MW, Zhuang HL, Yan J, Ward TZ, Puretzky AA, Rouleau CM et al (2016) Ultrathin nanosheets of $CrSiTe_3$: a semiconducting two-dimensional ferromagnetic material. J Mater Chem C 4:315–322
100. Wildes AR, Simonet V, Ressouche E, McIntyre GJ, Avdeev M, Suard E et al (2015) Magnetic structure of the quasi-two-dimensional antiferromagnet $NiPS_3$. Phys Rev B 92:224408
101. Lebègue S, Björkman T, Klintenberg M, Nieminen RM, Eriksson O (2013) Two-dimensional materials from data filtering and ab initio calculations. Phys Rev X 3:031002
102. Han GH, Duong DL, Keum DH, Yun SJ, Lee YH (2018) van der Waals metallic transition metal dichalcogenides. Chem Rev 118:6297–6336
103. Ataca C, Şahin H, Ciraci S (2012) Stable, single-layer MX_2 transition-metal oxides and dichalcogenides in a honeycomb-like structure. J Phys Chem C 116:8983–8999
104. Cong X, Cheng C, Liao Y, Ye Y, Dong C, Sun H (2015) Intrinsic charge storage capability of transition metal dichalcogenides as pseudocapacitor electrodes. J Phys Chem C 119:20864–20870
105. Kan M, Adhikari S, Sun Q (2014) Ferromagnetism in MnX_2 (X = S, Se) monolayers. Phys Chem Chem Phys 16:4990–4994
106. Ma Y, Dai Y, Guo M, Niu C, Zhu Y, Huang B (2012) Evidence of the existence of magnetism in pristine VX_2 monolayers (X = S, Se) and their strain-induced tunable magnetic properties. ACS Nano 6:1695–1701
107. Gao D, Xue Q, Mao X, Wang W, Xu Q, Xue D (2013) Ferromagnetism in ultrathin VS_2 nanosheets. J Mater Chem C 1:5909–5916
108. Pan H (2014) Electronic and magnetic properties of vanadium dichalcogenides monolayers tuned by hydrogenation. J Phys Chem C 118:13248–13253
109. Lv HY, Lu WJ, Shao DF, Liu Y, Sun YP (2015) Strain-controlled switch between ferromagnetism and antiferromagnetism in 1T-CrX_2 (X = Se, Te) monolayers. Phys Rev B 92:214419
110. Wang C, Zhou X, Pan Y, Qiao J, Kong X, Kaun CC, Ji W (2018) Layer and doping tunable ferromagnetic order in two-dimensional CrS_2 layers. Phys Rev B 97:245409
111. Kudrnovský J, Turek I, Drchal V, Máca F, Weinberger P, Bruno P (2004) Exchange interactions in III–V and group-IV diluted magnetic semiconductors. Phys Rev B 69:115208
112. Máca F, Kudrnovský J, Drchal V, Bouzerar G (2008) Magnetism without magnetic impurities in ZrO_2 oxide. Appl Phys Lett 92:212503
113. Bonilla M, Kolekar S, Ma Y, Diaz HC, Kalappattil V, Das R, Eggers T, Gutierrez HR, Phan MH, Batzill M (2018) Strong room-temperature ferromagnetism in VSe_2 monolayers on van der Waals substrates. Nat Nanotechnol 13:289–293
114. Zhou Y, Wang Z, Yang P, Zu X, Yang L, Sun X, Gao F (2012) Tensile strain switched ferromagnetism in layered NbS_2 and $NbSe_2$. ACS Nano 6:9727–9736
115. Manchanda P, Sharma V, Yu H, Sellmyer DJ, Skomski R (2015) Magnetism of Ta dichalcogenide monolayers tuned by strain and hydrogenation. Appl Phys Lett 107:032402
116. Zheng H, Yang B, Wang D, Han R, Du X, Yan Y (2014) Tuning magnetism of monolayer MoS_2 by doping vacancy and applying strain. Appl Phys Lett 104:132403
117. Liu B, Wu LJ, Zhao YQ, Wang LZ, Cai MQ (2016) A first-principles study of magnetic variation via doping vacancy in monolayer VS_2. J Mag Mag Mat 420:218–224

118. Lin X, Ni J (2014) Charge and magnetic states of Mn-, Fe-, and Co-doped monolayer MoS_2. J Appl Phys 116:044311
119. Cheng YC, Zhu ZY, Mi WB, Guo ZB, Schwingenschlögl U (2013) Prediction of two-dimensional diluted magnetic semiconductors: doped monolayer MoS_2 systems. Phys Rev B 87:100401
120. Ataca C, Ciraci S (2011) Functionalization of single-layer MoS_2 honeycomb structures. J Phys Chem C 115:13303–13311
121. Yue Q, Chang S, Qin S, Li J (2013) Functionalization of monolayer MoS_2 by substitutional doping: a first-principles study. Phys Lett A 377:1362–1367
122. Priyanka M, Ralph S (2016) 2D transition-metal diselenides: phase segregation, electronic structure, and magnetism. J Phys Condens Matter 28:064002
123. Shu H, Luo P, Liang P, Cao D, Chen X (2015) Layer-dependent dopant stability and magnetic exchange coupling of iron-doped MoS_2 nanosheets. ACS Appl Mater Interfaces 7:7534–7541
124. Mishra R, Zhou W, Pennycook SJ, Pantelides ST, Idrobo JC (2013) Long-range ferromagnetic ordering in manganese-doped two-dimensional dichalcogenides. Phys Rev B 88(14):144409
125. He J, Wu K, Sa R, Li Q, Wei Y (2010) Magnetic properties of nonmetal atoms absorbed MoS_2 monolayers. Appl Phys Lett 96:082504

Chapter 6
Transition Metal Dichalcogenides for Energy Storage Applications

Liangxu Lin, Shaowei Zhang and Dan A. Allwood

Abstract Energy storage techniques based on supercapacitors and secondary batteries play important roles in the current energy fields. They all face some technical challenges which need to be addressed urgently to satisfy the increasing demand for modern clean energy technologies. In these electrochemical energy storage devices, two-dimensional monolayered transition metal dichalcogenides (2D TMDs) may play particular roles in improving many aspects of performances owing to their thin structure, large surface area, high surface tenability, and both "Faradaic" and "non-Faradaic" electrochemical behaviors. This chapter gives an overview of energy storage techniques based on conventional and newly developed supercapacitors and secondary batteries and discusses on how to engineer 2D TMDs to enable them to find promising applications in the area.

6.1 Introduction

Electrochemical energy storage devices, in particular supercapacitors and Li-ion batteries, are essential elements of modern energy technologies. They could be key to storing and delivering clean energy (e.g., solar and wind power), potentially enabling electronic devices and electric vehicles to have uninterruptible clean power supplies [1–3].

The increasing global challenges in energy, environment, and climate change mean that such energy storage techniques are vital for the sustainable development

L. Lin (✉)
University of Wollongong, Wollongong, AU 2522, Australia
e-mail: liangxu@uow.edu.au

Wuhan University of Science and Technology, Wuhan 430081, China

S. Zhang (✉)
University of Exeter, Exeter EX4 4QF, UK
e-mail: s.zhang@exeter.ac.uk

D. A. Allwood (✉)
The University of Sheffield, Sheffield S1 3JD, UK
e-mail: d.allwood@sheffield.ac.uk

N. S. Arul and V. D. Nithya (eds.), *Two Dimensional Transition Metal Dichalcogenides*,
https://doi.org/10.1007/978-981-13-9045-6_6

of our society. However, vehicles and power equipment nowadays still largely rely on non-renewable resources due to the lack of highly efficient energy storage and delivery technologies [1]. For example, the energy density of current supercapacitor is unsuitably low for long time operation, whereas the power density of the current secondary battery is not high enough to drive heavy-duty devices. How to design and develop novel electrode materials to store and deliver energy more efficiently has become one of the main challenges in the field of energy storage. Recent development has suggested that two-dimensional (2D) materials such as thin transition metal dichalcogenides (TMDs) could find promising applications in both supercapacitors and secondary batteries. This chapter introduces the current status of supercapacitors and secondary batteries (e.g., Li-ion battery) and discusses how thin TMDs could be engineered and used to improve the performance of these two types of energy storage device.

6.2 Supercapacitor

6.2.1 Current Status and Challenges

Electrochemical capacitors (supercapacitors) are electric energy storage devices which store and deliver energy at the electrolyte/electrode interface through reversible ion adsorption/desorption and redox reactions on the surface of the electrode material [4]. The former mainly involves pure ion adsorption/desorption, so is also called "double-layer capacitor" or "non-Faradaic capacitor", while the latter is named as "Faradaic capacitor" as a redox reaction is involved [4]. A "non-Faradaic capacitor" shows high power density, high safety, and an almost unlimited lifetime [2]. Correspondingly, the power density of a "Faradaic capacitor" is usually degenerated to a certain extent due to the slow redox reaction, but it could provide higher energy density by forming "pseudocapacitance" on the electrode surface [2].

Generally, the energy density (Wh kg^{-1}) of an electrical vehicle represents how far it can go, and the power density (W kg^{-1}, the power delivery efficiency) indicates how quickly it can speed up [2].

Compared with electrochemical secondary batteries (e.g., Li-ion batteries), supercapacitors have distinct advantages of high safety, rapid charge/discharge rates and an almost unlimited lifetime, showing much higher power delivery abilities (e.g., 100 kW kg^{-1} for many seconds) [2]. Nevertheless, even after decades of efforts, practical applications of supercapacitors are still largely limited by their unsuitably low energy densities (~several Wh kg^{-1}), which are far lower than those of secondary batteries (Fig. 6.1). In the early stage of supercapacitor research, electrode materials were mainly based on activated carbon in consideration of its low cost and chemical stability [4–8]. Although significant progresses have been made on tuning the pore size and improving the Brunauer–Emmett–Teller (BET) surface area of porous carbon, the capacitance (or the energy density) of these supercapacitors remained

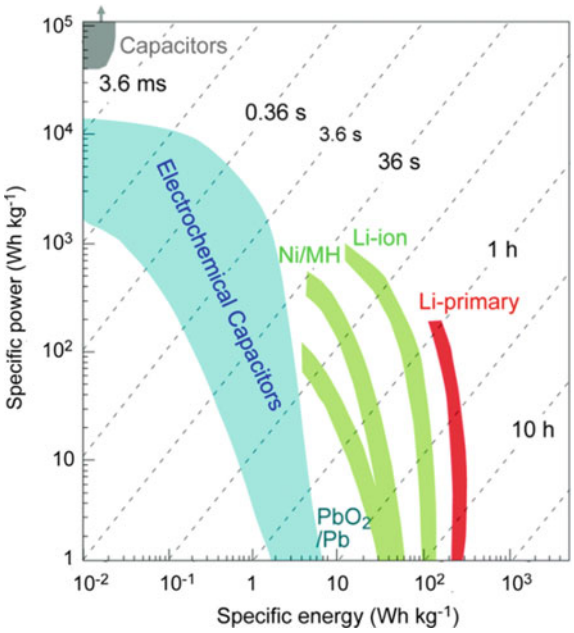

Fig. 6.1 Ragone plot showing specific power against specific energy. Times shown in the figure are the time constants determined by dividing the energy density by the power [2]. Copyright 2008. Reproduced with permission from Nature

unsatisfactory. For example, a supercapacitor based on activated carbon, with a pore size ranged from 2 to 5 nm and BET surface area up to 1000–2000 $m^2\ g^{-1}$, only had a specific capacitance of 100–120 F g^{-1} and related energy density of 3.47–4.17 Wh kg^{-1} with 1 V operation window [8]. Carbon nanotubes have also been used for supercapacitors, but their performance remained poor [9–11]. Researchers in this field therefore proposed to combine metal oxide nanoparticles and/or conducting polymer with activated carbon to improve the capacitance via the formation of near-surface "pseudocapacitance" ("Faradaic capacitance") [12, 13]. Unfortunately, such a kind of hybrid structure also led to considerable degeneration of power density and lifetime due to the following:

(1) Rapid charge transport became difficult without intimate contact between nanoparticles and carbon materials, sacrificing the ion transport channels, and decreasing the power density;
(2) The relatively thick (compared with atomically thin graphene) nanoparticles with poor electrical conductivity (e.g., 10^{-5}–10^{-6} S cm^{-1} in the case of manganese dioxide/MnO_2) [14] also increased the electron transport length and ion transport distance;
(3) The redox reaction only occurred on the topmost surface of the nanoparticles (if they were not small enough), meaning that most of the material was wasted, reducing energy capacity and increasing the cost. How to make an efficient supercapacitor electrode with high energy density and retain high power density and long lifetime has become a major issue.

In electrochemical reactions, the kinetics of electrode processes such as adsorption/desorption kinetics and mass transfer efficiencies dominate the performance of energy storage devices in many aspects. A high-performance supercapacitor requires an electrode with high electrical conductivity and large surface area. Activated and/or three-dimensional (3D) graphene developed recently could meet these criteria. In 3D graphene, the thin graphene wall could provide an ideal super short electron transport length/ion transport distance as well as high conductivity and large BET surface area, which could improve the energy density, power density, and lifetime of the supercapacitor. In a research work of Zhu et al. [15], activated graphene was prepared from conventional graphene oxide (GO) sheets, showing a BET surface area up to 3100 $m^2\ g^{-1}$, pore size range of 0.3–10 nm and a high electrical conductivity of 500 S cm^{-1}. A packed supercapacitor cell fabricated from these activated graphene materials exhibited power and energy densities of 75 kW kg^{-1} and 70 Wh kg^{-1}, respectively. This supercapacitor also showed a good durability/stability and retained 97% capacitance after 10,000 charge/discharge cycles. The preparation of 3D graphene has been improved significantly in recent years. For example, Zhang et al. [16] have prepared 3D graphene with N doping (doping ratio was up to 15.8 at.%) using the thermal annealing method (Fig. 6.2a). The 3D network was built by immersing a 3D interconnected and porous network structure into GO (Fig. 6.2b–c) suspension, followed by thermal annealing in Ar, XeF_2, and NH_3 gases step by step. This preparation has led to porous structure with N doping (Fig. 6.2d–e) and high capacity of 380 F g^{-1}. Although the energy density obtained from 3D graphene or activated graphene was very close to those of some lead–acid batteries [15], it was still considerably lower than those of current Li-ion batteries. To further improve the energy density of 3D graphene-based supercapacitor, several strategies have been proposed, including the old one using metal oxide nanoparticles. Nevertheless, such a hybrid structure is unsuitable for efficient electrochemical mass transfer due to the reasons discussed above.

6.2.2 Role of 2D TMDs in Supercapacitors

Like graphene, 2D TMDs are also thin materials (~1 nm thick, in the case of monolayer) with ideal super short electron transport length and small ion transport distance. Hybrid supercapacitors from graphene and other 2D materials show many advantages over their conventional counterparts, including:

- intimate contact between thin 2D materials and graphene ensures rapid charge transport between the materials;
- the entire 2D material participates in the electrochemical processes and contributes to both Faradaic and non-Faradaic capacitances, reducing considerably the materials' usage and improving the energy density;
- the thin structure of 2D material retains the small electron transport length and short ion transport distance of graphene, accelerating the charge/discharge rates;

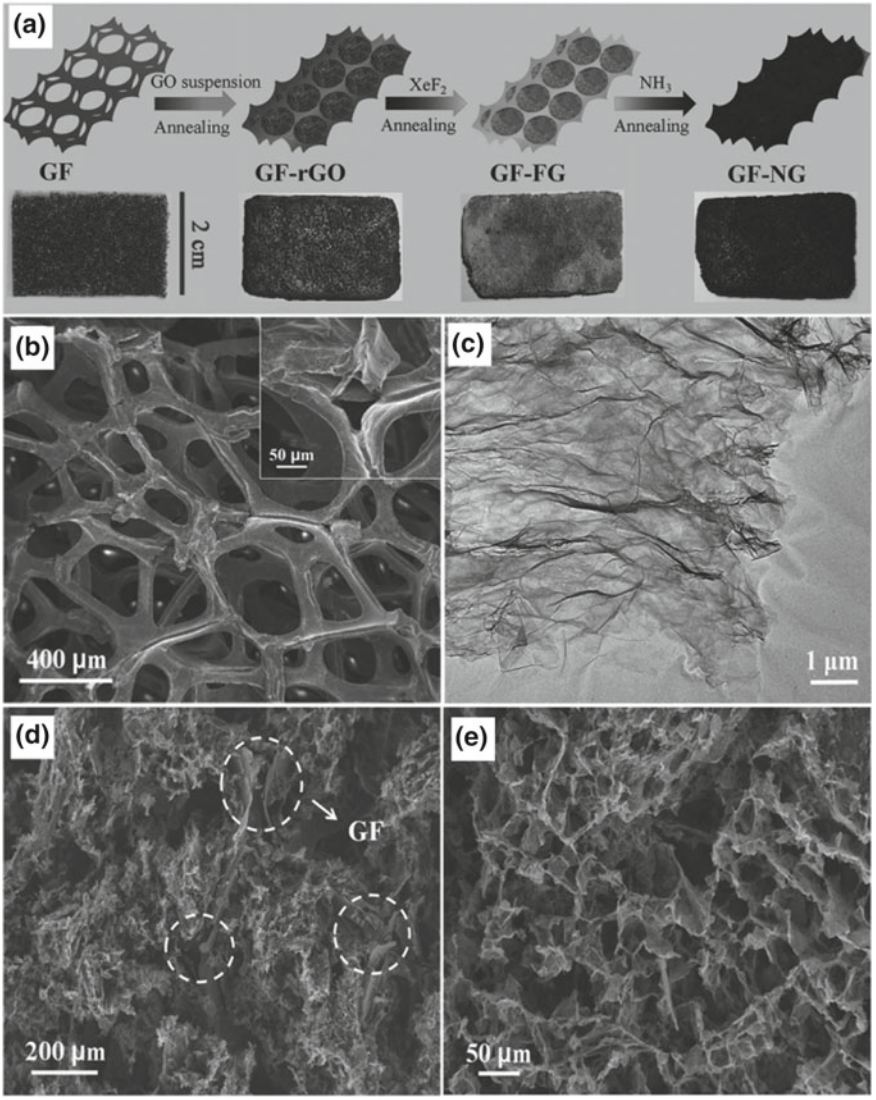

Fig. 6.2 **a** Schematic of the fabrication of the 3D graphene network, **b** SEM of 3D graphene framework (inset was high-resolution SEM image), **c** TEM image of GO, **d**, **e** low (**d**) and high-magnification cross-sectional SEM of the 3D graphene (**e**) [17]. Copyright 2017. Reproduced with the permission from Wiley-VCH Verlag GmbH

- the electrical conductivity of 2D materials is generally improved substantially from their bulk or nanoparticle counterparts, further enhancing the charge and discharge rates;
- the highly exposed surface of 2D materials allows them to be readily modified to further improve their electrochemical performances.

Supercapacitors based on 2D TMDs combine many features of both "non-Faradaic" and "Faradaic" capacitors. They could do energy storage/delivery through ion adsorption and desorption and also redox reactions on the surface with high energy density. Nevertheless, in comparison with some secondary batteries, this near-surface redox reaction is essentially different by avoiding the intercalation/extraction of the ions. As a result, the near-surface redox reaction provides a much higher efficiency in power delivery than in the case of a traditional battery.

Although the work on hybrid supercapacitors from 2D TMDs is still in its very early stage, the successful production of single- and multi-layered TMD sheets ensures their availability for future applications in supercapacitors. They could be engineered to have a very high specific surface area for surface redox reactions and ion adsorption/desorption processes. Even in few-layered TMDs, simple/quick ion intercalation and some special electrochemical properties (high reversibility, high rate, and capacitive mechanism) are highly expectable, which is totally different from the case with their micron-sized bulk counterparts. For example, a recently published research discovered interesting pseudocapacitance behavior of thin titanium disulfide (TiS_2) sheets (~50–270 nm, 2–10 layers) in Li^+ electrolyte [18]. The 2D TiS_2 had an interplanar spacing of ~5.7 Å and contained both 1T (Fig. 6.3a) and 2H phases (only existing in nanocrystal (NC) phase). The unit cell volume of 2D-TiS_2 was larger than that of bulk TiS_2 (B-TiS_2, Fig. 6.3b) in their pristine states. During the reversible Li^+ intercalation/extraction process, the 2D-TiS_2 exhibited a smaller *c*-axis lattice expansion (5.93 Å) as compared to B-TiS_2 (6.17 Å from pristine 5.66 Å) and did not show any significant crystallographic changes, which could directly extend the lifetime of the device and improve its safety during energy storage operations. Further studies suggested that the charge storage characteristics of 2D-TiS_2 were corresponding with the intercalation pseudocapacitance (Fig. 6.3c), resulting in both higher energy and power densities than in the case of B-TiS_2 (Fig. 6.3d). In 2D-TiS_2 NCs, the rate-limiting step for lithium-ion storage was also a quasi-2D process and similar to that of 2D surface adsorption reactions (much quicker than Li^+ intercalation/extraction process of conventional Li-ion batteries).

The above findings on few-layered TiS_2 suggest that 2D TMDs could be highly promising in supercapacitor applications, though the work on supercapacitors from pure 2D TMD monolayers is rather limited. This high application potential has also been confirmed by several studies on 2D TMD-like materials. As early as in 2007, Soon et al. discovered that thin edge-oriented molybdenum disulfide (MoS_2) film had comparable supercapacitor performance to that of carbon nanotube arrays [19]. A study by Cao et al. in 2013 [20] suggested that few-layered MoS_2 (Fig. 6.4a) actually had a theoretical capacity over that of graphite. Starting from few-layered MoS_2 sheets (Fig. 6.4a), they fabricated a micrometer-sized supercapacitor (Fig. 6.4b) and

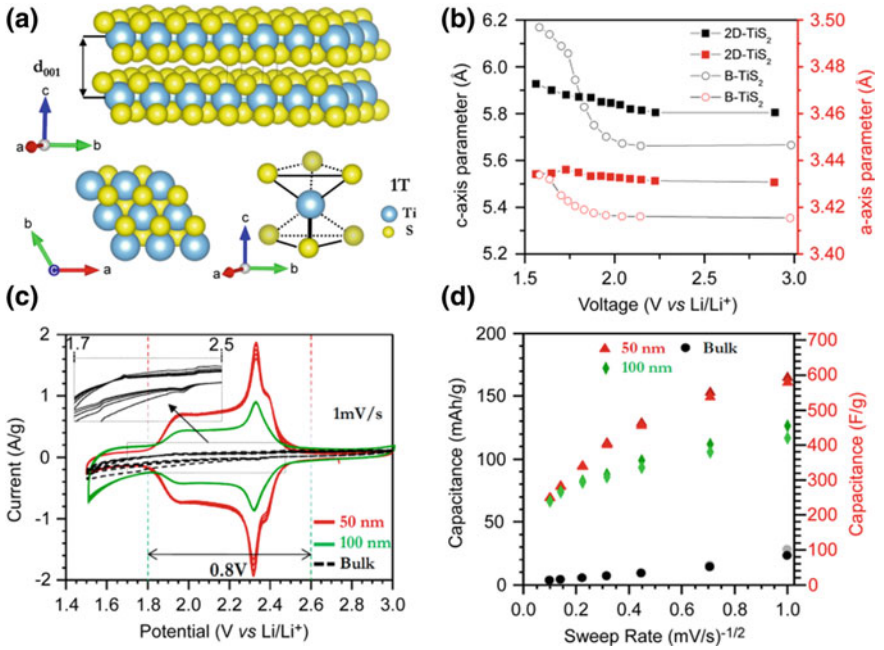

Fig. 6.3 **a** Crystalline structure of TiS_2, **b** In situ variations of the a-, and c-axis lattice parameters of lithium titanium sulfides with the potential during the first intercalation, **c** Cyclic voltammetry curves (CVs) at 1 mV s^{-1} in a Li^+ electrolyte for 2D-TiS_2 NCs, in comparison with the case of B-TiS_2, **d** Capacity versus $V^{-1/2}$ [18]. Copyright 2015. Reproduced with the permission from the American Chemical Society

demonstrated its very stable area and volumetric capacitances of 8 mF cm^{-2} and 178 F cm^{-3}, respectively. Such capacitances were evidently higher than those reported for many high-performance micro-supercapacitors, e.g., 0.5–3 mF cm^{-2} for onion-like carbon [21] and graphene-based micro-supercapacitors [22]. More recently prepared 2D 3R-MoS_2 thin film using a direct deposition technique [23] (Fig. 6.4c) and designed a high-performance film supercapacitor using the as-prepared thin 2D 3R-MoS_2 sheets (Fig. 6.4c), which showed a high capacitance of 330 F cm^{-3} and long lifetime (capacitance retention over 97% after 5000 charge and discharge cycles). The volumetric energy and power densities of this device were 1.6–2.4 mW h cm^{-3} (close to those of some Li-ion thin-film batteries, Fig. 6.4d) and 40–80 W cm^{-3} (over two orders higher than in the cases of using other thin materials such as transition metal carbides and/or nitrides/MXenes, Fig. 6.4d), respectively. These results suggested that thin MoS_2 could be a suitable and promising electrode material for high-efficiency supercapacitors.

Since energy storage requires a high electrical conductivity, 1T-MoS_2 has been considered a more promising electrode material. It is metallic and has electrical conductivity 10^7 times higher than that of the 1H/2H phase. Acerce et al. prepared

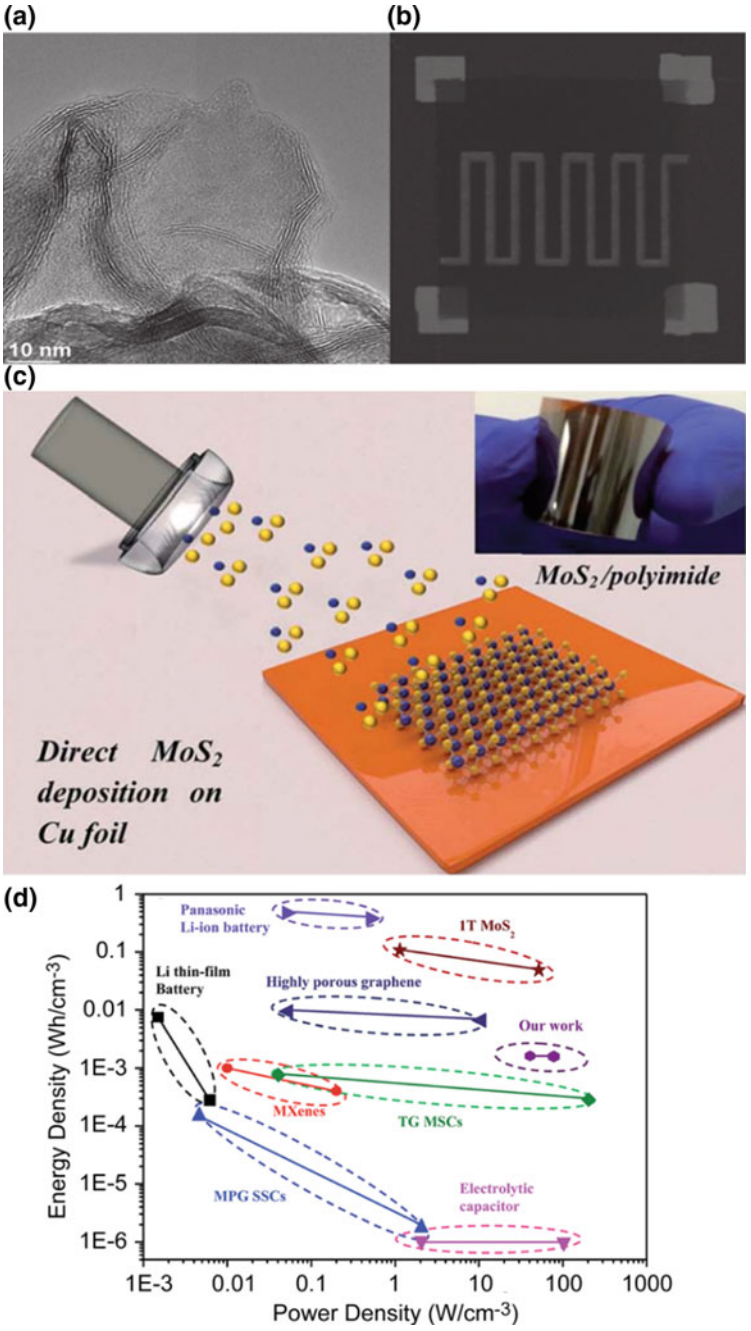
(a)
10 nm
(b)
(c)
MoS2/polyimide
Direct MoS2 deposition on Cu foil
(d)
Panasonic Li-ion battery
1T MoS2
Li thin-film Battery
Highly porous graphene
Our work
MXenes
TG MSCs
MPG SSCs
Electrolytic capacitor
Energy Density (Wh/cm-3)
Power Density (W/cm-3)
1
0.1
0.01
1E-3
1E-4
1E-5
1E-6
1E-3
0.01
0.1
1
10
100
1000

◀**Fig. 6.4** **a** HRTEM image of 2D MoS_2 nanosheets with 2–7 layers, **b** A photograph showing the MoS_2 film micro-supercapacitor [23]. Copyright 2013. Reproduced with permission from Wiley-VCH Verlag GmbH. **c** Direct deposition of a MoS_2 film on a substrate by sputtering, the inset showing thin 3R-MoS_2 film deposited on flexible polyimide substrate, **d** Ragone plot of the maximum energy and power densities from the commonly used power sources and a supercapacitor based on 2D 3R-MoS_2 sheets [24]. Copyright 2015. Reproduced with the permission from the Royal Society of Chemistry

monolayered 1T MoS_2 sheets (~70% phase ratio) via the chemical exfoliation of bulk 2H-MoS_2 powders (Fig. 6.5a) [25] and applied them onto a flexible polyimide substrate (Fig. 6.5b) with thickness up to 5 μm (Fig. 6.5c). Basic CV measurements of the electrode in various aqueous electrolytes (Fig. 6.5d) indicated that the specific gravimetric capacitance was almost 20 times as high as that in the case of using 2H-MoS_2 monolayers. The volumetric capacitances of the 1T-MoS_2 sheets ranged from 400 to 700 F cm^{-3}, significantly higher than those given above for few-layered 2H- and 3R-MoS_2 sheets. Apart from the high capacitance, 1T MoS_2 sheets were suitable for high-voltage operation in organic electrolytes (Fig. 6.5e) and exhibited over 5000 charge and discharge cycles with 95% capacitance retention. Acerce et al. [25] therefore concluded that the high performance of 1T-MoS_2 sheets in supercapacitor was mainly attributed to their hydrophilicity (water contact angle <30°) and high electrical conductivity (10–100 S cm^{-1}).

Based on the results described and discussed above, it could be considered that monolayered MoS_2 NCs should be a very interesting material for high-performance supercapacitors. Recently, Lin et al. reported the fabrication of monolayered 2H Mo-S NCs (~20 nm) with and without S-depletion [26, 27] (Fig. 6.6a, b). The NCs showed excellent electrocatalytic activity in the hydrogen evolution reaction and were also able to split water driven by solar lights. Such a performance was mainly attributed to the dramatically improved density of the active edge, a metallic surrounding region and a semiconducting core (Fig. 6.6c). The metallic feature was further enhanced upon suitable S-depletion on the surface. Combining S-depleted NCs with expanded graphene (EG) gave a double-layer capacitance of ~1.7 times as high as the sum of the NCs and EG (Fig. 6.6d). The metallic feature of the Mo-S NCs was revealed by density of state calculation. The metallic surrounding region means that the 2D Mo-S NCs may have similar high electrical conductivity to that of 2D 1T-MoS_2 for electrochemical processes. The hybrid structure from such NCs and graphene can be potentially used to develop high-performance supercapacitors. Unfortunately, only very limited work on small monolayered NCs has been carried out due to the technical difficulties in materials and device fabrication.

2D tungsten disulfide (WS_2) has also been used to make supercapacitors. As reported by Tu et al. [28], nanostructures based on 2D 2H-WS_2 sheets were formed via in situ anchoring on reduced graphene oxide (rGO). Although the high specific capacitance of 2508 F g^{-1} was achieved at a very slow scan rate of 1 mV s^{-1}, this work still confirmed the feasibility of hybrid structure of 2D TMDs and graphene in energy storage applications. Since 1T-WS_2 is metastable in most cases, the use of stable 2H-WS_2 is practically more feasible. Incorporating graphene to build a hybrid

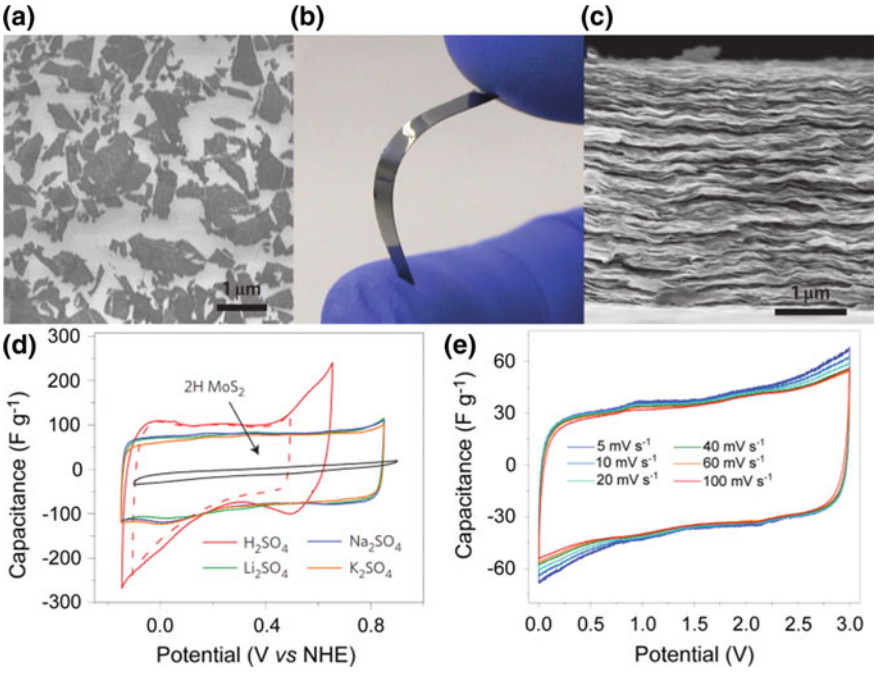

Fig. 6.5 **a** SEM image of monolayered 1T MoS_2, **b** A photograph showing the electrode composed of thick film of 1T MoS_2, **c** SEM side view of the electrode, **d** CV curves of MoS_2 in 0.5 M sulfate-based electrolyte solutions, **e** CV curves of 1T MoS_2 in 1 M TEA BF_4/MeCN electrolyte [22]. Copyright 2015. Reproduced with permission from Nature

supercapacitor should be a good strategy to avoid the re-stacking of 2D TMDs, which could retain the high electrical conductivity of the materials (re-stacking of 2D sheets such as 2H MoS_2 and WS_2 would significantly decrease the electrical conductivity [29]). A similar strategy was also used in recent work [30] to avoid the agglomeration and re-stacking of 2D TMDs. The fabricated composite was composed of 2D molybdenum selenide ($MoSe_2$) sheets, graphene, and nickel–cobalt sulfide ($CoNi_2S_4$), as illustrated in Fig. 6.7.

From CV curves, the maximum specific capacitance of the composite was calculated to be around 1141 F g^{-1} at 1 A g^{-1} rate with the three-electrode technique. Although this measurement technique sometimes is not as reliable as the two-electrode technique from the packed device (see the best practice method to determine the capacitance from Stoller et al. [31]), the demonstrated capacitance and cycle life (capacitance retention of 108% after 2000 cycles) were rather encouraging. Other 2D TMDs were also investigated for supercapacitors. For example, vanadium disulfide (VS_2), which unlike MoS_2 and WS_2, is metallic. This feature means that monolayered or few-layered VS_2 could offer great potentials as supercapacitors. As confirmed by Feng et al. in 2011, few-layered VS_2 nanosheets could be used to build a high-performance supercapacitor [32]. Such a supercapacitor had a specific capac-

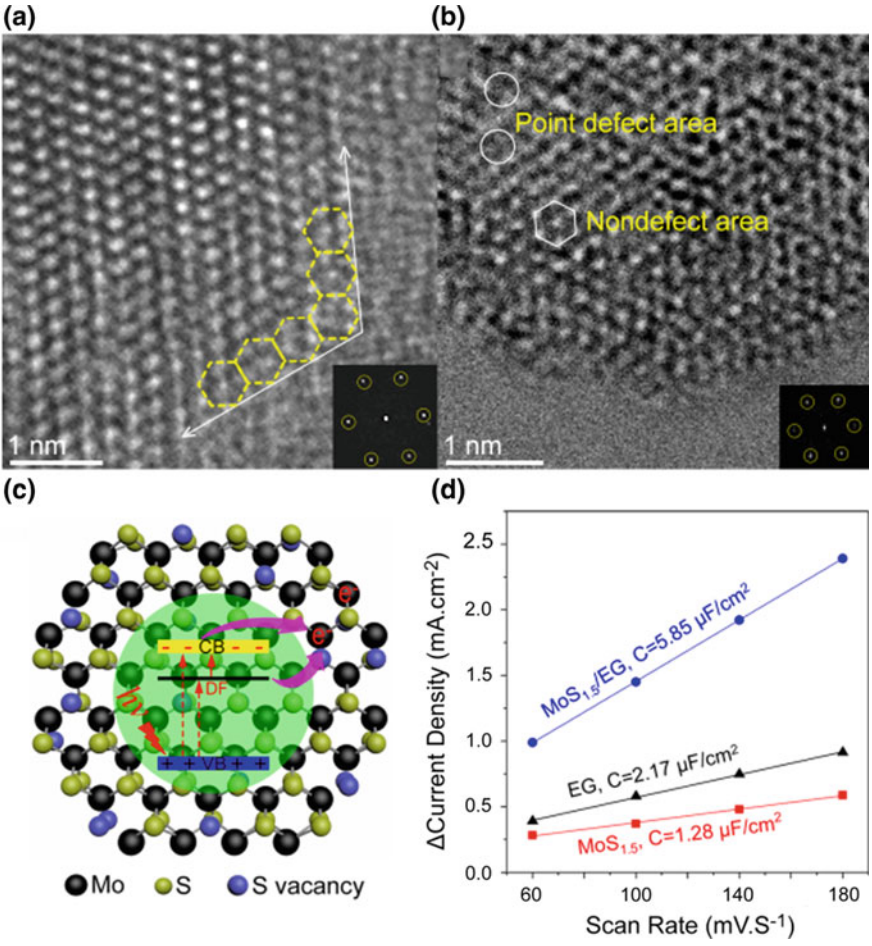

Fig. 6.6 **a** TEM image of an MoS_2 NC, **b** TEM image of an S-depleted Mo-S NC, **c** Schematic illustration of the metallic and semiconductor hybrid structure of Mo-S NC, **d** Double-layer capacitance of Mo-S NC before and after S-depletion, and S-depleted Mo-S NCs on EG [26, 27]. Copyright 2016, 2017. Reproduced with permission from the American Chemical Society and Elsevier

itance of 4760 μF cm^{-2} in a 150 nm in-plane configuration without degradation after 1000 charge/discharge cycles. Other TMDs such as thin CoS_2 [16] and WSe_2 [33] structures have also been explored for supercapacitors, but only limited work has been done on supercapacitors based on their 2D counterparts, especially that on monolayered TMDs required for the high-performance demonstration.

Unlike conventional forms of TMDs such as nanoparticles, 2D materials can be used effectively in flexible supercapacitors, which have already been comprehensively reviewed by several groups [34–37]. The flexible supercapacitors could be a composite of 2D TMDs, graphene, and conducting polymer (with/without a flexible

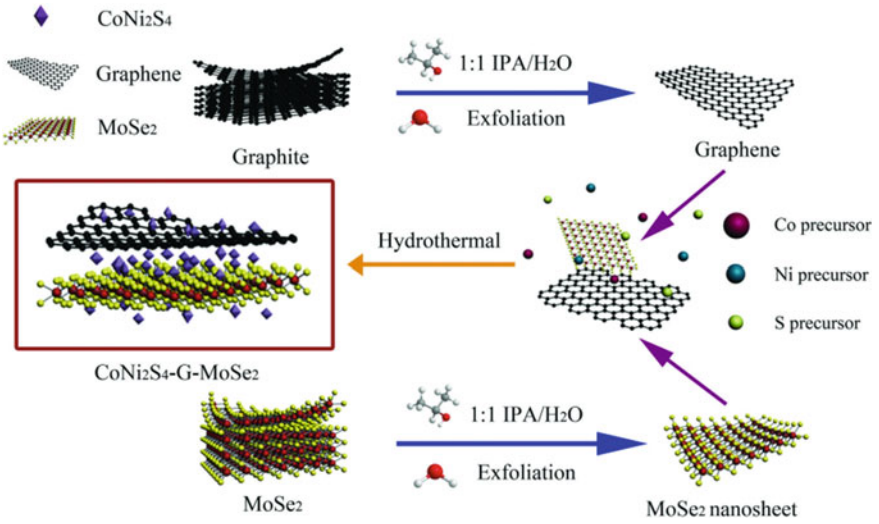

Fig. 6.7 Preparation of $CoNi_2S_4$-G-$MoSe_2$ nanocomposite for hybrid supercapacitors [30]. Copyright 2016. Reproduced with permission from Wiley-VCH Verlag GmbH

substrate). They were fundamentally demonstrated by Acerce et al., using highly electrically conductive 2D 1T-MoS_2 as the pure electrode material (Fig. 6.5) [22]. Another example of flexible supercapacitor was based on WS_2 nanosheets [38], in which a device with volumetric capacitance of 0.97 mW h cm^{-3} and 82% retention after 10,000 cycles was demonstrated. Nevertheless, for an industrially-relevant flexible supercapacitor, packing of the cell will need smart design on the device, especially when solid electrolytes and 3D printing techniques are involved. As mentioned earlier, the agglomeration of 2D TMDs could be avoided via building hybrid electrodes. This process would normally decrease the loading of the TMDs, weakening both area and volumetric capacitances. Although the 2D TMD has considerably higher power delivery capabilities than conventional Li-batteries, how to densely pack the composite without degenerating the energy density has become one of the main challenges. A smart idea to deal with this challenge could be the use of 3D graphene with appropriate pore sizes, which can hold dense 2D TMDs nanomaterials to retain super high area and volumetric capacitances. However, little demonstration work on such prototypes has been carried out.

In recent years, van der Waals heterostructures from pure 2D TMDs have also attracted a great deal of attention. The heterostructure is similar to that of 2D TMDs on graphene sheet described above. Figure 6.8a shows how the 2D building blocks assemble like Lego pieces [39]. The heterostructure could be fabricated via both mechanically assembled stacks and physical epitaxy/CVD approaches [40]. Previous investigations of this kind of heterostructure were more focused on electronic properties and band gap engineering, rather than on its energy storage applications. In a recent report by Pomerantseva et al., potential advantages of such 2D heterostruc-

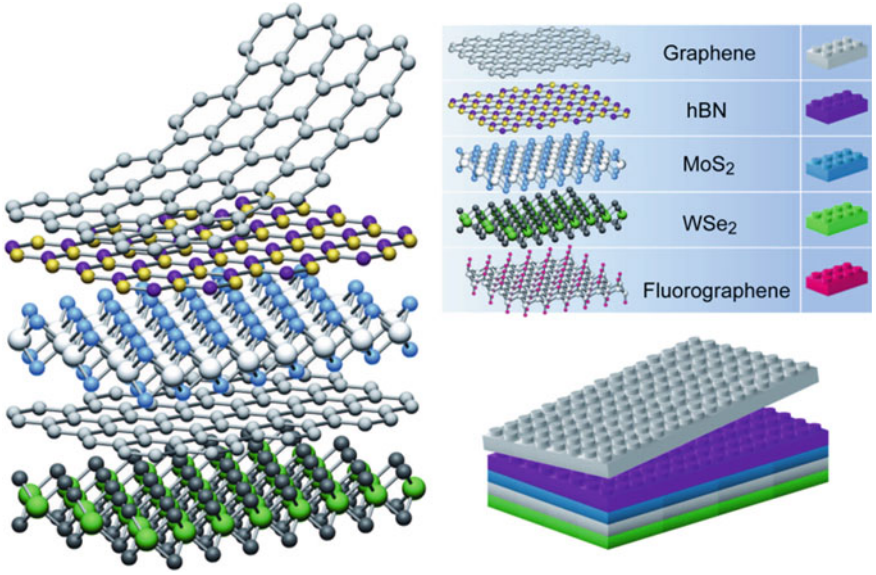

Fig. 6.8 Building van der Waals heterostructures analogous to Lego construction [39]. Reproduced with permission from Nature

tures for energy storage applications have been well identified [41]. As summarized in this report, individual 2D sheets may have both advantages and disadvantages in energy storage applications. For example, graphene has high electrical conductivity and mechanical strength, but the capacity is not sufficiently high due to the sole charge storage on the surface. Other 2D materials such as TMDs show high initial capacities but undergo a conversion reaction on the first discharge cycle, which gives poor capacity retention. Disadvantages of 2D TMDs in energy storage applications could be potentially avoided via building heterostructures with different 2D sheets (e.g., MXene and TMO/transition metal oxides). Pomerantseva et al. further proposed approaches to the construction of relevant heterostructures [41]. Although such heterostructures may potentially enable supercapacitors to have super high performance in many aspects (e.g., lifetime, energy, and power density), practical fabrication techniques and property examinations still have not been fully explored.

Despite the limited work on supercapacitors based on the strictly monolayered 2D TMD materials, the research highlighted above suggested that 2D TMDs could be very promising materials for building novel supercapacitors. The research also proposed several feasible strategies for design and construction of 2D TMD-based supercapacitors, i.e., improvement of electrical conductivity, formation of thin structures, hybrid structures to avoid the re-stacking of TMDs, and heterostructures from 2D TMDs. With further development in the fabrication techniques, next-generation high-performance supercapacitors based on 2D TMDs and other 2D materials could

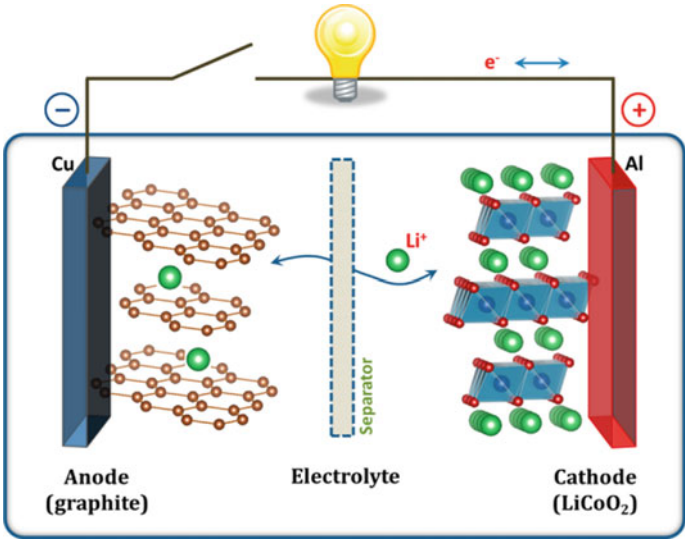

Fig. 6.9 Schematic illustration of the first Li-ion battery [42]. Reproduced with permission from the American Chemical Society

realistically be produced and used for energy storage, which would be a big step forward in the field.

6.3 Rechargeable Batteries

6.3.1 Current Status and Challenges

Rechargeable batteries are energy storage devices which store and deliver energy through reversible chemical reactions at both electrodes. A typical reversible chemical reaction involves displacement at solid anodes and insertion reactions at cathodes. Taking the first Li-ion battery as an example (Fig. 6.9), it uses a cathode on a copper current collector (positive electrode), an anode on an aluminum current collector (negative electrode), and an electrolyte made of lithium salt in an organic solvent. The charge process corresponds to the ions' flow from the cathode to the anode through the electrolyte and a separator. The reversed process is named as discharge, which corresponds to the ions' flow from the anode to the cathode. During the discharge process, the anode undergoes an oxidation reaction (losing electrons) and the cathode undergoes a reduction reaction (gaining electrons). These chemical reactions mean that rechargeable batteries generally have much higher energy density but lower power density (energy delivery efficiency) than those of supercapacitors (Fig. 6.1).

Like supercapacitors, rechargeable batteries also play important roles in the energy applications because of their recharging ability and mobility. The most commonly used rechargeable batteries include lead acid, NiCd, NiMH, and Li-ion batteries (Table 6.1, comparison of portable batteries, Battery University). Among them, Li-ion batteries exhibit many advantages such as high energy density, very low toxicity, high Coulombic efficiency, and maintenance-free operation. Although other types of battery such as those based on sodium-ions have been proposed in recent years in response to the resource depletion issue of Li, their energy density values are well below those of currently used Li-ion batteries. To date, various types of Li-ion batteries have been developed, and they all have one common characteristic of "lithium-ion". Most Li-ion batteries consist of a carbon/graphite anode and a metal oxide cathode. Although Li-ion batteries are more expensive than other secondary batteries, their high cycle life and low maintenance actually reduce the total cost per cycle (Table 6.1). They are considered to be much suitable to replace many applications previously served by lead and nickel-based batteries and are the most popular energy storage devices in current portable electrical devices. Nevertheless, for safety control, Li-ion batteries need to have a protection circuit. This risk arises from the undesirable dendrites formed on the anode, which penetrate the separator and cause electrical shorting, the melting of lithium and thermal runaway.

Li-ion batteries have led to great changes in our daily life (e.g., in mobile phones and laptops), but such energy storage techniques still need considerable improvements. Future energy storage system need to have longer cycle lives, smaller devices, and higher energy densities. Currently, the achievement of high energy capacity (e.g., >3.0 Ah) with portable Li-ion batteries largely relies on smart cell engineering, i.e., creating numerous cell units in a device or a large volume. Modifications of the active materials via size and morphology control have also been attempted, but this strategy has nearly reached its limits [42].

Although Li-ion batteries with over 30,000 safe charge/discharge cycles at an acceptable rate have been demonstrated [44], the achievement of larger energy density is still challenging. As is well known, in an individual battery cell, the output current I and the operating time Δt can be increased by improving the electrode area (e.g., the surface area of active electrode materials) and the power $P = IV$ (V is the potential or voltage). The energy density is highly dependent on the open-circuit voltage (OCV) of a cell. Increasing the voltage would be a good way to further improve the energy density, but it is technically difficult. As illustrated in Fig. 6.10, the operating window of the electrolyte is the energy gap between the lowest unoccupied molecular orbit (LUMO) and highest occupied molecular orbit (HOMO) of a liquid electrolyte (or the gap between the bottom of the conduction band/CB and the top of the valence band/VB of a solid electrolyte). Electrochemical potentials of the anode (μ_A) above the LUMO and electrochemical potentials of the cathode (μ_c) below the HOMO both reduce the electrolyte unless the electrode–electrolyte reactions are blocked by a passivating solid-electrolyte interphase (SEI). The SEI causes an irreversible loss of the capacity, which is unfavorable for the fabrication of batteries with a long lifetime. Approaches have also been developed to modify the electrochemical potentials of both anode and cathode, resulting in the improved window for higher

Table 6.1 Comparison of various rechargeable batteries [43]

Specifications	Lead acid	NiCd	NiMH	Li-ion		
				Cobalt	Manganese	Phosphate
Specific energy (Wh/kg)	30–50	45–80	60–120	150–250	100–150	90–120
Internal resistance	Very low	Very low	Low	Medium	Low	Very low
Cycle life	200–300	1000	300–500	500–1000	500–1000	1000–2000
Charge time	8–16 h	1–2 h	2–4 h	2–4 h	1–2 h	1–2 h
Charge temperature (°C)	−20 to 50	0–45				
Discharge temperature (°C)	−20 to 50	−20 to 65		−20 to 60		
Maintenance requirement	3–6 months	Every 90 days in full use		Maintenance-free		
Safety requirements	Thermally stable	Thermally stable, fuse protection		Mandatory protection circuit		
In use since	Late 1980s	1950	1990	1991	1996	1999
Toxicity	Very high	Very high	Low	Low		
Coulombic efficiency (%)	~90	~70–90		99		
Cost	Low	Moderate		High		

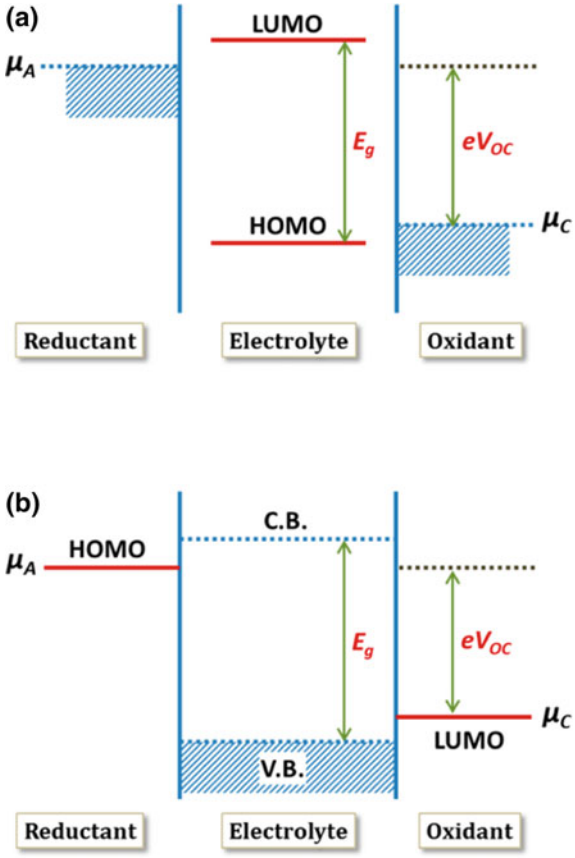

Fig. 6.10 Relative energies of the electrolyte window E_g and the electrode electrochemical potentials μ_A and μ_c ($LiCoO_2$) without electrode/electrolyte reaction: **a** liquid electrolyte with solid electrodes; **b** solid electrolyte with liquid or gaseous reactants [42]. Reproduced with permission from the American Chemical Society

energy density. Nevertheless, little work on these high-voltage electrode materials has been reported because the organic liquid carbonate electrolytes are normally unstable at a voltage > 5 V. Furthermore, since chemical reactions are usually involved in the charge/discharge processes of electrochemical secondary batteries, cycle life and power density are significantly inferior to those of supercapacitors. It is still a big challenge to develop feasible strategies to retain the cycle life at an acceptable rate in a safe and affordable battery with much larger energy density.

6.3.2 Role of 2D TMDs in Rechargeable Batteries

2D materials such as TMDs also have great application potential in secondary batteries, particularly in Li- and Na-ion batteries. A good example of this is TiS_2 sheets, which have been previously explored for supercapacitors (Fig. 6.3a). TiS_2

sheets exhibit several ideal features that are useful for high-performance Li-ion batteries: (1) no significant volume change on Li-ion intercalation/extraction; (2) energy and power densities higher than those of their conventional bulk counterparts; (3) in nano-phases, the Li-ion intercalation/extraction process is rapid, which is totally different from the slow process commonly involved with the charge/discharge of conventional Li-ion batteries. These discoveries suggest that 2D TMDs could play some particular roles in improving many aspects of Li-ion batteries, such as energy/power density, cycle lifetime, and safety issue. For example, graphite (negative electrode) has only a theoretical capacity of 372 mA h g^{-1}, but MoS_2 sheets could have one over 1000 mAh g^{-1} [45]. A theoretical investigation predicted that 1T-MoS_2 monolayers possess comparable Li storage capacity and diffusion kinetics to those of $LiFePO_4$ [46].

Recent experimental achievements on 2D TMDs have further revealed their great application potential in Li-ion batteries. In most cases, the batteries tested were based on 3D hybrid structures from graphene in consideration of its high surface area and efficient charge transportation. For example, thin MoS_2 layers were formed on 3D graphene via a commonly used CVD technique [23]. Using this hybrid structured material as the anode, Cao et al. fabricated a Li-ion battery which showed high capacities of 877 and 665 mAh g^{-1} in the first 50 cycles at current densities of 100 and 500 mA g^{-1}, respectively. The packed battery also exhibited excellent high current density performance of 466 mAh g^{-1} at a high current density of 4 A g^{-1}. Similar hybrid structured materials also have been produced by other groups. In 2015, Zhou et al. [47] prepared few-layered ($\leq$5 layers) MoS_2 on 3D carbon nanosheets (Fig. 6.11a, b). They demonstrated a specific capacity of 709 mAh g^{-1} at 2A g^{-1} and 95.2% retention after over 500 deep charge/discharge cycles. Such a high performance was attributed to the following: (1) the highly flexible carbon nanosheets prevented the 2D MoS_2 from peeling off; (2) the well-crystallized MoS_2 coupled with carbon nanosheets and enabled fast and stable transport of both electrons and ions across the interface especially in high-rate charge/discharge cycling processes. More recently, Jiang et al. [48] proposed and fabricated robust 3D porous architectures from interconnected monolayered MoS_2-graphene hybrid nanosheets (Fig. 6.11c, d). The 3D composite showed a large reversible capacity (up to 1200 mAh g^{-1}, at the scan rate of 100 mA g^{-1}), a good cycling stability (95% retention after 200 cycles), and a high-rate performance (436 mAh g^{-1} at the scan rate of 2 A g^{-1}), making it a very promising candidate for advanced anode materials for lithium-ion batteries [48].

Other 2D TMDs have also been investigated for use in Li-ion batteries. VS_2 is a typical example because it has metallic features, providing great potential into the enhancement of power densities of the batteries. A theoretical modeling study carried out in 2013 [49] predicted that VS_2 monolayers can be utilized as a promising anode material for Li-ion batteries with high energy density up to 466 mAh g^{-1}. Such thin VS_2 sheets could lead to fast charge/discharge rates with low Li diffusion barrier, which is similar to that in the case of MoS_2 or graphite. By introducing graphene to form a VS_2/graphene heterostructure, the capacity can be further increased to 569 mAh g^{-1}. In this heterostructure, the diffusion barrier is considerably lower than that in the case of bulk VS_2 and comparable to that of graphitic anode (~0.2 eV)

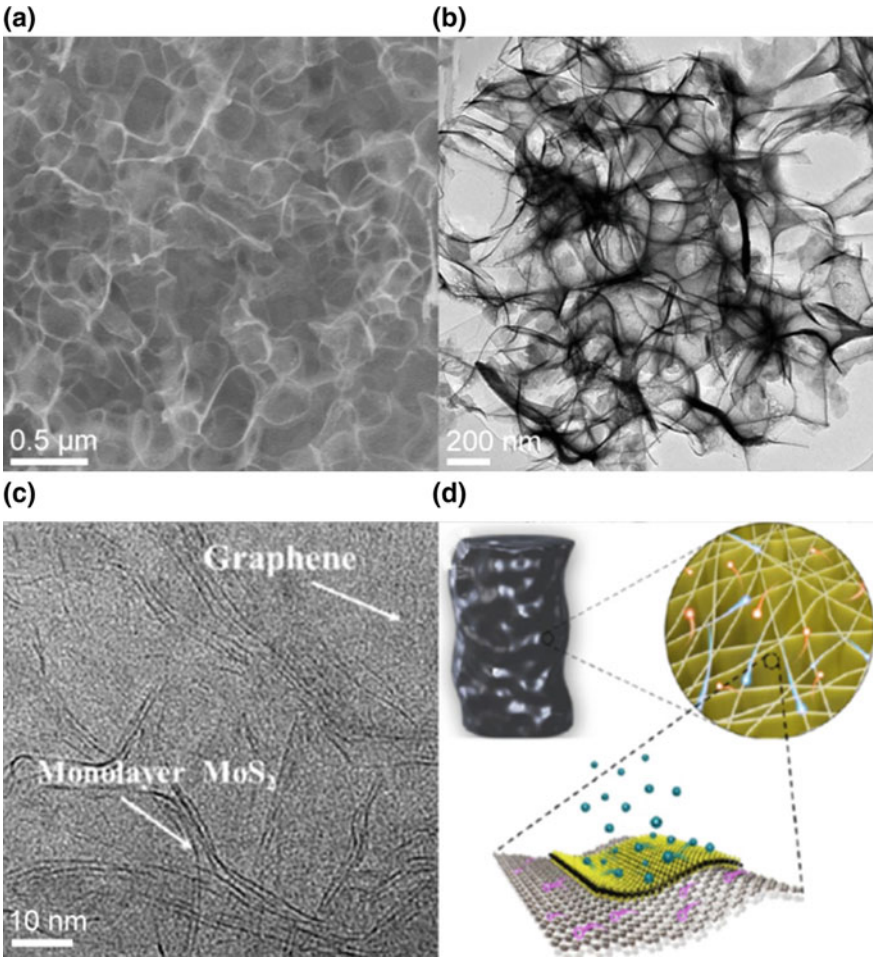

Fig. 6.11 **a**–**b** TEM images of few-layered MoS_2 anchored on 3D carbon nanosheets [47]. Copyright 2015. Reproduced with permission from the American Chemical Society. **c** High magnification TEM image of MoS_2-graphene hybrid nanosheets, **d** A diagram showing the 3D porous architectures with building blocks of MoS_2/graphene hybrid nanosheets [48]. Reproduced with permission from the American Chemical Society

[50]. Actually, VS_2 monolayers could have much higher theoretical energy density. Recent calculations [51] predict that a VS_2 monolayer could adsorb three layers of Li, two layers of Mg, one layer of K and 1/9 layer of Al on each of its sides. The multi-layer adsorptions of VS_2 monolayers increase the theoretical capacities to 1397, 1863, 466, and 78 mAh g^{-1} for Li, Mg, K, and Al ion storage, respectively. Although only limited experimental work on 2D VS_2 for Li-ion battery applications has been carried out, the reported results so far have confirmed that 2D VS_2 is indeed a very promising material for Li-ion batteries, as predicted by previous theoretical

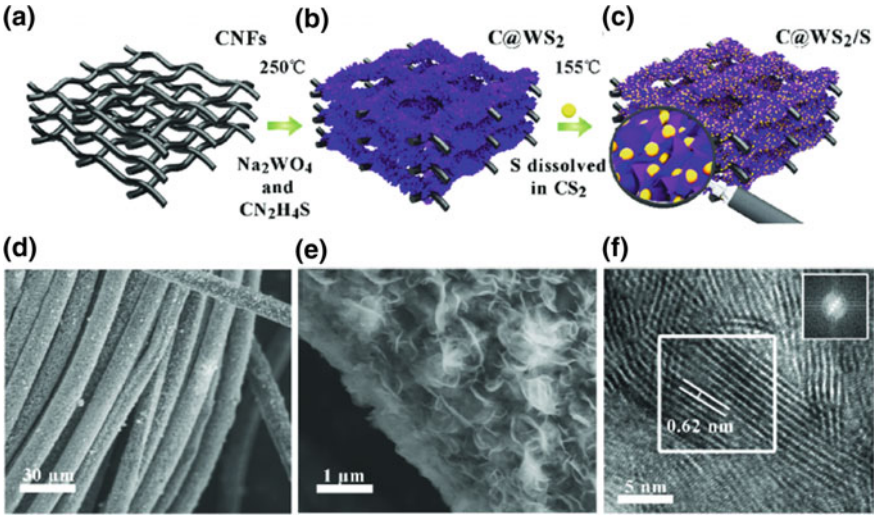

Fig. 6.12 **a–c** Schematic illustration of WS_2 sheets vertically aligned on CNFs and loading of S using hydrothermal deposition, **d–f** SEM and TEM images of C@WS_2/S material [54]. Reproduced with permission from Wiley-VCH Verlag GmbH

calculations. For example, Cai et al. [52] fabricated an all-solid-state lithium battery from VS_2 nanosheets and demonstrated the capacity of 532.2 mAh g^{-1} at the current density of 50 mA g^{-1}. This capacity is already higher than the early prediction (466 mAh g^{-1}) [48], despite the fact that the VS_2 nanosheets tested were still not thin enough (with a thickness of 50 nm).

2D WS_2 sheets also lead to high energy density when used in Li-ion batteries. In a recent report [53], WS_2 nanosheets were deposited on carbon nanofibers (CNFs) and then incorporated with S to form a hybrid material of C@WS_2/S (see schematic illustration in Fig. 6.12a–c). As seen from SEM and TEM images, the CNFs exhibited coarse surface composed of many WS_2 nanosheets (about 10 layers, up to 1 μm in size, Fig. 6.12d–f). The composite was evaluated for Li-S battery application. It showed a high specific capacity of 502 mAh g^{-1} at a charge/discharge rate of 2C (2A s^{-1}). It was also stable for long cycling uses, retaining 90% capacity after 1500 cycles. The high capacity may be partially contributed by the enriched S in the composite. In addition, the high capacity in the case of using 2D WS_2 has been further demonstrated by a quite recent study [53], in which 2D WS_2 nanosheets were fabricated on CNTs and used as the anode material. Li-ion batteries fabricated by using them showed high capacities of 1000 and 688.3 mAh g^{-1} at current densities of 0.1 and 1 A g^{-1}, respectively.

Apart from thin MoS_2, VS_2, and WS_2 materials described above, other 2D TMDs have been attempted for Li-ion battery applications [55]. Nevertheless, theoretical studies still need to be carried out to explore them further, in particular, when more complex chemical compositions (e.g., with doping and defects) are involved. For

example, in the case of $MnSbS_4$ monolayers, although they are not pure TMDs, they still can be considered as Mn-doped TMDs. Theoretical calculations predict that such monolayers could lead to very high capacity up to 879 mAh g^{-1} in the cases of Li, Na, and Mg ion storage. It is expected that similar TMDs doped with other transition metals also will be explored for further performance improvements required by future high-efficiency energy storage.

In consideration of the resource depletion issue with Li, researchers have also attempted to use other types of ions such as Na to replace Li. In 2015, Yang et al. systematically investigated several types of TMD monolayers used as the anode of a sodium ion battery [56]. At the average voltage and capacity, TMDs based on Ti, Zr, Nb, and Mo were suitable for the anodes of sodium ion batteries with voltages of 0.49–0.95 V and theoretical capacities of 260–339 mA h g^{-1} (Fig. 6.13a). The results indicated that 2D TiS_2 and NbS_2 were highly promising in high-power Na-ion batteries, with small ion migration barriers of 0.22 and 0.07 eV, respectively. Similarly, high OCV of VS_2 monolayers was also calculated by other researchers [57]. Apart from the theoretical calculations, several experimental studies on the Na storage based on thin VS_2 sheets have been reported recently. They all demonstrated the high capacitance of 2D VS_2, which matched with that predicted by the theoretical calculations. For example, layer-by-layer stacked VS_2 nanosheets (thickness around 20 nm, Fig. 6.13b) had capacity values of 250 and 150 mAh g^{-1} at 0.2 and 20 A g^{-1}, respectively [58]. Hierarchical flower-like nanomaterials composed of VS_2 nanosheets (Fig. 6.13c) exhibited capacitances of around 600 and 277 mAh g^{-1} at 0.1 and 20 A g^{-1}, respectively [59]. These high capacitances were partially contributed by the intercalation pseudocapacitance. 2D VS_2 with a few stacked layers (e.g., <5 layers) might perform even better, increasing further the power density. Unfortunately, a little work has been done so far in this and other aspects.

As predicted (Fig. 6.13a), 2D TiS_2 should also have a high capacitance in Na storage. According to a recent research [60], 2D TiS_2 showed a highly stable cycling performance, but its capacity (~146 mAh g^{-1}) was far lower than that predicted. Considerable experimental work still needs to be carried out to achieve the high performance of 2D TiS_2. 2D MoS_2, however, performed differently. In 2014, the stable Na charge capacity of 230 mAh g^{-1} with high Coulombic efficiency (~99%) was demonstrated based on 2D MoS_2. These values were already close to those predicted (Fig. 6.13a). The composite electrode tested consisted of reduced GO and chemically exfoliated few-layered MoS_2 sheets [61]. In a study by Yang et al., a high capacity around 500 mAh g^{-1} was achieved at the current density of 0.1 A g^{-1}, by forming directly the composite of few-layered MoS_2 nanosheets (<10 layers, ~15 nm) and carbon conductors [62]. In this work, a similar Na storage capacity (~500 mAh g^{-1}) was also demonstrated in the case of using few-layered $MoSe_2$ nanosheets to replace the few-layered MoS_2 nanosheets. The capacity can be further enhanced to >600 mAh g^{-1} by forming a hybrid structure with $MoSe_2$ vertically aligned on the MoS_2 nanosheets [62].

Similarly, a high performance of $MoSe_2$ nanosheets was attributed to more exposed active sites. This strategy was also used to build Na-ion batteries from 2D SnS_2. In a research by Chao et al. [63], a 3D graphene foam substrate was prepared

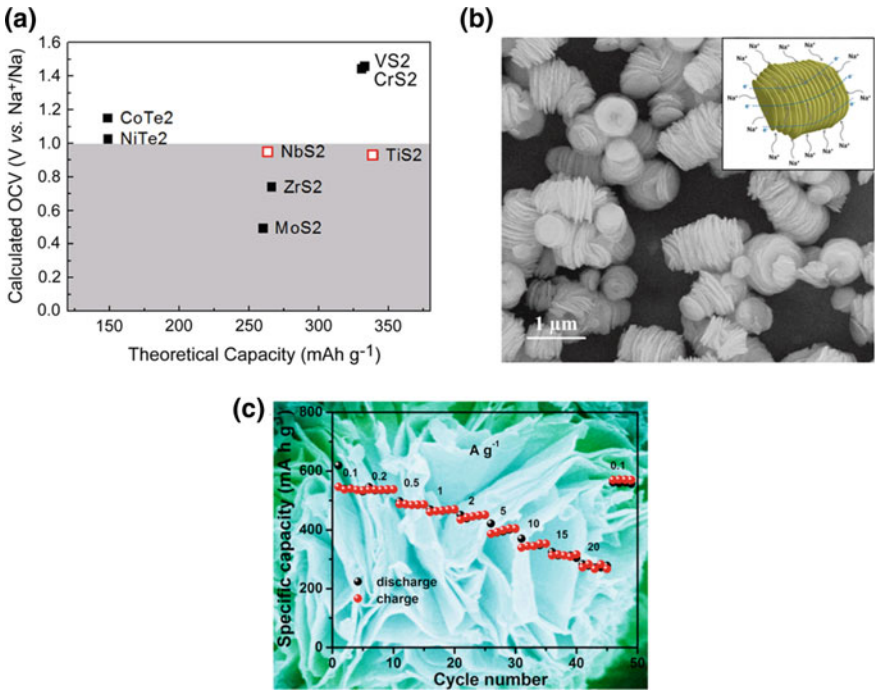

Fig. 6.13 **a** Calculated average OCV values of different TMD monolayers (The desirable voltage for a sodium anode ranges from 0.0 to 1.0 V) [56]. Copyright 2017. Reproduced with permission from the American Chemical Society. **b** SEM image of layer-by-layer stacked VS_2 nanosheets (the inset is a schematic of Na^+ intercalation and charge transportation) [58]. Copyright 2017. Reproduced with permission from Elsevier. **c** SEM image of hierarchical flower-like nanomaterials composed of VS_2 nanosheets (the inset shows the rate capability at various current densities, the scale bar of the full image length is around 10 μm) [59]. Copyright 2018. Reproduced with permission from Elsevier

using a CVD method. Then, 2D self-branched SnS_2 nanoarrays were synthesized and aligned vertically on the 3D graphene using a facile hot bath in-processing intervention method (Fig. 6.14a). The size and density of SnS_2 nanoarrays can be well controlled by adjusting the reaction parameters (Fig. 6.14b–e). SEM observations on the surface of the 3D graphene revealed the dense arrays of 2D self-branched SnS_2 nanoarrays comprising big nanoflake cores and small nanosheet branches (Fig. 6.14b–e) having respectively 12 and four layers of SnS_2. Thanks to the highly exposed unsaturated S-edges of the nanoarrays, the 2D SnS_2 on the 3D graphene exhibited very high performance in Na storage. Specifically, capacities of 900 and 400 mAh g^{-1} were achieved with current densities of 0.2 and 10 A g^{-1}, respectively. The first-principle calculations further revealed that the exposed S-edges provided feasible active sites for Na absorption with lower edge formation energy. The fast Na^+ storage was mainly attributed to the alloying-based reaction which has a theoretical capacity of 1136 mAh g^{-1} [63].

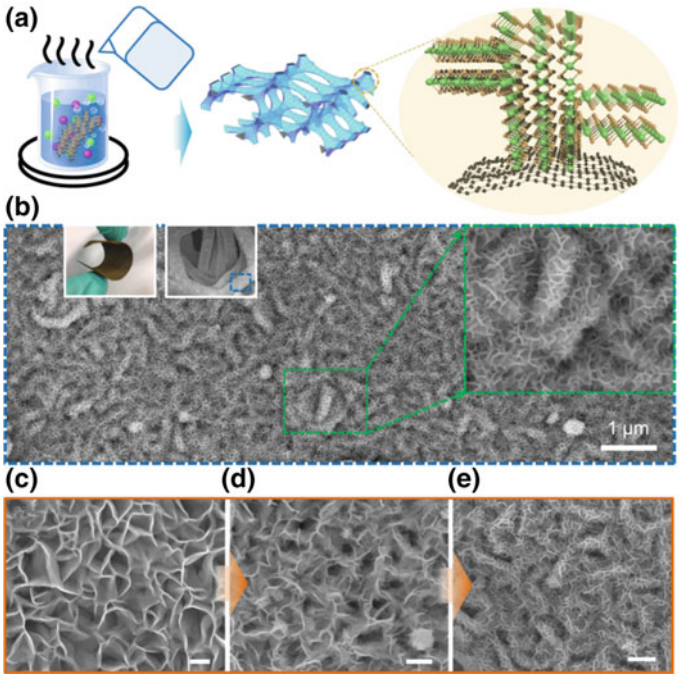

Fig. 6.14 **a** Schematics of fabricated 2D self-branched SnS_2 nanoarrays on 3D graphene, **b** SEM image of 2D self-branched SnS_2 nanoarrays on 3D graphene (the insets are a photograph and SEM images at different magnifications, **c–e** SEM image (scale bar of 200 nm) of SnS_2 nanoarrays prepared under different conditions [54]. Copyright 2017. Reproduced with permission from Wiley-VCH Verlag GmbH

Apart from using vertically aligned 2D TMDs, another novel strategy of building van der Waals heterostructures of 2D materials, has been proposed to improve the performance in secondary battery applications (Fig. 6.8). With this strategy, various 2D materials are combined together to break through the limitations of single-material systems. For example, by combining blue phosphorene (P) with 2D NbS_2 or TaS_2 to form van der Waals heterostructures, both structural stability and capacity can be improved significantly (Fig. 6.15a). Specifically, the capacity of blue P/NbS_2 was calculated to be as high as ~528.26 mAh g^{-1} which is much higher than that (485.31 mAh g^{-1}) in the case of using heterostructured black P/graphene material [64]. Furthermore, the formation of such a heterostructure also reduced Young's modulus of the material, making it more useful in flexible energy storage devices.

On nanoscale, the edge defect and the enhanced energy gap would reduce the electrical conductivity of 2D TMDs. The electrical conductivity between layers of some 2D TMDs, such as MoS_2, is also poor due to the hopping transport [29]. Considering this, Xiang et al. investigated heterostructured borophone and 2D MoS_2 sheets used as anode materials of secondary batteries (Fig. 6.15b) by using the first-principles cal-

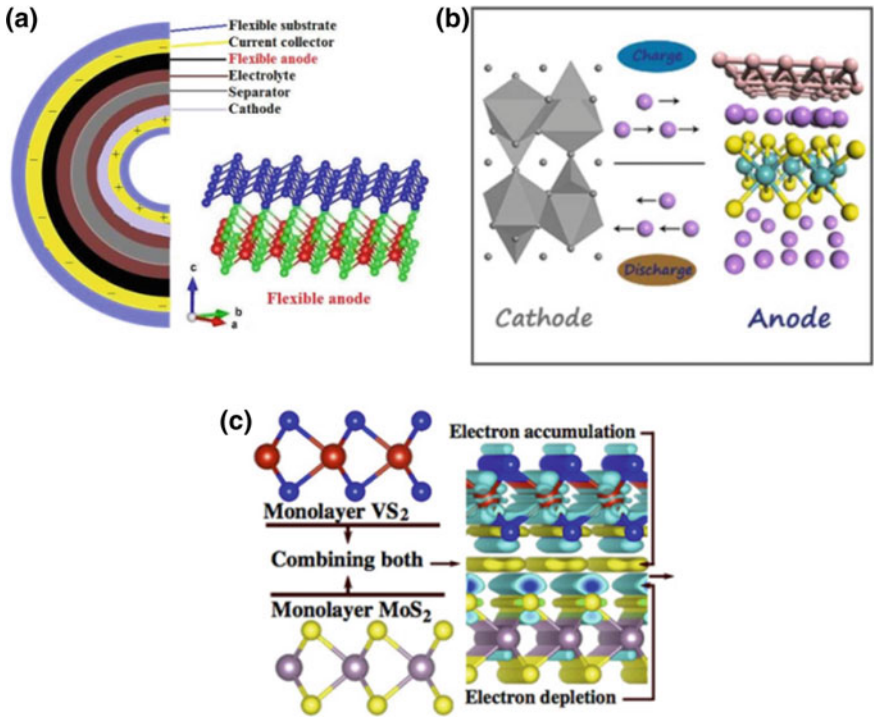

Fig. 6.15 **a** A schematic showing the heterostructure of 2D blue P and 2D NbS_2/TaS_2 monolayers, and an example of flexible devices based on this heterostructures [64]. Copyright 2016. Reproduced with permission from the American Chemical Society. **b** A schematic showing the heterostructure of 2D B and MoS_2 monolayers, and the charge/discharge processes in the case of using this heterostructure as the anode of a Li-ion battery [65]. Copyright 2018. Reproduced with permission from the American Chemical Society, **c** A schematic showing how the heterostructure from the 2D VS_2 and MoS_2 monolayers overcomes the disadvantages their monolayers for ion batteries [66]. Copyright 2017. Reproduced with permission from the American Chemical Society

culations [65]. Their results suggest that substantial electrons could be transferred from MoS_2 to borophene, producing strong electronic coupling which assists the improvement in the Li affinity. Incorporating borophene into 2D MoS_2 also increases the elastic modulus of the material, which is desirable for a long lifetime operation. Moreover, the heterostructure is predicted to have a high Li storage capacity of 539 mAh g^{-1} along with low-ion hopping barriers. More recently, heterostructures from two different types of 2D TMDs were investigated as hybrid anodes for both Li and Na storages [66]. One example was a heterostructure composed of 2D MoS_2 and 2D VS_2 monolayers (Fig. 6.15c). Owing to the interfacial charge accumulation between the monolayered MoS_2 and VS_2, the chemically active VS_2 monolayers can be stabilized in energy and phonon vibrations. Such a hybrid structure enabled the MoS_2 surface to adsorb high density of Li and Na ions, achieving a high capacity of 584 mAh g^{-1} for Li/Na storage. Furthermore, the energy barriers for the Li/Na diffusion

remained close to those in the cases of monolayered MoS_2 and VS_2. In addition to the advantages described above, the 2D heterostructures could potentially avoid the problem caused by the formation of SEI layers during energy storage [41]. Nevertheless, such 2D heterostructures in secondary batteries have not been demonstrated so far.

6.4 Summary and Prospective

Supercapacitors and secondary batteries are key devices for modern energy storage applications. They could be further developed to satisfy the increasing demands of our society. However, both of them suffer from several disadvantages which need to be addressed properly or at least alleviated. For example, the energy density of supercapacitors and the power density of secondary batteries should be further improved appropriately. Ever for the current Li-ion batteries, the energy density achieved so far is still not sufficiently high for future uses in heavy-duty devices, especially when other technical parameters such as high safety, small volume of the device, and long lifetime need to be considered as well. The developments in recent years suggest that 2D TMDs could potentially fill the gap between the performance and requirements for future energy storage.

Like graphene, 2D TMDs are also thin and have both super short electron transport length and small ion transport distance in ideal electrochemical processes. The electrochemical process on the surface of 2D TMDs has both rapid "Faradaic" and "non-Faradaic" features. It is essentially different from and considerably quicker than using a conventional anode material (e.g., graphite). Even as few-layered structures, 2D TMDs still exhibit simple and rapid ion intercalation/extraction features. Along with the highly exposed active surface, the use of 2D TMDs has been proven feasible in improving the performances of both supercapacitors and secondary batteries and has various advantages over the conventional materials. Theoretical and experimental investigations carried out so far have revealed that the energy density of a supercapacitor can be improved substantially by using a hybrid structure composed of conducting materials and 2D TMDs. On the other hand, the power density and lifetime of Li- and Na-ion batteries from 2D TMDs also have been demonstrated, indicating that 2D TMDs are highly promising candidate materials for future energy storage applications.

Nevertheless, significant amounts of future work on 2D TMDs for energy storage applications are still required, including:

1. Demonstrations of energy storage devices based on strictly monolayered or few layered (<5 layers) TMDs are rather limited, probably due to the technical difficulties with fabrication. The development of feasible fabrication techniques for super thin 2D TMDs and their small crystals is, therefore, essential.

2. Several 2D TMDs suffer from poor electrical conductivity. Apart from the reported one based on hybrid structures of 3D graphene and 2D TMDs, other novel strategies need to be introduced to address this problem.
3. Theoretical investigations on 2D TMDs to overcome their disadvantages. For example, using chemical doping to improve the conductivity and the surface activity.
4. In both supercapacitors and secondary batteries, van der Waals heterostructures from 2D TMDs and other 2D materials could potentially overcome the disadvantages of using single material and result in considerable improvements in many aspects. Nevertheless, theoretical investigations and experimental demonstrations are still limited, which could be a fruitful area for future research.
5. 2D TMDs could be highly suitable for making small flexible energy storage devices. Some theoretical studies have been conducted to reduce the hardness of some 2D TMDs and more similar modeling and experimental investigations are expected.

Based on the achievements so far, more promising applications of 2D TMDs in energy storage devices such as the supercapacitors and Li-/Na-ion secondary batteries are highly expected. Moreover, it can be reasonably expected that 2D TMDs would accelerate the development of clean energy technology to help meet the energy needs of our society.

References

1. Braff WA, Mueller JM, Trancik JE (2016) Value of storage technologies for wind and solar energy. Nat. Clim. Change 6:964–970
2. Simon P, Gogotsi Y (2008) Materials for electrochemical capacitors. Nat Mater 7:845–854
3. Miller JR, Simon P (2008) Electrochemical capacitors for energy management. Science 321:651–652
4. Zhao C, Zheng W (2015) A review for aqueous electrochemical supercapacitors. Front Energy Res 3:23
5. Faraji S, Ani FN (2015) The development supercapacitor from activated carbon by electroless plating-a review. Renew Sust Energ Rev 42:823–834
6. Choi H, Yoon H (2015) Nanostructured electrode materials for electrochemical capacitor applications. Nanomaterials 5:906–936
7. Béguin F, Presser V, Balducci A et al (2014) Carbon and electrolytes for advanced supercapacitors. Adv Mater 26:2219–2251
8. Fernández JA, Morishita T, Toyoda M et al (2008) Performance of mesoporous carbons derived from poly (vinyl achohol) in electrochemical capacitors. J Power Sources 175:675–679
9. Izadi-Najafabadi A, Yasuda S, Kobashi K et al (2010) Extracting the full potential of single-walled carbon nanotubes as durable supercapacitor electrodes operable at 4 V with high power and energy density. Adv Mater 22:E235–E241
10. Futaba DN, Hata K, Yamada T et al (2006) Shape-engineerable and highly densely packed single-walled carbon nanotubes and their application as super-capacitor electrodes. Nat Mater 5:987–994
11. Chmiola J, Yushin G, Gogotsi Y et al (2006) Anomalous increase in carbon capacitance at pore sizes less than 1 nanometer. Science 313:1760–1763

12. Bi R, Wu X, Cao F et al (2010) Highly dispersed RuO_2 nanoparticles on carbon nanotubes: facile synthesis and enhanced supercapacitance performance. J Phys Chem C 114:2448–2451
13. Brezesinski T, Wang J, Tolbert SH et al (2010) Ordered mesoporous α-MoO_3 with iso-oriented nanocrystalline walls for thin-film pseudocapacitors. Nat Mater 9:146–151
14. Lang X, Hirata A, Fujita T et al (2011) Nanoporous metal/oxide hybrid electrode for electrochemical supercapacitors. Nat Nanotechnol 6:232–236
15. Zhu Y, Murali S, Stoller MD et al (2011) Carbon-based supercapacitors produced by activation of graphene. Science 332:1537–1541
16. Zhang L, Wu HB, Lou XW (2012) Unusual CoS_2 ellipsoids with anisotropic tube-like cavities and their application in supercapacitors. Chem Commun 48:6912–6914
17. Zhang W, Chuan X, Ma C et al (2017) Nitrogen-superdoped 3D graphene networks for high-performance supercapacitors. Adv Mater 29:1701677
18. Muller GA, Cook JB, Kim HS et al (2015) High performance pseudocapacitor based on 2D layered metal chalcogenide nanocrystals. ACS Nano 15:1911–1917
19. Soon JM, Loh KP (2007) Electrochemical double-layer capacitance of MoS_2 nanowall films. Electrochem Solid-State Lett 10:A250–A254
20. Cao X, Shi Y, Shi W et at (2013) Preparation of MoS_2-coated three-dimensional graphene networks for high-performance anode material in Lithium-ion batteries. Small 9:433–3438
21. Gao W, Singh N, Song L et al (2011) Direct laser writing of micro-supercapacitors on hydrated graphite oxide films. Nat Nanotechnol 6:496–500
22. Pech D, Brunet M, Durou H et al (2010) Ultrahigh-power micrometre-sized supercapacitors based on onion-like carbon. Nat Nanotechnol 5:651–654
23. Cao L, Yang S, Gao W et al (2013) Direct laser-patterned micro-supercapacitors from paintable MoS_2 films. Small 9:2905–2910
24. Choudhary N, Patel M, Ho YH et al (2015) Directly deposited MoS2 thin film electrodes for high performance supercapacitors. J Mater Chem A 3:24049–24054
25. Acerce M, Voiry D, Chhowalla M (2015) Metallic 1T phase MoS_2 nanosheets as supercapacitor electrode materials. Nat Mater 10:313–318
26. Lin L, Miao N, Wen Y et al (2016) Sulphur-depleted monolayered molybdenum disulfide nanocrystals for superelectrochemical hydrogen evolution reaction. ACS Nano 10:8929–8937
27. Lin L, Miao N, Huang J et al (2017) A photocatalyst of Sulphur depleted monolayered molybdenum sulfide nanocrystals for dye degradation and hydrogen evolution reaction. Nano Energy 38:544–552
28. Tu C, Lin L, Xiao B et al (2016) Highly efficient supercapacitor electrode with two-dimensional tungsten disulfide and reduced graphene oxide hybrid nanosheet. J Power Sources 320:78–85
29. Yu Y, Huang S, Li Y et al (2014) Layer-dependent electrocatalysis of MoS_2 for hydrogen evolution. Nano Lett 14:553–558
30. Shen J, Wu J, Pei L et al (2016) $CoNi_2S_4$-graphene-2D-$MoSe_2$ as an advanced electrode material for supercapacitors. Adv Energ Mater 6:1600341
31. Stoller MD, Ruoff RS (2010) Best practice methods for determining and electrode material's performance for ultracapacitors. Energy Environ Sci 3:1294–1301
32. Feng J, Sun X, Wu CZ et al (2011) Metallic few-layered VS_2 ultrathin nanosheets: high two-dimensional conductivity for in-plane supercapacitors. J Am Chem Soc 133:17832–17838
33. Chakravarty D, Late DJ (2015) Microwave and hydrothermal syntheses of WSe_2 micro/nanorods and their application in supercapacitors. RSC Adv 5:21700–21709
34. Liu J, Cao H, Jiang B et al (2016) Newborn 2D materials for flexible energy conversion and storage. Sci. China Mater 59:459–474
35. Gao L (2017) Flexible device applications of 2D semiconductors. Small 13:1603994
36. Liu Y, Peng X (2017) Recent advances of supercapacitors based on two-dimensional materials. Appl. Mater. Today 8:104–115
37. Han Y, Ge Y, Chao Y et al (2018) Recent progress in 2D materials for flexible supercapacitors. J. Energ. Chem. 27:57–72
38. Liu S, Zeng Y, Zhang M et al (2017) Bindier-free WS_2 nanosheets with enhanved crystallinity as a stable negative electrode for flexible asymmetric supercapacitors. J Mater Chem A

39. Geim AK, Grigorieva IV (2013) Van der Waals heterostructures. Nature 499:419–425, 5:21460–21466
40. Novoselov KS, Mishchenko A, Carvalho A et al (2016) 2D materials and van der Waals heterostructures. 353:461
41. Pomerantseva E, Gogotsi Y (2017) Two-dimensional heterostructures for energy storage. Nat Energy 2:17089
42. Goodenough JB, Park KS (2012) The Li-ion rechargeable battery: a perspective. J Am Chem Soc 135:1167–1176
43. Battery University: BU-107: Comparison table of secondary batteries. http://batteryuniversity.com/learn/article/secondary_batteries
44. Zaghib K, Dontigny M, Guerifi A et al (2011) Safe and fast-charging Li-ion battery with long shelf life for power applications. J Power Sources 196:3949–3954
45. Xiao J, Choi D, Cosimbescu L et al (2010) Exfoliated MoS_2 nanocomposite as an anode material for lithium ion batteries. Chem Mater 22:4522–4524
46. Xu B, Wang L, Chen HJ et al (2014) Adsorption and diffusion of lithium on 1T-MoS_2 monolayer. Compunt Mater Sci 93:86–90
47. Zhou JW, Qin J, Zhang X et al (2015) 2D space-confined synthesis of few-layer MoS_2 anchored on carbon nanosheets for lithium-ion battery anode. ACS Nano 9:3837–3848
48. Jiang L, Lin B, Li X et al (2016) Monolayer MoS_2-graphene hybrid aerogels with controllable porosity for lithium-ion batteries with high reversible capacity. ACS Appl Mater Interfaces 8:2680–2687
49. Jing Y, Zhou Z, Cabrera CR et al (2013) Metallic VS_2 monolayer: a promising 2D anode material for lithium ion batteries. J Phys Chem C 117:25409–25413
50. Mikhaleva NS, Visotin MA, Kuzubov AA et al (2017) VS_2/graphene heterostructures as promising anode material for Li-ion batteries. J Phys Chem C 121:24179–24184
51. Wang D, Liu Y, Meng X et al (2017) Two-dimensional VS_2 monolayers as potential anode materials for lituium-ion batteries and beyond: first-principles calculations. J Mater Chem A 5:21370–21377
52. Cai L, Zhang Q, Mwizerwa JP et al (2018) Highly crystalline layered VS_2 nanosheets for all-solid-state lithium batteries with enhanced electrochemical performances. ACS Appl Mater Interfaces 10:10053–10063
53. Ren J, Wang Z, Yang F et al (2018) Freestanding 3D single-wall carbon nanotubes/WS2 nanosheets foams as ultra-long-life anodes for rechargeable lithium ion batteries. Electrochim Acta 267:133–140
54. Lei T, Chen W, Huang J et al (2017) Multi-functional layered WS_2 nanosheets for enhancing the performance of lithium-sulfur batteries. Adv Energy Mater 7:1601843
55. Chaturvedi A, Hu P, Aravindan V et al (2017) Unveiling two-dimensional TiS_2 as an insertion host for the construction of high energy Li-ion capacitors. J Mater Chem A 5:9177–9181
56. Yang E, Ji H, Jung Y et al (2015) Two-dimensional transition metal dichalcogenide monolayers as promising sodium ion battery anodes. J Phys Chem C 119:26374–26380
57. Putungan DB, Lin S, Kuo J (2016) Metallic VS_2 monolayer polytypes as potential sodium-ion battery anode via ab initio random structure searching. ACS Appl Mater Interfaces 8:18754–18762
58. Sun R, Wei Q, Sheng J et al (2017) Novel layer-by-layer stacked VS_2 nanosheets with intercalation pseudocapacitance for high-rate sodium ion charge storage. Nano Energy 35:396–404
59. Yu D, Pang Q, Gao Y et al (2018) Hierarchical flower-like VS_2 nanosheets-a high rate-capacity and stable anode material for sodium-ion battery. Energy Storage Mater 11:1–7
60. Chaturvedi A, Edison E, Arun N et al (2018) Two dimensional TiS_2 as a promising insertion anode for Na-ion battery. Chem Select 3:524–528
61. David L, Bhandavat R, Singh G (2014) MoS_2/graphene composite paper for sodium-ion battery electrodes. ACS Nano 8:1759–1770
62. Yang J, Zhu J, Xu J et al (2017) $MoSe_2$ nanosheet array with layered MoS_2 heterostructures for superior hydrogen evolution and lithium storage performance. ACS Appl Mater Interfaces 9:44550–44559

63. Chao D, Liang P, Chen Z et al (2016) Pseudocapacitive Na-Ion storage boosts high rate and areal capacity of self-branched 2D layered metal chalcogenide Nanoarrays. ACS Nano 10:10211–10219
64. Peng Q, Wang ZY, Sa BS et al (2016) Blue phosphorene/MS_2 (M=Nb, Ta) heterostructures as promising flexible anodes for lithium-ion batteries. ACS Appl Mater Interfaces 8:13449–13457
65. Xiang P, Chen XF, Liu J et al (2018) Borophene as conductive additive to boost the performance of MoS_2-based anode materials. J Phys Chem C 122:9302–9311
66. Samad A, Shin YH (2017) MoS_2@VS_2 nanocomposite as a superior hybrid anode material. ACS Appl Mater Interfaces 9:29942–29949

Chapter 7
2D Transition Metal Dichalcogenides for Solution-Processed Organic and Perovskite Solar Cells

G. Kakavelakis, L. Gouda, Y. Tischler, I. Kaliakatsos and K. Petridis

Abstract The construction of low cost, printable compatible, solution processed, of high performance, stable solar cells is one of the scientific milestones of the next ten years. The discovery of graphene launched a new era in the materials science, and the research implemented in the exceptional properties of the two-dimensional (2D) materials. The chemical, physical, electrical and mechanical properties of 2D materials match with the requirements that the various building blocks of the third-generation photovoltaics should have in order for these devices to deliver exceptional performance and become attractive alternatives to silicon-based solar cells. The 2D library of materials expands in a very high pace and nowadays includes 150 exotic layered materials. Among them are the transition metal dichalcogenides (2D-TMDs). Recent advances in atomically thin 2D-TMDs (e.g., MoS_2, WS_2, $MoSe_2$ and WSe_2) have introduced numerous promising technologies in nanotechnologies, photonics, sensing, energy storage and solar cells to name few. This chapter highlights the contributions of 2D-TMDs toward the construction of high efficiency and of long lifetime, solution-processed organic and perovskite solar cells.

List of Abbreviations of the TMDs

MoS_2	Molybdenum Disulfide
MoS_2@Au	Gold nanoparticles decorated MoS_2

G. Kakavelakis (✉)
Department of Materials Science and Technology, University of Crete, Gallos, Greece
e-mail: gkakavelakis@materials.uoc.gr

L. Gouda · Y. Tischler
Department of Chemistry and the Institute of Nanotechnology, Bar-Ilan University, Ramat-Gan, Israel

I. Kaliakatsos · K. Petridis (✉)
Department of Electronic Engineering, Hellenic Mediterranean University, Crete, Greece
e-mail: c.petridischania@gmail.com

N. S. Arul and V. D. Nithya (eds.), *Two Dimensional Transition Metal Dichalcogenides*,
https://doi.org/10.1007/978-981-13-9045-6_7

ce-MoS_2	Chemically exploited 2D M_OS_2
O-ce-MoS_2	UV-ozone-treated ce-MoS_2
O-MoS_2	UV-ozone-treated MoS_2
m-MoS_2	Modified MoS_2
$MoSe_2$	Molybdenum Diselenide
$NbSe_2$	Niobium Diselenide
TaS_2	Tantalum Disulfide
TiS_2	Titanium Disulfide
WS_2	Tungsten Disulfide
WS_2-Au	Gold nanoparticles decorated WS_2
WSe_2	Tungsten Diselenide

7.1 Introduction

The integration of graphene and other two-dimensional (2D) materials (e.g., transition metal dichalcogenides (TMDs) and TMDs oxides) into energy devices provides an interesting proposal to tackle challenges driven by the emerging energy demands and the global environmental concerns [1]. Inspired by the great achievements of the graphene and graphene-related materials (GRMs) in the past decade [2], TMDs (MX_2, M: transition metal, X:S, Se, Te) represent a vast family of materials (with more than >100 different compositions), with key physical, chemical, mechanical and electrical properties for energy-related devices especially due to their 2D morphology.

Their incorporation and utilization are triggering a new field that promises the introduction of new artificial materials with semiconducting, metallic and insulating properties and the construction of high performance, stable and environmentally friendly energy converging devices, e.g., solar cells [3]. Among the fabrication methods of 2D-TMDs, the solution processing methodologies, such as sonication-assisted exfoliation, electrochemical Li-intercalation and exfoliation, electrochemical Li-intercalation and exfoliation, hydro/solvothermal synthesis and colloidal synthesis, are capable of fabricating solution-processed 2D-TMDs in high yield and large scale, which are essential for the third-generation solar cell devices [4].

Some of the parameters that determine the performance and the stability of a planar architecture solar cell device are (a) the absorption spectrum of the active layer; (b) the conductivity of the selected hole and electron transport layers (HTL and ETL); (c) the relative work functions (WF) of the solar cell building blocks; and (d) tolerance of the employed transporting materials and electrodes against degradation factors, e.g., humidity, temperature, ion migration and light exposure. Advances in organic solar cells (OSCs) and perovskite solar cells (PSCs) are still underway through research implemented to boost the efficiency and the stability of the selected interlayers and electrodes. TMDs WF tunability and energy bandgap (depending on their thickness—number of layers and synthesis) are their main advantages to be exploited in a photovoltaic cell as transport layer material or within the active layer

in the case of ternary solar cells in order to boost their performance and prolong their operational lifetime. Their main impact on these devices is (a) the enhancement of their photovoltaic performance and (b) the extended stability under various degradation protocols. These contributions are attributed to the TMDs (a) superior carrier mobilities caused by ballistic transport; (b) enhanced photoluminescence that is a result of quantum confinement effects; and (c) the absence of dangling bonds which enhances their resistance to reactions with other chemical species [5].

Thus, TMDs have huge potential and are highly promising alternatives to the traditional HTL and ETL materials in OSCs and PSCs. In particular, layered TMDs such as MoS_2, WS_2, WSe_2, $MoSe_2$, $NbSe_2$, TaS_2 and TiS_2 nanosheets are promising materials to be utilized as transporting layers or within the active layer of OSCs and PSCs.

In this chapter, we will summarize the most important findings of the application of solution-processed 2D-TMDs in OSCs and PSCs. Moreover, particular attention will be given to the improvement of the photovoltaic performance and the enhanced operational stability the TMDs induce into these third-generation solar cell devices. At the end, we will attempt to highlight the perspectives of this field.

7.2 Transition Metal Dichalcogenides in Organic Photovoltaics (OPVs)

OSCs are characterized by some unique and attractive features, such as lightweight, transparency, flexibility, ease of manufacturing scale-up through the roll-to-roll coating processes and low fabrication costs, which make them a very attractive technology of high potential [6]. One of the most essential building blocks for the optimum operation of the OSCs is their charge selective transport layers otherwise known as ETL and HTL. The ETL and HTL facilitate the transportation of the photogenerated carriers and their effective collection in the respective electrodes. In Fig. 7.1 are depicted the two possible OPVs architectures (conventional and inverted) and the different positions where the 2D-TMDs can be placed within the device are highlighted.

7.2.1 TMDCs in the HTL of OPVs

One of the most prominently used HTL materials is the conductive conjugated polymer poly(3,4-ethylenedioxy-thiophene):poly(styrenesulfonate) (PEDOT:PSS) [7]. However, the high acidity and hydroscopicity of PEDOT:PSS can cause the corrosion of indium tin oxide (ITO) as well as of the metal electrode [8]. Other alternative materials, such as transition metal oxides (e.g., V_2O_5, MoO_3, WO_3, NiO_X), have been utilized [9]. Despite the improved stability [10] and better energy level alignment [11] these materials have exhibited, the required expensive, complicated deposition

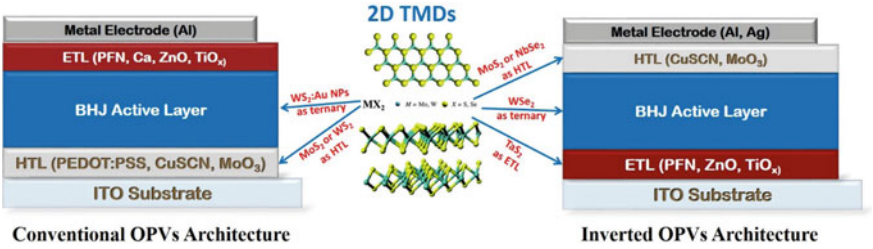

Fig. 7.1 Schematic diagram showing both (left) the conventional and (right) the inverted OPVs architectures. The picture in the center depicts the structure of the various 2D-TMDs, and the blue arrows indicate the different layers in which these TMDs have been placed in the OPVs building blocks

processes (through vacuum deposition) to be deposited and additional high temperature annealing processing, has diverted scientific community's attention to other solution processed, annealing free, materials with high hole mobility such as TMDs. The latter advantages of easy processing, no need of additional annealing, solution processability, high efficiency and low trap density, make them ideal candidate materials to be exploited in the HTL of an OSC devices. Table 7.1 summarizes the reported results regarding the utilization of 2D-TMDs as HTLs in both normal and inverted architecture OPVs.

Until 2013, only a few attempts were reported for the application of 2D-TMDs and especially of the exfoliated molybdenum disulfide (MoS_2), as transporting layers within the OSCs; this was mainly due to ambiguous WF value of the MoS_2 and the inhomogeneous and aggregated morphology of spin cast MoS_2 thin films. Yun et al. [12] were the first to report a facile and simple method for the n and p doping of single layers (thickness of 1.1–1.2 nm, lateral size 100–300 nm) of MoS_2 in order to (a) tune their WF and utilize them as HTL and ETL within normal and inverted OSCs, respectively and (b) optimize the morphology of the doped MoS_2 layers in order to build planar devices with the optimum performance. The p-doped MoS_2 layers were utilized as HTL in a normal structured OSC whereas the n-doped used as ETL in an inverted setup. Both of the doped MoS_2-based HTL and ETL-based OSCs were performed superior than the undoped MoS_2-based devices due to (a) better-aligned transport layers with the energy levels of the donor (P3HT) and the acceptor (PCBM) and (b) similar morphology of the doped MoS_2 transport layers with the undoped films. Critical factor for all the ascribed improvements was the concentration of the employed dopants; the n and the p character were increased with the dopants concentration whereas for the planarization of the doped MoS_2 morphology there was an optimum value for each dopant.

Gu et al. [13] proposed the integration of chemical exfoliated solution-processed MoS_2 nanosheets (lateral size between 400 and 800 nm) into OSCs as an efficient HTL. The MoS_2 was double spin coated between the silver anode and the active layer of the OSC. Its performance was tested in two systems (active layer): P3HT:PC_{61}BM and PTB7:PC_{71}BM. Key to the optimum performance of MoS_2 as

Table 7.1 Summary of the results of 2D-TMDs-based HTLs in OPVs

TMD	OSC Active Layer/building block (architecture)	WF (−eV)	V_{oc} (V)	J_{sc} (mA/cm^2)	FF	PCE (%)	ΔPCE (%)	Other improvements	References
p-and n-doped single layer of exfoliated MoS_2	P3HT:PCBM/p-doped MoS_2 (normal)	4.76	0.59	8.62	0.66	3.4	200 (undoped MoS_2)	N/A	Yun et al. [12]
	P3HT:PCBM/n-doped MoS_2 (ETL) (inverted)	3.5	0.61	8.16	0.55	2.73	161 (undoped MoS_2)	N/A	
MoS_2 nanosheets (chemical exfoliation)	PTB7:$PC_{71}BM$/ HTL (normal)	–	0.72	15.9	0.71	8.11	7.55 (e-MoO_3)	N/A	Gu et al. [13]
$NbSe_2$ nanosheets (chemical exfoliation)	PTB7:$PC_{71}BM$/HTL (inverted)	–	0.72	16.04	0.70	8.1	7.42 (e-MoO_3)	N/A	Gu et al. [14]
UVO-treated MoS_2 nanosheets/PEDOT:PSS (sonication exfoliated)	P3HT:PCBM/HTL (normal)	4.9	0.52	8.14	0.67	2.87	2.13 (PEDOT:PSS)	Ambient Conditions Stability	Le et al. [16]
Salt-assisted liquid phase exfoliated MoS_2	P3HT:$PC_{61}BM$ (normal)	–	0.57	7.1	0.44	1.81	−27.6 (PEDOT:PSS)	N/A	Niu et al. [17]

(continued)

Table 7.1 (continued)

TMD	OSC Active Layer/building block (architecture)	WF (−eV)	V_{oc} (V)	J_{sc} (mA/cm^2)	FF	PCE (%)	ΔPCE (%)	Other improvements	References
MoS_2 nanosheets decorated with MoO_3 NPs	PBDTTT-CF:$PC_{71}BM$ (normal)	4.79	–	–	–	6.9	10 (conventional MoS_2)	Ambient Conditions Stability	Yun et al. [18]
Modified chemical exfoliated MoS_2 nanosheets (using lithium intercalation)	PTB7:$PC_{71}BM$ (normal)	–	0.73	14.71	0.676	7.26	1.96 (non-modified MoS_2)	Self-stability	Liu et al. [19]
UV-ozone-treated sonication exfoliated WS_2 nanosheets	P3HT:PCBM/WS_2 /PEDOT:PSS/(normal)	5.1	0.52	8.71	0.67	3.07	6.9 (PEDOT:PSS)	N/A	Le et al. [20]
MoS_2 sheets decorated with Au NPs	PTB7/$PC_{71}BM$/HTL (normal)	–	0.72	15.44	0.65	7.25	17.31 (bare MoS_2)	N/A	Yang et al. [21]
UVO-treated ce-MoS_2 nanosheets	PTB7/$PC_{71}BM$ /(normal)	4.93	0.73	14.98	0.69	7.64	0.52 (PEDOT:PSS)	N/A	Yang et al. [22]

(continued)

Table 7.1 (continued)

TMD	OSC Active Layer/building block (architecture)	WF (−eV)	V_{oc} (V)	J_{sc} (mA/cm^2)	FF	PCE (%)	ΔPCE (%)	Other improvements	References
UVO-treated MoS_2 and WS_2	P3HT:$PC_{60}BM$ (normal)	4.8 (5-min UVO treat.)	0.6	7.81	0.63	2.96 (MoS_2)	−8.35 (PEDOT:PSS)	Ambient Conditions Stability	Kwon et al. [23]
		4.95 (5-min UVO treat.)	0.61	7.87	0.64	3.08 (WS_2)	−4.64 (PEDOT:PSS)	Ambient Conditions Stability	
UVO-treated WS_x and MoS_x nanodots	P3HT:PCBM/HTL (normal)	5.0–5.1	0.61	7.81	0.62	3 (WS_x)	−7.12 (PEDOT:PSS)	Ambient Conditions Stability	Le et al. [24]
			0.6	7.87	0.62	2.95 (MoS_x)	−8.66 (PEDOT:PSS)	Ambient Conditions Stability	
UVO-treated MoS_2 quantum dots	PTB7-Th:$PC_{71}BM$ (normal)	4.9–5.2 (for 8 and 30-min treat-ment time)	0.79	16.9	0.65	8.66	1.04 (PEDOT:PSS)	Ambient Conditions Stability	Xing et al. [27]
PEDOT:PSS/WS_2	PTB7-Th:$PC_{71}BM$ (normal)	–	0.79	15.67	0.58	7.24	10.36 (PEDOT:PSS)	Storage Stability	Xing et al. [28]

HTL is the good coverage of the active layer so to prohibit any current leakage pathways due to direct contact between Ag electrode and the active layer. The record power conversion efficiency (PCE) results were achieved with the PTB7:$PC_{71}BM$ system with PCEs higher than 8.1%. The excellent performance of the MoS_2 as HTL was reconfirmed through transient photovoltage measurements. The latter measurements clearly showed the superiority regarding the transportation of holes (less trapped photogenerated charges) through MoS_2 compared to the reference devices that employed traditional vacuum e-evaporated molybdenum oxide (e-MoO_3) HTLs.

The same research group [14] investigated the potential of chemical exfoliated [15] niobium diselenide ($NbSe_2$) nanosheets (thickness of 1.6 nm, lateral size of 200–400 nm) as an ideal HTL material in OSCs. As in the case of the spin-coated MoS_2, the uniform and full coverage of the active layer with $NbSe_2$ nanosheets is the key for the construction of high performance OSCs. The record efficiency was 8.1% with the average values for 20 cells to be 7.95%. The devices exhibited improved efficiencies compared to e-MoO_3 HTL-based devices. The improved performance was ascribed, as transient photovoltage and photocurrent measurements showed, to the nanoflakes construction of the employed $NbSe_2$ nanosheets which contained fewer traps (one of order less than in the case of e-MoO_3); as a result, lower recombination rates were occurred. Additionally, the devices used $NbSe_2$ nanosheets in HTL, demonstrated longer carrier lifetimes which was an indication that the photogenerated carriers were effectively collected by the electrodes.

Le et al. [16] suggested the use of spin-coated ultraviolet ozone (UVO)-treated, sonication exfoliated MoS_2 nanosheets (1 nm in thickness and 100–300 nm in lateral size) as an interlayer between the anode and the PEDOT:PSS in a P3HT:PCBM OSC. The device exhibited enhanced stability without degradation of its photovoltaic performance compared to the PEDOT:PSS HTL based on device. As a result of the UVO treatment, the work function (WF) of the MoS_2 decreased from -3.9 eV to -4.9 and -5.2 eV for 15 and 30 min UVO treatment, respectively. This tuning in the WF decreased the hole extraction barrier and improved the performance of the device. The best-performed device was this one that exploited both UVO (for 15-min treated) MoS_2/PEDOT:PSS HTL between the active medium and the ITO. These devices performed better compared to the HTL-free devices or the MoS_2 HTL based on reference devices. Moreover, the non-encapsulated MoS_2/PEDOT:PSS HTL OSCs exhibited superior stability under air atmosphere compared to the reference cells. The main finding was that the values of FF and V_{oc} demonstrated no significant difference for the PEDOT:PSS and the MoS_2/PEDOT:PSS HTL-based OSCs for 120 h of testing. On the other hand, the MoS_2/PEDOT:PSS HTL-based OSCs exhibited superior stability compared to the PEDOT:PSS respective devices regarding the behavior of the J_{sc}. It was concluded that placing the MoS_2 between the PEDOT:PSS and the ITO protects the latter from the hydroscopic nature of PEDOT:PSS and thus prolongs the stability of the device.

To overcome the long time takes the liquid exfoliation of TMDs using ultrasounds, Niu et al. [17] reported a modified liquid phase ultrasonication method that employed low-cost inorganic salts in order to exfoliate bulk 2D TMD materials faster. This new proposed technique yielded single and few layer 2D sheets of TMDs (65% of the

as-made TMD 2D sheets are 1–5 layers, with lateral size of hundreds of nanometers to several micrometers) including MoS_2, $MoSe_2$, WS_2 and WSe_2 in large quantities and of high quality. Atomic force microscopy (AFM) measurements showed that the lateral size of the fabricated flakes ranged from a hundred nanometers to several micrometers whereas the thicknesses varied from 0.75 to 3.5 nm. For the proof of concept of the applicability of the MoS_2 films, the authors utilized them as HTL in normal P3HT:PCBM OSCs; as a result, the open circuit voltage (V_{oc}) improved from 0.34 V (HTL-free devices) to 0.58 V. Moreover, and compared to the PEDOT:PSS HTL based on devices, all the MoS_2 cells demonstrated lower reverse saturation current and a higher rectification ratio up to 10^2; this was a direct demonstration for the suitability of MoS_2 as a hole transport and electron blocking layer for OSCs. The record results were obtained for the vacuum filtration deposited MoS_2 HTL-based cells with 1.81% PCE. The latter performance was superior to that of HTL-free devices (0.02%) but inferior to that of the PEDOT:PSS OSCs (2.34%). The inferior performance compared to the PEDOT:PSS cells was attributed into (a) high roughness (55 nm) due to the rough surface morphology of the filter paper used during the vacuum filtration and (b) the lower transmittance (approximately of 6%) at 550 nm as the UV–Vis measurements showed.

Yun et al. [18] in order to deal with the serious drawback the PEDOT:PSS is characterized as an HTL regarding its stability studied a different solution-processed HTL material consisted from bi- or tri-layer MoS_2 nanosheets (~230 nm lateral dimension and thickness of ~1.17 nm) with MoO_3 nanoparticles (NPs) (average diameter of 19 nm). The MoS_2/MoO_3-based HTL composite PBDTTT-CF:$PC_{71}BM$ OSC (under normal structure) performed better than the PEDOT:PSS HTL-based OSC with respect to (a) higher power conversion efficiency (6.9% over 6.8%) and (b) superior air stability of the device. The air stability of the MoO_3/MoS_2-based cell was exceptional long (over 16 days). During the stability tests period, MoO_3/MoS_2-based cell retained to 80% of its initial value. In contrast, the PEDOT:PSS cells completely failed within four days of testing. This enhanced stability was ascribed to (a) better chemical inertness compared to the PEDOT:PSS and (b) better uniform and full covered surface morphology compared to commercial MoO_3 (c-MoO_3).

The authors Liu et al. [19] have proposed a chemical synthesis route to overcome the instability issues for the M_OS_2 2D nanosheets and its implication for optoelectronic application. The chemically exploited 2D M_OS_2 (ce-MoS_2) in DI water has great tendency to agglomerate, which has no interest for electronic applications. The chemical modification of a 2D nanosheet surface with surfactant, favored via electrostatic interaction, was demonstrated to have hindrance behavior for the agglomeration. From the other hand, the insulating nature of these surfactant molecules limits its implication for optoelectronic applications. The author Liu et al. proposed the use of self-assembled hexadecyltrimethylammonium chloride surfactant (CTAC) with 2D M_OS_2. This proposal resolved the issues of agglomeration and insulation behavior. The performed Zeta potential measurements showed Zeta potentials shift from −47.2 mV to +34.7 mV that confirmed the chemical modification of 2D M_OS_2 with the CTAC. The authors performed also, XPS measurements which evident that the properties of 2D M_OS_2 remained unchanged after the modification. The stability

of the modified MoS_2 (m-M_OS_2) was monitored by change in the absorption coefficients of single-layered M_OS_2 peak at 672 nm. The absorption of pristine M_OS_2 stock solution was drastically dropped with storage time (within 3 days) whereas for the modified one remained unchanged (99%) up to 100 days, confirming no agglomeration of the 2D sheets. Further the authors implicated m-2D M_OS_2 and pristine 2D M_OS_2 as HTLs in the ITO/M_OS_2/PCBM/PFN/Al stacked solar cell structures. Both devices initially showed similar performance (pristine 7.12% and modified 7.23%), which confirmed that the transport properties remained unchanged for m-2D M_OS_2-based devices. The solar cells fabricated from three days stored pristine 2D M_OS_2 HTL, showed an initial drop of performance to 5.35%, whereas the solar cell fabricated with 100 days stored m-2DM_OS_2 solution exhibited stable performances as its initials. The authors concluded that the stability of m-2D M_OS_2-based OSCs was due to electrostatic repulsion and steric hindrance effect of CTAC molecules at the 2D M_OS_2 surface.

Le et al. [20] have demonstrated the use of 2D WS_2 nanosheets (of thickness of 0.7–1.4 nm and lateral size of 300 nm) as better HTL for P3HT:PCBM solar cells. The 2D WS_2 nanosheets have similar structure and properties like 2D M_OS_2, which are recently demonstrated as HTL and owing to improve the solar cell performance. The authors synthesized 2D WS_2 nanosheets using a simple sonication method. The formation of 2D WS_2 nanosheets was confirmed by Raman and UV–Vis absorption spectroscopy. After successful synthesis of WS_2 nanosheets, the authors performed UVO treatment, which believed to increase the WF of the material. The implemented WF measurements showed an increase from 4.9 to 5.1 eV after 30 min of UVO treatment. It was considered that the UVO treatment partially converted the WS_2 to WO_x, which was further confirmed in XPS measurements, showing formation of O 1 s after the UVO treatments. The authors fabricated neat solar cells without HTL, i.e., ITO/PCBM/LiF/Al solar cells which exhibited low PCE of 1.84% mainly due to poor fill factor (FF) of 55%. The solar cell fabricated with PEDOT:PSS as HTL, showed improved J_{sc} 8.14 mA, PCE (2.87%), V_{oc} 0.52 V and FF (67%). The authors continuously replaced the PEDOT:PSS with WS_2 nanosheets as HTL. The UVO-untreated device demonstrated similar performance as the without HTL devices; contrary the UVO-processed OSCs exhibited progress to all of its photovoltaic parameters: J_{sc} of 8.06 mA, V_{oc} of 0.59 V, FF 61% and PCE of 2.40%. These improvements were attributed to the better energy band alignment of HTL with the PCBM. The sample that employed both PEDOT:PSS and UVO-treated WS_2 nanosheet as HTL showed the highest performance of 3.07%. The authors concluded that the combination of PEDOT:PSS and UVO-treated WS_2 nanosheet as HTL was the way to improve the OPV performance.

One of the most popular techniques to compromise the tradeoff between charge transport and light absorption and simultaneously to improve the efficiency of thin film active layer OSCs is the incorporation of metallic nanoparticles (NPs) within the various building blocks of these devices. The utilization of metallic NPs increases the absorption cross section of the active layers through the exploitation of (a) light scattering (from the large size metal NPs, larger than 50 nm) or (b) the localized surface plasmon resonance (LSPR) (from the smaller diameter NPs, smaller than

50 nm). Yang et al. [21] followed this light trapping strategy and showed theoretically and experimentally that the decoration of thin films of MoS_2 with gold (Au) NPs improved the photovoltaic performance of PTB7:$PC_{71}BM$-based OSCs. More specifically, the decoration of the surface of ultrathin (~1 nm) MoS_2 nanosheets (lateral size of 200–300 nm) with 20 nm in diameter Au NPs and the use of MoS_2@Au composite as HTL in normal structures enhanced the PCE of the pristine devices (with MoS_2 HTL) by 17.3% mainly due to the enhancement of the J_{sc} (enhancement by 15.6%, the other two parameters FF and V_{oc} remained unaffected). The enhancement of the PCE was ascribed to (a) the LSPR of the Au NPs at 750 nm (when emerged within PTB7:PCBM) that matched with the absorption of the PTB7:PCBM blend; (b) the ultra-small thickness of the MoS_2 nanosheets that did not screen the re-emitted wave from the Au NPs nano-antennas; and (c) the position of the Au NPs on the surface of the MoS_2.

The effect of the different local crystalline structures on MoS_2 sheets when employed as HTL in OSCs was revealed by the work of Yang et al. [22]. The UVO treatment of ce-MoS_2, resulted to nanosheets free of defects (oxygen atoms filled the defects, vacuum places of sulfur atoms), known as O-ce-MoS_2 nanosheets (thickness of 2–3 nm and lateral sizes of 200–300 nm). The latter were employed as HTL in normal architecture PTB7:$PC_{71}BM$ OSCs that performed superior to the ce-MoS_2 HTL and PEDOT:PSS HTL based on OSCs. This was attributed to the UVO treatment that (a) reduced the defects, the electron trap states and the O-ce-MoS_2-based cells demonstrated higher J_{sc} and FF values (14.98 from 14.29 mA/cm^2 and 0.699 from 0.563, that caused higher PCE (7.65% than 4.99% of the ce-MoS_2 HTL-based OSCs)) and (b) to the better energy alignment between the O-ce-MoS_2 (WF −4.9 eV) with the PTB7 (HOMO of −5.15 eV) than with the ce-MoS_2 (−4.5 eV).

Kwon et al. [23] reviewed in their paper the application of atomically thin TMDs as HTL in OSCs. The metal sulfides (MeS_2), such as MoS_2 and WS_2, were the materials replace the PEDOT:PSS, mainly due to latter stability issues. As the result of the UVO treatment (for 5 min), the WF of the MoS_2 and the WS_2 was decreased from −4.6 and −4.75 eV to 4.8 and 4.95 eV, respectively. This means that the lowest hole injection barrier belongs to UVO-treated WS_2 that was reflected higher achieved PCE. The UVO treatment did not only tune the WF of the MeS_2 HTL but also enhanced the transmission at 550 nm, from 91.7 to 94% for MoS_2 and from 92.4 to 94.6% for WS_2. The positive effect of the UVO treatment was also reflected the photovoltaic performance of MeS_2 HTL-based OSCs, from 2.72 (in the untreated MoS_2) to 2.96% (after 5 min of UVO treatment) for the MoS_2 and from 2.79 to 3.08% for the WS_2. The improved performance of the UVO-treated MeS_2 HTL based on OSCs compared to the pristine ones was attributed to the increase of the transmittance, variation of the WF and the removal of the surface contamination due to UVO processing. Although the photovoltaic performance of the UVO-treated MeS_2 HTL-based OSCs were inferior to the PEDOT:PSS HTL based on cells, the stability was significantly improved (Fig. 7.2).

Le et al. [24] demonstrated the great potential of synthesis WS_x and MoS_x nanodots for the use as HTL in OSCs. The use of solvothermal (at low temperatures, <200 °C) produced WS_x and MoS_x as HTLs resulted in similar photovoltaic perfor-

mances as the PEDOT:PSS respective devices and moreover to superior stabilities when the aforementioned TMDs were UVO processed. The thickness of the applied WS_x and MoS_x HTLs was between one and three nm whereas their sizes were 1–3 nm. After the UVO treatment for 30 min, the WF of the WS_x and MoS_x was increased from 4.4 and 4.3 eV to 5 and 5.1 eV, respectively. The record results were achieved for the 30-min UVO-treated WS_x and MoS_x nanodot HTL-based OSCs. The highest reported PCEs were of the order of 3 and 2.95% for the WS_x and MoS_x HTL-based OSCs, respectively. These were similar performances compared to the PEDOT:PSS reference devices. The well-satisfied photovoltaic performance of the

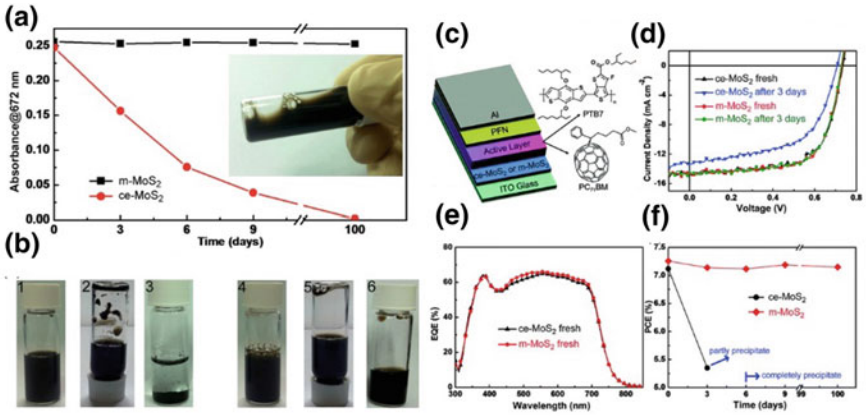

Fig. 7.2 **a** Normalized absorbance of solutions of ce-MoS_2 and m-MoS_2 at 672 nm as a function of storage time. The inset is the image of m-MoS2 colloidal dispersion stored for ~100 days. **b** Images (1, 2, 3) of ce-MoS_2 and (4, 5, 6) of m-MoS2 colloidal dispersions stored for 0 day (1, 4), 3 days (2, 5) and 9 days (3, 6), respectively. **c** Chemical structures of PTB7 and $PC_{71}BM$ and schematic of the OPVs architecture: ITO/ce-MoS_2 or m-MoS_2/PTB7:PC71BM/PFN/ Al. **d** J–V curves of devices fabricated by using different MoS_2 dispersions with various storage times. **e** Corresponding EQE spectra for devices with freshly prepared ce-MoS_2 and m-MoS_2 dispersions. **f** Stability of the devices fabricated by using ce-MoS_2 or m-MoS_2 dispersions with various periods of time. Reproduced with permission from Ref. [19]. **g** OPVs with MoS_2 flakes as the HTL. **h** J–V curves and (i) EQE spectra of the OPV devices with PEDOT:PSS, ce-MoS_2 and O-ce-MoS_2 as HTLs, respectively. **j** The steady-state photoluminescence spectra of the PTB7 film deposited on ce-MoS_2 and O-ce-MoS_2 thin films on a quartz substrate, respectively. **k** Charge collection probability as a function of internal voltage for OPVs based on ce-MoS_2 and O-ce-MoS_2 HTLs. **l** Ultraviolet photoemission spectra of ce-MoS_2, O-ce-MoS_2 and PEDOT:PSS deposited on ITO substrates. **m** Energy level diagram of the PTB7:$PC_{71}BM$ photoactive layer sandwiched between the ITO anode and the Al cathode utilizing ce-MoS_2 and O-ce-MoS_2 as the HTL, respectively. Reproduced with permission from Ref. [22] **n** Simulated extinction spectra of isolated Au NPs in water, PEDOT:PSS and the PTB7:$PC_{71}BM$ blend. Simulated electric field ($|E|^2$) distribution around an Au NP compared with the incident light electric field in **o** water, **p** PEDOT:PSS and **q** PTB7:$PC_{71}BM$ blend. **r** Schematic of the device architecture. **s** UV–Vis absorption spectra of PTB7:$PC_{71}BM$ films with MoS_2 HTL and MoS_2@Au HTL (the absorption enhancement after the incorporation of Au NPs onto MoS_2 sheets is provided). **t** J–V curves and **u** EQE spectra of the OPVs with MoS_2 HTL and MoS2@Au HTL. The calculated EQE enhancement against wavelength is also presented in (**u**). Reproduced with permission from Ref. [21]

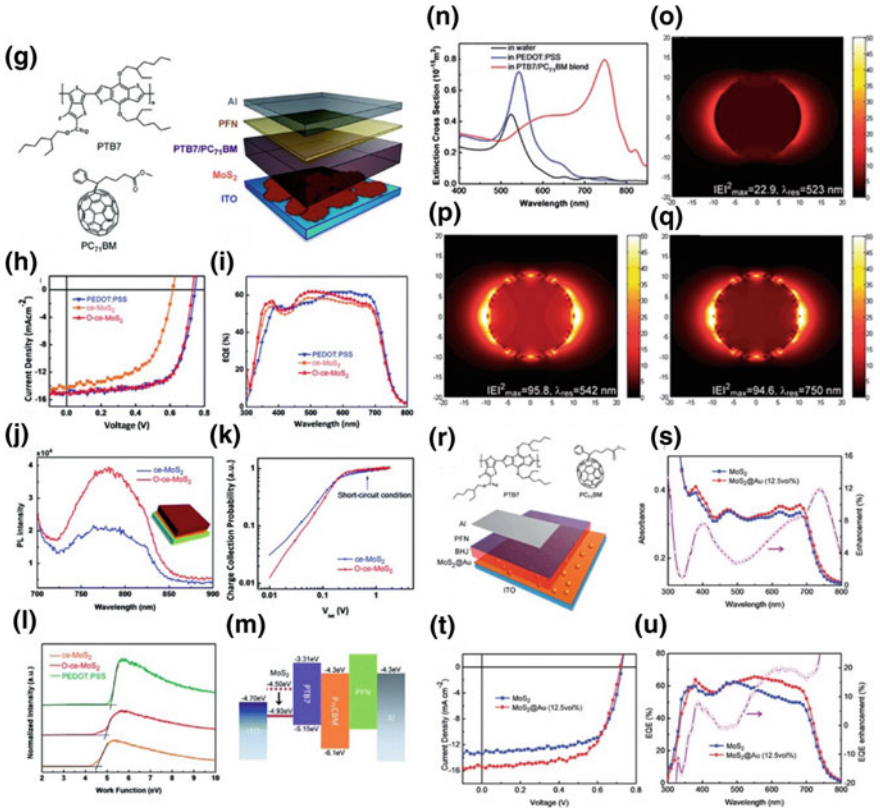

Fig. 7.2 (continued)

WS_x and MoS_x nanodot HTL-based OSCs was attributed to the lowering of the energy barrier between ITO and active layer. The stability of the WS_x and MoS_x HTL-based, without encapsulation, OSCs demonstrated under atmospheric conditions was superior compared to the PEDOT:PSS-based cells; the latter were deteriorated after 24 h whereas the WS_x and MoS_x HTL-based OSCs remained their PCE over the 50% of its initial values for the same period.

It has been reported that quantum dots (QDs) constructions employing materials such as PbS, TiO_2, graphene and MoS_2 [25, 26] formed pinhole-free, thickness-controllable and uniform spin-coated films. This is a very promising alternative since other 2D-TMDs materials production techniques do not provide such of high standards films, and this is detrimental to OSC performance. Xing et al. [27] were from the 1st ones that tested UVO MoS_2 (O-MoS_2) QDs (average size of 3.3 nm, thickness of 0.5–2.5 nm) as a HTL in OCS. The UVO treatment was necessary in order to tune the WF of the film and be appropriately matched with the energy levels of the donor material. By controlling the time of the UVO treatment, the authors managed to tune the WF of the MoS_2 QDs to the levels required, depending on

the selected donor material (P3HT and PTB7-Th). The optimum UVO treatment period also reflected the record photovoltaic performances achieved. As a result, a record PCE for PTB7-Th-based OSCs was reported at 8.7% which was higher 71 and 12% than MoS_2 QDs and O-MoS_2 nanosheets-based OSCs, respectively. This was mainly ascribed to smoother surface (that is very much affected by the OZO treatment time) of the O-MoS_2 QDs compared to the O-MoS_2 nanosheets that allowed the better contact with the active layer. Moreover, the stability of the non-encapsulated PTB7-Th-based OSCs was much improved due to the replacement of the acid and hydrophilic PEDOT:PSS (@ 25 °C and 30% humidity). The PEDOT:PSS-based OSCs dropped to about half of their efficiency after eight days of operation whereas the O-MoS_2 QDs retained the 64% of their PCE after 47 days of operation under similar conditions.

Xing et al. [28] demonstrated a new innovative method to exfoliate the TMD 2D nanosheets. These authors used a mixture of TMD crystal, graphite and PEDOT:PSS solution. This reaction mixture employed for repeated ultrasonication and centrifugation before resulted in the final 2D nanosheet product. The PEDOT:PSS was adsorbed onto surface of graphite/TMD nanocrystals and acted as a surfactant to dissociate TMD nanosheets after the sonication. In this method, the authors synthesized MoS_2, WS_2 nanosheets and characterized them with the Raman and XRD measurements. The ink prepared by sonication and centrifugation of PEDOT:PSS/WS_2 mixture was employed in OSCs as an HTL, in the ITO/HEL/P3HT:PCBM/Ca/Al and ITO/HEL/PTB7-Th:PCBM/Ca/Al device structures. The device PEDOT:PSS with WS_2 as HTL showed improved device performance with reduction in the series resistance and also reduction in the negative currents in the IV. It indicated that the WS_2 incorporation reduced the nonradiative recombination pathways and recombination currents, thus increased the performance of the solar cells.

7.2.2 TMDCs into ETL of OPVs

Table 7.2 summarizes the reported results regarding the utilization of 2D-TMDs as the ETL in both conventional and inverted OPVs.

Le et al. [29] have demonstrated that tantalum disulfides (TaS_2) ultrasonic assisted exfoliated nanosheets were very promising candidates for both anode and cathode transporting layers in normal and inverted OSCs. The authors applied UVO and non-treated TaS_2 nanosheets (thickness of 1 nm and lateral size of ~70 nm) as HTL and ETL in normal and inverted OSCs, respectively. The TaS_2 HTL and ETL based on devices had improved photovoltaic performances compared to the reference non-TaS_2 OSCs (HTL-free devices). Even though TaS_2 is structurally similar to MoS_2 and WS_2, its electrical properties are superior to those materials since its electrical resistivity is much lower (10^{-3} to 18 and 0.1 Ω cm, respectively). This makes TaS_2 very attractive and promising material to be employed as transport layer within OSC systems. In the case of the UVO-treated TaS_2 nanosheets, their WF was tuned as a function of the UVO treatment period. The normal OSC structure employed

Table 7.2 Summary of the results of 2D-TMDs—based ETLs in OPVs

TMD	OSC Active Layer/Building Block (architecture)	WF (−eV)	J_{sc} (mA/cm^2)	V_{oc} (V)	FF	PCE (%)	ΔPCE (%)	Other improvements	References
UVO-treated and non-treated TaS_2 nanosheets	P3HT:PCBM/UVO TaS_2 (normal)	4.9–5.1	7.87	0.61	0.64	3.06	−6.7 (PEDOT:PSS)	N/A	Le et al. [16]
	P3HT:PCBM/untreated TaS_2 (inverted)	4.4	8.76	0.60	0.52	2.73	9.2 (TiO_x)	N/A	
Liquid exfoliated MoS_2 nanosheets decorated with Au NPs	PBDTTT-CT/PC71BM (normal)	–	13.4	0.69	0.53	4.91	59.93 (bare MoS_2)	N/A	Chuang et al. [30]

30 min UVO-treated TaS_2 HTL provided PCEs comparable to the PEDOT:PSS OSCs (~3.06% vs. 3.28% for the PEDOT:PSS). From the other hand, the inverted systems employed non-treated TaS_2 as an ETL demonstrated the higher improvement with respect to the achieved PCE compared to the ETL free devices: from 0.22 to 2.73%. The better photovoltaic performance for both the UVO-treated and non-treated TaS_2 nanosheets based on devices compared to the free HTL and ETL cells, respectively, was ascribed to the matched energy levels between the active layer and the HTL and ETL materials.

Chuang et al. [30] proposed the use of liquid phase exfoliated monolayer or few layers of MoS_2 nanosheets (planar size of 100 nm) decorated with Au NPs (average size of six nm) as an ETL in OSCs. The incorporation of metal NPs has shown to be a promising way for increasing the light harvesting of solar cells of all the technologies [31, 32]. TEM images revealed that the Au NPs were grown on the surface of the MoS_2 sheets and not within the volume of these nanostructures. Moreover, the UV–Vis absorption spectroscopy measurements were shown an intense peak at 535 nm which corresponded to the localized surface plasmonic resonance (LSPR) of the Au NPs. The employment of such nanocomposites as ETL enhanced the photovoltaic performance of inverted OSCs due to surface plasmonic effect—light trapping technique. The record results were obtained in the PBDTTT-CT/$PC_{71}BM$ system and for an optimum concentration of Au NPs onto MoS_2 nanosheets. Above this optimum concentration value, the device performance started to degrade due to NPs aggregation. As was expected, the PCE was enhanced from 4.41% of the reference MoS_2 ETL based on OSC to 4.91% in the MoS_2-Au NPs ETL based on OSCs. This enhancement was attributed to the coupling of the plasmonic resonance effects of Au NPs and the MoS_2 nanosheets; the improved performance was reconfirmed by the higher obtained J_{sc} and EQE values and spectra for the plasmonic-based OSC (Fig. 7.3).

7.2.3 TMDCs into the Active Layer of OPVs

Bulk heterojunction (BHJ) OSCs main disadvantage compared to the silicon solar cells is their low PCE. The main reasons for this inferior performance are: (1) limited absorption width (~100 nm) [33]; (2) the low charge mobility [34]; (3) and the low exciton diffusion length (~10 nm) [35]. One strategy to address in an extent the aforementioned drawbacks of the OSCs is to move from binary systems to ternary ones: A third element is utilized within the active layer [36]. Careful selection of the third material dictates (1) the matching of its energy levels between the energy levels of the donor and the acceptor material; (2) the balance of the electron and the hole mobilities after the immersion of the third material; (3) the complementary absorption of the third material to the absorption of the donor; and (4) the morphological matching of the third material with the donor and acceptor of the OSC. Table 7.3 summarizes the reported results regarding the utilization of 2D-TMDs as ternary components in both conventional and inverted OPVs.

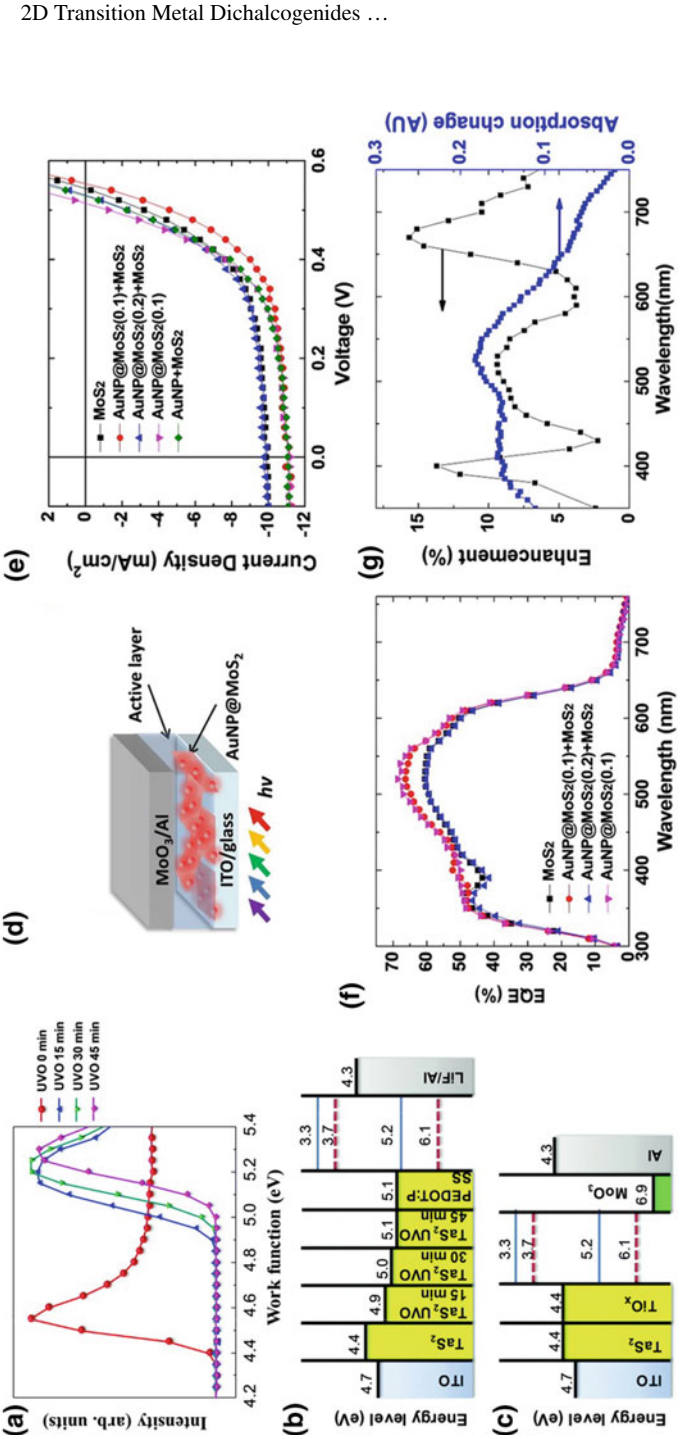

Fig. 7.3 **a** Changes in the secondary electron spectra of TaS_2 film with UV-O_3 treatment exposure. Schematic band diagram of **b** N-OPV and **c** I-OPV. Reproduced with permission from Ref. [29]. **d** the schematic representation of the device structure in this work. **e** J-V curves of the OPVs prepared with various MoS_2 nanocomposites. **f** corresponding EQE spectra of these devices and **g** the calculated EQE enhancement of the device prepared with the AuNP@MoS_2 nanocomposites. The change in the absorption spectra after the AuNP@MoS_2 nanocomposite incorporation was also presented for easy comparison. Reproduced with permission from Ref. [30]

Table 7.3 Summary of the results of 2D-TMDs—based ternary active layers in OPVs

TMD	OSC Active Layer/Building Block (architecture)	WF (−eV)	J_{sc} (mA/cm^2)	V_{oc} (V)	FF	PCE (%)	ΔPCE	Other improvements	References
WS_2 nanosheets decorated with Au NPs	PCDTBT:WS_2–Au NPs: $PC_{71}BM$/(normal)	4.35 (CB) to 6.31 (VB)	12.3	0.89	0.58	6.3	12.5 (binary system)	N/A	Sygletou et al. [37]
Liquid exfoliated WSe_2 flakes	PTB7:$PC_{71}BM$/active layer (inverted)	3.6 (C.B.) to 4.9 (V.B.)	17.69	0.731	0.71	9.3	14.56 (binary system)	More balanced hole and electron mobilities	Kakavelakis et al. [38]

A novel and facile method to decorate various 2D materials (graphene oxide (GO), boron nitride (BN) and tungsten disulfide (WS_2)) nanosheets with metal nanoparticles has been proposed by Sygletou et al. [37]; in particular, the authors presented a top-down technique where NS-NPs assemblies were formed under ambient conditions via a solution laser assisted process (at 248 nm, 20 ns pulse duration) in the presence of a metallic precursor. It was found the metal NPs (diameters from 1 to 15 nm) were anchored on the plane and at the edges of the employed 2D material-based nanosheets. The decoration process was very controllable through (a) the laser fluence (100 and 1000 mJ/cm^2 were tested); (b) the number of pulses irradiated the mixed solution of the selected 2D material and the metallic precursor; and (c) the concentration of the metallic precursor into the mixed solution (1%, 1.5 and 2.5% v/v Au concentrations were tested). The general trend was that the gold plasmon resonance frequency (@ 545 nm) becomes more pronounced with the fluence and the number of ultraviolet pulses employed. For the proof of concept, the authors used a WS_2–Au NPs composite within the active layer of a ternary bulk heterojunction OPV. Due to the better energy alignment (compared to the binary system), the input of additional interfaces that lead further exciton dissociations and metal nanoparticles induced scattering effects, the PCE of the ternary system was enhanced by 13% and reached the value of 6.3%. The best performance was achieved for the 1.5% v/v concentration of Au NPs within the WS_2. The enhanced acquired PCE was mainly attributed to the higher J_{sc} due to improved (a) charge separation; (b) transportation; and (c) collection.

Kakavelakis et al. [38] provided important information regarding the application of 2D crystals in the inverted BHJ OSCs. It was the 1st work that showed quantitative the interplay between 2D crystals and fullerene domains size. The authors, when the lateral size of the liquid phase exfoliated (LPE) WSe_2 flakes, were matched with that of the fullerene ($PC_{71}BM$), managed to report the highest ever reported PCE for 2D material-based OSCs, ~9.3%. More particular, the authors exploited the LPE of bulk WSe_2 crystals in ethanol, by combining an ultrasonication process with sedimentation-based separation (SBS) to produce three different WSe_2 samples with fine-tuned area (~70, ~240, and ~720 nm^2) and thickness (~2.6, ~6.1 and ~8.5 nm). The as-prepared WSe_2 flakes were mixed within the PTB7:$PCB_{71}M$ blend and employed as the active layer in a ternary inverted OSC. The cell that employed WSe_2 flakes with area similar to the $PC_{71}BM$ (240 nm^2) provided the record performance (~9.3%), yielding an increase of the PCE of 15% with respect to the binary reference system (8.1%). The main enhancements were introduced to (1) the J_{sc} that was improved by 11% and (2) the FF that was enhanced from 68.7 to 71.7%. These improvements were ascribed to (1) area matching between the $PC_{71}BM$ and the WSe_2; (2) energy matching of the WSe_2 interlayer with that of donor and acceptor materials of the OSC; (3) exciton generation by the absorption induced by the WSe_2 (direct energy bandgap of 1.3 eV in the single-layer limit); (4) enhanced exciton generation in the interface between WSe_2 and PCBM; and (5) improved electron extraction to the cathode due to balanced charge carriers' mobility (Fig. 7.4).

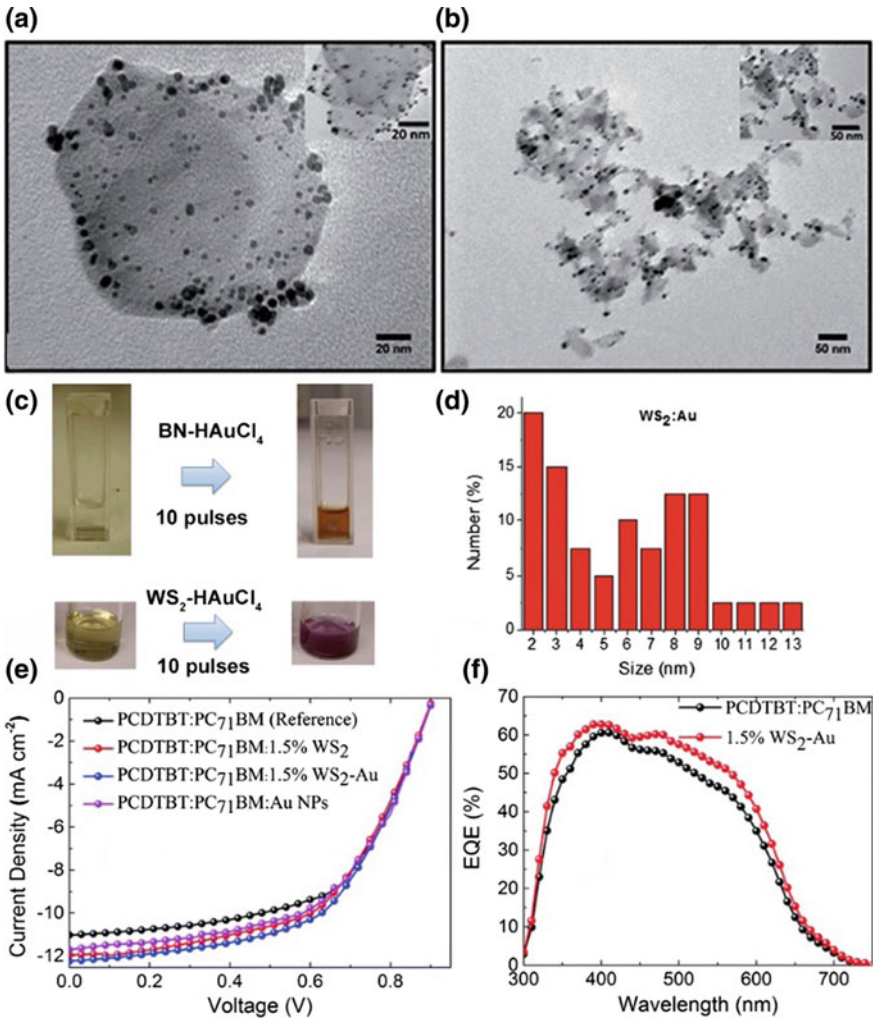

Fig. 7.4 TEM images of BN-Au (**a**) and WS_2-Au (**b**) NPs assemblies following the illumination of the mixed solutions with a single UV pulse. **c** Images of the pristine and laser irradiated dispersions. **d** Size distribution of the Au NPs grafted onto the WS_2 NS. **e** J-V curves for the optimized devices incorporating the reference PCDTBT:PC_{71}BM, the PCDTBT:Au:PC_{71}BM, the PCDTBT:WS_2:PC_{71}BM and the PCDTBT:WS2-Au:PC_{71}BM blends. **f** IPCE spectra for the control device and the one containing the WS_2-Au assemblies as a ternary component. Reproduced with permission from Ref. [37]. **g** Schematic representation of the WSe_2 flakes separation, the device architecture and the energy level diagram. **h** J-V curves of the PTB7:PC_{71}BM-based OPVs and **i** IPCE measurements of solar cells based on WSe_2 flakes having different sizes. $J-V^2$ characteristics under dark conditions of the fabricated devices for the calculation of **j** electron and **k** hole mobility using the Mott−Gurney equation. Reproduced with permission from Ref. [38]

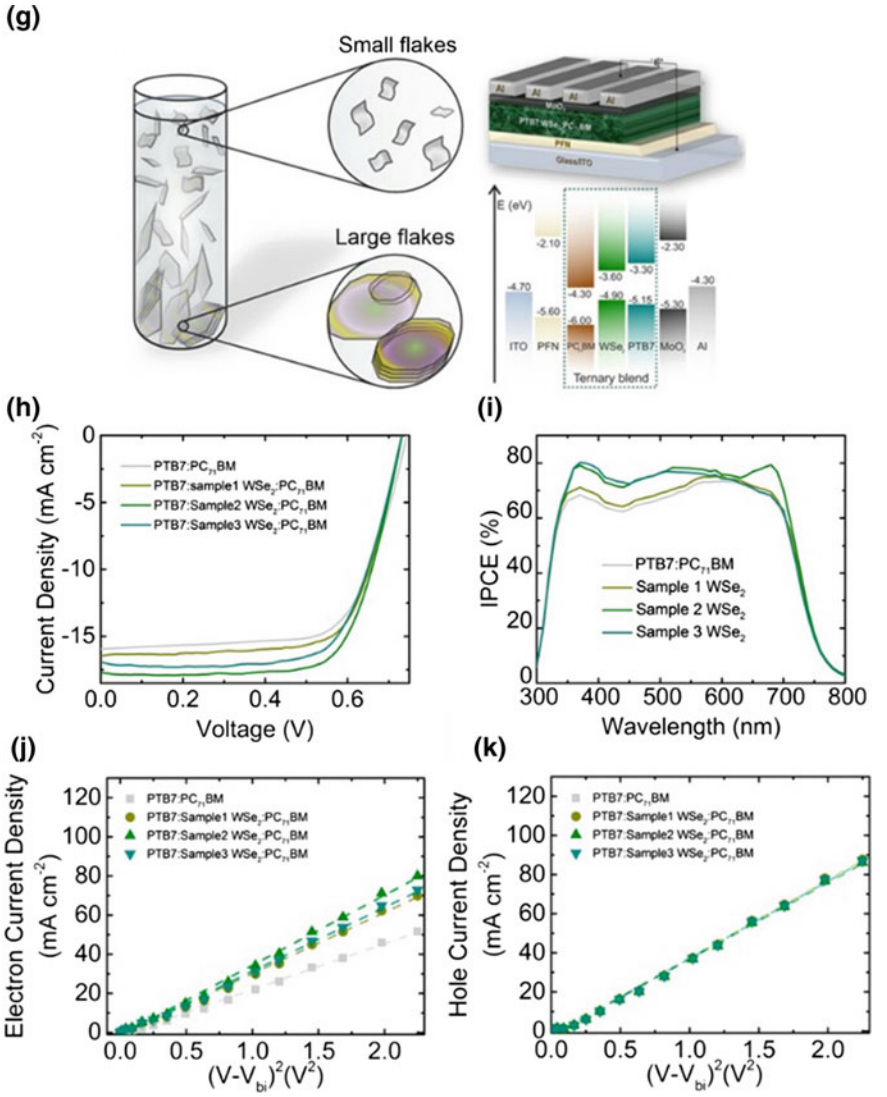

Fig. 7.4 (continued)

7.3 Application of Transition Metal Dichalcogenides in PSCs

The great success and progress of graphene and GRMs in third-generation solution-processed photovoltaics [39] has inspired the researcher of the field to explore and apply also other 2D layered materials beyond graphene and in particular the 2D-

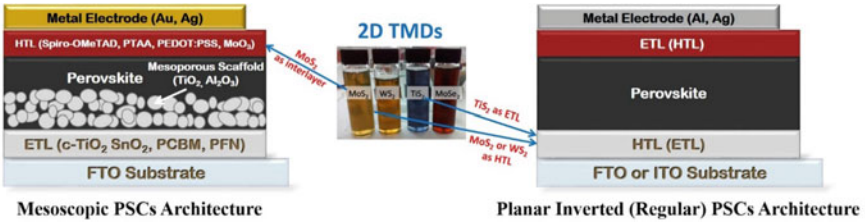

Fig. 7.5 Schematic diagram showing both (left) the mesoscopic and (right) the planar (regular and inverted) PSC architectures. The picture in the center depicts various 2D-TMDs (MoS_2, WS_2, TiS_2 and $MoSe_2$) dispersions, and the blue arrows indicate the different layers in which these TMDs have been placed in the PSC building blocks

TMDs in highly emerging PSCs. Importantly, 2D-TMDs due to their outstanding (a) chemical, physical and electronic properties and (b) acceptability on doping or functionalization processes to further improve their properties (e.g., enhancement of their conductivity, tuning of their WF) constitute an excellent new class of materials to be tested in this highly emerging photovoltaic technology. Moreover, 2D-TMDs are characterized by an energy bandgap that overcomes the major limitation of graphene, which is the absence of a bandgap. This allows the application of the 2D-TMDs as ETLs (or hole blocking) or HTLs (or electron blocking) materials. These materials can be fabricated on large area into a single layer or few layers utilizing chemical vapor deposition (CVD) or liquid phase exfoliation, to demonstrate their superior electrical and optical properties. The presence of (a) lone pairs of electrons at the surfaces of 2D-TMDs, (b) non-covalent interaction and (c) the absence of dangling bonds could enhance their resistance to reactions with other chemical elements [5] and as a result enhancing the stability of PSCs when employed in one of their transporting layers. The most commonly reported 2D-TMDs utilized in the field of PSCs, after the necessary chemical processing, are few layers of the inorganic MoS_2 and WS_2 [40]. In Fig. 7.5 are depicted the two possible PSCs architectures (mesoscopic and planar) and the different positions where the 2D-TMDs can be placed within the device are highlighted.

7.3.1 TMDs Interfacing Metal Halide Perovskites

The first demonstration of the huge potential of TMDs toward efficient charge-extraction materials when interfacing metal halide perovskite photoactive materials was presented by Peng et al. back in 2016 [41]. Despite the benefits of the current state-of-the-art HTM used in PSCs, such as the ultrafast charge separation and injection at the $MAPbI_3$/spiro-OMeTAD interface [42], they present striking disadvantages toward the commercialization of these devices. On the one hand, spiro-OMeTAD (the most commonly exploited HTM used in PSCs) is in fact of higher cost than gold in weight that is in contradiction with the need of low-cost solar cells.

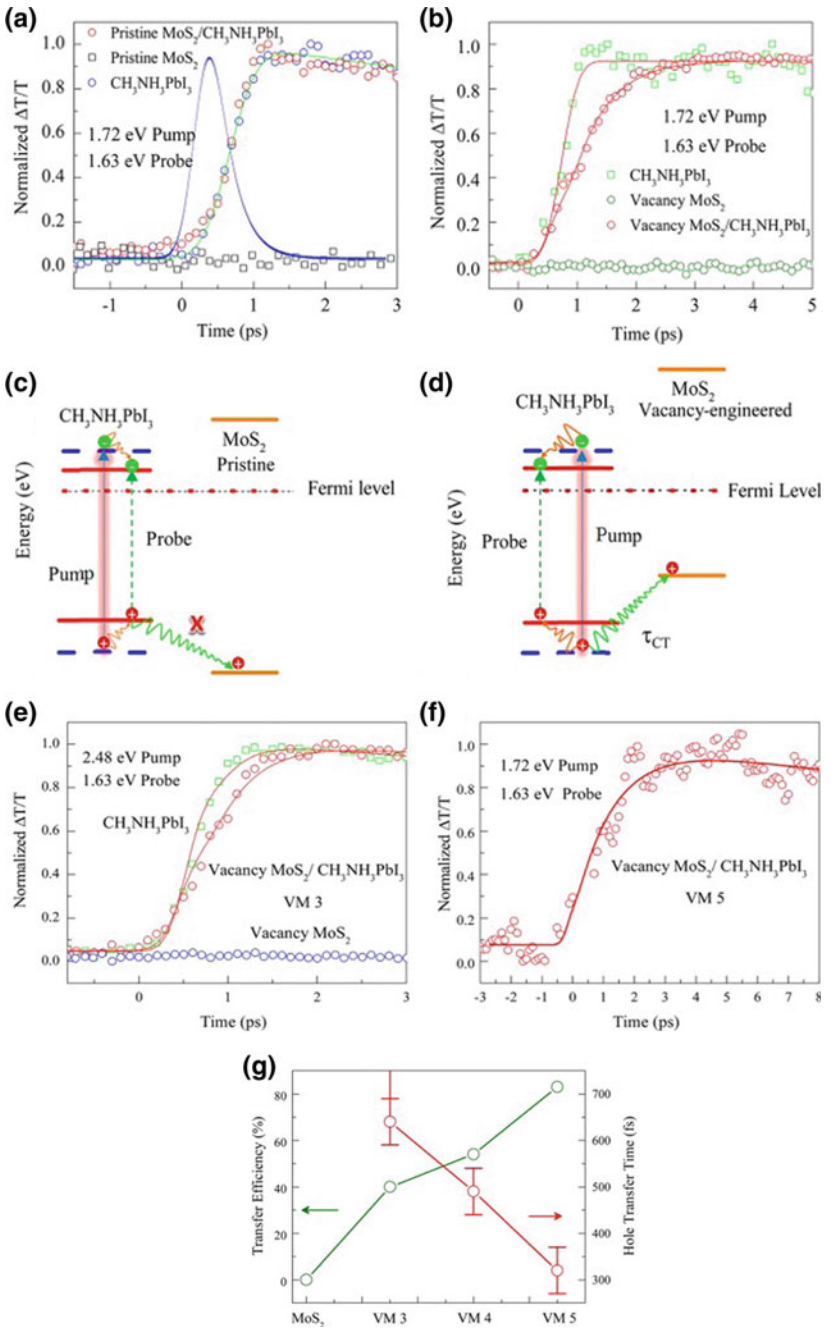
(a)
Pristine MoS2/CH3NH3PbI3
Pristine MoS2
CH3NH3PbI3
1.72 eV Pump
1.63 eV Probe
Normalized ΔT/T
Time (ps)
(b)
1.72 eV Pump
1.63 eV Probe
CH3NH3PbI3
Vacancy MoS2
Vacancy MoS2/CH3NH3PbI3
Normalized ΔT/T
Time (ps)
(c)
CH3NH3PbI3
MoS2
Pristine
Fermi level
Probe
Pump
Energy (eV)
(d)
CH3NH3PbI3
MoS2
Vacancy-engineered
Fermi Level
Probe
Pump
τCT
Energy (eV)
(e)
2.48 eV Pump
1.63 eV Probe
CH3NH3PbI3
Vacancy MoS2/ CH3NH3PbI3
VM 3
Vacancy MoS2
Normalized ΔT/T
Time (ps)
(f)
1.72 eV Pump
1.63 eV Probe
Vacancy MoS2/ CH3NH3PbI3
VM 5
Normalized ΔT/T
Time (ps)
(g)
Transfer Efficiency (%)
Hole Transfer Time (fs)
MoS2
VM 3
VM 4
VM 5

◀**Fig. 7.6** **a** Transient absorption signals at 1.63 eV upon excitation at 1.72 eV. The invariance of the photobleach rise times indicates the absence of charge transfer between the pristine MoS_2 monolayer and $CH_3NH_3PbI_3$. The blue dashed line is the pump−probe laser cross-correlation of the spatially resolved micro pump−probe setup. **b** The increasing rise time indicates that the hole transfer takes place. **c** Schematic illustrating the type I band alignment and the absence of charge transfer between the pristine MoS_2 monolayer and $CH_3NH_3PbI_3$. **d** Schematic of the type II energy alignment at the vacancy-engineered $MoS_2/CH_3NH_3PbI_3$ interface favoring hole transfer from the perovskite to the vacancy-engineered MoS_2 monolayer. **e** Photobleaching signals at 1.63 eV after excitation at 2.48 eV in $CH_3NH_3PbI_3$, vacancy-engineered $MoS_2/CH_3NH_3PbI_3$ heterostructure and vacancy-engineered MoS_2 monolayer. **f** Evolution of the photobleaching signals at 1.63 eV after excitation at 1.72 eV as the bleach builds up. Prolonged oxygen plasma treatment of the MoS_2 monolayer resulted in the quenching of the PL. **g** Hole transfer efficiency and hole transfer time as a function of S vacancy density. The higher S vacancy density results in a higher hole transfer rate and efficiency. Reproduced with permission from Ref. [41]

On the other hand, being organic in nature and the need of a doping procedure to improve its conductivity raises stability issues in the solar cell. Thus, the motivation of the authors for this work was to overcome the aforementioned limitations of HTMs by testing CVD fabricated MoS_2 single-layer film that is of significantly lower cost and higher carrier mobility material compared to spiro-OMeTAD. However, using ultraviolet photoelectron spectroscopy (UPS) the authors realized that CVD fabricated MoS_2 single layer has a valence band (VB) of −6.28 eV, and since the VB of $MAPbI_3$ is −5.79, CVD fabricated MoS_2 cannot efficiently collect the photoexcited holes of $MAPbI_3$ due to the valence band barrier that is built at their interface. Very surprisingly, they also demonstrated that the intrinsic band offset at the $MAPbI_3/MoS_2$ interface was overcome by creating sulfur vacancies in MoS_2 using a mild plasma treatment due to the reduction in the band offset (increased work function); using this approach, ultrafast hole transfer was reported from $MAPbI_3$ to MoS_2 that occurred within 320 fs with 83% efficiency following photoexcitation (these results were extracted using ultrafast transient absorption spectroscopy and photoluminescence quenching measurements). Importantly, this work highlighted the feasibility of applying defect-engineered 2D-TMDs as charge-extraction layers in perovskite-based optoelectronic devices (Fig. 7.6).

7.3.2 2D-TMDs as Hole Transporters in PSCs

Table 7.4 summarizes the reported results regarding the utilization of 2D-TMDs as HTLs in both mesoscopic and planar PSCs. The same year Kim et al. [43] proposed for the first time the utilization of CVD produced thin films (~2 nm thick) of MoS_2 and WS_2 as HTLs in mixed halide $MAPbI_{3-x}Cl_x$ planar inverted PSCs. The motivation toward this work was to address the stability related drawbacks of the PEDOT:PSS hole transporter (acidic nature, aqueous processed material). The 2D-TMDs-based HTL exhibited similar PCEs, with respect to the reference devices based on PEDOT:PSS. The PCEs of MoS_2 & WS_2 devices were 9.53 and 8.02%,

respectively, versus 9.93% for the PEDOT:PSS-based devices. The lower PCE of the WS_2-based devices was mainly attributed to the lower measured open circuit voltage (V_{oc}) due to its lower work function (−4.95 eV compared to the −5 eV of the MoS_2 and the 5.25 eV of the PEDOT:PSS with respect to the valence band of $CH_3NH_3PbI_{3-x}Cl_x$).

A few months afterward, Capasso et al. [44] addressed the aforementioned stability-related challenges of Spiro-OMeTAD-based PSCs with the use of LPE, spin-coated MoS_2 2D-flakes (~3 nm in thickness) as an interlayer between $MAPbI_3$ active absorber and the Spiro-OMeTAD state-of-the-art hole transporter in a mesoscopic PSC device. MoS_2 had a dual role: (1) to prevent the formation of shunt contacts between the perovskite and the Au electrode and (2) to provide a more suitable energy band alignment between the active layer and the HTL that facilitates the fast transportation of holes into the HTL. Because of the uniform deposition of MoS_2 onto perovskite absorber and the favorite energy alignment between the valence band (VB) of MoS_2 and the $MAPbI_3$ (as confirmed by top view SEM images and UPS measurements, respectively), the measured short circuit current density was significantly enhanced compared to the respective ones in reference (MoS_2-free) devices. Moreover, the MoS_2 flakes addition enhanced the stability of the devices preserving almost completely the initial PCE of ~13.3% for over 550 h, while in the case of the MoS_2-free devices, the PCE was constantly decreased and after a 550 h of the aging test under illumination the PCE dropped about 34% compared to the initial value). The improved stability was ascribed to the surface passivation of the perovskite layer provided by the MoS_2, which prevented the iodine migration from the perovskite into the HTL. The use of solution-processed MoS_2 flakes has also been successfully demonstrated for the high performance of large active area (~1.05 cm^2) cells.

One year later, Dasgupta et al. [45] demonstrated the application of impressive homogeneous, pinhole-free, spin-coated deposited LPE p-doped MoS_2 thin films (five layers) operated as HTL in $MAPbI_3$ planar inverted PSCs. The record device exhibited PCE of 6.01% which was superior to the HTL-free reference cells by 241%. However, these devices exhibited significantly lower PCE compared to the previously reported works exploiting MoS_2 as the HTL. The supremacy of the MoS_2 HTL based compared to the HTL-free PSCs was attributed to the suitable energy band alignment, after the doping of the MoS_2 through UV-ozone treatment, between the VB of the inorganic HTL and the VB of $MAPbI_3$ that facilitated the fast hole extraction (within 320 fs) and thus more efficient collection.

Again in 2017, Huang et al. [46] proposed the incorporation of water soluble, low temperature processed (to acquire the desired 1T phase, at 90 °C), thin films (~11 nm) of 2D-TMDs such as MoS_2 and WS_2 as HTLs in planar inverted PSCs. The authors reported higher PCEs for the MoS_2 and WS_2 HTL-based cells compared to the PEDOT:PSS-based PSCs by 15.4 and 20%, respectively. This was attributed to (1) the better energy band alignment between the VB of the selected TMD and perovskite absorber layer leading to higher acquired V_{oc}; (2) the lower series resistance and the higher shunt resistance of the 2D TMD-based HTLs compared to the reference PEDOT:PSS devices. Moreover, the TMD HTL-based non-encapsulated solar cells

Table 7.4 Summary of the results of 2D-TMDs-based HTLs in PSCs

TMD	Perovskite/building block (architecture)	WF (−eV)	J_{sc} (mA/cm^2)	V_{oc} (V)	FF	PCE (%)	ΔPCE (%)	Other improvements	References
VD MoS_2	MAPbI3-xClx/HTL (planar inverted)	−5.0	14.89	0.96	0.67	9.53	−4.02 (PEDOT:PSS)	N/A	Kim et al. [43]
CVD WS_2	$MAPbI_{3-x}Cl_x$/HTL (planar inverted)	−4.95	15.91	0.82	0.64	8.01	−19.34 (PEDOT:PSS)	N/A	Kim et al. [43]
LPE MoS_2	$MAPbI_3$/HT interlayer (mesoscopic)	−5.1	21.5	0.93	0.67	13.3	+6.34 (MoS_2-free)	Self-stability, scalability	Capasso et al. [44]
UV-O_3-treated LPE MoS_2	$MAPbI_3$/HTL (planar inverted)	N/A	12.60	0.84	0.57	6.01	+341 (no HTL)	N/A	Dasgupta et al. [45]
LPE MoS_2	$MAPbI_{3-x}Cl_x$/HTL (planar inverted)	−5.13	20.94	0.88	0.78	14.35	+15.35 (PEDOT:PSS)	Self-stability	Huang et al. [46]
LPE WS_2	$MAPbI_{3-x}Cl_x$/HTL (planar inverted)	−5.18	21.22	0.97	0.73	15.00	+20.58 (PEDOT:PSS)	Self-stability	Huang et al. [51]
LPE MoS_2-PAS	$MAPbI_3$/additive in HTL (planar inverted)	N/A	24.04	0.99	0.69	16.47	+6.8 (PEDOT:PSS undoped)	Self-stability	Dai et al. [47]
LPE MoS_2	$MAPbI_3$/HT interlayer (planar inverted)	N/A	20.71	1.01	0.78	16.42	+5.8 (PTAA)	MPP ambient stability, scalability	Kakavelakis et al. [48]
MoS_2 (theoretical work)	$MAPbI_3$/HTL (planar inverted)	N/A	26.25	0.93	0.84	20.53	+97 (no HTL)	N/A	Kohnehpoushi et al. [49]

exhibited superior stability, under nitrogen storage conditions; the WS_2- and MoS_2-based PSCs retained 72 and 78% of their PCE after 56 days within the glove box whereas the PEDOT:PSS cells degraded to zero % over 35 days (mainly due to hygroscopic feature of PEDOT:PSS).

The main reason for the low performances of the PSCs that use 2D-TMDs as the sole bottom HTL was mainly due to the poor coverage and passivation of the ITO transparent electrode that resulted from the low dispensability of the TMDs in the most of commonly used solvents. To overcome this limitation, Dai et al. [47] introduced phenyl acetylene silver (PAS), a metalorganic compound, to modify MoS_2. PAS functionalized MoS_2 compound improved the dispersibility of the TMD in common solvents such as of DMF and water. A conductive polymer PEDOT:PSS blend with the MoS_2 led to a significantly enhanced performance of planar inverted PSCs achieving 16.47% as well as largely increased stability.

Until recently, the stability of 2D-TMDs HTL-based PSCs was checked under dark or under nitrogen environment conditions. In 2018, Kakavelakis et al. [48] addressed for the first time on the stability of solution-processed planar inverted $MAPbI_3$ PSCs under prolonged illumination conditions along with the continuous operation at MPPT in ambient atmospheric conditions. The authors' approach was also successfully applied in larger area solar cells (with active layer of 0.5 cm^2). They demonstrated state of the art of long-term stability in the aforementioned stress conditions; after 568 h of continuous operation, the PCE retained ~80% of its initial ~17% PCE (T_{80} time), using MoS_2 nanoflakes as the hole transporting interlayer between the $MAPbI_3$ perovskite absorber and PTAA HTL. This extended stability was attributed to (1) the interlayer operating as a shield for the perovskite to contact the doped PTAA; (2) the stronger mechanical strength of the MoS_2/PTAA compared to the bare doped PTAA under electrical biasing stress; (3) prohibiting water molecules to reach the active layer from ITO and HTL material; and (4) the stopping of indium ions migration from ITO toward the interface between the HTL and the perovskite active layer. Beside the improved stability of the devices, the introduction of the MoS_2 facilitated the more efficient hole charge extraction (these results were extracted using transient photocurrent and transient photovoltage measurements) from the perovskite semiconductor due to almost perfect energy band alignment that secured also the electron blocking by the MoS_2 interlayer. Additionally, the use of MoS_2 contributed to the reduction of the bimolecular recombination at the perovskite/HTL interface as revealed the intensity-dependent measurement of the short circuit current density. These improvements resulted in a slightly higher performance (~6% higher) of the MoS_2-based compared to the MoS_2-free PSCs.

Finally, Kohnehpoushi et al. [49] recently simulated a low-cost architecture that satisfies the market criteria due to the utilization of low cost, stable inorganic HTL and ETL transporting layers in PSCs. This work was mainly focused in addressing the high fabrication cost (high cost of most organic materials employed, e.g., PEDOT:PSS, Spiro-OMeTAD, PTAA, PCBM) that is still a main drawback for the establishment and domination of PSCs. The authors following the current existing research trend for the exploitation of low-cost nanosheets of 2D-TMDs simulated the use of MoS_2-based HTLs in planar inverted $MAPbI_3$ PSC configurations. The

authors very clearly demonstrated the impact of determining the optimum thickness of the HTL (and the ETL) and of the perovskite layer, to lower as much as possible the recombination rates and maximize the solar light harvesting, respectively. The authors calculated for 1.34-nm-thick MoS_2, 350-nm-thick $MAPbI_3$ layer, the maximum PCE, 20.53% which is 96% higher than the one of the HTL-free device. The record performances were calculated for devices employed aluminum (Al) or silver (Ag) electrodes that lower even more the cost of the PSCs (Fig. 7.7).

7.3.3 2D-TMDs as Electron Transporters in PSCs

Table 7.5 summarizes the reported results regarding the utilization of 2D-TMDs as HTLs in both mesoscopic and planar PSCs. The first demonstration of TMDs placed in the ETL of PSCs was made by Ahmed et al. [50] in 2016. In this work in order, the authors to boost the absorption spectrum of the $MAPbI_3$ at its band edges without complicating the cell configuration, by introducing nanoparticles, for example [32], or increase the thickness of the active layer, suggested the use of an ETL nanocomposite build by MoS_2 nanosheets impeded within the TiO_2 layer. The utilization of the MoS_2 into the ETL succeeded to extend the absorption spectrum of the device from 350 to 800 nm (see Fig. 7.1d). The record results were obtained for 20 wt% impeded MoS_2 flakes into the TiO_2 matrix. Above this concentration, induced agglomeration of MoS_2 causing the CB of MoS_2 to be lower than the one of TiO_2 which hinders the electrical properties of the ETL nanocomposite. Due to absorption complementarily contributed by the MoS_2, the PCE was enhanced from 3.74 to 4.43% compared to the pristine TiO_2 ETL-based device. The immersion of the MoS_2 flakes into the TiO_2 matrix did not only contributed to higher absorption but also improved the conductivity of the TiO_2 which resulted in the faster electron transport along the interface of active and ETL. This lowered the recombination rates and enhanced the more efficient charge collection.

For the next almost two years, there were few reports of progress regarding the utilization of 2D-TMDs as ETLs in PSCs since it was more than obvious that the most commonly exploited TMDs (MoS_2 and WS_2) performed better as HTLs of these devices. However, very surprisingly in early 2018 and almost at the same time two different groups reported the use of titanium disulfide (TiS_2) as efficient and stable ETLs for PSCs. The motivation of the authors of both works was to overcome the tradeoff between the performance and the processing temperature that TiO_2 ETL presents. By using LPE, 2D-TiS_2 as a low temperature processed ETL replacing the state-of-the-art TiO_2 highly efficient and stable planar normal PSCs, was fabricated.

On the one hand, Huang et al. [51] exploited a room temperature and aqueous solution-processed UV-ozone-treated 2D-TiS_2 film as ETL achieved 18.79% PCE. This value is the highest ever reported performance for a solution and room temperature processed planar normal PSC. Another important finding of this work was that the pristine (UV-ozone free) TiS_2 ETL-based PSCs resulted in significantly lower PCEs compared to the UV-ozone-treated TiS_2 ETL (~9.5%). This was due

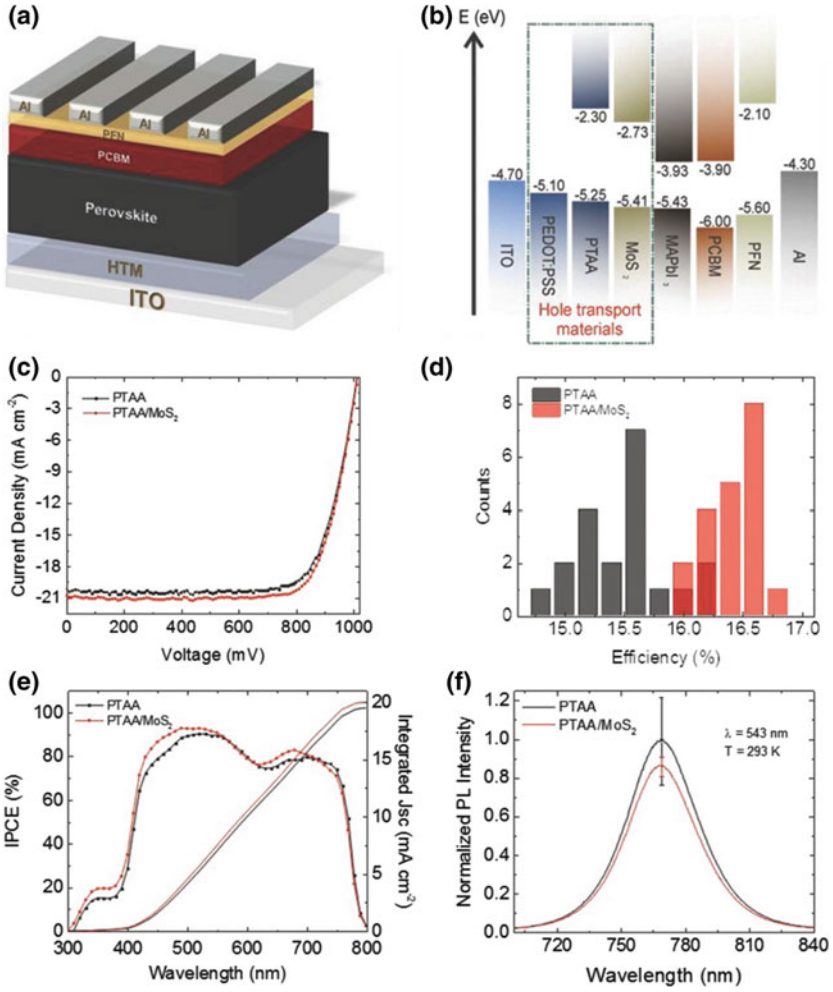

Fig. 7.7 Schematic of **a** the device architecture and **b** the energy band diagram of the fabricated planar inverted PSCs. **c** The J–V curves of PSCs based on PTAA (black) and PTAA/MoS_2 bilayer (red) HTMs measured under AM 1.5G (100 mW cm^{-2}) illumination conditions. **d** PCE distribution of the devices with (red) and without (black) MoS_2 interlayer. **e** EQE spectra of the PTAA (red) and PTAA/MoS_2 (black) based devices. **f** Photoluminescence spectra of $CH_3NH_3PbI_3$/PTAA (black) and MoS_2/PTAA/glass (red) substrates. Reproduced with permission from Ref. [48]. **g** The J -V curves and **h** the changes of PCE as a function of time for $CH_3NH_3PbI_3$ PSCs based on PEDOT:PSS blended with different concentration of MoS_2-PAS. Reproduced with permission from Ref. [47]. **i** Lifetime test under continuous illumination at the MPP tracking of devices with (red scatter) and without MoS_2 (black scatter) in ambient conditions. Inset: Actual MPP values obtained for both devices. **j** State-of-the-art lifetimes reported in continuous device operation in the above-mentioned conditions of high-efficiency PSCs in both ambient (black marked) and inert conditions (blue marked). Reproduced with permission from Ref. [48]. **k** J-V curves of the large-area cells (1.05 cm^2 active area) with (blue curve) and without MoS_2 (red curve) measured under one sun illumination conditions. (l) Photograph of a large-area cell with the MoS_2 interlayer. Reproduced with permission from Ref. [44]

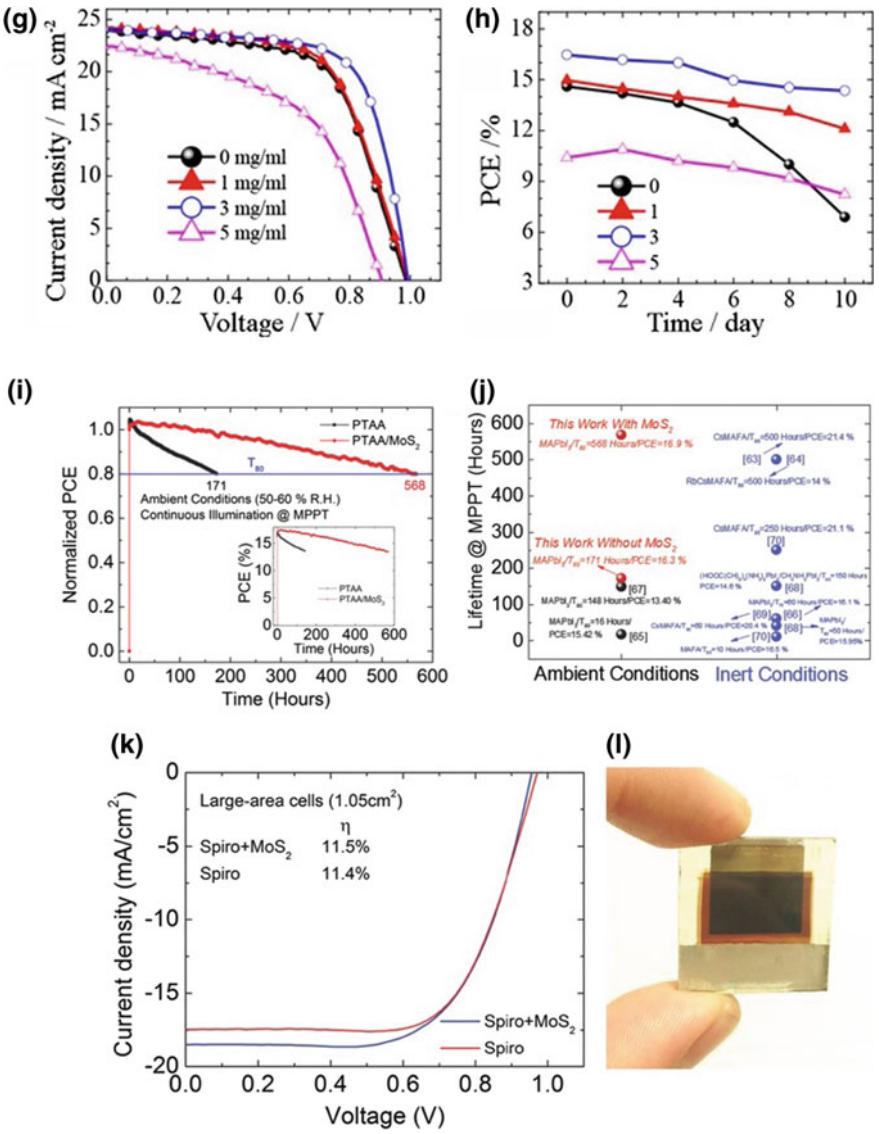

Fig. 7.7 (continued)

Table 7.5 Summary of the results of 2D-TMDs—based ETLs in PSCs

TMD	Perovskite/Building Block (architecture)	WF (−eV)	J_{sc} (mA/cm^2)	V_{oc} (V)	FF	PCE (%)	ΔPCE (%)	Other improvements	References
CVD MoS_2	MAPbI3-xClx/additive in ETL (planar normal)	N/A	13.36	0.65	0.51	4.43	+18 (TiO_2 undoped)	N/A	Ahmed et al. [50]
LPE UV-O_3-treated TiS_2	$MAFAPbI_{3-x}Br_x$/ETL (planar normal)	−4.64	24.75	1.00	0.75	18.79	+40 (no ETL)	Humidity stability	Huang et al. [51]
LPE TiS_2	$MAFAPbI_3$/ETL (planar normal)	N/A	23.38	1.05	0.71	17.37	+2 (TiO_2)	UV-light stability, flexibility and bendability	Yin et al. [52]

to the unfavorable band alignment between the ETL and perovskite energy levels, while such a treatment of the TiS_2 film with UV-ozone resulted in an almost perfect alignment band of the two materials. Additionally, the UVO-treated 2D-TiS_2 ETL-based devices demonstrated an extremely high stability, and the average PCEs of non-encapsulated cells remained over 95% of initial PCEs after being stored at atmospheric conditions with relative humidity of ~10% for more than 800 h.

On the other hand, Yin et al. [52] prepared the 2D-TiS_2 nanosheets by a simple solution exfoliation method and demonstrated that 2D-TiS_2 can be applied as an effective ETL in normal planar PSCs. The optimum concentration of the TiS_2 flakes in the dispersion resulted in PSCs with very high PCE of 17.37%. Photoluminescence quenching and time-resolved photoluminescence measurements revealed that TiS_2 can extract the charges and transport them as efficient as the state-of-the-art TiO_2 ETL, resulting in comparable photovoltaic performances of the respective devices. Furthermore, TiS_2-based devices were significantly more stable in constant UV-light exposure compared to TiO_2-based cells. Flexible PSCs were also fabricated using the low temperature processed TiS_2 presenting acceptable PCEs and bending tolerance. Benefiting from the merits of solution and low temperature processability, high mobility and suitable energy level, the proposed TiS_2 fabrication method could aid scalable production of PSCs with high efficiency, excellent UV stability and realization flexible PSCs (Fig. 7.8).

7.4 Conclusions and Perspectives

Third-generation photovoltaics such as OSCs and PSCs are very promising photovoltaic elements that are expected to contribute in the near future to satisfying of the vast global demand for energy. Both of these technologies are under intense research investigation, to improve their performance, lower their fabrication cost and enhance their stability and lifetime, and thus, become competitive technologies to silicon as alternatives or complementary solar cell elements in various applications. 2D-TMDs are solution-processed elements that can be incorporated in the case of OSCs in all the building blocks whereas in the case of PSCs can be utilized mainly into the transporting layers. Their main impact in OSCs includes (a) higher PCE, reaching efficiencies higher than 9% and (b) extension of OSCs lifetimes mainly by replacing the PEDOT:PSS. In the case of PSCs, the improved operational characteristics were attributed to (a) facilitation of the charge extraction; (b) improvement of the device long-term stability (under various degradation and stress protocols); (c) increased scalability of these devices; and (d) the construction of solar cells at low temperatures.

However, the challenges to be tackled are numerous. The success of the establishment of the 2D-TMDs based on solar cells is very much dependent on the development and the optimization of production methods for the fabrication of uniform, solution-processed TMD films with high yield and in industrial scale. These demands are beyond the fabrication of the films but reach also the low-cost deposition tech-

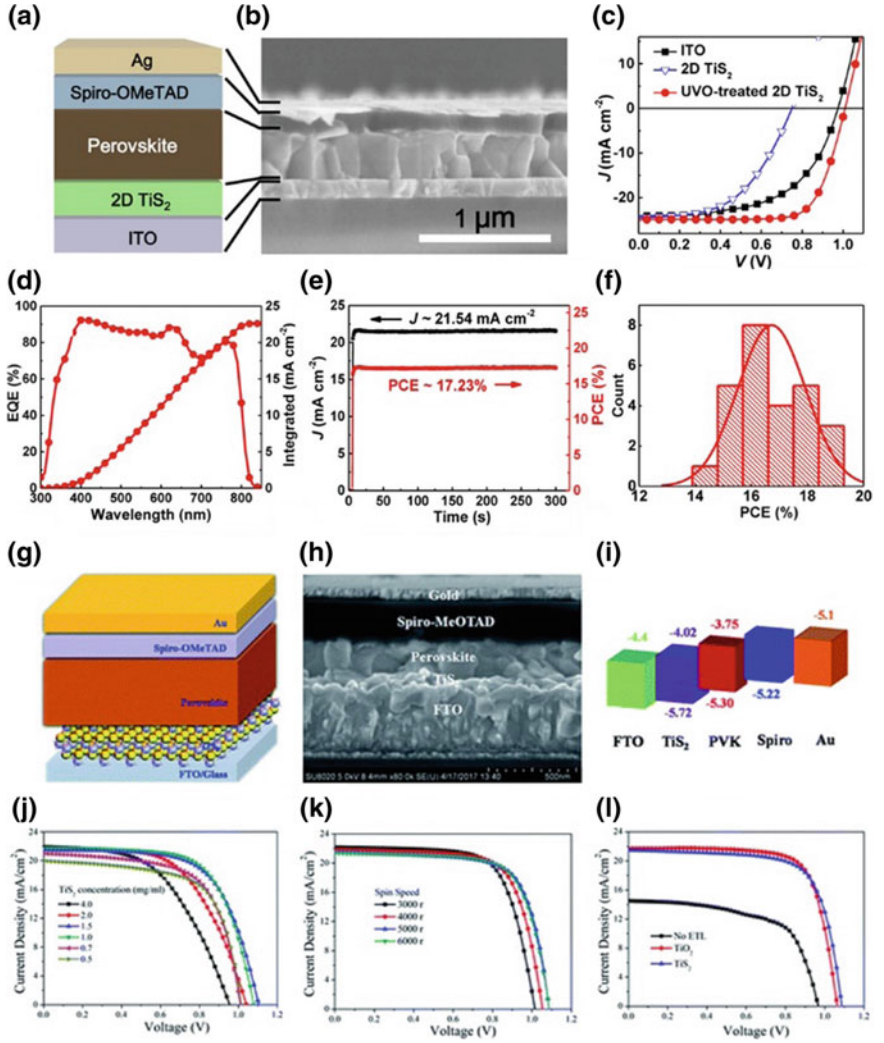

Fig. 7.8 **a** Schematic illustration of the device configuration and **b** cross-sectional SEM image of the corresponding device. **c** Typical J-V curves of the PSCs with different ETLs under one sun illumination conditions. **d** EQE spectra of the PSCs with UV-O_3-treated 2D-TiS_2 as ETL. **e** Steady-state efficiency of the PSCs with UVO-treated 2D-TiS_2 as ETL. **f** Distribution of the PCEs of PSCs with UVO-treated 2D-TiS_2. Reproduced with permission from Ref. [51]. **g** Device schematic and **h** cross-sectional SEM image of PSCs with the 2D-TiS_2 ETL. **i** Corresponding energy level diagram of PSC with TiS_2 as ETL. **j** J-V curves of the PSCs with TiS_2 ETLs that were prepared with different concentration of solution. **k** J-V curves of the PSCs with TiS_2 ETLs that were coated with different spin speed. **l** J-V curves of the best-performing PSCs with ETLs (TiS_2 or TiO_2) and without an ETL. **m** Ultraviolet photocatalytic activity for decomposition of water in Na_2SO_4 solution by using TiO_2 and on TiS_2 film on FTO glass as photoanodes. **n** Long-term UV-light stability of the PSCs with TiO_2 or TiS_2 film as the ETLs. **o** J-V curves of the flexible devices with TiS_2 as ETLs. J-V curves of the flexible PSCs before and after 300 bending cycles with a radius of curvature of **p** 12, **q** 7 and **r** 5 mm, respectively. The insets show the corresponding bending images. Reproduced with permission from Ref. [52]

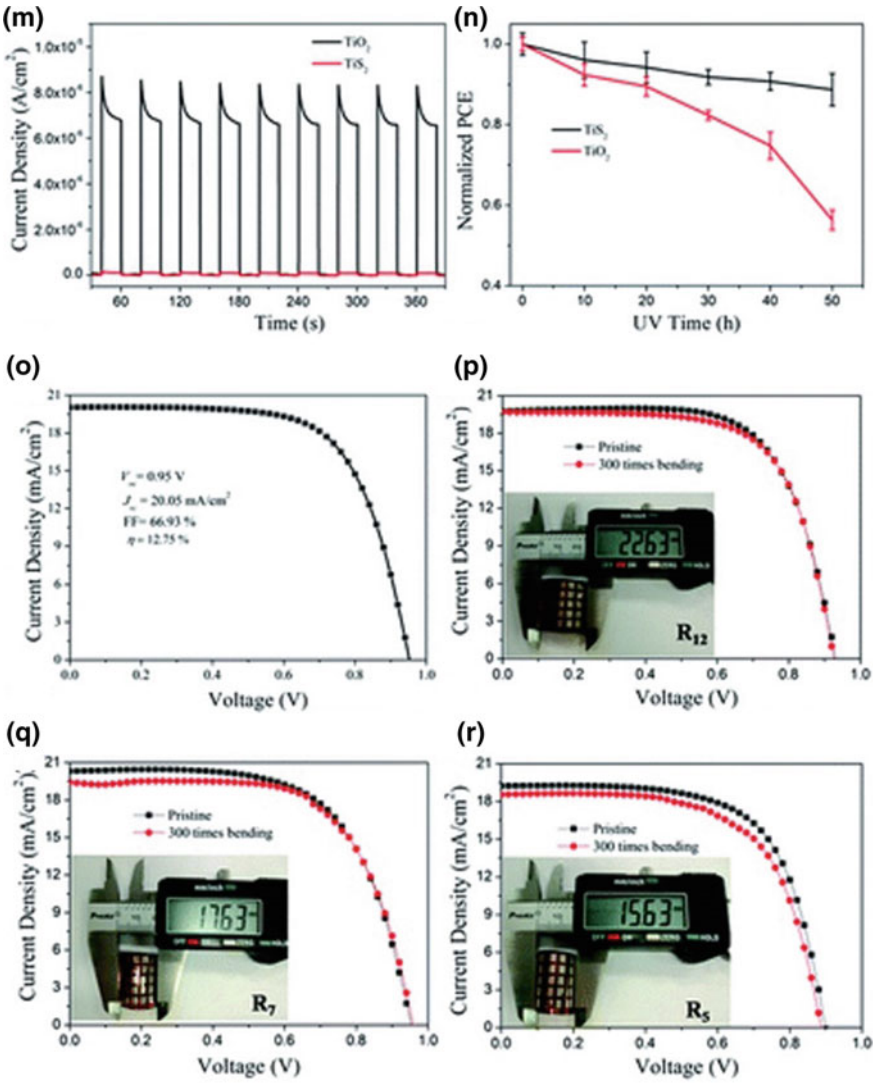

Fig. 7.8 (continued)

niques, e.g., spray coating away, from the expensive CVD methods. The implemented research regarding the utilization of 2D-TMDs within OSCs and PSCs has thus far involved a limited number of materials. The further testing of other available TMDs beyond the MoS_2 and WS_2 as HTL in OSCs and PSCs should be attempted. It is noteworthy that TMDs represent a large group of materials including TiS_2, TaS_2, ReS_2 and ZrS_2 which have similar structural features but versatile chemical and electronic

properties. These innovative materials should be further tested in OSCs and PSCs as electrodes and/or as transport layers.

Acknowledgements The authors would like to acknowledge the Strategic Partnership Alliance Project, entitled "Electronics Beyond Silicon Era"—ELBYSIER (2015-1-ELKA203-013988) under the Erasmus Plus Program for supporting this work.

References

1. Bonaccorso F, Colombo L, Yu G, Stoller M, Tozzini V, Ferrari AC et al (2015) Graphene, related two-dimensional crystals, and hybrid systems for energy conversion and storage. Science 347:1246501–1246509
2. Cao X, Tao C, Zhang X, Zhao W, Zhang H (2016) Solution-processed two-dimensional metal dichalcogenide-based nanomaterials for energy storage and conversion. Adv Mater 28:6167–6196
3. Kakavelakis G, Kymakis E, Petridis K (2018) 2D materials beyond graphene for metal halide perovskite solar cells. Adv Mater Interf https://doi.org/10.1002/admi.201800339
4. Ortiz-Quiles EO, Cabrera CR (2017) Exfoliated molybdenum disulfide for dye sensitized solar cells. FlatChem 2:1–7
5. Marcia M, Hirsch A, Hauke F (2017) Perylene-based non-covalent functionalization of 2D materials. FlatChem 1:89–103
6. Yu G, Cao J, Hummelen J, Heeger A (1995) Polymer photovoltaic cells: enhanced efficiencies via a network of internal donor-acceptor heterojunctions. Science 270:1789–1791
7. Jonas F, Krafft W, Muys B (1995) Conductive coatings, technical applications and properties. Macromol Symp 100:169–173
8. Voroshazi E, Verreet B, Buri A, Muller R, Di Nuzzo D, Heremans P (2011) Influence of cathode oxidation via the hole extraction layer in polymer: fullerene solar cells. Org Electron 12:736–744
9. Shrotriya V, Li G, Yao Y, Chu CW, Yang Y (2006) Transition metal oxides as the buffer layer for polymer photovoltaic cells. Appl Phys Lett 88:073508
10. Girotto C, Voroshazi E, Cheyns D, Heremans P, Rand BP (2011) Solution-processed MoO_3 thin films as a hole-injection layer for organic solar cells. ACS Appl Mater Interfaces 3:3244–3247
11. Shizuo T, Koji N, Yasunori T (1996) Metal oxides as a hole-injecting layer for an organic electroluminescent device. J Phys D Appl Phys 29:2750–2753
12. Yun JM, Noh YJ, Yeo JS, Go YJ, Na SI, Jeong HG et al (2013) Efficient work-function engineering of solution processed MoS_2 thin-films for novel hole and electron transport layers leading to high-performance polymer solar cells. J Mater Chem C 1:3777–3783
13. Gu X, Cui W, Li H, Wu Z, Zheng Z, Lee ST et al (2013) A solution-processed hole extraction layer made from ultrathin mos_2 nanosheets for efficient organic solar cells. Adv Energy Mater 3:1262–1268
14. Gu X, Cui W, Song T, Liu C, Shi X, Wang S et al (2014) Solution-processed 2D niobium diselenide nanosheets as efficient hole-transport layers in organic solar cells. Chemsuschem 7:416–420
15. Murphy DW, Di Salvo FJ, Hull GW, Waszczak JV (1976) Convenient preparation and physical properties of lithium intercalation compounds of Group 4B and 5B layered transition metal dichalcogenides. Inorg Chem 15:17–21
16. Le QV, Nguyen TP, Jang HW, Kim SY (2014) The use of UV-ozone-treated MoS_2 nanosheets for extended air stability in organic photovoltaic cells. Phys Chem Chem Phys 16:13123–13128
17. Niu L, Li K, Zhen H, Chui YS, Zhang W, Yan F et al (2014) Salt-assisted high-throughput synthesis of single- and few-layer transition metal dichalcogenides and their application in organic solar cells. Small 10:4651–4657

18. Yun JM, Noh YJ, Lee CH, Na SI, Lee S, Jo SM et al (2014) Exfoliated and partially oxidized MoS_2 nanosheets by one-pot reaction for efficient and stable organic solar cells. Small 10:2319–2324
19. Liu W, Yang X, Zhang Y, Xu M, Chen H (2014) Ultra-stable two-dimensional MoS_2 solution for highly efficient organic solar cells. RSC Adv 4:32744–32748
20. Le QV, Nguyen TP, Kim SY (2014) UV-ozone-treated WS2 hole-extraction layer in organic photovoltaic cells. Phys Status Solidi RRL 8:390–394
21. Yang X, Liu W, Xiong M, Zhang Y, Liang T, Yang J et al (2014) Au nanoparticles on ultrathin MoS_2 sheets for plasmonic organic solar cells. J Mater Chem A 2:14798–14806
22. Yang X, Fu W, Liu W, Hong J, Cai Y, Jin C et al (2014) Engineering crystalline structures of two-dimensional MoS_2 sheets for high-performance organic solar cells. J Mater Chem A 2:7727–7733
23. Kwon KC, Kim C, Le QV, Gim S, Jeon JM, Ham JY et al (2015) Synthesis of atomically thin transition metal disulfides for charge transport layers in optoelectronic devices. ACS Nano 9:4146–4155
24. Le QV, Nguyen TP, Park M, Sohn W, Jang HW, Kim SY (2016) Bottom-up synthesis of mes_x nanodots for optoelectronic device applications. Adv Opt Mater 4:1796–1804
25. Ding Z, Hao Z, Meng B, Xie Z, Liu J, Dai L (2015) Few-layered graphene quantum dots as efficient hole-extraction layer for high-performance polymer solar cells. Nano Energy 15:186–192
26. Yang HB, Dong Y, Wang X, Khoo S, Liu B (2014) Cesium carbonate functionalized graphene quantum dots as stable electron-selective layer for improvement of inverted polymer solar cells. ACS Appl Mater Interfaces 6:1092–1099
27. Xing W, Chen Y, Wang X, Lv L, Quyang X, Ge Z et al (2016) MoS_2 quantum dots with a tunable work function for high-performance organic solar cells. ACS Appl Mater Interfaces 8:26916–26923
28. Xing W, Chen Y, Wu X, Xu X, Ye P, Zhu T et al (2017) PEDOT:PSS-assisted exfoliation and functionalization of 2D nanosheets for high-performance organic solar cells. Adv Funct Mater 27:1701622
29. Le QV, Nguyen TP, Choi KS, Cho YH, Hong YJ, Kim SY (2014) Dual use of tantalum disulfides as hole and electron extraction layers in organic photovoltaic cells. Phys Chem Chem Phys 16:25468–25472
30. Chuang MK, Yang SS, Chen FC (2015) Metal nanoparticle-decorated two-dimensional molybdenum sulfide for plasmonic-enhanced polymer photovoltaic devices. Materials 8:5414–5425
31. Petridis C, Savva K, Kymakis E, Stratakis E (2017) Laser generated nanoparticles based photovoltaics. J Colloid Interface Sci 489:28–37
32. Kakavelakis G, Petridis C, Kymakis E (2017) Recent advances in plasmonic metal and rare-earth-element upconversion nanoparticle doped perovskite solar cells. J Mater Chem A 5:21604–21624
33. Kohler A, Bassler H (2015) Electronic processes in organic semiconductors: an introduction. Wiley-VCH, Hoboken, NJ
34. Foster S, Deledalle F, Mitani A, Kimura T, Kim K-B, Okachi T et al (2014) Electron collection as a limit to polymer: PCBM solar cell efficiency: effect of blend microstructure on carrier mobility and device performance in PTB7:PCBM. Adv Energy Mater 4:1400311
35. Mikhnenko OV, Azimi H, Schrarber M, Morana M, Blom PW, Loi MA (2012) Exciton diffusion length in narrow bandgap polymers. Energy Environ Sci 5:6960–6965
36. Stylianakis M, Konios D, Petridis C, Kakavelakis G, Stratakis E, Kymakis E (2017) Ternary solution-processed organic solar cells incorporating 2D materials. 2D Mater 4:042005
37. Sygletou M, Tzourmpakis P, Petridis C, Konios D, Fotakis C, Kymakis E et al (2016) Laser induced nucletion of plasmonic nanoparticles on two-dimensional nanosheets for organic photovoltaics. J Mater Chem A 4:1020–1027
38. Kakavelakis G, Castillo AE, Pellegrini V, Ansaldo A, Tzourmpakis P, Brescia R et al (2017) Size-tuning of WSe_2 flakes for high efficiency inverted organic solar cells. ACS Nano 11:3517–3531

39. Petridis C, Kakavelakis G, Kymakis E (2018) The renaissance of graphene-related materials in photovoltaics with the emergence of metal-halide perovskite solar cells. Energy Environ Sci 11:1030–1061
40. Matte HS, Gomathi A, Manna AK, Late DJ, Datta R, Pati SK et al (2010) MoS_2 and WS_2 analogues of graphene. Angew Chem Int Ed 49:4059–4062
41. Peng B, Yu G, Zhao Y, Xu Q, Xing G, Liu X et al (2016) Achieving ultrafast hole transfer at the monolayer MoS_2 and $CH_3NH_3PbI_3$ perovskite interface by defect engineering. ACS Nano 10:6383–6391
42. Marchioro A, Teuscher J, Friedrich D, Kunst M, Van de Krol R, Moehl T, Gratzel M et al (2014) Unravelling the mechanism of photoinduced charge transfer processes in lead iodide perovskite solar cells. Nat Photonics 8:250–255
43. Kim YG, Kwon KC, Le QV, Hong K, Jang HW, Kim SY (2016) Atomically thin two-dimensional materials as hole extraction layers in organolead halide perovskite photovoltaic cells. J Power Sources 319:1–8
44. Capasso A, Matteocci F, Najafi L, Prato M, Buha J, Cina L et al (2016) Solar cells: few-layer MoS2 flakes as active buffer layer for stable perovskite solar cells. Adv Energy Mater 6:1600920
45. Dasgupta U, Chatterjee S, Pal AJ (2017) Thin-film formation of 2D MoS_2 and its application as a hole-transport layer in planar perovskite solar cells. Sol Energy Mater Sol Cells 172:353–360
46. Huang P, Wang ZW, Liu Y, Zhang KC, Yuan L, Zhou Y et al (2017) Water-soluble 2D transition metal dichalcogenides as the hole-transport layer for highly efficient and stable p–i–n perovskite solar cells. ACS Appl Mater & Interfaces 9:25323–25331
47. Dai R, Wang Y, Wang J, Deng X (2017) Metal–organic-compound-modified MoS2 with enhanced solubility for high-performance perovskite solar cells. Chemsuschem 10:2869
48. Kakavelakis G, Paradisanos I, Paci B, Generosi A, Papachatzakis M, Maksudov T et al (2018) Extending the continuous operating lifetime of perovskite solar cells with a molybdenum disulfide hole extraction interlayer. Adv Energy Mater 8:1702287
49. Kohnehpoushi S, Nazari P, Nejand BA, Eskandar M (2018) MoS_2: a two-dimensional hole-transporting material for high-efficiency, low-cost perovskite solar cells. Nanotechnology 29:205201
50. Ahmed MI, Hussain Z, Khalid A, Amin HMN, Habib A (2016) Absorption enhancement in $CH_3NH_3PbI_3$ solar cell using a TiO_2/MoS_2 nanocomposite electron selective contact. Mater Res Express 3:045022
51. Huang P, Yuan L, Zhang K, Chen Q, Zhou Y, Song B et al (2018) Room-temperature and aqueous solution-processed two-dimensional TiS_2 as an electron transport layer for highly efficient and stable planar n–i–p perovskite solar cells. ACS Appl Mater Interfaces 10:14796–14802
52. Yin G, Zhao H, Feng J, Sun J, Yan J, Liu Z et al (2018) Low-temperature and facile solution-processed two-dimensional TiS_2 as an effective electron transport layer for UV-stable planar perovskite solar cells. J Mater Chem A 6:9132–9138

Chapter 8
Transition Metal Dichalcogenides for Biomedical Applications

Linji Gong and Zhanjun Gu

Abstract The intriguing properties of two-dimensional transition metal dichalcogenides (2D TMDs) have led to the rapid development of research on these emerging 2D inorganic graphene-like nanomaterials in various fields, such as electronic devices, sensors, catalysis, and energy storage. Recently, 2D TMDs exhibit great potentials and advantages in biological systems due to their tunable optical properties, tailorable electronic characteristics, ultrahigh surface area, versatile surface chemistry, and good biocompatibility. In this chapter, we summarize the latest progress of the use of 2D TMDs for biological applications, ranging from bioanalysis, antibacterial and wound repair, bioimaging, drug delivery, and cancer therapy to tissue engineering and medical devices. Specifically, the nanotoxicology and biosafety profiles of TMDs are reviewed to meet the concern of nanomedicine from the public and scientific community. Moreover, the current challenges and future perspectives on the development of 2D TMDs for biomedical applications are also outlined. It is expected that these promising 2D TMDs will have a great practical foundation and play an important role in next-generation biomedicine.

Keywords Transition metal dichalcogenides · Nanomaterials · Bioimaging · Nanomedicine · Nanosafety

Abbreviations

2D	Two-dimensional
2D TMDs	Two-dimensional transition metal dichalcogenides
$\cdot O^{2-}$	Superoxide radical
·OH	Hydroxyl radical

L. Gong · Z. Gu (✉)
CAS Key Laboratory for Biomedical Effects of Nanomaterials and Nanosafety, Institute of High Energy Physics, Chinese Academy of Sciences, Beijing 100049, People's Republic of China
e-mail: zjgu@ihep.ac.cn

University of Chinese Academy of Sciences, Beijing 100049, People's Republic of China
gonglj@ihep.ac.cn

N. S. Arul and V. D. Nithya (eds.), *Two Dimensional Transition Metal Dichalcogenides*,
https://doi.org/10.1007/978-981-13-9045-6_8

$^1O_2$	Singlet oxygen
BBB	Blood–brain barrier
BMSCs	Bone marrow mesenchymal stem cells
BP	Black phosphorus
BSA	Bovine serum albumin
CCK-8	Cell counting kit-8
Ce6	Chlorin e6
CpG	Cytosine-phosphate-guanine
CS	Chitosan
CT	Computed tomography
CurvIS	Curved image sensor
CVD	Chemical vapor deposition
DHE	Dihydroethidine
DOX	Doxorubicin
ECM-like	Extracellular matrix-like
EMT	Epithelial-mesenchymal transition
EPR	Enhanced permeability and retention
FA	Folic acid
FL	Fluorescent imaging
GO	Graphene oxide
GSH	Glutathione
GT	Gene therapy
HA	Hyaluronic acid
HELFs	Human embryonic lung fibroblasts
HSPs	Heat shock proteins
HU	Hounsfield units
i.t.	Intratumorally
i.v.	Intravenously
ICG	Indocyanine green
MB	Methylene blue
MRI	Magnetic resonance imaging
MTT	Methylthiazolyldiphenyltetrazolium bromide
MWT	Microwave thermal therapy
NFs	Nanoflowers
NIR	Near-infrared
NMP	*N*-methylpyrrolidone
NSC	Neural stem cell
PANI	Polyaniline
PAT	Photoacoustic tomography
PDA	Polydopamine
PEG	Polyethylene glycol
PEI	Polyetherimide
PET	Positron emission tomography
PLGA	Poly(lactic-*co*-glycolic acid)
PS	Photosensitizer

PTT	Photothermal therapy
PVP	Polyvinylpyrrolidone
QDs	Quantum dots
RES	Reticuloendothelial system
rGO	Reduced graphene oxide
ROS	Reactive oxygen species
RSV	Resveratrol
SH	Sulfhydryl
SPECT	Single-photon emission computed tomography
TBO	Toluidine blue O
Tf-SH	Thiol-functionalized transferrin

8.1 Introduction

Two-dimensional transition metal dichalcogenides (2D TMDs) with unique planar topography and versatile physicochemical properties have attracted great attention and become the hot spot of fundamental research and technological applications in recent years [1–4]. 2D TMDs consist of transition metal atoms (M) and chalcogen atoms (X) with a MX_2 stoichiometry, where M ranges from Group IVB to Group VIII (e.g., Ti, V, Mo, Ta, W, and Re), and X stands for the chalcogen (S, Se, and Te) [1, 5]. The special layered structure and various combinations of transition metals and chalcogens endow 2D TMDs with versatile properties, such as ultrahigh surface area, versatile surface chemistry, unique electronic characteristics, tunable optical properties, and good biocompatibility, all of which make these materials suitable for applications in various fields including electronic devices, sensors, catalysis, energy storage, and biomedicine [6].

The increasing demand for biomedicine and rapid growth of nanobiotechnology have catalyzed and promoted the expansion of multifunctional TMDs nanosheets in the field of biomedical application [7–13]. One of the advantages of 2D TMDs for biomedical uses may be ascribed to their easy and feasible preparation methods. To date, both top-down (e.g., mechanical exfoliation, liquid exfoliation, lithium intercalation, chemical exfoliation) and bottom-up approaches (e.g., chemical vapor deposition (CVD), hydro/solvothermal methods) have been applied to prepare almost all 2D TMDs [14–16]. Then, their ultrahigh surface area and versatile surface chemistry, such as surface atomic vacancy and surface charge, enable them to link with polymers and target molecules, and/or deliver imaging agents, drugs, genes, and photosensitizers for cancer diagnosis and therapy [17, 18]. The large surface area is propitious to decorate with biocompatible polymers and further reduce the cytotoxicity and improve the dispersibility and biocompatibility of TMDs [17, 19]. Moreover, the specific surface chemistry also helps to interact with surrounding biological molecules or cellular components for the application of antibacterial strips [20] and wound repair [21]. TMDs can act as reinforcing agents within biopolymers or scaffolds for constructing extracellular matrix-like (ECM-like) materials for tissue engineering [22]

and bone regeneration [23]. Ultrathin-layered TMDs with the super photo-absorption coefficient have been developed for the soft bio-optoelectronic device in ophthalmology [24]. Also, most of the TMDs possess high photothermal conversion efficiency in the near-infrared (NIR) region and have the potential to be a novel photothermal agent for photoacoustic tomography (PAT) imaging and phototherapy [25–27]. Some TMDs (e.g., MoS_2, WS_2, TaS_2, ReS_2) with high atomic number have been reported to be suitable for X-ray-computed tomography (CT) contrast agents [28] and radiosensitizers [29] due to their strong X-ray attenuation performance. More importantly, the toxicity and safety profiles are the first factors of concern when applying TMDs in biological applications. Researches on the toxicity profile of TMDs nanosheets show that this newly developed 2D material exhibits lower cytotoxicity than many other nanostructures [9, 10], ensuring their further applications for the direction of nanomedicine.

Here, we will summarize the latest progress of the utilization of 2D TMDs for biomedical field, ranging from bioanalysis, antibacterial and wound repair, bioimaging, diagnosis, drug delivery, and cancer therapy to tissue engineering and medical devices. Specifically, the nanotoxicology and biosafety profiles of TMDs are reviewed to meet the concern of nanomedicine from the public and scientific community. Moreover, the current challenges and future perspectives on the development of 2D TMDs for biomedical applications are also outlined.

8.2 Bioanalysis and Disease Diagnosis

Development of techniques for early and effective diagnosis of diseases is of highly desired and paramount importance. The last decade has witnessed the rapid growth of the application of TMDs in bioanalysis and disease diagnosis [30]. Owing to the versatile physiochemical properties, such as easy preparation, layered structure, large surface area, desirable optical properties, tunable electric properties, favorable catalytic properties, and good biocompatibility, TMDs nanosheets have been widely developed as fluorescent biosensors, electrochemical biosensors, photoelectrochemical biosensors, field-effect transistor (FET) biosensors, and nanopore biosensors, to fast, sensitively and selectively detect or analyze various biomolecules (e.g., DNA, RNA, glucose, cholesterol, dopamine, cholesterol, protein, antigen, enzyme, glutathione (GSH), and biomarkers) and the surrounding environment (e.g., pH, H_2O_2, ATP) and cells (e.g., cancer cells, bacteria, virus). The readers can find out the related contents of the mechanism and application of 2D TMDs-based biosensors in other chapter.

8.3 Antibacterial and Wound Repair

From ancient times, our forefathers had known that water, wine, and vinegar stored in silver-coated containers could efficiently limit bacterial contamination [31]. With the rapid development of modern medicine in the twentieth century, many antibiotics were produced to prevent bacterial infections, which led to a dramatic decline in mortality rates all over the world. However, it was unexpected that the misuse or long-term use of antibiotics gives rise to the uncertain outbreaks of infectious diseases caused by drug-resistant bacteria. Thus, we are bound to seek more efficient alternately antibacterial strategies to prevent the rise of bacterial infections.

Nanomaterials-based antibacterial agents have come into the picture in the past decade. Compared with antibiotics, nanomaterials could inhibit the growth of bacteria with various mechanisms, such as the deconstruction of cell wall/membrane, the production of reactive oxygen species (ROS), the interaction with the biological macromolecules, the interruption of electron transport, and the release of metal ions in bacteria [32, 33]. Not limited to nano-silver [33–35], TMDs nanomaterials, such as MoS_2 [36–39], WS_2 [39–42] and their composites [43–45], also show high antibacterial activity. For example, it was reported that the antibacterial ability of chemically exfoliated MoS_2 nanosheets was better than that of the untreated MoS_2 powders [36]. This phenomenon may be ascribed to the larger surface area and better electronic properties of the nanoscale MoS_2 sheet. The antimicrobial mechanisms mainly include membrane and oxidation stress caused by the increased interaction rate between MoS_2 nanosheets and bacteria and the production of ROS. Similarly, Navale et al. [41] also tested the antibacterial performances of WS_2 nanosheets against four bacterial strains through oxidative and membrane stress approaches. But they found that WS_2 did not produce ROS, which was contradictory to the case of its structural analog, MoS_2. Notably, this outcome is consistent with the later work by Liu et al. [42]. Under UV irradiation, as shown in Fig. 8.1, the phototoxicity of CdS, MoS_2 as well as WS_2 nanoparticles toward Escherichia coli (*E. coli*) was different (CdS > MoS_2 > WS_2) [39]. When exposed to the same mass concentration (such as 50 mg/L) of those three nanoparticles, the inhibition ratios of *E. coli* were 96.7, 38.5, and 31.2%, respectively. Different from the above-mentioned outcomes [41, 42], WS_2 and MoS_2 could produce ROS including superoxide radical ($\cdot O^{2-}$), singlet oxygen ($^1O_2$), and hydroxyl radical (·OH) under UV irradiation [39], while CdS generated only $\cdot O^{2-}$ and $^1O_2$ [39]. In addition, due to the photon energy (3.4 eV) of the incident UV light is higher than the band gap of WS_2 (2.1 eV) and CdS (2.5 eV), the photocorrosion process will appear: $WS_2 + 6h^+ \xrightarrow{hv} W^{6+} + 2S$. Moreover, under the irradiation of UV light, CdS and WS_2 could release metal ions, but no detectable amount of Mo ion was found [39]. Thus, the dominant antibacterial mechanism of MoS_2 may be ascribed to the generation of ROS, while both ROS production and toxic metal ions release contribute to the toxic mechanism of CdS and WS_2. In addition, some TMDs-based nanocomposites also have been fabricated to further increase the antibacterial activity. For example, Navale et al. [41] found that reduced graphene oxide (rGO) and WS_2 were not able to produce $\cdot O^{2-}$ or ROS but

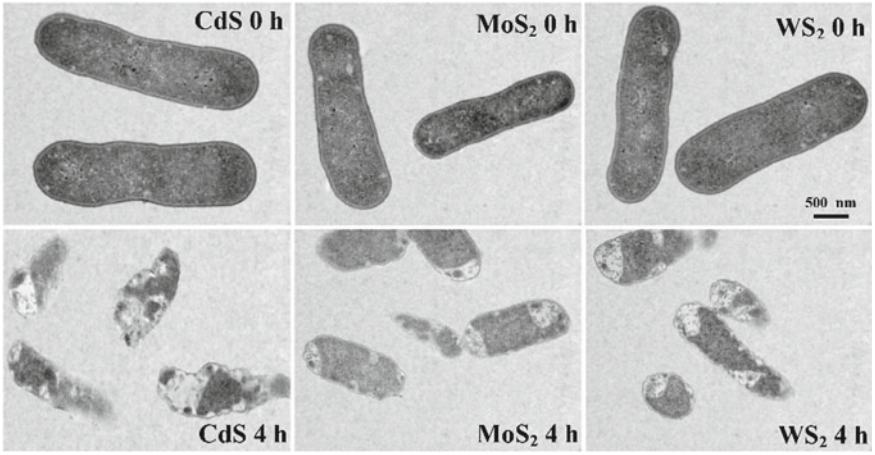

Fig. 8.1 Antibacterial ability of CdS, MoS_2, and WS_2. TEM micrographs of *E. coli* cells exposed to three sulfide nanoparticles before and after 4 h UV irradiation. (Reprinted with permission from Ref. [39]. Copyright 2017, Elsevier.)

the rGO-WS_2 composite could generate both. It was shown that the higher antibacterial effects were observed in the group of rGO-WS_2 nanocomposite than solo WS_2 or rGO.

The antibacterial properties of TMDs give them the opportunity to play a role in antimicrobial therapy. For example, Yin et al. [21] fabricated a versatile antibacterial agent based on polyethylene glycol (PEG) modified MoS_2 nanoflowers (PEG-MoS_2 NFs) for safe and synergetic wound antibacterial applications. Firstly, the PEG-MoS_2 NFs with good biocompatibility can be easily uptaken by cells. Second, the peroxidase-like activity enables it to efficiently catalyze H_2O_2 to produce cytotoxic ·OH, which has a higher antibacterial capacity. Besides, PEG-MoS_2 NFs with a large surface area and high NIR absorption will be propitious to further improve the bacteria-killing effects by NIR-induced hyperthermia. In mice model, the PEG-MoS_2 NFs and low concentration of H_2O_2 solutions were dropped on the wound area of mice after bacterial infection. The wound-healing results demonstrated that the PEG-MoS_2 NFs with peroxidase catalytic and NIR absorption capacities could significantly inhibit the growth of resistant bacteria in wounds. Similarly, Huang et al. [46] also found that silk fibroin-modified $MoSe_2$ nanosheets with low cytotoxicity and favorable peroxidase-like ability showed rapid wound-healing efficacy in vivo. Different from Yin's work [21], silk fibroin-$MoSe_2$ films were posted on the skin of infection area. Cao et al. [20] also designed an efficient and benign antibacterial depot by the integration of Ag^+ and MoS_2 nanosheets. Compared with an equal amount of $AgNO_3$, the depot showed higher broad-spectrum antibacterial ability due to the efficient release of Ag^+. In addition, the antibacterial system exhibited negligible biotoxicity, high antibacterial activities and avoided the waste of Ag. Besides wound bacterial infection, artificial implants also provide a hospitable place for bacterial

adherence and growth. Therefore, it is necessary to develop new-style multifunctional artificial implants with excellent self-antibacterial capabilities. Feng et al. [47] fabricated Ti implant coated with chitosan-assisted MoS_2 ($CS@MoS_2$) hybrid via electrophoretic deposition. The implant exhibited significantly antibacterial efficacy under the combined irradiation of 660 and 808 nm light than the irradiation separately, which might stem from the synergistic function of both $^1O_2$ and hyperthermia. After the implantation of $CS@MoS_2$-Ti in mice, the photodynamic process can produce ROS under 660 nm visible light while the photothermal process will enhance the temperature of the Ti implants when exposed to an 808 nm light. This research demonstrated that TMDs-based artificial implants with novel self-antibacterial abilities showed great promising for in situ disinfection.

8.4 Bioimaging

Over the past decades, TMDs have emerged as promising candidates in bioimaging and diagnosis due to their versatile physicochemical properties including layered structure, tunable band gaps, fluorescence properties, and low cytotoxicity. On the one hand, TMDs can be used as imaging agents for diagnosis or imaging-guided therapy, which have been illustrated with many works in recent years. On the other hand, and more importantly, molecular imaging technologies, such as fluorescent imaging (FL), PAT imaging, CT imaging, positron emission tomography (PET) imaging, and single-photon emission computed tomography (SPECT) imaging, can be applied to monitor the in vivo tracking, biodistribution, transportation, and clearance processes of TMDs nanoparticles to meet the concern of drug delivery and nanosafety.

8.4.1 Fluorescent Imaging

Compared with the traditional organic fluorescent molecule, semiconductor quantum dots (QDs) with tunable wavelength, good photostability, and high quantum yields throw light on the development of in vivo bioimaging [7, 48–51]. Nevertheless, the cellular toxicity of traditional inorganic QDs (such as cadmium-containing QDs) severely restricts its biomedical applications [52]. Therefore, it is highly significant to develop newly fluorescent nanomaterial. The emerging TMDs with easily tunable structures and optical properties plus good compatibility show alternative potential application for fluorescent bioimaging. Firstly, the large surface area and versatile surface chemistry of TMDs will enable them to be good fluorescein carriers. For examples, Cy5.5-labeled WS_2-Fe_3O_4@SiO_2-PEG [53] or BSA-MoS_2 [54] can be applied for in vivo NIR fluorescence imaging to realize the visualization and localization of the biodistribution of the nanocomposite in the small animal. Compared with TMDs nanosheets, 0D TMDs QDs (e.g., MoS_2 QDs) with lateral sizes less than 10 nm show unique optical and electrical properties for their stronger quantum con-

finement and edge effects [55–57]. For instance, the monodispersed MoS_2 QDs with different uniform lateral diameters of ~3.5 nm [55], ~2.9 nm [56], and ~2.6 nm [57] show fluorescence quantum yield of 9.65, 3.1, and 5.6% and fluorescence lifetime of 4.66, 11.0, and 12 ns, respectively. Those optical features suggest that the MoS_2 QDs is suitable for the applications of bioanalysis and cellular bioimaging.

8.4.2 Photoacoustic Tomography Imaging

PAT imaging is a newly developed noninvasive diagnostic imaging technology based on the photoacoustic effects in biological tissue [58]. Compared with the traditional optical imaging modality, this emerging PAT imaging offers remarkably increased penetration depth and spatial resolution [59]. Therefore, PAT imaging may be contributed to study the in vivo tracking of nanoparticles.

Based on the excellent NIR-absorbance performance and strong photothermal effects, TMDs can produce thermal signals by thermal expansion or bubble formation [27], which enables their suitability for PAT imaging. For example, one of the first explorations of TMDs-based PAT imaging was published by Cheng et al. [59]. They used WS_2-PEG nanosheets as a photoacoustic agent to display its tumor accumulation by the degree of photoacoustic signals. When the tumor-bearing mice were intratumorally (i.t.) injected with the as-prepared WS_2-PEG (2 mg/mL, 20 μL) and subsequently imaged at different time points, strong photoacoustic signals in the tumor region could be detected to show and visualize the efficient accumulation of WS_2-PEG nanosheets in tumor through the enhanced permeability and retention (EPR) effect. After that, for the sake of the easy-to-fabricate feature and effective NIR light-to-heat conversion capability, various TMDs with different morphology and components (e.g., MoS_2 nanosheets [54, 60–66], MoS_2 nanodots [67–69], $MoSe_2$ nanosheets [70, 71], WS_2 nanosheets [72, 73], WS_2 nanodots (Fig. 8.2) [74], TiS_2 nanosheets [75], VS_2 nanosheets [76], ReS_2 nanosheets [77, 78], MoS_2 or WS_2-based nanocomposites [79–82], and some ternary chalcogenide nanosheets (Cu_2MnS_2 [83] and Ta_2NiS_5 [84]) have also been developed for PAT imaging applications.

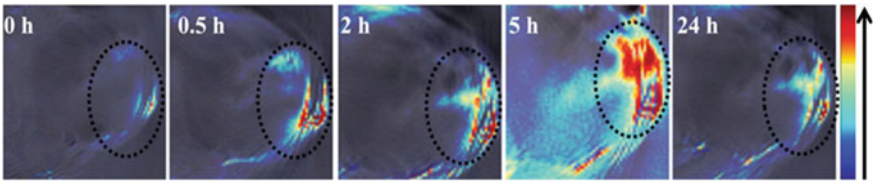

Fig. 8.2 TMDs-based photoacoustic tomography imaging. PAT images of tumor before and after intravenously (i.v.) injection with WS_2@PEI nanoparticles at various time points. (Reprinted with permission from Ref. [74]. Copyright 2016, Wiley-VCH.)

8.4.3 Computed Tomography Imaging

X-ray CT imaging is a well-established biomedical imaging technique being routinely used in various researches and clinical diagnosis [9, 28]. CT imaging is a non-invasive bioimaging tool which provides a 3D visual reconstruction of the targeted tissues with deep penetration and high resolution [9]. In CT imaging, the weakness X-ray contrast signals can be enhanced and amplified by the use of contrast agents [9, 59]. As a rule, the X-ray absorption coefficient (μ) is formalized as follows: $\mu = \left(\rho Z^4\right)/\left(AE^3\right)$, where A is the atomic mass and E is the X-ray energy [28]. Therefore, CT contrast agents possessing higher density (ρ) or high atomic number (Z) tend to have stronger X-rays absorbability.

As with gold and lanthanides nanoparticles-based CT imaging agents [28], TMDs that comprise high atomic number metal elements (e.g., Mo, Ta, W, Re; their atomic number is 42, 73, 74, and 75, respectively) have also been reported to be suitable for CT imaging in recent years. For example, PEG [53, 59, 72, 85, 86], BSA [87], PEI [74], hyaluronic acid (HA) [88], or polyvinylpyrrolidone (PVP) [73] modified biocompatible WS_2 nanosheets or nanodots was successfully prepared for in vitro and in vivo CT imaging. The X-ray attenuation coefficient of the W atom at 100 keV is 4.438 cm^2/kg, which is higher than that of iodine (1.94 cm^2/kg at 100 keV) [85]. WS_2 shows higher Hounsfield units (HU) value indeed when compared with commercial iodine-based clinic used contrast agents (e.g., Iohexol [85], Iobitridol [73], Iopromide [59, 86, 87]) at the same concentration in those works. It is noted that the widely used small molecular CT contrast agent, such as Iobitridol, can be rapidly cleared from the blood within minutes [89]. Therefore, biocompatible nanoscale materials-based CT contrast agents may have significant advantages compared with those traditional iodine-based small molecular contrast agents.

The excellent CT contrast ability in vitro of WS_2 nanosheets encouraged researchers further to pursue their in vivo CT imaging applications. For example, BEL-7402 tumor-bearing mice were i.v. injected with PEGylated WS_2 QDs solution (15 mg/mL, 200 μL) and then time-dependent whole-body CT imaging was collected [86]. Before administration of WS_2-PEG nanoparticles, the CT signals of the liver, spleen, and tumor region were very weak, as shown in Fig. 8.3. In contrast, we could observe the obvious enhancement of contrast signals in liver and spleen after i.v. injection, suggesting the uptake of WS_2-PEG nanoparticles by the reticuloendothelial system (RES). After 2 h post-injections, the remarkably enhanced contrast signals in tumorous regions were detected, which could be contributed to the gradual accumulation of nanoparticles in tumors through passive targeting approach. Additionally, the contrast signals in the bladder were also gradually enhanced, indicating that the ultrasmall WS_2 QDs might be cleared out through renal filtration and own better biocompatible and biodegradable properties. Similarly, polymer functionalized ReS_2 [77, 78] and TaS_2 [89] nanosheets also can act as promising contrast agents for CT bioimaging due to the strong X-ray attenuation performance of Re and Ta. Besides, TMDs can conjugate with other components such as Au [90], Bi_2S_3 [79] or doped with Gd^{3+} ion [71, 72, 91] to realize better CT imaging effects. Those

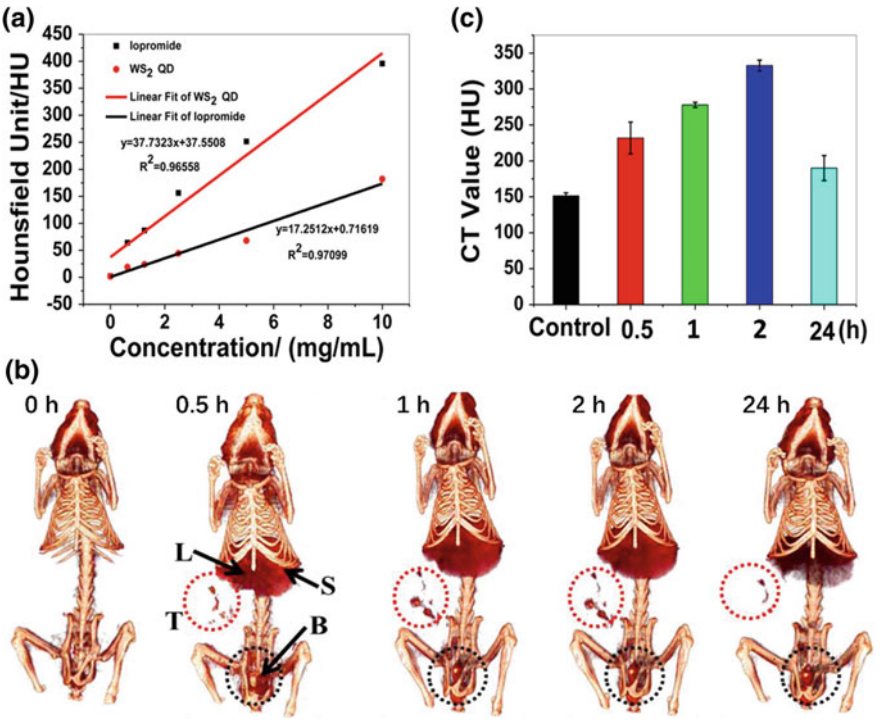

Fig. 8.3 TMDs-based computed tomography imaging. **a** Hounsfield unit values of iopromide and WS_2 QDs. **b** CT images of tumor before and after i.v. injection of WS_2 QDs solution at different time points. **c** Corresponding HU value of CT images. (Adapted with permission from Ref. [86]. Copyright 2015, American Chemical Society.)

examples demonstrated that CT imaging could be applied to investigate the in vivo biodistribution, transportation, and clearance processes of nanoparticles to realize multifunction of nanomedicine.

8.4.4 Multimodal Imaging

It is worth noting that each imaging modality has its own advantages and drawbacks. Therefore, the development of novel "all-in-one" bioimaging agents to combine different imaging modalities is of highly desired and full of promising.

With the repaid development of molecular imaging, nanoparticles-based multimodal bioimaging has become a booming trend. On the one hand, the inherent excellent NIR-absorbance performance and strong X-ray attenuation ability endow some TMDs with dual-modal PAT and CT imaging capability, to integrate the advantages of CT and PAT imaging. For example, Miao et al. [78] prepared colloidal

ReS_2 nanosheets by liquid exfoliation method for in vivo PAT and CT imaging. The obtained PVP-ReS_2 nanosheets possess excellent photothermal conversion efficiency (79.2%), which is higher than those of MoS_2 (24.37%) [92] and WS_2 (32.83%) [87]. The photoacoustic signals in the tumorous region were significantly enhanced and reached the strongest at around 1 h after i.v. injection, indicating the efficient accumulation of ReS_2 nanosheets via the EPR effect. In addition, the ReS_2 nanosheets are also suitable for the application of CT imaging. When the tumor-bearing mice were i.t. injected with PVP-ReS_2 solutions (10 mg/mL, 50 μL), an obvious contrast signal enhancement of the tumorous region was detected. Hence, the ReS_2 nanosheets and other TMDs such as MoS_2 [68, 79], $MoSe_2$ [93], WS_2 [59, 68, 73, 74, 86, 88] with inherent versatile imaging capability can serve as a multifunctional contrast agent for both PAT and CT imaging. On the other hand, some functional moieties (e.g., magnetic particle, radioisotope), with other imaging capabilities, can be modified onto the surface of 2D TMDs to realize multimodal bioimaging. As mentioned above, PAT imaging provides useful information on in vivo tracking and biodistribution of nanoparticles inside the tissue, while magnetic resonance imaging (MRI) possesses high spatial resolution and excellent soft-tissue contrast effects with a noninvasive feature. Thus, the combination of PAT and MRI imaging will further improve the ability of diagnostic imaging. For example, Chen et al. [76] for the first time found that PEGylated VS_2 nanodots could be used for T1-weighted MRI and PAT imaging-guided photothermal therapy (PTT) due to its paramagnetism and high NIR-absorbance feature. Meanwhile, there are many works reporting that iron oxide (IO) [53, 62, 80, 81, 94–97] or Gd^{3+} ion [63, 71, 72, 91, 98] modified TMDs can serve as dual-modal contrast agents for PAT and MRI imaging. Liu et al. [62] successfully prepared iron oxide-decorated MoS_2 nanosheets via a sulfur chemistry strategy to form MoS_2-IO-PEG composites, which possess both the superparamagnetic feature and T2 contrast capability. All the tumors and livers of mice after 24 h post-injection of MoS_2-IO-PEG exhibited obvious darkening effects in T2-weighted MRI images when compared to untreated mice. The results showed the effective aggregation of MoS_2-IO-PEG nanocomposites in tumors. Pan et al. [71] fabricated Gd^{3+}-doped $MoSe_2$ nanosheets via a simple liquid phase method and then employed this $MoSe_2(Gd^{3+})$-PEG nanosheets as a theranostic agent for PAT and MRI dual-modal bioimaging and PTT. In a similar work, Gd^{3+} ions were used to enhance the contrast action of WS_2 nanosheets in both MRI and CT imaging and also further increased the efficacy of radiotherapy [72]. 2D TMDs nanosheets also can be easily modified with radioisotope tracer including ^{64}Cu [62, 99], ^{188}Re [100], ^{89}Zr [101], and $^{99m}Tc^{4+}$ [76, 77] to enable noninvasive nuclear imaging such as PET and SPECT imaging. For instance, $^{99m}Tc^{4+}$ ions, as a wide clinic used radioisotope tracer, could be firmly and efficiently anchored on the surface of VS_2 nanosheets through a chelator-free labeling strategy [76]. The signals of in vivo tumor SPECT imaging were gradually increased from time after the i.v. injection of ^{99m}Tc-VS_2@lipid-PEG, indicating the timely accumulation of nanoparticles by EPR effect. The delivery efficiency of ^{99m}Tc-VS_2@lipid-PEG was calculated up to 5.1 ± 1.2% ID/g at 24 h [76]. It was demonstrated that nuclear imaging could help to precisely reveal the biodistribution and tracking in vivo of administrated nanoparticles. In a word, taking full

advantages of the high NIR and X-ray absorbance capabilities and functionalized by magnetic components or radioisotope tracer, TMDs can serve as an "all-in-one" nanoplatforms for multimodal in vivo tumor imaging including PA, CT, MRI, PET, and SPECT imaging and imaging-guided therapy (Table 8.1).

8.5 Cancer Therapy

8.5.1 Photothermal Therapy

PTT is an invasive therapeutic modality, which typically employs external laser (usually NIR light) to cause hyperthermia within tumor tissues. Hyperthermia (41–43 °C) can effective thermal ablate cancer cells via the change of the tumor microenvironment, induction of apoptosis, and induction of gene and protein synthesis [108]. PTT also causes serious side effects to surrounding normal tissues. Moreover, PTT is often hard to completely ablate the deep-located cancer cells due to the insufficient penetration of laser. Thus, 2D TMDs nanosheets with better NIR light absorbance property and excellent photothermal conversion performance will bring about an alternative and feasible solution for promoting the efficiency of PTT.

In 2013, it was reported that MoS_2 nanosheets exhibited better photothermal performance than that of Au and graphene and thus can be used as NIR photothermal agents [109]. The MoS_2 nanosheets were chemically exfoliated via the Morrison method. The as-prepared MoS_2 nanosheets have a mass extinction coefficient up to 29.2 L/(g cm) at 800 nm, which is approximately 7.8-fold of graphene oxide [3.6 L/(g cm)] [109] higher than that of gold nanorods [13.89 L/(g cm)] [110]. The in vitro photothermal experiment showed better HeLa cells killing efficacy when incubated with MoS_2 and subsequently treated with NIR irradiation (800 nm, 20 min). After that, the application of TMDs in the field of PTT has exponentially increased. For example, Wang et al. [111] for the first time used a versatile "bottom-up" one-pot synthesis method to successfully synthesize PEGylated MoS_2 nanosheets for highly efficient PTT. Ultrathin MoS_2 nanosheets with a smaller diameter were prepared via the solvothermal procedure, which is very different from traditional "up-down" strategy via exfoliation from bulk MoS_2 [59, 92, 109]. The $(NH_4)_2MoS_4$ was utilized as a novel precursor to synchronously provide both Mo and S sources, and PEG-400 aqueous solution was used as the solvent to control the size and enhance the colloidal stability and biocompatibility of MoS_2 nanosheets. The as-prepared MoS_2 nanosheets with no significant cytotoxicity were confirmed by in vitro cell viability assay of 4T1 cells incubated with nanosheets, even at the concentration up to 500 μg/mL. Encouraged by the better in vitro photothermal cells killing performance, MoS_2 nanosheets also exhibits excellent antitumor efficiency in vivo, demonstrating MoS_2 nanosheets have a great potential for PTT.

Like MoS_2, WS_2 nanosheet is another representative example of the TMDs family and also shows promising NIR photothermal agents. Cheng et al. [59] synthesized

Table 8.1 The applications of 2D TMDs for bioimaging and cancer therapy

TMD	Modification	Bioimaging	Therapy	References
TiS_2	PEG	PAT	PTT	[75]
VS_2	PEG, $^{99m}Tc^{4+}$	PAT/MRI/SPECT	PTT	[76]
MoS_2	BSA, Gd^{3+}	PAT/MRI	PTT	[63]
	^{64}Cu, Fe_3O_4, PEG	PAT/MRI/PET	PTT	[62]
	BSA		MWT	[102]
	mPEG-PLGA, DOX, Fe_3O_4	CT/MRI	MWT/chemotherapy	[95]
	PEG, Ce6	PAT	PTT/PDT	[61]
	BSA	FL/PAT	PTT/PDT	[54]
	PEG, DOX		PTT/chemotherapy	[103]
	Chitosan, DOX	CT	PTT/chemotherapy	[92]
	PEI, HA, DOX	PET	PTT/chemotherapy	[99]
	Fe_3O_4, ICG, Pt(IV), PEI	PAT/MRI	PTT/PDT/chemotherapy	[81]
	PEG, CpG		PTT/immunotherapy	[104]
	PANI, PEG	PAT/CT	PTT/RT	[68]
	Bi_2S_3, PEG	PAT/CT	PTT/RT	[79]
$MoSe_2$	BSA, ICG	PAT	PTT	[70]
	PEG, Gd^{3+}	PAT/MRI	PTT	[71]
	PDA, DOX		PTT/chemotherapy	[105]
TaS_2	PEG, DOX	CT	PTT/chemotherapy	[89]
WS_2	PEG	PAT/CT	PTT	[59]
	PVP	PAT/CT	PTT	[73]
	BSA, MB	CT	PTT/PDT	[87]
	Fe_3O_4, PEG, DOX	FL/CT/MRI	PTT/chemotherapy	[53]
	PEI, siRNA	PAT/CT	PTT/gene therapy	[74]
	LA-PEG	PAT/CT	PTT/RT	[86]
	PEG, ^{188}Re	SPECT	PTT/RT	[100]
	PEG, Gd^{3+}	PAT/CT/MRI	PTT/RT	[72]
	Fe_3O_4, $sSiO_2$, MnO_2, PEG	FL/PAT/MRI	PTT/RT	[97]
	HA, PANI, Ce6	FL/PAT/CT	PTT/PDT/RT	[88]
WSe_2	BSA, MB		PTT/PDT	[106]
ReS_2	PVP	PAT/CT	PTT	[78]
	BSA, RSV, FA		PTT/chemotherapy	[107]
	PEG, $^{99m}Tc^{4+}$	PAT/CT/SPECT	PTT/RT	[77]

MB methylene blue; *BSA* bovine serum albumin; *RSV* resveratrol; *FA* folic acid; *PVP* polyvinylpyrrolidone; *PDA* polydopamine; *PLGA* poly($_{D,L}$-lactide-*co*-glycolide acid); *ICG* indocyanine green; *HA* hyaluronic acid; *PANI* polyaniline; *Ce6* chlorin e6; *CpG* cytosine-phosphate-guanine; *MWT* microwave thermal therapy; *Tf-SH* thiol-functionalized transferrin

PEGylated WS_2 nanosheets with strong NIR-absorbance performance for in vivo CT and PAT imaging-guided PTT. The WS_2-PEG nanosheets with the diameter of 50-100 nm and thickness of ~1.6 nm were revealed by TEM and AFM, respectively. The mass extinction coefficient of the as-prepared PEGylated WS_2 nanosheets was calculated to be 23.8 L/(g cm) at 808 nm. Compared to the uncoated WS_2 nanosheets, PEGylated WS_2 nanosheets have better biocompatibility with no significant cytotoxicity, making it suitable for further biomedicine application. The excellent in vivo photothermal antitumor outcome was achieved in the group of treated with WS_2-PEG solution (2 mg/kg of i.t. injection, 20 μL) and NIR laser (808 nm, 0.8 W/cm^2, 5 min). The tumor surface temperatures rapidly increased from ~30 to ~65 °C within 5 min. As a result, the treated tumors have been completely inhibited without obvious reoccurrences and the mice survived over 45 days. The PVP-ReS_2 nanosheets with ultrahigh photothermal conversion efficiency (79.2%) were also found to remarkable ablate and eradicate the tumors without recurrence [78]. In addition, Li et al. [112] were the first to discover that chemically exfoliated WS_2 nanosheets could not only efficiently inhibit Aβ aggregation due to the selective adsorption of Aβ monomers on the surface of WS_2 nanosheets through van der Waals and electrostatic interactions but also cross the blood–brain barrier (BBB) and dissociate preformed Aβ aggregates upon NIR irradiation. Moreover, a similar work further confirmed the inhibition of Aβ aggregation by MoS_2 and found that MoS_2 nanoparticles could block the Aβ-formed Ca^{2+} channel and maintain the calcium homeostasis [113]. These phenomena will open a new avenue for PTT of Alzheimer's disease and enlarge the biological application fields of WS_2 nanosheets.

The photothermal conversion efficiency of many TMDs (such as those mentioned above, MoS_2 [109] and WS_2 [59]) was experimentally investigated only based on the optical part and described by the mass extinction coefficient, which reflects the wavelength-selective absorbing feature and the absorbance capability of nanoparticles [78, 114]. However, the photothermal conversion performance of an agent mainly depends on two independent factors: the mass extinction coefficient (ε) and photothermal conversion efficiency (η) [78, 115]. Photothermal conversion efficiency often represents the ability of the conversion from light energy to heat energy [78]. Therefore, many works also studied the photothermal conversion efficiency of TMDs, which was shown in Table 8.2. For example, $MoSe_2$ nanosheets have revealed a photothermal conversion efficiency of 57.9% [116], which is higher than that of MoS_2 (24.37%) [92], Nb_2C nanosheets (36.4%) [115], Ta_4C_3 nanosheets (44.7%) [117], black phosphorus (BP) QDs (28.4%) [118], and Au nanorods (21%) [119–121]. Besides the typical MoS_2 [23, 62–64, 67, 69, 80, 109, 111, 122–133] and WS_2 [73, 85, 134–136], many other TMDs (e.g., $MoSe_2$ [70, 71, 93, 116, 132, 137, 138], TiS_2 [75, 139], SnS [140], VS_2 [76], ReS_2 [78]) with different component and surface chemistry also have been demonstrated as efficient NIR light-driven agents for PTT.

Although the TMDs-based photothermal agents have achieved remarkable antitumor efficacy in PTT, some heat-resistant cancer cells are hard to be eradicated by PTT alone. It is infeasible to directly increase the laser power, which will inevitably damage to the surrounding healthy tissue. On account of the heat resistance of cancer cells stem from the intrinsic heat shock response, we can develop novel strategies

Table 8.2 The photothermal conversion performance of various agents including traditional photothermal agents and novel 2D nanomaterials

Material	Photothermal conversion efficiency (η, %)	Mass extinction coefficient [ε, L/(g cm)]	Wavelength (λ, nm)	References
TiS_2	–	26.8	808	[75]
VS_2	31.5	22.6	808	[76]
MoS_2	24.37	29.2	808	[92, 109]
$MoSe_2$	57.9	11.1	808	[116]
$MoTe_2$	33.8	3.15	808	[141]
SnS	36.1	16.2	808	[140]
TaS_2	39	–	808	[89]
WS_2	32.83	21.8	808	[87]
WSe_2	35.07	–	808	[106]
ReS_2	79.2	4.35	808	[78]
Ti_3C_2	30.6	25.2	808	[142]
Nb_2C	36.4	37.6	808	[115]
Ta_4C_3	44.7	4.06	808	[117]
Ta_2NiS_5	35	25.6	808	[84]
Bi_2Se_3	34.6	11.5	808	[143]
BP QDs	28.4	14.8	808	[118]
Nano-rGO	–	24.6	808	[144]
Au nanorods	21	13.9	808	[120]

to inhibit the production of heat shock proteins (HSPs) (such as Hsp70 and Hsp90) by regulating the related genes expression [74, 126, 145, 146]. For example, Zhang et al. [74] decorated a positively charged polyetherimide (PEI) onto the surface of MoS_2 to efficient carrying negatively charged survivin-siRNA. Firstly, hyperthermia could increase cell membrane permeability and thus enhance the cellular uptake of the as-prepared WS_2@PEI-siRNA nanocomposite. Then, the silencing of survivin could downregulate the Hsp70 expressions, making heat-resistant cancer cells more susceptible to PTT. As a result, all the WS_2@PEI-siRNA involved in vitro and in vivo experiments showed a remarkable synergistic GT/PTT efficacy (Fig. 8.4). Besides the regulation of genes expression by loading siRNA onto WS_2, using protein inhibitor to disturb the function of Hsp90 also a feasible approach to enhance PTT efficacy. Ariyasu and Mu et al. [126] utilized CS@MoS_2 as a carrier to load cyclic peptide sequence (Cype), which could specifically bind to N-middle domain of intracellular Hsp90. The as-prepared CS@MoS_2-Cype nanocomposite could effectively induce tumor ablation through the process of necrosis and enhance apoptosis under 808 nm NIR light irradiations, resulting in significant enhancement of photothermal treatment.

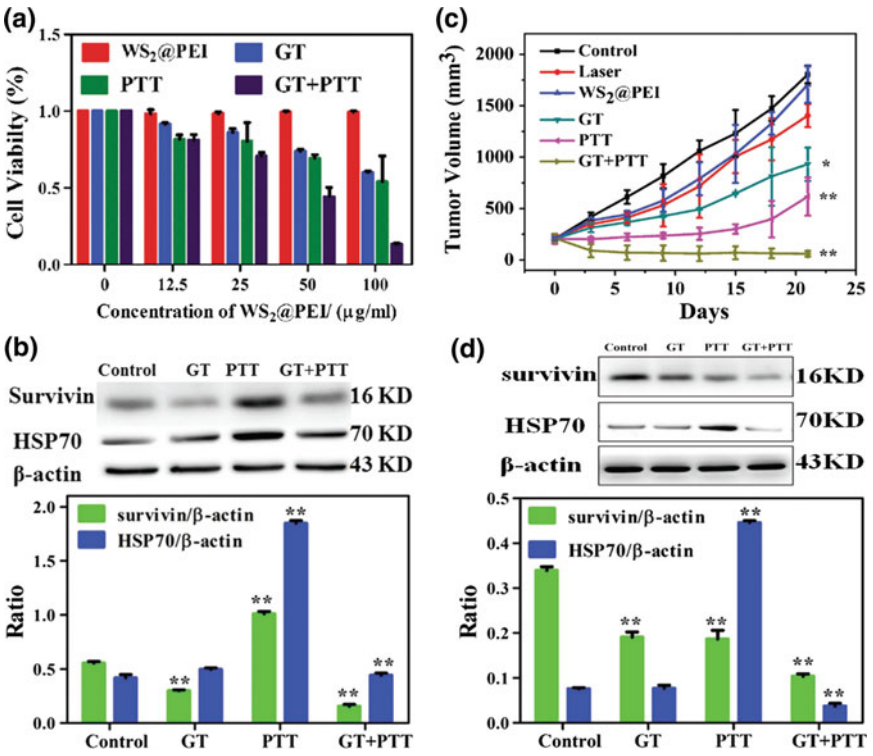

Fig. 8.4 TMDs-based PTT/GT combination therapy. **a** Photothermal effect of WS_2@PEI-siRNA on BEL-7402 cells. **b** The protein expressions of survivin and HSP70 of BEL-7402 cells from different treatments for 24 h. **c** Tumor volume growth curves of mice after combined PTT/GT therapy. **d** The protein expression levels of survivin and HSP70 of tumors from different groups. (Reprinted with permission from Ref. [74]. Copyright 2016, Wiley-VCH.)

8.5.2 Microwave Thermal Therapy

The employ of nanomaterials to induce localized heating within tumor tissue for the thermal ablation of cancer cells is a general strategy in nanomedicine, mainly including three approaches: the absorption of NIR light, magnetically induced heating, and radiofrequency ablation [147]. In the above-mentioned section, we can conclude that the applications of TMDs in PTT usually rely on the external incident light, especially the NIR light due to the strong absorption by agents, high tissue penetration depths, and low absorption of hemoglobin and water in the region around 650–900 nm [148]. In the photothermal process, light induces the generation of hyperthermia to ablate cancer cells. Different from light-mediated PTT, the hyperthermia situations in microwave thermal therapy (MWT) are triggered by external radiofrequency (microwave) irradiation. The clinic translation of PTT is limited by the penetration depths of NIR light (typically 1–3 mm [149]), while microwave possesses a deeper

tissue penetration, faster heat generation, and wider ablation zones [102]. Moreover, the microwave has been proofed as a friendly heat source to be applied for tumor ablations in clinical [95, 150].

Recently, TMDs have also been found to be suitable for MWT. For example, Wang et al. [102] successfully synthesized layered MoS_2 NFs via a hydrothermal process for cancer MWT for the first time. The MoS_2 NFs was then modified by bovine serum albumin (BSA) to improve its biostability and biocompatibility. The average temperature of solutions was rapidly increased to as high as 42 °C after treated with microwave (1.8 W, 450 MHz) for 1 min and 53 °C for 5 min. In the animal experiment, ICR mice were i.t. injected with BSA-MoS_2 NFs (20 mg/kg) and then irradiated by microwave for 5 min in the tumor region after two hours injection. Tumors on mice were completely eliminated after microwave treatment, preliminary demonstrating the as-prepared layered BSA-MoS_2 NFs have the potentials to be promising microwave hyperthermia sensitizers for cancer MWT. After that, Tang and Fu et al. [95] developed biocompatible mPEG-PLGA microcapsules with doxorubicin (DOX) hydrochloride (DOX·HCl), MoS_2 nanosheets and Fe_3O_4 nanoparticles encapsulated for MRI/CT dual-modal imaging-guided microwave-induced tumor therapy. These microcapsules possess at least seven advantages include: (1) easy to prepare; (2) hybrid organic-inorganic composites, biocompatible, degradable, and no significant toxicity; (3) superselective arterial blocking; (4) superior microwave sensitive property; (5) controlled release DOX·HCl under the microwave irradiation; (6) in vivo MRI/CT dual-modal imaging; (7) synergetic chemotherapy and MWT. Following up this work, the same research group [151] performed a systematic study of MoS_2-mediated microcapsules (MSMC)-based microwave embolization agents for large orthotopic transplantation tumor therapy. To eradicate the large orthotopic transplantation tumor, a novel microwave embolization agent was prepared by enclosing MoS_2 nanosheets in the sodium alginate microcapsules. This agent not only has a good biocompatibility and body-clearable but also exhibits excellent embolic and microwave susceptible properties. Moreover, as shown in Fig. 8.5, microcapsules can be dispersed in the margin of tumors after the arterial injection and then induce the embolic effect on the blood vessels, which remarkably increases the microwave ablation efficiency by reducing heat loss and cutting off the feeding of nutrition [151]. The results show that the ablation zone was enlarged 5 times compared to the microwave alone group. The excellent antitumor efficacy was contributed to the synergistic therapy of enhanced MWT and transcatheter arterial embolization.

8.5.3 Photodynamic Therapy

Photodynamic therapy (PDT) is a clinically approved, minimally invasive therapeutic method [152]. PDT procedure requires three important components: photosensitizer (PS), light, and oxygen [152]. In the presence of oxygen and under light irradiation, the administrated photosensitizing molecules absorb the light energy to produce toxic ROS (e.g., $^1O_2$) to kill cancer cells and induce the inflammatory reaction. But the

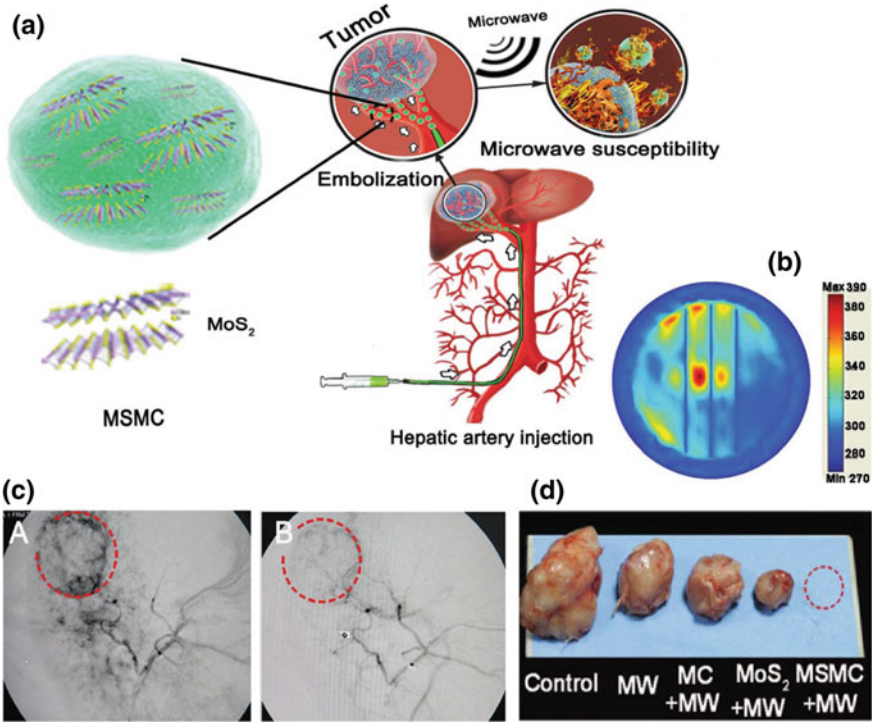

Fig. 8.5 TMDs-based microwave thermal therapy. **a** Schematic illustration of the MSMC used for the microwave ablation and the chemoembolization therapy. **b** The simulated microwave susceptibility for MSMC under the microwave irradiation. **c** Digital subtraction angiography images of the liver before and after embolization of MSMC. **d** Tumor tissues removed from the mice. (Adapted from Ref. [151]. Copyright 2017, The Royal Society of Chemistry.)

efficacy of PDT is hindered by the tissue penetration depth of external light, the insufficient water-solubility of PSs, the targeting delivery of PSs, and the efficiency of ROS generation. For example, the hypoxic tumor microenvironments attenuate the production of singlet oxygen in a photodynamic process and hence reduce therapeutic efficacy. The combination of PTT with PDT may be a novel and feasible strategy to tackle the problems. PTT-caused hyperthermia may soften microvasculature and then increase intratumoral blood flow, which further transports more oxygen into the tumor to improve PDT efficiency [25, 90].

2D TMDs, as a kind of excellent photothermal agent, possess great promising for the combination of PTT and PDT. For example, 2D TMDs have large surface areas, which endow them as photosensitizer carriers to load and delivery molecular PSs. In addition, 2D TMDs-mediated PTT can enhance PDT efficiency by increasing intratumoral oxygen concentrations as well as by promoting the cellular delivery of PSs. Moreover, TMDs own the tunable size and optical properties, which endue them with unique photosensitive behaviors. It is reported that the ultrasonic-exfoliated MoS_2

nanodots can produce massive toxic $^1O_2$ upon a light irradiation [39, 54, 153], even higher than commercial photosensitizer PpIX [154]. BSA-coated MoS_2 nanosheets have also been found to be a photosensitizer for the in vivo NIR light (808 nm) triggered photodynamic cancer treatment [54]. Most importantly, the combination of PTT and PDT can promote the cancer killing efficiency in a synergistic manner.

Yong et al. [87] pioneered the utilization of TMDs for PTT/PDT combined therapy. Water-soluble BSA modified WS_2 nanosheets were prepared by a H_2SO_4 exfoliation strategy. Methylene blue (MB) molecules, a common photosensitizer, were then loaded onto the surface of the as-prepared BSA-WS_2. The greatest HeLa cell prohibition was observed when incubated with BSA-WS_2@MB and exposed to an 808 nm laser (1 W/cm^2, 15 min) and then a 665 nm LED lamp (50 mW/cm^2, 5 min). MB could efficiently product singlet oxygen under irradiation in a controllable manner. The synergistic effects may be ascribed to WS_2-based PTT and MB-based PDT. Not long after, the first 2D TMD-based PDT/PTT combined therapy in the animal model was reported by Liu et al. [61]. The chlorin e6 (Ce6) was selected as the photosensitizer and physically adsorbed onto the surface of MoS_2 nanosheets. The as-prepared MoS_2-PEG/Ce6 nanocomposites could remarkably increase the intracellular uptake of Ce6 molecules because mild hyperthermia could increase cell membrane permeability. The cancer cell growth was significantly inhibited upon the separate exposure of laser with wavelengths at 808 nm (0.45 W/cm^2, 20 min) and 660 nm (5 W/cm^2, 20 min). In similar works, MB-loaded WSe_2-BSA complexes (Fig. 8.6) and PEG-MoS_2-Au-Ce6 nanocomposites also demonstrated to be the promising therapeutic agent for the combination of phototherapy [90, 106].

To increase the release of photosensitizers, a pH-sensitive charge-convertible peptide [LA-K11(DMA)] was modified on the surface of MoS_2 nanosheets and subsequently loading a positively charged photosensitizer (toluidine blue O, TBO) [155]. Under acidic conditions (e.g., tumor microenvironment), the negatively charged LA-K11(DMA) peptide was converted into a positively charged one, reducing the interaction between TBO and MoS_2. Moreover, light-induced hyperthermia could promote the release of TBO, leading to a synergistic tumor therapy. In addition, the promotion of the targeting ability of photosensitizers is also of great importance for PDT [156, 157]. Herein, folic acid (FA) was selected to be decorated on the surface of MoS_2-UCNPs to form a tumor-targeting nanocomposite [157]. To study the target specificity of the as-prepared MoS_2-UCNPs-FA/ZnPc, two types of FR-positive cells and one type of FR-negative cell were incubated with MoS_2-UCNPs/ZnPc or MoS_2-UCNPs-FA/ZnPc, respectively [157]. Strong ZnPc fluorescence was observed in the group of FR-positive cells incubated with MoS_2-UCNPs-FA/ZnPc, while FR-positive cells incubated with MoS_2-UCNPs/ZnPc, and all FR-negative cells emitted negligible ZnPc red fluorescence. These results accelerated the application of 2D TMDs-based nanoplatforms in phototherapy.

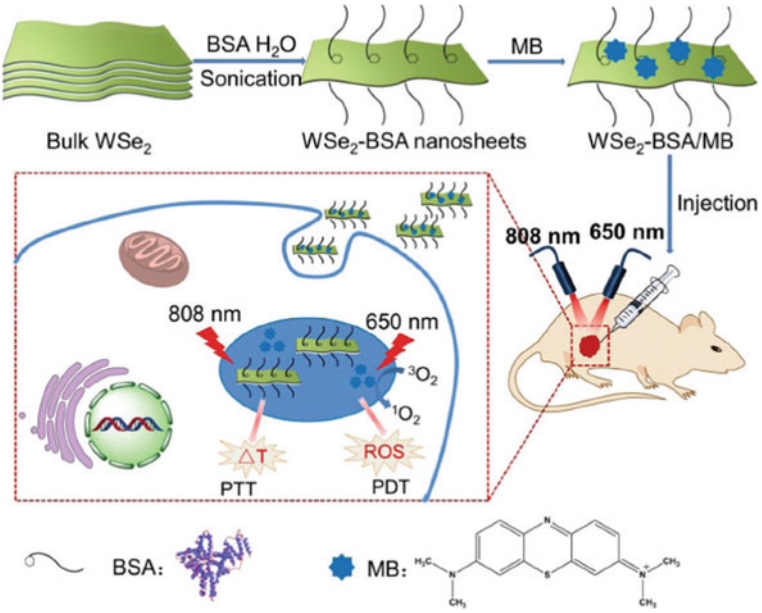

Fig. 8.6 TMDs-based photodynamic therapy. Schematic illustration of the MB-loaded WSe_2-BSA nanosheets for combined PTT/PDT therapy. (Reprinted from Ref. [106]. Copyright 2017, The Royal Society of Chemistry.)

8.5.4 Chemotherapy

Chemotherapy, which utilizes chemotherapeutic drugs for the inhibition and damage of cancer cells, is one of the widely used antitumor approaches in clinical [25]. However, chemotherapy or drugs also meet some shortcomings, such as drug resistance, drug efflux, short circulation time, low specificity or selectivity, insufficient drug-controlled release nanocarriers.

Recent years, 2D TMDs nanomaterials have been demonstrated to be an efficient promoter of chemotherapy. Firstly, TMDs with an ultrahigh surface area and versatile surface chemistry will enable them to feasibly link and delivery drugs. Then, TMDs, as an excellent photo-absorb agent, could trigger the smart drug release at the desired site and time in an external light-controlled manner. In addition, hyperthermia can improve the sensitivity of cancer cells to drugs and increase the drug uptake and accumulation. Moreover, the combination of PTT and chemotherapy can obtain an enhanced synergistic antitumor effect. Therefore, it is necessary to develop the novel and smart NIR light-responsive drug-controlled release systems for chemotherapy.

In the last decade, various NIR light and pH-responsive drug-controlled release systems based on 2D TMDs have been successfully developed [53, 82, 89, 92, 94, 96, 103, 105, 107, 141, 158–163]. For example, as shown in Fig. 8.7, Yin et al. [92] employed CS@MoS_2 as DOX carriers to construct a NIR light-triggered drug

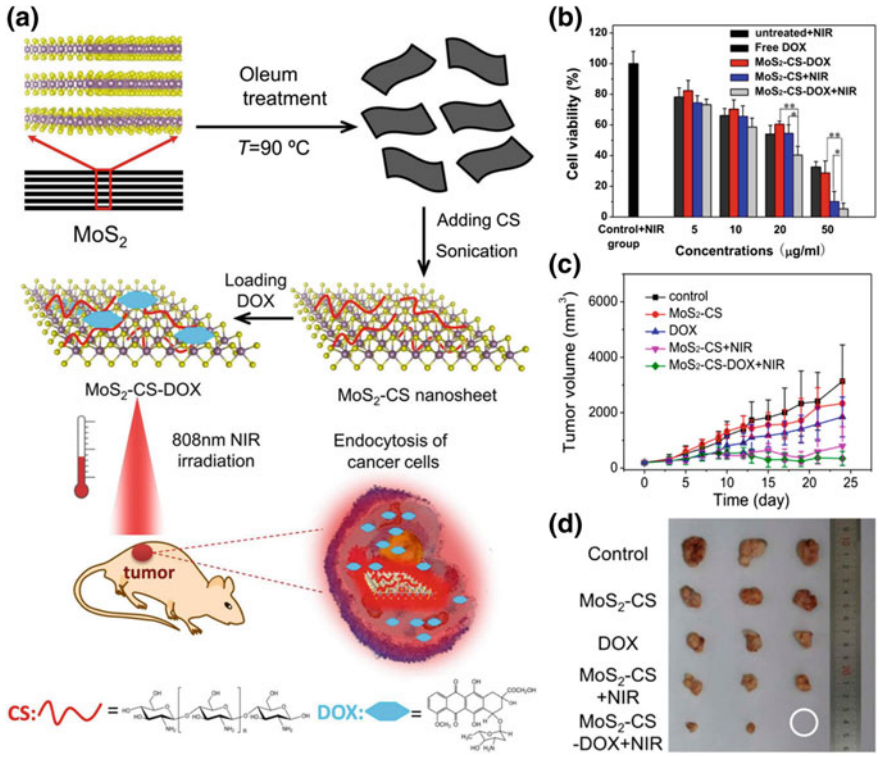

Fig. 8.7 TMDs-based Chemo/PTT combination therapy. **a** Schematic illustration of the CS@MoS_2-based photothermal-triggered drug delivery system for efficient cancer therapy. **b** Cytotoxicity of KB cells treated with CS@MoS_2 with or without irradiation. **c**, **d** The antitumor efficacy of synergistic Chemo/PTT therapy. (Reproduced with permission from Ref. [92]. Copyright 2014, American Chemical Society.)

release system for effective cancer treatment. The DOX loading data showed that the saturated loading rate of CS@MoS_2 was up to ~32% at pH 8.00. In the presence of 808 nm laser irradiations (0.8 W/cm^2, 10 min), 12.4% DOX was released within 1 h in PBS buffer (pH 5.00); while only ~6% DOX was measured without irradiation. This feature will be beneficial to the release of DOX in the acidic tumor microenvironments under external irradiation. In addition, only 0.2% of DOX was released in the next hour in the absence of laser. The accumulated release of DOX was up to 38%, while 80% of DOX was released when the laser power increases to 1.4 W/cm^2. It means that the release of DOX was in a pH and light-controlled manner.

In a similar work, PEG-TaS_2-DOX could also realize the controlled drug releases triggered by NIR light, and moderate acidic pH, leading to the accumulation of drugs [89]. After arriving at the mild acidic tumor microenvironment, those nanoplatforms could effectively release the chemotherapeutic drugs and synergistically damage the cancer cells under the irradiation of external NIR laser.

To realize the slow release of drug and reduce its systemically side effects, Wang et al. [65, 66, 164] designed a series of injectable MoS_2 and drug co-encapsulated implant for NIR light-triggered synergistic PTT and chemotherapy. For example, they fabricated a PLGA/MoS_2/DOX (PMD) oleosol by homogenizing Poly(lactic-*co*-glycolic acid) (PLGA), MoS_2, and DOX together into *N*-methylpyrrolidone (NMP) [164]. The release of encapsulated DOX was relatively slow at pH 7.4 as well as at acidic pH condition (pH 5.4) due to the shielding effect of hydrophobic of PLGA. However, in an acidic solution, the DOX release rate was increased from 8.7 to 31.8% in the light-treated group [164]. Moreover, the PMD hydrogel could restrain their access to body fluid circulation. Such a pH/light dual-stimuli-responsive drug release implant significantly enhanced cancer therapeutic efficacy and mitigated the side effects on normal tissues.

In addition, the chemotherapeutic effects are often reduced by low specific delivery. To address this problem, Liu's group designed a novel targeting approaches based on MoS_2-mediated disulfide chemistry for drug-targeted chemotherapy [165–167]. The copolymer P(OEGA)-*b*-P(VBA-*co*-KH570) (POVK) was modified on the surface of MoS_2 nanosheets and subsequently loaded with DOX [165]. Then, thiol-functionalized transferrin (Tf-SH) was selected as the targeting ligand and anchored onto the surface of MoS_2 through disulfide bonds (–S–S), which could be easily cleaved in the presence of the reductive intracellular GSH. The as-prepared DOX-POVK-MoS_2-Tf nanocomposites showed good stability in physiological condition but rapidly release DOX upon the synergistic trigger of GSH and acidic conditions. The excellent in vitro antitumor outcomes demonstrated that the transferrin-decorated MoS_2-enabled nanocarriers are promising for targeting chemo-photothermal therapy.

8.5.5 Immunotherapy

Activating the body's own immune system for targeting and eradicating cancer cells has long been a goal in immunology [168]. After decades of development, cancer immunotherapy comes of age and has been regarded as the fourth most important cancer therapy modality, after surgery, radiation therapy, and chemotherapy [168, 169]. As an emerging tumor treatment strategy, cancer immunotherapy offers advantages to patients that include higher overall response rates, promoted durable antitumor responses, reduced metastasis, recurrence, decreased side effects, and better tolerance for some special patients more than traditional treatments [169, 170].

Nano-delivery systems hold great potential for further improving the efficiency of cancer immunotherapy due to their versatile physiochemical properties and advantages in efficient tissue-specific delivery, enhanced tumor microenvironment responsiveness [170]. Various types of nanovehicles (e.g., inorganics [171], nanoscale metal-organic frameworks (nMOFs) [172–174], polymers [175], liposomes [176], DNA hybrid [177]) have been studied for anti-metastatic cancer immunotherapy. But up to now, the TMDs-based immunomodulators are relatively scarce. Pardo et al.

[178] reported that WS_2 nanotubes (INT-WS_2) and inorganic fullerene-like MoS_2 (IF-MoS_2) nanoparticles could induce low levels of the proinflammatory cytokines IL-1β, IL-6, IL-8, and TNF-α in human bronchial cells and activate the antioxidant response. Owing to the excellent photothermal performance and delivering capability of TMDs, Han and Wang et al. [104] found that cytosine-phosphate-guanine (CpG) and PEG-functionalized MoS_2-PEG-CpG nanoconjugates could disturb the proliferative activity of 4T1 cells upon NIR irradiation (808 nm, 2 W/cm^2, 10 min), realizing in vitro photothermal-enhanced cancer immunotherapy. The negatively charged CpG was hard to cross the cell membrane and could be easily biodegraded by nucleases, making it difficult to cross the cell membrane [104]. Fortunately, MoS_2 nanocarriers can efficiently promote the intracellular accumulation of CpG and then increase DC (dendritic cells) maturation and TNFα generation, and finally improve the immune response level. The results demonstrated that TMDs-based NIR light-responsive nanovehicles could specifically eradicate tumor-associated immune cells or induced an inflammatory immune response by activating killer T cells [179]. Those preliminary studies will stimulate the development of nanomaterial-based photo-triggered cancer immunotherapy.

8.5.6 Radiotherapy

Radiotherapy or radiation therapy (RT), as an important procedure for many types of cancer, employs ionizing radiation to kill cancer cells [25, 180]. The high energy ionizing radiations in radiotherapy can directly damage intracellular DNA to cause its structural and functional changes and simultaneously indirectly break DNA by the free radicals. In the indirect process, the water and biomolecules are dissociated by ionizing radiation to generate toxic-free radicals including ROS. However, RT also has some drawbacks, such as the requirement of elevated doses, the side effects to normal tissue, and the radioresistance of hypoxic cancer cells [29, 180].

With the development of emerging nanomedicine, two feasible approaches come into being to enhance the efficiency of RT [25]. Since the high Z element possesses strong X-ray attenuation ability, the first strategy is to improve the effectiveness of external ionizing radiation by using nanoradiosensitizers which contain elements with high atomic number (e.g., Au, Gd, Hf, Ta, W, Bi) [29]. The high Z element could increase energy deposition and then generate secondary and Auger electrons, which can efficiently cause DNA damages and suppress cell growth [72, 77, 100]. The other is to modulate tumor microenvironment (e.g., hypoxia, H_2O_2, low pH) or disturb cellular biochemical process (e.g., cell cycle, DNA repair) by using multifunctional nanoparticles [29, 181]. For example, hyperthermia not only can directly kill cancer cells but also inhibit the repair of damaged DNA by inducing protein aggregation [146]. In addition, as mentioned above, hyperthermia can increase intratumoral blood flow, which may relieve the hypoxic microenvironment, making cancer cells more susceptible to radiation [146]. Moreover, hyperthermia can damage the cancer cells

which are resistant to ionizing radiation. Hence, the combination of PTT and RT may be a feasible approach to improve the therapeutic effects of RT alone.

Some TMDs (e.g., MoS_2 [68], WS_2 [72, 86, 88, 97, 100], ReS_2 [77]) with strong X-ray attenuation ability have the potential for facilitating the combination of PTT and RT into one system. For example, Yong et al. [86] designed biocompatible WS_2-PEG with ultrasmall size (3 nm) via a facile H_2SO_4 exfoliation strategy. The as-prepared WS_2-PEG possesses good water-solubility, low cytotoxicity, high absorbance in the NIR region, and more importantly, strong X-ray attenuation performance. After the treatment of NIR light plus X-ray radiation, the remarkable DNA breaking was observed in the group of 4T1 cells incubated with WS_2-PEG, as shown in Fig. 8.8. Encouraged by the excellent outcomes of in vitro experiment, the tumor-bearing mice were i.t. injected with WS_2-PEG solutions and then treated with PTT and RT separately. Three weeks later, tumor growth in the treated group was significantly delayed. In addition, the Liu group also reported the use of PEGylated WS_2 nanocomposites (e.g., Gd^{3+}-doped WS_2-PEG [72], MnO_2 coated $WS_2@Fe_3O_4/sSiO_2$ [97]) as multifunctional agents for RT involved combination cancer therapy. In those works, W and Gd atoms strongly deposit X-ray energy to promote the generation of toxic ROS for radiosensitization. Besides, the catalytic MnO_2 with pH-responsive ability can decompose tumor endogenous H_2O_2 and relieve tumor hypoxia to further reverse the radioresistance of hypoxic cancer cells. WS_2-mediated PTT could also effectively kill the radioresistant cancer cells, leading to the remarkably PTT-enhanced RT therapeutic effects. Differ from external-beam radiation therapy, radioisotope ions labeled WS_2-PEG (^{188}Re-WS_2-PEG) could realize "self-sensitization" to enhance the synergistic effects of PTT and internal radioisotope therapy without the demand of external X-ray source [100]. After the treatment, the tumors were gradually eradicated and the mice survived for more than 60 days.

8.5.7 Radioprotection

Although radiotherapy is a widely used and highly effective treatment for cancer therapy, it also causes inevitable damage to healthy tissues in the body. Radioprotection, which makes use of radioprotectants to protect healthy tissues from radiation damage, is becoming increasingly important [182, 183]. There is an urgent demand for designing highly efficient radioprotectants to relieve the pain of patients.

Ionizing radiation can directly damage cellular DNA and indirectly damage DNA by the generation of cytotoxic free radicals. On this account, the strategy of radioprotective often originates from the scavenging of free radicals. Different from radiosensitizers, which aim to improve the generation of free radicals in tumor tissues, radioprotectors provide a feasible approach to shield healthy tissues from radiation damage. The most remarkable radioprotectors are the sulfhydryl (SH) compounds, such as cysteine and cysteamine, which could protect animals from total body exposure to irradiation [184]. Amifostine, which is the first selective-target and broad-spectrum radioprotector [184, 185], has been used as a protector for radiotherapy as well as

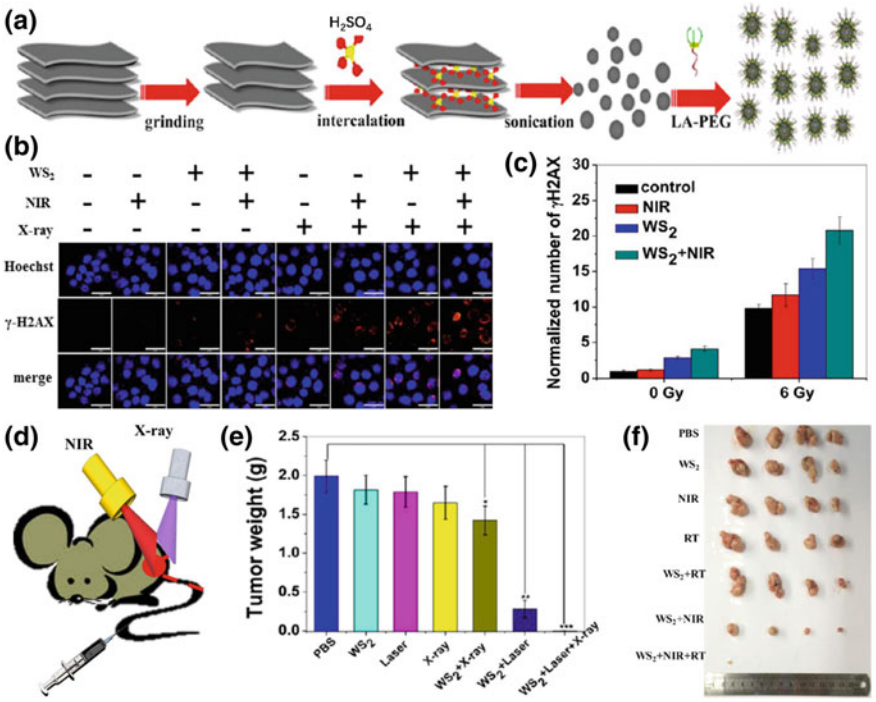

Fig. 8.8 TMDs-based PTT/RT combination therapy. **a** Synthetic process diagram of WS_2 QDs. **b** Representative fluorescence images of DNA fragmentation and nuclear condensation induced by WS_2 QDs and external NIR laser and X-ray treatment. **c** Corresponding normalized number of γ-H2AX after WS_2 QDs and external NIR laser and X-ray treatment. **d** Scheme of the WS_2 QDs-based PTT/RT combined therapy. **e**, **f** The antitumor efficacy of combined PTT/RT therapy. (Reproduced with permission from Ref. [86]. Copyright 2015, American Chemical Society.)

chemotherapy due to its quick accumulation in normal tissues and little penetration into tumors [184]. But the side effects and short blood circulation half-life [186] of amifostine seriously impede its extensive uses. Therefore, it is of great importance to developing more ideal radioprotectors to address these critical challenges.

The emerging nanobiotechnology provides such an opportunity for developing alternative radioprotectors [183]. Ceria (CeO_2) nanoparticles are one of the most representative nanoradioprotectors revealed to show remarkable free radical scavenging performance and radioprotection effects in vivo and in vitro [187–190]. In addition, some carbon nanomaterials (e.g., bamboo charcoal [191], multiwalled carbon nanotubes [192], graphene [193], graphdiyne [182]) also have free radical scavenging ability for radioprotection. Yim et al. [194] deeply studied the ROS scavenging mechanisms in vitro of TMDs nanosheets based on experimentally ROS detections and theoretically simulations. They thought that the radical-mediated oxidation of TMDs and hydrogen transfer from the oxidized TMDs to radicals were the two main steps involving ROS scavenging. Recently, the Zhang group pioneered the study of

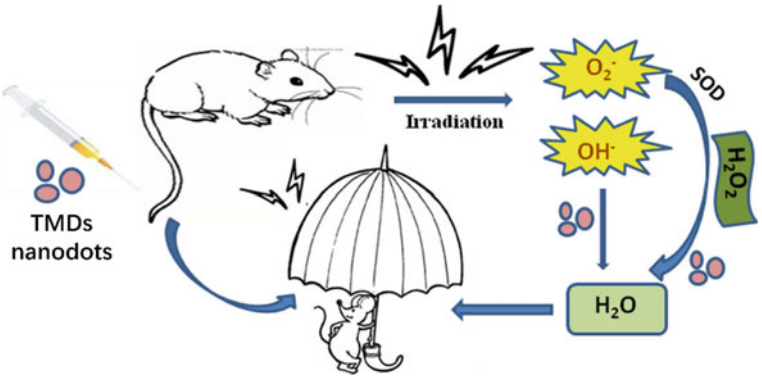

Fig. 8.9 TMDs-based radioprotection. Schematic illustration of the radioprotective process of the ultrasmall MoS_2, WS_2, and WSe_2 nanodots. (Reproduced with permission from Ref. [196]. Copyright 2017, American Chemical Society.)

TMDs-based radioprotectors for radioprotection in vivo [195–197]. For example, they designed ultrasmall cysteine-protected MoS_2 dots with high catalytic properties as radioprotectants. The electrochemical measurements showed that the as-prepared cysteine-protected MoS_2 dots exhibit strong in vitro catalytic activities for H_2O_2 and oxygen reduction reactions. The catalytic capability of the ultrasmall MoS_2 dots might stem from its size effect and surface atomic defects. The A31 cells were incubated with cysteine-MoS_2 dots in different concentrations and then exposed to various gamma radiation doses. At the same doses of radiations, the survival rates of cells were significantly increased with increasing cysteine-MoS_2 concentrations, suggesting an efficient protective phenomenon against external radiation damages in vitro. The tail moment experiments showed effectively DNA repair in the cysteine-MoS_2 dots-treated group. The reason is that the catalytic properties enable MoS_2 dots to scavenge free radicals via rapid reactions with $\cdot O_2^-$ and H_2O_2 and thus reduce DNA damage. It is well known that radiation can destroy healthy cells in the body, especially bone marrow cells and cells in the gastrointestinal tract [198]. So, we can assess the level of in vivo radioprotection by analyzing the DNA concentrations of bone marrow cells. After 7 days post-exposure to radiation, the total DNA in bone marrow cells and bone marrow nucleated cells recovered to the health level in the MoS_2-treated group, resulting in the enhanced surviving fraction of mice. It is worth to note that cysteine with SH group also can scavenge free radical and repair DNA, which is mentioned above. But the author observed only a low survival rate of cysteine-treated mice, clearly indicating that the principal radioprotection effects originated from MoS_2 instead of cysteine. Similarly, they also developed highly catalytic ultrasmall (sub-5 nm) cysteine-protected WS_2 [196] and WSe_2 [197] dots with renal clearance to scavenge free radicals for radioprotection (Fig. 8.9).

8.5.8 Combination Therapy

The current trend in nanomedicine has gradually shifted from monotherapy to combination therapy for enhanced treatment efficacy [199]. In Table 8.1, we can conclude that significant progress has been achieved in 2D TMDs nanomaterials-mediated multimodal combination therapy in the recent decade. Since their multifunctional physicochemical properties, such as high surface area, versatile surface chemistry, excellent photothermal conversion efficacy, and strong X-ray attenuation ability, 2D TMDs can be designed on demand for the combination of diagnostic applications (e.g., FL, PAT, CT) and therapeutic applications including PTT, MWT, PDT, chemotherapy, and RT. The combined therapy can not only overcome the shortcoming of monotherapy but also may obtain the remarkable superadditive (namely "1 + 1 > 2") effects in the battle against cancer.

8.6 Tissue Engineering

Tissue engineering aims to develop biological substitutes that restore, maintain, or improve damaged tissue and organ functionality [200]. During the past ten years, multifunctional nanomaterials have been served as alternative biomaterials to traditional implants and recognized as promising candidates for bone, vascular, neural, and bladder tissue engineering applications.

As a new type of inorganic biomaterials analogous to graphene, TMDs not only attract extensively interest in bioimaging and cancer therapy but also show great potentials for tissue engineering although research works in this field are only at a beginning stage. On the one hand, TMDs with versatile physicochemical properties can act as reinforcing agents within biopolymers. Due to the high Young's modulus and functional group, WS_2 nanotubes have been utilized to increase and reinforce the mechanical properties of biodegradable poly(propylene fumarate), which is widely investigated for bone tissue engineering [201]. In addition, the atomic defects of 2D MoS_2 (mostly due to sulfur vacancies) can offer a facile binding center for four-arm poly(ethylene glycol)-thiol (PEG-SH) via covalent conjugation, forming a high-water content gel [202]. The hydrogel obtained from vacancy-driven gelation exhibits better cytocompatibility and elastomeric and robust mechanical behavior. On the other hand, TMDs reinforced nanofibers or scaffolds with excellent biocompatibility and various fascinating properties can be applied to tissue engineering, especially stem cells proliferation and bone regeneration. It is well known that electrospinning is a simple yet effective approach to fabricate ECM-like nanofibrous materials with desirable performances for tissue engineering [203]. For example, prepared by electrospinning technology, as shown in Fig. 8.10, the polyacrylonitrile/MoS_2 composite nanofibers showed low cytotoxicity and natural ECM-like structure [203]. Moreover, they could guide effective adhesion and differentiation of bone marrow mesenchymal stem cells (BMSCs) on nanofibers. This phenomenon indicated that the as-prepared

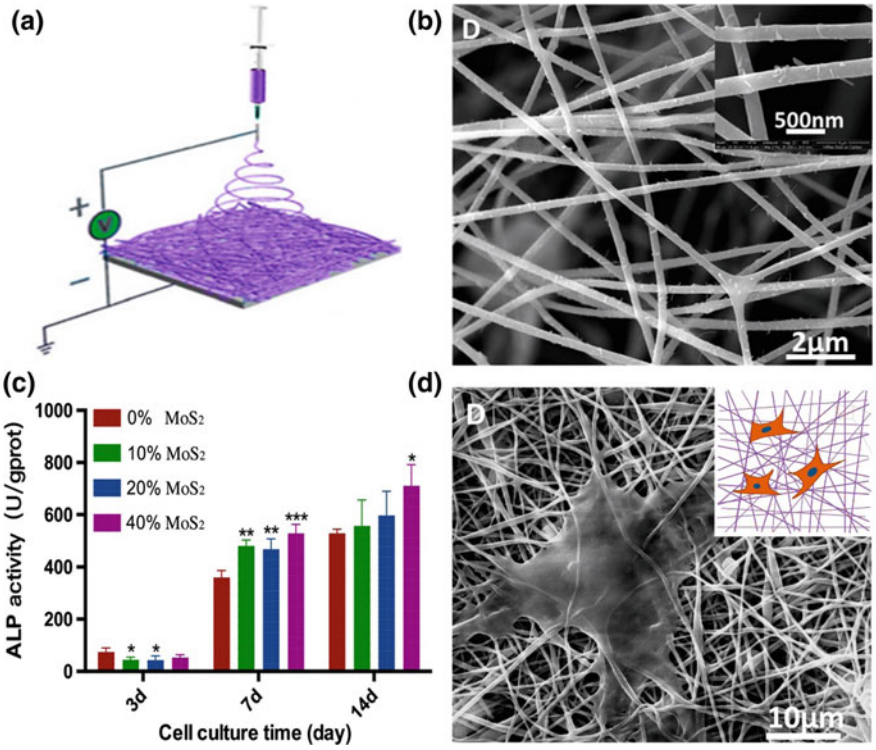

Fig. 8.10 The use of TMDs for tissue regeneration. **a** Schematic illustration of the fabrication of MoS_2 composite nanofibers by electrospinning technology. **b** SEM images of MoS_2 composite nanofibers with 40% MoS_2 (w/w). **c** Alkaline Phosphatase activity of BMSCs cultured on different MoS_2 composite nanofibers in various incubation periods. **d** SEM images of BMSCs cultured on 20% MoS_2 composite nanofibers on day 3. (Reproduced with permission from Ref. [203]. Copyright 2017, American Chemical Society.)

MoS_2 nanofibers could promote the growth of stem cells and positively regulate cellular proliferation and osteogenic differentiation. Similarly, nanostructured MoS_2 also has the potential to promote the differentiation of neural stem cell (NSC) and the maturation of neurons.

Wang et al. [22] designed nanostructured MoS_2 thin films (MTFs) on glass slides via a bottom-up hydrothermal process. When seeded and cultured NSCs on an MTF, they found that biocompatible MTFs played important roles in promoting cell attachment on films and directing NSC differentiation. Motivated by their comparable performance than tissue culture plate, these MoS_2 thin films were then used to assemble with an electrospun PVDF support substrate matrix to construct 3D living conduit scaffolds for nerve regeneration. 3D bioprinting is another emerging popular technique to fabricate extracellular matrix biomaterials for tissue engineering including bone regeneration in recent decades [204]. For example, Wang et al. [23] for the

first time reported a bifunctional 3D-printed bioceramic scaffold for simultaneous tumor therapy and tissue regeneration. The as-fabricated porous scaffold with good biocompatibility comprised two functional parts: akermanite ($Ca_2MgSi_2O_7$) as the matrix material for osteogenesis and angiogenesis, and MoS_2 nanosheets as photothermal agent for NIR tumor ablation. After implanting the hybrid scaffolds into the center of tumors and then exposed to an 808 nm laser, the temperature in tumor tissue rapidly increased to ~50 °C. Moreover, akermanite contained scaffolds could contribute to the attachment, proliferation, and osteogenic differentiation of BMSCs and promote bone regeneration in the rabbit model, indicating that the scaffolds have the potential to act as bioactive materials for bone regeneration. This studies provide a promising strategy to overcome tumor-induced bone defects and opens a new way for the combination of tumor therapy and tissue engineering by using TMDs-based multifunctional inorganic nanomaterials.

8.7 Medical Devices

Since TMDs possess versatile promising physicochemical properties, such as electrical, mechanical, and catalytic property, it has attracted significant attention particularly in biomedical devices for many types of diseases.

Medical strips, such as woundplast, are the most commonly used external medication. Strips usually consist of rubberized fabric and infused therapeutic drugs for hemostasis, wound antibiosis and skin infection, and so on. Recently, nanotechnology has shown the potentials to revolutionize traditional medical strips. For example, some nanomaterials with enzymatic property (e.g., peroxidase) have been successfully used to fabricate strips for effective and sensitive detecting H1N1 virus [205]. Cao et al. [20] infused the cysteine-MoS_2 with Ag^+ ions and then coated with a layer of cationic polyelectrolyte to fabricate an antibacterial depot for wound disinfection in vivo (Fig. 8.11). The biocompatible MoS_2 nanosheets not only possess antibacterial ability [21] but also can efficiently adsorb Ag^+ and then release it to the cell walls. Inspired by Cao's work [20], $MoSe_2$ hybrid nanosheets were twined by silk fibroin to form macroscopic films [46] (Fig. 8.11). Then, the films were posted on the *E. coli* infected skin wounds on the mice. Due to the superior peroxidase-like activity, $MoSe_2$ nanosheets can catalyze the decomposition of H_2O_2 into ·OH radicals, which possess high antibacterial ability without bacterial resistance. Therefore, a rapid and effective wound disinfection and healing efficacy were observed after treating with silk fibroin-coated $MoSe_2$ films and low-dose H_2O_2 in vivo. Those proof-of-concept studies demonstrated the feasibility of wound disinfection in wound care management using catalytic TMDs-based medical strips [20, 21, 46].

Soft bioelectronics, employing soft materials whose modulus is well matched with soft human tissues, have been extensively used in internal environment owing to their soft mechanical properties that lead to minimize tissue damages and immune responses [24]. For instance, there is still a challenge to fabricate implantable artificial retina simultaneously with the function of optoelectronic sensing and retinal stimu-

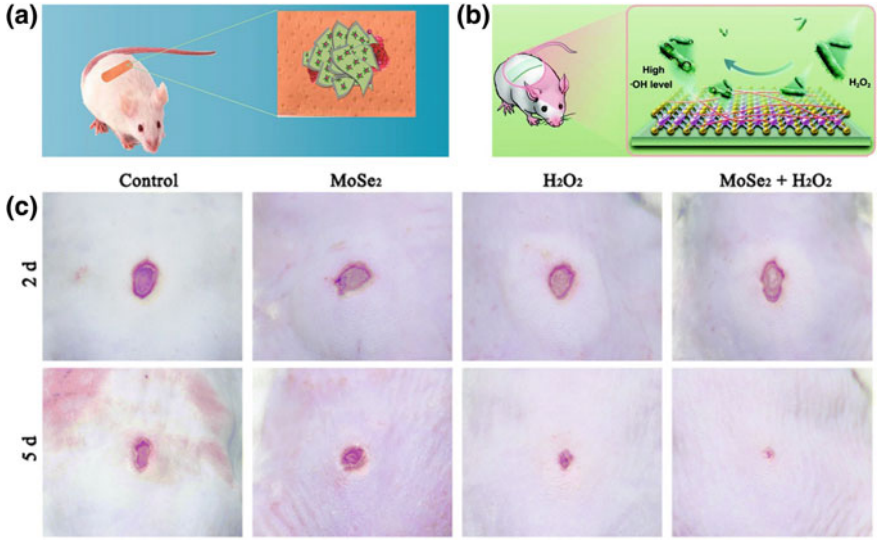

Fig. 8.11 TMDs-based woundplast for wound disinfection. **a**, **b** Schematic illustration of the preparation TMDs-based woundplast (Reprinted with permission from Ref. [20]. Copyright 2017, American Chemical Society.) **c** The wound repair process on the mice by the use of the silk fibroin-$MoSe_2$ films (Adapted from Ref. [46]. Copyright 2017, The Royal Society of Chemistry.)

lation. Therefore, Choi and his co-workers [24] designed an ultrasoft, high-density and hemispherically curved image sensor (CurvIS) array based on the atomically thin MoS_2-graphene heterostructure, as shown in Fig. 8.12. The soft, ultrathin, as well as super photo-absorption coefficient enables MoS_2 nanosheets as a photodetector to achieve high-quality imaging, while the ultrathin graphene acts as electrodes to conduct photocurrent. The CurvIS array exhibits many advantages including the high-density array design, hemispherical shape, small optical aberration, and simplified optics. It was found that the soft MoS_2-graphene CurvIS array successfully stimulated a rat's retinal nerves in response to the pulsed external optical signals. This deep work might greatly promote the application of 2D ultrathin nanomaterials-based implantable soft bio-optoelectronic device in ophthalmology.

8.8 Toxicity and Biosafety

8.8.1 Nanotoxicity Mechanisms of TMDs

The clinical translation of nanomaterials and nanotechnology gives rise to the high awareness of nanotoxicity and nanosafety originated from the public and scientific community. The toxicity of TMDs is of great importance and should be first con-

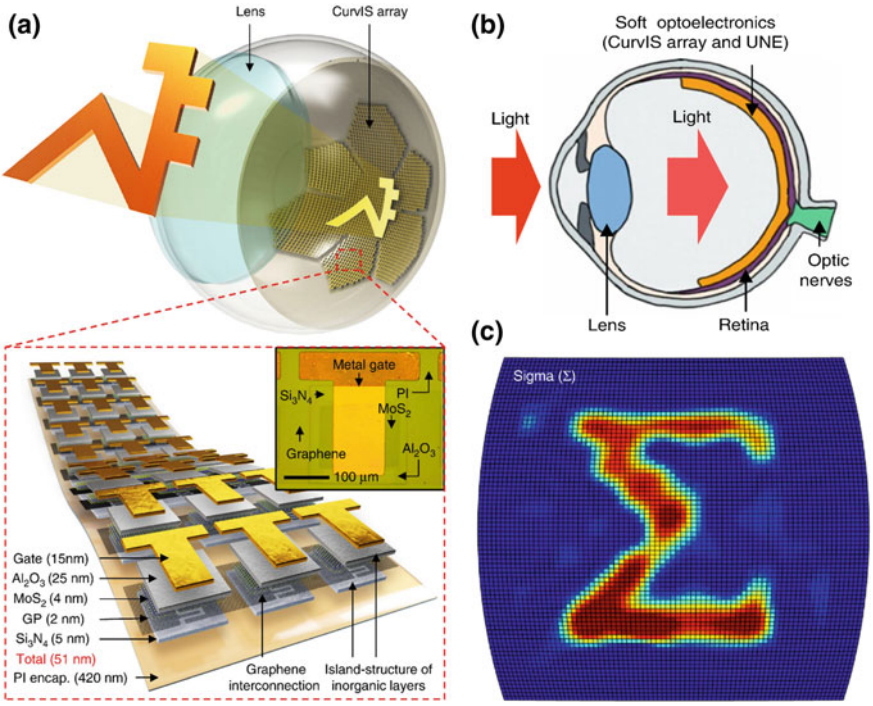

Fig. 8.12 TMDs-based soft bioelectronics for ophthalmology. **a** Schematic illustration of the high-density CurvIS array based on the MoS_2-graphene heterostructure. **b** Schematic illustration showing the ocular structure with the soft optoelectronic device. **c** Sigma-shaped image captured by the CurvIS array (Reproduced with permission from Ref. [24]. Copyright 2017, Springer Nature.)

sidered to guarantee their safe uses in the biomedical field. Therefore, since TMDs have shown great promising in disease diagnostic, bioimaging and cancer therapy, we are bound to pay more attention to study their biological effects and toxicology profiles in vitro and in vivo.

The interaction of 2D TMDs nanosheets with biosystems plays a vital role in understanding the nanotoxicity mechanisms of TMDs and guiding their safe and biomedical application. A deep study on cellular-level revealed the nano-bio interactions of MoS_2 nanosheets (the representative example of 2D TMDs family) with cancer cells from the aspect of endocytosis/exocytosis and autophagy [206]. As shown in Fig. 8.13, the main internalization processes and intracellular tracks of MoS_2 nanosheets consist of three different pathways: endocytosis through macropinocytosis, transportation from early endosomes to lysosomes, secretion of the internalized MoS_2 via exocytosis. Moreover, autophagy is also involved in the accumulation of MoS_2 in the lysosomes. So far, as the Achilles' heel, the biosafety evaluation and toxicity mechanisms of different types of TMDs in the biosystems are still not well revealed and understood [207].

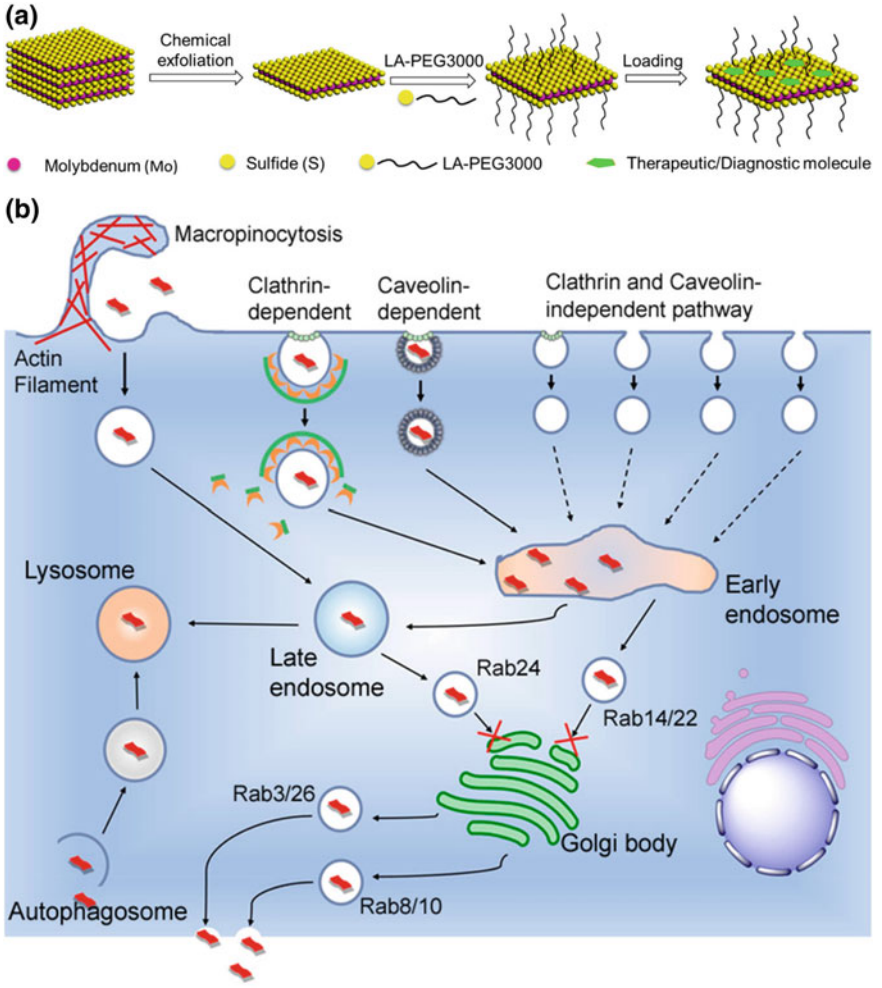

Fig. 8.13 The nano-bio interactions of MoS_2 nanosheets with cancer cells. **a** Scheme of the preparation of MoS_2 nanosheets with therapeutic/diagnostic molecules. **b** Schematic diagram illustrating the intracellular fates of MoS_2-based nanosheets. The process consists of three different pathways: endocytosis through macropinocytosis, transportation from early endosomes to lysosomes, secretion of the internalized MoS_2 via exocytosis. (Reproduced with permission from Ref. [206]. Copyright 2018, American Chemical Society.)

On the one hand, when TMDs nanoparticles enter the body, it may cause many stress reactions such as ROS production as it can be regarded as foreign components by cells and tissues. ROS usually generated from different routes such as the direct production, the interaction with cellular organelles, and the catalysis of intracellular H_2O_2 and so on. However, various negative effects, especially cell apoptosis or necrosis, will be appeared when the ROS level is too high. So, we must find out the safe concentrations and permissible doses of TMDs to ensure the minimum harmfulness to healthy tissues. It is worth mentioning that the generation of ROS caused by TMDs is an effective strategy to prohibit the growth of bacteria and cancer cells for antibacterial and antitumor, respectively. On the other hand, TMDs can be gradually biodegraded by various degradative components or the physiological environment, resulting in the release of free metal ions from TMDs, which may be also contributed to the toxicology profiles. For example, similar to CdS nanoparticles, Shang et al. demonstrated that the antibacterial activity of WS_2 was not only caused by ROS generation but also related to the release of toxic tungsten ions under UV irradiation [39]. Besides, the outstanding physicochemical properties such as the large surface area, surface atomic vacancy, and surface charge enabled TMDs nanosheets to interact with surrounding biological molecules via electrostatic interaction, covalent conjugation, or van de Waals forces. For example, the interaction of MoS_2 with protein can be investigated by all-atom molecular dynamics simulations [208–210]. The simulation results show that the secondary and tertiary structures of β-sheet protein were quickly damaged after adsorbing onto the MoS_2 surface [208]. In a later work, Villin Headpiece (HP35), a model protein widely used in protein folding studies, was chosen to further study the potential toxicity of MoS_2 nanosheets to proteins at the atomic level. MoS_2 nanosheets exhibit robust denaturing capability to severely destroy the secondary structures of HP35 within hundreds of nanoseconds. The dispersion interaction between protein and MoS_2 monolayer is contributed to the main driving force behind the adsorption process. Those interesting works illustrated the nanotoxicology origination from the atomic and theoretical levels, which help us to understand the underlying molecular mechanism. Then, Zou et al. [211] revealed for the first time that single-layer MoS_2 ($SLMoS_2$) accelerated proliferation and promoted myogenic differentiation and epithelial-mesenchymal transition (EMT) in human embryonic lung fibroblasts (HELFs) via the Akt-mTOR-p70S6 K signaling pathway, which is triggered by the generation of ROS. In contrast, after BSA binding, the cellular uptake of $SLMoS_2$ and the production of intracellular ROS were markedly reduced, and the $SLMoS_2$-activated phosphorylation of Akt-dependent signaling pathways was also mitigated. This studies demonstrated that serum proteins binding provides an effective strategy to reduce the potential nanotoxicity of MoS_2 nanosheets. So, after being uptake into tissue, TMDs will be coated by serum proteins, forming a protective protein corona.

8.8.2 *Effects of Physicochemical Factors on Nanotoxicity*

Compared to the corresponding bulk material, TMDs nanosheets have unique properties which can greatly affect the biological interaction of TMDs with cells. According to previous studies, the biocompatibility and nanotoxicity of TMDs nanosheets may vary with different synthesis methods, surface modification, size, shape, number of layers, surface charge, chemical composition, dose as well as the exposure time and route [212, 213]. The mainly physicochemical factors influencing biocompatibility of 2D TMDs nanosheets are as follows.

(1) **Preparation methods**

Chemically exfoliation is a well-known and widely used method to prepare biocompatible 2D TMDs for biosensing and cancer treatment. However, little is known about the degree of exfoliation of the nanosheets impacting on their toxicological behaviors. In one such recent work, Chng et al. [214] systematically compared the toxicity in vitro of MoS_2 nanosheets, which were chemically exfoliated using various lithium intercalating agents. All the results of the methylthiazolyldiphenyltetrazolium bromide (MTT) and water-soluble tetrazolium salt (WST-8) assays on A549 cells indicated that the *tert*-butyllithium (*t*-Bu-Li) and *n*-butyllithium (*n*-Bu-Li) exfoliated MoS_2 nanosheets showed higher cytotoxicity than MoS_2 exfoliated by methyllithium (Me-Li). In fact, the cytotoxicity of Me-Li-exfoliated nanosheets was similar to that of bulk MoS_2. *t*-Bu-Li and *n*-Bu-Li provide more efficient exfoliation over Me-Li, indicating that MoS_2 nanosheets exhibit stronger toxicity with increased exfoliation and decreased layer number. In contrast, a separate work by Wang et al. [215] has reported the increasing toxicological potential of three aqueous suspended forms of MoS_2 with increasing thickness or aggregates. It was observed that the aggregated and layered MoS_2 nanomaterials did not induce significant in vitro cytotoxic effect on BEAS-2B and THP-1 cell lines. Compared to lithiation-exfoliated MoS_2 (Lit-MoS_2) and Pluronic F87-dispersed MoS_2 (PF87-MoS_2), aggregated MoS_2 (Agg-MoS_2) induces stronger in vitro proinflammatory and profibrogenic responses. Moreover, Agg-MoS_2 caused acute lung inflammation in mice model, while both Lit-MoS_2 and PF87-MoS_2 had little effect. The observed phenomenon suggests that exfoliation attenuates the toxicity of Agg-MoS_2. Hence, it is a tremendous need to standardize the preparation of TMDs for toxicity tests.

In addition, the cytotoxicity of 2D TMDs may vary with different preparation methods. For example, Appel et al. [217] carefully investigated the toxicology profiles of mechanically exfoliated and CVD-grown pristine 2D TMDs (ME-WS_2, MEMoS_2, and CVD MoS_2) through various biocompatibility tests, including live-dead cell assays, ROS generation assays, and cellular morphology assessment. It turns out that both mechanically exfoliated and CVD-grown TMDs do not decrease cell viability and induce genetic defects when the concentrations of TMDs as high as 100 μg/mL.

(2) **Surface modification**

Taking MoS_2 as an example, Liu et al. [103] firstly studied the in vitro toxicity of pristine and PEGylated MoS_2 nanosheets using MTT assay. HeLa cells were incubated with various concentrations of MoS_2 or MoS_2-PEG for 24, 48, and 72 h. It was found that pristine MoS_2 nanosheets exhibited slight cytotoxicity (cell viability is ~73%, MoS_2 at 0.16 mg/mL) after culturing for 3 days, while PEGylated MoS_2 nanosheets showed negligible cytotoxicity (cell viability over 90%). The intracellular ROS levels in MoS_2 treated cells were subsequently assessed by using dihydroethidine (DHE) probe, indicating minimal oxidative stress induced by MoS_2. Moreover, PEGylated MoS_2 nanosheets also exhibited no significant cytotoxicity at a series of concentrations up to 500 μg/mL [111]. The novel outcomes of this work may be ascribed to the PEG-mediated one-pot solvothermal procedure. The "bottom-up" strategy improves the colloidal stability and bio-tolerance of MoS_2 nanosheets in the physiological environment. A separate study conducted by Pumera group also revealed that thiobarbituric acid functionalized MoS_2 nanosheets showed more protective effects than non-functionalized MoS_2 [218]. Thereafter, many works have been developed based on biocompatible polymers, liposomes, and even cellular components functionalized approaches to reduce the cytotoxicity of MoS_2 nanosheets. The excellent biocompatibility inspires the researchers to further pursue the biomedical applications of MoS_2.

(3) **Size and morphology**

Nanoparticle size and morphology play important roles when interacting with biological molecules and cells present in physiological conditions. In one such study, three kinds of cells (THP-1, AGS, and A549 cells) were incubated with three sizes (50, 117, and 177 nm) of MoS_2 at varying concentrations for 24 h [219]. The results showed that AGS cells were the most susceptible to 117 nm MoS_2 at the highest concentrations, while THP-1 showed the highest toxicity toward the smallest MoS_2 sheets (50 nm), indicating that the cytotoxicity of MoS_2 nanosheets varies with its sizes and cell types. Besides, some studies reported that the ultrasmall TMDs may be faster and easier to be cleared out of the kidney and body [67, 195–197]. Not only the 2D-layered TMDs nanosheets but other morphological TMDs such as radar-like MoS_2 nanoparticles [123], flowerlike MoS_2 nanoflakes [21, 102, 122, 158], multiwall WS_2 nanotubes [220], fullerene-like nanoparticles (IFWS_2 [220], $MoSe_2$ [221]) also have been demonstrated to be favorable biocompatibility in a certain concentration range.

(4) **Chemical Composition**

The chemical compositions are also key factors impacting on the toxicology profiles of TMDs nanosheets. Pumera group pioneered the study of the nanotoxicity of 2D materials including graphene, black phosphorus, and TMDs. In a work, they found that MoS_2 and WS_2 induced slight cytotoxicity in the A549 cells after 24 h exposure, even at high concentration up to 400 μg/mL, while WSe_2 showed higher toxicity compared to MoS_2 and WS_2 [222]. Moreover, the studied Group 6 TMDs (MoS_2,

WS_2, WSe_2) exhibited significantly lower cytotoxicity than different synthesized graphene oxide (GO) and layered GaSe tested on the same cell lines in the same conditions, while black phosphorus showed a generally intermediate cytotoxicity between GO and TMDs [222–225]. They subsequently compared the toxicological behavior of Group 6 TMDs with Group 5 vanadium dichalcogenides (VS_2, VSe_2, VTe_2) under similar experimental conditions [216]. For the same chalcogen element, VS_2 consistently shows higher toxicity for both MTT and WST-8 assay at all concentrations than that of MoS_2 and WS_2; the similar tendency was also observed among WSe_2 and VSe_2. They also compared the cytotoxicity of the Group 5 transition metal ditellurides (VTe_2, $NbTe_2$, $TaTe_2$) to understand their biological effects for the future applications [226]. The results suggest that VTe_2 is highly toxic to A549 cells with 92.5% of cells elimination at a concentration of 200 μg/mL, whereas $NbTe_2$ and $TaTe_2$ are mildly toxic. For the same metal element, the metal sulfides (WS_2, VS_2) display higher cell viability relative to their corresponding metal selenides (WSe_2, VSe_2) [216]. In addition, a recent work revealed that the toxicity of Pt dichalcogenides follows the trend of $PtTe_2 > PtSe_2 > PtS_2$ [227]. It is concluded that TMDs consist of vanadium element which is inherently more toxic than Mo and W, while sulfides are generally less toxic compared to their selenide and telluride counterparts for TMDs.

8.8.3 Nanotoxicity and Biodegradability of TMDs

To date, many research works have been conducted to evaluate the in vitro cytotoxicity of 2D TMDs through CCK-8, MTT assays, or WST-8 assay. Most of the results showed that 2D TMDs were non-cytotoxic or negligible cytotoxic within a certain range of concentrations, which importantly encouraged the in vivo applications of TMDs. In this regard, researches concerning the evaluations on the biosafety and biodegradability in vivo of 2D TMDs are urgently required. Many studies have reported that the TMDs nanosheets treated mice could survive for more than one month. For example, Liu et al. [103] assessed the biocompatibility of PEGylated MoS_2 nanosheets to BALB/c mice at the dose of 3.4 mg/kg. The results showed that PEGylated MoS_2 nanosheets may not be noticeably toxic to mice within one month. In a similar work, WS_2-PEG (20 mg/kg of i.v. injection) and NIR irradiation (808 nm, 0.8 W/cm^2, 5 min) treated BALB/c mice showed no obvious abnormal behavior and noticeable organ damage within 45 days [59]. The blood biochemistry assay revealed that all measured indexes of the blood test fell within normal reference ranges, indicating the excellent histocompatibility of WS_2-PEG. In addition, 4T1 tumor-bearing mice died within 16 days, while the TiS_2-PEG and PTT treated mice survived over 60 days, suggesting no obvious toxicity to mice at the tested dose [75]. In another in vivo toxicology assays, i.v. injected ReS_2-PEG nanosheets did not induce obvious organ damages, hepatic or kidney disorder at the dose of 20 mg/kg [77]. Besides, Yu et al. [228] conducted the first investigation of the toxicity of CS@MoS_2 micro-sheets in adult zebrafish. It was found that CS@MoS_2 at

high concentrations (20 mg/L) induced a proinflammatory response and apoptosis in the gills and liver.

More importantly, the long-term biodistribution, degradation, and excretion of PEGylated MS_2 (M = Mo, W, Ti) were carefully evaluated and compared by Hao et al. [229]. After i.v. injection, these three kinds of PEGylated TMDs nanosheets were found mainly to be accumulated in liver and spleen. Notably, large amounts of injected W or Ti were still retained in the RES for months, while MoS_2-PEG could be almost completely degraded and then excreted. PEGylated MoS_2 and TiS_2 will be oxidized into water-soluble Mo^{VI}-oxide species (such as MoO_4^{2-}), water-insoluble TiO_2 aggregates, respectively, while WS_2-PEG was hardly oxidized for the higher chemical stability. The histological and blood analysis demonstrated that these three kinds of PEGylated MS_2 nanosheets have no obvious long-term toxicity at the tested dose [229]. In a separate work, ultrasmall VS_2 nanodots converted from their sheet materials via ultrasonic exfoliation exhibited effective body excretion without appreciable toxicity [76]. Dark black VS_2@lipid-PEG solutions were found to be gradually oxidized into light yellow after air exposure 30 days. The results confirmed that V element in VS_2 nanostructures was oxidized from V^{3+}/V^{4+} to the high valence state (V^V). Thus, VS_2@lipid-PEG nanoparticles might be gradually oxidized and degraded into water-soluble and degradable V^V-oxide species.

8.9 Conclusions and Outlook

The utilization of multifunctional TMDs nanosheets for biomedical applications is of great importance and has achieved remarkable advancement. In this chapter, we summarized the latest progress of inorganic 2D TMDs in bioanalysis, antibacterial and wound repair, drug delivery, bioimaging, cancer therapy, tissue engineering, and medical devices. In particular, the nanotoxicology and biosafety profiles of TMDs are reviewed to ensure their further biomedical use. The abundant chemical compositions, unique physicochemical properties, and diverse biological effects endow the emerging TMDs nanosheets with the potential for next-generation biomedicine.

However, the investigation of these 2D TMDs in biomedicine is only in its infancy, and two critical challenges are to be concerned. From the materials point of view, the first is the standardization of the synthesis methods of 2D TMDs nanosheets. Different parameters and synthesis methods will lead to diverse characteristics, such as size and layer number, which will impact their physicochemical properties and even biological effects. Thus, we need to standardize the preparation of 2D TMDs in a controllable and repeatable manner to obtain the materials with desired structure and property. Moreover, detailed biosafety and toxicity evaluations of these 2D TMDs are urgently demanded from the biosafety point. Although the current evaluation has demonstrated that 2D TMDs exhibit relatively low toxicity, their potential long-term biosafety and in vivo biodegradation in the diverse animal model, and related toxicity mechanisms are still insufficient and should be systemically assessed to reduce the awareness of nanotoxicity.

In conclusion, although the various remarkable progresses of 2D TMDs in biomedical field that has achieved in the last decade are exciting, more research efforts are needed to be undertaken to accelerate the clinical translations of the emerging 2D TMDs.

Acknowledgements The authors gratefully acknowledge the help from Jiani Xie and Shuang Zhu. This work was supported by the National Basic Research Programs of China (Grant Nos. 2016YFA0201600 and 2015CB932104), the National Natural Science Foundation of China (Grant Nos. 31571015, 11621505, 11435002, and 21320102003), and the Youth Innovation Promotion Association CAS (Grant No. 2013007).

Conflict of Interest
The authors declare no conflict of interest.

References

1. Manzeli S, Ovchinnikov D, Pasquier D, Yazyev OV, Kis A (2017) 2D transition metal dichalcogenides. Nat Rev Mater 2:17033. https://doi.org/10.1038/natrevmats.2017.33
2. Tan C, Cao X, Wu XJ, He Q, Yang J, Zhang X, Chen J, Zhao W, Han S, Nam GH, Sindoro M, Zhang H (2017) Recent advances in ultrathin two-dimensional nanomaterials. Chem Rev 117(9):6225–6331. https://doi.org/10.1021/acs.chemrev.6b00558
3. Samadi M, Sarikhani N, Zirak M, Zhang H, Zhang H-L, Moshfegh AZ (2018) Group 6 transition metal dichalcogenide nanomaterials: synthesis, applications and future perspectives. Nanoscale Horiz 3(2):90–204. https://doi.org/10.1039/c7nh00137a
4. Bhimanapati GR, Lin Z, Meunier V, Jung Y, Cha J, Das S, Xiao D, Son Y, Strano MS, Cooper VR, Liang L, Louie SG, Ringe E, Zhou W, Kim SS, Naik RR, Sumpter BG, Terrones H, Xia F, Wang Y, Zhu J, Akinwande D, Alem N, Schuller JA, Schaak RE, Terrones M, Robinson JA (2015) Recent advances in two-dimensional materials beyond graphene. ACS Nano 9(12):11509–11539. https://doi.org/10.1021/acsnano.5b05556
5. Chhowalla M, Shin HS, Eda G, Li LJ, Loh KP, Zhang H (2013) The chemistry of two-dimensional layered transition metal dichalcogenide nanosheets. Nat Chem 5(4):263–275. https://doi.org/10.1038/nchem.1589
6. Kolobov AV, Tominaga J (2016) Emerging applications of 2D TMDCs. In: Two-dimensional transition-metal dichalcogenides. Springer series in materials science, vol 239. Springer International Publishing, Cham, pp 473–512. https://doi.org/10.1007/978-3-319-31450-1_14
7. Chen Y, Tan C, Zhang H, Wang L (2015) Two-dimensional graphene analogues for biomedical applications. Chem Soc Rev 44(9):2681–2701. https://doi.org/10.1039/c4cs00300d
8. Chimene D, Alge DL, Gaharwar AK (2015) Two-dimensional nanomaterials for biomedical applications: emerging trends and future prospects. Adv Mater 27(45):7261–7284. https://doi.org/10.1002/adma.201502422
9. Kurapati R, Kostarelos K, Prato M, Bianco A (2016) Biomedical uses for 2D materials beyond graphene: current advances and challenges ahead. Adv Mater 28(29):6052–6074. https://doi.org/10.1002/adma.201506306
10. Kalantar-zadeh K, Ou JZ, Daeneke T, Strano MS, Pumera M, Gras SL (2015) Two-dimensional transition metal dichalcogenides in biosystems. Adv Funct Mater 25(32):5086–5099. https://doi.org/10.1002/adfm.201500891
11. Liu T, Liu Z (2018) 2D MoS_2 nanostructures for biomedical applications. Adv Healthc Mater 7(8):1701158. https://doi.org/10.1002/adhm.201701158
12. Yang B, Chen Y, Shi J (2018) Material chemistry of two-dimensional inorganic nanosheets in cancer theranostics. Chem 4(6):1284–1313. https://doi.org/10.1016/j.chempr.2018.02.012

13. Li X, Shan J, Zhang W, Su S, Yuwen L, Wang L (2017) Recent advances in synthesis and biomedical applications of two-dimensional transition metal dichalcogenide nanosheets. Small 13(5):1602660. https://doi.org/10.1002/smll.201602660
14. Coleman JN, Lotya M, O'Neill A, Bergin SD, King PJ, Khan U, Young K, Gaucher A, De S, Smith RJ, Shvets IV, Arora SK, Stanton G, Kim HY, Lee K, Kim GT, Duesberg GS, Hallam T, Boland JJ, Wang JJ, Donegan JF, Grunlan JC, Moriarty G, Shmeliov A, Nicholls RJ, Perkins JM, Grieveson EM, Theuwissen K, McComb DW, Nellist PD, Nicolosi V (2011) Two-dimensional nanosheets produced by liquid exfoliation of layered materials. Science 331(6017):568–571. https://doi.org/10.1126/science.1194975
15. Nicolosi V, Chhowalla M, Kanatzidis MG, Strano MS, Coleman JN (2013) Liquid exfoliation of layered materials. Science 340(6139). https://doi.org/10.1126/science.1226419
16. Brent JR, Savjani N, O'Brien P (2017) Synthetic approaches to two-dimensional transition metal dichalcogenide nanosheets. Prog Mater Sci 89:411–478. https://doi.org/10.1016/j.pmatsci.2017.06.002
17. Zhu S, Gong L, Xie J, Gu Z, Zhao Y (2017) Design, synthesis, and surface modification of materials based on transition-metal dichalcogenides for biomedical applications. Small Methods 1(12):1700220. https://doi.org/10.1002/smtd.201700220
18. Yin F, Gu B, Lin Y, Panwar N, Tjin SC, Qu J, Lau SP, Yong K-T (2017) Functionalized 2D nanomaterials for gene delivery applications. Coord Chem Rev 347:77–97. https://doi.org/10.1016/j.ccr.2017.06.024
19. Li Z, Wong SL (2017) Functionalization of 2D transition metal dichalcogenides for biomedical applications. Mater Sci Eng, C 70:1095–1106. https://doi.org/10.1016/j.msec.2016.03.039
20. Cao F, Ju E, Zhang Y, Wang Z, Liu C, Li W, Huang Y, Dong K, Ren J, Qu X (2017) An efficient and benign antimicrobial depot based on silver-infused MoS_2. ACS Nano 11(5):4651–4659. https://doi.org/10.1021/acsnano.7b00343
21. Yin W, Yu J, Lv F, Yan L, Zheng LR, Gu Z, Zhao Y (2016) Functionalized nano-MoS_2 with peroxidase catalytic and near-infrared photothermal activities for safe and synergetic wound antibacterial applications. ACS Nano 10(12):11000–11011. https://doi.org/10.1021/acsnano.6b05810
22. Wang S, Qiu J, Guo W, Yu X, Nie J, Zhang J, Zhang X, Liu Z, Mou X, Li L, Liu H (2017) A nanostructured molybdenum disulfide film for promoting neural stem cell neuronal differentiation: toward a nerve tissue-engineered 3D scaffold. Adv Biosyst 1(5):1600042. https://doi.org/10.1002/adbi.201600042
23. Wang X, Li T, Ma H, Zhai D, Jiang C, Chang J, Wang J, Wu C (2017) A 3D-printed scaffold with MoS_2 nanosheets for tumor therapy and tissue regeneration. NPG Asia Mater 9(4):e376. https://doi.org/10.1038/am.2017.47
24. Choi C, Choi MK, Liu S, Kim MS, Park OK, Im C, Kim J, Qin X, Lee GJ, Cho KW, Kim M, Joh E, Lee J, Son D, Kwon SH, Jeon NL, Song YM, Lu N, Kim DH (2017) Human eye-inspired soft optoelectronic device using high-density MoS_2-graphene curved image sensor array. Nat Commun 8(1):1664. https://doi.org/10.1038/s41467-017-01824-6
25. Gong L, Yan L, Zhou R, Xie J, Wu W, Gu Z (2017) Two-dimensional transition metal dichalcogenide nanomaterials for combination cancer therapy. J Mater Chem B 5(10):1873–1895. https://doi.org/10.1039/c7tb00195a
26. Chen Y, Wang LZ, Shi JL (2016) Two-dimensional non-carbonaceous materials-enabled efficient photothermal cancer therapy. Nano Today 11(3):292–308. https://doi.org/10.1016/j.nantod.2016.05.009
27. Chen H, Liu T, Su Z, Shang L, Wei G (2018) 2D transition metal dichalcogenide nanosheets for photo/thermo-based tumor imaging and therapy. Nanoscale Horiz 3(2):74–89. https://doi.org/10.1039/c7nh00158d
28. Lusic H, Grinstaff MW (2013) X-ray-computed tomography contrast agents. Chem Rev 113(3):1641–1666. https://doi.org/10.1021/cr200358s
29. Gong LJ, Xie JN, Zhu S, Gu ZJ, Zhao YL (2018) Application of multifunctional nanomaterials in tumor radiosensitization. Acta Phys Chim Sin 34(2):140–167. https://doi.org/10.3866/pku.Whxb201707174

30. Wang L, Xiong Q, Xiao F, Duan H (2017) 2D nanomaterials based electrochemical biosensors for cancer diagnosis. Biosens Bioelectron 89(Pt 1):136–151. https://doi.org/10.1016/j.bios.2016.06.011
31. Peng B, Zhang X, Aarts D, Dullens RPA (2018) Superparamagnetic nickel colloidal nanocrystal clusters with antibacterial activity and bacteria binding ability. Nat Nanotechnol 13(6):478–482. https://doi.org/10.1038/s41565-018-0108-0
32. Zheng H, Ma R, Gao M, Tian X, Li Y-Q, Zeng L, Li R (2018) Antibacterial applications of graphene oxides: structure-activity relationships, molecular initiating events and biosafety. Sci Bull 63(2):133–142. https://doi.org/10.1016/j.scib.2017.12.012
33. Le Ouay B, Stellacci F (2015) Antibacterial activity of silver nanoparticles: a surface science insight. Nano Today 10(3):339–354. https://doi.org/10.1016/j.nantod.2015.04.002
34. Chernousova S, Epple M (2013) Silver as antibacterial agent: ion, nanoparticle, and metal. Angew Chem Int Ed 52(6):1636–1653. https://doi.org/10.1002/anie.201205923
35. Franci G, Falanga A, Galdiero S, Palomba L, Rai M, Morelli G, Galdiero M (2015) Silver nanoparticles as potential antibacterial agents. Molecules 20(5):8856–8874. https://doi.org/10.3390/molecules20058856
36. Yang X, Li J, Liang T, Ma C, Zhang Y, Chen H, Hanagata N, Su H, Xu M (2014) Antibacterial activity of two-dimensional MoS2 sheets. Nanoscale 6(17):10126–10133. https://doi.org/10.1039/c4nr01965b
37. Pandit S, Karunakaran S, Boda SK, Basu B, De M (2016) High antibacterial activity of functionalized chemically exfoliated MoS_2. ACS Appl Mater Interfaces 8(46):31567–31573. https://doi.org/10.1021/acsami.6b10916
38. Zhang W, Shi S, Wang Y, Yu S, Zhu W, Zhang X, Zhang D, Yang B, Wang X, Wang J (2016) Versatile molybdenum disulfide based antibacterial composites for in vitro enhanced sterilization and in vivo focal infection therapy. Nanoscale 8(22):11642–11648. https://doi.org/10.1039/c6nr01243d
39. Shang E, Niu J, Li Y, Zhou Y, Crittenden JC (2017) Comparative toxicity of Cd, Mo, and W sulphide nanomaterials toward *E. coli* under UV irradiation. Environ Pollut 224:606–614. https://doi.org/10.1016/j.envpol.2017.02.044
40. Bang GS, Cho S, Son N, Shim GW, Cho BK, Choi SY (2016) DNA-assisted exfoliation of tungsten dichalcogenides and their antibacterial effect. ACS Appl Mater Interfaces 8(3):1943–1950. https://doi.org/10.1021/acsami.5b10136
41. Navale GR, Rout CS, Gohil KN, Dharne MS, Late DJ, Shinde SS (2015) Oxidative and membrane stress-mediated antibacterial activity of WS_2 and rGO-WS_2 nanosheets. RSC Adv 5(91):74726–74733. https://doi.org/10.1039/c5ra15652a
42. Liu X, Duan G, Li W, Zhou Z, Zhou R (2017) Membrane destruction-mediated antibacterial activity of tungsten disulfide (WS_2). RSC Adv 7(60):37873–37880. https://doi.org/10.1039/c7ra06442j
43. Awasthi GP, Adhikari SP, Ko S, Kim HJ, Park CH, Kim CS (2016) Facile synthesis of ZnO flowers modified graphene like MoS_2 sheets for enhanced visible-light-driven photocatalytic activity and antibacterial properties. J Alloys Compd 682:208–215. https://doi.org/10.1016/j.jallcom.2016.04.267
44. Chen CS, Yu WW, Liu TG, Cao SY, Tsang YH (2017) Graphene oxide/WS_2/Mg-doped ZnO nanocomposites for solar-light catalytic and anti-bacterial applications. Sol Energy Mater Sol Cells 160:43–53. https://doi.org/10.1016/j.solmat.2016.10.020
45. Pal A, Jana TK, Roy T, Pradhan A, Maiti R, Choudhury SM, Chatterjee K (2018) MoS_2-TiO_2 nanocomposite with excellent adsorption performance and high antibacterial activity. Chemistryselect 3(1):81–90. https://doi.org/10.1002/slct.201702618
46. Huang X-W, Wei J-J, Liu T, Zhang X-L, Bai S-M, Yang H-H (2017) Silk fibroin-assisted exfoliation and functionalization of transition metal dichalcogenide nanosheets for antibacterial wound dressings. Nanoscale 9(44):17193–17198. https://doi.org/10.1039/c7nr06807g
47. Feng Z, Liu X, Tan L, Cui Z, Yang X, Li Z, Zheng Y, Yeung KWK, Wu S (2018) Electrophoretic deposited stable chitosan@MoS_2 coating with rapid in situ bacteria-killing ability under dual-light irradiation. Small 14(21):1704347. https://doi.org/10.1002/smll.201704347

48. Dubertret B, Skourides P, Norris DJ, Noireaux V, Brivanlou AH, Libchaber A (2002) In vivo imaging of quantum dots encapsulated in phospholipid micelles. Science 298(5599):1759–1762. https://doi.org/10.1126/science.1077194
49. Gao X, Cui Y, Levenson RM, Chung LW, Nie S (2004) In vivo cancer targeting and imaging with semiconductor quantum dots. Nat Biotechnol 22(8):969–976. https://doi.org/10.1038/nbt994
50. Michalet X, Pinaud FF, Bentolila LA, Tsay JM, Doose S, Li JJ, Sundaresan G, Wu AM, Gambhir SS, Weiss S (2005) Quantum dots for live cells, in vivo imaging, and diagnostics. Science 307(5709):538–544. https://doi.org/10.1126/science.1104274
51. Bruns OT, Bischof TS, Harris DK, Franke D, Shi Y, Riedemann L, Bartelt A, Jaworski FB, Carr JA, Rowlands CJ, Wilson MWB, Chen O, Wei H, Hwang GW, Montana DM, Coropceanu I, Achorn OB, Kloepper J, Heeren J, So PTC, Fukumura D, Jensen KF, Jain RK, Bawendi MG (2017) Next-generation in vivo optical imaging with short-wave infrared quantum dots. Nat Biomed Eng 1:0056. https://doi.org/10.1038/s41551-017-0056
52. Oh E, Liu R, Nel A, Gemill KB, Bilal M, Cohen Y, Medintz IL (2016) Meta-analysis of cellular toxicity for cadmium-containing quantum dots. Nat Nanotechnol 11(5):479–486. https://doi.org/10.1038/nnano.2015.338
53. Yang G, Gong H, Liu T, Sun X, Cheng L, Liu Z (2015) Two-dimensional magnetic WS_2@$Fe3O_4$ nanocomposite with mesoporous silica coating for drug delivery and imaging-guided therapy of cancer. Biomaterials 60:62–71. https://doi.org/10.1016/j.biomaterials.2015.04.053
54. Song C, Yang C, Wang F, Ding D, Gao Y, Guo W, Yan M, Liu S, Guo C (2017) MoS_2-Based multipurpose theranostic nanoplatform: realizing dual-imaging-guided combination phototherapy to eliminate solid tumor via a liquefaction necrosis process. J Mater Chem B 5(45):9015–9024. https://doi.org/10.1039/c7tb02648j
55. Dai W, Dong H, Fugetsu B, Cao Y, Lu H, Ma X, Zhang X (2015) Tunable fabrication of molybdenum disulfide quantum dots for intracellular microRNA detection and multiphoton bioimaging. Small 11(33):4158–4164. https://doi.org/10.1002/smll.201500208
56. Gu W, Yan Y, Cao X, Zhang C, Ding C, Xian Y (2016) A facile and one-step ethanol-thermal synthesis of MoS_2 quantum dots for two-photon fluorescence imaging. J Mater Chem B 4(1):27–31. https://doi.org/10.1039/c5tb01839k
57. Chen SC, Lin CY, Cheng TL, Tseng WL (2017) 6-mercaptopurine-induced fluorescence quenching of monolayer MoS_2 nanodots: applications to glutathione sensing, cellular imaging, and glutathione-stimulated drug delivery. Adv Funct Mater 27(41):1702452. https://doi.org/10.1002/adfm.201702452
58. Wang LV, Hu S (2012) Photoacoustic tomography: in vivo imaging from organelles to organs. Science 335(6075):1458–1462. https://doi.org/10.1126/science.1216210
59. Cheng L, Liu J, Gu X, Gong H, Shi X, Liu T, Wang C, Wang X, Liu G, Xing H, Bu W, Sun B, Liu Z (2014) PEGylated WS_2 nanosheets as a multifunctional theranostic agent for in vivo dual-modal CT/photoacoustic imaging guided photothermal therapy. Adv Mater 26(12):1886–1893. https://doi.org/10.1002/adma.201304497
60. Chen JQ, Liu CB, Hu DH, Wang F, Wu HW, Gong XJ, Liu X, Song L, Sheng ZH, Zheng HR (2016) Single-layer MoS_2 nanosheets with amplified photoacoustic effect for highly sensitive photoacoustic imaging of orthotopic brain tumors. Adv Funct Mater 26(47):8715–8725. https://doi.org/10.1002/adfm.201603758
61. Liu T, Wang C, Cui W, Gong H, Liang C, Shi X, Li Z, Sun B, Liu Z (2014) Combined photothermal and photodynamic therapy delivered by PEGylated MoS_2 nanosheets. Nanoscale 6(19):11219–11225. https://doi.org/10.1039/c4nr03753g
62. Liu T, Shi S, Liang C, Shen S, Cheng L, Wang C, Song X, Goel S, Barnhart TE, Cai W, Liu Z (2015) Iron oxide decorated MoS_2 nanosheets with double PEGylation for chelator-free radiolabeling and multimodal imaging guided photothermal therapy. ACS Nano 9(1):950–960. https://doi.org/10.1021/nn506757x
63. Chen L, Zhou X, Nie W, Feng W, Zhang Q, Wang W, Zhang Y, Chen Z, Huang P, He C (2017) Marriage of albumin-gadolinium complexes and MoS_2 nanoflakes as cancer theranostics for

dual-modality magnetic resonance/photoacoustic imaging and photothermal therapy. ACS Appl Mater Interfaces 9(21):17786–17798. https://doi.org/10.1021/acsami.7b04488
64. Liu CB, Chen JQ, Zhu Y, Gong XJ, Zheng RQ, Chen NB, Chen D, Yan HX, Zhang P, Zheng HR, Sheng ZH, Song L (2018) Highly sensitive MoS_2-indocyanine green hybrid for photoacoustic imaging of orthotopic brain glioma at deep site. Nano-Micro Lett 10(3):48. https://doi.org/10.1007/s40820-018-0202-8
65. Wu C, Zhao J, Hu F, Zheng Y, Yang H, Pan S, Shi S, Chen X, Wang S (2018) Design of injectable agar-based composite hydrogel for multi-mode tumor therapy. Carbohydr Polym 180:112–121. https://doi.org/10.1016/j.carbpol.2017.10.024
66. Zhao J, Li J, Zhu C, Hu F, Wu H, Man X, Li Z, Ye C, Zou D, Wang S (2018) Design of phase-changeable and injectable alginate hydrogel for imaging-guided tumor hyperthermia and chemotherapy. ACS Appl Mater Interfaces 10(4):3392–3404. https://doi.org/10.1021/acsami.7b17608
67. Liu T, Chao Y, Gao M, Liang C, Chen Q, Song GS, Cheng L, Liu Z (2016) Ultra-small MoS_2 nanodots with rapid body clearance for photothermal cancer therapy. Nano Res 9(10):3003–3017. https://doi.org/10.1007/s12274-016-1183-x
68. Wang J, Tan X, Pang X, Liu L, Tan F, Li N (2016) MoS_2 quantum dot@polyaniline inorganic-organic nanohybrids for in vivo dual-modal imaging guided synergistic photothermal/radiation therapy. ACS Appl Mater Interfaces 8(37):24331–24338. https://doi.org/10.1021/acsami.6b08391
69. Zhao J, Zhou C, Li M, Li J, Li G, Ma D, Li Z, Zou D (2017) Bottom-up synthesis of ultra-small molybdenum disulfide-polyvinylpyrrolidone nanosheets for imaging-guided tumor regression. Oncotarget 8(63):106707–106720. https://doi.org/10.18632/oncotarget.22477
70. Chen J, Li X, Liu X, Yan H, Xie Z, Sheng Z, Gong X, Wang L, Liu X, Zhang P, Zheng H, Song L, Liu C (2018) Hybrid $MoSe_2$-indocyanine green nanosheets as a highly efficient phototheranostic agent for photoacoustic imaging guided photothermal cancer therapy. Biomater Sci 6(6):1503–1516. https://doi.org/10.1039/c8bm00104a
71. Pan J, Zhu X, Chen X, Zhao Y, Liu J (2018) Gd^{3+}-doped $MoSe_2$ nanosheets used as a theranostic agent for bimodal imaging and highly efficient photothermal cancer therapy. Biomater Sci 6(2):372–387. https://doi.org/10.1039/c7bm00894e
72. Cheng L, Yuan C, Shen S, Yi X, Gong H, Yang K, Liu Z (2015) Bottom-up synthesis of metal-ion-doped WS_2 nanoflakes for cancer theranostics. ACS Nano 9(11):11090–11101. https://doi.org/10.1021/acsnano.5b04606
73. Wang S, Zhao J, Yang H, Wu C, Hu F, Chang H, Li G, Ma D, Zou D, Huang M (2017) Bottom-up synthesis of WS_2 nanosheets with synchronous surface modification for imaging guided tumor regression. Acta Biomater 58:442–454. https://doi.org/10.1016/j.actbio.2017.06.014
74. Zhang C, Yong Y, Song L, Dong X, Zhang X, Liu X, Gu Z, Zhao Y, Hu Z (2016) Multifunctional WS_2@Poly(ethylene imine) nanoplatforms for imaging guided gene-photothermal synergistic therapy of cancer. Adv Healthc Mater 5(21):2776–2787. https://doi.org/10.1002/adhm.201600633
75. Qian XX, Shen SD, Liu T, Cheng L, Liu Z (2015) Two-dimensional TiS_2 nanosheets for in vivo photoacoustic imaging and photothermal cancer therapy. Nanoscale 7(14):6380–6387. https://doi.org/10.1039/c5nr00893j
76. Chen Y, Cheng L, Dong Z, Chao Y, Lei H, Zhao H, Wang J, Liu Z (2017) Degradable vanadium disulfide nanostructures with unique optical and magnetic functions for cancer theranostics. Angew Chem Int Ed 56(42):12991–12996. https://doi.org/10.1002/anie.201707128
77. Shen SD, Chao Y, Dong ZL, Wang GL, Yi X, Song GS, Yang K, Liu Z, Cheng L (2017) Bottom-up preparation of uniform ultrathin rhenium disulfide nanosheets for image-guided photothermal radiotherapy. Adv Funct Mater 27(28):1700250. https://doi.org/10.1002/adfm.201700250
78. Miao ZH, Lv LX, Li K, Liu PY, Li Z, Yang H, Zhao Q, Chang M, Zhen L, Xu CY (2018) Liquid exfoliation of colloidal rhenium disulfide nanosheets as a multifunctional theranostic agent for in vivo photoacoustic/ct imaging and photothermal therapy. Small 14(14):1703789. https://doi.org/10.1002/smll.201703789

79. Wang S, Li X, Chen Y, Cai X, Yao H, Gao W, Zheng Y, An X, Shi J, Chen H (2015) A facile one-pot synthesis of a two-dimensional MoS_2/Bi_2S_3 composite theranostic nanosystem for multi-modality tumor imaging and therapy. Adv Mater 27(17):2775–2782. https://doi.org/10.1002/adma.201500870
80. Yu J, Yin W, Zheng X, Tian G, Zhang X, Bao T, Dong X, Wang Z, Gu Z, Ma X, Zhao Y (2015) Smart MoS_2/Fe_3O_4 nanotheranostic for magnetically targeted photothermal therapy guided by magnetic resonance/photoacoustic imaging. Theranostics 5(9):931–945. https://doi.org/10.7150/thno.11802
81. Liu B, Li C, Chen G, Liu B, Deng X, Wei Y, Xia J, Xing B, Ma P, Lin J (2017) Synthesis and optimization of MoS_2@Fe_3O_4-ICG/Pt(IV) Nanoflowers for MR/IR/PA bioimaging and combined PTT/PDT/chemotherapy triggered by 808 nm laser. Adv Sci 4(8):1600540. https://doi.org/10.1002/advs.201600540
82. Meng XD, Liu ZQ, Cao Y, Dai WH, Zhang K, Dong HF, Feng XY, Zhang XJ (2017) Fabricating aptamer-conjugated PEGylated-MoS_2/Cu1.8S theranostic nanoplatform for multiplexed imaging diagnosis and chemo-photothermal therapy of cancer. Adv Funct Mater 27(16):1605592. https://doi.org/10.1002/adfm.201605592
83. Ke K, Yang W, Xie X, Liu R, Wang LL, Lin WW, Huang G, Lu CH, Yang HH (2017) Copper manganese sulfide nanoplates: a new two-dimensional theranostic nanoplatform for MRI/MSOT dual-modal imaging-guided photothermal therapy in the second near-infrared window. Theranostics 7(19):4763–4776. https://doi.org/10.7150/thno.21694
84. Zhu H, Lai Z, Fang Y, Zhen X, Tan C, Qi X, Ding D, Chen P, Zhang H, Pu K (2017) Ternary chalcogenide nanosheets with ultrahigh photothermal conversion efficiency for photoacoustic theranostics. Small 13(16):1604139. https://doi.org/10.1002/smll.201604139
85. Cui X-Z, Zhou Z-G, Yang Y, Wei J, Wang J, Wang M-W, Yang H, Zhang Y-J, Yang S-P (2015) PEGylated WS_2 nanosheets for X-ray computed tomography imaging and photothermal therapy. Chin Chem Lett 26(6):749–754. https://doi.org/10.1016/j.cclet.2015.03.034
86. Yong Y, Cheng X, Bao T, Zu M, Yan L, Yin W, Ge C, Wang D, Gu Z, Zhao Y (2015) Tungsten sulfide quantum dots as multifunctional nanotheranostics for in vivo dual-modal image-guided photothermal/radiotherapy synergistic therapy. ACS Nano 9(12):12451–12463. https://doi.org/10.1021/acsnano.5b05825
87. Yong Y, Zhou L, Gu Z, Yan L, Tian G, Zheng X, Liu X, Zhang X, Shi J, Cong W, Yin W, Zhao Y (2014) WS_2 nanosheet as a new photosensitizer carrier for combined photodynamic and photothermal therapy of cancer cells. Nanoscale 6(17):10394–10403. https://doi.org/10.1039/C4NR02453B
88. Wang J, Pang X, Tan X, Song Y, Liu L, You Q, Sun Q, Tan F, Li N (2017) A triple-synergistic strategy for combinational photo/radiotherapy and multi-modality imaging based on hyaluronic acid-hybridized polyaniline-coated WS_2 nanodots. Nanoscale 9(17):5551–5564. https://doi.org/10.1039/c6nr09219e
89. Liu Y, Ji X, Liu J, Tong WWL, Askhatova D, Shi J (2017) Tantalum sulfide nanosheets as a theranostic nanoplatform for computed tomography imaging-guided combinatorial chemo-photothermal therapy. Adv Funct Mater 27(39):1703261. https://doi.org/10.1002/adfm.201703261
90. Liu L, Wang J, Tan X, Pang X, You Q, Sun Q, Tan F, Li N (2017) Photosensitizer loaded PEG-MoS_2-Au hybrids for CT/NIRF imaging-guided stepwise photothermal and photodynamic therapy. J Mater Chem B 5(12):2286–2296. https://doi.org/10.1039/c6tb03352k
91. Xu J, Gulzar A, Liu Y, Bi H, Gai S, Liu B, Yang D, He F, Yang P (2017) Integration of IR-808 sensitized upconversion nanostructure and MoS_2 nanosheet for 808 nm NIR light triggered phototherapy and bioimaging. Small 13(36):1701841. https://doi.org/10.1002/smll.201701841
92. Yin W, Yan L, Yu J, Tian G, Zhou L, Zheng X, Zhang X, Yong Y, Li J, Gu Z, Zhao Y (2014) High-throughput synthesis of single-layer MoS_2 nanosheets as a near-infrared photothermal-triggered drug delivery for effective cancer therapy. ACS Nano 8(7):6922–6933. https://doi.org/10.1021/nn501647j

93. Mao B, Bao T, Yu J, Zheng L, Qin J, Yin W, Cao M (2017) One-pot synthesis of MoSe2 hetero-dimensional hybrid self-assembled by nanodots and nanosheets for electrocatalytic hydrogen evolution and photothermal therapy. Nano Res 10(8):2667–2682. https://doi.org/10.1007/s12274-017-1469-7
94. Jing X, Zhi Z, Wang D, Liu J, Shao Y, Meng L (2018) Multifunctional nanoflowers for simultaneous multimodal imaging and high-sensitivity chemo-photothermal treatment. Bioconjug Chem 29(2):559–570. https://doi.org/10.1021/acs.bioconjchem.8b00053
95. Tang S, Fu C, Tan L, Liu T, Mao J, Ren X, Su H, Long D, Chai Q, Huang Z, Chen X, Wang J, Ren J, Meng X (2017) Imaging-guided synergetic therapy of orthotopic transplantation tumor by superselectively arterial administration of microwave-induced microcapsules. Biomaterials 133:144–153. https://doi.org/10.1016/j.biomaterials.2017.04.027
96. Xie W, Gao Q, Wang D, Guo Z, Gao F, Wang X, Cai Q, S-s Feng, Fan H, Sun X, Zhao L (2018) Doxorubicin-loaded Fe_3O_4@MoS_2-PEG-2DG nanocubes as a theranostic platform for magnetic resonance imaging-guided chemo-photothermal therapy of breast cancer. Nano Res 11(5):2470–2487. https://doi.org/10.1007/s12274-017-1871-1
97. Yang G, Zhang R, Liang C, Zhao H, Yi X, Shen S, Yang K, Cheng L, Liu Z (2018) Manganese dioxide coated WS_2@Fe_3O_4/sSiO_2 nanocomposites for pH-responsive MR imaging and oxygen-elevated synergetic therapy. Small 14(2):1702664. https://doi.org/10.1002/smll.201702664
98. Anbazhagan R, Su YA, Tsai HC, Jeng RJ (2016) MoS_2-Gd chelate magnetic nanomaterials with core-shell structure used as contrast agents in in vivo magnetic resonance imaging. ACS Appl Mater Interfaces 8(3):1827–1835. https://doi.org/10.1021/acsami.5b09722
99. Dong X, Yin W, Zhang X, Zhu S, He X, Yu J, Xie J, Guo Z, Yan L, Liu X, Wang Q, Gu Z, Zhao Y (2018) Intelligent MoS_2 nanotheranostic for targeted and enzyme-/pH-/NIR-responsive drug delivery to overcome cancer chemotherapy resistance guided by PET imaging. ACS Appl Mater Interfaces 10(4):4271–4284. https://doi.org/10.1021/acsami.7b17506
100. Chao Y, Wang G, Liang C, Yi X, Zhong X, Liu J, Gao M, Yang K, Cheng L, Liu Z (2016) Rhenium-188 labeled tungsten disulfide nanoflakes for self-sensitized. Near-infrared enhanced radioisotope therapy. Small 12(29):3967–3975. https://doi.org/10.1002/smll.201601375
101. Cheng L, Kamkaew A, Shen S, Valdovinos HF, Sun H, Hernandez R, Goel S, Liu T, Thompson CR, Barnhart TE, Liu Z, Cai W (2016) Facile preparation of multifunctional WS_2/WO_x nanodots for chelator-free Zr-89-labeling and in vivo PET imaging. Small 12(41):5750–5758. https://doi.org/10.1002/smll.201601696
102. Wang SP, Tan LF, Liang P, Liu TL, Wang JZ, Fu CH, Yu J, Dou JP, Hong L, Meng XW (2016) Layered MoS_2 nanoflowers for microwave thermal therapy. J Mater Chem B 4(12):2133–2141. https://doi.org/10.1039/c6tb00296j
103. Liu T, Wang C, Gu X, Gong H, Cheng L, Shi X, Feng L, Sun B, Liu Z (2014) Drug delivery with PEGylated MoS_2 nano-sheets for combined photothermal and chemotherapy of cancer. Adv Mater 26(21):3433–3440. https://doi.org/10.1002/adma.201305256
104. Han Q, Wang X, Jia X, Cai S, Liang W, Qin Y, Yang R, Wang C (2017) CpG loaded MoS_2 nanosheets as multifunctional agents for photothermal enhanced cancer immunotherapy. Nanoscale 9(18):5927–5934. https://doi.org/10.1039/c7nr01460k
105. Wang C, Bai J, Liu YW, Jia XD, Jiang X (2016) Polydopamine coated selenide molybdenum: a new photothermal nanocarrier for highly effective chemo-photothermal synergistic therapy. ACS Biomater Sci Eng 2(11):2011–2017. https://doi.org/10.1021/acsbiomaterials.6b00416
106. Jia XD, Bai J, Ma ZF, Jiang XU (2017) BSA-exfoliated WSe_2 nanosheets as a photoregulated carrier for synergistic photodynamic/photothermal therapy. J Mater Chem B 5(2):269–278. https://doi.org/10.1039/c6tb02525k
107. Huang QL, Wang SR, Zhou J, Zhong XY, Huang YL (2018) Albumin-assisted exfoliated ultrathin rhenium disulfide nanosheets as a tumor targeting and dual-stimuli-responsive drug delivery system for a combination chemo-photothermal treatment. RSC Adv 8(9):4624–4633. https://doi.org/10.1039/c7ra13454a

108. Wust P, Hildebrandt B, Sreenivasa G, Rau B, Gellermann J, Riess H, Felix R, Schlag PM (2002) Hyperthermia in combined treatment of cancer. Lancet Oncol 3(8):487–497. https://doi.org/10.1016/s1470-2045(02)00818-5
109. Chou SS, Kaehr B, Kim J, Foley BM, De M, Hopkins PE, Huang J, Brinker CJ, Dravid VP (2013) Chemically exfoliated MoS_2 as near-infrared photothermal agents. Angew Chem Int Ed 52(15):4160–4164. https://doi.org/10.1002/anie.201209229
110. Robinson JT, Welsher K, Tabakman SM, Sherlock SP, Wang H, Luong R, Dai H (2010) High performance in vivo near-IR (>1 μm) imaging and photothermal cancer therapy with carbon nanotubes. Nano Res 3(11):779–793. https://doi.org/10.1007/s12274-010-0045-1
111. Wang S, Li K, Chen Y, Chen H, Ma M, Feng J, Zhao Q, Shi J (2015) Biocompatible PEGylated MoS_2 nanosheets: controllable bottom-up synthesis and highly efficient photothermal regression of tumor. Biomaterials 39:206–217. https://doi.org/10.1016/j.biomaterials.2014.11.009
112. Li M, Zhao AD, Dong K, Li W, Ren JS, Qu XG (2015) Chemically exfoliated WS_2 nanosheets efficiently inhibit amyloid beta-peptide aggregation and can be used for photothermal treatment of Alzheimer's disease. Nano Res 8(10):3216–3227. https://doi.org/10.1007/s12274-015-0821-z
113. Han Q, Cai S, Yang L, Wang X, Qi C, Yang R, Wang C (2017) Molybdenum disulfide nanoparticles as multifunctional inhibitors against Alzheimer's disease. ACS Appl Mater Interfaces 9(25):21116–21123. https://doi.org/10.1021/acsami.7b03816
114. Zhang H, Chen H-J, Du X, Wen D (2014) Photothermal conversion characteristics of gold nanoparticle dispersions. Sol Energy 100:141–147. https://doi.org/10.1016/j.solener.2013.12.004
115. Lin H, Gao S, Dai C, Chen Y, Shi J (2017) A two-dimensional biodegradable niobium carbide (MXene) for photothermal tumor eradication in NIR-I and NIR-II biowindows. J Am Chem Soc 139(45):16235–16247. https://doi.org/10.1021/jacs.7b07818
116. Lei Z, Zhu W, Xu S, Ding J, Wan J, Wu P (2016) Hydrophilic $MoSe_2$ nanosheets as effective photothermal therapy agents and their application in smart devices. ACS Appl Mater Interfaces 8(32):20900–20908. https://doi.org/10.1021/acsami.6b07326
117. Lin H, Wang Y, Gao S, Chen Y, Shi J (2018) Theranostic 2D tantalum carbide (MXene). Adv Mater 30(4):1703284. https://doi.org/10.1002/adma.201703284
118. Sun Z, Xie H, Tang S, Yu XF, Guo Z, Shao J, Zhang H, Huang H, Wang H, Chu PK (2015) Ultrasmall black phosphorus quantum dots: synthesis and use as photothermal agents. Angew Chem Int Ed 54(39):11526–11530. https://doi.org/10.1002/anie.201506154
119. Hessel CM, Pattani VP, Rasch M, Panthani MG, Koo B, Tunnell JW, Korgel BA (2011) Copper selenide nanocrystals for photothermal therapy. Nano Lett 11(6):2560–2566. https://doi.org/10.1021/nl201400z
120. Zeng J, Goldfeld D, Xia Y (2013) A plasmon-assisted optofluidic (PAOF) system for measuring the photothermal conversion efficiencies of gold nanostructures and controlling an electrical switch. Angew Chem Int Ed 52(15):4169–4173. https://doi.org/10.1002/anie.201210359
121. Wang B, Wang JH, Liu Q, Huang H, Chen M, Li K, Li C, Yu XF, Chu PK (2014) Rose-bengal-conjugated gold nanorods for in vivo photodynamic and photothermal oral cancer therapies. Biomaterials 35(6):1954–1966. https://doi.org/10.1016/j.biomaterials.2013.11.066
122. Feng W, Chen L, Qin M, Zhou X, Zhang Q, Miao Y, Qiu K, Zhang Y, He C (2015) Flower-like PEGylated MoS_2 nanoflakes for near-infrared photothermal cancer therapy. Sci Rep 5:17422. https://doi.org/10.1038/srep17422
123. Huang Z, Qi Y, Yu D, Zhan J (2016) Radar-like MoS_2 nanoparticles as a highly efficient 808 nm laser-induced photothermal agent for cancer therapy. RSC Adv 6(37):31031–31036. https://doi.org/10.1039/C6RA03226E
124. Li X, Gong Y, Zhou XQ, Jin H, Yan HH, Wang SG, Liu J (2016) Facile synthesis of soybean phospholipid-encapsulated MoS_2 nanosheets for efficient in vitro and in vivo photothermal regression of breast tumor. Int J Nanomed 11:1819–1833. https://doi.org/10.2147/ijn.s104198

125. Tan LF, Wang SP, Xu K, Liu TL, Liang P, Niu M, Fu CH, Shao HB, Yu J, Ma TC, Ren XL, Li H, Dou JP, Ren J, Meng XW (2016) Layered MoS_2 hollow spheres for highly-efficient photothermal therapy of rabbit liver orthotopic transplantation tumors. Small 12(15):2046–2055. https://doi.org/10.1002/smll.201600191
126. Ariyasu S, Mu J, Zhang X, Huang Y, Yeow EKL, Zhang H, Xing B (2017) Investigation of thermally induced cellular ablation and heat response triggered by planar MoS_2-based nanocomposite. Bioconjug Chem 28(4):1059–1067. https://doi.org/10.1021/acs.bioconjchem.6b00741
127. Chen L, Feng Y, Zhou X, Zhang Q, Nie W, Wang W, Zhang Y, He C (2017) One-pot synthesis of MoS_2 nanoflakes with desirable degradability for photothermal cancer therapy. ACS Appl Mater Interfaces 9(20):17347–17358. https://doi.org/10.1021/acsami.7b02657
128. Huang B, Wang D, Wang G, Zhang F, Zhou L (2017) Enhancing the colloidal stability and surface functionality of molybdenum disulfide (MoS_2) nanosheets with hyperbranched polyglycerol for photothermal therapy. J Colloid Interface Sci 508:214–221. https://doi.org/10.1016/j.jcis.2017.08.062
129. Li Z, Yang Y, Yao J, Shao Z, Chen X (2017) A facile fabrication of silk/MoS_2 hybrids for photothermal therapy. Mater Sci Eng C Mater Biol Appl 79:123–129. https://doi.org/10.1016/j.msec.2017.05.010
130. Park CH, Yun H, Yang H, Lee J, Kim BJ (2017) Fluorescent block copolymer-MoS_2 nanocomposites for real-time photothermal heating and imaging. Adv Funct Mater 27(5):1604403. https://doi.org/10.1002/adfm.201604403
131. Zhang Y, Xiu W, Sun Y, Zhu D, Zhang Q, Yuwen L, Weng L, Teng Z, Wang L (2017) RGD-QD-MoS_2 nanosheets for targeted fluorescent imaging and photothermal therapy of cancer. Nanoscale 9(41):15835–15845. https://doi.org/10.1039/c7nr05278b
132. Zhang YB, Jia GZ, Wang P, Zhang Q, Wei XY, Dong EM, Yao JH (2017) Size effect on near infrared photothermal conversion properties of liquid-exfoliated MoS_2 and MoSe2. Superlattices Microstruct 105:22–27. https://doi.org/10.1016/j.spmi.2016.11.058
133. Park CH, Lee S, Pornnoppadol G, Nam YS, Kim SH, Kim BJ (2018) Microcapsules containing pH-responsive, fluorescent polymer-integrated MoS_2: an effective platform for in situ pH sensing and photothermal heating. ACS Appl Mater Interfaces 10(10):9023–9031. https://doi.org/10.1021/acsami.7b19468
134. Liu Q, Sun C, He Q, Khalil A, Xiang T, Liu D, Zhou Y, Wang J, Song L (2015) Stable metallic 1T-WS_2 ultrathin nanosheets as a promising agent for near-infrared photothermal ablation cancer therapy. Nano Res 8(12):3982–3991. https://doi.org/10.1007/s12274-015-0901-0
135. Macharia DK, Yu N, Zhong R, Xiao Z, Yang J, Chen Z (2016) Synthesis of WS_2 nanowires as efficient 808 nm-laser-driven photothermal nanoagents. J Nanosci Nanotechnol 16(6):5865–5868. https://doi.org/10.1166/jnn.2016.11747
136. Nandi S, Bhunia SK, Zeiri L, Pour M, Nachman I, Raichman D, Lellouche JM, Jelinek R (2017) Bifunctional carbon-dot-WS_2 nanorods for photothermal therapy and cell imaging. Chem Eur J 23(4):963–969. https://doi.org/10.1002/chem.201604787
137. Yuwen LH, Zhou JJ, Zhang YQ, Zhang Q, Shan JY, Luo ZM, Weng LX, Teng ZG, Wang LH (2016) Aqueous phase preparation of ultrasmall $MoSe_2$ nanodots for efficient photothermal therapy of cancer cells. Nanoscale 8(5):2720–2726. https://doi.org/10.1039/c5nr08166a
138. Zhong CL, Zhao X, Wang LJ, Li YX, Zhao YY (2017) Facile synthesis of biocompatible $MoSe_2$ nanoparticles for efficient targeted photothermal therapy of human lung cancer. RSC Adv 7(12):7382–7391. https://doi.org/10.1039/c6ra27384j
139. Zhu Z, Zou Y, Hu W, Li Y, Gu Y, Cao B, Guo N, Wang L, Song J, Zhang S, Gu H, Zeng H (2016) Near-infrared plasmonic 2D semimetals for applications in communication and biology. Adv Funct Mater 26(11):1793–1802. https://doi.org/10.1002/adfm.201504884
140. Ren QL, Li B, Peng ZY, He GJ, Zhang WL, Guan GQ, Huang XJ, Xiao ZY, Liao LJ, Pan YS, Yang XJ, Zou RJ, Hu JQ (2016) SnS nanosheets for efficient photothermal therapy. New J Chem 40(5):4464–4467. https://doi.org/10.1039/c5nj03263f
141. Ma N, Zhang M-K, Wang X-S, Zhang L, Feng J, Zhang X-Z (2018) NIR light-triggered degradable $MoTe_2$ nanosheets for combined photothermal and chemotherapy of cancer. Adv Funct Mater:1801139. https://doi.org/10.1002/adfm.201801139

142. Lin H, Wang X, Yu L, Chen Y, Shi J (2017) Two-dimensional ultrathin MXene ceramic nanosheets for photothermal conversion. Nano Lett 17(1):384–391. https://doi.org/10.1021/acs.nanolett.6b04339
143. Xie H, Li Z, Sun Z, Shao J, Yu XF, Guo Z, Wang J, Xiao Q, Wang H, Wang QQ, Zhang H, Chu PK (2016) Metabolizable ultrathin bi2se3 nanosheets in imaging-guided photothermal therapy. Small 12(30):4136–4145. https://doi.org/10.1002/smll.201601050
144. Robinson JT, Tabakman SM, Liang Y, Wang H, Casalongue HS, Vinh D, Dai H (2011) Ultrasmall reduced graphene oxide with high near-infrared absorbance for photothermal therapy. J Am Chem Soc 133(17):6825–6831. https://doi.org/10.1021/ja2010175
145. Xia C, Wang H, Jiao F, Gao F, Wu Q, Shen Y, Zhang Y, Qian X (2018) Rational synthesis of MoS_2-based immobilized trypsin for rapid and effective protein digestion. Talanta 179:393–400. https://doi.org/10.1016/j.talanta.2017.11.027
146. Bettaieb A, Wrzal PK, Averill-Bates DA (2013) Hyperthermia: cancer treatment and beyond. In: Cancer treatment—conventional and innovative approaches. https://doi.org/10.5772/55795
147. Day ES, Morton JG, West JL (2009) Nanoparticles for thermal cancer therapy. J Biomech Eng 131(7):074001–074005. https://doi.org/10.1115/1.3156800
148. Weissleder R (2001) A clearer vision for in vivo imaging. Nat Biotechnol 19(4):316–317. https://doi.org/10.1038/86684
149. Yun SH, Kwok SJJ (2017) Light in diagnosis, therapy and surgery. Nat Biomed Eng 1(1):0008. https://doi.org/10.1038/s41551-016-0008
150. Qian GJ, Wang N, Shen Q, Sheng YH, Zhao JQ, Kuang M, Liu GJ, Wu MC (2012) Efficacy of microwave versus radiofrequency ablation for treatment of small hepatocellular carcinoma: experimental and clinical studies. Eur Radiol 22(9):1983–1990. https://doi.org/10.1007/s00330-012-2442-1
151. Fu C, He F, Tan L, Ren X, Zhang W, Liu T, Wang J, Ren J, Chen X, Meng X (2017) MoS_2 nanosheets encapsulated in sodium alginate microcapsules as microwave embolization agents for large orthotopic transplantation tumor therapy. Nanoscale 9(39):14846–14853. https://doi.org/10.1039/c7nr04274d
152. Agostinis P, Berg K, Cengel KA, Foster TH, Girotti AW, Gollnick SO, Hahn SM, Hamblin MR, Juzeniene A, Kessel D, Korbelik M, Moan J, Mroz P, Nowis D, Piette J, Wilson BC, Golab J (2011) Photodynamic therapy of cancer: an update. CA Cancer J Clin 61(4):250–281. https://doi.org/10.3322/caac.20114
153. Ji DK, Zhang Y, Zang Y, Li J, Chen GR, He XP, Tian H (2016) Targeted intracellular production of reactive oxygen species by a 2D molybdenum disulfide glycosheet. Adv Mater 28(42):9356–9363. https://doi.org/10.1002/adma.201602748
154. Dong H, Tang S, Hao Y, Yu H, Dai W, Zhao G, Cao Y, Lu H, Zhang X, Ju H (2016) Fluorescent MoS_2 quantum dots: ultrasonic preparation, up-conversion and down-conversion bioimaging, and photodynamic therapy. ACS Appl Mater Interfaces 8(5):3107–3114. https://doi.org/10.1021/acsami.5b10459
155. Peng MY, Zheng DW, Wang SB, Cheng SX, Zhang XZ (2017) Multifunctional nanosystem for synergistic tumor therapy delivered by two-dimensional MoS_2. ACS Appl Mater Interfaces 9(16):13965–13975. https://doi.org/10.1021/acsami.7b03276
156. Jia L, Ding L, Tian J, Bao L, Hu Y, Ju H, Yu JS (2015) Aptamer loaded MoS_2 nanoplates as nanoprobes for detection of intracellular ATP and controllable photodynamic therapy. Nanoscale 7(38):15953–15961. https://doi.org/10.1039/c5nr02224j
157. Han J, Xia H, Wu Y, Kong SN, Deivasigamani A, Xu R, Hui KM, Kang Y (2016) Single-layer MoS_2 nanosheet grafted upconversion nanoparticles for near-infrared fluorescence imaging-guided deep tissue cancer phototherapy. Nanoscale 8(15):7861–7865. https://doi.org/10.1039/c6nr00150e
158. Chen L, Feng W, Zhou X, Qiu K, Miao Y, Zhang Q, Qin M, Li L, Zhang Y, He C (2016) Facile synthesis of novel albumin-functionalized flower-like MoS_2 nanoparticles for in vitro chemo-photothermal synergistic therapy. RSC Adv 6(16):13040–13049. https://doi.org/10.1039/C5RA27822H

159. Deng R, Yi H, Fan FY, Fu L, Zeng Y, Wang Y, Li YC, Liu YL, Ji SJ, Su Y (2016) Facile exfoliation of MoS_2 nanosheets by protein as a photothermal-triggered drug delivery system for synergistic tumor therapy. RSC Adv 6(80):77083–77092. https://doi.org/10.1039/c6ra13993k
160. Shao T, Wen J, Zhang Q, Zhou Y, Liu L, Yuwen L, Tian Y, Zhang Y, Tian W, Su Y, Teng Z, Lu G, Xu J (2016) NIR photoresponsive drug delivery and synergistic chemo-photothermal therapy by monodispersed-MoS_2-nanosheets wrapped periodic mesoporous organosilicas. J Mater Chem B 4(47):7708–7717. https://doi.org/10.1039/c6tb02724e
161. Lei Q, Wang SB, Hu JJ, Lin YX, Zhu CH, Rong L, Zhang XZ (2017) Stimuli-Responsive "Cluster Bomb" for Programmed Tumor Therapy. ACS Nano 11(7):7201–7214. https://doi.org/10.1021/acsnano.7b03088
162. Wang KW, Chen QQ, Xue W, Li S, Liu ZH (2017) Combined chemo-photothermal antitumor therapy using molybdenum disulfide modified with hyperbranched polyglycidyl. ACS Biomater Sci Eng 3(10):2325–2335. https://doi.org/10.1021/acsbiomaterials.7b00499
163. Liao W, Zhang L, Zhong Y, Shen Y, Li C, An N (2018) Fabrication of ultrasmall WS_2 quantum dots-coated periodic mesoporous organosilica nanoparticles for intracellular drug delivery and synergistic chemo-photothermal therapy. Onco Targets Ther 11:1949–1960. https://doi.org/10.2147/OTT.S160748
164. Wang S, Chen Y, Li X, Gao W, Zhang L, Liu J, Zheng Y, Chen H, Shi J (2015) Injectable 2D MoS_2-integrated drug delivering implant for highly efficient NIR-triggered synergistic tumor hyperthermia. Adv Mater 27(44):7117–7122. https://doi.org/10.1002/adma.201503869
165. Zhang A, Li A, Tian W, Li Z, Wei C, Sun Y, Zhao W, Liu M, Liu J (2017) A target-directed chemo-photothermal system based on transferrin and copolymer-modified MoS_2 nanoplates with pH-activated drug release. Chem Eur J 23(47):11346–11356. https://doi.org/10.1002/chem.201701916
166. Zhao W, Li AH, Chen C, Quan FY, Sun L, Zhang AT, Zheng YW, Liu JQ (2017) Transferrin-decorated, MoS_2-capped hollow mesoporous silica nanospheres as a self-guided chemo-photothermal nanoplatform for controlled drug release and thermotherapy. J Mater Chem B 5(35):7403–7414. https://doi.org/10.1039/c7tb01648d
167. Zhang A, Li A, Zhao W, Yan G, Liu B, Liu M, Li M, Huo B, Liu J (2018) An efficient and self-guided chemo-photothermal drug loading system based on copolymer and transferrin decorated MoS_2 nanodots for dually controlled drug release. Chem Eng J 342:120–132. https://doi.org/10.1016/j.cej.2018.02.081
168. Mellman I, Coukos G, Dranoff G (2011) Cancer immunotherapy comes of age. Nature 480(7378):480–489. https://doi.org/10.1038/nature10673
169. Song W, Musetti SN, Huang L (2017) Nanomaterials for cancer immunotherapy. Biomaterials 148:16–30. https://doi.org/10.1016/j.biomaterials.2017.09.017
170. Wang ZJ, Liu WH, Shi JY, Chen N, Fan CH (2018) Nanoscale delivery systems for cancer immunotherapy. Mater Horiz 5(3):344–362. https://doi.org/10.1039/c7mh00991g
171. Ge R, Liu C, Zhang X, Wang W, Li B, Liu J, Liu Y, Sun H, Zhang D, Hou Y, Zhang H, Yang B (2018) Photothermal-activatable Fe_3O_4 superparticle nanodrug carriers with PD-L1 immune checkpoint blockade for anti-metastatic cancer immunotherapy. ACS Appl Mater Interfaces 10(24):20342–20355. https://doi.org/10.1021/acsami.8b05876
172. Lu K, He C, Guo N, Chan C, Ni K, Weichselbaum RR, Lin W (2016) Chlorin-based nanoscale metal-organic framework systemically rejects colorectal cancers via synergistic photodynamic therapy and checkpoint blockade immunotherapy. J Am Chem Soc 138(38):12502–12510. https://doi.org/10.1021/jacs.6b06663
173. Ni K, Lan G, Chan C, Quigley B, Lu K, Aung T, Guo N, La Riviere P, Weichselbaum RR, Lin W (2018) Nanoscale metal-organic frameworks enhance radiotherapy to potentiate checkpoint blockade immunotherapy. Nat Commun 9(1):2351. https://doi.org/10.1038/s41467-018-04703-w
174. Lan G, Ni K, Xu Z, Veroneau SS, Song Y, Lin W (2018) Nanoscale metal-organic framework overcomes hypoxia for photodynamic therapy primed cancer immunotherapy. J Am Chem Soc 140(17):5670–5673. https://doi.org/10.1021/jacs.8b01072

175. He C, Duan X, Guo N, Chan C, Poon C, Weichselbaum RR, Lin W (2016) Core-shell nanoscale coordination polymers combine chemotherapy and photodynamic therapy to potentiate checkpoint blockade cancer immunotherapy. Nat Commun 7:12499. https://doi.org/10.1038/ncomms12499
176. Noh YW, Kim SY, Kim JE, Kim S, Ryu J, Kim I, Lee E, Um SH, Lim YT (2017) Multifaceted immunomodulatory nanoliposomes: reshaping tumors into vaccines for enhanced cancer immunotherapy. Adv Funct Mater 27(8):1605398. https://doi.org/10.1002/adfm.201605398
177. Zhu G, Liu Y, Yang X, Kim YH, Zhang H, Jia R, Liao HS, Jin A, Lin J, Aronova M, Leapman R, Nie Z, Niu G, Chen X (2016) DNA-inorganic hybrid nanovaccine for cancer immunotherapy. Nanoscale 8(12):6684–6692. https://doi.org/10.1039/c5nr08821f
178. Pardo M, Shuster-Meiseles T, Levin-Zaidman S, Rudich A, Rudich Y (2014) Low cytotoxicity of inorganic nanotubes and fullerene-like nanostructures in human bronchial epithelial cells: relation to inflammatory gene induction and antioxidant response. Environ Sci Technol 48(6):3457–3466. https://doi.org/10.1021/es500065z
179. Rajendrakumar SK, Uthaman S, Cho CS, Park IK (2018) Nanoparticle-based phototriggered cancer immunotherapy and its domino effect in the tumor microenvironment. Biomacromol 19(6):1869–1887. https://doi.org/10.1021/acs.biomac.8b00460
180. Wang H, Mu X, He H, Zhang XD (2018) Cancer radiosensitizers. Trends Pharmacol Sci 39(1):24–48. https://doi.org/10.1016/j.tips.2017.11.003
181. Zhu S, Gu Z, Zhao Y (2018) Harnessing tumor microenvironment for nanoparticle-mediated radiotherapy. Adv Therap 0(0):1800050. https://doi.org/10.1002/adtp.201800050
182. Xie J, Wang N, Dong X, Wang C, Du Z, Mei L, Yong Y, Huang C, Li Y, Gu Z, Zhao Y (2018) Graphdiyne nanoparticles with high free radical scavenging activity for radiation protection. ACS Appl Mater Interfaces. https://doi.org/10.1021/acsami.8b00949
183. Xie J, Wang C, Zhao F, Gu Z, Zhao Y (2018) Application of multifunctional nanomaterials in radioprotection of healthy tissues. Adv Healthc Mater 0(0):1800421. https://doi.org/10.1002/adhm.201800421
184. Hall EJ, Giaccia AJ (2012) Radiobiology for the radiologist. Wolters Kluwer Health
185. Kouvaris JR, Kouloulias VE, Vlahos LJ (2007) Amifostine: the first selective-target and broad-spectrum radioprotector. Oncologist 12(6):738–747. https://doi.org/10.1634/theoncologist.12-6-738
186. Grdina DJ, Murley JS, Kataoka Y (2002) Radioprotectants: current status and new directions. Oncology 63(Suppl. 2):2–10. https://doi.org/10.1159/000067146
187. Tarnuzzer RW, Colon J, Patil S, Seal S (2005) Vacancy engineered ceria nanostructures for protection from radiation-induced cellular damage. Nano Lett 5(12):2573–2577. https://doi.org/10.1021/nl052024f
188. Colon J, Hsieh N, Ferguson A, Kupelian P, Seal S, Jenkins DW, Baker CH (2010) Cerium oxide nanoparticles protect gastrointestinal epithelium from radiation-induced damage by reduction of reactive oxygen species and upregulation of superoxide dismutase 2. Nanomed Nanotechnol Biol Med 6(5):698–705. https://doi.org/10.1016/j.nano.2010.01.010
189. Xue Y, Luan Q, Yang D, Yao X, Zhou K (2011) Direct evidence for hydroxyl radical scavenging activity of cerium oxide nanoparticles. J Phys Chem C 115(11):4433–4438. https://doi.org/10.1021/jp109819u
190. Li H, Yang ZY, Liu C, Zeng YP, Hao YH, Gu Y, Wang WD, Li R (2015) PEGylated ceria nanoparticles used for radioprotection on human liver cells under gamma-ray irradiation. Free Radic Biol Med 87:26–35. https://doi.org/10.1016/j.freeradbiomed.2015.06.010
191. Xie J, Yong Y, Dong X, Du J, Guo Z, Gong L, Zhu S, Tian G, Yu S, Gu Z, Zhao Y (2017) Therapeutic nanoparticles based on curcumin and bamboo charcoal nanoparticles for chemo-photothermal synergistic treatment of cancer and radioprotection of normal cells. ACS Appl Mater Interfaces 9(16):14281–14291. https://doi.org/10.1021/acsami.7b02622
192. Cirillo G, Hampel S, Klingeler R, Puoci F, Iemma F, Curcio M, Parisi Ortensia I, Spizzirri Umile G, Picci N, Leonhardt A, Ritschel M, Büchner B (2010) Antioxidant multi-walled carbon nanotubes by free radical grafting of gallic acid: new materials for biomedical applications. J Pharm Pharmacol 63(2):179–188. https://doi.org/10.1111/j.2042-7158.2010.01211.x

193. Qiu Y, Wang Z, Owens ACE, Kulaots I, Chen Y, Kane AB, Hurt RH (2014) Antioxidant chemistry of graphene-based materials and its role in oxidation protection technology. Nanoscale 6(20):11744–11755. https://doi.org/10.1039/C4NR03275F
194. Yim D, Kim JE, Kim HI, Yang JK, Kang TW, Nam J, Han SH, Jun B, Lee CH, Lee SU, Kim JW, Kim JH (2018) Adjustable intermolecular interactions allowing 2D transition metal dichalcogenides with prolonged scavenging activity for reactive oxygen species. Small 14(16):1800026. https://doi.org/10.1002/smll.201800026
195. Zhang XD, Zhang J, Wang J, Yang J, Chen J, Shen X, Deng J, Deng D, Long W, Sun YM, Liu C, Li M (2016) Highly catalytic nanodots with renal clearance for radiation protection. ACS Nano 10(4):4511–4519. https://doi.org/10.1021/acsnano.6b00321
196. Bai XT, Wang JY, Mu XY, Yang J, Liu HX, Xu FJ, Jing YQ, Liu LF, Xue XH, Dai HT, Liu Q, Sun YM, Liu CL, Zhang XD (2017) Ultrasmall WS_2 quantum dots with visible fluorescence for protection of cells and animal models from radiation-induced damages. ACS Biomater Sci Eng 3(3):460–470. https://doi.org/10.1021/acsbiomaterials.6b00714
197. Liu HX, Wang JY, Jing YQ, Yang J, Bai XT, Mu XY, Xu FJ, Xue XH, Liu LF, Sun YM, Liu Q, Dai HT, Liu CL, Zhang XD (2017) Renal clearable luminescent WSe_2 for radioprotection of nontargeted tissues during radiotherapy. Part Part Syst Charact 34(6):1700035. https://doi.org/10.1002/ppsc.201700035
198. Radioprotection: taking the Toll Road (2008). Science 320 (5873):151–151. https://doi.org/10.1126/science.320.5873.151g
199. Fan W, Yung B, Huang P, Chen X (2017) Nanotechnology for multimodal synergistic cancer therapy. Chem Rev 117(22):13566–13638. https://doi.org/10.1021/acs.chemrev.7b00258
200. Zhang L, Webster TJ (2009) Nanotechnology and nanomaterials: Promises for improved tissue regeneration. Nano Today 4(1):66–80. https://doi.org/10.1016/j.nantod.2008.10.014
201. Lalwani G, Henslee AM, Farshid B, Parmar P, Lin L, Qin YX, Kasper FK, Mikos AG, Sitharaman B (2013) Tungsten disulfide nanotubes reinforced biodegradable polymers for bone tissue engineering. Acta Biomater 9(9):8365–8373. https://doi.org/10.1016/j.actbio.2013.05.018
202. Jaiswal MK, Carrow JK, Gentry JL, Gupta J, Altangerel N, Scully M, Gaharwar AK (2017) Vacancy-driven gelation using defect-rich nanoassemblies of 2D transition metal dichalcogenides and polymeric binder for biomedical applications. Adv Mater 29(36):1702037. https://doi.org/10.1002/adma.201702037
203. Wu S, Wang J, Jin L, Li Y, Wang Z (2018) Effects of polyacrylonitrile/MoS_2 composite nanofibers on the growth behavior of bone marrow mesenchymal stem cells. ACS Appl Nano Mater 1(1):337–343. https://doi.org/10.1021/acsanm.7b00188
204. Hussey GS, Dziki JL, Badylak SF (2018) Extracellular matrix-based materials for regenerative medicine. Nat Rev Mater 3(7):159–173. https://doi.org/10.1038/s41578-018-0023-x
205. Jiang B, Duan D, Gao L, Zhou M, Fan K, Tang Y, Xi J, Bi Y, Tong Z, Gao GF, Xie N, Tang A, Nie G, Liang M, Yan X (2018) Standardized assays for determining the catalytic activity and kinetics of peroxidase-like nanozymes. Nat Protoc 13(7):1506–1520. https://doi.org/10.1038/s41596-018-0001-1
206. Zhu X, Ji X, Kong N, Chen Y, Mahmoudi M, Xu X, Ding L, Tao W, Cai T, Li Y, Gan T, Barrett A, Bharwani Z, Chen H, Farokhzad OC (2018) Intracellular mechanistic understanding of 2D MoS_2 nanosheets for anti-exocytosis-enhanced synergistic cancer therapy. ACS Nano 12(3):2922–2938. https://doi.org/10.1021/acsnano.8b00516
207. Yan L, Zhao YL, Gu ZJ (2016) Nanotoxicity of near infrared nanomaterials. In: Near-infrared nanomaterials: preparation, bioimaging and therapy applications. The Royal Society of Chemistry, pp 355–402. (Chapter 11). https://doi.org/10.1039/9781782623939-00355
208. Ling Y, Gu Z, S-g Kang, Luo J, Zhou R (2016) Structural damage of a β-sheet protein upon adsorption onto molybdenum disulfide nanotubes. J Phys Chem C 120(12):6796–6803. https://doi.org/10.1021/acs.jpcc.5b11236
209. Gu Z, Yang Z, Kang SG, Yang JR, Luo J, Zhou R (2016) Robust denaturation of villin headpiece by MoS_2 nanosheet: potential molecular origin of the nanotoxicity. Sci Rep 6:28252. https://doi.org/10.1038/srep28252

210. Gu Z, Plant LD, Meng X-Y, Perez-Aguilar JM, Wang Z, Dong M, Logothetis DE, Zhou R (2018) Exploring the nanotoxicology of MoS_2: a study on the interaction of mos2 nanoflakes and K^+ channels. ACS Nano 12(1):705–717. https://doi.org/10.1021/acsnano.7b07871
211. Zou W, Zhang X, Zhao M, Zhou Q, Hu X (2017) Cellular proliferation and differentiation induced by single-layer molybdenum disulfide and mediation mechanisms of proteins via the Akt-mTOR-p70S6K signaling pathway. Nanotoxicology 11(6):781–793. https://doi.org/10.1080/17435390.2017.1357213
212. Kenry Lim CT (2017) Biocompatibility and nanotoxicity of layered two-dimensional nanomaterials. Chemnanomat 3(1):5–16. https://doi.org/10.1002/cnma.201600290
213. Wei Y, Quan L, Zhou C, Zhan Q (2018) Factors relating to the biodistribution & clearance of nanoparticles & their effects on in vivo application. Nanomedicine (Lond) 13(12):1495–1512. https://doi.org/10.2217/nnm-2018-0040
214. Chng EL, Sofer Z, Pumera M (2014) MoS_2 exhibits stronger toxicity with increased exfoliation. Nanoscale 6(23):14412–14418. https://doi.org/10.1039/c4nr04907a
215. Wang X, Mansukhani ND, Guiney LM, Ji Z, Chang CH, Wang M, Liao YP, Song TB, Sun B, Li R, Xia T, Hersam MC, Nel AE (2015) Differences in the toxicological potential of 2D versus aggregated molybdenum disulfide in the lung. Small 11(38):5079–5087. https://doi.org/10.1002/smll.201500906
216. Latiff NM, Sofer Z, Fisher AC, Pumera M (2017) Cytotoxicity of exfoliated layered vanadium dichalcogenides. Chem Eur J 23(3):684–690. https://doi.org/10.1002/chem.201604430
217. Appel JH, Li DO, Podlevsky JD, Debnath A, Green AA, Wang QH, Chae J (2016) Low cytotoxicity and genotoxicity of two-dimensional MoS_2 and WS_2. ACS Biomater Sci Eng 2(3):361–367. https://doi.org/10.1021/acsbiomaterials.5b00467
218. Rosli NF, Latiff NM, Sofer Z, Fisher AC, Pumera M (2018) In vitro cytotoxicity of covalently protected layered molybdenum disulfide. Appl Mater Today 11:200–206. https://doi.org/10.1016/j.apmt.2018.02.001
219. Moore C, Movia D, Smith RJ, Hanlon D, Lebre F, Lavelle EC, Byrne HJ, Coleman JN, Volkov Y, McIntyre J (2017) Industrial grade 2D molybdenum disulphide (MoS_2): an in vitro exploration of the impact on cellular uptake, cytotoxicity, and inflammation. 2d Mater 4(2):025065. https://doi.org/10.1088/2053-1583/aa673f
220. Goldman EB, Zak A, Tenne R, Kartvelishvily E, Levin-Zaidman S, Neumann Y, Stiubea-Cohen R, Palmon A, Hovav AH, Aframian DJ (2015) Biocompatibility of tungsten disulfide inorganic nanotubes and fullerene-like nanoparticles with salivary gland cells. Tissue Eng Part A 21(5–6):1013–1023. https://doi.org/10.1089/ten.TEA.2014.0163
221. Wu X, Tian X, Chen T, Zeng A, Yang G (2018) Inorganic fullerene-like molybdenum selenide with good biocompatibility synthesized by laser ablation in liquids. Nanotechnology 29(29):295604. https://doi.org/10.1088/1361-6528/aac1b1
222. Teo Wei Z, Chng Elaine Lay K, Sofer Z, Pumera M (2014) Cytotoxicity of exfoliated transition-metal dichalcogenides (MoS_2, WS_2, and WSe_2) is lower than that of graphene and its analogues. Chem Eur J 20(31):9627–9632. https://doi.org/10.1002/chem.201402680
223. Chng ELK, Pumera M (2015) Toxicity of graphene related materials and transition metal dichalcogenides. RSC Adv 5(4):3074–3080. https://doi.org/10.1039/c4ra12624f
224. Latiff N, Teo WZ, Sofer Z, Huber S, Fisher AC, Pumera M (2015) Toxicity of layered semiconductor chalcogenides: beware of interferences. RSC Adv 5(83):67485–67492. https://doi.org/10.1039/c5ra09404f
225. Latiff NM, Teo WZ, Sofer Z, Fisher AC, Pumera M (2015) The cytotoxicity of layered black phosphorus. Chem Eur J 21(40):13991–13995. https://doi.org/10.1002/chem.201502006
226. Chia HL, Latiff NM, Sofer Z, Pumera M (2018) Cytotoxicity of group 5 transition metal ditellurides (MTe_2; M = V, Nb, Ta). Chem Eur J 24(1):206–211. https://doi.org/10.1002/chem.201704316
227. Rosli NF, Mayorga-Martinez CC, Latiff NM, Rohaizad N, Sofer Z, Fisher AC, Pumera M (2018) Layered $PtTe_2$ matches electrocatalytic performance of Pt/C for oxygen reduction reaction with significantly lower toxicity. ACS Sustain Chem Eng 6(6):7432–7441. https://doi.org/10.1021/acssuschemeng.7b04920

228. Yu Y, Yi Y, Li Y, Peng T, Lao S, Zhang J, Liang S, Xiong Y, Shao S, Wu N, Zhao Y, Huang H (2018) Dispersible MoS_2 micro-sheets induced a proinflammatory response and apoptosis in the gills and liver of adult zebrafish. RSC Adv 8(32):17826–17836. https://doi.org/10.1039/c8ra00922h
229. Hao J, Song G, Liu T, Yi X, Yang K, Cheng L, Liu Z (2017) In vivo long-term biodistribution, excretion, and toxicology of pegylated transition-metal dichalcogenides MS_2 (M = Mo, W, Ti) nanosheets. Adv Sci 4(1):1600160. https://doi.org/10.1002/advs.201600160

Linji Gong received his Bachelor's degree in chemistry from Nanchang University in China in 2015. He is currently a graduate student under the supervision of Prof. Yuliang Zhao and Prof. Zhanjun Gu at CAS key Laboratory for Biomedical Effects of Nanomaterials and Nanosafety, Institute of High Energy Physics, Chinese Academy of Sciences. He is now studying the synthesis of nanomaterials and exploring their biosafety and biomedical applications.

Zhanjun Gu received his B.E. degree (2002) from Huazhong University of Science and Technology and his Ph.D. degree (2007) from the Institute of Chemistry, Chinese Academy of Science, under the direction of Prof. Jiannian Yao. He then became a Postdoctoral Fellow at the University of Georgia. In 2009, he joined the faculty at CAS Key Lab for Biomedical Effects of Nanomaterials and Nanosafety, Institute of High Energy Physics, Chinese Academy of Science. His current research interests include nanomaterials synthesis, optical spectroscopy, and bioapplications of nanomaterials.

Chapter 9
Transition Metal Dichalcogenides in Sensors

Rajeswari Ponnusamy and Chandra Sekhar Rout

Abstract Transition metal dichalcogenides (TMDs), an emerging 2D analogy of graphene, with their captivating physiochemical properties find applications in advanced point-of-care diagnosis of various health-related issues. Specially, multidimensional structures of TMDs and its structure-dependent electronic, optical and electrocatalytic properties are apt for the design of different types (electrochemical, photoluminescence and colorimetric) of biosensing devices. Henceforth, this chapter outlines the biosensing applications of TMDs and its recent developments. Introduction part of this chapter will give a brief knowledge about the principle mechanisms of the different sensing methods followed by the importance of TMDs. Second p art, particularly concerned to address the recent advances in the different TMDs-based biosensors for the detection of diverse analytes. Present challenges preceded by the suggestions of its amelioration for day-to-day life clinical applications and opportunities are proposed at the end.

9.1 Introduction

Advanced personalized health care utilizes modern tools and techniques to detect and diagnose various diseases by the introduction of nanotechnology in biosensors. Simplicity, cost-effectiveness and rapid response of biosensors make it as a powerful tool in the detection of biological analytes such as small molecules, nucleic acid and proteins, and heavy metal ions. Analyte molecules are extracted from the biological systems and used as a biomarker for particular disease. Since the analytes are available in (less than micromolar) low concentrations, selection of sensing material is a matter of utmost importance for better signal amplification. Hitherto, different nanostructures of metal oxides [1–3], metal nanoparticles [4, 5], carbon-based materials [6] and its hybrids were studied as biosensors. Carbon-based nanomaterials have unique properties such as high conductivity, fast electron transfer rate,

R. Ponnusamy · C. S. Rout (✉)
Centre for Nano and Material Sciences, Jain University, Jain Global Campus, Ramanagaram, Bangalore 562112, India
e-mail: csrout@gmail.com; r.chandrasekhar@jainuniversity.ac.in

N. S. Arul and V. D. Nithya (eds.), *Two Dimensional Transition Metal Dichalcogenides*,
https://doi.org/10.1007/978-981-13-9045-6_9

biocompatibility and flexibility which can be effectively utilized in the development of biosensors [7, 8]. In the search of new materials for biosensing, researchers found transition metal dichalcogenides as a best substitution to carbonaceous materials.

Transition metal dichalcogenides (TMDs) are promising for a wide range of applications (solar energy harvesting, catalytic energy conversion, photocatalysis, optoelectronics, supercapacitors and so on) due to its exceptional chemical and physical properties that are not available in other nanomaterials [9–13]. Graphene-like two-dimensional lattice structure is the characteristic of TMDs where the metal and chalcogens formed a hexagonal arrangement. However, this hexagonal structure is not thin as graphene because of the sandwiched X-M-X structure, where M is a transition metal element from 3 to 12 groups and X is a chalcogen which are arranged in three layers. Intra-plane atoms strongly held together by covalent bonding whereas the interaction with its neighbouring atoms is weak by van der Waals forces, facilitating the easy exfoliation of sheets for the improved biosensing activity.

Transition metal disulphides including MoS_2, WS_2, VS_2 and SnS_2, and the transition metal diselenides mainly $MoSe_2$ and WSe_2, are the most widely studied among the TMDs. However, remaining sulphide (S_2)- and selenide (Se_2)- based compounds and ditellurides are at their infant stage in the synthesis as well as various field implementation. A vast variety of synthetic methods including chemical vapour deposition [14–16], mechanical cleavage [17, 18], wet chemical synthesis [19, 20], ultrasound and liquid phase exfoliation [21–23], chemical or electrochemical Li-intercalation [24, 25] etc. are assisted in the preparation of TMDs mainly to obtain 2D layered structure. Similar to transition metal oxide materials, size and shape of the TMDs can be tailored from zero to three dimensions (0D, 1D, 2D and 3D) for its constructive applications [26–30].

The basic aim of this chapter is to provide the recent advances in the development of TMD-based biosensors. It will also bring the basic knowledge about the biosensors and the different biosensing methods with their underlying mechanisms. The structure–property relation in TMDs that affects the sensing behaviour is also briefly described in it. Then, the recent progress of the TMDs-based electrochemical, optical and colorimetric biosensor for the detection of different analytes such as small molecules, nucleic acids, DNA and heavy metal ions is also reviewed. The chapter closes with the major challenges in the current TMD biosensors, and the potential opportunities are also proposed at the end.

9.2 Biosensors

9.2.1 Fundamentals

Advantageous characteristics that determine the practical applicability of nanomaterials in the biosensor design are defined below.

- **Linear range**: It is attributed to the accuracy of measured response for a set of measurements with different doses of analyte which generally follows a straight line. Linearity over the bioavailability of the particular analyte is most desirable.
- **Sensitivity**: It is an essential parameter of biosensors that derived from the slope of the calibration plot (analyte concentration vs. sensor response) and is defined as the change of measured signal per unit analyte concentration.
- **Response time**: It is usually quantified as time taken to reach 90% of the steady-state response to a step change in concentration (not more than 30 s).
- **Selectivity**: It is the ability to respond only to the particular target analyte among the co-substances/contaminants.
- **Stability**: It is the degree of susceptibility to ambient disturbances over a period of time with reproducible results.
- **Limit of detection**: It is the minimum concentration of analyte that a sensor can detect or a concentration that gives a response signal exceeding three times the standard deviation of a blank sample.

An ideal working electrode material that has wide linear range, high sensitivity, quick response, low detection limit, good selectivity and long-term stability is promising for practical applications.

9.2.2 Types of Biosensor

Biosensor can be classified either based on the transduction mechanism or type of receptor used. According to the receptor type, biosensors can be labelled as enzymatic, immuno, DNA and aptamer sensors. Electrochemical, optical, piezoelectric, electronic and colorimetric are the common biosensors of transduction category.

Electrochemical biosensors

Electrochemical biosensors are frequently used in the detection of various biomolecules due to its low cost, simplicity and high performance. It can be divided further into two types as enzymatic and non-enzymatic biosensors. In enzymatic sensors, using a specific material, bioreceptor molecules such as enzymes, antibodies, tissues and nucleic acids will initially immobilize on the working electrode surface. For the immobilization of bioreceptors, specific approaches, namely physical adsorption via van der Waals interaction, chemical adsorption by the covalent bonding, entrapment, cross-linking, etc., were used. In course of measurement, bioreceptor acts as a transducer and the subsequent electrical signal resulted by the reaction of bioactive material with the analyte species is generated. Analytical methods like chronoamperometry, squarewave pulse voltammetry (SWV), differential pulse voltammetry (DPV) and electrochemical impedance spectroscopy (EIS) have been used in the enzyme-based biosensing to detect the analyte molecules. The first enzyme-based electrochemical biosensor was developed by Clark for the detection of glucose molecules, and glucose oxidase (GOx) enzyme is used for the immobilization.

Non-enzymatic electrochemical biosensors work based on the principle of charge transfer between the working electrode surface and the analyte that dissolved in a particular electrolyte solution. A typical electrochemical set-up consists of three different electrodes specifically a working, a counter and a reference electrode. Generally, cyclic voltammetry will be used for the initial evaluation of sensing activity of the material, in combination with any of the analytical methods mentioned for enzymatic biosensors.

Fluorescence biosensors

Optical methods (via fluorescence changes or colorimetric changes) are more convenient for the ultrasensitive detection of biospecies due to its simplicity and low detection limit. Every optical sensor assay must contain an active centre/probe that interacts strongly with the target analyte and a chromophore or fluorophore that can strongly couple with the active centre. An active centre of fluorescence biosensors works as fluorescence probe or quencher, and the change in fluorescence intensity measures the level of analyte added. In the case of less emissive active centres, dye labelling will be introduced where the active centre plays a quencher role by absorbing its emissive radiation. Quenching is usually governed by the fluorescence resonance energy transfer (FRET) mechanism that happens between the donor–acceptor pair formed by the dye molecules and the active centre. Traditional organic dyes, such as cyanine, FAM and Texas Red, that can emit in the UV near infrared region of electromagnetic spectrum are frequently used in the FRET-based sensors for labelling. Fluorescent proteins have been considered in the living cell experiments for FRET processes. In contrast, as a fluorescent probe, intrinsic emissive radiation of the active centre gets quenched by the analyte species. For the quantitative measure of target materials, conventional fluorescence spectrophotometers are used to study the respective intensity changes.

Colorimetric biosensor

It is one of the simplest analytical methods that can be used for the determination of different biomolecular species as well as heavy metal ions. Colorimetric sensors use either peroxidise enzymes to get the coloured reaction or peroxidase mimetics for label-free detection. In colorimetric analyses, the analyte molecules could be detected by two ways: (i) by measuring the change in absorption intensity at a particular wavelength, i.e. colour appearing or fading; and (ii) by monitoring a change in the absorption wavelength (blue or red shift for new colours). The results can directly be read out from the colour change, and the spectral changes can be recorded using a simple UV-Vis spectrophotometer. Here, for signal amplification, various aptamers (oligonucleotides or peptide molecules) were bind with the target.

9.3 TMDs in Biosensor

9.3.1 Basic Properties of TMDs

Based on their atomic configuration in the individual slab, TMDs can exist in two different crystallographic forms, namely octahedral (1T) and trigonal prismatic (2H). Generally, 1T phase is metallic in nature and less stable which will be transformed to semiconducting 2H phase easily. Metallic nature of 1T phase is more advantageous in electrochemical sensing [31], but almost all synthesized TMDs are crystallized in semiconducting 2H form. A recent report by Nayak et al. states that a pressure of 22 GPa at 280 K can transform the semiconducting WS_2 into metallic. During this transformation, a 6-order decrease in resistivity, a 2-order decrease in mobility and a 4-order increase in carrier concentration can be realized [32]. Another efficient and easiest way to improve the poor conductivity of 2H TMDs is hybridization/functionalization with carbonaceous materials, metal NPs, organic compounds, etc.

A recent review on MoS_2-based biosensor by Barua et al. has addressed the possibility of different dimension-wise sensing application [33]. Excitation wavelength-dependent photoluminescence of 0D quantum dots that arise due to a quantum confinement effect could be convenient for optical biosensing. Large surface area of 2D layered structures is beneficial for the electrochemical sensing, and its tuneable band gap makes it suitable for fluorescent biosensing too [29]. However, the properties of the 1D structured TMDs are not explored, and so there is a huge potential for 1D-based biosensors. Current status of the different TMDs-based biosensors is summarized in the subsequent sections.

9.3.2 Electrochemical Sensors

In electrochemical sensing, different TMD nanomaterials and its hybrids were utilized for the assessment of wide variety of bio-analytes, mainly small molecules (glucose, hydrogen peroxide, dopamine, etc.), DNA, proteins, etc. For the detection of the bio-analytes, potentiometric and amperometric methods were generally employed in electrochemical biosensors. In recent days, with the help of DPV, SWV and EIS, ultrasensitive detection of biospecies is possibly achieved. Some of the reports that deal with TMDs-based electrochemical biosensing have been briefly reviewed below.

Detection of glucose

Glucose is one of the utmost studied analytes by electrochemical methods in the area of biosensing. Materials including metals [34, 35], bimetallics [36–38], metal oxides [39–41], carbon materials [8, 42, 43], different hybrids/nanocomposites [44–46], etc. are extensively used in the biosensor matrix design for glucose sensing. 2D layered

TMDs also showed interesting performance in glucose oxidation which is briefly discussed here. Both glucose oxidase (GOx)-assisted enzymatic and non-enzymatic methods are repeatedly used in the construction of TMDs-based glucose sensors. GOx is an ideal enzyme that used considerably in glucose biosensor fabrication due to its catalytic ability in the glucose oxidation [47, 48]. It is obvious that the large surface area of MoS_2 nanosheets (NSs) can be conveniently decorated with nobel metal (Au, Pd, Pt) nanoparticles (NPs) to avail the superior electrocatalytic properties. Practically, it was realized in microwave-assisted synthesized MoS_2 NSs while hybridizing with Au NPs [49]. Uniformly distributed 5 nm sized Au NPs (Fig. 9.1a, b) not only increase the conductivity of the MoS_2 matrix (Fig. 9.1c) but also facilitate the electron transfer between the GOx and electrode. Typical cyclic voltammetric (CV) scans shown in Fig. 9.1d on different modified electrodes undoubtedly explain the importance of Au NPs and GOx. This hybrid sensor can detect the glucose in the concentration range from 10 to 300 μM. SnS_2, an n-type semiconductor in TMDs family, has been combined with carbonaceous materials and nobel metals and used in glucose detection. Li et al. decorated the SnS_2 on multiwalled carbon nanotubes surface (MWCNTs) [50]. GOx immobilized MWCNTs-SnS_2 composite showed a surface-controlled, reversible two-proton and two-electron transfer reaction with an electron transfer rate of 3.96 s^{-1}. They also used SnS_2 nanoflakes in glucose sensing by decorating it with Au NPs. Here, GOx was immobilized on the matrix to improve the direct electrochemistry of glucose. The scan rate-dependent redox peak currents indicating a quasi-irreversible surface-controlled reaction on GOx/AuNPs-SnS_2-chitosan/glassy carbon electrode (GCE) and GOx-modified sensor exhibited a better sensitivity of 21.8 mA $M^{-1}cm^{-2}$ than the bare SnS_2-based sensor [51]. Later, SnS_2 nanoplates were exfoliated by an organic solvent-free ultrasonication method and used as glucose biosensor. This exfoliated SnS_2 nanoplates significantly improved the hydrophilicity of the electrode and the electron transfer microenvironment upon decoration [52]. The sensitivity of 28.9 μA mM^{-1} cm^{-2} achieved in exfoliated SnS_2 is the highest among reported for CNT- and GOx-based direct electrochemical glucose sensing.

Bonding between the sulphur of MoS_2 and Cu and its considerably increased specific surface can support large number of electroactive species which facilitate the mass and electron transfer in sensing [53, 54]. So, with the use of CV and chronoamperometric methods, electrochemical and electrocatalytic performances of 3D nano-flower-like Cu/layered MoS_2 composite (CuNFs-MoS_2 NPs) prepared by layer-by-layer deposition were explored. The morphology of the prepared CuNFs-MoS_2 NPs was investigated by SEM and TEM analyses. Quantitative detection of H_2O_2 at neutral pH (PBS) and glucose at basic pH (NaOH) by amperometric I-t method suggests that it can be applied in real sample analyses like tap water and blood serum (Fig. 9.2) [55]. In other cases, Ni and $Ni(OH)_2$ nanoparticles were functionalized on MoS_2 nanosheets to get the improved electrochemical sensing activity in glucose detection. Huang and his co-workers used Ni as a supporting material with MoS_2, and the fabricated sensor showed an excellent sensitivity of 1824 μA mM^{-1} cm^{-2} in alkaline media [56]. TEM images in Fig. 9.3 a, b clearly showed the uniformly distributed Ni NPs (size: 4–8 nm) on MoS_2 which attributes the obtained

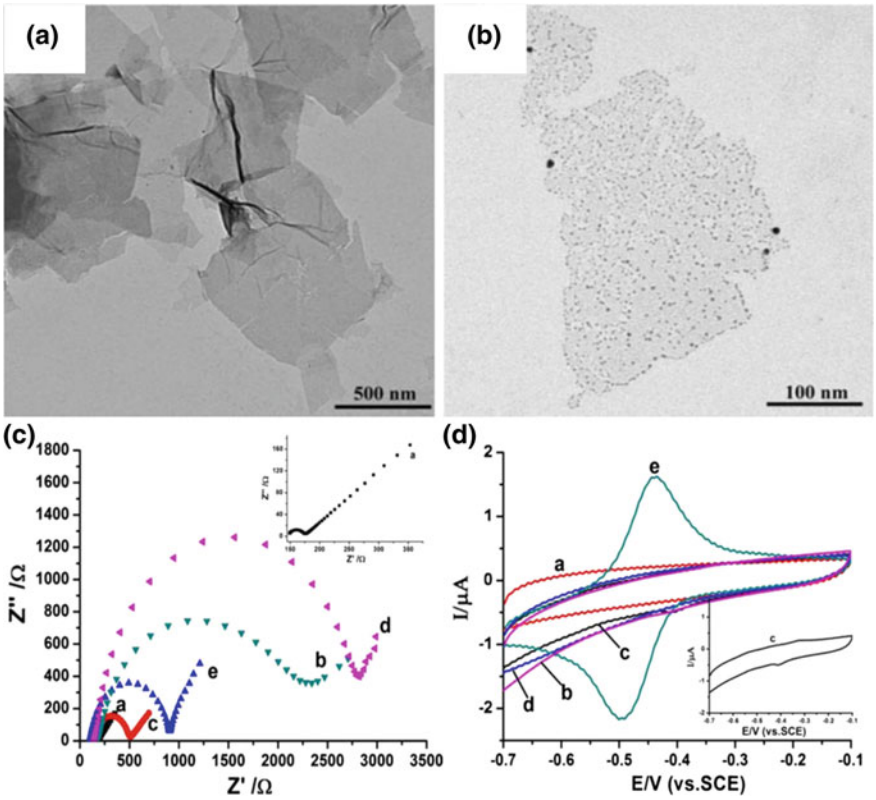

Fig. 9.1 TEM images of **a** MoS_2; **b** AuNPs@MoS_2 nanostructures; **c** EIS spectra of bare GCE; **a** MoS_2/GCE; **b** AuNPs@MoS_2/GCE; **c** Nafion-GOx-MoS_2/GCE; **d** Nafion-GOx-AuNPs@MoS_2/GCE; and **e** inset EIS of bare GCE; **d** CVs of bare GCE; **a** MoS_2/GCE; **b** AuNPs@MoS_2/GCE; **c** Nafion-GOx-MoS_2/GCE; **d** Nafion-GOx-AuNPs@MoS_2/GCE; **e** in N_2-saturated 0.1 M PBS at the scan rate of 100 mV/s. Reprinted with permission from [49]. Copyright 2014 Springer Nature

high-level electrocatalytic activity (Fig. 9.3c). This hybrid is very selective in detecting the glucose molecules in the presence of common interferents (dopamine, uric acid, ascorbic acid, Fig. 9.3d). Ji et al. had modified the glassy carbon electrode with two-step electrodeposited $Ni(OH)_2$/MoSx nanocomposite and studied its glucose-sensing behaviour. In CV tests, enhanced anodic and cathodic peak currents were observed for $Ni(OH)_2$/MoSx due to the oxidation of glucose into gluconolactone and the representative redox reactions are stated as follows [57]:

$$(Ni(OH)_2 + OH^- \leftrightarrow NiOOH + H_2O + e^- \quad (1)$$

$$NiOOH + \text{glucose} \rightarrow (Ni(OH)_2 + \text{glucanolactone} \quad (2)$$

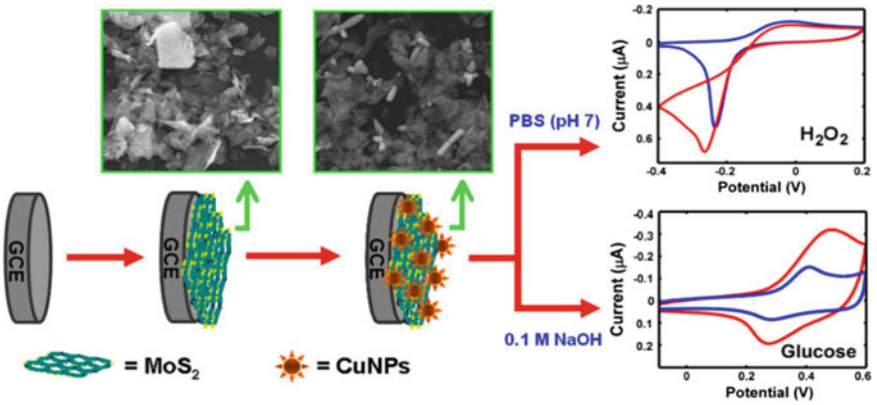

Fig. 9.2 Schematic representation of synthesis and sensing mechanism of Cu NFs/MoS_2/GCE for H_2O_2 and glucose. Reprinted with permission from [55]. Copyright 2016 Elsevier

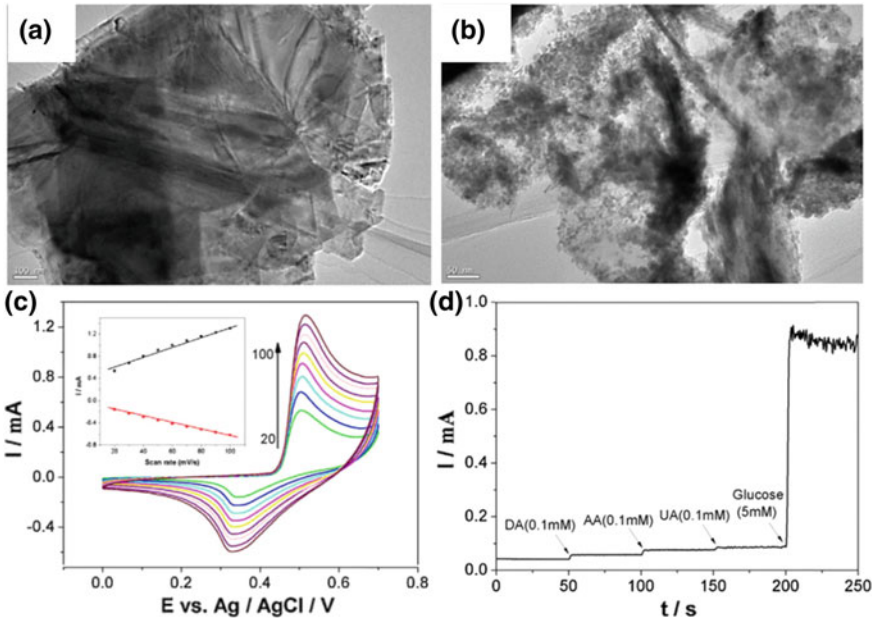

Fig. 9.3 TEM images of **a** MoS_2; **b** Ni-MoS_2 nanosheets; **c** scan rate-dependent CV response of GCE/Ni-MoS_2/Nafion in 0.1 M NaOH with 1.0 mM glucose; and **d** specificity test of GCE/Ni-MoS_2/Nafion. Reprinted with permission from [56]. Copyright 2014 Elsevier

More available surface area of $Ni(OH)_2$ nanoparticles can adsorb more glucose molecules, and the active sulphides of MoS_x will assist the dissociation of glucose. Finally, a good linear response over the glucose concentration of 10–1300 μM was achieved using this non-enzymatic sensor.

Detection of H_2O_2

Hydrogen peroxide (H_2O_2), a major reactive oxygen species in living organisms, has been generated during the incomplete reduction of oxygen and plays a significant role in signal transduction and oxidation pathway of cells. Besides, as an oxidative stress marker, it helps to diagnose the diseases like cancer, cardiovascular and neuro-degenerative disorders. Hence, the detection of H_2O_2 level is essential and imperative which can be done possibly by different TMDs grown by various methodologies as asserted. Beyond the layered structure, particle-shaped TMDs can also be synthesized and utilized in the construction of sensitive H_2O_2 biosensor. An example demonstrating the synthesis of ultrasmall MoS_2 nanoparticles was reported by Wang et al. [58]. This MoS_2 nanoparticle of size 1–2 nm was harvested from 2 μm sized MoS_2 via an easy ultrasonication process. It is also stated that these nanoparticles would adhere more strongly on GCE even in the Nafion-free environment. While testing the sensing ability towards H_2O_2 in the N_2 saturated 0.1 M PBS at-0.25 V potential, a sensitivity of 2.58×10^3 mA cm^{-2} M^{-1} over the wide concentration range of 5–100 nM and 160 mA cm^{-2} M^{-1} for 100 nM to 100 μM was achieved in it. Furthermore, it showed an amazing sensitivity in the real-time analysis of H_2O_2 that released from RAW 264.7 cells. They also demonstrated that the MoS_2 nanoparticle is a potent working electrode material to detect various bio-analytes such as glucose, because H_2O_2 is the main product in the GOx-catalysed reactions.

Detection of analytes by biomolecular (e.g. metalloproteins)-based biosensors has the practical limitations such as unintended orientation of biomolecules on the electrode, low electrochemical signal from the biomolecules and slow and varying electron transfer rate. It is well known from the previous reports that encapsulation of graphene with metal dichalcogenides can improve the efficiency by preserving the effective carrier mobility of graphene during the electron transfer at the interface and can facilitate the charge transfer from the metalloproteins. Hence, Jinho et al. [59] had made the first attempt to fabricate the electrochemical biosensor composed of myoglobin (Mb) on MoS_2 nanoparticles encapsulated with graphene oxide and tested it for H_2O_2 detection. In cyclic voltammograms, compared to Mb/GO, Mb/MoS_2, an enhanced redox signal was observed for Mb/GO@MoS_2 which also has the ability of sensing very low concentration (detection limit: 20 nM) of H_2O_2 in amperometric measurement. Karthik et al. prepared the grass-like VS_2 via simple sonochemical route and employed in non-enzymatic electrochemical sensing of H_2O_2 [60]. The recorded high-magnification images revealed the grass-like (GL) structure which could be composed of randomly oriented leaf-like flakes. So they believed that the as-prepared VS_2 are potential for electrochemical sensing and experimented it. Figure 9.4a, b shows the VS_2 grass-like structure and the comparative CV curves of bare GCE and GL-VS_2 modified GCE electrodes in the presence and absence of H_2O_2. The higher electrocatalytic response, lower reduction potential and increase in the active surface area (Fig. 9.4c) of GL-VS_2 resulted in the high sensitivity of 0.23 μA μM^{-1} cm^{-2} for H_2O_2 sensing.

Sarkar et al. [61] for the first time designed a VS_2 NPs-based amperometric sensor for the detection of H_2O_2 and glucose. High conducting property and cheap

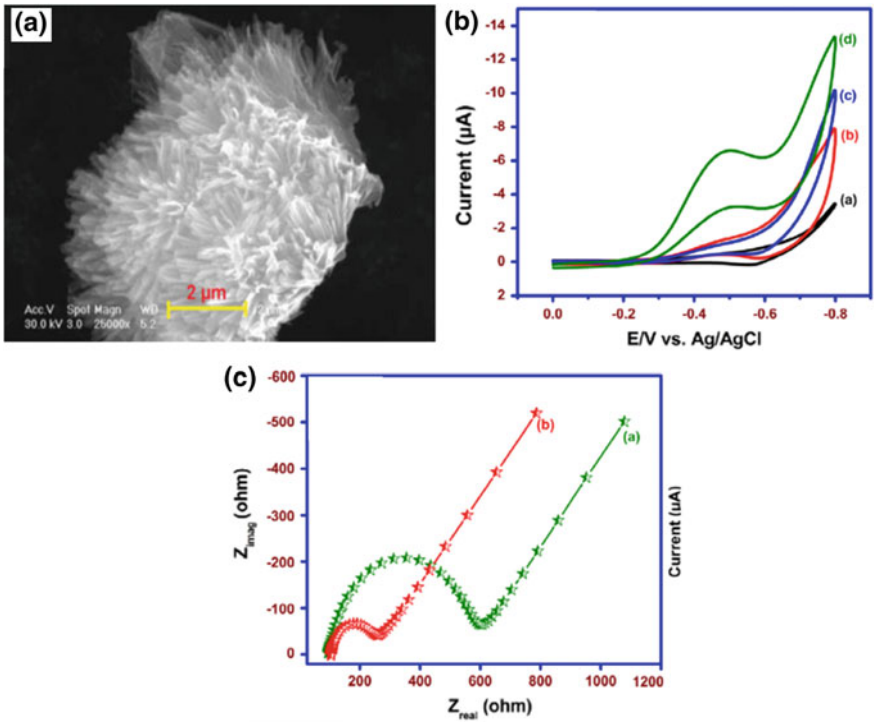

Fig. 9.4 **a** FESEM image of GL-VS_2; **b** CVs of **a** bare GCE; **b** GL-VS_2/GCE; **c**, **d** in presence of 400 µM H_2O_2; **c** EIS of bare GCE (**a**), GL-VS_2/GCE (**b**) in 0.1 M KCl containing 5 mM $[Fe(CN)_6]^{3-/4-}$. Reprinted with permission from [60]. Copyright 2018 Elsevier

cost of VS_2 NPs encouraged them to study its electrochemical sensing behaviour. The calibration plot of I-t curve exhibits a sensitivity of 37.96 µA mM^{-1} over the range 0.5–2000 µM with 0.224 µM detection limit. They also revealed its effective non-enzymatic sensing capability towards glucose. Metallic 1T-phase of WS_2 could act as a better immobilization material to use in the heme-based H_2O_2 sensors due to its desirable properties like high surface-to-volume ratio, high conductivity and capacitive behaviour. To enhance the charge transfer rate of the haemoglobin (Hb) in H_2O_2 sensing, Toh et al. had utilized the 1T-WS_2 sheets as immobilization source [31]. The schematic representation of the construction of working electrode assembly is depicted in Fig. 9.5. Glutaraldehyde (GTA) is used for entrapment and the synergistic interactions between 1T-WS_2 and Hb attained a limit of detection of 36 nM. This t-BuLi-exfoliated 1T-WS_2 is more advantageous in H_2O_2 sensing, than its counterparts like MoS_2, $MoSe_2$ and WSe_2.

The sensing performance of the layered TMDs can be improved by the intercalation of other electrode materials. For example, cubic-PtW nanocrystals were grown on MoS_2 nanosheets and studied for H_2O_2 sensing. Smallest electron transfer resistance (PtW/MoS_2/GCE < MoS_2/GCE < GCE) in electrochemical impedance

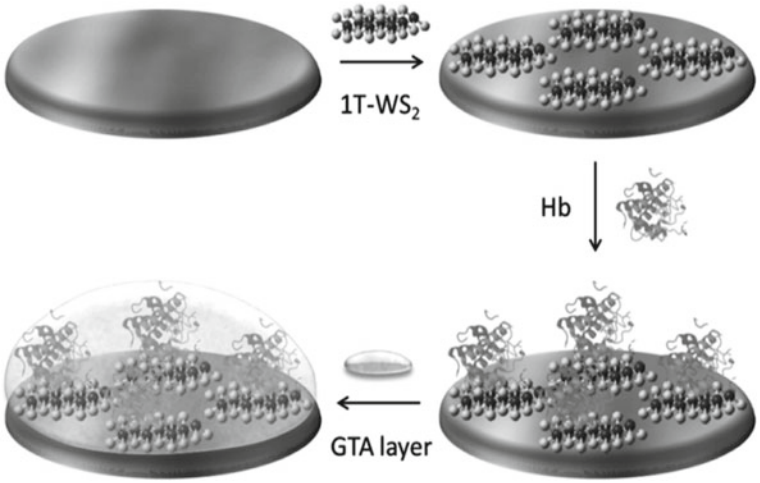

Fig. 9.5 Scheme for the construction of GTA/Hb/1T-WS_2/GCE. Reprinted with permission from [31]. Copyright 2016 John Wiley and Sons

spectroscopy and quick response (<5 s) in amperometry for each H_2O_2 dose are originating from the more available active sites induced by PtW on MoS_2 surface (Fig. 9.6). The real sample analysis on H_2O_2 released from 4T1 breast cancer cells also exposed its potential application in sensing of biosystems [62]. Solvothermally synthesized hybrid SnS_2/Pt nanoparticles with porous structure also showed good electrocatalytic activity towards H_2O_2 reduction. It is the first attempt for its preparation by hydrothermal route. High surface area of SnS_2, efficient electrochemical activity of Pt NPs and their interesting synergistic effects find a better position in the sensing platform for this material [63]. Summary of the recently reported TMDs-based glucose and H_2O_2 biosensors is provided in Table 9.1.

Detection of DNA

Because of its exceptional physical and electrochemical properties, MoS_2 has also been used in the development of electrochemical biosensor for the detection of DNA. The basic principle that involved in the DNA detection by MoS_2 is its differential affinity towards single-stranded DNA (ssDNA) and double-stranded DNA (dsDNA). Based on this principle, MoS_2 nanoflakes synthesized by Loo et al. showed excellent sensitivity towards the ssDNA and dsDNA [64]. Wang et al. too experienced the differential affinity of MoS_2 nanosheets while performing the assay of the gene sequence [65]. Here, MoS_2 nanosheets were synthesized via ultrasound exfoliation, and the modified electrode was prepared on carbon paste electrode (CPE). Most importantly, they avoided the costly fluorophore labelling and used methylene blue, a classic electroactive indicator to read the surface changes of electrode after DNA immobilization and hybridization. The amount of target DNA can be estimated from the decrease in reduction peak currents of MB in DPV, and the detection limit is

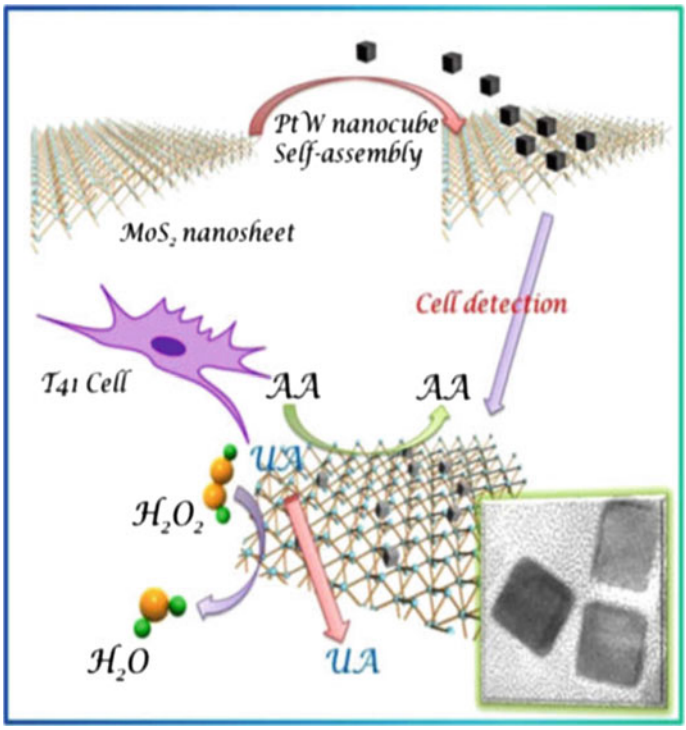

Fig. 9.6 Scheme of PtW/MoS_2 nanocomposite synthesis and its sensing mechanism of H_2O_2 released from living cells. Reprinted with permission from [62]. Copyright 2016 Elsevier

1.9×10^{-17} M for the proposed sensor. Similar methodology was followed by Yang et al. [66] where the free-standing ZnO nanosheets were electrodeposited on MoS_2 to detect the specific DNA sequence. The strong electrostatic interaction between negatively charged DNA and positively charged ZnO makes the ZnO/MoS_2 nanocomposite capable of immobilizing DNA. This free-standing ZnO/MoS_2 structure showed good differences in the redox current values of MB while adding probe DNA and its complement. It also exhibited the low limit of detection (6.6×10^{-16} M) for PML/RARA fusion gene. Thionin-functionalized MoS_2 also displayed a stable and enhanced electrochemical sensing behaviour towards DNA [67]. In the presence of ionic liquid (1-butyl-3-methylimidazolium hexafluorophosphate), bulk MoS_2 was exfoliated easily and thionin was attached by the charge transfer process. During dsDNA detection, thionin as a cationic phenothiazine dye can strongly bind with dsDNA through intercalation and electrostatic interaction that leads the inhibition of its own electrochemical signal. A linear response from the thionin-MoS_2 modified electrode was obtained in the range 0.2–2.0 nM in SWV measurements. Besides, it can also be used for the sensing of ssDNA and RNA. Cao et al. exploited the signal amplification strategy in DNA sensing for AuNPs/MoS_2/Gr composite elec-

Table 9.1 Summary of recent reports on different TMDs-based glucose and H_2O_2 biosensors

Material	Analyte	Linear range	Sensitivity	LOD	References
Nafion-GOx-Au NPs@MoS_2	Glucose	10–300 μM	–	2.8 μM	[49]
GOx/MWCNTs-SnS_2	Glucose	0.02–1.95 nM	21.65 mA M^{-1} cm^{-2}	0.004 nM	[50]
GOx/Au NPs-SnS_2-chitosan	Glucose	0.02–1.32 mM	21.8 mA M^{-1} cm^{-2}	0.001 mM	[51]
SnS_2 nanoplates	Glucose	0.0625–2.8 mM	28.9 μA mM^{-1} cm^{-2}	0.0125 mM	[52]
Cu NFs/MoS_2/GCE	Glucose	1–20, 20–70 μM	–	0.32 μM	[55]
	H_2O_2			0.021 μM	
		0.04–1.88, 1.88–35.6 μM			
Ni-MoS_2 hybrid	Glucose	Up to 4 mM	1824 μA mM^{-1} cm^{-2}	0.31 μM/L	[56]
$Ni(OH)_2$/MoSx-GCE	Glucose	10–1300 μM	–	5.8 μM	[57]
Ultrasmall MoS_2/GOD	H_2O_2	2.0–16.0 mM	152 mA M^{-1} cm^{-2}	2.5 nM	[58]
GL-VS_2	H_2O_2	0.1–260 μM	0.23 μA $μM^{-1}$ cm^{-2}	26 nM	[60]
VS_2 NPs	H_2O_2	0.5–2000 μM	37.96 μA mM^{-1}	0.224 μM	[61]
	Glucose				
		0.5–3000 μM	41.96 μA mM^{-1}	0.211 μM	
GTA/Hb/1T-WS_2	H_2O_2	2–38, 48–1728 μM	–	0.036 μM	[23]
PtW/MoS_2	H_2O_2	1 μM–0.2 mM	1.71 μA $μM^{-1}$ cm^{-2}	5 nM	[62]
SnS_2/Pt NPs	H_2O_2	1–185, 385–2185 μM	–	0.33 μM	[63]

trode which showed high selectivity among single-base mismatched and three-base mismatched sequences of DNA. Streptavidin-horseradish peroxide functionalized AuNPs were used for signal amplification, and hence, the designed sensor detected the DNA down to 2.2×10^{-15} M [68].

Again, an organic–inorganic mixed matrix was fabricated by Yang et al. where polyaniline (PANI) was hybridized with MoS_2 [69]. Their series of experiments on the synthesis conditions provide direct evidence for the influence of MoS_2 dose on immobilization of probe DNA and its hybridization. At the optimum concentration of 0.054 g MoS_2, PANI-MoS_2 composite possesses high surface area and its detection limit is 2.0×10^{-16} M in cauliflower mosaic virus 35S (CaMV35S) gene sequence detection. Moreover, either internal self-signals (PBS system) or external indicator

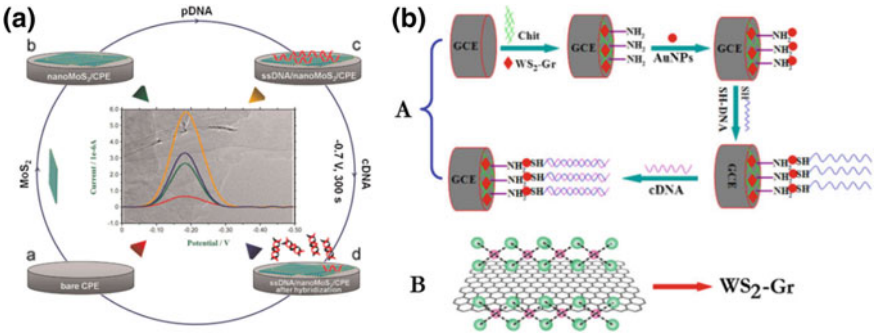

Fig. 9.7 Schemes of DNA sensing by **a** thin-layer MoS_2 NSs. Reprinted with permission from [65]. Copyright 2015 Elsevier. **b** WS_2-Gr nanocomposites. Reprinted with permission from [71]. Copyright 2014 Elsevier

signals (MB), PANI-MoS_2 displayed an enhanced electrochemical activity over PANI and bare MoS_2.

Unlike MoS_2, only a limited number of attempts were made to use WS_2 as an electrode material in biosensors because of its relatively low conductivity. To improve it, Shuai et al. hybridized acetylene black (AB) with WS_2 to effectively sense DNA molecules [70]. Subsequently, the electrode was modified with target DNA, auxiliary DNA and hairpin DNA's H1, H2 for hybridization chain reactions (HCR). The formed double helices from HCR are used to immobilize horseradish peroxidase enzyme which produces signal amplification in DNA detection by the catalytic reaction of H_2O_2 + hydroquinone system. In the DPV study, a linear relationship between the current and log of DNA concentrations was observed over the range of 0.001−100 pM. Huang et al. had made WS_2-Graphene (Gr) composite to overcome the conductivity deficiency in WS_2 and tested against DNA. As synthesized composite exhibits good dispersibility in water which played an important role during the electrochemical sensing. Here, chitosan was used to bind the composite on GCE, and then, thiolated probe ssDNA (5′-SH-$(CH_2)_6$-TCT TTG GGA CCA CTG TCG-3′) was linked on it. When target DNA 5′-CGA CAG TGG TCC CAA AGA-3-3′ is introduced, a lower redox current appeared in DPV scans and the detectable concentration of the fabricated electrode is 0.00001–0.5 nM [71]. Figure 9.7a, b represents the schemes of DNA detection by MoS_2 nanosheets and WS_2-Gr nanocomposites, respectively.

Detection by TMD-carbon hybrids

Despite the fact that MoS_2 is a remarkable material in electrochemical sensing, different functional groups were decorated on MoS_2 to further improve its properties and to widen the applications. Especially, carbonaceous materials were combined with MoS_2 due to its large specific surface area and excellent biocompatibility which are used in the detection of various analytes. For instance, Chu et al. [72] had integrated MoS_2 and graphene through hydrothermal and ultrasonication processes and used it to design a label-free, amplification-free ultrasensitive tumour DNA electrochemical sensor. The designed sensor can detect the trace amount of DNA in the range of 10^{-16} to 10^{-13} M. Determination of honokiol content is of great importance, since it used in Chinese herbal medicine to treat various problems. So Zhao et al. hybridized MoS_2 with graphene to improve its electrical conductivity and used for the tracing of honokiol level [73]. By a two-electron redox reaction, honokiol was reduced in the presence of MoS_2/graphene nanohybrid and its detection limit is estimated to be 6.2×10^{-10} M. Song et al. also prepared layered MoS_2-graphene nanocomposite which is hybridized further with horseradish peroxidase for H_2O_2 sensing. This MoS_2-graphene-HRP composite biosensor exhibits a fast amperometric response with a high sensitivity of 679.7 $\mu A\ mM^{-1}\ cm^{-2}$ [74]. Similar to this, graphene had been compounded with VS_2 to defeat its poorer electronic conductivity and this hybrid compound was harvested by hydrothermal method. The AuNPs/VS_2-GR/HRP-modified aptamer sensor detected the trace level of platelet-derived growth factor BB (PGDF-BB) molecules successfully via signal amplification [75].

Detection by TMD non-carbon hybrids

To acquire more interesting and superior electrocatalytic properties in TMDs, different organic and inorganic materials were amalgamized by different synthetic strategies. For example, a simple electrochemical sensor was constructed using MoS_2 films which is modified with chitosan (CS) and decorated with Ag NPs. The uniform decoration of Ag NPs and the formation of Ag-MoS_2/CS composite were verified with TEM images shown in Fig. 9.8a. Then, the determination of tryptophan was carried out by DPV (Fig. 9.8b) where the linearly increased current with each dose of tryptophan was obtained [76]. PANI, a conducting polymer, also assisted in the composite making and resulted in an outstanding conductivity. On MoS_2 NSs, self-doped PANI (SPAN) was deposited and utilized for the first time in chloramphenicol (CAP) sensing by Yang et al. [77]. This SPAN/MoS_2 hybrid showed remarkable synergistic effect in CAP reduction than the sole MoS_2 and SPAN. The typical DPV scans and the corresponding calibration plot are displayed in Fig. 9.9.

In this route, organic Cu nanowires (OCu) were used to modify the surface of MoS_2 to get the better mobility in electrochemical analysis [78]. MoS_2-OCu nanohybrids can detect H_2O_2 and ascorbic acid simultaneously without any enzyme addition. The OCu nanowires act as a spacer to isolate MoS_2 NSs which in turn ensure sufficient reactive sites for the redox reactions of the analytes. Because of the unique characteristics, such as high conductivity, biocompatibility, anti-oxidant characteristics and better electron affinity, etc., noble metal NPs are frequently used in hybridization of

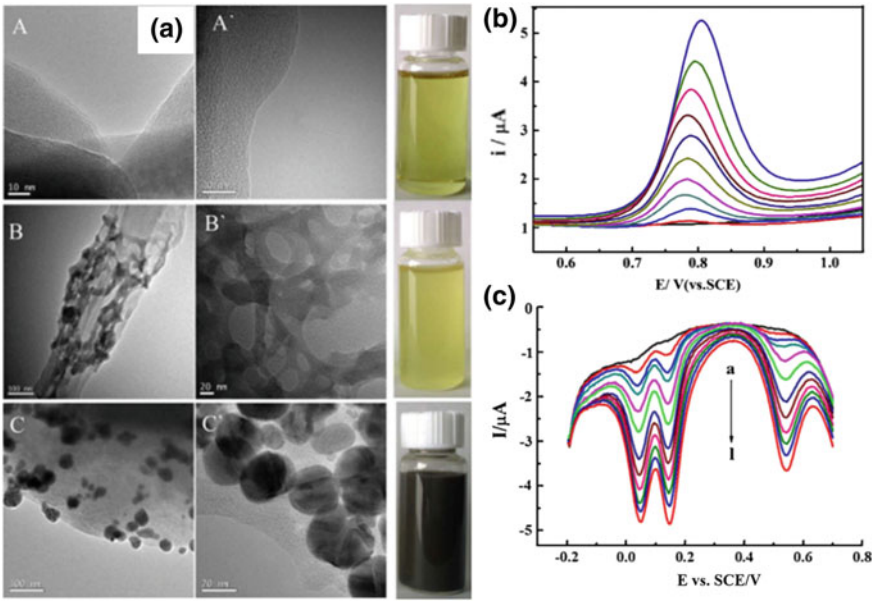

Fig. 9.8 **a** TEM images of MoS_2 films (A, A′), MoS_2/CS films (B, B′), Ag-MoS_2/CS films (C, C′) at different magnifications; **b** DPVs of Ag-MoS_2/CS/GCE with different concentration of tryptophan (0.5, 3.0, 10.0, 20.0, 30.0, 40.0, 50.0, 60.0, 75.0, 95.0 and 120.0 μM, respectively) in 0.1 M PBS. Reprinted with permission from [76]. Copyright 2014 Elsevier. **c** DPVs of WS_2-GR electrode with mixtures (a to l: 1×10^{-6},3×10^{-6},5×10^{-6},7×10^{-6}, 1×10^{-5}, 2×10^{-5}, 3×10^{-5}, 4×10^{-5}, 5×10^{-5}, 6×10^{-5},8×10^{-5},10×10^{-5}) of CT, HQ and RS in 0.1 M PBS. Reprinted with permission from [81]. Copyright 2013 Elsevier

TMDs. In the nanocomposite of SnS_2, platinum (Pt) NPs were assembled on SnS_2 nanoflakes and its enzymatic glucose-sensing activity was tested [79]. The possible reactions involved in the oxidation of glucose at the GO_x/PtNP@SnS_2 modified GCE electrode are:

$$\mathrm{GOx(FAD)} + 2\mathrm{e}^- + 2\mathrm{H}^+ \leftrightarrow \mathrm{GO_X(FADH_2)} \tag{3}$$

$$\mathrm{GO_x(FADH_2)} + \mathrm{O_2} \rightarrow \mathrm{GO_x(FAD)} + \mathrm{H_2O_2} \tag{4}$$

$$\mathrm{Glucose} + \mathrm{GO_x(FAD)} \rightarrow \mathrm{Gluconolactone} + \mathrm{GO_x(FADH_2)} \tag{5}$$

Another work reported by Su et al. demonstrated that Au NPs addition greatly enhanced the electron transfer kinetics and electrocatalytic activities of the MoS_2. Also, in dopamine sensing, this AuNP@MoS_2 nanocomposite showed a detection limit of 80 nM which is attributed to the cooperative effect that aroused from excellent conductivity of AuNPs and high surface area of MoS_2 [49]. Lin et al. also prepared

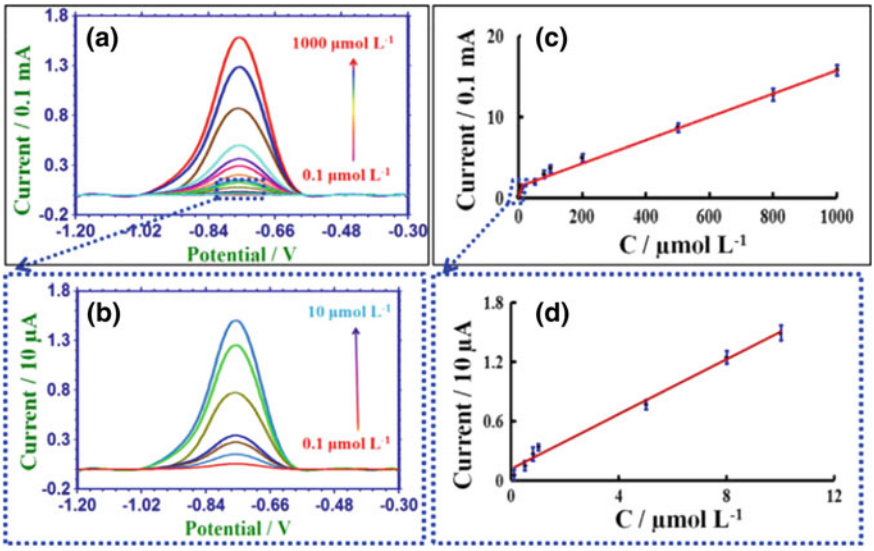

Fig. 9.9 DPV curves of SPAN-MoS_2 (1:3)/CPE in PBS with chloramphenicol concentrations varying from 0.1 to 1000 µM (**a**), enlarged view of 0.1–10 µM (**b**), (**c**, **d**) calibration plots of a and b. Reprinted with permission from [77]. Copyright 2015 Elsevier

MoS_2-AuNPs hybrid and quantified the concentration of cholesterol in egg yolk and pork liver samples with the help of cholesterol oxidase [80].

Detection of other biomolecules

Besides the above discussed analytes, the application of large surface area of 2D layered TMDs with its intriguing properties can be expanded for the sensing of other biospecies. Some of the recent reports with interesting results are discussed here briefly. At first, WS_2 NSs with GR composite was synthesized by L-cysteine-assisted solution-phase method. Three dihydroxybenzene isomers, catechol (CC), resorcinol (RS) and hydroquinone (HQ), were taken as a model to check out the feasibility of as-prepared WS_2-GR biosensor. The sensor showed distinct cathodic peaks at the potentials 0.05, 0.16 and 0.55 V for HQ, CC and RS, respectively (Fig. 9.8c). It corroborates that WS_2-GR composite can simultaneously detect the dihydroxybenzene isomers without any enzymes [81]. A multilayered film comprised of chitosan, SnS_2 NPs and single-walled carbon nanotubes (SWCNTs) was successfully synthesized and used as a multifunctional biosensor to detect the biomolecules dopamine (DA), uric acid (UA) and ascorbic acid (AA) [82]. In CV, well-separated voltammetric signals with the peak-to-peak separation of 171, 136 and 307 mV were obtained for DA-UA, DA-AA and UA-AA, respectively, which confirm its multi-potentiality in electrochemical sensing. Interestingly, for the tracing of 17β-estradiol, one of the environmental endogenous estrogens, Au NPs modified VS_2 nanoflowers-based sensor was developed by Huang et al. [83]. Aptamer immobi-

lized Au NPs/VS_2/GCE electrode showed amplified signals towards 17β-estradiol because of high loading ability of VS_2 for Au NPs along with its own surface area. The analyte 17β-estradiol can be detected up to 1.0×10^{-12} M using this novel sensor. For this purpose, Au NPs/WS_2/GCE electrode also applied and detected the 17β-estradiol concentrations in serum and water samples [84]. Very recently, miRNAs were also electrochemically sensed by the MoS_2-$CuFe_2O_4$ nanocomposite [85]. The proposed PDMS microfluidic sensing system can detect the paratuberculosis (pTb)-specific miRNAs in highly sensitive and selective manner with a detection limit of 0.48 pM. A label-free electrochemical aptasensor was designed by Liu et al. using leaf-like VS_2-Au NPs for the sensitive detection of platelet-derived growth factor BB. The results obtained from the real urine sample analysis using this sensor are well comparable with the ELISA method [86]. TMDs can be used as an efficient electrode material in the sensing of antimicrobials, nucleobases, vitamins, etc. From a simple hydrothermal process, strontium-doped $MoSe_2$ was harvested by Sakthivel et al. to detect an antimicrobial agent [87]. With the increased active surface area of 0.104 cm^2, $SrMoSe_2$ exhibits a 1.83 times higher reduction peak current for metronidazole (MTZ). During the reduction, via a four-electron process, nitro group ($-NO_2$) of MTZ was reduced to hydroxylamine group ($-NHOH$) by $SrMoSe_2$. Sensitivity of $SrMoSe_2$ on MTZ was calculated to be 1.13 $\mu A\ \mu M^{-1}\ cm^{-2}$. Vitamin B_2, also known as riboflavin biosensor, was constructed by Wang et al. [88] using reduced MoS_2/graphene/homo adenine single-stranded DNA/Au electrode (rMoS_2-graphene/A_{32}/Au). In DPV, rMoS_2-graphene/A_{32}/Au composite displayed a wide linear range of 0.025–2.25 μM for riboflavin. The good electrocatalytic activity of poly(xanthurenic acid) (PXa)-MoS_2 composite film was found by yang et al. during guanine and adenine sensing [89]. Negative charge of PXa-MoS_2 nanocomposite prompted the adsorption of positively charged guanine and adenine on it which resulted the low detection limits of 1.7×10^{-8} and 3.0×10^{-8} M, respectively. One of the major public health threats chikungunya that caused by a chikungunya virus (CHIGV) also can be sensed by TMD-based electrochemical sensor. Recently, Singhal et al. developed a MoS_2 nanosheets deposited screen printed gold electrode for CHIGV sensing [90]. The developed biosensor showed a linearity over the range of 0.1 nM to 100 μM with 3.4 nM as detection limit. It is demonstrated that introduction of hydrogen in titanium disulphide ($HxTiS_2$) can result in peculiar electrical conductivity of 6.76×10^4 S/m [91]. Hence, it can be effectively employed in the electrochemical sensing platform. A recent report says that $HxTiS_2$-PANI nanocomposite prepared by Li-intercalation and exfoliation method is highly selective in Cu^{2+} ions detection that endowed from the coordination interaction between Cu^{2+} cations and the N atoms of the imine moieties in PANI. The detection limit for Cu^{2+} ions by this sensor is 0.7 nM, and the linear range is 25 nM to 5 μM [92]. Details of various analytes (DNA, metal ions, proteins, etc.) that sensed by different TMDs were listed in Table 9.2.

Table 9.2 List of TMDs-based electrochemical biosensors for DNA and other biospecies detection

Material	Analyte	Analytical method	Linear range	LOD	References
MoS_2 nanosheets	DNA	DPV	1.0×10^{-16} to 1.0×10^{-10} M	1.9×10^{-17} M	[65]
ZnO/MoS_2	DNA	DPV	1.0×10^{-15} to 1.0×10^{-6} M	6.6×10^{-16} M	[66]
MoS_2-thionin	DNA	SWV	0.09 to 1.9 ng mL^{-1}	–	[67]
AuNPs/MoS_2/Gr/GCE	DNA	DPV	0.000005–5	0.0022 fM	[68]
PANI-MoS_2	DNA	DPV	1.0×10^{-15} to 1.0×10^{-6} M	2.0×10^{-16} M	[69]
WS_2-AB	DNA	DPV	0.001–100 pM	0.12 fM	[70]
WS_2-Gr/GCE	DNA	DPV	0.01–500 pM	0.0023 pM	[71]
MoS_2/graphene	DNA	DPV	1.0×10^{-16}–1.0×10^{-13} M	1×10^{-17} M	[72]
MoS_2/graphene	Honokiol	DPV	1.0 nM to 2.5 μM	62 nM	[73]
VS_2-Gr	PGDF-BB	DPV	0.001–1 nM	0.03 pM	[75]
Ag-MoS_2/CS/GCE	Tryptophan	DPV	0.5–120 mM	0.05 mM	[76]
SPAN-MoS_2	Chloramphenicol	DPV	0.1–1000 μM	6.5×10^{-8} mol L^{-1}	[77]
MoS_2-OCu	Ascorbic acid	AM	0.015–11.75 mM	0.022 μM	[78]
MoS_2-Au NPs	Cholesterol	AM	0.5–48 μM	0.26 μM	[80]
WS_2-GR/GCE	Catechol	DPV	1–100 μM	0.2 μM	[81]
	Resorcinol		1–100 μM	0.1 μM	
	Hydroquinone		1–100 μM	0.1 μM	
Aptamer/Au NPs/VS_2/GCE	17β-estradiol	DPV	1.0×10^{-11} to 1.0×10^{-8} M	1.0 pM	[83]
Aptamer/Au NPs/WS_2/GCE	17β-estradiol	DPV	$1.0 \times 10^{-11-5}$ to 0×10^{-9} M	2.0 pM	[84]
MoS_2-$CuFe_2O_4$	pTb specific miRNA	SWV	–	0.48 pM	[85]
Au NP/VS_2	PGDF-BB	DPV	0.001–1 nM	0.4 pM	[86]
$SrMoSe_2$/GCE	metronidazole	DPV	0.05–914.92 μM	0.001 μM	[87]
rMoS_2-graphene/A_{32}/Au	riboflavin	DPV	0.0025–2.25 μM	0.020 μM	[88]
PXa-MoS_2	Adenine guanine	DPV	0.5–10 μM	3.0×10^{-8} M	[89]

(continued)

Table 9.2 (continued)

Material	Analyte	Analytical method	Linear range	LOD	References
			0.5–10 μM	1.7×10^{-8} M	
H_xTiS_2-PANI/GCE	Cu (II) ions	SWASV	25 nM to 5 μM	0.7 nM	[92]

SWASV-square wave anodic striping voltammetry

9.3.3 Optical Biosensors

The simplicity, fast detection and direct visible read out features of optical biosensors are fascinating and feasible for the medical diagnosis and the pollutant monitoring. Fluorescence sensing and colorimetric sensing are the two major subclasses of optical biosensors [93]. 2D layered structure of TMDs has triggered intensive interest owing to its tunable optical and electronic properties that depend on the number of layers. For instance, indirect band gap of bulk MoS_2 becomes direct when the number of layers reduced to one [94]. Efficient fluorescence quenching ability for fluorophores and photoluminescence emission properties make the TMDs beneficial for the construction of fluorescent-based sensing devices. Hence, in the forthcoming sections, interesting results from the recent reports on fluorescence and colorimetric sensing performances of TMDs were presented.

Fluorescence sensors

In fluorescence (FL) sensors, based on the morphological features and optical properties, TMDs can be employed either as a fluorescence probe or quencher. Like electrochemical sensors, TMDs-based FL sensors are also proficient in detecting the different analytes including small molecules, DNA, proteins, metal ions, pathogens, etc.

TMD composites in metal ions detection

Hybridization of 2D TMDs with other nanomaterials such as noble metals, carbon materials and transition metal oxides paved the way to explore its synergistically enhanced properties in variety of sensing applications. For example, a fluorescent turn-on biosensor based on graphene QDs/MoS_2 NSs was designed by Shi and his co-workers [95] for the detection of epithelial cell adhesion molecule (EpCAM). Initially, via fluorescence resonance energy transfer (FRET) mechanism, the fluorescence signal of GQDs was diminished (Fig. 9.10). Upon addition of target protein, the stronger affinity interaction between the aptamer and EpCAM restored the same by detaching the GQDs from MoS_2 NSs. In this process, the target could be detected by monitoring the change in the fluorescence signal. To enrich the fluorescence properties of MoS_2 nanosheets in the direction of sensing, Liu et al. [96] doped boron (B) and nitrogen (N) in it. B, N-MoS_2 NSs with increased band gap of 1.61 eV acted as a facile sensing platform for label-free detection of Hg^{2+}. The observed fluorescence

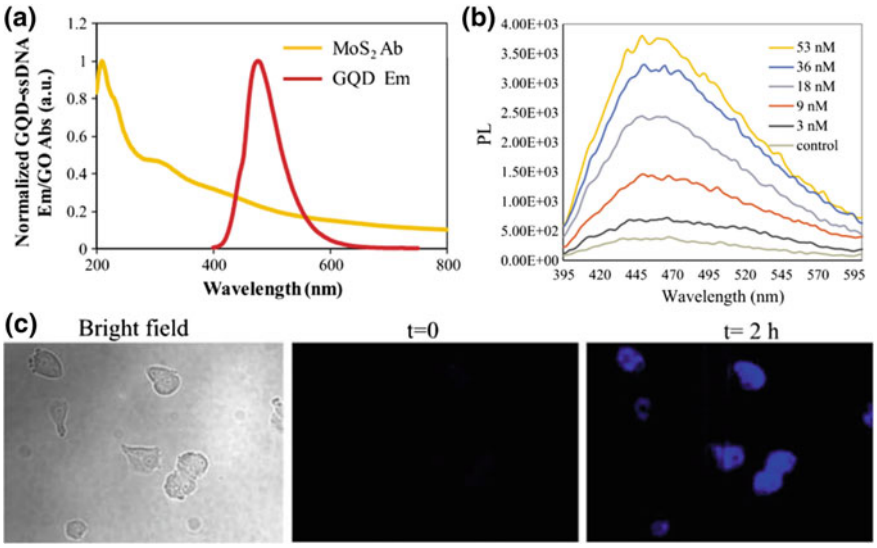

Fig. 9.10 **a** spectral overlapping between MoS_2 absorption and graphene QDs emission; **b** fluorescence spectral response of GQDs-PEG-aptamer/MoS_2 for different concentrations of EpCAM; **c** MCF-7 cell detection by GQDs-PEG-aptamer/MoS_2. Reprinted with permission from [95]. Copyright 2017 Elsevier

quenching after the introduction of Hg^{2+} could have proceeded with the photoinduced electron transfer from the CB of B, N-MoS_2 to complex Hg^{2+} where the redox potential of Hg^{2+}/Hg^{+} lies between the energy gap of the matrix. They have extended the same doping strategy in WS_2 NSs to get the enhanced fluorescence. Further, the B, N-WS_2 NSs were used in the label-free detection of Hg^{2+}. In this fashion, WSe_2:CdS and $MoSe_2$:CdS nanohybrid quantum dots (NHDs) were synthesized by Karfa et al. via hydrothermal and top-down approaches, respectively [97]. $MoSe_2$:CdS NHDs showed excellent excitation wavelength-dependent fluorescence and used as a turn-off fluorescence probe for the detection of Pb^{2+}. The real-time analysis (human sera and polluted industrial water) made on the NHDs-coated paper sensor showed a good response towards the trace level (20 μg/L) of Pb^{2+}. It is believed that onto the surface of nanoparticles, metal ions will be adsorbed and a nanoparticle-metal matrix will be formed, leading to PL quenching.

Wang et al. have synthesized the photoluminescent MoS_2 quantum dots by hydrothermal method using sodium molybdate and cysteine as precursors [98]. As a photoluminescent probe, MoS_2 QDs had successfully detected 2,4,6-trinitrophenol (TNP) with a high detection limit of 95 nM via PL quenching. The analysis of Stern–Volmer quenching constant suggested that the high sensitivity very likely originated from a combination of PL resonance energy transfer, electronic energy transfer and electrostatic interaction between MoS_2 QDs and TNP. Interestingly, cysteine-MoS_2 QDs prepared by Wu's group showed good dispersion in aqueous solution and

blue emission at 428 nm [99]. They have applied the as-prepared cysteine-MoS_2 QDs in dual-mode PL sensing for the effective detection of Al^{3+} and Fe^{3+} simultaneously. In typical sensing, the blue fluorescence was gradually enhanced for Al^{3+} (turn-on) and quenched for Fe^{3+} ions (turn-off).

Chemical doping of inorganic compounds is the easiest way to enhance the fluorescent quantum yield of MoS_2 NSs rather than organic compounds or DNA molecular doping. Wang et al. realized it in MoS_2 NSs prepared via hydrothermal method with lead (II) (Pb^{2+}) and sulphide (S^{2-}) ions doping which also can be exploited to design a label-free fluorescent "turn-on/turn-off" sensor for the detection of Pb^{2+} and S^{2-} heavy metal ions. Various analytical techniques demonstrated the origin of FL enhancement/quenching as the Pb^{2+}-induced formation of $PbSO_4$ at MoS_2 surface and its transformation into PbS by S^{2-} ions, respectively [100]. This formula could be expanded in the area of high-performance optical modulators, solar cells and biological applications.

TMDs in DNA sensing

First and foremost, pristine TMDs like MoS_2, WS_2, VS_2, etc. are employed in DNA molecular sensing. Available reports addressed both the fluorescent dye-labelled and label-free detection of DNA molecules. Generally, all the single layered TMDs are possibly composed of X-M-X sandwich structure, where the X (S, Se, Te) and M (Mo, W, V, etc.) denote chalcogenide and transition metal ion, respectively. This unique morphological characteristic of TMDs facilitates the specific absorption of ssDNA via van der Waals force between nucleobases and the basal planes of TMDs, so the fluorescence gets reduced. In contrast, due to weaker affinity, dsDNA restores the emission behaviour of fluorophores and these differential affinities were utilized for the tracing of nucleic acid levels. Huang et al. followed the hybridization chain reactions (HCRs) strategy in DNA detection using MoS_2 NSs. Two complementary hairpin DNA probes, HP1 and HP2, with FAM were employed in the typical sensing system. After adsorption of FAM-probes, MoS_2 quenches the fluorescence ability of FAM. When the target DNA is introduced, it hybridized with the anchoring end of HP1 followed by the opening of HP2. The as-formed long-chain HP1-HP2 duplex was desorbed from the sheet due to their weaker interactions with MoS_2 and hence the strong fluorescence signal generated again [101].

Selection of transition metal in layered TMD perhaps influences their application in the fluorescence biosensing platform. To check this, Loo et al. had made the comparative study on the fluorescence-sensing performances of MoS_2 and WS_2 nanoflakes [64]. Both MoS_2 and WS_2 nanoflakes exhibited the similar degree of fluorescence quenching (~71 to 75%), at the optimal amount of nucleic acid. However, a better performance in the areas of detection range (9.60–366 nM) and selectivity (97.8%) was achieved with MoS_2 nanoflakes than WS_2. Hence, it is proven that transition metal in layered TMD nanoflakes is strongly affecting their quenching efficiency in DNA detection. Likewise, interaction of collagen peptide was tested with both MoS_2 and WS_2 by Sun et al. where WS_2 provides strong fluorescence enhancement [102] and the interaction between target peptide and matrix is shown in Fig. 9.11a.

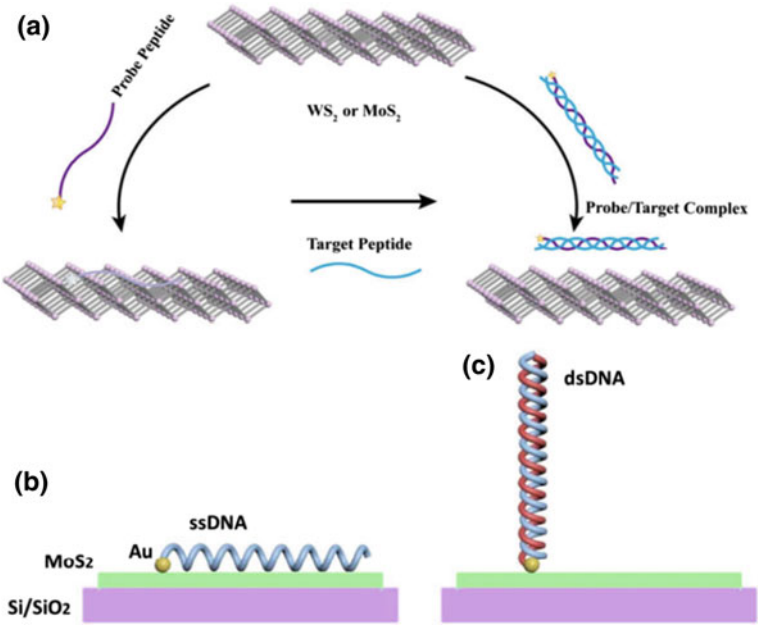

Fig. 9.11 Schemes illustrating **a** interaction of peptide with WS_2 or MoS_2. Reprinted with permission from [102]. Copyright 2017 Nature Publishing Group. **b** adsorption of ssDNA and **c** dsDNA on Au-MoS_2 surface. Reprinted with permission from [104]. Copyright 2016 American Chemical Society

Effective utilization of target sample in the fluorescence sensing not only provides high throughput analysis but enables the ultrasensitive detection of DNA molecules. Huang et al. had applied the microfluidic technique in DNA detection in order to reduce the sample volume. To investigate this, a dye-labelled probe (5'-TAMRA-TGCGAACCAGGAATT-3′) and its complementary DNA (5′-AATTCCTGGTTCGCA-3′) were used and are mixed with MoS_2 nanosheets in a zigzag microchannel. Using this methodology, a detection limit of attomole level for DNA was achieved [103]. A slightly altered tactics was used by Jin and his group members for the detection of DNA [104]. As an alternative for dye labelling, thiol functionalization was employed while using Au-modified MoS_2 as a fluorescence probe to detect the target. The PL emission of MoS_2 observed at 1.84 eV gets tiny blue shift initially by Au deposition and continuously shifted with increasing concentration of A30-thiol target. Given that the bond formation between the Au and thiol group helps for the enhanced adsorption of DNA on MoS_2 surface (Fig. 9.11b). From the absence of peak shift after the target DNA mixing and its clear blue shift with mismatched DNA, one can easily differentiate the target DNA through PL analysis and the interactions of Au-MoS_2 with A30-SH also verified by DFT calculations.

MoS_2 nanosheets were also used in the design of protein fluorescent biosensor where the combination of terminal protection of small-molecule-linked DNA

(TPSMLD) and Exo III-aided DNA recycling amplification was adopted for the streptavidin protein testing. The minimum level (LOD) of streptavidin protein that can be detected by this route is 0.67 ng/mL. The high specificity of MoS_2 was confirmed from the less fluorescent signal observed in the presence of bovine serum, recombinant human TNF-α and immunoglobulin G [105]. A water-soluble thiol-functionalized atomic-thick-sheet fluorescent MoS_2 nanosheet was reported to sense dopamine through PL quenching. This sensor is working based on "turn-off" response and quenched the PL intensity in the range from 0.05 to 20 μM with a lower limit of 0.027 μM. The possible mechanism of do pamine sensing is stated as charge transfer by the stacking of MoS_2 layers through C–O···H–O bonding interaction [106].

Rhodamine B isothiocyanate (RhoBS) fluorescent dye adsorbed MoS_2 nanosheets were used by Yang et al. to detect Ag^+ ions in aqueous solution and living *E.coli* cells [107]. On the surface of MoS_2, Ag^+ reacts with RhoBS and detached from the surface as Ag nanoparticles. Hence the fluorescence intensity of RhoBS-MoS_2 complex was recovered and so it is a "turn-on" mode. As a non-toxic nanoprobe, it can sense Ag^+ ions down to 10 nM with great selectivity. Zhu et al. for the first time, employed the fluorogenic MoS_2 for the detection of DNA and small molecules like adenosine [108]. They have used a simple 'mix and detect' assay format to sense the analyte molecules within a few minutes. In 2014, aptamer-functionalized MoS_2 nano biosensor also exploited in the sensitive detection of prostate-specific antigen (PSA) [109]. When the target PSA binded to the aptamer, resulting in the release of aptamer probe away from the surface of the MoS_2 nanosheets. Thus the quenched fluorescence was restored and the sensor showed the 'turn-on' response to PSA. Further, by considering MoS_2 as a FL probe, a digital sensing assay was made by Singh et al. to detect the pathogens [110]. Initially, FL of fluorescin-tagged aptamer (Apt-FAM) was diminished by primary ssDNA as shown in Fig. 9.12. However, the target pathogen *S.typhimurium* binds to Apt-FAM and retaining its FL emission and the presence of target was noted from a digital 'yes' or 'no' type of response. The selectivity of MoS_2 is good for *S.typhimurium* over *E.coli* and *P.vulgaris* with a detection limit of 10 $CFU.mL^{-1}$. Similar kind of detection was made electrochemically to detect the food pathogen and chikungunya virus using MoS_2 as working electrode material [90, 111]. FRET-based fluorescence-sensing behaviour of water-soluble VS_2 QDs was disclosed for the first time by Du et al. [112]. In their work, 3.3 nm sized VS_2 QDs with unusual optical properties were used for the tracing of glutathione (GSH). By mixing MnO_2 nanosheets with VS_2 QDs, due to the FRET process, the inherent FL emissions of VS_2 QDs are lessened. Then it is recovered by the addition of GSH and this principle was applied for the sensing of GSH under UV and NIR excitations. On the contrary, with the cooperation of FAM-aptamer, fluorescence quenching ability of VS_2 NSs was exploited in the detection of protein, cytochrome C (Cyt C). It hinders the fluorescence of probe which is recollected again by incubating Cyt C target and giving a linear detection over the range of 0.75 nM to 50 μM [113].

Taking the advantage of intense emission merits of TMD QDs, exploring the shape, size and surface modification related sensing behaviour would be remarkable in the path of multifunctional sensor device designing. Dhenadhayalan et al. [114] reported the interesting results obtained from the three distinct surface functionalized

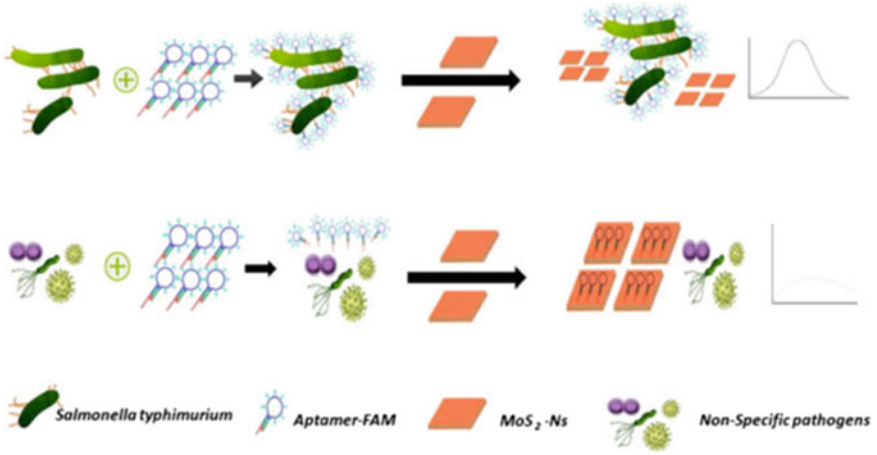

Fig. 9.12 Schematic representation of pathogens detection by MoS_2 Ns binded with Apt-FAM probe. Reprinted with permission from [110]. Copyright 2016 Springer Nature

$MoSe_2$ QDs. The $MoSe_2$/COOH, $MoSe_2/NH_2$ and $MoSe_2$/SH were synthesized by hydrothermal method and tested against Cu^{2+}, TNP and melamine (MA) respectively. The higher sensitivity of 4.6, 45.3 and 27. 7 nM in the detection of Cu^{2+}, TNP and MA follows the different mechanism as metal ion induced fluorescence turn-on, electron transfer and FRET process respectively which makes $MoSe_2$ a perfect chemosensor.

In the optical sensing platform, rarely p-type WSe_2 also used for the detection of DNA molecules. On the p-type WSe_2 monolayer, Han et al. hybridized Cy3 fluorescent dye and the doping and de-doping effect has been used as a mechanism of DNA sensing [115]. When the relative concentration of Cy3/probe DNA (p-DNA) is increased, PL intensity quenched and red shifted because of the p-type doping charge transfer effect (i.e. injection of excess holes). In contrast, target DNA (t-DNA) hybridization de-quenched and increased the PL intensity of WSe_2/Cy3/p-DNA system along with the repositioning of peak (blue shift). This de-doping effect is possibly originated from the charge and energy transfer to WSe_2 from Cy3/p-DNA/t-DNA. In addition to this, single layer TaS_2 NSs were prepared by Zhang et al. based on the lithium-intercalation method and tested for fluorescence biosensor [116]. While comparing the results of fluorescent detection of DNA, this TaS_2 possess high fluorescence quenching abilities and differential affinities towards ssDNA and dsDNA than MoS_2 and TiS_2. The 6-carboxyfluorescein (FAM)-labelled ssDNA probe exhibited strong fluorescence emission at the excitation of 494 nm (FAM) which then diminished by TaS_2 addition. It reveals the strong interaction between the ssDNA and TaS_2. However, the fluorescent emission was restored when the target DNA influenza A virus subtype H1N1 gene was added in it. This result suggests that dsDNA is having weaker interaction with TaS_2 than ssDNA. Table 9.3 summarizes the TMD-based fluorescent biosensors for the detection of different analytes.

Table 9.3 Summary of TMD-based fluorescent biosensors for the detection of different analyte molecules

Material	Target	Mode of operation	LOD	References
MoS_2-GQDs	EpCAM	Turn-on	450 pM	[95]
B, N-MoS_2	Hg^{2+}	Turn-on	Less than 1 nM	[96]
$MoSe_2$: CdS NHDs WSe_2:CdS NHDs	Pb^{2+}	Turn-off	0.5 μg L^{-1} 6.3 μg L^{-1}	[97]
MoS_2 QDs	2,4,6-trinitrophenol	Fluorescence quenching	95 nM	[98]
Cys-MoS_2 QDs	Al^{3+}	Turn-on	–	[99]
	Fe^{3+}	Turn-off		
MoS_2 Ns	Pb^{2+}	Turn-on	0.22 μM	[100]
	S^{2-}	Turn-off	0.42 μM	
RhoBS-MoS_2	Ag^{+}	Fluorescence recovery	< 10 nM	[107]
$MoSe_2$/COOH $MoSe_2/NH_2$ $MoSe_2$/SH	Cu^{2+}	Turn-on	4.6 nM	[114]
	2,4,6-trinitrophenol	Electron transfer	45.3 nM	
	Melamine	Energy transfer	27. 7 nM	
MoS_2 NSs	DNA	Turn-off	15 pM	[101]
MoS_2 Ns	DNA	Turn-off	500 pM	[103]
Au-MoS_2	DNA	Blueshift in PL peak	–	[104]
Single layered MoS_2 NSs	DNA	Dye quencher	0.5 fmol	[108]
p-WSe_2/Cy3	DNA	Doping and de-doping effect	–	[115]
TaS_2	DNA	Fluorescence quenching	0.05 nM	[116]
WS_2	Collagen peptide	Fluorescence recovery	21 nM	[102]
MoS_2 Ns	Streptavidin-biotin	Turn-on	0.67 ng/mL	[105]
TGA-MoS_2	Dopamine	Charge transfer	27 nM	[106]
MoS_2 Ns	Salmonella typhimurium	Digital YES/NO	10 CFU/mL	[109]
VS_2 QDs	Glutathione	Turn-on	3.5 μM	[112]
VS_2 Ns	Cytochrome C	Fluorescence quenching	0.50 nM	[113]

Ns nanosheets, *QDs* quantum dots, *PSA* prostate specific antigen, *TGA* thioglycolic acid, *GQDs* graphene quantum dots, *EpCAM* epithelial cell adhesion molecule

9.3.4 Colorimetric Sensors

Colorimetric sensing method is very simple as well as attractive due to its instant detection of analytes where it can be visualized directly by naked eyes. These sensors are potent for portable and inexpensive day-to-day life sensing applications as it does not require any sophisticated instrumentation for the analysis. For the detection of analytes, optical properties like absorption or surface plasmon resonance have been utilized. However, in most colorimetric methods, to catalyse the enzymatic chromogenic substance 3,3,5,5,-tetramethylbenzidine (TMB) and to produce the blue coloured reaction, peroxidase enzymes such as horseradish peroxidase (HRP) were adapted. On the other hand, the need for the development of peroxidase mimetics has been increased due to the expensive and time-consuming preparative procedures in the natural enzyme-based colorimetric methods. At this time, intrinsic peroxidase mimetic behaviour in TMDs was explored and are efficiently applied in the sensing of various biomolecules. In 2013, Lin's group has reported the peroxidase-like activity of WS_2 nanosheets and the colorimetric detection of H_2O_2 and glucose [117]. They also reported the analytical behaviour of MoS_2 nanosheets which is capable of catalysing TMB in the presence of H_2O_2. The catalytic activity of MoS_2

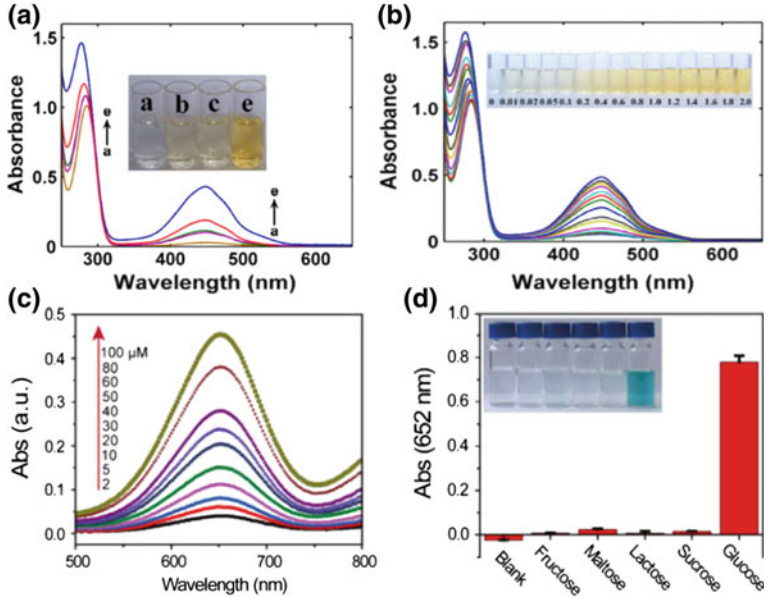

Fig. 9.13 **a** UV spectral changes of blank (**a**), $Fe^{2+}/OPD/H_2O_2$ (**b**), $MoS_2/OPD/H_2O_2$ (**c**), $Fe^{2+}/MoS_2/OPD/H_2O_2$ (**d**, theoretical) at t-1172 s; **b** absorption of spectra of $MoS_2/OPD/H_2O_2$ in the presence of different concentrations of Fe^{2+} ions (0–2.0 μM) Reprinted with permission from [121]. Copyright 2016 Elsevier. **c** UV Vis absorption spectra of VS_2 POx at different concentrations of H_2O_2 (2–100 μM); **d** anti-interference test of VS_2 POx over glucose with coexisting substances in fruit juice. Reprinted with permission from [125]. Copyright 2017 Springer Nature

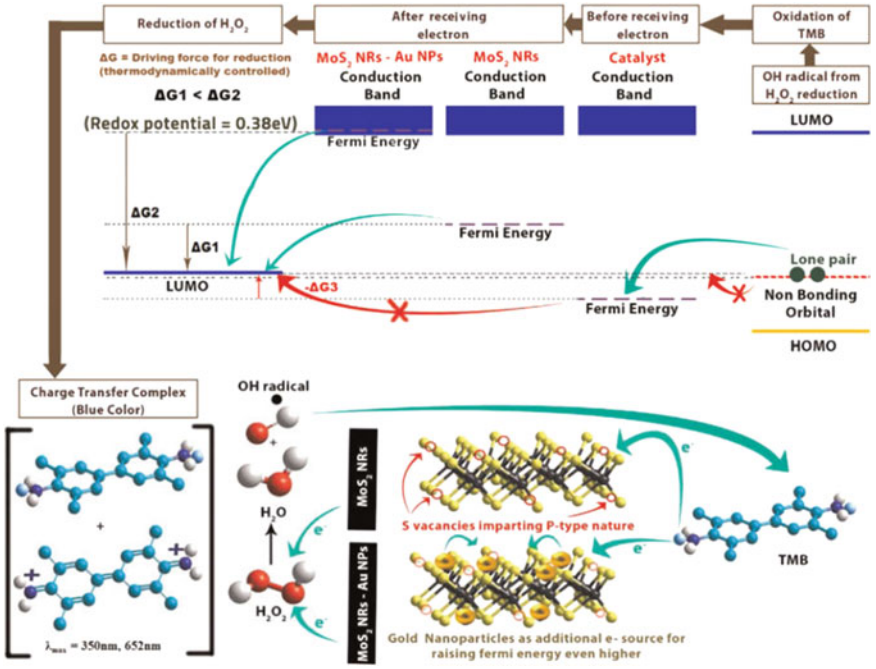

Fig. 9.14 Possible mechanism of colorimetric catalytic reactions during cholesterol sensing by TMB + MoS_2 NRs-Au NPs. Reprinted with permission from [123]. Copyright 2015 Elsevier

follows Michaelis-Menten kinetics and is dependent on temperature, pH, H_2O_2 concentration and reaction time [118]. Guo et al. also followed the similar strategy for their hydrothermally synthesized layered MoS_2 and achieved the sensitivity of 0.125–1.75 μM for H_2O_2 with a LOD of 0.08 μM [119]. Chen et al. synthesized the WS_2 nanosheets (NSs) and functionalized the Hemin (iron protoporphyrin) on its few layered structure via van der Waals interactions [120]. This assembled structure not only resolved the issues of Hemin (oxidative self-degradation and molecular aggregation) but also showed several advantages over HRP and other peroxidase mimetics, such as ease of preparation, low cost, stability, dispersibility and high catalytic efficiency. In glucose detection, hemin/WS_2 NSs showed a linear range 0.5×10^{-5} to 2.0×10^{-4} mol.L^{-1} with a LOD of 1.5 μM. Recently, luminescent MoS_2 nanosheet-based peroxidase mimetics was reported by Wang et al. for the label-free colorimetric sensing of Fe^{2+} ions [121]. It produces a yellow-coloured reaction during the catalytic oxidation of peroxidase substrate *o*-phenylendiamine (OPD) in the presence of H_2O_2 (Fig. 9.13a). Further addition of Fe^{2+} greatly enhanced the catalytic activity of nanosheets (Fig. 9.13b), and the origin of enhanced sensitivity and selectivity was analysed by multivariate curve resolution by alternating least squares (MCR-ALS) and time-dependent UV-Vis spectral studies and found to be its large reaction rate constant. Since the catalytic activity of the nanomaterials depends on

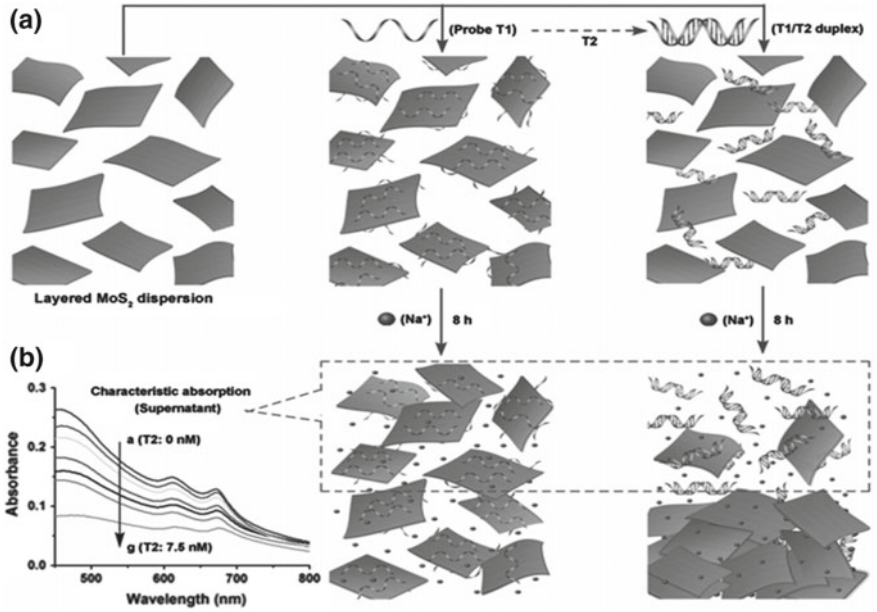

Fig. 9.15 **a** Illustration of label-free DNA biosensor based on ssDNA induced dispersion of 2D MoS_2 in aqueous salt solution; **b** absorption spectra of layered MoS_2 in the presence of different concentrations of target DNA (T2) for fixed concentration of probe DNA (T1). Reprinted with permission from [124]. Copyright 2015 John Wiley and Sons

their size and dispersibility, beyond the layered structure of MoS_2, particle-shaped MoS_2 functionalized with PVP also synthesized by Yu and his co-workers which is tested for H_2O_2 detection [122]. The biocompatibility of this 5 nm sized PVP-MoS_2 NPs is good which was verified by in vitro cytotoxicity and haemolysis studies. They have also obtained reliable results while measuring glucose concentration in serum by colorimetric strategy as well as electronic glucometer based on the electrochemical method. Increased cholesterol-related diseases demand for the economic, quick and reliable detection approach to check the level of cholesterol. Combining the high surface area MoS_2 along with gold nanoparticles, a long appreciated material in the colorimetric route, it is proven that synergistically enhanced detection of cholesterol is possible. Nirala et al. had experimented it and explained the mechanism of colorimetric catalytic reaction as high aspect ratio and electron transfer that provides better loading capacity and binding efficiency through the strong mechanical bonding with the analytes (Fig. 9.14) [123].

Like peroxidase mimetics activities, size-dependent optical absorption behaviour of MoS_2 can be utilized in the detection of DNA oligonucleotides. Based on the discrimination ability of MoS_2 on ssDNA and dsDNA, Li et al. considered it for the DNA sensor construction [124]. Aggregation of layered MoS_2 is more in a salt solution where the sedimentation of layered MoS_2 occurred subsequently. The coag-

ulation between MoS_2 layers gets inhibited upon the adsorption of ssDNA on its surface, which retains its original optical absorption ability. Whereas, dsDNA stayed away from the surface and hence the dispersion behaviour was remarkably weakened. Therefore, for the detection of DNA molecules, the size-dependent change in the optical absorption of layered MoS_2 can be effectively utilized (Fig. 9.15). VS_2 nanosheets, due to their unique properties and also its richness in natural enzymes, can possibly exploited in biocatalytic applications. Of late, for the first time, peroxidase-like activity was found in layered VS_2 nanosheets and reported by Huang's group [125]. Like MoS_2 and WS_2, VS_2 also possess good glucose detection capabilities in colorimetric measurements, with H_2O_2 as a co-substrate (Fig. 9.13c, d). The above survey clears that enzyme-mimic TMD nanomaterials could be useful in medical diagnosis of various bio-analytes.

9.4 Conclusions and Future Prospects

Herein, the recent works on TMDs-based electrochemical, photoluminescence and colorimetric biosensors were highlighted and discussed. Based on the current reports, it is absolutely clear that TMDs with peculiar layered structure and high specific surface area finds great variety of applications, especially in biosensors. However, finding solutions to some of the unresolved challenges can improve the sensing performance of TMDs. The performance of TMDs in biosensor is strongly related to different parameters like shape, size, number of layers, etc. Hence, the synthesis of composite materials with dimensionally different TMDs should be made for advanced sensing. Simple preparation routes also to be established for the fabrication of different TMD materials. Besides, large-scale synthesis of TMDs for industrial applications is still challenging because most of the reported TMD electrochemical biosensors were designed and fabricated at lab-scale. Mechanism of electron transfer between the TMDs and the biomaterials should be completely investigated for the better understanding of its interactions which can offer the improved sensitivity beyond the current detection limit. From the family of TMDs, only MoS_2 and WS_2 were mainly focused for biosensing applications. While other TMD nanomaterials were unnoticed by the researchers even they are potential to serve as working electrode in biosensor device. So, in the future, more light should shed to study the sensing activity of other TMD materials.

Acknowledgements Dr. P. R sincerely thanks Science and Engineering Research Board (DST-SERB), Government of India, New Delhi for the award of National Post Doctoral Fellowship (PDF/2016/001002).

References

1. Solanki PR, Kaushik A, Agrawal VV, Malhotra BD (2011) Nanostructured metal oxide-based biosensors. Npg Asia Mater 3:17
2. Shi X, Gu W, Li B, Chen N, Zhao K, Xian Y (2014) Enzymatic biosensors based on the use of metal oxide nanoparticles. Microchim Acta 181(1):1–22
3. George JM, Antony A, Mathew B (2018) Metal oxide nanoparticles in electrochemical sensing and biosensing: a review. Microchim Acta 185(7):358
4. Xia Y (2016) Optical sensing and biosensing based on non-spherical noble metal nanoparticles. Anal Bioanal Chem 408(11):2813–2825
5. Wang J (2012) Electrochemical biosensing based on noble metal nanoparticles. Microchim Acta 177(3):245–270
6. Justino CIL, Gomes AR, Freitas AC, Duarte AC, Rocha-Santos TAP (2017) Graphene based sensors and biosensors. TrAC Trends Anal Chem 91:53–66
7. Sha R, Badhulika S, Mulchandani A (2018) Graphene-based biosensors and their applications in biomedical and environmental monitoring. In: Schöning MJ, Poghossian A (eds) Label-free biosensing: advanced materials, devices and applications. Springer International Publishing, Cham, pp 261–290
8. Wang Z, Dai Z (2015) Carbon nanomaterial-based electrochemical biosensors: an overview. Nanoscale 7(15):6420–6431
9. Li H, Shi Y, Chiu M-H, Li L-J (2015) Emerging energy applications of two-dimensional layered transition metal dichalcogenides. Nano Energy 18:293–305
10. Peng W, Li Y, Zhang F, Zhang G, Fan X (2017) Roles of two-dimensional transition metal dichalcogenides as cocatalysts in photocatalytic hydrogen evolution and environmental remediation. Ind Eng Chem Res 56(16):4611–4626
11. Elham R, Rasoul M, Martin P (2018) Nanohybrids of two-dimensional transition-metal dichalcogenides and titanium dioxide for photocatalytic applications. Chem A Eur. J. 24 (1):18–31
12. Bissett MA, Worrall SD, Kinloch IA, Dryfe RAW (2016) Comparison of two-dimensional transition metal dichalcogenides for electrochemical supercapacitors. Electrochim Acta 201:30–37
13. Pumera M, Sofer Z, Ambrosi A (2014) Layered transition metal dichalcogenides for electrochemical energy generation and storage. J Mater Chem A 2(24):8981–8987
14. Schmidt H, Wang S, Chu L, Toh M, Kumar R, Zhao W, Castro Neto AH, Martin J, Adam S, Özyilmaz B, Eda G (2014) Transport properties of monolayer mos$_2$ grown by chemical vapor deposition. Nano Lett 14(4):1909–1913
15. Zhenyu D, Zhenwei W, Xin H, Xi-Xiang Z, AH N (2017) Large-area chemical vapor deposited MoS_2 with transparent conducting oxide contacts toward fully transparent 2D electronics. Adv Funct Mater 27(41):1703119
16. Okada M, Sawazaki T, Watanabe K, Taniguch T, Hibino H, Shinohara H, Kitaura R (2014) Direct chemical vapor deposition growth of WS_2 atomic layers on hexagonal boron nitride. ACS Nano 8(8):8273–8277
17. Ovchinnikov D, Allain A, Huang Y-S, Dumcenco D, Kis A (2014) Electrical transport properties of single-layer WS_2. ACS Nano 8(8):8174–8181
18. Iqbal MW, Iqbal MZ, Khan MF, Shehzad MA, Seo Y, Park JH, Hwang C, Eom J (2015) High-mobility and air-stable single-layer WS_2 field-effect transistors sandwiched between chemical vapor deposition-grown hexagonal BN films. Sci Rep 5:10699
19. Vattikuti SVP, Byon C, Reddy CV (2015) Synthesis of MoS_2 multi-wall nanotubes using wet chemical method with H_2O_2 as growth promoter. Superlattices Microstruct 85:124–132
20. Wet chemical thinning of molybdenum disulfide down to its monolayer (2014). APL Materials 2(9):092509
21. Štengl V, Tolasz J, Popelková D (2015) Ultrasonic preparation of tungsten disulfide single-layers and quantum dots. RSC Advances 5(109):89612–89620

22. Fu X, Ilanchezhiyan P, Mohan Kumar G, Cho HD, Zhang L, Chan AS, Lee DJ, Panin GN, Kang TW (2017) Tunable UV-visible absorption of SnS_2 layered quantum dots produced by liquid phase exfoliation. Nanoscale 9(5):1820–1826
23. Zhang X, Xiang J, Mu C, Wen F, Yuan S, Zhao J, Xu D, Su C, Liu Z (2017) SnS_2 nanoflakes anchored graphene obtained by liquid phase exfoliation and MoS_2 nanosheet composites as lithium and sodium battery anodes. Electrochim Acta 227:203–209
24. Qiao W, Yan S, Song X, Zhang X, He X, Zhong W, Du Y (2015) Luminescent monolayer MoS_2 quantum dots produced by multi-exfoliation based on lithium intercalation. Appl Surf Sci 359:130–136
25. Fan X, Xu P, Zhou D, Sun Y, Li YC, Nguyen MAT, Terrones M, Mallouk TE (2015) Fast and efficient preparation of exfoliated 2H MoS_2 nanosheets by sonication-assisted lithium intercalation and infrared laser-induced 1T to 2H phase reversion. Nano Lett 15(9):5956–5960
26. Dong HH, Ju HD, Seob CJ, Minsu P, Seok ST (2014) Dual role of blue luminescent MoS_2 quantum dots in fluorescence resonance energy transfer phenomenon. Small 10(19):3858–3862
27. Feldman Y, Frey GL, Homyonfer M, Lyakhovitskaya V, Margulis L, Cohen H, Hodes G, Hutchison JL, Tenne R (1996) Bulk synthesis of inorganic fullerene-like MS_2 (M = Mo, W) from the respective trioxides and the reaction mechanism. J Am Chem Soc 118(23):5362–5367
28. Scheffer L, Rosentzveig R, Margolin A, Popovitz-Biro R, Seifert G, Cohen SR, Tenne R (2002) Scanning tunneling microscopy study of WS_2 nanotubes. Phys Chem Chem Phys 4(11):2095–2098
29. Lin Y-C, Dumcenco DO, Huang Y-S, Suenaga K (2014) Atomic mechanism of the semiconducting-to-metallic phase transition in single-layered MoS_2. Nat Nanotechnol 9:391
30. Qinbai Y, Qipeng L, Xiao Z, Chaoliang T, Hua Z (2018) Three-dimensional architectures constructed from transition-metal dichalcogenide nanomaterials for electrochemical energy storage and conversion. Angew Chem Int Ed 57(3):626–646
31. Jun TR, M-MC C, Zdenek S, Martin P (2017) 1T-Phase WS_2 protein-based biosensor. Adv Funct Mater 27 (5):1604923
32. Nayak AP, Yuan Z, Cao B, Liu J, Wu J, Moran ST, Li T, Akinwande D, Jin C, Lin J-F (2015) Pressure-modulated conductivity, carrier density, and mobility of multilayered tungsten disulfide. ACS Nano 9(9):9117–9123
33. Barua S, Dutta HS, Gogoi S, Devi R, Khan R (2018) Nanostructured MoS_2-based advanced biosensors: a review. ACS Appl Nano Mater 1(1):2–25
34. Liu W, Wu X, Li X (2017) Gold nanorods on three-dimensional nickel foam: a non-enzymatic glucose sensor with enhanced electro-catalytic performance. RSC Adv 7(58):36744–36749. https://doi.org/10.1039/c7ra06909j
35. Tee SY, Teng CP, Ye E (2017) Metal nanostructures for non-enzymatic glucose sensing. Mater Sci Eng, C 70:1018–1030
36. Zhan H, Li J, Liu Z, Zheng Y, Jing Y (2015) A highly sensitive electrochemical OP biosensor based on electrodeposition of Au–Pd bimetallic nanoparticles onto a functionalized graphene modified glassy carbon electrode. Anal Methods 7(9):3903–3911
37. Janyasupab M, Liu C-W, Zhang Y, Wang K-W, Liu C-C (2013) Bimetallic Pt–M (M = Cu, Ni, Pd, and Rh) nanoporous for H_2O_2 based amperometric biosensors. Sens Actuators B: Chem 179:209–214
38. Ghodselahi T, Arsalani S, Neishaboorynejad T (2014) Synthesis and biosensor application of Ag@Au bimetallic nanoparticles based on localized surface plasmon resonance. Appl Surf Sci 301:230–234
39. Liu Y, Zhang X, He D, Ma F, Fu Q, Hu Y (2016) An amperometric glucose biosensor based on a MnO_2/graphene composite modified electrode. RSC Adv 6(22):18654–18661
40. Ponnusamy R, Chakraborty B, Rout CS (2018) Pd-Doped WO_3 Nanostructures as Potential Glucose Sensor with Insight from Electronic Structure Simulations. J Phys Chem B 122(10):2737–2746
41. Chen H, Rim YS, Wang IC, Li C, Zhu B, Sun M, Goorsky MS, He X, Yang Y (2017) Quasi-two-dimensional metal oxide semiconductors based ultrasensitive potentiometric biosensors. ACS Nano 11(5):4710–4718

42. Zhu Z (2017) An overview of carbon nanotubes and graphene for biosensing applications. Nano-Micro Lett 9(3):25
43. Wang L, Zhang Q, Chen S, Xu F, Chen S, Jia J, Tan H, Hou H, Song Y (2014) Electrochemical sensing and biosensing platform based on biomass-derived macroporous carbon materials. Anal Chem 86(3):1414–1421
44. Song J, Xu L, Zhou C, Xing R, Dai Q, Liu D, Song H (2013) Synthesis of graphene oxide based CuO nanoparticles composite electrode for highly enhanced nonenzymatic glucose detection. ACS Appl Mater Interfaces 5(24):12928–12934
45. Zhang Q, Luo Q, Qin Z, Liu L, Wu Z, Shen B, Hu W (2018) Self-assembly of graphene-encapsulated Cu composites for nonenzymatic glucose sensing. ACS Omega 3(3):3420–3428
46. Huang W, Ding S, Chen Y, Hao W, Lai X, Peng J, Tu J, Cao Y, Li X (2017) 3D NiO hollow sphere/reduced graphene oxide composite for high-performance glucose biosensor. Sci Rep 7(1):5220
47. Shan C, Yang H, Han D, Zhang Q, Ivaska A, Niu L (2010) Graphene/AuNPs/chitosan nanocomposites film for glucose biosensing. Biosens Bioelectron 25(5):1070–1074
48. Salimi A, Sharifi E, Noorbakhsh A, Soltanian S (2007) Immobilization of glucose oxidase on electrodeposited nickel oxide nanoparticles: direct electron transfer and electrocatalytic activity. Biosens Bioelectron 22(12):3146–3153
49. Su S, Sun H, Xu F, Yuwen L, Fan C, Wang L (2014) Direct electrochemistry of glucose oxidase and a biosensor for glucose based on a glass carbon electrode modified with MoS_2 nanosheets decorated with gold nanoparticles. Microchim Acta 181(13):1497–1503
50. Li J, Yang Z, Tang Y, Zhang Y, Hu X (2013) Carbon nanotubes-nanoflake-like SnS_2 nanocomposite for direct electrochemistry of glucose oxidase and glucose sensing. Biosens Bioelectron 41:698–703
51. Li J, Yang Z, Zhang Y, Yu S, Xu Q, Qu Q, Hu X (2012) Tin disulfide nanoflakes decorated with gold nanoparticles for direct electrochemistry of glucose oxidase and glucose biosensing. Microchim Acta 179(3):265–272
52. Lee K-T, Liang Y-C, Lin H-H, Li C-H, Lu S-Y (2016) Exfoliated SnS_2 nanoplates for enhancing direct electrochemical glucose sensing. Electrochim Acta 219:241–250
53. Zhong X, Yang H, Guo S, Li S, Gou G, Niu Z, Dong Z, Lei Y, Jin J, Li R, Ma J (2012) In situ growth of Ni–Fe alloy on graphene-like MoS_2 for catalysis of hydrazine oxidation. J Mater Chem 22(28):13925–13927
54. Chen Y-Y, Dong M, Wang J, Jiao H (2012) Mechanisms and energies of water gas shift reaction on Fe-, Co-, and Ni-Promoted MoS_2 catalysts. J Phys Chem C 116(48):25368–25375
55. Lin X, Ni Y, Kokot S (2016) Electrochemical and bio-sensing platform based on a novel 3D Cu nano-flowers/layered MoS_2 composite. Biosens Bioelectron 79:685–692
56. Huang J, He Y, Jin J, Li Y, Dong Z, Li R (2014) A novel glucose sensor based on MoS_2 nanosheet functionalized with Ni nanoparticles. Electrochim Acta 136:41–46
57. Ji S, Yang Z, Zhang C, Miao Y-E, Tjiu WW, Pan J, Liu T (2013) Nonenzymatic sensor for glucose based on a glassy carbon electrode modified with $Ni(OH)_2$ nanoparticles grown on a film of molybdenum sulfide. Microchim Acta 180(11):1127–1134
58. Wang T, Zhu H, Zhuo J, Zhu Z, Papakonstantinou P, Lubarsky G, Lin J, Li M (2013) Biosensor based on ultrasmall MoS_2 nanoparticles for electrochemical detection of H_2O_2 released by cells at the nanomolar level. Anal Chem 85(21):10289–10295
59. Yoon J, Lee T, Bapurao GB, Jo J, Oh B-K, Choi J-W (2017) Electrochemical H_2O_2 biosensor composed of myoglobin on MoS_2 nanoparticle-graphene oxide hybrid structure. Biosens Bioelectron 93:14–20
60. Karthik R, Vinoth Kumar J, Chen S-M, Sundaresan P, Mutharani B, Chi Chen Y, Muthuraj V (2018) Simple sonochemical synthesis of novel grass-like vanadium disulfide: A viable non-enzymatic electrochemical sensor for the detection of hydrogen peroxide. Ultrason Sonochem 48:473–481
61. Sarkar A, Ghosh AB, Saha N, Bhadu GR, Adhikary B (2018) Newly designed amperometric biosensor for hydrogen peroxide and glucose based on vanadium sulfide nanoparticles. ACS Appl Nano Mater 1(3):1339–1347

62. Zhu L, Zhang Y, Xu P, Wen W, Li X, Xu J (2016) PtW/MoS_2 hybrid nanocomposite for electrochemical sensing of H_2O_2 released from living cells. Biosens Bioelectron 80:601–606
63. Li K, Yan S, Chen H, Wang B, Li G, Shi Y, Xu X (2015) Facile solvothermal synthesis of hybrid SnS_2/platinum nanoparticles for hydrogen peroxide biosensing. J Bionanoscience 9(5):335–340
64. Loo AH, Bonanni A, Ambrosi A, Pumera M (2014) Molybdenum disulfide (MoS_2) nanoflakes as inherently electroactive labels for DNA hybridization detection. Nanoscale 6(20):11971–11975
65. Wang X, Nan F, Zhao J, Yang T, Ge T, Jiao K (2015) A label-free ultrasensitive electrochemical DNA sensor based on thin-layer MoS_2 nanosheets with high electrochemical activity. Biosens Bioelectron 64:386–391
66. Yang T, Chen M, Kong Q, Luo X, Jiao K (2017) Toward DNA electrochemical sensing by free-standing ZnO nanosheets grown on 2D thin-layered MoS_2. Biosens Bioelectron 89:538–544
67. Wang T, Zhu R, Zhuo J, Zhu Z, Shao Y, Li M (2014) Direct detection of DNA below ppb level based on thionin-functionalized layered MoS_2 electrochemical sensors. Anal Chem 86(24):12064–12069
68. Cao X (2014) Ultra-sensitive electrochemical DNA biosensor based on signal amplification using gold nanoparticles modified with molybdenum disulfide, graphene and horseradish peroxidase. Microchim Acta 181(9):1133–1141
69. Tao Y, Le M, Huaiyin C, Shizhong L, Weihua L, Kui J (2016) Synthesis of thin-layered molybdenum disulfide-based polyaniline nanointerfaces for enhanced direct electrochemical DNA detection. Adv Mater Interfaces 3(7):1500700
70. Shuai H-L, Huang K-J, Chen Y-X (2016) A layered tungsten disulfide/acetylene black composite based DNA biosensing platform coupled with hybridization chain reaction for signal amplification. J Mater Chem B 4(6):1186–1196
71. Huang K-J, Liu Y-J, Wang H-B, Gan T, Liu Y-M, Wang L-L (2014) Signal amplification for electrochemical DNA biosensor based on two-dimensional graphene analogue tungsten sulfide–graphene composites and gold nanoparticles. Sens Actuators B: Chem 191:828–836
72. Chu Y, Cai B, Ma Y, Zhao M, Ye Z, Huang J (2016) Highly sensitive electrochemical detection of circulating tumor DNA based on thin-layer MoS_2/graphene composites. RSC Adv 6(27):22673–22678
73. Zhao X, Xia X, Yu S, Wang C (2014) An electrochemical sensor for honokiol based on a glassy carbon electrode modified with MoS_2/graphene nanohybrid film. Anal Methods 6(23):9375–9382
74. Song H, Ni Y, Kokot S (2014) Investigations of an electrochemical platform based on the layered MoS_2–graphene and horseradish peroxidase nanocomposite for direct electrochemistry and electrocatalysis. Biosens Bioelectron 56:137–143
75. Huang K-J, Liu Y-J, Zhai Q-F (2015) Ultrasensitive biosensing platform based on layered vanadium disulfide–graphene composites coupling with tetrahedron-structured DNA probes and exonuclease III assisted signal amplification. J Mater Chem B 3(41):8180–8187
76. Xia X, Zheng Z, Zhang Y, Zhao X, Wang C (2014) Synthesis of Ag-MoS_2/chitosan nanocomposite and its application for catalytic oxidation of tryptophan. Sens Actuators B: Chem 192:42–50
77. Yang R, Zhao J, Chen M, Yang T, Luo S, Jiao K (2015) Electrocatalytic determination of chloramphenicol based on molybdenum disulfide nanosheets and self-doped polyaniline. Talanta 131:619–623
78. Li D, Liu X, Yi R, Zhang J, Su Z, Wei G (2018) Electrochemical sensor based on novel two-dimensional nanohybrids: MoS_2 nanosheets conjugated with organic copper nanowires for simultaneous detection of hydrogen peroxide and ascorbic acid. Inorg Chem Front 5(1):112–119
79. Wang L, Li J, Pan Y, Min L, Zhang Y, Hu X, Yang Z (2017) Platinum nanoparticle-assembled nanoflake-like tin disulfide for enzyme-based amperometric sensing of glucose. Microchim Acta 184(7):2357–2363. https://doi.org/10.1007/s00604-017-2209-0

80. Lin X, Ni Y, Kokot S (2016) Electrochemical cholesterol sensor based on cholesterol oxidase and MoS_2-AuNPs modified glassy carbon electrode. Sens Actuators B: Chem 233:100–106
81. Huang K-J, Wang L, Liu Y-J, Gan T, Liu Y-M, Wang L-L, Fan Y (2013) Synthesis and electrochemical performances of layered tungsten sulfide-graphene nanocomposite as a sensing platform for catechol, resorcinol and hydroquinone. Electrochim Acta 107:379–387
82. Yan P, Yu-Zhong Z, Yong L (2013) Layer-by-layer self-assembled multilayer films of single-walled carbon nanotubes and tin disulfide nanoparticles with chitosan for the fabrication of biosensors. J Appl Polym Sci 128(1):647–652
83. Huang K-J, Liu Y-J, Shi G-W, Yang X-R, Liu Y-M (2014) Label-free aptamer sensor for 17β-estradiol based on vanadium disulfide nanoflowers and Au nanoparticles. Sens Actuators B: Chem 201:579–585
84. Huang K-J, Liu Y-J, Zhang J-Z, Liu Y-M (2014) A novel aptamer sensor based on layered tungsten disulfide nanosheets and Au nanoparticles amplification for 17β-estradiol detection. Anal Methods 6(19):8011–8017
85. Chand R, Ramalingam S, Neethirajan S (2018) A 2D transition-metal dichalcogenide MoS_2 based novel nanocomposite and nanocarrier for multiplex miRNA detection. Nanoscale 10(17):8217–8225
86. Liu X, Shuai H-L, Huang K-J (2015) A label-free electrochemical aptasensor based on leaf-like vanadium disulfide-Au nanoparticles for the sensitive and selective detection of platelet-derived growth factor BB. Anal Methods 7(19):8277–8284
87. Sakthivel M, Sukanya R, Chen S-M, Dinesh B (2018) Synthesis of two-dimensional Sr-Doped $MoSe_2$ nanosheets and their application for efficient electrochemical reduction of metronidazole. J Phys Chem C 122(23):12474–12484
88. Wang Y, Zhuang Q, Ni Y (2015) Fabrication of riboflavin electrochemical sensor based on homoadenine single-stranded DNA/molybdenum disulfide–graphene nanocomposite modified gold electrode. J Electroanal Chem 736:47–54
89. Yang T, Chen M, Nan F, Chen L, Luo X, Jiao K (2015) Enhanced electropolymerization of poly(xanthurenic acid)–MoS_2 film for specific electrocatalytic detection of guanine and adenine. J Mater Chem B 3(24):4884–4891
90. Singhal C, Khanuja M, Chaudhary N, Pundir CS, Narang J (2018) Detection of chikungunya virus DNA using two-dimensional MoS_2 nanosheets based disposable biosensor. Sci Rep 8(1):7734
91. Lin C, Zhu X, Feng J, Wu C, Hu S, Peng J, Guo Y, Peng L, Zhao J, Huang J, Yang J, Xie Y (2013) Hydrogen-incorporated TiS_2 ultrathin nanosheets with ultrahigh conductivity for stamp-transferrable electrodes. J Am Chem Soc 135(13):5144–5151
92. Gan X, Zhao H, Chen S, Yu H, Quan X (2015) Three-dimensional Porous HxTiS2 nanosheet-polyaniline nanocomposite electrodes for directly detecting trace Cu(II) Ions. Anal Chem 87(11):5605–5613
93. Askim JR, Mahmoudi M, Suslick KS (2013) Optical sensor arrays for chemical sensing: the optoelectronic nose. Chem Soc Rev 42(22):8649–8682
94. Mak KF, Lee C, Hone J, Shan J, Heinz TF (2010) Atomically Thin MoS_2: a new direct-gap semiconductor. Phys Rev Lett 105(13):136805
95. Shi J, Lyu J, Tian F, Yang M (2017) A fluorescence turn-on biosensor based on graphene quantum dots (GQDs) and molybdenum disulfide (MoS_2) nanosheets for epithelial cell adhesion molecule (EpCAM) detection. Biosens Bioelectron 93:182–188
96. Liu X, Li L, Wei Y, Zheng Y, Xiao Q, Feng B (2015) Facile synthesis of boron- and nitride-doped MoS_2 nanosheets as fluorescent probes for the ultrafast, sensitive, and label-free detection of Hg^{2+}. Analyst 140(13):4654–4661
97. Karfa P, Madhuri R, Sharma PK (2017) Multifunctional fluorescent chalcogenide hybrid nanodots ($MoSe_2$:CdS and WSe_2:CdS) as electro catalyst (for oxygen reduction/oxygen evolution reactions) and sensing probe for lead. J Mater Chem A 5(4):1495–1508
98. Wang Y, Ni Y (2014) Molybdenum disulfide quantum dots as a photoluminescence sensing platform for 2,4,6-trinitrophenol detection. Anal Chem 86(15):7463–7470

99. Qian W, Xiaojie W, Yingnan J, Weiyi S, Chuanxi W, Minghui Y, Chi Z (2018) MoS_2-QD-based dual-model photoluminescence sensing platform for effective determination of Al^{3+} and Fe^{3+} simultaneously in various environment. ChemistrySelect 3(8):2326–2331
100. Wang Y, Hu J, Zhuang Q, Ni Y (2016) Label-free fluorescence sensing of lead(II) ions and sulfide ions based on luminescent molybdenum disulfide nanosheets. ACS Sustain Chem & Eng 4(5):2535–2541
101. Huang J, Ye L, Gao X, Li H, Xu J, Li Z (2015) Molybdenum disulfide-based amplified fluorescence DNA detection using hybridization chain reactions. J Mater Chem B 3(11):2395–2401
102. Sun X, Fan J, Fu C, Yao L, Zhao S, Wang J, Xiao J (2017) WS_2 and MoS_2 biosensing platforms using peptides as probe biomolecules. Sci Rep 7(1):10290
103. Huang Y, Shi Y, Yang HY, Ai Y (2015) A novel single-layered MoS_2 nanosheet based microfluidic biosensor for ultrasensitive detection of DNA. Nanoscale 7(6):2245–2249
104. Jin K, Xie L, Tian Y, Liu D (2016) Au-modified monolayer MoS_2 sensor for DNA detection. J Phys Chem C 120(20):11204–11209
105. Xiang X, Shi J, Huang F, Zheng M, Deng Q, Xu J (2015) MoS_2 nanosheet-based fluorescent biosensor for protein detection via terminal protection of small-molecule-linked DNA and exonuclease III-aided DNA recycling amplification. Biosens Bioelectron 74:227–232
106. Xu B, Su Y, Li L, Liu R, Lv Y (2017) Thiol-functionalized single-layered MoS_2 nanosheet as a photoluminescence sensing platform via charge transfer for dopamine detection. Sens Actuators B: Chem 246:380–388
107. Yang Y, Liu T, Cheng L, Song G, Liu Z, Chen M (2015) MoS_2-Based nanoprobes for detection of silver ions in aqueous solutions and bacteria. ACS Appl Mater Interfaces 7(14):7526–7533
108. Zhu C, Zeng Z, Li H, Li F, Fan C, Zhang H (2013) Single-layer MoS_2-based nanoprobes for homogeneous detection of biomolecules. J Am Chem Soc 135(16):5998–6001
109. Kong R-M, Ding L, Wang Z, You J, Qu F (2015) A novel aptamer-functionalized MoS_2 nanosheet fluorescent biosensor for sensitive detection of prostate specific antigen. Anal Bioanal Chem 407(2):369–377
110. Singh P, Gupta R, Sinha M, Kumar R, Bhalla V (2016) MoS_2 based digital response platform for aptamer based fluorescent detection of pathogens. Microchim Acta 183(4):1501–1506
111. Singh C, Ali MA, Kumar V, Ahmad R, Sumana G (2018) Functionalized MoS_2 nanosheets assembled microfluidic immunosensor for highly sensitive detection of food pathogen. Sens Actuators B: Chem 259:1090–1098
112. Du C, Shang A, Shang M, Ma X, Song W (2018) Water-soluble VS_2 quantum dots with unusual fluorescence for biosensing. Sens Actuators B: Chem 255:926–934
113. Yin X, Cai J, Feng H, Wu Z, Zou J, Cai Q (2015) A novel VS_2 nanosheet-based biosensor for rapid fluorescence detection of cytochrome c. New J Chem 39(3):1892–1898
114. Dhenadhayalan N, Lin T-W, Lee H-L, Lin K-C (2018) Multisensing capability of $MoSe_2$ quantum dots by tuning surface functional groups. ACS Appl Nano Mater 1(7):3453–3463
115. Kyu Hyun H, Jun Young K, Seong Gi J, Changwon S, Jeongyong K, Jinsoo J (2017) Sensitive optical bio-sensing of p-type WSe_2 hybridized with fluorescent dye attached DNA by doping and de-doping effects. Nanotechnology 28(43):435501
116. Ying Z, Bing Z, Changfeng Z, Xiao Z, Chaoliang T, Hai L, Bo C, Jian Y, Junze C, Ying H, Lianhui W, Hua Z (2015) Single-layer transition metal dichalcogenide nanosheet-based nanosensors for rapid, sensitive, and multiplexed detection of DNA. Adv Mater 27(5):935–939
117. Lin T, Zhong L, Song Z, Guo L, Wu H, Guo Q, Chen Y, Fu F, Chen G (2014) Visual detection of blood glucose based on peroxidase-like activity of WS_2 nanosheets. Biosens Bioelectron 62:302–307
118. Lin T, Zhong L, Guo L, Fu F, Chen G (2014) Seeing diabetes: visual detection of glucose based on the intrinsic peroxidase-like activity of MoS_2 nanosheets. Nanoscale 6(20):11856–11862
119. Guo X, Wang Y, Wu F, Ni Y, Kokot S (2015) A colorimetric method of analysis for trace amounts of hydrogen peroxide with the use of the nano-properties of molybdenum disulfide. Analyst 140(4):1119–1126
120. Chen Q, Chen J, Gao C, Zhang M, Chen J, Qiu H (2015) Hemin-functionalized WS_2 nanosheets as highly active peroxidase mimetics for label-free colorimetric detection of H_2O_2 and glucose. Analyst 140(8):2857–2863

121. Wang Y, Hu J, Zhuang Q, Ni Y (2016) Enhancing sensitivity and selectivity in a label-free colorimetric sensor for detection of iron(II) ions with luminescent molybdenum disulfide nanosheet-based peroxidase mimetics. Biosens Bioelectron 80:111–117
122. Yu J, Ma X, Yin W, Gu Z (2016) Synthesis of PVP-functionalized ultra-small MoS_2 nanoparticles with intrinsic peroxidase-like activity for H_2O_2 and glucose detection. RSC Adv 6(84):81174–81183
123. Nirala NR, Pandey S, Bansal A, Singh VK, Mukherjee B, Saxena PS, Srivastava A (2015) Different shades of cholesterol: gold nanoparticles supported on MoS_2 nanoribbons for enhanced colorimetric sensing of free cholesterol. Biosens Bioelectron 74:207–213
124. Lin LB, Lin ZH, Lu L, Yu Y, Lei LJ, Qun LH, Bing LN (2015) Size-dependent optical absorption of layered MoS_2 and DNA oligonucleotides induced dispersion behavior for label-free detection of single-nucleotide polymorphism. Adv Func Mater 25(23):3541–3550
125. Huang L, Zhu W, Zhang W, Chen K, Wang J, Wang R, Yang Q, Hu N, Suo Y, Wang J (2017) Layered vanadium(IV) disulfide nanosheets as a peroxidase-like nanozyme for colorimetric detection of glucose. Microchim Acta 185(1):7

Chapter 10
Electronic Devices Based on Transition Metal Dichalcogenides

Jiaxu Yan and Ze Xiang Shen

Abstract In spite of the tremendous development in the semiconductor industry, the Moore's Law is believed to soon reach its limit and traditional microelectronic devices are currently facing challenges such as high energy consumption and the short-channel effect. As an alternative, two-dimensional (2D) layered transition metal dichalcogenide (TMDC) materials show the ability to restrain the carriers in a 1 nm physical limit and demonstrate high carrier mobility, tunable band gap, and excellent manufacture compatibility, which will hopefully give birth to revolutionary changes in nanoelectronics. In this chapter, we review the most recent progress of 2D TMDC in field-effect transistors (FETs). We present the achievements in carrier mobility and electrical contacts. We also point out the emerging directions for further development.

Keywords Transition metal dichalcogenides · Field-effect transistors · Mobility · Electrical contact

10.1 Introduction

In the era of digital information, the core status of semiconductor technology is increasingly prominent. With the 10 nm technology node and beyond, the semiconductor industry faces unprecedented challenges over power consumption issues caused by the short-channel effects. In order to overcome the power consumption

J. Yan
Key Laboratory of Flexible Electronics (KLOFE),
Jiangsu National Synergistic Innovation Center for Advanced Materials (SICAM), Institute of Advanced Materials (IAM),
Nanjing Tech University (Nanjing Tech), Nanjing,
People's Republic of China

J. Yan · Z. X. Shen (✉)
Division of Physics and Applied Physics,
School of Physical and Mathematical Sciences (SPMS), Nanyang Technological University,
Nanyang Link 21,
Singapore 637371, Singapore
e-mail: zexiang@ntu.edu.sg

N. S. Arul and V. D. Nithya (eds.), *Two Dimensional Transition Metal Dichalcogenides*,
https://doi.org/10.1007/978-981-13-9045-6_10

problem brought about by large-scale integration and maintain the cost advantage brought by Moore's Law, the new device technology in the post-Moore era, featuring new materials, new structures, and new principles, has become an important frontier of nanoelectronics.

Discovery of graphene has diverted the interest to the two-dimensional (2D) layered materials as the most promising alternative for the next-generation nanoelectronics, owing to its excellent carrier mobility. Unfortunately, the lack of band gap limits the further possible applications in semiconductor technology. Among the 2D materials family, the transition metal dichalcogenides (TMDCs), in which transition metal (M) is sandwiched between two chalcogen atoms (X), have various band gaps and solve the biggest bottleneck of graphene, ranging from the visible to the near-infrared [1]. Among TMDCs, MoS_2, WS_2, $MoSe_2$, and WSe_2 are semiconductor materials with a band gap of 1–2 eV, good air stability and process compatibility and can be synthesized by chemically vapor deposition (CVD) method, which are best suited for transistors in digital electronics [2]. In addition, TMDCs can be easily combined to form Van der Waals heterojunctions for the possible applications of tunneling transistors, photodiodes, photodetectors, and other prototype devices [3], independent of the limitations of lattice matching in traditional semiconductor epitaxy growth.

10.1.1 2D TMDC-Based Transistors

In principle, the semiconductor TMDCs possess the three main advantages as the channel materials for the efficient switching devices: Optimum balance between high mobility and on/off ratio, ultrathin 2D layered structure with the thickness of <1 nm and great process compatibility with traditional Si-based technologies. Figure 10.1 compares the on/off ratio and mobility of various unconventional channel materials. Semiconducting TMDCs (s-TMDCs) are placed at vantage points compared to other semiconductors [4]. Such high mobility can still be maintained at the limit thickness due to the atomic-scale clean surfaces without chemical dangling bonds. Unlike conventional semiconductors in which the mobility drop drastically with the sixth power of the thickness decrease to 10 nm or less, TMDCs can maintain high mobility even in the case of a single layer, e.g., 410 $cm^2\ V^{-1}\ s^{-1}$ at room temperature [5], is much higher than Si with equivalent thickness.

As early as 1996, T. Löher et al. conducted a preliminary study on the principle of carrier transport at the interface between $MoTe_2$ and WSe_2 [6]. In the same year, R. Tenne et al. reported on the electrical properties exhibited by the WSe_2 thin-film devices, and its carrier mobility could reach 19.2 cm^2/Vs [7]. However, after more than ten years, due to bottlenecks in the material preparation process, research on TMD semiconductor devices entered a low tide. Until the last decade, with the improvement of controllability of TMDC semiconductor materials and the emergence of new device structures, the application of TMDCs to semiconductor devices has once again entered the academic field of vision. In 2004, Podzorov et al. [8]

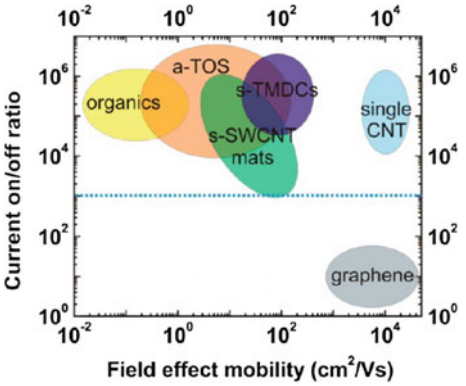

Fig. 10.1 Summary of on/off ratio and mobility of possible next-generation channel materials [4]. Copyright 2014. Reproduced with permission from the American Chemical Society

began to study the transition metal sulfide FETs, which opened the study sequence of TMDCs-FET. In this way, the MoS_2 device possesses high mobility, high on/off ratio, and ideal subthreshold slope are of special interests. Although the theoretical mobility of MoS_2 devices can reach 200–400 $cm^2\ V^{-1}\ s^{-1}$ [5], previously experimental mobilities are too low (lower than 10 $cm^2\ V^{-1}\ s^{-1}$ [9, 10]) for practical devices.

Subsequent studies by Chen et al. [11] and Konar et al. [12] show that the mobility of the device can be effectively enhanced by introducing a high dielectric constant of the gate dielectric layer. The reason is that the high dielectric constant gate medium can effectively reduce the Coulomb impurity scattering by dielectric screening.

The first monolayer MoS_2 field-effect transistor with high on/off ratio (up to 10^8) was realized in 2011 by the Kis group, setting off a research boom in TMDC [13] (Fig. 10.2). The carrier mobility at room temperature can reach 60–70 $cm^2\ V^{-1}\ s^{-1}$ and the device had a low subthreshold swing (74 mV dec^{-1}). In addition, MoS_2-based FET also has good electrostatic regulation [14] and can well avoid short-channel effects [15]. In 2012, Kim et al. [16] reported a multilayer MoS_2 FETs with a single back-gated insulator of 50-nm-thick Al_2O_3 by atomic layer deposition (ALD). The corresponding devices show high electron mobility (>100 cm^2/Vs), near-ideal subthreshold swings (~70 mV/dec), and a stable saturation current over a large voltage window. They further verify the experimental results through simulations based on Shockley's long-channel transistor model and calculations of scattering mechanisms. Zou et al. [17] demonstrated high-performance top-gated MoS_2 transistors using a unique design of a hexagonal boron nitride (h-BN)/HfO_2 dielectric heterostructure, in which few-layer BN grown by CVD serves as a buffer layer and high-κ HfO_2 suppresses Coulomb scattering. The device shows high room-temperature mobility up to 104 cm^2/Vs, and the on/off ratio can reach close to 10^8.

The atomic thickness of <1 nm effectively suppresses the short-channel effect and reduces the power consumption during operation, which is expected to extend the lifespan of Moore's Law [18]. Si transistors will fail below 5 nm gate lengths due to severe short-channel effects, in which direct source-to-drain tunneling occurs

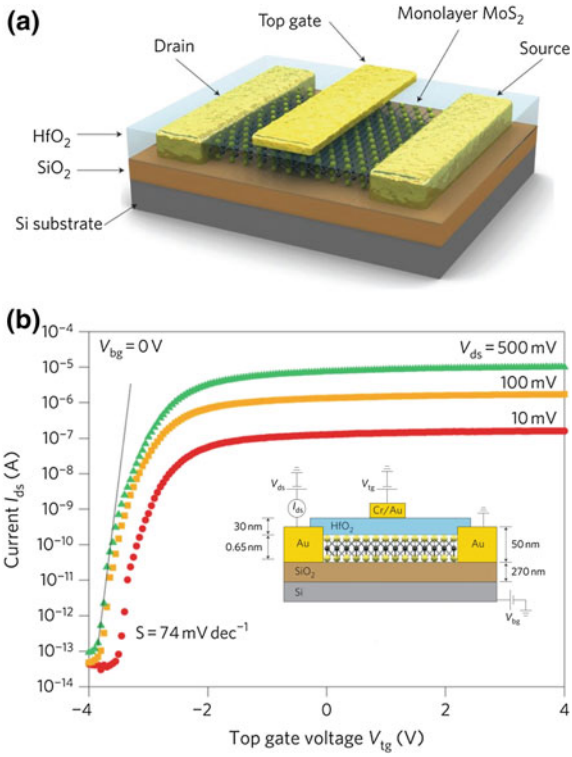

Fig. 10.2 **a** Schematic model of MoS_2 monolayer transistors. Monolayer MoS_2 is covered by 30 nm of ALD-deposited HfO_2 as a gate dielectric. **b** $I_{ds} - V_{tg}$ curve recorded for a bias voltage ranging from 10 to 500 mV. For $V_{ds} = 500$ mV, the I_{on}/I_{off} ratio is $>1 \times 10^8$ in the measured range while the subthreshold swing $S = 74$ mV dec^{-1}. Insert: Cross-sectional view of the monolayer MoS_2 FET [13]. Copyright 2011. Reproduced with permission from Nature

with the loss of gate electrostatic control on the channel. MoS_2 has been shown theoretically more than two orders of magnitude reduction in leakage currents to Si in the OFF state, as shown in Fig. 10.3a, b. In 2016, Desai et al. constructed a MoS_2 field-effect transistor (FET) with a 1 nm physical gate (Fig. 10.3c) with excellent switching characteristics with an on/off current ratio of 10^6 and a subthreshold swing of 65 mV/dec (Fig. 10.3d) using a single-walled carbon nanotube as the gate electrode, demonstrating that MoS_2 can be used as the ideal channel materials at the sub-5 nm scaling limit [19].

In layer dependence study, Li et al. [20] found that the thinner the conductive material, the lower the electron mobility for the MoS_2 field-effect transistor when number of layers, NL is <5 (Fig. 10.4a–c). It is mainly because the interaction distance between the charged impurities, i.e., adsorbed gas molecules, and the carrier is shortened as the thickness of MoS_2 is reduced, especially to the single atomic layer, which leads to the enhancement of the interface Coulomb scattering. The scattering ability of the carrier is far more than the phonon scattering, which greatly affects the electronic transport. More specifically, as thickness increases, the effect of the substrate or charge impurities can be mitigated to some extent, leading to a mobility enhancement. For thick samples (NL > 5), the situation is changed [21]. The additional interlayer resistance associated with an increasing NLs reverses this

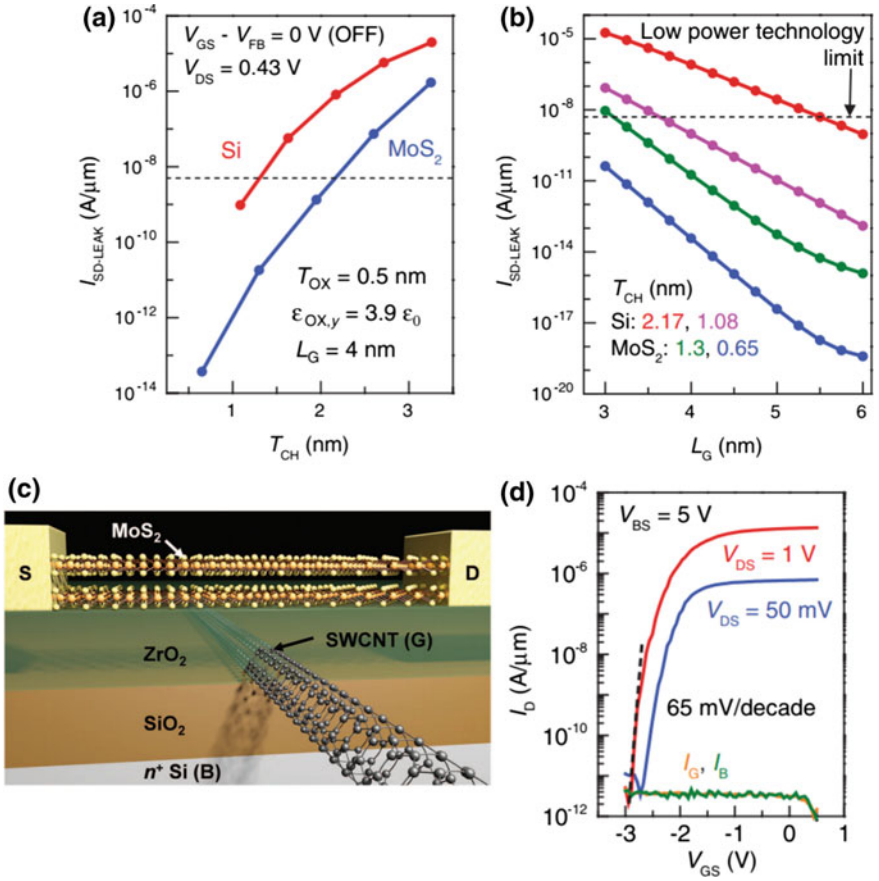

Fig. 10.3 Calculated direct source-to-drain tunneling leakage current ($I_{SD\text{-}LEAK}$) (**a**) and $I_{SD\text{-}LEAK}$ versus gate length (**b**) with the change of channel thickness for Si and MoS_2 at OFF state. **c** Schematic of FET with a MoS_2 channel and single-walled carbon nanotube (SWCNT) gate. **d** $I_D - V_{GS}$ characteristics of a bilayer MoS_2 channel SWCNT gated FET at $V_{BS} = 5$ V and $V_{DS} = 50$ mV and 1 V [19]. Copyright 2016. Reproduced with permission from the American Chemical Society

trend and leads to an effectively lower total mobility of the devices. According to the resistor network model (Fig. 10.4d, f), a non-monotonic trend of carrier mobility for multilayer MoS_2 materials as a function of channel thickness is shown, giving rise to a maximum mobility value for a finite layer thickness. For example, to achieve the maximum potential of MoS_2 for high-performance device applications, a ~10-nm-thick multilayer MoS_2 flake should be adopted. Similar trends in mobility were also found by Lin et al. at low temperature [22].

As mentioned above, unlike the process challenges and power consumption in conventional Si channel materials for sub-5 nm CMOS technology nodes, TMDCs

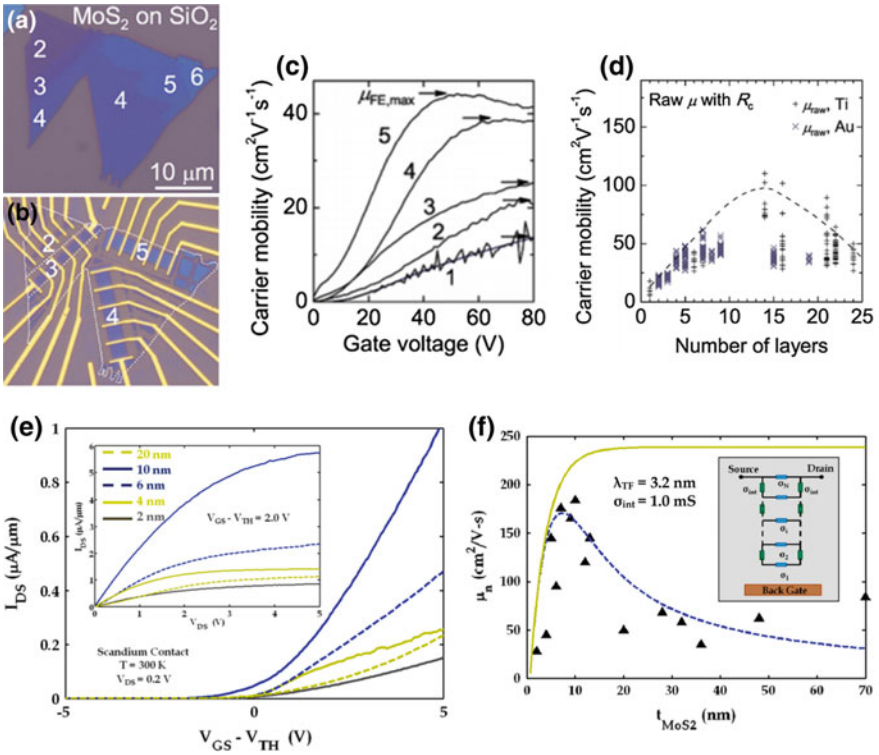

Fig. 10.4 **a** Optical images for MoS_2 flakes with various layer number and **b** corresponding FET devices. **c** and **d** carrier mobility as a function of channel thickness [20]. **e** Transfer characteristics of MoS_2 FETs with different thickness for $V_{DS} = 0.2$ V. Insert: The output characteristics for a gate overdrive voltage of 2 V. **f** Summarized effective carrier mobility as a function of the MoS_2 thickness. The dotted line is a fit to the experimental data (triangle) using a resistor network model (inset), while the solid line is the calculated mobility without any interlayer resistance [21]. Copyright 2013. Reproduced with permission from the American Chemical Society

are ideal channel materials owing to their ultrathin body thickness and good mobility at nm thinness.

In addition, chemical vapor deposition (CVD) of TMD is a compatible growth method with CMOS process integration and suitable for ultrathin body formation. In 2014, Chen et al. [23] integrated few-layer MoS_2 with a silicon-based fin field-effect transistor (Fin-FET), which is fully compatible with silicon-based complementary metal–oxide–semiconductor (CMOS) process. In 2016, they further reported silicon-based integrated U-shaped MoS_2 transistors (Fig. 10.5). Using doped poly-Si as the source/leak, CVD MoS_2 deposition creates a channel between the source and leak. The 10 nm grid length of the MoS_2 p-MOSFET device exhibits excellent performance: Switch ratio > 10^5, I_{on} > 150 μA/μm [24].

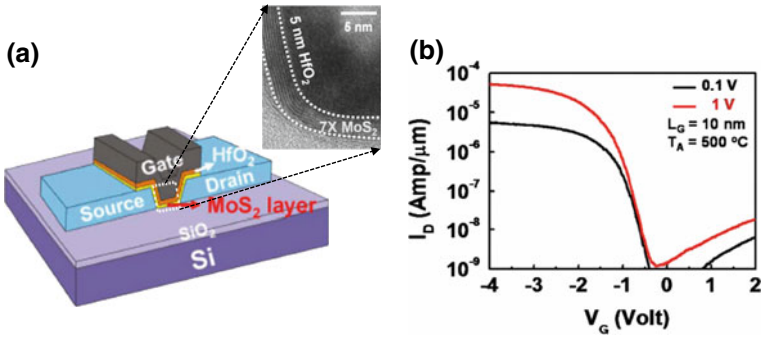

Fig. 10.5 **a** Schematic model of the U-shape MoS_2 p-MOSFET device. Insert: cross-sectional TEM image of U-shape MoS_2 transistor. **b** I_D versus V_G of a 10 nm channel MoS_2 transistor with $I_{on}/I_{off} > 10^5$ [24]. Copyright 2016. Reproduced with permission from IEEE

10.2 Factors Related to Electronic Performance

In theoretical, due to the intrinsic phonon scattering, the room-temperature mobility is predicted at ~410 $cm^2\ V^{-1}\ s^{-1}$, which is set as an upper limit for the experimental achievement [5, 25]. However, the experimentally obtained carrier mobility is too low to be applicable to real device [26, 27]. Figure 10.6 shows the typical structure of the FET and the flow of electrons. The electrons are first injected into the channel from the source electrode. The channel is then injected into the drain electrode. In this process, there are mainly three interfaces that affect device performance. One is the contact between the metal electrode (A region) and the MoS_2 channel (B region), in which a large contact resistance may exist [28]. The study of the metal-MoS_2 contact interface is called contact electronics. Second is that MoS_2 can metallize when it contacts with a metal electrode. A new barrier is formed between the metallized MoS_2 (B′ region) and the non-metallized MoS_2 (C region) interface in the channel. Third, carriers are scattered by Coulomb impurities or phonons (C region) at the interface formed between the MoS_2 channel and the gate insulating layer. There are two main aspects responsible for the device performance in TMDCs-based FETs [29]: (1) carrier injection at the electrode/channel contacts and (2) carrier scattering within the conduction channels. Therefore, we only consider the relevant factors at the A/B interfaces and C region. This part will discuss TMDC transistor contacts, including the main means to reduce the contact resistance and the electronic transport properties in TMDC using MoS_2 as an example.

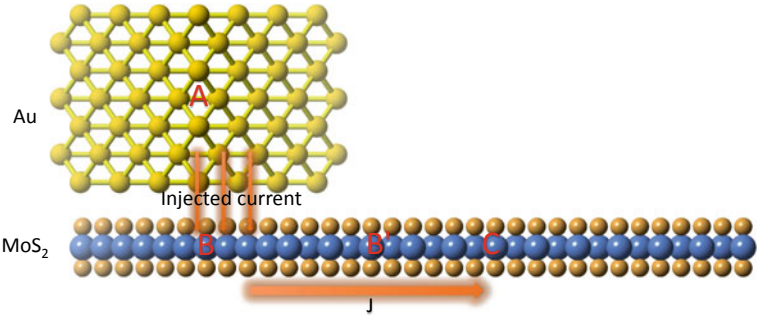

Fig. 10.6 Schematic cross-sectional view of a typical FET and the pathway of electrons. A, B, B′ and C represent different regions from Au to MoS_2

10.3 TMDC Electrical Contact

Since TMDC has no chemical bonds on the surface, it cannot bond with metal, leading to high Schottky barrier and low carrier injection efficiency. The contact resistance is typically more than an order of magnitude higher than that in Si-based MOSFETs, and this is a major limiting factor in device currents especially in short-channel conditions. Therefore, lowering contact resistance is the key issue for improving TMDC transistor performance. In the past few years, various methods have been used to effectively reduce the contact resistance, mainly including metal-TMDC, graphene-TMDC, TMDC phase-change contacts and tunneling contacts (Fig. 10.7). This section describes the progress of the current TMDC transistor electrical contact from these four aspects.

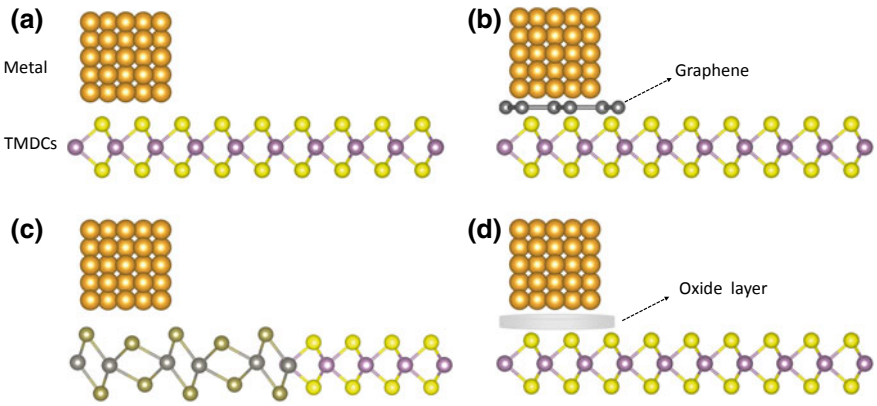

Fig. 10.7 Electrical contact types of 2D semiconductor TMDC transistor: **a** Metal–semiconductor contact; **b** graphene contact; **c** phase transition contact; **d** tunneling contact

10.4 Metal-TMDC Contact

Typical metal-single-layer TMDC contact resistance is in the order of 1–100 kΩ μm, which is 1–3 orders of magnitude higher compared to that of Si-based CMOS devices. Generally speaking, the method of reducing the metal-TMDC contact resistance is divided into two categories: The first is to choose the type of contact electrode metal, making its work function similar to that of the channel material; the second is doping the channel material, changing the carrier density of the channel material, and hence improving the contact resistance of the interface. This part will systematically explain the reduction in the contact resistance from these two aspects.

10.4.1 Effect of Different Metals on Contact

Interfacial Schottky barrier, proportional to the energy-level difference of two coupled materials, can be reduced by making contact between n-type (or p-type) semiconductor and low (or high) work function metals. In 2012, Das et al. [21] compared the difference in the performance of MoS_2 devices using different contact electrodes metals (Pt, Ni, Sc, and Ti). They found that for an n-type MoS_2 device, a low work function metal Sc can achieve higher performance electron injection and low contact resistance (Fig. 10.8a). Walia et al. [30] compared metals Al, W, Au, and Pt as contact electrodes and found that the Al and W electrode with low work function are able to facilitate the electron transport, while the hole transport is dominant with high work function metal electrodes, e.g., Au and Pt (Fig. 10.8b). In 2012, Tománek et al. [28] conducted theoretical studies on the electronic structure, bonding, and geometry of metal-monolayer MoS_2 contact regions using ab initio density functional theory. They found that the charge carrier density at the Au–MoS_2 interface is very low and the electron transport is mainly of a tunneling nature with low electron injection efficiency; while the Ti–MoS_2 interface displays a high density of delocalized states at the Fermi level that can form a low-resistance ohmic contact. It is worth noting that the measured output I-V characteristics using Au contacts are linear, indicating electrically ohmic contacts to MoS_2. Such observation seems counterintuitive to the above analysis that high work function metal (i.e., Au) will increase the Schottky barrier for n-type MoS_2. Actually, owing to the ultrathin MoS_2, a tunneling current is responsible for the observed linear or electrically ohmic behavior even with high work function metal contacts. In 2013, Banerjee et al. [31] reported a high-performance multilayer MoS_2 transistors with low contact resistance (~0.8 kΩ μm) using Ti as the electrode. It was found that the edge contacts between Ti and MoS_2 increased electron injection efficiency between channels. Later, the layer-dependent interfacial barrier at Au/MoS_2 contacts was reported [32]. The barrier increases from 0.3 to 0.6 eV as the layer number of MoS_2 changes from five to one layer, as a result of quantum confinement. Furthermore, the dependence of electrical transport properties on channel lengths ranging from 2 μm down to 50 nm in MoS_2-based MOSFETs

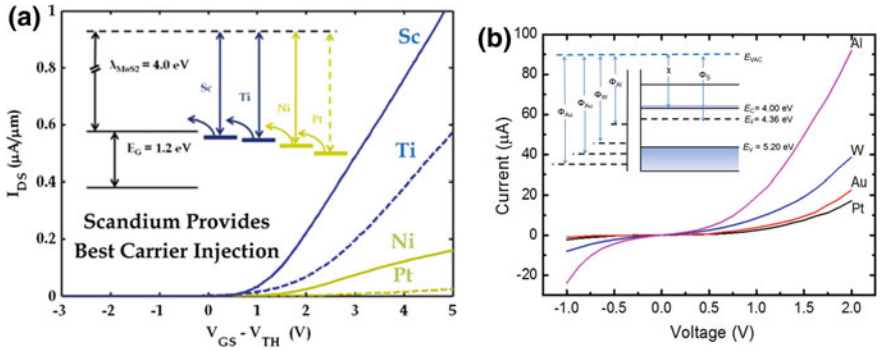

Fig. 10.8 I-V characteristics for different metal/MoS_2 contacts under identical bias conditions [21, 30]. Copyright 2013. Reproduced with permission from the American Chemical Society and Institute of Physics. Insert: The realistic band alignments

was examined [15]. No obvious short-channel effects on the device with 100 nm channel length were found. In 2014, using tunneling barriers (Van der Waals gap of metal-TMDC interface), Schottky barrier (Fermi level difference at metal-TMDC interface) and orbital overlap (overlapping of electron cloud of metal-TMDC interface), three indices were systematically evaluated for interfacial contact between different metals and a single layer of MoS_2 [33, 34]. They found that metals Ti and Mo can form ohmic contacts with a single layer of MoS_2. The former originates from the Ti–MoS_2 interface with small tunneling barrier and improved the electron injection efficiency; while the latter is due to the higher lattice matching of the Mo–MoS_2 contact interface, resulting in higher electron injection efficiency. Subsequently, in experiments, the team measured the contact resistance between MoS_2–Ti and MoS_2–Mo is 1.3 kΩ μm [35] and 2 kΩ μm [36], respectively.

10.4.2 Effect of Doping on Contact

Heavy doping reduces the Schottky barrier height, and the metal–semiconductor contact current is greatly enhanced by tunneling. For conventional semiconductors, doping can be precisely controlled by impurity diffusion or ion implantation. For two-dimensional TMDC semiconductor materials, their atomically smooth surfaces without dangling bonds and atomic-scale thickness hinder the effective doping. However, their ultrathin 2D nature allows the exploration of novel approaches, such as chemical and molecular doping. Javey et al. have performed a series of pioneering studies on surface charge doping in TMDC FETs [37, 38]. In 2012, they adopted the patterned NO_2 molecules chemisorption on WSe_2 for hole injection to lower the contact resistance. Later, using potassium, degenerate n-doping of few-layer MoS_2 and WSe_2 semiconductors were achieved. In 2013, Ye et al. proposed a sim-

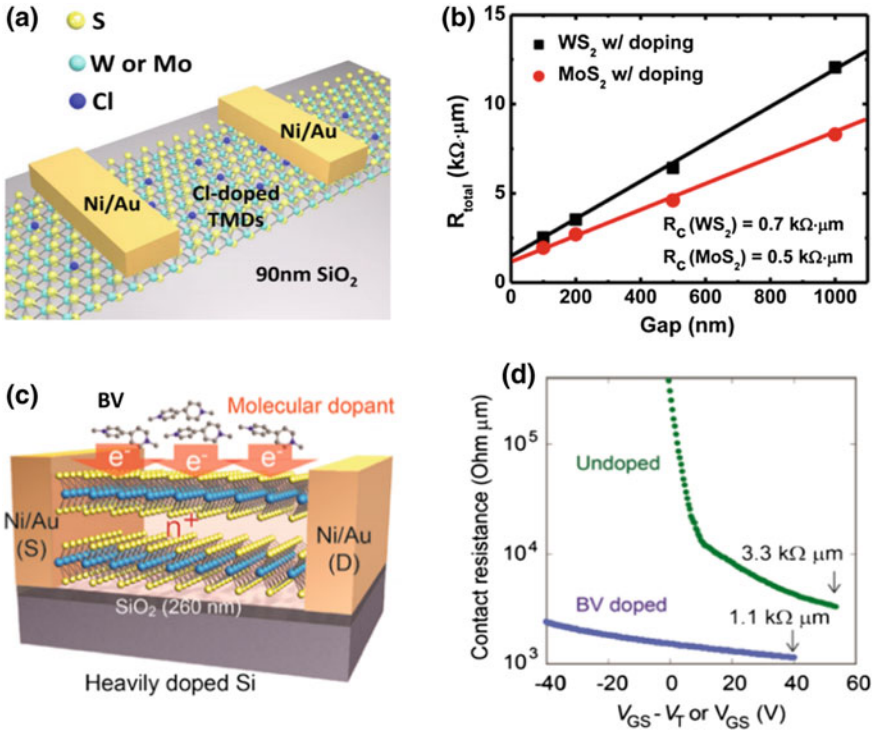

Fig. 10.9 **a** Schematic illustration of a Cl-doped back-gated MoS_2/WS_2 FET and the measured contact resistance, **b** after doping [42]. Copyright 2014. Reproduced with permission from the American Chemical Society. **c** Schematic illustration of a BV surface charge transfer doped back-gated MoS_2 FET and **d** the measured contact resistance before (green curve) and after (blue curve) BV doping [41]. Copyright 2014. Reproduced with permission from the American Chemical Society

ple method to incorporate doping in few-layer MoS_2 FETs by soaking the devices in polyethyleneimine (PEI) solutions as n-type surface dopants [39]. Owing to the reduction in sheet resistance and contact resistance, the device performances in ON-current and mobility are effectively improved. At present, there are many reports on surface charge transport doping of two-dimensional semiconductor TMDC [37–41]. In 2014, the Javey team used benzyl viologen (BV) as a surface charge transport donor to achieve effective n-type doping of MoS_2 [41]. They found that MoS_2 FET fabricated by using the Ni/Au electrode has a contact resistance of 3.3 kΩ μm before the doping and a contact resistance of 1.1 kΩ μm after the doping (Fig. 10.9c, d). Moreover, this doping method has the characteristics of air stable and no degradation. In addition, the effect of doping can be eliminated by soaking in toluene reagent.

The alternative approach is to introduce new elements into TMDC channel materials to achieve effective doping. Yang et al. [42] proposed a method of soaking thin slices of MoS_2 into dichloroethane (DCE) to achieve n-type chlorine doping of 2D TMDC materials. After doping, the chlorine atoms occupy the sulfur atom vacancy

in MoS_2 and WS_2, causing the Fermi level to shift upward and the Schottky barrier is reduced. The contact resistance of Ni–WS_2 and Ni–MoS_2 systems is effectively reduced to 0.7 and 0.5 kΩ μm (Fig. 10.9a, b). Due to the presence of many sulfur atom vacancies in MoS_2 and WS_2, the doping concentration of corresponding chlorine atoms is very high. The multilayer WS_2 and MoS_2 can achieve high doping densities of 6.0×10^{11} cm^{-2} and 9.2×10^{12} cm^{-2} at zero grid voltage. For MoS_2 FET devices with ferromagnetic Co electrodes, with the insertion of a thin MgO [43] or TiO_2 [44] oxide barrier between the Co electrode and the MoS_2 flake, the Schottky barrier height can be reduced drastically. Here, the integration of a thin oxide layer could simultaneously bypasses the conductivity mismatch problem while minimizing carrier depletion near the contacts.

The high-κ dielectric oxides can also serve as the effective charge transfer dopants for the doping of monolayer MoS_2. In 2015, Rai et al. [45] adopted (ATO) amorphous titanium suboxide thin film as a high-κ dopant in monolayer MoS_2 transistor using an Ag/Au electrode. The effective n-doping of ATO resulted in low contact resistance of about 180 Ω μm, with the room-temperature mobility increased to 102 cm^2 V^{-1} s^{-1}. Theoretical calculations show that ATO doping is an interface with oxygen vacancies modulation. ATO doping not only effectively reduces the Schottky barrier, but also acts as a high dielectric material that can effectively shield Coulomb impurity scattering. Subsequently, in 2017, Pop et al. [46] performed *n*-type doping of MoS_2 by depositing a layer of unsaturated alumina AlO_x on the channel surface of a single-layer MoS_2 transistor. The contact resistance is reduced to 480 Ω μm, and the ON-current is increased to 700 μA/μm.

10.4.3 Graphene-TMDC Contact

Graphene-TMDC contact refers to the use of graphene as an electrode and TMDC as a contact material for channel formation (Fig. 10.7b). Graphene is a 2D semimetal with ultra-high mobility and can realize the atomic-scale contact interface with TMDC. Graphene has a zero band gap, and its work function can be controlled by the gate voltage effectively reducing the Schottky barrier. Graphene can form two kinds of graphene-based contacts to TMDCs, i.e., top contact and edge contact. For graphene top contacts, Liu et al. [47] have shown that with proper gate voltage control, graphene and MoS_2 can form a good contact, realizing a true zero barrier and linear output characteristic at low temperatures (less than 19 K). Due to a very small contact barrier, their MoS_2-FETs achieve a low-temperature field-effect mobility of 1300 cm^2 V^{-1} s^{-1} (Fig. 10.10a). Here, one should note that there is still a large contact resistance for graphene top contacts, due to the existing Van der Walls gap between graphene and MoS_2. To reduce the contact resistance height, Thong et al. [48] developed a nickel-etched graphene electrode on MoS_2 using a dry transfer method and a metal-

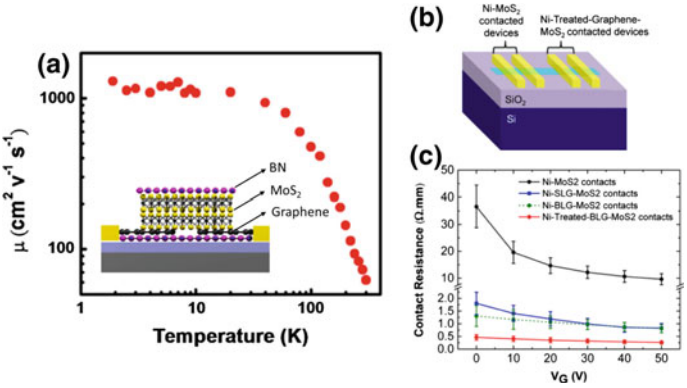

Fig. 10.10 **a** The measured field-effect mobility of a BN/graphene/MoS_2/BN FET with graphene contacts [47]. Copyright 2015. Reproduced with permission from the American Chemical Society. **b** Schematic illustration of back-gated MoS_2 FET fabricated with four different types of contacts and **c** the corresponding measured contact resistances [48]. Copyright 2015. Reproduced with permission from the American Chemical Society

catalyzed graphene treatment process (Fig. 10.10b). The contact resistance between nickel-etched graphene electrode and MoS_2 are only approximately 200 Ω μm. Compared to pure nickel electrodes, the contact resistance is reduced by two orders of magnitude due to the very low work function of the nickel graphene electrode and the presence of zigzag edges on the treated graphene (Fig. 10.10c), which enhances the tunneling efficiency between graphene and nickel [49].

To reduce the effects of MoS_2's extrinsic scattering, Dean et al. [50] proposed a Van der Waals heterojunction device, where the device is wrapped in the two layers of h-BN MoS_2, using graphene as electrodes. Magnetic transport results show that six layers of MoS_2 devices at low temperatures get a Hall mobility record of up to 34,000 $cm^2\ V^{-1}\ s^{-1}$, confirming that the previous low-temperature characteristics were dominated by external interface impurities, including both long-range Coulomb impurities and short-range defects, instead of the scattering centers within the bulk. They also used this structure to fabricate dual-grid FETs. Studies have shown that they have high-quality electrical contact. The mobility of carriers at both ends is 33–151 $cm^2\ V^{-1}\ s^{-1}$ at room temperature, and the subthreshold swing is 80 mV/dec [51].

10.4.3.1 Phase-Change Contact

Phase-change contact refers to the use of multiple phases of a two-dimensional material for different parts of a device: The semiconductor phase acts as a channel, the

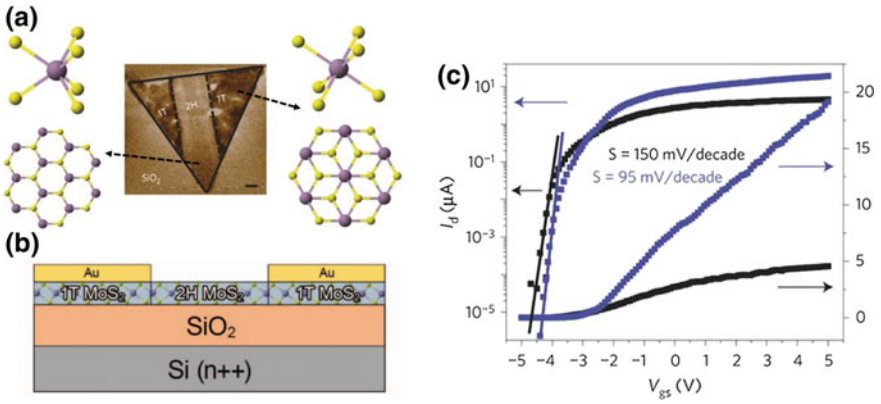

Fig. 10.11 **a** Atomic models and optical images of 2H- and 1T-TMDs. The different color contrast shows locally patterned 2H (bright color) and 1T (dark color) phases [54]. Copyright 2014. Reproduced with permission from Nature. **b** Schematic of device structure with 1T phase contact. **c** Transfer characteristics of top-gated MoS_2 FET. Blue curves represent devices with 1T phase contact and the black curves are with Au contact on the 2H phase [55]. Copyright 2014. Reproduced with permission from the Institute of Physics

metal phase acts as an electrode, and the two phases are connected by chemical bonds, making contact in a seamless manner (Fig. 10.7c). The method of the phase-change contact interface has no Van der Waals energy gap and has atomic-level contact boundaries, enabling the efficient injection of carriers. As shown in Fig. 10.11a, monolayer MoS_2 delivers two distinct symmetries: the trigonal prismatic 2H and octahedral 1T phases. The 2H phase exhibits semiconducting and the 1T is metallic. Through intralayer atomic plane gliding, the 1T phase was the first reported to transform from 2H–MoS_2 by Li and K intercalation [52, 53]. One can use the metal 1T phase as the electrode and the semiconductor 2H phase as the channel material to create a seamless MoS_2 FET [54, 55]. Tests have shown that the contact resistance is 200–300 Ω μm at zero gate voltage, which mainly comes from the apparent atomic-level grain boundary between the 1T phase and the 2H phase (Fig. 10.11b). This is one of the lowest reported contact resistances. Phase-change contact opens up a new route for phase engineering toward the future development of integrated design of TMDC FETs. However, current means of inducing phase transitions are implemented through solution processing methods [53] or Ar-plasma bombardment [56] with organic adsorbents or induced defects. To reduce the contact resistance via phase engineering technique, a facile, clean, controllable, and scalable approach is desperately needed.

10.4.3.2 Tunneling Contact

When an ultrathin insulating layer is inserted into the contact interface between the metal and the two-dimensional TMDC, a metal–insulator–semiconductor (MIS) is formed, which can reduce the Schottky barrier height and contact resistance (Fig. 10.7d). Such MIS sandwich structures were designed to reduce the Schottky barriers of metal contacts to Si [57], Ge [58], and Group III–V semiconductors [59, 60]. The reduction of the effective Schottky barrier height has been ascribed to the attenuation of metal-induced gap states in the insulator and/or electronic dipole formation at the insulator–semiconductor interface [61]. Recently, inserting an ultrathin tunneling layer into the metal-MoS_2 interface is adopted to reduce the Schottky barrier height and various insulating oxides are involved, such as MgO [44], TiO_2 [43], Ta_2O_5 [61]. Initially, the thin insulating layer in the MIS structure used was MgO and TiO_2. The experimental results show that the insulating layer can effectively reduce the Schottky barrier height, but the contact resistance has not been quantified. In 2016, Wong et al. used Ta_2O_5 as the tunneling layer to fabricate a MoS_2–Ta_2O_5–Ti/Au MIS structure. Via thickness optimization analysis of the insulating layer, it was found that when the Ta_2O_5 is 1.5 nm, the Schottky barrier of the metal in contact with CVD-MoS_2 is reduced to 29 meV. However, these ultrathin oxide tunneling layers are difficult to be deposited directly on the MoS_2 surface without dangling bonds. Thus, 2D insulating materials are proposed instead of 3D oxide insertion. Wang et al. [62] used CVD h-BN as the tunneling insulation layer to reduce the Schottky barrier height and improved the metal-MoS_2 contact resistance. The 1–2 layers of h-BN have atomic-level ultrathin thicknesses, producing only a small tunneling resistance, which greatly reduces the Schottky barrier height from 158 to 32 meV and the contact resistance from 5.2 to 1.8 kΩ μmm. The MoS_2 FET can have field-effect mobility of 73 $cm^2\ V^{-1}\ s^{-1}$ and output current of 330 μA/μm at room temperature due to the optimization of the tunneling contact. At 77 K, the mobility and output current increase to 321.4 $cm^2\ V^{-1}\ s^{-1}$ and 572 μA/μm, respectively. Subsequently, Cui et al. [63] produced a mechanically stripped monolayer *h*-BN wrapped monolayer MoS_2. The sandwich structure, using metal Co as the electrode, realizes a low-temperature ohmic contact. The *h*-BN not only reduces the Schottky barrier of the interface as a tunneling insulating layer, but also modulates the work function of the metal electrode Co, resulting a greatly improved contact interface at a low temperature of 20 K. The contact resistance at a carrier concentration of $5.3 \times 10^{12}/cm^2$ was approximately 3 kΩ μm, and the extracted Schottky barrier was 16 meV. Good contact made the SdH oscillation of monolayer MoS_2 observable under lower carrier concentration, which provided a rare platform for the study of the inherent properties of monolayer MoS_2 (Fig. 10.12).

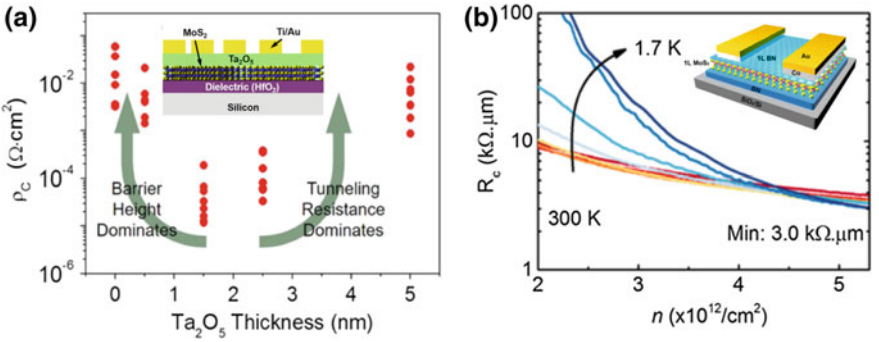

Fig. 10.12 **a** Measured contact resistance as a function of Ta_2O_5 layer thickness in FETs [61]. **b** Measured contact resistance as a function of temperature for Co/h-BN/1L MoS_2 FET [63]. Copyright 2017. Reproduced with permission from the American Chemical Society

10.5 TMDC Mobility

Although TMDC is an important candidate for extended Moore's Law, recent studies have shown that their electron transport is limited by many external factors. The experimental mobility reported so far is far below the theoretical limit of phonon scattering. For example, the theoretical phonon-limited mobility of single-layer MoS_2 and WS_2 at room temperature is approximately 410 $cm^2\ V^{-1}\ s^{-1}$ [5] and 1100 $cm^2\ V^{-1}\ s^{-1}$ [64], respectively; however, for these two materials, the experimental values can only reach 150 $cm^2\ V^{-1}\ s^{-1}$ [65] and 80 $cm^2\ V^{-1}\ s^{-1}$ [66]. Therefore, the mobility problem seriously affects the performance of TMDC device. Through the study of electron transport [2, 67–69], these external factors mainly include semiconductor–dielectric interface coulomb impurity (CIs) scattering, intrinsic electron-phonon (*e-ph*) scattering, oxide surface-optical (SO) phonon scattering, and defects (Fig. 10.13). They will significantly reduce the carrier scattering free path, thereby reducing the mobility.

10.5.1 Intrinsic Electron-Phonon Scattering

In the absence of any external scattering source, the mobility of the material is limited by the interaction between electrons and different types of lattice phonons (Fig. 10.13a). The intrinsic phonon limit mobility is a very important concept that determines the highest mobility that can be achieved for perfect samples without impurities and defects, which can be used as a yardstick to evaluate the quality of experimental samples. Kaasbjerg et al. [5] found that the internal phonon scattering rates are derived from the interactions between electrons and longitudinal acoustic (LA) phonons, transverse acoustical (TA) phonons, intravalley polar TO phonons,

intervalley polar LO, and homopolar optical phonons. The sum of the intensity of these effects will change with temperature: As shown in Fig. 10.14a, below 100 K, the internal phonon-limited mobility in monolayer MoS_2 is mainly determined by the acoustic phonon and follows a $\mu \sim T^{-1.7}$ temperature dependence. As the temperature rises, the role of carriers and internal phonons is dominated by LO phonons, so that the phonon-limited mobility is linear with T^{-1}.

At 300 K, if Coulomb impurity scattering and the surface of the optical phonon scattering are not considered, the mobility can be achieved 410 $cm^2\ V^{-1}\ s^{-1}$ in monolayer MoS_2 dominated by optical phonon scattering via intra and intervalley deformation potential couplings and the Fröhlich interaction.

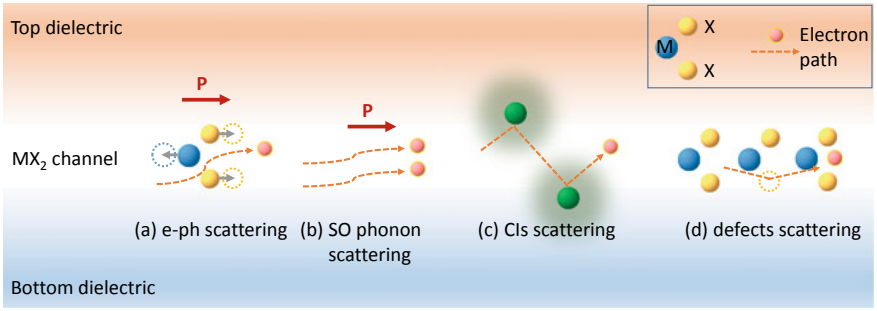

Fig. 10.13 Electron transport mechanism in MoS_2 channel device. **a** Electron-phonon scattering; **b** SO phonon scattering; **c** coulomb impurity scattering; **d** defection scattering [69]. Copyright 2014. Reproduced with permission from Wiley-VCH Verlag GmbH & Co. KGaA

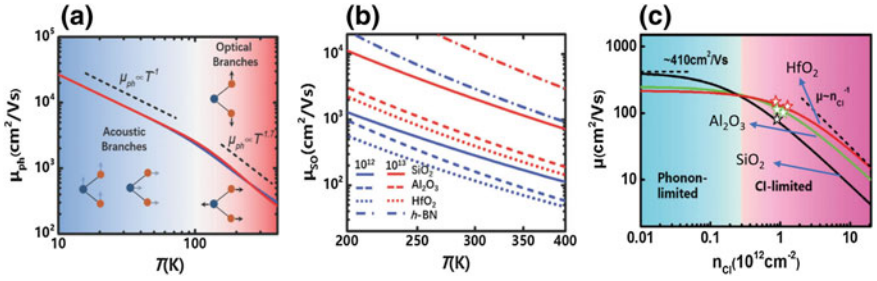

Fig. 10.14 **a** Phonon-limited carrier mobility in monolayer MoS_2 with varying the temperature. **b** Calculated surface-optical (SO) phonon-limited carrier mobility for different substrates [69]. Copyright 2004. Reproduced with permission from Wiley-VCH Verlag GmbH & Co. KGaA. **c** Predicted carrier mobility as a function of the concentration of Coulomb impurities (CIs) on SiO_2, Al_2O_3, and HfO_2 substrate, compared to the starred experimental data [65]. Copyright 2014. Reproduced with permission from Wiley-VCH Verlag GmbH & Co. KGaA

10.5.2 Optical Phonons on Oxide Surfaces

In semiconductors, electrons can excite phonons in the surrounding dielectric material through long-range Coulomb interactions if the dielectrics support polar vibrational modes. In high-κ insulators, e.g., HfO_2, the chemical bonds between metal–oxygen atoms are very likely to polarize, creating a locally polarized electric field at the interface. In silicon [70, 71], organic transistor [72, 73], and graphene [74, 75] devices, it has been widely observed that the remote interfacial phonon or surface-optical (SO) phonon is determined by the phonon mode energy of the interface material, and the lower the energy its phonon mode is, the more significant the scattering of carrier transport is. As shown in Fig. 10.13b, the dielectric near MoS_2 provides support for the polar vibration mode, resulting in a SO phonon in the oxide surface. Yu et al. [69] calculated the temperature-dependent SO phonon-limited mobility μ_{SO} for different dielectric materials and different carrier concentration. As shown in Fig. 10.14b, they found that the high-κ dielectric significantly degrades FET carrier mobility. Because of the effect of carrier screening, the dominant mobility of remote interface phonon scattering will gradually increase with the increase of carrier concentration. At the same time, the remote interface phonon shows a strong temperature dependence, and its scattering will rapidly increase with the increase of temperature, resulting in a rapid decline in mobility. Therefore, SO phonon scattering is one of the main sources of high-temperature scattering of the MoS_2 FET device since SO phonons are more thermally populated at higher temperatures. Moreover, as the surface field strength of the material increases and the dielectric constant becomes larger, the energy of the surface-optical phonon will gradually decrease, leading to even stronger interfacial phonon scattering. For materials with multiple long-range phonon modes (hexagonal boron nitride (*h*-BN), etc.), the remote phonon scattering is a superposition of several modes.

10.5.3 Coulomb Impurity Scattering

In a 2D system, since the carriers are distributed on the surface, their transmission is severely scattered by the charged impurities (CIs) distributed at the interface of the channel and the dielectric. Each CI will produce a long-range Coulomb potential field $V(d)$, where d is the interaction distance. Figure 10.13c shows that the scattering potentials generated by the two CIs located on the upper and lower surfaces of the trench interface. The carriers in monolayer MoS_2 are confined within 1 nm, leading to a small d. Since the scattering potential $V(d)$ is proportional to $1/d$, the scattering intensity in monolayer MoS_2 is much stronger than on the thick ones. Experiments have shown that the CIs are one of the main factors affecting mobility in crystalline Si FETs [76], graphene [77], and monolayer MoS_2 [78]. In comparison with Si FETs, where impurities mainly originate from the residual metals ions and unsaturated Si bonds at the channel/dielectric interfaces, the sources of CIs in TMDCs include

gas molecules adsorbed during device fabrication, chemical residues, defects, and oxidation, the surface charge of the object, etc. To increase the carrier mobility, reducing the above sources of CI must be considered.

In the case of the same carrier concentration, the use of a high-κ dielectric layer such as HfO_2 can improve the electron mobility because of the dielectric screening effect on Coulomb scattering. Fischetti [78] established a CI scattering model and calculated the CI-limited mobility of single-layer MoS_2 at different temperatures and electron concentrations in high-κ (HfO_2) top-gate oxide structures. Since the screening depends on the temperature, the Coulomb impurity-limited mobility of a single layer of MoS_2 should be sensitive to the temperature. They also found that the introduction of high-κ oxidation would increase the mobility at room temperature by several times [79–81]. Subsequently, Yu et al. [65, 69] found through experiments and theoretical studies that high carrier concentration also acts as a screening effect for Coulomb impurities. As the concentration increased from 10^{12} to 10^{13} cm^{-2}, the mobility also increased.

However, the use of high-κ dielectrics will also bring the side effects on the room-temperature mobility due to SO phonon scattering in the polar dielectric, as we discussed in Sect. 3.2.2. In fact, the two competing factors deliver the contentious roles of the dielectric environment in improving or suppressing carrier mobility. For example, Liao et al. found a mobility degradation of 30–50% in top HfO_2 gated MoS_2 FET, as compared with back SiO_2 gated devices [82]. The observed mobility degradation is attributed to the strong SO phonon scattering in the high-κ dielectric. To address this controversy, Ma and Jena [83] performed a comparative study of the individual scattering mechanisms between SO phonon and CI scattering. When the average permittivity of the top and bottom dielectrics is smaller than 10, the mobility is improved. For the value is higher than 10, enhanced SO phonon scattering will determine the overall mobility. As shown in Fig. 10.12b, Yu et al. [65] systematically compared the performance of MoS_2 FET with a different gate dielectric, e.g., SiO_2, Al_2O_3, and HfO_2. They concluded that the screening of CI by high-κ dielectric is the dominant factor in the practical situation. When the CI density is reduced, SO phonon scattering will determine the highest mobility attainable at room temperature and low-κ dielectric will be preferable, such as SiO_2.

10.5.4 Scattering of Defects

Various kinds of structural defects such as vacancies and grain boundaries [84–88] are inevitably present in TMDCs by various methods (Fig. 10.13d). For example, MoS_2 samples grown by the CVD method have sulfur atom vacancy density up to $(1.2 \pm 0.4) \times 10^{13}$ cm^{-2}, i.e., 0.4%. These defects can result in highly localized band-to-band electronic states or tails that affect the electronic transport of TMDCs. A large number of theoretical calculations and experiments have been conducted on the effect of MoS_2 defects on the band structure and properties, such as the S atom vacancy in MoS_2 and their applications, e.g., in the petroleum industry to

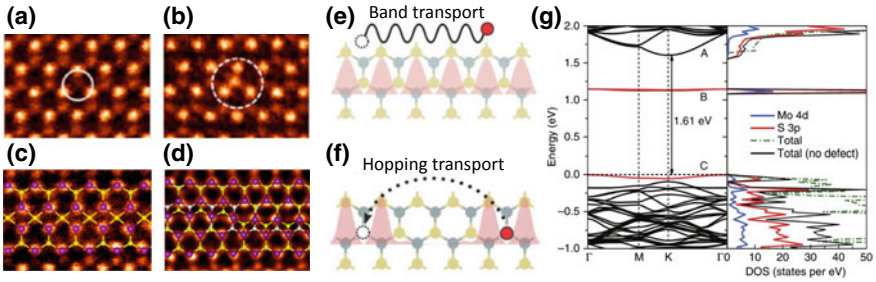

Fig. 10.15 Scanning transmission electron microscopy (STEM) images of S vacancy (**a**), MoS_2 antisite defect (**b**), grain boundaries (**c**, **d**) in monolayer MoS_2. Electron transport mechanism in perfect (**e**) and defective (**f**) MoS_2. **g** Band structure and partial density of states for monolayer MoS_2 [85]. Copyright 2013. Reproduced with permission from Nature

catalyze desulfurization [89, 90] and accelerate water decomposition [91, 92]. Qiu et al. [85] found that charge hopping transport at low carrier concentration through sulfur vacancy defects played an important role for the observed low mobility in monolayer MoS_2 (Fig. 10.15). In addition to sulfur atom defects, grain boundary defects are also widely present in the sample. van der Zande et al. [93] compared the mobility of mechanically exfoliated MoS_2 and CVD synthesized MoS_2 samples at room temperature and found that the performance of the device depends not only on the type of grain boundary, but also on the relative direction of current transport.

10.6 Summary and Outlook

In summary, as typical 2D materials, TMDCs possess excellent electrical properties, flexibility, and light transmission, and thus have broad application prospects in channel materials of FET devices. Currently, the research of TMDCs-based electronic devices mainly focuses on the mechanism of carrier transport and the improvement of transistor performance. In this chapter, we discuss the main scattering mechanisms that affect carrier transport and the methods to suppress scattering. The influence of metal–semiconductor contact on the performance of the devices is analyzed, as well as the current process methods to effectively reduce the contact resistance of TMDC.

2D semiconductor TMDC materials have shown advantages over traditional silicon materials in the field of electronic devices, such as the preparation of sub-10 nm channel devices [94–96], overcoming the short-channel effect of the incompatibility of silicon materials. Therefore, it still has enormous potential in nano-electronic devices field.

Future research will explore more exotic properties of TMDCs, e.g., superconductivity, spin-orbit coupling, toward the next-generation nanoelectronics. We believe that the technological impact of semiconducting TMDCs can likely be maximized.

Acknowledgements J.X.Y is supported by the National Natural Science Foundation of China (Grant No. 11704185) and the Natural Science Foundation of Jiangsu Province, China (Grant No. BK20171021). J.X.Y. and Z.X.S. gratefully acknowledge the Ministry of Education (MOE) for the following grants: AcRF Tier 1 (Reference No: RG103/16); AcRF Tier 2 (MOE2015-T2-1-148); AcRF Tier 3 (MOE2011-T3-1-005).

References

1. Mattheiss LF (1973) Band structures of transition-metal-dichalcogenide layer compounds. Phys Rev B 8:3719–3740
2. Wang QH, Kalantar-Zadeh K, Kis A, Coleman JN, Strano MS (2012) Electronics and optoelectronics of two-dimensional transition metal dichalcogenides. Nat Nanotechnol 7:699
3. Liu Y, Weiss NO, Duan X, Cheng HC, Huang Y, Duan X (2016) Van der Waals heterostructures and devices. Nat Rev Mater 1:16042
4. Jariwala D, Sangwan VK, Lauhon LJ, Marks TJ, Hersam MC (2014) Emerging device applications for semiconducting two-dimensional transition metal dichalcogenides. ACS Nano 8:1102–1120
5. Kaasbjerg K, Thygesen KS, Jacobsen KW (2012) Phonon-limited mobility in n-type single-layer MoS_2 from first principles. Phys Rev B 85:115317
6. Loher T, Tomm Y, Klein A, Su D, Pettenkofer C, Jaegermann W (1996) Highly oriented layers of the three-dimensional semiconductor CdTe on the two-dimensional layered semiconductors $MoTe_2$ and WSe_2. J Appl Phys 80:5718–5722
7. Tenne R, Galun E, Ennaoui A, Fiechter S, Ellmer K, Kunst M (1996) Characterization of oriented thin films of WSe_2 grown by van der Waals rheotaxy. Thin Solid Films 272:38–42
8. Podzorov V, Gershenson ME, Kloc C, Zeis R, Bucher E (2004) High-mobility field-effect transistors based on transition metal dichalcogenides. Appl Phys Lett 84:3301–3303
9. Novoselov KS, Jiang D, Schedin F, Booth TJ, Khotkevich VV, Morozov SV, Geim AK (2005) Two-dimensional atomic crystals. PNAS 102:10451–10453
10. Ayari A, Cobas E, Ogundadegbe O, Fuhrer MS (2007) Realization and electrical characterization of ultrathin crystals of layered transition-metal dichalcogenides. J Appl Phys 101:014507
11. Chen F, Xia J, Ferry DK, Tao N (2009) Dielectric screening enhanced performance in graphene FET. Nano Lett 9:2571–2574
12. Konar A, Fang T, Jena D (2010) Effect of high-κ gate dielectrics on charge transport in graphene-based field effect transistors. Phys Rev B 82:115452
13. Radisavljevic B, Radenovic A, Brivio J, Giacometti V, Kis A (2011) Single-layer MoS_2 transistors. Nat Nanotechnol 6:147–150
14. Liu H, Ye PD (2012) MoS_2 dual-gate MOSFET with atomic-layer-deposited Al_2O_3 as top-gate dielectric. IEEE Electron Device Lett 33:546–548
15. Liu H, Neal AT, Ye PD (2012) Channel length scaling of MoS_2 MOSFETs. ACS Nano 6:8563–8569
16. Kim S, Konar A, Hwang WS, Lee JH, Lee J, Yang J (2012) High-mobility and low-power thin-film transistors based on multilayer MoS_2 crystals. Nat Commun 3:1011
17. Xuming Z, Chun-Wei H, Lifeng W, Long-Jing Y, Wenqing L, Jingli W (2016) Dielectric engineering of a boron nitride/hafnium oxide heterostructure for high-performance 2D field effect transistors. Adv Mater 28:2062–2069
18. Schwierz F (2010) Graphene transistors. Nat Nanotechnol 5:487
19. Desai SB, Madhvapathy SR, Sachid AB, Llinas JP, Wang Q, Ahn GH (2016) MoS_2 transistors with 1-nanometer gate lengths. Science 354:99–102
20. Li SL, Wakabayashi K, Xu Y, Nakaharai S, Komatsu K, Li WW (2013) Thickness-dependent interfacial coulomb scattering in atomically thin field-effect transistors. Nano Lett 13:3546–3552

21. Das S, Chen HY, Penumatcha AV, Appenzeller J (2013) High performance multilayer MoS_2 transistors with scandium contacts. Nano Lett 13:100–105
22. Ming-Wei L, Ivan IK, Jason F, Xufan L, Alexander AP, Christopher MR (2016) Thickness-dependent charge transport in few-layer MoS_2 field-effect transistors. Nanotechnology 27:165203
23. Chen MC, Lin CY, Kai-Hsin L, Li LJ, Chen CH, Cheng-Hao C et al (2014) Hybrid Si/TMD 2D electronic double channels fabricated using solid CVD few-layer-MoS_2 stacking for Vth matching and CMOS-compatible 3DFETs. In: IEEE international electron devices meeting, pp 33.5.1–33.5.4
24. Kai-Shing L, Bo-Wei W, Lain-Jong L, Ming-Yang L, Chia-Chin Kevin C, Cho-Lun H et al (2016) MoS_2 U-shape MOSFET with 10 nm channel length and poly-Si source/drain serving as seed for full wafer CVD MoS_2 availability. In: IEEE symposium on VLSI technology, pp 1–2
25. Li X, Mullen JT, Jin Z, Borysenko KM, Buongiorno Nardelli M, Kim KW (2013) Intrinsic electrical transport properties of monolayer silicene and MoS_2 from first principles. Phys Rev B 87:115418
26. Yoon Y, Ganapathi K, Salahuddin S (2011) How good can monolayer MoS_2 Transistors be? Nano Lett 11:3768–3773
27. Liu H, Si M, Najmaei S, Neal AT, Du Y, Ajayan PM, Lou J, Ye PD (2013) Statistical study of deep submicron dual-gated field-effect transistors on monolayer chemical vapor deposition molybdenum disulfide films. Nano Lett 13:2640–2646
28. Popov I, Seifert G, Tomanek D (2012) Designing electrical contacts to MoS_2 monolayers: a computational study. Phys Rev Lett 108:156802
29. Li SL, Tsukagoshi K (2015) Carrier injection and scattering in atomically thin chalcogenides. J Phys Soc Jpn 84:121011
30. Walia S, Balendhran S, Wang Y, Kadir RA, Zoolfakar AS, Atkin P, Ou JZ, Sriram S, Kalantar-zadeh K, Bhaskaran M (2013) Characterization of metal contacts for two-dimensional MoS_2 nanoflakes. Appl Phys Lett 103:232105
31. Liu W, Kang J, Sarkar D, Khatami Y, Jena D, Banerjee K (2013) Role of metal contacts in designing high-performance monolayer n-type WSe_2 field effect transistors. Nano Lett 12:1983–1990
32. Li SL, Komatsu K, Nakaharai S, Lin YF, Yamamoto M, Duan X, Tsukagoshi K (2014) Thickness scaling effect on interfacial barrier and electrical contact to two-dimensional MoS_2 layers. ACS Nano 8:12836–12842
33. Kang J, Sarkar D, Liu W, Jena D, Banerjee K (2012) A computational study of metal-contacts to beyond-graphene 2D semiconductor materials. In: International electron devices meeting, pp 407–410
34. Kang J, Liu W, Sarkar D, Jena D, Banerjee K (2014) Computational study of metal contacts to monolayer transition-metal dichalcogenide semiconductors. Phys Rev X 4:031005
35. Liu W, Sarkar D, Kang J, Cao W, Banerjee K (2015) Impact of contact on the operation and performance of back-gated monolayer MoS_2 field-effect-transistors. ACS Nano 9:7904–7912
36. Kang J, Liu W, Banerjee K (2014) High-performance MoS_2 transistors with low-resistance molybdenum contacts. Appl Phys Lett 104:093106
37. Fang H, Chuang S, Chang TC, Takei K, Takahashi T, Javey A (2012) High-performance single layered WSe_2 p-FETs with chemically doped contacts. Nano Lett 12:3788–3792
38. Fang H, Tosun M, Seol G, Chang TC, Takei K, Guo J, Javey A (2013) Degenerate n-doping of few-layer transition metal dichalcogenides by potassium. Nano Lett 13:1991–1995
39. Du Y, Liu H, Neal AT, Si M, Ye PD (2013) Molecular doping of multilayer MoS_2 field-effect transistors: reduction in sheet and contact resistances. IEEE Electron Device Lett 34:1328–1330
40. Zhao P, Kiriya D, Azcatl A, Zhang C, Tosun M, Liu YS (2014) Air stable p-doping of WSe_2 by covalent functionalization. ACS Nano 8:10808–10814
41. Kiriya D, Tosun M, Zhao P, Kang JS, Javey A (2014) Air-stable surface charge transfer doping of MoS_2 by benzyl viologen. J Am Chem Soc 136:7853–7856
42. Yang L, Majumdar K, Liu H, Du Y, Wu H, Hatzistergos M (2014) Chloride molecular doping technique on 2D materials: WS_2 and MoS_2. Nano Lett 14:6275–6280

43. Chen JR, Odenthal PM, Swartz AG, Floyd GC, Wen H, Luo KY, Kawakami RK (2013) Control of Schottky barriers in single layer MoS_2 transistors with ferromagnetic contacts. Nano Lett 13:3106–3110
44. Dankert A, Langouche L, Kamalakar MV, Dash SP (2014) High-performance molybdenum disulfide field-effect transistors with spin tunnel contacts. ACS Nano 8:476–482
45. Rai A, Valsaraj A, Movva HCP, Roy A, Ghosh R, Sonde S (2015) Air stable doping and intrinsic mobility enhancement in monolayer molybdenum disulfide by amorphous titanium suboxide encapsulation. Nano Lett 15:4329–4336
46. McClellan CJ, Yalon E, Smithe KKH, Suryavanshi SV, Pop E (2017) Effective n-type doping of monolayer MoS_2 by AlO_x. In: 75th Annual device research conference (DRC), pp 1–2
47. Liu Y, Wu H, Cheng HC, Yang S, Zhu E, He Q (2015) Toward barrier free contact to molybdenum disulfide using graphene electrodes. Nano Lett 15:3030–3034
48. Leong WS, Luo X, Li Y, Khoo KH, Quek SY, Thong JTL (2015) Low resistance metal contacts to MoS_2 devices with nickel-etched-graphene electrodes. ACS Nano 9:869–877
49. Stokbro K, Engelund M, Blom A (2012) Atomic-scale model for the contact resistance of the nickel-graphene interface. Phys Rev B 85:165442
50. Dean CR, Young AF, Meric I, Lee C, Wang L, Sorgenfrei S (2010) Boron nitride substrates for high-quality graphene electronics. Nat Nanotechnol 5:722–726
51. Lee GH, Cui X, Kim YD, Arefe G, Zhang X, Lee CH (2015) Highly stable, dual-gated MoS_2 transistors encapsulated by hexagonal boron nitride with gate-controllable contact, resistance, and threshold voltage. ACS Nano 9:7019–7026
52. Eda G, Yamaguchi H, Voiry D, Fujita T, Chen M, Chhowalla M (2011) Photoluminescence from chemically exfoliated MoS_2. Nano Lett 11:5111–5116
53. Wypych F, Schöllhorn R (1992) 1T-MoS_2, a new metallic modification of molybdenum disulfide. Chem Commun 0:1386–1388
54. Kappera R, Voiry D, Yalcin SE, Branch B, Gupta G, Mohite AD, Chhowalla M (2014) Phase-engineered low-resistance contacts for ultrathin MoS_2 transistors. Nat Mat 13:1128–1134
55. Kappera R, Voiry D, Yalcin SE, Jen W, Acerce M, Torrel S (2014) Metallic 1T phase source/drain electrodes for field effect transistors from chemical vapor deposited MoS_2. APL Mater 2:092516
56. Zhu J, Wang Z, Yu H, Li N, Zhang J, Meng J (2017) Argon plasma induced phase transition in monolayer MoS_2. J Am Chem Soc 139:10216–10219
57. Lin L, Robertson J, Clark SJ (2011) Shifting Schottky barrier heights with ultra-thin dielectric layers. Microelectronic Eng 88:1461–1463
58. Tomonori N, Koji K, Akira T (2008) A significant shift of Schottky barrier heights at strongly pinned metal/germanium interface by inserting an ultra-thin insulating film. Appl Phys Exp 1:051406
59. Hu J, Saraswat KC, Wong HSP (2010) Metal/III-V Schottky barrier height tuning for the design of nonalloyed III-V field-effect transistor source/drain contacts. J Appl Phys 107:063712
60. Hu J, Nainani A, Sun Y, Saraswat KC, Philip Wong HS (2011) Impact of fixed charge on metal-insulator-semiconductor barrier height reduction. Appl Phys Lett 99:252104
61. Lee S, Tang A, Aloni S, Philip Wong HS (2016) Statistical study on the Schottky barrier reduction of tunneling contacts to CVD synthesized MoS_2. Nano Lett 16:276–281
62. Jingli W, Qian Y, Chun-Wei H, Xuming Z, Lei L, Shanshan C (2016) High mobility MoS_2 transistor with low Schottky barrier contact by using atomic thick h-BN as a tunneling layer. Adv Mater 28:8302–8308
63. Cui X, Shih EM, Jauregui LA, Chae SH, Kim YD, Li B et al (2017) Low-temperature ohmic contact to monolayer MoS_2 by van der waals bonded Co/*h*-BN electrodes. Nano Lett 17:4781–4786
64. Zhang W, Huang Z, Zhang W, Li Y (2014) Two-dimensional semiconductors with possible high room temperature mobility. Nano Res 7:1731–1737
65. Yu Z, Ong ZY, Pan Y, Cui Y, Xin R, Shi Y (2015) Realization of room-temperature phonon-limited carrier transport in monolayer MoS_2 by dielectric and carrier screening. Adv Mater 28:547–552

66. Cui Y, Xin R, Yu Z, Pan Y, Ong ZY, Wei X et al (2015) High-performance monolayer WS_2 field-effect transistors on high-κ dielectrics. Adv Mater 27:5230–5234
67. Li ZL, Tsukagoshi K, Orgiu E, Samori P (2016) Charge transport and mobility engineering in two-dimensional transition metal chalcogenide semiconductors. Chem Soc Rev 45:118–151
68. Salvatore GA, Münzenrieder N, Barraud C, Petti L, Zysset C, Büthe L et al (2013) Fabrication and transfer of flexible few-layers MoS_2 thin film transistors to any arbitrary substrate. ACS Nano 7:8809–8815
69. Zhihao Y, Zhun-Yong O, Songlin L, Jian-Bin X, Gang Z, Yong-Wei Z, Yi S, Xinran W (2014) Analyzing the carrier mobility in transition-metal dichalcogenide MoS_2 field-effect transistors. Adv Funct Mater 27:1604093
70. Moore BT, Ferry DK (1980) Remote polar phonon scattering in si inversion layers. J Appl Phys 51:2603–2605
71. Fischetti MV, Neumayer DA, Cartier EA (2001) Effective electron mobility in Si inversion layers in metal–oxide–semiconductor systems with a high-κ insulator: the role of remote phonon scattering. J Appl Phys 90:4587–4608
72. Veres J, Ogier SD, Leeming SW, Cupertino DC, Mohialdin Khaffaf S (2003) Low-k insulators as the choice of dielectrics in organic field-effect transistors. Adv Funct Mater 13:199–204
73. Hulea IN, Fratini S, Xie H, Mulder CL, Iossad NN, Rastelli G, Ciuchi S, Morpurgo AF (2006) Tunable Frohlich polarons in organic single-crystal transistors. Nat Mater 5:982–986
74. Chen JH, Jang C, Xiao S, Ishigami M, Fuhrer MS (2008) Intrinsic and extrinsic performance limits of graphene devices on SiO_2. Nat Nanotechnol 3:206–209
75. DaSilva AM, Zou K, Jain JK, Zhu J (2010) Mechanism for current saturation and energy dissipation in graphene transistors. Phys Rev Lett 104:236601
76. Ando T, Fowler AB, Stern F (1982) Electronic properties of two-dimensional systems. Rev Mod Phys 54:437–672
77. Das Sarma S, Adam S, Hwang EH, Rossi E (2011) Electronic transport in two-dimensional graphene. Rev Mod Phys 83:407–470
78. Ong ZY, Fischetti MV (2013) Mobility enhancement and temperature dependence in top-gated single-layer MoS_2. Phys Rev B 88:165316
79. Radisavljevic B, Kis A (2013) Mobility engineering and a metal–insulator transition in monolayer MoS_2. Nat Mater 12:815–820
80. Ghatak S, Pal AN, Ghosh A (2011) Nature of electronic states in atomically thin MoS_2 field-effect transistors. ACS Nano 5:7707–7712
81. Amani M, Chin ML, Birdwell AG, O'Regan TP, Najmaei S, Liu Z et al (2013) Electrical performance of monolayer MoS_2 field-effect transistors prepared by chemical vapor deposition. Appl Phys Lett 102:193107
82. Jingli W, Songlin L, Xuming Z, Johnny H, Lei L, Xiangheng X, Changzhong J, Weida H, Jianlu W, Jinchai L (2015) Integration of high-k oxide on MoS_2 by using ozone pretreatment for high-performance MoS_2 top-gated transistor with thickness-dependent carrier scattering investigation. Small 11:5932–5938
83. Ma N, Jena D (2014) Charge scattering and mobility in atomically thin semiconductors. Phys Rev X 4:011043
84. Yu Z, Pan Y, Shen Y, Wang Z, Ong ZY, Xu T (2014) Towards intrinsic charge transport in monolayer molybdenum disulfide by defect and interface engineering. Nat Commun 5:5290
85. Qiu H, Xu T, Wang Z, Ren W, Nan H, Ni Z (2013) Hopping transport through defect-induced localized states in molybdenum disulphide. Nat Commun 4:2642
86. Fuhr JD, Saul A, Sofo JO (2004) Scanning tunneling microscopy chemical signature of point defects on the MoS_2 (0001) surface. Phys Rev Lett 92:026802
87. Lu CP, Li G, Mao J, Wang LM, Andrei EY (2014) Bandgap, mid-gap states, and gating effects in MoS_2. Nano Lett 14:4628–4633
88. Zhou W, Zou X, Najmaei S, Liu Z, Shi Y, Kong J et al (2013) Intrinsic structural defects in monolayer molybdenum disulfide. Nano Lett 13:2615–2622
89. Moses PG, Hinnemann B, Topsøe H, Norskov JK (2007) The hydrogenation and direct desulfurization reaction pathway in thiophene hydrodesulfurization over MoS_2 catalysts at realistic conditions: a density functional study. J Catal 248:188–203

90. Paul JF, Payen E (2003) Vacancy formation on MoS_2 hydrodesulfurization catalyst: DFT study of the mechanism. J Phys Chem B 107:4057–4064
91. Voiry D, Yamaguchi H, Li J, Silva R, Alves DCB, Fujita T et al (2013) Enhanced catalytic activity in strained chemically exfoliated WS_2 nanosheets for hydrogen evolution. Nat Mater 12:850–855
92. Karunadasa HI, Montalvo E, Sun Y, Majda M, Long JR, Chang CJ (2012) A molecular MoS_2 edge site mimic for catalytic hydrogen generation. Science 335:698–702
93. van der Zande AM, Huang PY, Chenet DA, Berkelbach TC, You Y, Lee GH et al (2013) Grains and grain boundaries in highly crystalline monolayer molybdenum disulphide. Nat Mater 12:554–561
94. Xu K, Chen D, Yang F, Wang Z, Yin L, Wang F et al (2017) Sub-10 nm nanopattern architecture for 2D material field-effect transistors. Nano Lett 17:1065–1070
95. Nourbakhsh A, Zubair A, Sajjad RN, Tavakkoli A, Chen KGW, Fang S et al (2016) MoS_2 field-effect transistor with sub-10 nm channel length. Nano Lett 16:7798–7806
96. Li X, Mengzhou L, Shuopei W, Hua Y, Luojun D, Jian T et al (2017) Graphene-contacted ultrashort channel monolayer MoS_2 transistors. Adv Mater 29:1702522